Book of Abstracts and Proceedings of Second International Congress on Trends and Advances in Global Research and Applications



TAGRA 2025

13 - 14 December, 2025
Erzurum, Türkiye

Powered by

Book of Abstracts and Proceedings of

2nd International Congress on Trends and Advances in Global Research and Applications (TAGRA 2025)

13 - 14 December, 2025
Erzurum, Türkiye

Edited by
Muhammet Kaan YEŞİLYURT

ISBN:

978-605-73167-5-2

Publishing

TAGRA 2025 was organized in partnership with Congreteria, Syntagra, and High Technology Community of Ataturk University

hosted by

Atatürk University
Vocational School of Technical Sciences

and sponsored by Atatürk University, and DEGZ Robotics

Atatürk University

degz

BOOK OF ABSTRACTS AND PROCEEDINGS
OF

2ND INTERNATIONAL CONGRESS ON TRENDS AND ADVANCES IN GLOBAL RESEARCH AND APPLICATIONS

(TAGRA 2025)

13-14 DECEMBER 2025, ERZURUM, TÜRKİYE

Edited by
Muhammet Kaan YEŞİLYURT

Redacted by Hilal Kübra SAĞLAM
Reviewed by Hayrunnisa NADAROĞLU

Published, 2025 – ACA Publishing https://www.acapublishing.com/
ISBN: 978-605-73167-5-2

This work is subject to copyright. All rights are reserved, whether the whole or part of the material is concerned. Nothing from this publication may be translated, reproduced, stored in a computerized system, or published in any form or in any manner, including, but not limited to electronic, mechanical, reprographic, or photographic, without prior written permission from the publisher, except in the cases of brief quotations embodied in critical reviews and certain other noncommercial uses permissible by copyright law.

The book is not intended for commercial profit. The individual contributions in this publication and any liabilities arising from them remain the responsibility of the authors. It is the responsibility of the author to abide by the publishing ethics rules. The publisher is not responsible for possible damages, which could be a result of content derived from this publication.

https://congreteria.com/e/tagra2025
info@syntagra.com

CONTENTS

BOARDS 16
FOREWORD 19
Message from the Organizing Committee 20
Congress at a Glance 21
Chair's Opening Speech 22
CONGRESS PROGRAM 24
Sat, December 13 25
Sun, December 14 38
KEYNOTE SPEAKERS 52
Ahmad Ali 53
Faiz Arith 54
Zainab Yunusa 55
Prathap Singh S 56
Hamed Niroumand 57
Dr. Md. Habibur Rahman 58
Dalmo S. Amorim Jr. 59
Ismayadi Ismail 60
Peyil Esengul Kyzy 61
CONTRIBUTIONS 62
1. ABSTRACTS 63
1.1. KEYNOTE SPEECHES 64
Prevention and Mitigation Strategies for Sinkholes Using Soil Improvement Techniques 65
Graphenated Carbon Nanotubes: Bridging 1D–2D–3D Carbon for Advanced Functional Systems 66
AI and Bioinformatics Synergy: Transforming Data Into Precision Healthcare 67
Applications of Carbon Based Nanomaterials in Microwave Devices 68
Fabrication and Characterization of Functionally Graded A356 Alloy and Its Composite 69
A Shift Toward Simplicity: Current Progress, Technical Challenges, and Future Prospects of ETL-Free Perovskite Solar Cells 70
Unim-R Polyherbal Oil: Efficacy and Safety Assessment in Carrageenan and CFA-Induced Arthritis with Cytokine Profiling 71
Asymptotic Solution of Singular Perturbed Volterra-Type Integral Equations 72
1.2. ATTENDED POSTER PRESENTATIONS 73
Production of Low-Fat Mayonnaise Using Pomegranate Peel Powder and Evaluation of Its Physicochemical and Sensory Properties 74
QSPR Study on Photo Oxidation Reaction of Aromatic Micro Pollutants Using the Genetic Algorithm - Support Vector Machine 75
1.3. ORAL PRESENTATIONS 76
Comparison of Fabricated TiO2 Gas Sensor with MQ135 for Spoiled Fruit Detection 77
Preparation of WO3-X Nanoparticles by UVA-Irradiation for Colorimetric Sensing of Cr(VI) 78
Tetrachloroperylene Dianhydride as a Simple and Capable Sensor; Case Study: Cyanide Anion and

Primary Aliphatic Amines 79
Nitrogen-Doped Carbon Quantum Dots for Sensitive Colorimetric Assay of V(V) 80
Solution of Second Order Singular Perturbation Problem Using Cubic B-Spline Functions 81
Numerical Solution of Singularly Perturbed Differential Equations Using Interpolation and Collocation 82
Comparative Morphology of the Spleen in Mammals, Birds, and Amphibians (Frogs) 83
Enhanced Salinity Detection Using Zinc Oxide Nanorod Coated Tapered D-Shape Plastic Optical Fibers 84
Development of a Sensor Array (MQ2, MQ4 and MICS5524) for Methane Gas Detection with IOT-based Monitoring 85
Methane Detection from Food Waste Digestion Using Titanium Dioxide-Graphene Gas Sensor with IOT Integration 86
Gross and Micromorphological Evaluation of Yak (Bos Grunnies) Hindlimb Muscle Under Refrigeration and Freezing Conditions 87
Energy Efficiency-Focused Entropy Analysis: Investigation of Nanofluid Heat Transfer Processes 88
Numerical Analysis of Heat Transfer in Laminar Flow with Star-Cross Section Channel and Central and Circular Pipes 89
Fluorescence Spectroscopy in the Study of Animal Meats 90
Electrospun Carbon-Based Nanofibers for Advanced Material Applications 91
Graphene/Cellulose Nanocomposite Accelerate Oral Wound Healing in Diabetic Rats by Mitigating Oxidative Stress and Apoptosis in Gingival Fibroblasts. 92
Comparison of Metal-Oxide Semiconductor Sensors for Ethanol Detection at Room Temperature 93
Study of Elemental (Micro- and Macro-) Nutrient Content in Dracocephalum ıMberbe Bunge from the Alai Range, Kyrgyzstan 94
Comparative Effects of Cold Plasma and Microwave Pretreatments on Bioactive Compounds in Hydroalcoholic Quince Leaf Extracts 95
Investigation of the Cellular Effects of Infrared Electromagnetic Waves and Carbon Nanotubes on HT29 Cell Line 96
Cellular Toxicity of Laser, Iron Oxide and Manganese Oxide Nanoparticles on the Viability of Breast Cancer Cells Line 97
Structural Analysis of La-Doped MoO_3 Hole Transport Layers and Their Correlation with Perovskite Solar Cell Performance 98
Integrated Geophysical, Geochemical and Hydrogeological Methods to Investigation of Groundwater Contamination: A Case Study of Osubi, and its Environ Southern Nigeria 99
Integrated Electrical Resistivity Investigation of Subsurface Peat and Clay Deposits in Orile Whitesand, Orile–Iganmu, Lagos, Southwestern Nigeria 100
Improving the Pharmacological Properties of Curcumin by Nanoclay 101
An Evaluation of Optimum Inclination Angle for Fixed-angle Solar Panel Installations in Erzurum Province 102
Unraveling the Mechanism of TiCN Film-Coated NiTi Substrate Toxicity: Evidence of Mitochondrial Electron Transport Dysfunction in Gingival Cells from Diabetic Rats 103
Functional Nanoparticle Incorporated Bioprinted Scaffolds 104
Mechanistic Insights Into Tissue Regeneration Using Carbon-Based Nanoparticles in 3d Bioprnting 105

Fe-Pt Nanoparticles: Synthesis and Characterization 106

Product Innovation and Processing Technologies for Agroforestry Food Products.....107

Non-Invasive Marine Monitoring with Baited Remote Underwater Video (BRUV) Systems: Capabilities, Limitations, and Regional Opportunities.....108

Preserving Genetic Diversity: Why Türkiye Needs a National GenBank.....109

Chemical Composition, Physico-Chemical Properties and Amino Acid Profile of Muffins Enriched with Cricket Powder (*Acheta Domesticus*).....110

Innovative Pathways for Circular Economy: Repurposing Coal Mine Waste in Construction Materials 111

An Integrated Web-Based System for Managing MEDEK, MÜDEK, and YÖKAK Accreditation Processes 112

Network Pharmacology and Machine Learning-Driven Virtual Screening with Dynamics Simulations of Natural Compounds for Glioblastoma 113

Use of Nanoparticles for Drilling Fluid in Petroleum Industry.....114

Towards High-Efficiency $CsPbI_3$ Perovskite Solar Cells: A Computational Pathway to Material and Device Optimization, ...115

Evaluation of the Sensitivity and Specificity of the Diagnostic Electrochemical Biosensor Using MicroRNAs Biomarkers Involved in Multiple Sclerosis 116

Influence of Low-Temperature Annealing on Copper Iodide as Hole Transporting Layer for Perovskite Solar Cell Applications 117

Integrated Geophysical and Hydrochemical Assessment of Groundwater Contamination and Aquifer Vulnerability in the Ifewara Area, Southwestern Nigeria 118

Development of AI-Machine Learning with the One Health Framework in the Prevention of Foodborne Disease in the “Program Makanan Bergizi Gratis Indonesia” 119

Sustainable Nanomaterial Production: Carbon Quantum Dots Synthesized from Biological Waste.....120

Optical and Biological Properties of Carbon Quantum Dots Synthesized from Daucus Carota Ssp. Sativus Var. Atrorubens Extract.....121

Synthesis and Characterization of Ni-Doped ZnO Nanorods for Potential Use in Solar Cells 122

Zinc Oxide Nanostructure Buffer Layers for Improved Charge Transport and Efficiency in DSSC..123

Traditional Arts and Mathematics.....124

Effect of Temperature on the Structural and Thermal Properties of Perna Viridis Shells 125

Classification of Biomaterials and Their Biomedical Applications.....126

Demand Prediction in Textile Production: A Machine Learning-Based Approach 127

Alternative Wing Designs for UAVs 128

Examination of the Effect of Genistein on CD36 Lipid Receptor and Lipid Profile in Liver Cancer Cell Line.....129

Purification of Exopolysaccharides from Thermophilic Bacillus licheniformis SO2 Strain by Three-Phase Separation (TPP) System and Determination of Their in Vitro Biological Activities.....130

Risk Assessment of Occupational Hazards in Asphalt Production Plants Using the Fine-Kinney Method 131

Bioprinted Scaffolds Incorporated by Functional Nanoparticles.....132

Harnessing Interface Engineering to Unlock Performance in Lead-Free, ETL-Free Perovskite Solar Cells:

a SCAPS-1D Defect Tolerance Study 133

The Impact of Multi-Tagger Consistency on Semi-Supervised Natural Language Processing Models: A Bert-Based Tagging Approach 134

2. FULL-TEXT PAPERS 135

2.1. KEYNOTE SPEECHES 136

Modelling Economic Variables in Offshore Oilwell Drilling 137

Keywords 137
Abstract 137
1. Introduction 137
2. Literature review 137
3. Methodology 138
4. Case Study 141
5. Results 144
6. Conclusion 145
References 145

2.2. ATTENDED POSTER PRESENTATIONS 147

Copper-Based Metal-Organic Framework Cu(BDC) as a Reusable Heterogeneous Catalyst for Efficient *N*-Arylation of NH-Heterocycles 148

Keywords 148
Abstract 148
1. Introduction 148
2. Materials and Methods 148
3. Results and Discussion 149
4. Conclusion 150
References 150

2.3. ORAL PRESENTATIONS 151

Design and Manufacture of PLC Controlled Laboratory Wear Device for in Vitro Biomedical Applications 152

Keywords 152
Abstract 152
1. Introduction 152
2. Materials and Methods 153
3. Results and Discussion 154
4. Conclusion 154
References 155

Investigation Contact- and Contact-Free Wear Resistance of Titanium for Biomedical Applications: Correlation with Wear Depth and Volume Loss 156

Keywords 156
Abstract 156
1. Introduction 156
2. Materials and Methods 156
3. Results and Discussion 157
4. Conclusion 158
References 158

Effect of Sliding Wear Mechanism of Titanium Biomaterials: 3D Finite Element Analysis 160

Keywords 160

Abstract 160
1. Introduction 160
2. Materials and Methods 161
3. Results and Discussion 161
4. Conclusion 163
References 163

Electrochemical Synthesis of CoBi2O4 Nanostructures 164

Keywords 164
Abstract 164
1. Introduction 164
2. Materials and Methods 164
3. Results and Discussion 165
4. Conclusion 165
Acknowledgments 166
References 166

Removal of Heavy Metals in Ice Tea Beverages Using Electrochemically Synthesized Glutathione Modified Electrodes 167

Keywords 167
Abstract 167
1. Introduction 167
2. Results and Evaluatıon 168
3. General Evaluation and Conclusion 169
References 169

Efficient *N*-Arylation of *NH*-Heterocycles Catalyzed by the Copper-Based Metal-Organic Framework Cu(BDC): A Reusable Heterogeneous Catalyst 170

Keywords 170
Abstract 170
1. Introduction 170
2. Materials and Methods 170
3. Results and Discussion 171
4. Conclusion 172
References 173

Application of Dynamic Light Scattering Method in Nanofluids 174

Keywords 174
Abstract 174
1. Introduction 174
.2 Application of DLS 179
3. Conclusion 181
References 181

The Effect of Fractal Phenomena on the Thermal Conductivity of Nanofluids 182

Keywords 182
Abstract 182
1. Introduction 182
2. Materials and methods 184
3. Results and Discussion 187
4. Conclusion 187
References 188

Design and Thermodynamic Analysis of a Geothermal-Based Tri-Generation System for Simultaneous Production of Power, Fresh Water, and Domestic Hot Water....189

Keywords....189
Abstract....189
1. Introduction....189
2. System Description....190
3. Thermodynamic Modeling of the Proposed System....191
4. Results and Discussion....195
5. Conclusion....200
References....200

Effect of Using a Vertical Heat Exchanger on Performance in a Vapor Compression Heat Pump Using R417a Gas as an Alternative to R22....202

Keywords....202
Abstract....202
1. Introduction....202
2. Experimental Studies....202
3. Results and Discussion....204
4. Conclusion....205
References....205

Cauliflower Disease Classification Using Vision Transformer Architecture....206

Keywords....206
Abstract....206
1. Introduction....206
2. Materials and Methods....206
3. Results and Discussion....207
4. Conclusion....208
References....208

Experimental and Numerical Investigation of the Thermo-Hydraulic Performance of Mini-Channel Graphite Foam and Aluminum Heat Sinks....209

Keywords....209
Abstract....209
1. Introduction....209
2. Numerical Analysis....210
3. Results and Discussion....213
4. Conclusions....214
References....214

Performance Assessment of Thermoelectric Cooling Applied to Photovoltaic Panels....216

Keywords....216
Abstract....216
1. Introduction....216
2. Materials and Methods....216
3. Results and Discussion....217
4. Conclusion....219
References....219

Investigation of Erzurum Ilıca District Liquefaction Potential With Different Methods....220

Keywords....220
Abstract....220

1. Introduction....220
2. Materials and Methods....221
3. Results and Discussion....221
4. Conclusion....226
References....227

Hydrogeochemistry, Petrography, and Groundwater Quality in the Waru–Apo Area (Abuja FCT, Nigeria)....228

Keywords....228
Abstract....228
1. Introduction....228
2. Materials and Methods:....229
3. Results and Discussion:....229
References....233

Oxidation Mechanism in Vegetable Oils and Methods for Enhancing Oxidative Stability....235

Keywords....235
Abstract....235
1. Introduction....235
2. Research and Findings....236
3. Materials and Methods....237
4. Conclusion and Discussion....237
References....238

Optical Properties of a Novel Pyrazoline Derivative in Diverse Micelle Systems....239

Keywords....239
Abstract....239
1. Introduction....239
2. Materials and Methods....240
3. Results and Discussion....241
4. Conclusion....244
References....244

Therapeutic Effect of the SN-38–Fe2O3 Nanoparticle Combination Targeting Dopamine Receptors in Colorectal Cancer Cells....245

Keywords....245
Abstract....245
1. Introduction....245
2. Materials and Methods....246
3. Results and Discussion....246
4. Conclusion....249
References....249

Therapeutic Potential of Ginseng Against Cancer Exosome–Induced Toxicity in Neuronal and Endothelial Cells....250

Keywords....250
Abstract....250
1. Introduction....250
2. Materials and Methods....251
3. Results and Discussion....252
4. Conclusion....254
References....255

Perceptions of Artificial Intelligence in Türkiye: A Descriptive Analysis of TGSS Data 256
Keywords 256
Abstract 256
1. Introduction 256
2. Materials and Methods 257
3. Findings 261
4. Differences in Perception of Artificial Intelligence by Region 268
5. Conclusion and Recommendations 271
Future Research 272
References 272

Analysis of the RL Circuit Using the Physics-Informed Neural Network (PINN) Method 274
Keywords 274
Abstract 274
1. Introduction 274
2. Mathematical Model and Analytical Solution of the RL Circuit 275
3. Physics-Informed Neural Networks 275
4. Method 275
5. Result 276
6. Conclusion 277
Future Work 278
References 278

The Impact of Amorphous Boron Waste on the Long-Term Mechanical Properties of Steel Fiber-Reinforced 279
Keywords 279
Abstract 279
1. Introduction 279
2. Materials and Methods 280
3. Results and Discussion 282
4. Conclusion 283
References 283

The Critical Role of Rare Elements in Renewable Energy Systems and Türkiye 284
Keywords 284
Abstract 284
1. Introduction 284
2. Materials and Methods 285
3. Results and Discussion 289
4. Türkiye’s Position and Strategic Approach 290
5. Conclusion 291
References 291

Eco-Friendly Synthesis of Carbon Quantum Dots (CQDs) and Their Use in the Detection of Mycotoxins 293
Keywords 293
Abstract 293
1. Introduction 293
2. Results 295
3. Conclusion 295
Acknowledgements 295
References 295

Nature-Based Healing Approach: Horticultural Therapy Gardens 297
Keywords 297
Abstract 297
1. Introduction 297
2. Materials and Methods 298
3. Results 298
4. Conclusion 300
References 300
Urban Water Management Approaches for Resilient Cities 301
Keywords 301
Abstract 301
1. Introduction 301
2. Materials and Methods 303
3. Conclusion 304
References 305
Synthesis and Bioactivities of Zinc Oxide (ZnO) Nanoparticles 306
Keywords 306
Abstract 306
1. Introduction 306
2. Results and Discussion 307
3. Conclusion 308
References 308
Use of Metal Oxide Nanoparticles in the Food Industry: Toxicological Risks and Effects on Child Nutrition 310
Keywords 310
Abstract 310
1. Introduction 310
2. Nano-encapsulation Applications 312
3. Effects on Microbiota 313
4. Discussion 314
5. Conclusion 315
References 315
Occupational Health and Safety Practices in the Solar Energy Sector 316
Keywords 316
Abstract 316
1. Introduction 316
2. Materials and Methods 317
3. Results and Discussion 320
4. Conclusion 321
References 322
Advances in Albumin-Based Nanocarriers: Novel Engineering Strategies and Functional Enhancements 323
Keywords 323
Abstract 323
1. Introduction 323
2. Surface-Functionalized Albumin Nanoparticles for Targeted Delivery 324
3. Stimuli-Responsive Albumin Nanocarriers 324

4. Conclusion 325
References 325

A Two-Stage Evaluation Model Based on LBWA for Evaluating KOSGEB Entrepreneurship Support Projects 326

Keywords 326
Abstract 326
1. Introduction 326
2. Materials and Methods 327
3. Results and Discussion 328
4. Conclusion 331
References 331

Data-Driven Quality Control in Iron and Steel Production: Evaluating the Impact of Carbon Content and Process Parameters Using Machine Learning 333

Keywords 333
Abstract 333
1. Introduction 333
2. Materials and Methods 335
3. Experimental Setup and Results 338
4. Conclusion 341
References 341

New Approaches to Microneedle Technology and Alzheimer's Vaccine Applications 342

Keywords 342
Abstract 342
1. Introduction 342
2. The Basic Structure and Types of Microneedle Technology 343
3. Advantages of Microneedles in Vaccine Applications 343
4. Alzheimer’s Vaccines: Current Status and Approaches 344
5. Conclusion 344
Acknowledgments 344
References 344

The Study and Methodological Support for the Development of Natural Science Competencies in 5th-Grade Students of Secondary School No. 117 Named After Ch. Aitmatov in Bishkek 346

Keywords 346
Abstract 346
1. Relevance of the Study 346
2. Research Methods and Materials 347
3. Results and Discussion 347
4. Conclusions 348
References 348

Synergistic Effects of *Thymus vulgaris* Essential Oil Combined with Antibiotics Against Methicillin-Resistant *Staphylococcus aureus* 350

Keywords 350
Abstract 350
1. Introduction 350
2. Materials and Methods 351
3. Results and Discussion 351
4. Conclusion 351
References 352

Combining Black Seed Oil with Antibiotics: A Promising Strategy Against *Klebsiella pneumoniae* and *Acinetobacter baumannii* 353

Keywords 353
Abstract 353
1. Introduction 353
2. Materials and Methods 354
3. Results and Discussion 354
4. Conclusion 354
References 355

Characterization of Annealed and Unannealed Iron-Doped Tungsten Oxide Thin Films Grown by Co-Sputtering 356

Keywords 356
Abstract 356
1. Introduction 356
2. Materials and Methods 357
3. Results and Discussion 357
4. Conclusion 359
References 359

Microcontroller-Based Smart Monitoring Solutions for Critical Communication and Energy Infrastructures 360

Keywords 360
Abstract 360
1. Introduction 360
2. Materials and Methods 361
3. Results and Discussion 363
4. Conclusion 364
References 364

Effect of Concrete Strength Class, Maximum Aggregate Particle Size, and Curing Type on Ultrasonic Pulse Velocity 365

Keywords 365
Abstract 365
1. Introduction 365
2. Material and Method 366
3. Research Findings and Discussion 370
4. Conclusions 375
References 375

Remediation of Heavy Metal and Dye Pollution in Kyrgyzstan Using Nanotechnological and Biological Methods 376

Keywords 376
Abstract 376
1. Introduction 376
2. Biological Treatment Methods 378
3. Nanotechnological Purification Methods 378
4. Conclusion and Recommendation 379
References 379

A Comparative Study of Optimization-Based Control Strategies for a Two-Tank Liquid Level System 381

Keywords 381

Abstract 381
1. Introduction 381
2. Materials and Methods 382
3. Results and Discussion 386
4. Conclusion 390
References 390

Pharmacological Properties of Curcumin-Encapsulated Nanoclays 391

Keywords 391
Abstract 391
1. Introduction 391
2. Materials and Methods 392
3. Results and Discussion 392
4. Conclusions 394
References 394

Evaluation of Liquefaction Potential in Erzurum Aziziye District 395

Keywords 395
Abstract 395
1. Introduction 395
2. Introduction to the Field of Study and Examination of the Methods of Study 396
3. Field and Laboratory Studies 399
4. Assessment of Liquefaction Potential According to Different Earthquake Scenarios 399
5. Results 403
References 403

Chair's Closing Speech 404

Author Index 405

BOARDS

HONORARY BOARD

HONORARY CHAIR

Prof. Ahmet HACIMÜFTÜOĞLU — Atatürk University, TÜRKİYE

ORGANIZING BOARD

Chairs

SCIENTIFIC CHAIR

Prof. Hayrunnisa NADAROĞLU — Ataturk University, TÜRKİYE

ORGANIZING CHAIR

Asst. Prof. Muhammet Kaan YEŞİLYURT — Ataturk University, TÜRKİYE

CO-CHAIR

Asst. Prof. Hilal Kübra SAĞLAM — Ataturk University, TÜRKİYE

Secretariat

Dr. Rabiye KILIÇ — Ataturk University, TÜRKİYE
Dr. Aynur BABAGIL — Ataturk University, TÜRKİYE
Dr. Büşra YEŞİLYURT — Ataturk University, TÜRKİYE

Organizing Committee

Prof. Harun ARSLAN — Atatürk University, TÜRKİYE
Prof. Ebru BOZKURT — Atatürk University, TÜRKİYE
Prof. Ercan ÇELİK — Kyrgyzstan-Türkiye Manas University, KYRGYZSTAN
Prof. Esen TASĞIN — Ataturk University, TÜRKİYE
Prof. Mehmet YAVUZ — Kyrgyzstan-Türkiye Manas University, KYRGYZSTAN
Assoc. Prof. Rafet Çağrı ÖZTÜRK — Karadeniz Technical University, TÜRKİYE
Assoc. Prof. Efe Çetin YILMAZ — Kilis 7 Aralık University, TÜRKİYE
Asst. Prof. Cemil BAYRAM — Atatürk University, TÜRKİYE
Asst. Prof. Kaan CAN — Ataturk University, TÜRKİYE
Asst. Prof. Emir ÇEPNİ — Atatürk University, TÜRKİYE
Asst. Prof. Emine ÇORUH — Gümüşhane University, TÜRKİYE
Asst. Prof. Hayrunnisa MAZLUMOĞLU — Ataturk University, TÜRKİYE
Dr. Mansur MUSTAFAOĞLU — Erzurum, TÜRKİYE
Lect. Mahmut YEŞILYURT — İzmir Kavram Vocational School, TÜRKİYE

SCIENTIFIC BOARD

Committee of Advisors

- **Prof. Ahmet ADIGÜZEL** — Atatürk University, TÜRKİYE
- **Prof. Azize ALAYLI** — Sakarya University of Applied Sciences, TÜRKİYE
- **Prof. Ahmad ALİ** — University of Mumbai, INDIA
- **Prof. Özlem BARIŞ** — Kyrgyz-Turkish Manas University, KYRGYZSTAN
- **Prof. Ebru BOZKURT** — Atatürk University, TÜRKİYE
- **Prof. Ercan ÇELİK** — Kyrgyzstan-Türkiye Manas University, KYRGYZSTAN
- **Prof. Nazan DEMİR** — Muğla Sıtkı Koçman University, TÜRKİYE
- **Prof. Ümit DEMİR** — Gebze Technical University, TÜRKİYE
- **Prof. İhsan EFEOĞLU** — Atatürk University, TÜRKİYE
- **Prof. Abdollah ESMAEILI** — Federal University of Para (UFPA), BRAZIL
- **Prof. Mohd Nizar HAMIDON** — Universiti Putra Malaysia, MALAYSIA
- **Prof. Mostafa Abdelaty HASSIBELNABY** — Atatürk University, TÜRKİYE
- **Prof. Ekrem KALKAN** — Atatürk University, TÜRKİYE
- **Prof. Sibel KÜÇÜKOĞLU** — Selçuk University, TÜRKİYE
- **Prof. Rodrigo Ferrão De Paiva MARTINS** — Nova Schools of Science and Technology, PORTUGAL
- **Prof. Ahmet MAVİ** — Atatürk University, TÜRKİYE
- **Prof. Saravanan MUTHUPANDIAN** — Saveetha Institute of Medical and Technical Sciences, INDIA
- **Prof. Alper NUHOĞLU** — Ataturk University, TURKIYE
- **Prof. Ali OLAD** — Tabriz University, IRAN
- **Prof. Meral OLTULU** — Atatürk University, TÜRKİYE
- **Prof. Melda ŞIŞECIOĞLU** — Atatürk University, TÜRKİYE
- **Prof. Kamaruzzaman SOPHIAN** — National University of Malaysia, MALAYSIA
- **Prof. Hirofumi TANAKA** — Kyushu Institute of Technology, JAPAN
- **Prof. Raymond TUNG** — City University of New York, USA
- **Prof. Mehmet YAVUZ** — Kyrgyzstan-Türkiye Manas University, KYRGYZSTAN
- **Asst. Prof. Ahmed MOSA** — Al-Mansour University College, IRAQ
- **Asst. Prof. Ashok Kumar NADDA** — Jaypee University of Information Technology, INDIA
- **Asst. Prof. Prathap SINGH** — St. Joseph's Institute of Technology, INDIA
- **Dr. Manoochehr FARJAMINEZHAD** — Islamic Azad University, IRAN

Committee of Reviewers & Editors

- **Prof. Bishnu Pada BOSE** — Haldia Institute of Technology, INDIA
- **Prof. Elif Kılıç DELICE** — Atatürk University, TÜRKİYE
- **Prof. Aslıhan ESRINGÜ** — Atatürk University, TÜRKİYE
- **Prof. Esen TASĞIN** — Atatürk University, TÜRKİYE
- **Assoc. Prof. Abdulaziz Mohamed ATABANI** — Yuan Ze University, TAIWAN
- **Assoc. Prof. Alper CALAM** — Gazi University, TÜRKİYE
- **Assoc. Prof. Mahir Murat CENGIZ** — Atatürk University, TÜRKİYE
- **Assoc. Prof. Doğan ÇİLOĞLU** — Ataturk University, TÜRKİYE
- **Assoc. Prof. Efetobore G. Maju OYOVWIKOWHE** — University of Benin, NIGERIA
- **Assoc. Prof. Rafet Çağrı ÖZTÜRK** — Karadeniz Technical University, TÜRKİYE
- **Assoc. Prof. Sevda SARITAŞ** — Atatürk University, TÜRKİYE
- **Assoc. Prof. Efe Çetin YILMAZ** — Kilis 7 Aralık University, TÜRKİYE
- **Asst. Prof. Elif ERÇARIKÇI** — Atatürk University, TÜRKİYE

- **Asst. Prof. Parvaneh NASERZADEH** — Iran University of Medical Sciences, IRAN
- **Asst. Prof. Zhyldyzai OZBEKOVA** — Kyrgyz-Turkish Manas University, KYRGYZSTAN
- **Asst. Prof. Hilal Kübra SAĞLAM** — Atatürk University, TÜRKİYE
- **Asst. Prof. Hadi Ghasemi ZAVARAGH** — Technical and Vocational University, IRAN
- **Dr. Siti Amaniah Mohd CHACHULI** — Universiti Teknikal Malaysia Melaka, MALAYSIA

Committee of Session Chairs

- **Prof. Harun ARSLAN** — Atatürk University, TÜRKİYE
- **Prof. Ebru BOZKURT** — Atatürk University, TÜRKİYE
- **Prof. Elif Kılıç DELICE** — Atatürk University, TÜRKİYE
- **Prof. Aslıhan ESRINGÜ** — Atatürk University, TÜRKİYE
- **Prof. Mutlu KUNDAKÇI** — Atatürk University, TÜRKİYE
- **Prof. Alper NUHOĞLU** — Atatürk University, TÜRKİYE
- **Prof. Meral OLTULU** — Atatürk University, TÜRKİYE
- **Prof. Melda ŞIŞECIOĞLU** — Atatürk University, TÜRKİYE
- **Prof. Esen TAŞĞIN** — Atatürk University, TÜRKİYE
- **Assoc. Prof. Doğan ÇILOĞLU** — Atatürk University, TÜRKİYE
- **Assoc. Prof. Sinan KUL** — Atatürk University, TÜRKİYE
- **Asst. Prof. Cemil BAYRAM** — Atatürk University, TÜRKİYE
- **Asst. Prof. Kaan CAN** — Atatürk University, TÜRKİYE
- **Asst. Prof. Emir ÇEPNİ** — Atatürk University, TÜRKİYE
- **Asst. Prof. Bilal USANMAZ** — Atatürk University, TÜRKİYE
- **Dr. Mansur MUSTAFAOĞLU** — Erzurum, TÜRKİYE
- **Dr. Abbas RAZMI** — Erzurum, TÜRKİYE

TECHNICAL BOARD

HEAD OF BOARD

Dr. Rabiye KILIÇ — Atatürk University, TÜRKİYE

Lect. Mahmut YEŞILYURT — İzmir Kavram Vocational School, TÜRKİYE

Program Committee:

COORDINATOR

Tuğçe KARAGÖZ — ATA HTC

Osman KOLCU — ATA HTC

Fatma Melike YEŞILYURT — Kyrgyz-Turkish Manas University, KYRGYZSTAN

IT, AV & Logistics:

Ferdi DEMİR — ATA HTC

Alperen DAĞDELEN — ATA HTC

Serhat Baha ARICAN — ATA HTC

Nevzat AĞBAŞ

Elif KARAKAYA

Yaşar MUTAF

Publications Committee:

Hairat Abubakar BANARU

Tuğce KARAGÖZ — ATA HTC

Dilşat ÖZHATİNOĞLU — ATA HTC

Zeynep Nisa ŞAHİN — ATA HTC

Committee of Event Hosts:

İlayda PEKAR ÖZDEMİR — ATA HTC

Osman KOLCU — ATA HTC

Erhan KAHVECİ — ATA HTC

Dilşat ÖZHATİNOĞLU — ATA HTC

Zeynep Nisa ŞAHİN — ATA HTC

Elif KARAATA — ATA HTC

Committee of Facilitators:

Ahmet Celal HACIOĞLU — ATA HTC

Muhammet Çağrı YAZICI — ATA HTC

FOREWORD

We are pleased to extend our heartfelt gratitude to all participants, speakers, chairs, committee members, and contributors who have made the 2nd International Congress on Trends and Advances in Global Research and Applications (TAGRA 2025) a distinguished and truly memorable academic gathering. Building upon the success of the inaugural congress, TAGRA 2025 was held in a hybrid format in Erzurum, Türkiye, bringing together scholars from diverse fields to exchange ideas, present cutting-edge research, and foster new avenues for international collaboration.

TAGRA 2025 embodies the core mission of our congress series: providing an inclusive, interdisciplinary platform where advances in science, engineering, social sciences, marine sciences, and emerging technologies can be explored through rigorous and open academic dialogue. This year's congress brought together researchers, practitioners, and students from numerous countries, creating a vibrant environment enriched by diverse perspectives and innovative contributions.

During the congress, a wide range of plenary talks, invited lectures, thematic sessions, and oral and poster presentations offered participants the opportunity to engage with contemporary challenges, novel methodologies, and global research trends. The program featured contributions spanning scientific computation, engineering applications, artificial intelligence, environmental sciences, materials research, marine technologies, social sciences, educational studies, and many other domains. This broad thematic diversity is one of TAGRA's most defining strengths, enabling meaningful intersections between disciplines and encouraging holistic approaches to complex global issues.

On behalf of the Organizing Committee, we express our sincere appreciation to our plenary and invited speakers for sharing their expertise and for enriching the scientific content of the congress with their insightful perspectives. We also extend our gratitude to all authors for their valuable submissions and to the reviewers for their careful evaluations, constructive feedback, and dedication to academic excellence.

Our special thanks go to the chairs of the sessions, the coordinators of thematic tracks, and the members of the scientific, organizing, and advisory committees. Their commitment, professionalism, and tireless efforts have been instrumental in ensuring the smooth and successful realization of TAGRA 2025. We are equally grateful to our institutional partners, sponsors, and supporters for their continued collaboration and encouragement throughout this process.

We sincerely hope that all participants departed TAGRA 2025 with new ideas, strengthened academic networks, and fruitful inspirations for future research. It is our privilege to host such a diverse and dynamic community of scholars, and we look forward to welcoming you again at future TAGRA congresses.

On behalf of the Organizing Committee

Muhammet Kaan YEŞİLYURT

Organizing Chair

Message from the Organizing Committee

In a world where technology evolves at breakneck speed, how do we ensure our research keeps pace? Actually, academic events like this make us ensure we keep pace with the rest of the world. Aiming to bring together researchers and practitioners worldwide, the TAGRA events will be bringing together scientists, offering a unique platform to explore new developments in science and engineering and strengthen interdisciplinary collaboration as well as share innovative applications.

Organized with a multi-disciplinary approach, TAGRA also aims to bring together academics, researchers and industry professionals from all over the world in different fields to discuss the latest trends in science and technology and expand the global research vision. Offered with both face-to-face and online participation options, this flexible structure will increase the accessibility and enable us to reach a wider audience worldwide.

TAGRA is aimed to be not only a place for sharing academic knowledge, but also a meeting point where researchers can get inspired by each other and open doors to interdisciplinary collaboration and joint projects. In addition, participants will have the opportunity to access comprehensive information on the most up-to-date information and application techniques through oral and poster presentations, workshops and special sessions such as round-table talks, panel discussions, flash talks, and demonstrations/exhibits.

We eagerly look forward to seeing it come into reality in the coming events with your valuable contributions and spread of the word. Worldwide participation signifies our collective commitment to advancing scientific events. We do not want to become yet another event. We aim high, we aim for quality, we aim for yield, we aim for innovation, we aim for pure science, for all of us. Be the brick, be the cement, be the mold. Help us in making our way into it. As we embark on this journey together, do not just witness, be active contributors.

While we once again welcome you all, we would like to extend our sincere thanks and gratitude to everybody who made possible this event come into existence before we mark the new year, with special recognition to the organizing and scientific boards, to the technical board, and to our keynote speakers who devoted their valuable time to make this event complete in success.

Happy to have you all...

Congress at a Glance

The 2nd International Congress on Trends and Advances in Global Research and Applications (TAGRA 2025) was successfully held on 13–14 December 2025 in Erzurum, Türkiye, in a hybrid format that combined onsite and online participation. The congress hosted a rich and diverse scientific program, bringing together researchers, scholars, and practitioners from **12 countries** and multiple scientific domains.

The opening day, held onsite, commenced with a Plenary Session, featuring distinguished speakers from Australia, Malaysia, India, and Saudi Arabia. Throughout the first day, participants engaged in parallel scientific sessions across a variety of fields, including BioTech and BioEngineering, Marine Sciences, Interdisciplinary Studies, Nanomaterials, Mechanical Sciences, Architectural and Civil Engineering, and Optimization, Control and Decision Making.

The second day, conducted entirely online, expanded the thematic diversity of the congress with sessions in Agricultural and Food Science, Biomaterials, Biology–Biochemistry–Pharmacology, Solar Technology, Earth and Environmental Sciences, Thermal and Fluid Science, Electronics and Devices, Maths–Computation–Modeling, and Nano Frontiers: Materials and Applications. The program concluded with a Special Session dedicated to software-driven solutions for accreditation management in higher education institutions.

In total, **113** scientific presentations were delivered: **63** remotely presented and **50** face-to-face. The presentations included **9** keynote speeches, **100** oral presentations, **3** attended poster presentations, and **1** exhibit/demo presentation at a special session. The congress showcased **68 abstract-only** and **45 full-text** contributions from Türkiye **(50)**, Iran **(24)**, Malaysia **(15)**, Kyrgyzstan **(9)**, Nigeria **(5)**, India **(3)**, Brazil **(2)**, Poland **(1)**, Germany **(1)**, Saudi Arabia **(1)**, Australia **(1)**, and Indonesia **(1)**. The contributions were authored by a total of **224** people and presented by **107** speakers in **27** different sessions: **1** hybrid, **12** face-to-face and **13** online.

TAGRA 2025 demonstrated the growing international recognition of the congress series and affirmed its role as a dynamic platform for interdisciplinary scientific exchange. The strong participation, wide geographical representation, and diverse research topics reflect the commitment of the global academic community to advancing science, engineering, and emerging technologies. The Organizing Committee extends its gratitude to all contributors, session chairs, reviewers, and participants whose efforts and engagement ensured the success of this year’s congress.

Chair's Opening Speech

My dear professors, colleagues, dear students,

Distinguished professors, esteemed colleagues, and dear students, I greet you with respect and my warmest wishes.

Welcome to the International Congress on Trends and Advances in Global Research and Applications—TAGRA 2025.

Bringing together distinguished representatives from different geographies of the scientific world in Erzurum, both in person and online, is a great honor and pleasure for both myself and the organizing committee. Your participation in our congress is not only an indication of your interest in this event; it is also a concrete expression of our common will to share knowledge, strengthen the research culture, and advance science and engineering.

This year, TAGRA, with its multidisciplinary structure, is more than just a scientific meeting; it is an international scientific bridge that brings together different academic traditions, research perspectives, and cultural viewpoints on the same platform. Hosting participants from different countries is a strong indicator of our congress' global impact and academic appeal.

Our participant profile encompasses a wide range, from accomplished professors to young researchers, graduate students and undergraduate scientists. This diversity significantly contributes to TAGRA's dynamic, innovative and productive scientific atmosphere.

Our congress theme, "New Horizons in Science, Technology, and Applications," is a powerful vision aimed at understanding today's rapidly transforming science and technology ecosystem, discussing the new paradigms driving this transformation, and developing innovative perspectives for the future. The presentations are a tangible reflection of intensive research processes, academic experience, and dedication to science.

Throughout the event, current studies in strategic research areas such as Biotechnology and bioengineering, marine sciences, Nanomaterials, Optimization, control and decision making, Architecture and Construction, Mechanical Sciences, Agriculture and Food Sciences, Biomaterials, Biology, Biochemistry and Pharmacology, Earth and Environmental Sciences, Solar Technology, Mathematics, Computational and Modeling, Thermal and Fluid Science, Electronics

and Devices will be discussed. Each of these topics is not only a critical area that determines the direction of scientific developments; it is also a key theme in building a more just, sustainable and livable future.

The climate change, resource management problems, environmental vulnerabilities, and accelerating technological transformation that we face globally have made interdisciplinary collaborations inevitable. TAGRA 2025 serves as an important forum for strengthening these collaborations, generating knowledge, and discussing innovative solutions. On this occasion, I would like to express my gratitude to all my colleagues who contributed to the realization of our congress. I would like to express my gratitude to the Organizing Committee and the Congress secretariat team for their outstanding dedication in carrying out the organization process. I would also like to thank all our invited speakers and participants who will enrich our congress with their scientific contributions.

I hope that Erzurum’s historical texture and cultural richness will add meaning to this scientific gathering, and I wish you all a fruitful, inspiring, and scientifically fulfilling congress.

Now, with immense excitement and hope, I officially open TAGRA 2025.

Thank you and I wish you all a productive and inspiring congress.

Hayrunnisa Nadaroğlu

Scientific Chair

CONGRESS PROGRAM

1st Day Sat, Dec 13

Opening Session: Plenary Session

BioTech and BioEngineering: BioTechology and BioEngineering

Marine Sciences: Session for Marine Sciences

Interdisciplinary Session

Nanomaterials 1

Nanomaterials 2

Attended Poster Session

Optimization Control and Decision Making

Architectural and Civil

BioTech and BioEngineering

Mechanical Sciences

Nanomaterials

Optimization Control and Decision Making

2nd Day Sun, Dec 14

Gathering and Acquaintance

Agricultural and Food Science

Biomaterials

Biology Biochemistry and Pharmacology

Earth and Environmental Sciences

Solar Technology

Biomaterials

Biology Biochemistry and Pharmacology

Nano Frontiers: Materials and Applications

Maths, Computation and Modeling

Thermal and Fluid Science

Biology Biochemistry and Pharmacology

Electronics and Devices

Special Session

Sat, December 13

10:00 AM **1.1.**

10:00 AM – 1:00 PM

Opening Session: Plenary Session

Session | **Location:** Campus VSTS, C/Ground-2 - Main Hall |

Convener: Hayrunnisa Nadaroğlu (Department of Food Processing, Vocational School of Technical Sciences, Atatürk University, Erzurum, Türkiye)

10:30 – 10:40 AM **Opening Ceremony**

Speaker
Muhammet Kaan Yeşilyurt (Faculty of Engineering, Department of Mechanical Engineering, Ataturk University, Erzurum, Türkiye)

10:40 – 10:50 AM **Chairs' Speech**

10:50 – 11:10 AM **AI and Bioinformatics Synergy: Transforming Data Into Precision Healthcare**

Speaker
Md. Habibur Rahman (Department of Health Sciences, Novel Global Educational Foundation, NSW, Australia)

11:10 – 11:30 AM
Graphenated Carbon Nanotubes: Bridging 1D-2D-3D Carbon for Advanced Functional Systems

Speaker
Ismayadi Ismail (Nanomaterials Synthesis And Characterization Laboratory, Institute of Nanoscience and Nanotechnology, Universiti Putra Malaysia, 43400 Serdang, Selangor Darul Ehsan, Malaysia)

11:30 – 11:50 AM **Fabrication and Characterization of Functionally Graded A356 Alloy and Its Composite**

Speaker
Prathap Singh S (Department of Mechanical Engineering, St. Joseph's Institute of Technology, CHennai, India.)

11:50 AM – 12:10 PM
Unim-R Polyherbal Oil: Efficacy and Safety Assessment in Carrageenan and CFA-Induced Arthritis with Cytokine Profiling

Speaker
Ahmad Ali (Department of Life Sciences, University of Mumbai, Vidyanagari, Mumbai, India)

12:10 – 12:30 PM **Applications of Carbon Based Nanomaterials in Microwave Devices**

Speaker
Zainab Yunusa (Department of Electrical Engineering, University of Hafr Al Batin, Saudi Arabia)

12:30 – 12:50 PM
A Shift Toward Simplicity: Current Progress, Technical Challenges, and Future Prospects of ETL-Free Perovskite Solar Cells

Speaker
Faiz Arith (Faculty of Electronics and Computer Technology and Engineering, Universiti Teknikal Malaysia Melaka, Hang Tuah Jaya, Durian Tunggal, 76100, Melaka, Malaysia)

1:00 PM

2:00 – 3:00 PM

2:00 PM **1.2.**

BioTech and BioEngineering: BioTechology and BioEngineering

Session | **Location:** Campus VSTS, D/1-8 - Hall 3 |
Convener: Harun Arslan (Faculty of Fisheries, Ataturk University, Erzurum, Türkiye)

2:00 – 2:15 PM

Evaluation of the Sensitivity and Specificity of the Diagnostic Electrochemical Biosensor Using MicroRNAs Biomarkers Involved in Multiple Sclerosis

Speaker
Azizeh Shadidizaji (Department of Agriculture Biotechnology, Faculty of Agriculture, Ataturk University, Erzurum, Türkiye)

2:15 – 2:30 PM

~~Colostrum-Derived Exosomes as a Next-Generation Drug Delivery Platform: Mechanisms, Therapeutic Applications, and Future Perspectives~~

Speaker
Şeyma Aydın (Department of Genetics, Veterinary Faculty, Atatürk Üniversity, Erzurum, Türkiye)

2:30 – 2:45 PM

Synergistic Effects of Thymus Vulgaris Essential Oil Combined with Antibiotics Against MRSA (Methicillin-Resistant Staphylococcus aureus)

Speaker
Torkan Haghi (Department of Biology, Faculty of Science, Atatürk University, Erzurum, Türkiye)

2:45 – 3:00 PM

Purification of Exopolysaccharides from Thermophilic Bacillus licheniformis SO2 Strain by Three-Phase Separation (TPP) System and Determination of Their in Vitro Biological Activities

Speaker
Afranur Timur (Graduate Student, Atatürk Üniversity)

3:00 PM

2:00 – 3:20 PM

2:00 PM **1.3.**

Engineering Sciences: Session for Engineering Sciences

Session | **Location:** Campus VSTS, D/1-2 - Hall 2 |

Convener: Ahmet Numan Özakın (Department of Mechanical Engineering, Faculty of Engineering, Atatürk University, Erzurum, Türkiye)

2:00 – 2:15 PM **Evaluation of Liquefaction Potential in Erzurum Aziziye District**

Speaker
Onur Temiz (Department of Geological Engineering, Institute of Science, Atatürk University, Erzurum, Türkiye)

2:15 – 2:30 PM

Non-Invasive Marine Monitoring with Baited Remote Underwater Video (BRUV) Systems: Capabilities, Limitations, and Regional Opportunities

Speaker
Rafet Çağrı Öztürk (Department of Fisheries Technology Engineering, Faculty of Marine Sciences, Karadeniz Technical University, Trabzon, Türkiye)

2:30 – 2:45 PM **Investigation of Erzurum Ilıca District Liquefaction Potential With Different Methods**

Speaker
Hamit Çakıcı (Department of Architecture and Urban Planning, Pasinler Vocational School, Atatürk University, Erzurum, Türkiye)

2:45 – 2:55 PM **Preserving Genetic Diversity: Why Türkiye Needs a National GenBank**

Speaker
Rafet Çağrı Öztürk (Department of Fisheries Technology Engineering, Faculty of Marine Sciences, Karadeniz Technical University, Trabzon, Türkiye)

2:55 – 3:05 PM

An Evaluation of Optimum Inclination Angle for Fixed-angle Solar Panel Installations in Erzurum Province

Speaker
Muhammet Kaan Yeşilyurt (Faculty of Engineering, Department of Mechanical Engineering, Ataturk University, Erzurum, Türkiye)

3:20 PM

2:00 – 3:00 PM

2:00 PM **1.4.**

Interdisciplinary Session

Session | **Location:** Campus VSTS, D/1-6 - Hall 6 |

Convener: Aslıhan Esringü (Department of Landscape Architecture, Faculty of Architecture and Design, Atatürk University, 25249 Erzurum, Türkiye)

2:00 – 2:15 PM **Traditional Arts and Mathematics**

Speaker
Aydan Akkök (Department of Traditional Handicrafts, Vocational School of Technical Sciences, Atatürk University, Erzurum, Türkiye)

2:15 – 2:30 PM

Risk Assessment of Occupational Hazards in Asphalt Production Plants Using the Fine-Kinney Method

Speaker
Emine Çoruh (Faculty of Health Sciences, Department of Occupational Health and Safety, Gümüşhane University, Gümüşhane, Türkiye)

2:30 – 2:45 PM **Occupational Health and Safety Practices in the Solar Energy Sector**

Speaker
Selçuk Sincar (Department of Machinery and Metal Technologies, Vocational School of Technical Sciences, Ataturk University, Erzurum, Türkiye)

2:45 – 3:00 PM **The Critical Role of Rare Elements in Renewable Energy Systems and Türkiye**

Speaker
Hüseyin Güllüce (Machinery and Metal Technologies, Vocational School of Technical Sciences, Atatürk University, Erzurum, Turkiye)

3:00 PM

2:00 – 3:00 PM

2:00 PM **1.5.**

Nanomaterials 1

Session | **Location:** Campus VSTS, D/1-5 - Hall 5 |

Convener: Ebru Bozkurt (Department of Occupational Health and Safety, Vocational School of Technical Sciences, Atatürk University, 25240, Erzurum, Türkiye)

2:00 – 2:15 PM **Eco-Friendly Synthesis of Carbon Quantum Dots for Mycotoxin Detection**

Speaker
Hatice Yüncü (Department of Nanoscience and Nanoengineering, Institute of Science, Atatürk University, Erzurum, Türkiye)

2:15 – 2:30 PM

Removal of Heavy Metals in Ice Tea Beverages Using Electrochemically Synthesized Glutathione Modified Electrodes

Speaker
Ayşenur Şuvak (Department of Chemistry, Faculty of Science, Ataturk University, Erzurum, Türkiye)

2:30 – 2:45 PM **Electrochemical Synthesis of CoBi2O4 Nanostructures**

Speaker
Hulya Ozturk Doğan (Department of Chemical Technology, Vocational School of Technical Sciences, Atatürk University, Erzurum, Türkiye)

2:45 – 3:00 PM

Synthesis and Bioactivities of Zinc Oxide (ZnO) Nanoparticles from Lactobacillus plantarum

Speaker
Aysu Kırali (Department of of Nutrition and Dietetics, Faculty of Health Sciences, Atatürk University, Erzurum, Türkiye)

3:00 PM

2:00 PM **1.6.**

2:00 – 3:00 PM

Nanomaterials 2

Session | **Location:** Campus VSTS, D/1-1 - Hall 1 |

Convener: Mansur Mustafaoglu (Department of Nanoscience and Nanoengineering, Institute of Science, Atatürk University, Erzurum, Türkiye)

2:00 – 2:15 PM

Nitrogen-Doped Carbon Quantum Dots for Sensitive Colorimetric Assay of V(V)

Speaker

Habibollah Eskandari (Department of Chemistry, Faculty of Basic Sciences, University of Mohaghegh Ardabili, Ardabil 56199-11367, Iran)

2:00 – 2:15 PM

Preparation of WO3-X Nanoparticles by UVA-Irradiation for Colorimetric Sensing of Cr(VI)

Speaker

Habibollah Eskandari (Department of Chemistry, Faculty of Basic Sciences, University of Mohaghegh Ardabili, Ardabil 56199-11367, Iran)

2:15 – 2:30 PM

Efficient CO-Free Carbonylation of Aryl Halides Catalyzed by SBA-15-Supported Pd-1,10-Phenanthroline

Speaker

Yagoub Mansoori (Department of Applied Chemistry, Faculty of Science, University of Mohaghegh Ardabili, Ardabil, 56199-11367, Iran)

2:30 – 2:45 PM

Tetrachloroperylene Dianhydride as a Simple and Capable Sensor; Case Study: Cyanide Anion and Primary Aliphatic Amines

Speaker

Mohammad Reza Zamanloo (Department of Applied Chemistry, Faculty of Science, University of Mohaghegh Ardabili, Ardabil, Iran)

2:45 – 3:00 PM

Comparative Effects of Cold Plasma and Microwave Pretreatments on Bioactive Compounds in Hydroalcoholic Quince Leaf Extracts

Speaker

Bahram Fathi-Achachlouei (Department of Food Science and Technology, University of Mohaghegh Ardabili, Ardabil, Iran)

3:00 PM

2:00 PM **1.7.**

2:00 – 3:00 PM

Optimization Control and Decision Making

Session | **Location:** Campus VSTS, D/1-10 - Hall 4 |

Convener: Bilal Usanmaz (Department of Computer Engineering, Faculty of Engineering, Ataturk University, Erzurum, Türkiye.)

2:00 – 2:15 PM

A Comparative Study of Optimization-Based Control Strategies for a Two-Tank Liquid Level System

Speaker
Kaan Can (Department of Electrical and Electronics Engineering, Faculty of Engineering, Ataturk University, Erzurum, Türkiye)

2:15 – 2:30 PM

Perceptions of Artificial Intelligence in Turkey: A Descriptive Analysis of TGSS Data

Speaker
Esra Çelik (Department of Industrial Engineering, Faculty of Engineering, Atatürk University, Erzurum, Türkiye)

2:30 – 2:45 PM

Data-Driven Quality Control in Iron and Steel Production: Evaluating the Impact of Carbon Content and Process Parameters Using Machine Learning

Speaker
Tuba Irmak (Department of Industrial Engineering, Faculty of Engineering, Atatürk University, Erzurum, Türkiye)

2:45 – 3:00 PM

Analysis of the RL Circuit Using Physics-Informed Neural Network (PINN) Method

Speaker
Peruzet Aydın (Department of Computer Engineering, Institute of Science, Atatürk University, Erzurum, Türkiye)

3:00 PM

9:30–10:00 AM

12:30 AM / 3:00 PM

Attended Poster Session

Session | **Location:** Campus VSTS, D/1-5 - Hall 5

3:30–3:45 PM

QSPR Study on Photo Oxidation Reaction of Aromatic Micro Pollutants Using the Genetic Algorithm - Support Vector Machine

Speaker
Eslam Pourbasheer (University of Mohaghegh Ardabili, Ardabil Iran)

3:45–4:00 PM **Copper-Based Metal-Organic Framework Cu(BDC) as a Reusable Heterogeneous Catalyst for Efficient N-Arylation of NH-Heterocycles**

Speaker
Yagoub Mansoori (Department of Applied Chemistry, Faculty of Science, University of Mohaghegh Ardabili, Ardabil, 56199-11367, Iran)

4:30–4:45 PM

Production of Low-Fat Mayonnaise Using Pomegranate Peel Powder and Evaluation of Its Physicochemical and Sensory Properties

Speaker
Bahram Fathi-Achachlouei (Department of Food Science and Technology, University of Mohaghegh Ardabili, Ardabil, Iran)

13:00 PM / 3:30 PM

3:30 PM

3:30 – 4:30 PM

Architectural and Civil

Session | **Location:** Campus VSTS, D/1-10 - Hall 4 |

Convener: Meral Oltulu (Faculty of Engineering, Department of Civil Engineering, Ataturk University, Erzurum, Türkiye.)

3:30 – 3:45 PM

Effect of Concrete Strength Class, Maximum Aggregate Particle Size, and Curing Type on Ultrasonic Pulse Velocity

Speaker
Ibrahim Ishaq M Alkhattab (Department of Civil Engineering, Faculty of Engineering, Atatürk University, Erzurum, Türkiye)

3:45 – 4:00 PM

A Nature-Based Healing Approach: Horticultural Therapy Gardens

Speaker
Aslihan Esringü (Department of Landscape Architecture, Faculty of Architecture and Design, Atatürk University, 25249 Erzurum, Türkiye)

4:00 – 4:15 PM

The Impact of Amorphous Boron Waste on the Long-Term Mechanical Properties of Steel Fiber-Reinforced Concrete

Speaker
Meral Oltulu (Faculty of Engineering, Department of Civil Engineering, Ataturk University, Erzurum, Türkiye.)

4:15 – 4:30 PM

Urban Water Management Approaches for Resilient Cities

Speaker
Senanur seher Ağbaba (Graduate Student, Atatürk Üniversity)

4:30 PM

3:30 PM

3:30 – 4:30 PM

BioTech and BioEngineering

Session | **Location:** Campus VSTS, D/1-8 - Hall 3 |

Convener: Melda Şişecioğlu (Department of Molecular Biology and Genetics, Faculty of Science, Ataturk University, Erzurum, Türkiye)

3:30 – 3:45 PM

Combining Black Seed Oil with Antibiotics: A Promising Strategy Against Klebsiella pneumoniae and Acinetobacter baumannii

Speaker
Torkan Haghi (Department of Biology, Faculty of Science, Atatürk University, Erzurum, Türkiye)

3:45 – 4:00 PM

New Approaches to Microneedle Technology and Alzheimer's Vaccine Applications

Speaker
Hayrunnisa Nadaroğlu (Department of Food Processing, Vocational School of Technical Sciences, Atatürk University, Erzurum, Türkiye)

4:00 – 4:15 PM

Use of Metal Oxide Nanoparticles in the Food Industry: Toxicological Risks and Effects on Child Nutrition

Speaker
Behina Asadoghli (Department of Nutrition and Dietetics, Faculty of Health Sciences, Atatürk University, Erzurum, Türkiye)

4:15 – 4:30 PM

Examination of the Effect of Genistein on CD36 Lipid Receptor and Lipid Profile in Liver Cancer Cell Line

Speaker
Ebru Kılıç (Faculty of Health Sciences, Department of Nutrition and Dietetics, Atatürk University, Erzurum, Türkiye)

4:30 PM

3:30 – 4:45 PM

3:30 PM **1.8.**

Mechanical Sciences

Session | **Location:** Campus VSTS, D/1-5 - Hall 5 |
Convener: Doğan Çiloğlu (Deparment of Mechanical Engineering, Faculty of Engineering)

3:30 – 3:45 PM

Experimental and Numerical Investigation of the Thermo-Hydraulic Performance of Mini-Channel Graphite Foam and Aluminum Heat Sinks

Speaker
Zekeriya Kutlu (Department of Mechanical Engineering, Faculty of Engineering, Atatürk University, Erzurum, Türkiye)

3:45 – 4:00 PM

Performance Assessment of Thermoelectric Cooling Applied to Photovoltaic Panels

Speaker
Muhammet Harun Osta (Atatürk Üniversitesi)

4:00 – 4:15 PM

Effect of Using a Vertical Heat Exchanger on Performance in a Vapor Compressıon Heat Pump Using R417a Gas as an Alternakve to R22

Speaker
Fadime Şimşek (Department of Mechanical Engineering, Faculty of Engineering, Atatürk University, Erzurum, Türkiye)

4:15 – 4:30 PM

Alternative Wing Designs for UAVs

Speaker
Hüseyin Gündüz (Department of Mechanical Engineering, Faculty of Engineering, Atatürk University, Erzurum, Türkiye)

4:30 – 4:45 PM

Energy Efficiency-Focused Entropy Analysis: Investigation of Nanofluid Heat Transfer Processes

Speaker
Ali Sharifi (Faculty of Mechanical Engineering, University of Tabriz, Tabriz, Iran)

4:45 PM

3:30 PM **1.9.**

3:30 – 4:45 PM

Nanomaterials

Session | **Location:** Campus VSTS, D/1-1 - Hall 1 |

Convener: Esen Taşğın (Department of Nutrition and Dietetics, Faculty of Health Sciences, Atatürk University, Erzurum, Türkiye)

3:30 – 3:45 PM

Optical and Biological Properties of Carbon Quantum Dots Synthesized from Daucus Carota Ssp. Sativus Var. Atrorubens Extract

Speaker
Ezo palavan (Department of Molecular Biology and Genetics, Faculty of Science, Atatürk University, Erzurum, Türkiye)

3:45 – 4:00 PM

Sustainable Nanomaterial Production: Carbon Quantum Dots Synthesized from Biological Waste

Speaker
Taha Yasin Bayram (Department of Molecular Biology and Genetics, Institute of Science, Ataturk University, Erzurum, Türkiye)

4:00 – 4:15 PM

Optical Properties of a Novel Pyrazoline Derivative in Diverse Micelle Systems

Speaker
Ebru Bozkurt (Department of Occupational Health and Safety, Vocational School of Technical Sciences, Atatürk University, 25240, Erzurum, Türkiye)

4:15 – 4:30 PM

Oxidation Mechanism in Vegetable Oils and Methods for Increasing Oxidation Stability

Speaker
Büşra Aydın (Department of Chemical Engineering, Faculty of Engineering, Atatürk University, Erzurum, Türkiye)

4:30 – 4:45 PM

Characterization of Annealed and Unannealed Iron-Doped Tungsten Oxide Thin Films Grown by Co-Sputtering

Speaker
Hilal Kübra Sağlam (Department of Electrical and Electronics Engineering, Faculty of Engineering, Atatürk University, Erzurum, Türkiye)

4:45 PM

3:30 PM **1.10.**

3:30 – 4:30 PM

Optimization Control and Decision Making

Session | **Location:** Campus VSTS, D/1-2 - Hall 2 |

Convener: Elif Kılıç Delice (Faculty of Engineering, Department of Industrial Engineering, Ataturk University, Erzurum, Türkiye)

3:30 – 3:45 PM

Cauliflower Disease Classification Using Vision Transformer Architecture

Speaker

Rabiye Kılıç (Department of Computer Engineering, Faculty of Engineering, Atatürk University, Erzurum, Türkiye)

3:45 – 4:00 PM

Evaluation of Entrepreneurial Projects Using Multi-Criteria Decision-Making Methods: the Case of the KOSGEB Entrepreneurial Support Program

Speaker

Halil barış Gezmiş (Department of Industrial Engineering, Atatürk University, Erzurum, Türkiye)

4:00 – 4:15 PM

Microcontroller-Based Smart Monitoring Solutions for Critical Communication and Energy Infrastructures

Speaker

Tuba Çakıcı Can (Department of Electrical and Automation, Technical Science Vocational High School, Ataturk University, 25250, Erzurum, Türkiye)

4:15 – 4:30 PM

The Impact of Multi-Tagger Consistency on Semi-Supervised Natural Language Processing Models: A Bert-Based Tagging Approach

Speaker

Aleyna Karaosman (Department of Software Engineering, Institute of Science, Atatürk University, Erzurum, Türkiye)

4:30 PM

Sun, December 14

1:15 PM **1.11.**

1:15 – 1:30 PM

1:30 PM

Gathering and Acquaintance

Contribution | **Location:** Virtual Room, VCR/1-1 |

Convener: Cemil Bayram (Department of Pharmacology and Toxicology, Faculty of Veterinary, Ataturk University, Erzurum, Türkiye)

1:30 – 2:30 PM

1:30 PM **1.12.**

Agricultural and Food Science

Session | **Location:** Virtual Room, VCR/1-2 |

Convener: Emir Çepni (Department of Electrical and Electronics Engineering, Faculty of Engineering, Atatürk University, Erzurum, 25240, Türkiye)

1:30 – 1:45 PM

Advances in Albumin-Based Nanocarriers: Novel Engineering Strategies and Functional Enhancements

Speaker
Betül Çiçek (Department of Physiology, Faculty of Medicine, Erzincan Binali Yildirim University, Erzincan, Türkiye)

1:45 – 2:00 PM

Fluorescence Spectroscopy in the Study of Animal Meats

Speaker
Zhyldyzai Ozbekova (Department of Food Engineering, Faculty of Engineering, Kyrgyz-Turkish Manas University, Bishkek, Kyrgyz Republic)

2:00 – 2:15 PM

Product Innovation and Processing Technologies for Agroforestry Food Products

Speaker
Jamila Smanalieva (Food Chemistry, Faculty of Chemistry and Food Chemistry, Technische Universität Dresden, Germany)

2:15 – 2:30 PM

Chemical Composition, Physico-Chemical Properties and Amino Acid Profile of Muffins Enriched with Cricket Powder (Acheta Domesticus)

Speaker
Aichurok Mazhitova (Department of Food Engineering, Engineering Faculty, Kyrgyz-Turkish Manas University, Bishkek 720038, Kyrgyzstan)

2:30 PM

1:30 PM **1.13.**

1:30 – 2:30 PM

Biomaterials

Session | **Location:** Virtual Room, VCR/1-3 |
Convener: Abbas Razmi (Independent Researcher, Erzurum, Türkiye)

1:30 – 1:45 PM

Investigation of the Cellular Effects of Infrared Electromagnetic Waves and Carbon Nanotubes on HT29 Cell Line

Speaker
Farshad Lotfollahzadeh (Department of Physics, MAH., Islamic Azad University, Mahabad Iran)

1:45 – 2:00 PM

Cellular Toxicity of Laser, Iron Oxide and Manganese Oxide Nanoparticles on the Viability of Breast Cancer Cells Line

Speaker
Aysan Mansournia (Department of Physics, MAH. Islamic Azad University, Mahabad, Iran)

2:00 – 2:15 PM

Mechanistic Insights Into Tissue Regeneration Using Carbon-Based Nanoparticles in 3d Bioprnting

Speaker
Fatemeh Barati (Department of Medical Nanotechnology, Faculty of Advanced Technologies in Medicine, Iran University of Medical Sciences, Tehran, Iran)

2:15 – 2:30 PM

Bioprinted Scaffolds Incorporated by Functional Nanoparticles

Speakers
Fatemeh Barati (Department of Medical Nanotechnology, Faculty of Advanced Technologies in Medicine, Iran University of Medical Sciences, Tehran, Iran), Behnaz Ashtari (Department of Medical Nanotechnology, Faculty of Advanced Technologies in Medicine, Iran University od Medical Sciences. Tehran, Iran)

2:30 PM

1:30 PM **1.14.**

1:30 – 2:30 PM

Biology Biochemistry and Pharmacology

Session | **Location:** Virtual Room, VCR/1-4 |

Convener: Cemil Bayram (Department of Pharmacology and Toxicology, Faculty of Veterinary, Ataturk University, Erzurum, Türkiye)

1:30 – 1:45 PM

Comparative Morphology of the Spleen in Mammals, Birds, and Amphibians (Frogs)

Speaker
Bermet Kydyralieva (Biology Department,Faculty of Sciences, Kyrgyz-Turkish Manas University, Bishkek, Kyrgyzstan)

1:45 – 2:00 PM

Therapeutic Effect of the SN-38-FeO Nanoparticle Combination Targeting Dopamine Receptors in Colorectal Cancer Cells

Speaker
Özlem Ütme (Department of Medical Pharmacology, Faculty of Medicine, Şeyh Edebali University, Bilecik, Türkiye)

2:00 – 2:15 PM

Network Pharmacology and Machine Learning-Driven Virtual Screening with Dynamics Simulations of Natural Compounds for Glioblastoma

Speaker
Damilola Omoboyowa (Adekunle Ajasin University, Akungba-Akoko Ondo State, Nigeria)

2:15 – 2:30 PM

Graphene/Cellulose Nanocomposite Accelerate Oral Wound Healing in Diabetic Rats by Mitigating Oxidative Stress and Apoptosis in Gingival Fibroblasts.

Speaker
Sana Ghaffarzadeh (Department of Pharmacy, School of Pharmacy, Shahid Beheshti University of Medical Sciences, Tehran, Tehran, Iran.)

2:30 PM

1:30 PM

1:30 – 3:30 PM

Earth and Environmental Sciences

Session | **Location:** Virtual Room, VCR/1-1 |
Convener: Alper Nuhoğlu (Department of Environmental Engineering, Faculty of Engineering, Atatürk University, Erzurum, Türkiye)

1:30 – 1:50 PM

Prevention and Mitigation Strategies for Sinkholes Using Soil Improvement Techniques

Speaker
Hamed Niroumand (Department of Geotechnical and Hydraulic Engineering, Faculty of Civil and Environmental Engineering, Gdansk University of Technology, Gdansk, Poland.)

1:50 – 2:05 PM

Integrated Geophysical, Geochemical and Hydrogeological Methods to Investigation of Groundwater Contamination: A Case Study of Osubi, and its Environ Southern Nigeria

Speaker
Wasiu Osisanya (Department of Physics, College of Science, Federal University of Petroleum Resources, Effurun, Delta State, Nigeria)

2:05 – 2:20 PM

Innovative Pathways for Circular Economy: Repurposing Coal Mine Waste in Construction Materials

Speaker
Bishnu Pada Bose (Department of Civil Engineering, Haldia Institute of Technology, Haldia, India)

2:20 – 2:35 PM

Integrated Electrical Resistivity Investigation of Subsurface Peat and Clay Deposits in Orile Whitesand, Orile-Iganmu, Lagos, Southwestern Nigeria

Speaker
Wasiu Osisanya (Department of Physics, College of Science, Federal University of Petroleum Resources, Effurun, Delta State, Nigeria)

2:35 – 2:50 PM

Hydrogeochemistry, Petrography, and Groundwater Quality in the Waru-Apo Area (Abuja FCT, Nigeria)

Speaker
Hairat Abubakar (Department of Geology and Mining, Nasarawa State University, Keffi, Nigeria)

2:50 – 3:05 PM

Integrated Geophysical and Hydrochemical Assessment Of Groundwater Contamination And Aquifer Vulnerability In The Ifewara Area, Southwestern Nigeria

Speaker
Kamorudeen Alasi (Department of Physics with Electronics, University of Ilesa, Ilesa, Nigeria)

3:30 PM

1:30 PM

1:30 – 3:05 PM

Solar Technology

Session | **Location:** Virtual Room, VCR/1-5 |

Convener: Mutlu Kundakçı (Department of Physics, Faculty of Science, Ataturk University, Erzurum 25240, Türkiye)

1:30 – 1:45 PM

Structural Analysis of La-Doped MoO_3 Hole Transport Layers and Their Correlation with Perovskite Solar Cell Performance

Speaker
Zulfanizam Abdul Wahab (Universiti Teknikal Malaysia Melaka)

1:45 – 2:00 PM

Towards High-Efficiency $CsPbI_3$ Perovskite Solar Cells: A Computational Pathway to Material and Device Optimization,

Speaker
Nurul Farina Mohd Nazli (Faculty of Electronic and Computer Technology and Engineering (FTKEK), Universiti Teknikal Malaysia Melaka, Hang Tuah Jaya, 76100, Durian Tunggal, Malaysia)

2:00 – 2:15 PM

Influence of Low-Temperature Annealing on Copper Iodide as Hole Transporting Layer for Perovskite Solar Cell Applications

Speaker
Omsri Vinasha Aliyaselvam (Centre for Telecommunication Research & Innovation, Faculty of Electronic and Computer Engineering, Universiti Teknikal Malaysia Melaka, Malaysia)

2:15 – 2:30 PM

Synthesis and Characterization of Ni-Doped ZnO Nanorods for Potential Use in Solar Cells

Speaker
Thanies Murugan (Graduate Student, Universiti Teknikal Malaysia Melaka)

2:30 – 2:45 PM

Harnessing Interface Engineering to Unlock Performance in Lead-Free, ETL-Free Perovskite Solar Cells: a SCAPS-1D Defect Tolerance Study

Speaker
Nabilah Ahmad Jalaludin (Faculty of Electronics and Computer Technology and Engineering, Universiti Teknikal Malaysia Melaka)

3:05 PM

2:40 PM **1.15.**

2:40 – 4:10 PM

Biomaterials

Session | **Location:** Virtual Room, VCR/1-3 |
Convener: Abbas Razmi (Independent Researcher, Erzurum, Türkiye)

2:40 – 2:55 PM

Unraveling the Mechanism of TiCN Film-Coated NiTi Substrate Toxicity: Evidence of Mitochondrial Electron Transport Dysfunction in Gingival Cells from Diabetic Rats

Speaker
Parvaneh Naserzadeh (Colorectal Research Center, Iran University of Medical Sciences, Tehran, Iran)

2:55 – 3:10 PM

Functional Nanoparticle Incorporated Bioprinted Scaffolds

Speaker
Fatemeh Barati (Department of Medical Nanotechnology, Faculty of Advanced Technologies in Medicine, Iran University of Medical Sciences, Tehran, Iran)

3:10 – 3:25 PM

Effect of Sliding Wear Mechanism of Titanium Biomaterials: 3D Finite Element Analysis

Speaker
Efe Çetin Yılmaz (Department of Control Systems Electrical and Electronic Engineering, Engineering and Architecture Faculty, Kilis 7 Aralık University, Kilis, Türkiye)

3:25 – 3:40 PM

Classification of Biomaterials and Their Biomedical Applications

Speaker
Abbas Razmi (Independent Researcher, Erzurum, Türkiye)

3:40 – 3:55 PM

Design and Manufacture of PLC Controlled Laboratory Wear Device for in Vitro Biomedical Applications

Speaker
Ibrahim Elebeyd (Department of Electrical and Electronics Engineering, Graduate School of Natural and Applied Sciences, Kilis 7 Aralık University, Kilis, Türkiye. / Department of Electrical and Electronics Engineering, Faculty of Engineering, Firat University, Elazig, Türkiye)

3:55 – 4:10 PM

Investigation Contact- and Contact-Free Wear Resistance of Titanium for Biomedical Applications: Correlation with Wear Depth and Volume Loss

Speaker
Efe Çetin Yılmaz (Department of Control Systems Electrical and Electronic Engineering, Engineering and Architecture Faculty, Kilis 7 Aralık University, Kilis, Türkiye)

4:10 PM

2:40 PM

2:40 – 3:40 PM

Biology Biochemistry and Pharmacology

Session | **Location:** Virtual Room, VCR/1-4 |

Convener: Cemil Bayram (Department of Pharmacology and Toxicology, Faculty of Veterinary, Ataturk University, Erzurum, Türkiye)

2:40 – 2:55 PM

Gross and Micromorphological Evaluation of Yak (Bos Grunnies) Hindlimb Muscle Under Refrigeration and Freezing Conditions

Speaker

Nazgul Imanberdieva (Faculty of Sciences Department of Biology, Kyrgyz-Turkish Manas University, Bishkek, Kyrgyzstan)

2:55 – 3:10 PM

Study of Elemental (Micro- and Macro-) Nutrient Content in Dracocephalum ıMberbe Bunge from the Alai Range, Kyrgyzstan

Speaker

Nurgul Ermekova (Department of Biotechnology, Institute Of Graduate Studies, Kyrgyz Turkish Manas University)

3:10 – 3:25 PM

Effect of Temperature on the Structural and Thermal Properties of Perna Viridis Shells

Speaker

Rosnah Nawang (Nanomaterial Syntesis and Characterization Laboratory, Institute of Nanoscience and Nanotechnology, Universiti Putra Malaysia, Serdang Selangor, Malaysia)

3:25 – 3:40 PM

The Study and Methodological Support for the Development of Natural Science Competencies in 5th-Grade Students of Secondary School No. 117 Named After Ch. Aitmatov in Bishkek

Speaker

Gulnara Sharshenalieva (Department of General Biology and Technology of its Teaching, Institute of Natural Sciences, Kyrgyz State University named after I. Arabaev, Bishkek, Kyrgyz Republic)

3:40 PM

2:40 PM **1.16.**

2:40 – 4:10 PM

Nano Frontiers: Materials and Applications

Session | **Location:** Virtual Room, VCR/1-2 |

Convener: Emir Çepni (Department of Electrical and Electronics Engineering, Faculty of Engineering, Atatürk University, Erzurum, 25240, Türkiye)

2:40 – 2:55 PM

Enhanced Salinity Detection Using Zinc Oxide Nanorod Coated Tapered D-Shape Plastic Optical Fibers

Speaker

Siti Halma Johari (Fakulti Teknologi dan Kejuruteraan Elektronik dan Komputer, Universiti Teknikal Malaysia Melaka)

2:55 – 3:10 PM

Fe-Pt Nanoparticles: Synthesis and Characterization

Speaker

Zhazgul Kelgenbaeva (Institute of Chemistry and Phytotechnology, National Academy of Sciences of the Kyrgyz Republic, 720071, Bishkek, Kyrgyzstan)

3:10 – 3:25 PM

Pharmacological Properties of Curcumin-Encapsulated Nanoclays

Speaker

Shahriyar Karimdoust (Department of Geology, Payame Noor University, Ardebil, Iran)

3:25 – 3:40 PM

Zinc Oxide Nanostructure Buffer Layers for Improved Charge Transport and Efficiency in DSSC

Speaker

Juraina Md Yusof (Functional Nanotechnology Devices Laboratory, Institute of Nanoscience and Nanotechnology, Universiti Putra Malaysia, Malaysia)

3:40 – 3:55 PM

Improving the Pharmacological Properties of Curcumin by Nanoclay

Speaker

Shahriyar Karimdoust Betül(Department of Geology, Payame Noor University, Ardebil, Iran)

3:55 – 4:10 PM

Electrospun Carbon-Based Nanofibers for Advanced Material Applications

Speaker

Mohd Ali MAT NONG (Functional Nanotechnology Devices Laboratory (FNDL), Institute of Nanoscience and Nanotechnology Universiti Putra Malaysia, Serdang, Selangor, Malaysia.)

4:10 PM

3:15 PM **1.17.**

3:15 – 4:45 PM

Maths, Computation and Modeling

Session | **Location:** Virtual Room, VCR/1-5 |

Convener: Sinan Kul (Department of Computer Technologies, Vocational School of Technical Sciences, Atatürk University, Erzurum, Türkiye)

3:15 – 3:30 PM **Asymptotic Solution of Singular Perturbed Volterra-Type Integral Equations**

Speaker
Peyil Esengul kyzy (Department of Mathematics, Faculty of Sciences, Kyrgyz-Turkish Manas University, Bishkek, Kyrgyzstan)

3:30 – 3:45 PM **Demand Prediction in Textile Production: A Machine Learning-Based Approach**

Speaker
Mucize BELDEK TOMUK (Department of Industrial Engineering, Department of Production and Service Systems, Faculty of Engineering and Architecture, Eskisehir Osmangazi University, Eskişehir, Türkiye)

3:45 – 4:00 PM **Solution of Second Order Singular Perturbation Problem Using Cubic B-Spline Functions**

Speaker
Mehrdad LAKESTANI (Department of Applied Mathematics, University of Tabriz, Tabriz, Iran.)

4:00 – 4:15 PM

Development of AI-Machine Learning with the One Health Framework in the Prevention of Foodborne Disease in the "Program Makanan Bergizi Gratis Indonesia"

Speaker
I Made Dwi Mertha Adnyana (Department of Microbiology and Parasitology, Faculty of Medicine and Health Science, Universitas Jambi, Jambi, 36122, Indonesia)

4:15 – 4:30 PM

Numerical Solution of Singularly Perturbed Differential Equations Using Interpolation and Collocation

Speaker
Sedaghat Shahmorad (Department of Applied Mathematics, University of Tabriz, Tabriz, Iran.)

4:30 – 4:45 PM **Modelling Economic Variables in Offshore Oilwell Drilling**

Speaker
Dalmo S. Amorim Jr. (Department of Energy, IEE-USP, Institute of Energy and Environment, University of São Paulo, Brazil)

4:45 PM

3:40 PM **1.18.**

3:40 – 5:00 PM

Thermal and Fluid Science

Session | **Location:** Virtual Room, VCR/1-1 |

Convener: Mansur Mustafaoglu (Department of Nanoscience and Nanoengineering, Institute of Science, Atatürk University, Erzurum, Türkiye)

3:40 – 3:55 PM

Numerical Analysis of Heat Transfer in Laminar Flow with Star-Cross Section Channel and Central and Circular Pipes

Speaker
Mansur Mustafaoglu (Department of Nanoscience and Nanoengineering, Institute of Science, Atatürk University, Erzurum, Türkiye)

3:55 – 4:10 PM

The Effect of Fractal Phenomena on the Thermal Conductivity of Nanofluids

Speaker
Bahman rahmatinejad (Department of Mechanical Engineering, Technical and Vocational University (TVU) Tehran, Iran)

4:10 – 4:25 PM

Design and Thermodynamic Analysis of a Geothermal-Based Tri-Generation System for Simultaneous Production of Power, Fresh Water, and Domestic Hot Water

Speaker
Yaser Shokri (Department of Mechanical Engineering,Faculty of Engineering, University of Tabriz, Tabriz, Iran)

4:25 – 4:40 PM

Application of Dynamic Light Scattering Method in Nanofluids

Speaker
Bahman rahmatinejad (Department of Mechanical Engineering, Technical and Vocational University (TVU) Tehran, Iran)

4:40 – 5:00 PM

Use of Nanoparticles for Drilling Fluid in Petroleum Industry

Speaker
Abdollah Esmaeili (Geosciences Institute (IG/UFPA), Faculty of Geology, Universidade Federal do Pará (UFPA), Belém, PA, Brazil)

5:00 PM

3:50 PM **1.19.**

3:50 – 4:50 PM

Biology Biochemistry and Pharmacology

Session | **Location:** Virtual Room, VCR/1-4 |

Convener: Cemil Bayram (Department of Pharmacology and Toxicology, Faculty of Veterinary, Ataturk University, Erzurum, Türkiye)

3:50 – 4:05 PM

~~Quantitative Characterization of Essential Micro- and Macronutrients in Thymus ıNcertus Klok from the Alai Range, Kyrgyzstan~~

Speaker

Bakyt Borkoev (Department of Chemical Engineering, Faculty of Engineering, Kyrgyz-Turkish Manas University, Bishkek, Kyrgyz Republic)

4:05 – 4:20 PM

Therapeutic Potential of Ginseng Against Cancer Exosome-Induced Toxicity in Neuronal and Endothelial Cells

Speaker

Yunus Emre Aydın (Department of Medical Pharmacology, Faculty of Medicine, Şeyh Edebali University, Bilecik, Türkiye)

4:20 – 4:35 PM

Remediation of Heavy Metal and Dye Pollution in Kyrgyzstan Using Nanotechnological and Biological Methods

Speaker

Fatma Melike YEŞİLYURT (Department of Biology, Faculty of Science, Kyrgyz-Turkish Manas University, Bishkek, Kyrgyz Republic)

4:35 – 4:50 PM

~~Comparative Assessment of Micro- and Macronutrient Profiles in COusınıa Carduncellorıdea Regel & Schmalh from the Alai Range, Kyrgyzstan~~

Speaker

Kalipa Salieva (Department of Chemical Engineering, Faculty of Engineering, Kyrgyz-Turkish Manas University, Bishkek, Kyrgyz Republic)

4:50 PM

4:20 PM **1.20.**

4:20 – 5:20 PM

Electronics and Devices

Session | **Location:** Virtual Room, VCR/1-2 |

Convener: Kaan Can (Department of Electrical and Electronics Engineering, Faculty of Engineering, Ataturk University, Erzurum, Türkiye)

4:20 – 4:35 PM

Methane Detection from Food Waste Digestion Using Titanium Dioxide-Graphene Gas Sensor with IOT Integration

Speaker

Adam Zafry (Central for Telecommunication Research and Innovation (CeTRI), Faculty of Electronics & Computer Technology & Engineering, Universiti Teknikal Malaysia Melaka, 76100 Durian Tunggal, Melaka, Malaysi)

4:35 – 4:50 PM

Development of a Sensor Array (MQ2, MQ4 and MICS5524) for Methane Gas Detection with IOT-based Monitoring

Speaker

AFIQ IRHAM (Central for Telecommunication Research and Innovation (CeTRI), Faculty of Electronics & Computer Technology & Engineering, Universiti Teknikal Malaysia Melaka, 76100 Durian Tunggal, Melaka, Malaysia)

4:50 – 5:05 PM

Comparison of Metal-Oxide Semiconductor Sensors for Ethanol Detection at Room Temperature

Speaker

Raja Ahmad Arifikri Raja Ismail (Central for Telecommunication Research and Innovation (CeTRI), Faculty of Electronics & Computer Technology & Engineering, Universiti Teknikal Malaysia Melaka, 76100 Durian Tunggal, Melaka, Malaysia)

5:05 – 5:20 PM

Comparison of Fabricated TiO2 Gas Sensor with MQ135 for Spoiled Fruit Detection

Speaker

Yudesh Kumar Kumara Raja (Department of Electronic Industry, Faculty of Electronics & Computer & Engineering,Universiti Teknikal Malaysia Melaka, 76100 Durian Tunggal, Melaka, Malaysia)

5:20 PM

5:30 – 7:00 PM

5:30 PM

Special Session

Session | **Location:** Virtual Room, VCR/1-1 |
Convener: Kaan Yeşilyurt (Syntagra)

5:30 – 7:00 PM

An Integrated Web-Based System for Managing MEDEK, MÜDEK, and YÖKAK Accreditation Processes

Speaker

Mahmut Yeşilyurt (Department of Computer Technologies, İzmir Kavram Vocational School, İzmir, Türkiye)

7:00 PM

KEYNOTE SPEAKERS

Ahmad Ali



Senior Assistant Professor in the Department of Life Sciences

Head of the Molecular Biochemistry Laboratory at University of Mumbai

University of Mumbai
India

Dr. Ahmad Ali is currently working as Assistant Professor (Senior) in the Department of Life Sciences, University of Mumbai, Mumbai, India. Earlier he worked in the National Institute of Pharmaceutical Education and Research (NIPER). He studied at Jamia Hamdard, New Delhi for MSc Biochemistry and at University of Mumbai for PhD degree in Life Sciences. He has over 18 years of teaching and research experience. Presently he is heading the Molecular Biochemistry Laboratory in the Department where he is supervising MSc and PhD students. His areas of research are Protein and DNA Biochemistry with special contributions on Glycation of biomolecules, DNA damage, antiglycating and anti-aggregating properties of natural products. He has also made significant contributions in the area of traditional medicines and their therapeutic applications especially antidiabetic and anti-inflammatory potentials. Cyanobacterial systems are another thrust area in his lab where researchers are exploring various applications of these organisms in the field of bioremediation, cosmetics and health benefits. He has received several extramural grants from Government and private funding agencies. He has collaborators from National and International laboratories. He is also a recipient of EMBO Travel Grant to attend European Molecular Biology Organization (EMBO) Research Course and CSIR Travel grant to attend International conference. Recently he was invited for Erasmus Mobility program by the University of Agricultural Science and Veterinary Medicine at Cluj-Napoca, Romania. He is serving as the Reviewer and member of Editorial board of various international journals like Chemosphere, Frontiers in Plant Sciences and Microbiology, Glycobiology, International Journal of Biological Macromolecules, and other journals of Elsevier, Frontiers, Springer etc. He has contributed more than 75 research articles in peer-reviewed national and international journals. He is also author of one book and more than 30 book chapters from Springer, Taylor & Francis and Elsevier publishing houses. He has presented his work in many international and national conferences as Invited Speakers and Resource persons. He has also worked as a Member of the organizing committee for many of these conferences. Recently he was invited by the University of Debrecen, Debrecen, Hungary as a visiting Faculty to interact with the researchers from the University.

Faiz Arith



Manager at the Centre of Telecommunication Research and Innovation (CETRI)

Senior Lecturer and Head of the Micro and Nano Electronic Research Group at UTeM

Universiti Teknikal Malaysia Melaka
Malaysia

Dr Faiz Arith received the B. Eng. in Electrical & Electronic Engineering from the University of Fukui, Japan. Then, he obtained an M.Sc in Microelectronic from the National University of Malaysia and subsequently a Ph.D. in Semiconductor Materials and Devices from Newcastle University, United Kingdom. Currently, he is the Manager of the Centre of Telecommunication Research and Innovation and the Head of the Micro and Nano Electronic Research Group at Universiti Teknikal Malaysia, Melaka, Malaysia. His main research interest is semiconductor materials and devices including silicon carbide power semiconductor devices, solar cells, advanced packaging and optoelectronics devices. He has authored three book chapters, and more than 50 articles, and has won several international innovation competitions. To date, more than 20 research grants with a total value of more than USD 900,000 have been successfully secured as a researcher. Of these, 3 grants are from international agencies, Semiconductor Components Industries LLC (USA) and the Royal Society of Chemistry (UK) where he is the lead researcher. In addition, he also serves on the Editorial Board of Engineering Research Express (ERX), IOP UK Publisher and the Journal of Telecommunication, Electronic and Computer Engineering (JTEC). Apart from that, he has been awarded the Senior Member level in IEEE. Dr Faiz Arith is the recipient of the Excellent Service Award in 2013 and 2021 and several academic prestigious awards

Zainab Yunusa



Assistant Professor at Department of Electrical Engineering

University of Hafr Al Batin
Saudi Arabia

Zainab Yunusa has completed her PhD from Universiti Putra Malaysia, Malaysia. She has been working in the Department of Electrical Engineering, Bayero University Kano as a Senior Lecturer. She is currently an Assistant Professor in the Department of Electrical Engineering University of Hafr Al Batin Saudi Arabia. She has published many ISI indexed journals and presented papers in international conferences. Her research interests include Nanomaterials for electronics application and R.F microwave devices and applications.

Prathap Singh S



Assistant Professor at Department of Mechanical Engineering

St. Joseph's Institute of Technology
India

Dr. S. Prathap Singh is an accomplished researcher and educator specializing in mechanical engineering, with a strong focus on additive manufacturing, functionally graded materials, tribology, machining, and mathematical optimization. He is currently serving as an Assistant Professor in the Department of Mechanical Engineering at St. Joseph's Institute of Technology, Chennai.

With a Ph.D. from Anna University, his research revolves around the mechanical testing, characterization, tribological, and machining studies of functionally graded aluminum alloy A356 reinforced with silicon nitride. He has published 40 Scopus and Web of Science, and 9 Book Chapters extensively in high-impact international indexed journals and has a notable citation record.

Dr. Prathap Singh has guided several student research projects on advanced materials and manufacturing processes. He is an active reviewer for reputed journals and has delivered keynote lectures at international conferences. Additionally, he holds multiple patents and has contributed to consultancy projects. His professional memberships include ISTE and IAENG

Hamed Niroumand



Professor at Department of Geotechnical Engineering

Gdansk University of Technology
Poland

Dr. Hamed Niroumand is a faculty member and a professional engineer in geotechnical engineering. He is Associate Professor at Gdańsk University of Technology. He is 40 years old and has been working in his field since 2008. He has published 47 books, 350 journal and conference papers, and 45 patents in various countries such as Iran, USA, Germany and etc. His research topics include foundations, earth anchors, heritage and earth buildings, subsidence and sinkholes, numerical analysis, and nanotechnology. He has received over 20 awards and medals for his inventions and research, such as the best researcher award in the Ministry of Road and Urban Development (MRUD) in 2016. One of his notable achievements is receiving the 1st rank for youngest researcher in Iran for three consecutive years (2011, 2012, and 2013). He has also published numerous books on foundations, earth anchors, and heritage and earth buildings with prestigious publishers such as Elsevier, Taylor & Francis, and CRC. He has led and participated in various geotechnical projects and consulting and construction companies as a company CEO, project manager and professional engineer. He has organized and directed 35 international/national conferences of civil engineering and served as an editorial team member and reviewer for more than 100 scientific journals. He has held various academic positions such as head of department, and vice-chancellor for academic and research affairs in the university, and director of the strategic council for transportation infrastructures in the MRUD. He is the founder and chair of the Niroumand Research Group (NRG) since 2017, where he works with his master, PhD and post-doc students. He is passionate about teaching and mentoring students and collaborating with other researchers and professionals in his field in various countries.

Dr. Md. Habibur Rahman



Faculty of Health Sciences

Novel Global Educational Foundation
Australia

Md. Habibur Rahman is Registered Pharmacist and a member of the Novel Global Community Education Foundation (Australia). He earned his Ph.D. in Medical Science, and has contributed his expertise to several leading pharmaceutical organizations. His research is primarily focused on neuroscience, particularly the molecular mechanisms underlying clinical dementia, with emphasis on biomarker discovery and targeted diagnostic strategies. In addition to his neuroscience work, Dr. Rahman is an expert in molecular biology, with extensive experience in gene expression analysis, oxidative stress pathways, and neuroinflammation. He has been recognized among the top 2% of scientists worldwide (Stanford University, citation-based global ranking) for his impactful contributions. Dr. Rahman is also an active scientific communicator and public speaker, frequently presenting at international conferences and academic forums. He serves as a peer reviewer for several high-impact journals and is involved in multiple ongoing research collaborations in neuroscience and molecular medicine.

Dalmo S. Amorim Jr.



Senior Researcher in the Department of Energy

University of São Paulo
Brazil

Dr. Dalmo S. Amorim is a seasoned expert in the field of petroleum engineering, possessing a wealth of experience and knowledge. Currently a postdoctoral researcher in Energy at IEE-USP, Brazil, he has already earned significant educational accolades, including a PhD in Energy from IEE-USP, a Master's degree in Mineral Sciences from EP-USP, and a bachelor's Degree in Mining Engineering from EP-USP. He is a specialist in Drilling Engineering, a title acquired at Petrobras. Dalmo's professional journey spans over four decades, with roles at National Oilwell Varco and its affiliates, where he excelled as a Petroleum Engineer, becoming a Global Training Instructor on four continents and contributing to Engineering Support in various international capacities. Dr. Prof. Dalmo is also a professor of Petroleum Engineering, with expertise in Drilling Economics and Training Development. He is also a journal reviewer and a published author with contributions to leading journals and conferences. With an extensive background, he brings a deep understanding of drilling operations and a commitment to sharing his insights. He has presented his work in national and international conferences as an invited speaker.

Ismayadi Ismail



Researher at Nanomaterials Synthesis and Characterization Laboratory, Institute of Nanoscience and Nanotechnology

Universiti Putra Malaysia
Malaysia

Dr. Ismayadi Ismail is a researcher at the Institute of Nanoscience and Nanotechnology (ION2), Universiti Putra Malaysia (UPM), Malaysia and is based in the Nanomaterials Synthesis and Characterization Laboratory. He earned a B.Sc. (Hons.) in Materials Science (2001), an M.Sc. in Nanomaterials (2007), and a Ph.D. (with Distinction) in Magnetic Materials (2012). His research covers functional nanomaterials, magnetic and dielectric composites, and hybrid carbon architectures including graphenated carbon nanotubes for EMI shielding, microwave absorption, and energy-related devices. He has published 185 Scopus-indexed documents with a Scopus h-index of 29. He also served as Technical Manager and Approved Signatory for MS ISO/IEC 17025 laboratory accreditation, and holds editorial roles as Associate Editor of Nanoera and Editor of the Malaysian Journal of Microscopy. He reviews for journals such as Materials Letters and IEEE Transactions on Magnetics, and has delivered plenary and keynote lectures at national and international scientific meetings.

.

Peyil Esengul Kyzy



Professor of Mathematics, Faculty of Sciences

Kyrgyz-Turkish Manas University
Kyrgyzstan

Peyil Esengul Kyzy is an Assistant Professor of Mathematics at Kyrgyz-Turkish Manas University. She earned her B.Sc. in Applied Mathematics and Informatics, M.Sc. in Mathematics, and Ph.D. in Mathematics from Kyrgyz-Turkish Manas University. Her doctoral research focused on singularly perturbed parabolic differential equations and asymptotic analysis, under the supervision of Prof. Asan Omuraliev. Her research interests include singular perturbation theory, boundary layer problems, asymptotic methods, numerical analysis, and applied differential equations. Dr. Peyil Esengul Kyzy has published extensively in international peer-reviewed journals indexed in SCI, including Filomat, Soft Computing, Differential Equations, and Lobachevskii Journal of Mathematics. She has also contributed a book chapter published by IntechOpen and actively participates in international and national scientific conferences.

CONTRIBUTIONS

1.
ABSTRACTS

1.1.
KEYNOTE SPEECHES

Prevention and Mitigation Strategies for Sinkholes Using Soil Improvement Techniques

Hamed Niroumand [1]

1 Department of Geotechnical and Hydraulic Engineering, Faculty of Civil and Environmental Engineering, Gdansk University of Technology, Gdansk, Poland.

Corresponding Author: *niroumand.mrud@gmail.com*

Abstract

Sinkholes are a global challenge, and several countries are affected by them. Timely identification of sinkholes and monitoring of subsurface soil conditions are highly important. However, the main challenge for different countries lies in the methods of preventing and mitigating sinkholes. Accordingly, considering the distribution of sinkholes in various countries, this paper addresses the methods of sinkhole prevention and mitigation. The main approach in this paper is the use of soil improvement techniques in relation to sinkholes.

Keywords:

Sinkholes, Soil Improvement, Prevention Strategy

Graphenated Carbon Nanotubes: Bridging 1D–2D–3D Carbon for Advanced Functional Systems

Ismayadi Ismail [1]

1 Nanomaterials Synthesis and Characterization Laboratory, Institute of Nanoscience and Nanotechnology, Universiti Putra Malaysia, 43400 Serdang, Selangor Darul Ehsan, Malaysia

Corresponding Author: *ismayadi@upm.edu.my*

Abstract

This keynote presents a 10-year journey into graphenated carbon nanotubes (g-CNT), an advanced hybrid carbon architecture where graphene foliates emerge directly from the walls of carbon nanotubes to form an ultra-light and highly conductive three-dimensional aerogel. The talk invites the audience to explore how this unique structure evolved from fundamental discovery into a platform material for next generation energy and electronic systems. The keynote begins with the scientific motivation behind hybrid carbon design. It highlights the performance limits of graphene and carbon nanotubes when they are used on their own, including restacking, low interfacial activity, restricted charge transport pathways, and limited mechanical anchoring. These gaps form the basis for the development of a new architecture that integrates one dimensional conduction, two-dimensional surface interaction, and three-dimensional porosity. The talk then traces the experimental milestones from the first cotton like g-CNT aerogel produced using FCCVD to the introduction of sustainable precursors, morphology tuning, and refinement of the unzipping and regrowth mechanism. This foundation enables a deeper understanding of conductivity, surface polarization, ion transport, and mechanical behavior. The application segment showcases how g-CNT transitions from a laboratory curiosity to a functional material. Case studies include platinum free counter electrodes for dye sensitized solar cells, conductivity enhanced TiO_2 photoanodes, flexible supercapacitors built on MoS_2 and WS_2 nanowalls, and emerging opportunities in electromagnetic interference shielding for the 5G ecosystem. Each example highlights how the hierarchical carbon network improves device performance, stability, and scalability. The keynote concludes with a forward-looking perspective on hybrid carbon systems. It outlines a vision where architectured carbon materials can be tailored for specific functions, integrated into industrial composites, and paired with future two dimensional materials. The journey of g-CNT represents an early and significant step toward this future.

Keywords:

Carbon Materials, Hybrid Nanostructures, Graphenated Carbon Nanotubes, Energy and Electronic Devices, Hierarchical Conductive Networks

AI and Bioinformatics Synergy: Transforming Data Into Precision Healthcare

Md. Habibur Rahman [1]

1 Department of Health Sciences, Novel Global Educational Foundation, NSW, Australia

Corresponding Author: *globaldreamer111990@gmail.com*

Abstract

By transforming complicated, high-dimensional biomedical data into clinically actionable insights across the care continuum, the convergence of bioinformatics and artificial intelligence is transforming healthcare. In fields including oncology, neurology, and autoimmune illnesses, AI-driven algorithms now incorporate multi-omics profiles, medical imaging, and electronic health records to enable earlier diagnosis, molecular disease stratification, and customized treatment selection. Simultaneously, deep learning and machine learning-enhanced bioinformatics pipelines speed up in silico drug screening, biomarker validation, and target discovery, reducing development times and increasing the success rate of translational research. These developments enable intelligent clinical decision support systems that enhance rather than replace doctors by offering risk prediction, therapeutic optimization, and workflow automation. This improves patient outcomes and system efficiency. However, in order to minimize algorithmic bias and guarantee that AI-enabled bioinformatics serves a variety of patient populations, realizing this transformational potential necessitates systematic attention to data quality, model interpretability, regulatory and ethical frameworks, and equitable deployment.

Keywords:

Bioinformatics, Biomarker Discovery, Multi-Omics Integration, Machine Learning

Applications of Carbon Based Nanomaterials in Microwave Devices

Zainab Yunusa [1]

1 Department of Electrical Engineering, University of Hafr Al Batin, Saudi Arabia

Corresponding Author: *zee2yunusa@gmail.com*

Abstract

Nanomaterials are materials in the nanometer scale from 1 to 100 nm. Their numerous advantages which includes miniaturization and enhanced energy efficiency has made them popular to be deployed in many industrial applications including electronics, medicine, energy, environment, materials and consumer products. In this paper, our focus will be how we can use carbon based nanomaterials in microwave devices such as antenna. Carbon based nanomaterials are used in microstrip patch antennas to create conductive films for the patch, ground plane or feedline so as to enhance the bandwidth and return loss. Recent advances in carbon nanomaterials such as carbon nanotubes, graphene, graphene nanoribbons (GNRs) and other green carbon nanomaterials from organic sources such as rice husk and carbon charcoal have shown excellent results when deployed in electronics, bioelectronics, optoelectronics and photonic applications. In this paper we will present some case studies on development of microstrip patch antenna applications that proved to show excellent results with improved antenna performance parameters.

Keywords:

Carbon-Based Nanomaterials, Microwave Devices,

Fabrication and Characterization of Functionally Graded A356 Alloy and Its Composite

Prathap Singh S[1]

1 Department of Mechanical Engineering, St. Joseph's Institute of Technology, CHennai, India

Corresponding Author: *prathap.singh50@gmail.com*

Abstract

The primary goal of the study is to create an Aluminum A356 Functionally Graded alloy (A356 FG alloy) by vertical centrifugal casting after stir casting. After T6 heat treatment at various aging temperatures, the optimal aging temperature was determined to be 165℃. Using Vickers' microhardness instrument, the hardness was determined to be 50% greater in the higher hardness zone (Outer zone) for the sample aged at 165℃ compared to the as-cast Aluminum functionally graded alloy. Also, the tensile strength evaluation showed the highest tensile strength of 101.487 N/mm² in the 165℃ aged higher hardness zone. The microstructure was analyzed, and it was discovered that the heat-treated condition contained spheroidized eutectic silicon and magnesium silicide particles. The secondary investigation spatially dispersed high-hardness silicon nitride particles with Aluminum A356 alloy via vertical centrifugal casting to reinforce A356 with 10 wt.% Si_3N_4 Functionally Graded Composite (A356-10 wt.% Si_3N_4 FG Composite). On the fabricated FG composite, the optimal T6 heat treatment conditions obtained from the A356 FG alloy were implemented. Using Vicker's microhardness instrument, the hardness behavior was assessed. It was determined that the exterior surface exhibited a superior microhardness of 182 HV, which constituted a 73% increase compared to the interior surface. Also, the tensile strength evaluation showed the highest tensile strength of 131.067 N/mm² in the wealthy ceramic zone. The phase analysis and particle dissemination of the gradient were validated in the radial direction.

Keywords:

Aluminium Functionally Graded Composites, Centrifugal Casting Technique, Vicker'S Microhardness

A Shift Toward Simplicity: Current Progress, Technical Challenges, and Future Prospects of ETL-Free Perovskite Solar Cells

Faiz Arith [1], Fauziyah Salehuddin [1], Nabilah Ahmad Jaluluddin [1]

1 Faculty of Electronics and Computer Technology and Engineering, Universiti Teknikal Malaysia Melaka, Hang Tuah Jaya, Durian Tunggal, 76100, Melaka, Malaysia

Corresponding Author: *faiz.arith@utem.edu.my*

Abstract

This work presents a comprehensive overview of the development of ETL-free perovskite solar cells, highlighting their progress, current challenges, and prospects. By eliminating the electron transport layer (ETL), these devices simplify the solar cell architecture, reducing fabrication complexity and cost while maintaining competitive performance. The discussion begins with the fundamental principles and material innovations that have enabled ETL-free designs, including advances in perovskite composition, interface engineering, and device stability. Key obstacles such as charge extraction efficiency, interfacial recombination, and long-term operational stability are examined in detail. Various fabrication strategies, including surface passivation and multifunctional buffer layers, are compared for their effectiveness in addressing these issues. Looking ahead, the focus turns to scalable manufacturing approaches, improved reliability under real-world conditions, and exploration of novel perovskite compositions to enhance performance and commercial viability. Overall, the work aims to guide researchers toward simpler, more efficient, and cost-effective perovskite solar cells based on ETL-free architectures.

Keywords:

Charge Extraction, Device Stability, ETL-Free Perovskite Solar Cell, Fabrication Simplicity, Interface Engineering

Unim-R Polyherbal Oil: Efficacy and Safety Assessment in Carrageenan and CFA-Induced Arthritis with Cytokine Profiling

Pawan Sharma [1], Binita Mandal [1], Falek Bamme [1], Nikhat Shaikh [2], Tabassum Khan [3], Ahmad Ali [4]

1 Department of Life Sciences, University of Mumbai, Vidyanagari, Mumbai 400098, India
2 Regional Research Institute of Unani Medicine, Kharghar, New Mumbai 410210, India
3 Department of Pharmaceutical Chemistry & Quality Assurance, SVKM's Dr. Bhanuben Nanavati College of Pharmacy, Vile Parle(W), Mumbai 400056, India
4 Department of Life Sciences, University of Mumbai, Vidyanagari, Mumbai, India

Corresponding Author: *ahmadali@mu.ac.in*

Abstract

Arthritis is a chronic inflammatory condition that demands safer and more effective therapeutic alternatives. The present study investigated the anti-arthritic potential of UNIM-R, a polyherbal dermal oil formulated using Eucalyptus globulus oil, Ferula asafoetida resin, Matricaria chamomilla stem, Styrax benzoin resin, and Sesamum indicum seeds. The formulation was evaluated in carrageenan-induced paw oedema and Complete Freund's Adjuvant (CFA)-induced arthritis models in rats. Acute and chronic dermal toxicity studies were conducted in accordance with OECD guidelines to assess safety. In the CFA model, post-treatment profiling of key inflammatory biomarkers included TNF-α, IL-10, IFN-γ, hyaluronic acid, and PGE2. UNIM-R significantly attenuated carrageenan-induced oedema and improved clinical and biochemical indicators of inflammation in the CFA model. Cytokine analysis revealed marked suppression of pro-inflammatory mediators (TNF-α, IFN-γ, PGE2, hyaluronic acid) alongside an increase in the anti-inflammatory cytokine IL-10. The therapeutic response was comparable to standard diclofenac gel, demonstrating robust anti-inflammatory and immunomodulatory activity. Toxicity evaluations confirmed the absence of adverse dermal reactions, supporting its safety for topical application. These findings position UNIM-R as a promising polyherbal dermal intervention for arthritis management.

Keywords:

Polyherbal Formulation, Anti-Arthritic, CFA Model, Cytokine Modulation, OECD Toxicity Assessment

Asymptotic Solution of Singular Perturbed Volterra-Type Integral Equations

Asan Omuraliev [1], Peyil Esengul Kyzy [2], Ella Abylaeva [3]

1 I. Razzakov Kyrgyz State Technical University, Bishkek, Kyrgyzstan
2 Department of Mathematics, Faculty of Sciences, Kyrgyz-Turkish Manas University, Bishkek, Kyrgyzstan
3 Department of Applied Mathematics and Informatics, Faculty of Sciences, Kyrgyz-Turkish Manas University, Bishkek, Kyrgyzstan

Corresponding Author: *peyil.esengul@manas.edu.kg*

Abstract

The structure of the boundary layer in the asymptotics of a singularly perturbed Volterra-type integral equation is determined by the kernel of the integral equation. Researchers studying singularly perturbed integral equations have transformed them into integro-differential equations by differentiation, and then they have constructed the asymptotics. We will directly regularize the integral equation. To regularize the integral operator, we use the Dirac delta function, while other researchers using Lomov's method use integration by parts.

Keywords:

Integral Equation, Asymptotic Solution, Volterra-Type Integral Equations, Singular Perturbed

1.2.
ATTENDED POSTER PRESENTATIONS

Production of Low-Fat Mayonnaise Using Pomegranate Peel Powder and Evaluation of Its Physicochemical and Sensory Properties

Bahram Fathi-Achachlouei [1], Shayesteh Hassanloo [1], Fatemeh Ghannadiasl [1]

1 Department of Food Science and Technology, University of Mohaghegh Ardabili, Ardabil, Iran

Corresponding Author: *b_fathi@uma.ac.ir*

Abstract

In this study, Production and investigation of the physicochemical and sensory properties of low-fat mayonnaise using pomegranate peel powder was carried out. The objective of this research was to produce low-fat mayonnaise enriched with fiber and nutrients by replacing part of its fat content with pomegranate peel powder to develop a functional low-fat mayonnaise. The studied treatments included 4 formulations (Treatment1: Control, Treatment2-4: Mayonnaise containing 2%, 4% and 6% w/w pomegranate peel powders,respectively). Measurements of certain physicochemical properties such as pH, fat content, peroxide value, crude fiber content and total phenolic content (TPC), color and sensory properties were conducted over a 30-day storage period of the produced mayonnaise samples. The results of the statistical analysis showed that the addition of pomegranate peel powders in the production of low-fat mayonnaise had a significant effect on the physicochemical properties, sensory properties of the samples ($P< 0.05$). In terms of pH, the control treatment exhibited the lowest values compared to the enriched mayonnaise with pomegranate peel powders. The fat content of all produced low-fat sauces was lower than that of the control, with treatment 4 (containing 6% pomegranate peel powder) having the lowest fat content. Furthermore, treatment 4 exhibited the highest total phenolic content (TPC). Colorimetric results revealed that pomegranate peel powder directly influenced the redness and lightness intensity of the samples, increasing redness and reducing lightness. Moreover, pomegranate peel powder resulted in the greatest reduction in peroxide value and significantly delayed the formation of hydroperoxides ($P < 0.05$). The overall acceptability results from the sensory evaluation indicated that control sample received the highest scores in terms of sensory properties. In conclusion, the use of valuable agricultural by-products, including pomegranate peel powders, proved to be an innovative and effective strategy for producing low-fat mayonnaise enriched with fiber and nutrients.

Keywords:

Low-Fat Mayonnaise, Fiber, Pomegranate Peel Powder, Physicochemical and Sensory Properties

QSPR Study on Photo Oxidation Reaction of Aromatic Micro Pollutants Using the Genetic Algorithm - Support Vector Machine

Eslam Pourbasheer[1], Maryam Nouri Majd[1]

1 Department of Chemistry, Faculty of Science, University of Mohaghegh Ardabili, Ardabil, Iran

Corresponding Author: *e.pourbasheer@uma.ac.ir*

Abstract

Aromatic micropollutants (AMPs) are a group of organic chemical compounds that have an aromatic ring structure and may be substituted with various functional groups such as hydroxyl, amino, nitro or halogen. These pollutants are found in very low concentrations in surface water, ground water and waste water. Investigating the relationship between the chemical structure of Aromatic micropollutants and their reactivity in photocatalytic processes is crucial to improve the efficiency of removal methods and predict the environmental behavior of these pollutants. Developing models based on the structural features of AMPs can help predict the rate of degradation and understand their ultimate fate in nature. In this study, quantitative structure-activity relationship (QSAR) models were developed to predict the photooxidation reaction of aromatic micro-pollutants (AMPs) using the multiple linear regression (MLR) and support vector machine (SVM). The dataset consisted of 30 compounds, were divided into two training and test subsets by hierarchical clustering method. Genetic algorithm (GA) was used as a feature selection tool to identify the most relevant molecular descriptors. Model validation was performed using Y- randomization test, cross-validation, and external test set methods. The genetic algorithm- multiple linear regression (GA-MLR) model with three selected descriptors showed favorable statistical parameters (R2train=0.822, R2test=0.920). Comparison of the models' performance shows that, GA-SVM provided accurate results with strong statistical parameters for the training and test data sets (R2train=0.939, R2test=0.922). Analysis of the results showed that spheroid, atomic masses, and also difference between partial positively- and negatively-charged surface areas, of molecules play a decisive role in their activity. The developed models can be used as efficient tools in the targeted design of high-performance AMPs and understanding its photooxidation reaction behavior. The comparison between different models, allowed us to examine the advantages and limitations of linear and nonlinear models in analyzing the structure-reactivity relationship of Aromatic micropollutants.

Keywords:

QSAR, Support Vector Machine, Aromatic Micropollutants, Photooxidation

1.3.
ORAL PRESENTATIONS

Comparison of Fabricated TiO2 Gas Sensor with MQ135 for Spoiled Fruit Detection

Yudesh Kumar Kumara Raja [1], Siti Amaniah Mohd Chachuli [2]

1 Department of Electronic Industry, Faculty of Electronics & Computer & Engineering, Universiti Teknikal Malaysia Melaka, 76100 Durian Tunggal, Melaka, Malaysia

2 Central for Telecommunication Research and Innovation (CeTRI), Faculty of Electronics & Computer Technology & Engineering, Universiti Teknikal Malaysia Melaka, 76100 Durian Tunggal, Melaka, Malaysia

Corresponding Author: *yudesh011021@gmail.com*

Abstract

This study presents a cost-effective and innovative ethylene gas detection system designed to monitor fruit ripening and minimize postharvest losses. The system integrates a commercial MQ135 gas sensor with a single fabricated TiO_2-based sensor to detect ethylene gas through voltage variations under controlled parameters. The TiO_2 sensor was fabricated and characterized to evaluate its electrical properties, exhibiting a resistance value of 557.90 MΩ, indicating high sensitivity and stability. Experiments were conducted inside a custom-designed 3D-printed gas chamber at room temperature. Five selected fruits such as banana, mango, papaya, pear, and apple with weight of 20 gram were tested and monitored continuously for 85 hours. Real-time voltage data were transmitted to the Blynk Internet of Things (IoT) platform and automatically recorded in Google Sheets for continuous analysis. A cobalt(II) chloride test paper was also used as a colorimetric indicator to provide a visual confirmation of ethylene gas presence. Based on sensing response analysis, the TiO_2 sensor exhibited superior performance compared to the MQ135 sensor across all fruit samples. The sensing responses for MQ135 and TiO_2 were 96.97% and 95.45% for banana, 97.50% and 98.79% for apple, 82.14% and 87.88% for papaya, 84.00% and 90.91% for pear, and 74.19% and 82.42% for mango, respectively. The sensing response for MQ135 was approximately 96.97%, 97.50%, 82.14%, 84.00%, and 74.19% for banana, apple, papaya, pear, and mango, respectively. Whereas TiO_2 sensor exhibited sensing response of 95.45%, 98.79%, 87.88%, 90.91%, and 82.42% for banana, apple, papaya, pear, and for mango, respectively. These findings revealed that the fabricated TiO_2 sensor demonstrates better responsiveness and selectivity toward ethylene gas, making it a more efficient and reliable choice for real-time fruit ripening and spoilage monitoring through IoT-based smart sensing technology.

Keywords:

Ethylene Gas Detection, TiO_2 Sensor, MQ135 Gas Sensor, Internet of Things (IoT), Fruit Ripening Monitoring

Preparation of WO3-X Nanoparticles by UVA-Irradiation for Colorimetric Sensing of Cr(VI)

Ali Khodayari [1], Habibollah Eskandari [1], Haidar Abd Ali Abdulsada [1]

1 Department of Chemistry, Faculty of Basic Sciences, University of Mohaghegh Ardabili, Ardabil 56199-11367, Iran

Corresponding Author: *h_eskandari2001@yahoo.com*

Abstract

Nanomaterials based on WO3-x have emerged as highly promising materials due to their unique chemical and physical structures. The intentional introduction of oxygen vacancies in these nanostructures significantly enhances their optical and electronic properties. For instance, they are used in the fabrication of optical and gas sensors, smart windows with photochromic capabilities, and photocatalytic systems for converting carbon dioxide into clean fuels [1-3]. Hexavalent chromium (Cr(VI)) is a highly toxic heavy metal ion widely used in industries such as stainless steel, automotive parts, and leather production. Its release into the environment poses severe risks, as it can contaminate groundwater and accumulate in aquatic organisms like fish, eventually entering the human body through consumption. Excessive intake of Cr(VI) is associated with serious health hazards, prompting strict regulatory limits in wastewater and food safety standards [4]. There is an urgent need for simple, rapid, and sensitive detection techniques. Based on the research presented, this study successfully developed a simple and effective colorimetric method for the precise determination of Cr(VI). The method is based on the direct reaction of Cr(VI) with WO3-x nanoparticles synthesized via a UVA irradiation method. Under UVA light irradiation in a hydrochloric acid solution containing choline chloride, WO3-x nanoparticles (blue color) were produced. The intensity of the color, which decreased proportionally with the concentration of Cr(VI), was monitored spectrophotometrically. The proposed method demonstrated a wide linear range for Cr(VI) quantification from 1 to 30 µM, making it suitable for detecting trace levels of Cr(VI) with limit of detection equal to 0.22 µM. The method exhibited excellent selectivity for Cr(VI) over other potential interfering ions. The practical applicability of this colorimetric sensor was validated by successfully determining Cr(VI) concentrations in various real water samples, including tap water, river water, and lake water.

Keywords:

UVA Irradiation, Preparation of WO3-X Nanoparticles, Cr(VI) Colorimetric Sensing

Tetrachloroperylene Dianhydride as a Simple and Capable Sensor; Case Study: Cyanide Anion and Primary Aliphatic Amines

Mohammad Reza Zamanloo [1]

1 Department of Applied Chemistry, Faculty of Science, University of Mohaghegh Ardabili, Ardabil, Iran

Corresponding Author: *mrzamanloo@uma.ac.ir*

Abstract

Persistent radical-anions generating electrochemically or photochemically offer an exciting platform for investigation due to easily generation, structure–stability correlation, colour modulation and etc. A wide range of applications including molecular magnets, sensors, polymerization initiators, CO2 reduction and etc., have been developed recently for these intermediates [1-3]. Carbonyl compounds such as diimides or dianhydrides possessing low-lying frontier orbitals and known as organic π-acids, participate generally in electron transfer (ET) processes which engender persistent radical-anions. Herein, tetrachloroperylene dianhydride (TCP) is presented as a simple and capable electron accepting material that generate its colourful radical anion. This capability was utilized as a powerful and selective colorimetric sensing method to identify and determine some analytes. Many different anions including CN-, Halide anions, SCN- and etc., as well as different types of amines were investigated as electron donor in solution ET to TCP. Upon exposer to CN- and primary aliphatic amines, TCP solution was changed to a colourful state enabled colorimetric identification and determination of these species. Only CN- could participate in ET to TCP in between twenty examined anions and only primary aliphatic amines in between different various amines perform such a redox reaction, made TCP as a selective sensing agent. The response time of emerging detectable coloration was immediate in the case of CN-, while the amines have a two-step interaction with the substrate comprising a fast complexation followed by ET process with a 3h period. The ET process was followed using absorption and emission along with H NMR spectroscopy techniques. In order to evaluate the effect of the chemical structure of TCP comprising chlorine atoms and anhydride functionality on the ET interaction, the pristine perylene dianhydride and two imide counterparts were also checked which did not showed any comparable results. The following figure illustrates a representative scheme for the thermal ET process.

Keywords:

Electron Transfer, Anion-Radical, Perylene Dianhydride, Amine, Cyanide.

Nitrogen-Doped Carbon Quantum Dots for Sensitive Colorimetric Assay of V(V)

Rabah Sabah Khamees [1], Habibollah Eskandari [1], Ali Khodayari [1]

1 Department of Chemistry, Faculty of Basic Sciences, University of Mohaghegh Ardabili, Ardabil 56199-11367, Iran

Corresponding Author: *h_eskandari2001@yahoo.com*

Abstract

Carbon and graphene quantum dots (CQDs and GQDs) are highly attractive for a wide range of applications due to their excellent characteristics, including high photoluminescence, tunable bandgap, water solubility, and biocompatibility. These nanomaterials exhibit strong quantum confinement and edge effects, which can be further modulated through surface functionalization with groups such as -OH, -COOH, and -NH_2. Their capacity to participate in electron transfer and radical scavenging reactions makes them particularly useful for developing novel sensing platforms [1-3]. Furthermore, their synthesis from cost-effective precursors like citric acid facilitates scalable production. Vanadium is extensively used in steel production and other industrial processes, leading to its environmental release, primarily through the combustion of fossil fuels. Among its various oxidation states, V(V) is notably more toxic than its reduced forms, posing significant risks to ecosystems and human health [4]. Vanadium's dual role as both an essential trace element and a potential toxin underscores the need for accurate monitoring. This work introduces an innovative approach for the colorimetric detection of V(V) using nitrogen-doped CQDs (N-CQDs), synthesized via the thermal treatment of a mixture of citric acid and 3,4-diaminobenzoic acid. The synthesized N-CQDs were characterized using appropriate microscopic and spectroscopic techniques. In the detection mechanism, V(V) oxidizes 3-methyl-2-benzothiazolinone hydrazone in an aqueous solution containing sodium dodecyl sulfate and hydrochloric acid to generate a diazonium cation. This cation then couples with the N-CQDs to form a pink-colored azo dye. A linear calibration curve for V(V) was established in the range of 1.8–240 µM. The method achieved a low detection limit of 0.9 µM and a relative standard deviation of 1.7–5.3%. An interference study confirmed the method's high selectivity. To validate its practical utility, the method was successfully applied to the analysis of various environmental water samples.

Keywords:

N-Doped Carbon Quantum Dots, Coupling Reaction, Colorimetric Vanadium Detection

Solution of Second Order Singular Perturbation Problem Using Cubic B-Spline Functions

Fevzi Erdoğan [1], Mehrdad Lakestani [2]

1 Department of Mathematics, Van Yüzüncü Yil University, Van, Türkiye
2 Department of Applied Mathematics, University of Tabriz, Tabriz, Iran

Corresponding Author: *mlakestani@gmail.com*

Abstract

This study addresses a second-order singularly perturbed problem using cubic B-spline functions. We first examine the properties of these functions and then introduce their dual basis for function expansion. Next, we construct an operational matrix of derivatives for the cubic B-splines. A hybrid scheme is developed to solve the problem efficiently. The numerical results demonstrate the effectiveness of the proposed method.

Keywords:

Cubic B-Spline Functions, Singular Perturbation Problem, Numerical Methods

Numerical Solution of Singularly Perturbed Differential Equations Using Interpolation and Collocation

Fevzi Erdoğan [1], Sedaghat Shahmorad [2]

1 Department of Mathematics, Van Yüzüncü Yil University, Van, Türkiye
2 Department of Applied Mathematics, University of Tabriz, Tabriz, Iran

Corresponding Author: *sshahmorad@gmail.com*

Abstract

Presented in this paper is a numerical method based on interpolation and collocation for solving singularly perturbed boundary value problems whose solutions exhibit boundary layers. First, the general properties of such singularly perturbed boundary value problems are discussed. Next, a Lagrange interpolation scheme using Chebyshev nodes, combined with collocation at same points, which yields a uniformly convergent approach for solving this class of equations were constructed. Numerical examples demonstrate the theoretical results in practice.

Keywords:

Numerical Solution, Interpolation, Collocation

Comparative Morphology of the Spleen in Mammals, Birds, and Amphibians (Frogs)

Bermet Kydyralieva [1], Nurbek Aldayarov [2]

1 Biology Department, Faculty of Sciences, Kyrgyz-Turkish Manas University, Bishkek, Kyrgyzstan
2 Department of Biology, Faculty of Sciences, Kyrgyz-Turkish Manas University, Bishkek, Kyrgyzstan

Corresponding Author: *bermet.kidiraliyeva@manas.edu.kg*

Abstract

This microscopic study aims to characterize the structural organization of secondary encapsulated immune organs, specifically the spleen and lymph nodes, in the gray marmot (*Marmota baibacina*). The gray marmot serves as a principal reservoir in Central Asian plague foci and plays a critical role in zoonotic pathogen dynamics; however, its lymphoid anatomy remains poorly characterized. Previous ecological studies underscore the epidemiological significance of this species. Using light microscopy on fixed tissue samples from wild *M. baibacina*, the splenic parenchyma was observed to be organized into distinct white and red pulp compartments, consistent with typical mammalian secondary lymphoid architecture. The white pulp contains periarteriolar lymphoid sheaths and scattered lymphoid follicles, indicating active sites of antigen-driven lymphocyte proliferation. In contrast, the red pulp comprises a dense network of reticular cells and sinusoidal capillaries, facilitating blood filtration and immune cell trafficking. This structural organization closely parallels that observed in other mammalian species. Lymph nodes exhibit classical histoarchitecture, being encapsulated by dense connective tissue and comprising cortical regions with B-cell follicles and germinal centers, as well as paracortical T-cell zones. The reticular stromal framework supports lymphocyte compartmentalization and likely facilitates antigen presentation. Considering the relatively large body size of *M. baibacina*, it is inferred that lymph nodes are relatively few in number but well-developed, reflecting scaling patterns of adaptive immune responses across mammals. These morphological insights provide a foundational understanding of the gray marmot's immune system. Further immunohistochemical and functional investigations are warranted to delineate lymphocyte subpopulations, activation states, and immunological implications for plague ecology in this species.

Keywords:

Spleen, Comparative Morphology, Mammals, Birds, Amphibians

Enhanced Salinity Detection Using Zinc Oxide Nanorod Coated Tapered D-Shape Plastic Optical Fibers

Siti Halma Johari [1], Eliyana Ruslan [1], Siti Amaniah Mohd Chachuli [1], Siti Asma Che Aziz [1]

1 Central for Telecommunication Research and Innovation (CeTRI), Faculty of Electronics & Computer Technology & Engineering, Universiti Teknikal Malaysia Melaka, 76100 Durian Tunggal, Melaka, Malaysia

Corresponding Author: *siti.halma@utem.edu.my*

Abstract

Salinity detection plays a vital role in environmental monitoring, the food industry, and healthcare. Traditional methods such as conductivity meters or titration often involve bulky equipment, high costs, and limited sensitivity, making them less suitable for compact or cost-effective applications. This project focuses on the development of a zinc oxide (ZnO) coated tapered D-shape Plastic Optical Fiber (POF) sensor for saline concentration detection. The POF was fabricated with waist diameters of 500 µm, 550 µm, 600 µm, 650 µm, and 700 µm using a combination of chemical etching with acetone and deionized water, and mechanical polishing with sandpaper to enhance light interaction through the evanescent field. ZnO nanorods were grown on the tapered surface using the hydrothermal method, serving as a sensitive layer due to their high surface area and excellent optical properties. The sensors were tested with saline concentrations ranging from 0 g to 10 g, and a noticeable decrease in output voltage was observed as concentration increased. Among all samples, the ZnO-coated POF with a waist diameter of 600 µm showed the highest sensitivity at 0.1279 V/%, while the uncoated POF with a 700 µm diameter exhibited a sensitivity of 0.1127 V/%. The linearity of the ZnO-coated sensor was 95.46%, while the uncoated sensor reached 97.37%. These results demonstrate that ZnO coating significantly enhances sensor performance in terms of sensitivity, indicating the potential of ZnO-coated tapered POFs as a reliable, efficient, and cost-effective solution for accurate saline concentration monitoring in real-world applications.

Keywords:

Salinity, Plastic Optical Fiber, Zinc Oxide, Hydrothermal Method, Tapered D-Shape Fiber, Evanescent Wave

Development of a Sensor Array (MQ2, MQ4 and MICS5524) for Methane Gas Detection with IOT-based Monitoring

Afiq Irham [1], Siti Asma Che Aziz [1], Siti Amaniah Mohd Chachuli [1], Siti Halma Johari [1]

1 Central for Telecommunication Research and Innovation (CeTRI), Faculty of Electronics & Computer Technology & Engineering, Universiti Teknikal Malaysia Melaka, 76100 Durian Tunggal, Melaka, Malaysia

Corresponding Author: *afiqirhamrizal@gmail.com*

Abstract

The detection of methane gas is critically important for safety, environmental monitoring, and industrial process control, particularly in enclosed or high-risk areas such as laboratories, landfills, and gas pipelines. In confined spaces, excessive methane concentrations can result in explosions or suffocation, while its emission into the atmosphere significantly contributes to climate change due to its strong greenhouse effect. Conventional gas detection methods, such as gas chromatography and infrared sensing, tend to be expensive and require specialized handling. Therefore, this project focuses on the development of a sensor array integrating MQ2, MQ4, and MICS sensors, combined with an IoT-based monitoring platform, to enhance methane detection accuracy, real-time monitoring and provided sensing response performance comparison. The main objective of this project is to develop a methane gas detection system using a sensor array consisting of three commercial gas sensors which are MQ2, MQ4, and MICS5524. All the commercial was exposed to the methane gas for detection at the same time and environment simultaneously. The performance of each sensor will be analyzed by evaluating its sensing response and response time under six methane concentrations ranging from 5000 to 10,000 ppm. In parallel, the sensor array will be integrated with an IoT platform using Adafruit to enable real-time data monitoring and visualization. The results demonstrate that the combined sensor array successfully detected methane within the desired range, with the MQ2 sensor exhibiting highest sensing response at 7000 ppm concentrations, while MQ4 showed stable performance at higher ppm levels and the lowest sensing response of MICS 5524. The real-time monitoring system demonstrated reliable data monitoring to Adafruit with minimal latency and stable signal streaming. The successful integration of the sensor array with the IoT platform further proved the system's practicality and readiness for field deployment.

Keywords:

Commercial Gas Sensors, Gas Methane, Adafruit, Iot, mq2, mq4, mics5524,

Methane Detection from Food Waste Digestion Using Titanium Dioxide-Graphene Gas Sensor with IOT Integration

Adam Zafry [1], Siti Asma Che Aziz [1], Siti Halma Johari [1], Siti Amaniah Mohd Chachuli [1]

1 Central for Telecommunication Research and Innovation (CeTRI), Faculty of Electronics & Computer Technology & Engineering, Universiti Teknikal Malaysia Melaka, 76100 Durian Tunggal, Melaka, Malaysia

Corresponding Author: *mazafry@gmail.com*

Abstract

The study focuses on developing a low-cost and reliable methane gas sensor using a TiO_2–graphene composite material connected to an Adafruit platform for easy monitoring and data collection. Methane is a flammable gas commonly found in homes, industries, and the environment, so early detection is important to prevent accidents. TiO_2 is widely used in gas sensors because it is stable and inexpensive, but it has low electrical conductivity when used alone. To improve its sensing ability, graphene is added because it provides high conductivity, a large surface area, and strong chemical stability. When TiO_2 and graphene are combined, the composite creates more active sites for methane molecules and allows faster electron movement, which increases the sensor's sensitivity. The sensor works by measuring changes in electrical resistance when methane is present. These changes are sent to the IOT, such as an Adafruit IO, which processes the signal and displays the gas levels in real time. The Adafruit IO system is chosen because it is easy to use, supports many sensors, and can connect to displays or wireless modules for data logging and alerts. During testing, the TiO_2–graphene sensor showed sensing response, response time, and stable performance at room temperature or slightly elevated temperatures, making it more energy-efficient than many traditional sensors. The real-time readings provided by the Adafruit IO interface help users understand gas concentration levels quickly and clearly. Overall, the combination of the TiO_2–graphene sensing material with the Adafruit platform offers a simple, affordable, and effective solution for methane detection, demonstrating how nanomaterials and accessible electronics can work together to improve safety in practical applications.

Keywords:

Fabrication Gas Sensor, TiO2 Graphene, Adafruit IOT, Methane Gas, Response Time, Sensing Response

Gross and Micromorphological Evaluation of Yak (Bos Grunnies) Hindlimb Muscle Under Refrigeration and Freezing Conditions

Nazgul Imanberdieva [1], Nurbek Aldayarov [1]

1 Faculty of Sciences Department of Biology, Kyrgyz-Turkish Manas University, Bishkek, Kyrgyzstan

Corresponding Author: *nazgul.imanberdieva@manas.edu.kg*

Abstract

This study provides a comprehensive assessment of the macro- and micromorphological changes in yak (Bos grunnies) hindlimb muscle during storage under refrigeration (+4 °C) and freezing (-22 °C) conditions. Meat is a complex, nutritionally valuable food source, composed of muscle fibers, fat, connective tissue, blood, nerves, and vascular structures, with its quality dependent on the structural interplay among these components. Muscle and fat tissues are particularly critical in determining nutritional and functional properties. For experimental analysis, approximately 500 g of hindlimb muscle were collected from three yaks. An initial 50 g sample was fixed in 10% neutral buffered formalin as a control. The remaining tissue was subdivided into 12 samples of 50 g each, allocated to refrigeration (six samples) and freezing (six samples), and stored in dedicated plastic containers. Histological sections were prepared and stained using hematoxylin-eosin. The results revealed distinct macro- and micromorphological features, providing a detailed reference for veterinary-sanitary evaluation and for differentiating pathological changes in muscle tissues of varying origins. Refrigerated yak muscle should be stored for no longer than 7–10 days, as prolonged refrigeration leads to significant structural deterioration and promotes microbial growth, including pathogenic species. In frozen storage exceeding two months, muscle fiber deformation intensifies, accompanied by autolytic processes, inevitably resulting in qualitative deterioration. These findings provide standardized morphological data that can serve as a reference in future studies on meat quality, storage practices, and muscle tissue integrity in wild ungulates. The study emphasizes the critical influence of storage conditions on preserving the structural, nutritional, and hygienic properties of game meat.

Keywords:

Yak Meat, Histology, Muscle Tissue, Refrigeration, Freezing

Energy Efficiency-Focused Entropy Analysis: Investigation of Nanofluid Heat Transfer Processes

Mansur Mustafaoğlu [1], Muhammed Taha Topçu [2], Muhammet Kaan Yeşilyurt [2], Kadir Bilen [2], İlhan Volkan Öner [4], Ali Sharifi [4]

1 Department of Nanoscience and Nanoengineering, Institute of Science, Atatürk University, Erzurum, Türkiye
2 Department of Mechanical Engineering, Faculty of Engineering, Ataturk University, Erzurum, Türkiye
3 Department of Mechanical Engineering, Faculty of Engineering, Ataturk University, Erzurum, Türkiye
4 Faculty of Mechanical Engineering, University of Tabriz, Tabriz, Iran

Corresponding Author: *ali.sharifi@tabrizu.ac.ir*

Abstract

With the increasing importance of heat transfer applications, the development of new methods to increase energy efficiency and reduce energy consumption has become inevitable. In this context, the use of nanofluids as an alternative heat transfer medium offers higher heat transfer performance compared to conventional fluids, thereby reducing energy losses. Entropy analysis, a measure of energy quality, plays a critical role in evaluating the effectiveness of energy conversions in thermodynamic systems. Because entropy production represents the level of irreversibility and energy losses of a system, it stands out as an important parameter in the performance analysis of energy systems. In this study, the behavior of water–Al_2O_3 (aluminum oxide) nanofluid with variable thermophysical properties, within a square chamber with a moving and cold top wall, a fixed and hot bottom wall, and insulated side walls, was numerically investigated under natural convection conditions in terms of entropy production. Simulations were performed for a fixed Grashof number ($Gr = 10^4$), three different Reynolds numbers (Re = 100, 300, and 600), and two different nanoparticle volume fractions (ϕ = 0.01, 0.02, 0.03, and 0.04). The results revealed that total entropy production increased with increasing nanoparticle volume fraction at all Reynolds numbers examined. Furthermore, when the entropy production components were evaluated, it was determined that entropy production due to friction was negligible, and the largest contribution to total entropy production came from entropy production due to heat transfer.

Keywords:

Heat Transfer, Entropy Generation, Energy Conservation, Nanofluids

Numerical Analysis of Heat Transfer in Laminar Flow with Star-Cross Section Channel and Central and Circular Pipes

Mansur Mustafaoglu [1]

1 Department of Nanoscience and Nanoengineering, Institute of Science, Atatürk University, Erzurum, Türkiye

Corresponding Author: *mansour@atauni.edu.tr*

Abstract

The forced convection heat transfer behavior of water-titanium oxide (TiO_2) nanofluid was investigated numerically in a system consisting of a hollow tube in the middle of which water flows within a star-section channel. In this study, the motion and heat transfer of the nanofluid were modeled under the assumption of single-phase flow and the channel walls were evaluated under the condition of constant heat flux. Continuity, momentum and energy equations were solved numerically to describe the behavior of the fluid. Calculations were made using the finite volume method and the SIMPLE algorithm was preferred for pressure-velocity coupling. In the investigation, parameters such as Reynolds number, nanoparticle concentration in the nanofluid and particle diameter (in the range of 20-100 nm) were varied and the effects of these variables on the Nusselt number and overall heat transfer performance were analyzed. The accuracy of the obtained results was tested by comparing them with the simulation results of the same system using only pure water. The study findings show that the Nusselt number; The results show that the heat transfer coefficient increases significantly with increasing titanium oxide concentration in the nanofluid, decreasing the nanoparticle diameter, and increasing the Reynolds number. This demonstrates that nanofluids are an effective solution for enhancing heat transfer performance, especially in channels with complex geometries.

Keywords:

Heat Transfer, CFD, Water/(TiO_2) Nanofluids

Fluorescence Spectroscopy in the Study of Animal Meats

Zhyldyzai Ozbekova [1], Asylbek Kulmyrzaev [1]

1 Department of Food Engineering, Faculty of Engineering, Kyrgyz-Turkish Manas University, Bishkek, Kyrgyzstan

Corresponding Author: *zhyldyzai.ozbekova@manas.edu.kg*

Abstract

The potential of fluorescence spectroscopy was assessed to study cow, goat, sheep and yak meat. Meat samples were taken from muscles, viz. Gluteus medius (GM), Longissimus dorsi (LD) and Semitendinosus (ST). The moisture, fat and protein content of meat samples were measured. The emission fluorescence spectra of tryptophan (305–500 nm), riboflavin (410–700 nm) and vitamin A (340–540) were recorded directly on meat samples at 290, 382 and 322 nm, respectively. Principal component analysis (PCA), partial least squares regression (PLSR) and partial least squares discriminant analysis (PLSDA) were applied to process the spectra obtained. Moisture content with R2=0.94, protein content with R2=0.86, and fat content with R2=0.91 were predicted from the fluorescence emission spectra. The PLSDA applied at 410–700 nm fluorescence spectra showed 100, 100, 94.4 and 92.6% of discrimination for cow, goat, sheep and yak meat, respectively. This study demonstrates that fluorescence spectroscopy has a potential for the accurate, non-destructive and rapid prediction of meat composition and it could replace existing traditional analytical methods.

Keywords:

Chemical Parameters, Fluorescence Spectroscopy, Meat, Animal Species, Statistics

Electrospun Carbon-Based Nanofibers for Advanced Material Applications

Mohd Ali Mat Nong [1], Juraina Md Yusof [1], Suzila Sabil [2]

1 Functional Nanotechnology Devices Laboratory (FNDL), Institute of Nanoscience and Nanotechnology Universiti Putra Malaysia, Serdang, Selangor, Malaysia.
2 Kolej Komuniti Jelebu, Jalan Seperi, Kampung Chempedak, 71600 Kuala Klawang, Negeri Sembilan, Malaysia

Corresponding Author: *mohd_alee@upm.edu.my*

Abstract

The development of conductive and mechanically robust nanofibers remains a significant challenge for advanced applications in sensors, energy devices, and flexible electronics. This study addresses the need for enhanced nanofiber performance by fabricating carbon-based nanofibers reinforced with carbon fillers through an optimized electrospinning process. Polyacrylonitrile (PAN) (0.2–1.0 g) was dissolved in 10 mL of dimethylformamide (DMF) and subsequently blended with 0.2–1.0 g of carbon-based fillers. The mixture was sonicated for 30 minutes and stirred for 4 hours to achieve a uniform electrospinning solution. The solution was electrospun at a flow rate of 0.8 mL/hour, with a needle-to-collector distance of 20 cm and an applied voltage of 18 kV, using aluminum foil as the collection substrate. Characterization of the fabricated nanofibers was conducted using field emission scanning electron microscopy (FESEM) to examine fiber morphology, a four-point probe to evaluate electrical conductivity, and a universal testing machine to assess mechanical strength. The results show that the incorporation of carbon fillers significantly improved fiber uniformity, reduced bead formation, and enhanced both electrical conductivity and tensile performance. These improvements demonstrate that controlled carbon filler loading can effectively tailor the functional properties of PAN-based nanofibers. Overall, this work contributes to the development of high-performance electrospun nanofibers and highlights their potential for use in next-generation electronic and structural applications.

Keywords:

Electrospinning, Carbon-Based Nanofibers, Polyacrylonitrile (PAN), Conductivity, Mechanical Properties

Graphene/Cellulose Nanocomposite Accelerate Oral Wound Healing in Diabetic Rats by Mitigating Oxidative Stress and Apoptosis in Gingival Fibroblasts.

Sana Ghaffarzadeh [1], Jalal Pourahmad [2], Parvaneh Naserzadeh [3], Fatemeh Ghanbary [4], Mir-Jalal Hosseini [5]

1 Department of Pharmacy, School of Pharmacy, Shahid Beheshti University of Medical Sciences, Tehran, Tehran, Iran
2 Department of Toxicology and Pharmacology, School of Pharmacy, Shahids Beheshti University of Medical Sciences, Tehran, Iran
3 Endocrine Research Center, Institute of Endocrinology and Metabolism, Iran University of Medical Sciences, Tehran, Iran
4 Department of Chemistry, MAH.C., Islamic Azad University, Mahabad, Iran
5 Zanjan Applied Pharmacology Research Center, Health and Metabolic Diseases Research Institute, Zanjan University of Medical sciences, Zanjan, Iran

Corresponding Author: *sanna_gh@yahoo.com*

Abstract

Diabetes mellitus, a chronic metabolic disorder characterized by hyperglycemia, impairs oral wound healing through fibroblast dysfunction, persistent inflammation, and excessive apoptosis, leading to delayed closure and higher infection risk. While graphene-based nanomaterials show promise for tissue regeneration, their effects on fibroblast survival in diabetic oral wounds remain poorly understood. Here, we report the structural characterization and therapeutic evaluation of graphene/cellulose nanocomposites in a streptozotocin-induced diabetic rat oral wound model. Nanoparticles, synthesized with uniform graphene dispersion (38.9–77.6 nm) and strong interfacial bonding within a cellulose matrix, were confirmed by FTIR, XRD, XPS, and SEM. Untreated diabetic wounds displayed profound fibroblast injury, including reduced viability, elevated lipid peroxidation, reactive oxygen species, oxidized glutathione, cytochrome c release, and high apoptosis/necrosis rates versus healthy controls ($p < 0.001$). Nanoparticle treatment significantly restored viability ($p < 0.01$), suppressed oxidative stress ($p < 0.01$), normalized glutathione redox balance ($p < 0.001$), and reduced mitochondrial-mediated apoptosis, with most parameters approaching healthy levels within five days. These findings demonstrate that graphene/cellulose nanocomposites possess favorable nanoscale architecture and also confer potent cytoprotective effects in the diabetic wound microenvironment. This nanoplatform offers a promising strategy to counteract oxidative stress and enhance healing in diabetes-impaired oral tissues.

Keywords:

Graphene/Cellulose Nanocomposite, Diabetic Oral Wound Healing, Gingival Fibroblasts, Oxidative Stress, Apoptosis, Nanomedicine

Comparison of Metal-Oxide Semiconductor Sensors for Ethanol Detection at Room Temperature

Raja Ahmad Arifikri Raja Ismail [1], Nazreen Waeleh [2], Siti Amaniah Mohd Chachuli [1], Ömer Çoban [3]

1 Central for Telecommunication Research and Innovation (CeTRI), Faculty of Electronics & Computer Technology & Engineering, Universiti Teknikal Malaysia Melaka, 76100 Durian Tunggal, Melaka, Malaysia
2 Faculty of Electronic and Computer Engineering, Universiti Teknikal Malaysia Melaka (UTeM), 76100 Durian Tunggal, Melaka, Malaysia
3 Department of Electrical and Electronics Engineering, Faculty of Engineering, Atatürk University, Erzurum, Türkiye

Corresponding Author: *arif020208@gmail.com*

Abstract

Ethanol is a colorless, volatile, and flammable liquid that is widely used in industrial, medical, and consumer applications. However, prolonged ethanol exposure to humans at 1000 ppm and above can pose a serious health risk with symptoms such as throat irritation, dizziness, intoxication, and unconsciousness if the concentration continues to increase. This makes the detection of ethanol essential in applications such as industrial safety, breath analysis, and environmental monitoring. Thus, this study proposes a gas sensor to detect ethanol using three different metal-oxide semiconductors, which are Titanium Dioxide (TiO2), Nickel Oxide (NiO), and Zinc Oxide (ZnO) at room temperature. The sensors were fabricated using a screen-printing method by implementing an interdigitated electrode as the first layer and metal-oxide semiconductor paste as the second layer on a Kapton film. Silver paste was used as an interdigitated electrode and fired at 150ºC for 15 minutes in an oven. The metal-oxide semiconductor paste was prepared by mixing the sensing powder (TiO2, NiO, and ZnO) with a binder. All sensing layers were annealed at 200ºC for one hour in an oven. The results indicated that all sensors responded to 35,000 ppm of ethanol at room temperature. The sensing response was approximately 85.61%, 19.12%, and 11.64% for ZnO, NiO, and TiO2, respectively. The result revealed that ZnO is the best sensor for ethanol with the highest sensing response as compared to NiO and TiO2. This research can be applied in developing low-powered gas sensors that are effective in detecting ethanol presence to ensure workplace safety and monitoring procedures.

Keywords:

Gas Sensor, Zinc Oxide, Titanium Dioxide, Nickel Oxide, Ethanol, Room Temperature

Study of Elemental (Micro- and Macro-) Nutrient Content in Dracocephalum ıMberbe Bunge from the Alai Range, Kyrgyzstan

Nurbek Aldayarov [1], Nurgul Ermekova [2]

1 Department of Biology, Faculty of Sciences, Kyrgyz-Turkish Manas University, Bishkek, Kyrgyzstan
2 Department of Biotechnology, Institute of Graduate Studies, Kyrgyz Turkish Manas University, Bishkek, Kyrgyzstan

Corresponding Author: *1912.02025@manas.edu.kg*

Abstract

Dracocephalum imberbe Bunge (Lamiaceae) is a perennial species endemic to the Alai Range, Kyrgyzstan, traditionally used in ethnomedicine. Its aerial parts are employed in decoctions and infusions for respiratory and gastrointestinal ailments and exhibit mild anti-inflammatory effects. Quantitative assessment of macro- and micronutrient composition in both aerial and root tissues is critical for evaluating its biochemical profile, pharmacological potential, and safety. Analytical results indicate that all investigated elements in leaves and roots fall within acceptable ranges for medicinal plants, confirming the ecological purity of the samples. The aerial parts exhibit high concentrations of essential macronutrients, including potassium (K), calcium (Ca), magnesium (Mg), and phosphorus (P), while toxic elements such as cadmium (Cd), lead (Pb), mercury (Hg), and arsenic (As) remain at minimal levels. Slight deviations include marginally reduced copper (Cu) and values of chromium (Cr) and selenium (Se) approaching the upper limits of normative ranges, without exceeding permissible thresholds. Roots demonstrate elevated accumulation of barium (Ba), strontium (Sr), sodium (Na), and calcium (Ca), reflecting typical patterns of ion storage in subterranean tissues. Although lead (Pb) and molybdenum (Mo) concentrations are higher in roots than in aerial parts, they remain within acceptable limits. Comparative analysis underscores distinct element distribution between plant organs, with leaves preferentially accumulating essential macronutrients and roots concentrating certain non-essential or trace elements. Overall, D. imberbe exhibits a stable elemental profile, highlighting its suitability for medicinal applications and supporting its use in ethnopharmacology. These findings provide a foundation for quality assessment, standardization, and optimization as a botanical resource.

Keywords:

Ethnomedicine, Macronutrients and Micronutrient, Elemental Profile, Dracocephalum Imberbe, Kyrgyzstan

Comparative Effects of Cold Plasma and Microwave Pretreatments on Bioactive Compounds in Hydroalcoholic Quince Leaf Extracts

Bahram Fathi-Achachlouei [1], Rezvan Shaddel [1], Simin Tolouei [1]

1 Department of Food Science and Technology, University of Mohaghegh Ardabili, Ardabil, Iran

Corresponding Author: *b_fathi@uma.ac.ir*

Abstract

In recent years, there has been growing interest in plants rich in natural antioxidants and bioactive compounds, with quince leaves emerging as a notable example. Due to their high phenolic and antioxidant content, quince leaf extracts serve as effective natural antioxidants, offering a sustainable alternative to synthetic antioxidants. Over the past decade, emerging extraction technologies such as microwave, cold plasma, and ultrasound have gained significant attention in food science for their efficiency and environmental benefits. This study investigated the impact of cold plasma and microwave pretreatments on the chemical composition and antioxidant properties of hydroalcoholic extracts from quince leaves. The results demonstrated that a cold plasma and microwave pretreatments significantly increased ($P<0.05$) total chlorophyll content, whereas extending microwave pretreatment to 6 minutes led to a notable reduction compared to the control. Additionally, cold plasma and microwave pretreatments, significantly decreased moisture content. Ash content also declined significantly after 6 minutes of microwave and 15 minutes of cold plasma pretreatments, compared to the control. Both of cold plasma and microwave pretreatments, significantly enhanced ($P<0.05$) total phenolic content and antioxidant activity (especially pretreatment of cold plasma at 10 minutes was effective than microwave). However, color indices (L, *a*, b*) decreased significantly compared to the control due to cold plasma, but due to microwave pretreatment, there was no significant difference compared to the control. Based on the results of this research, cold plasma can be a better and more efficient method to extract and replace conventional thermal methods than the microwave pretreatment.

Keywords:

Cold Plasma, Microwave, Quince Leaves, Bioactive Compounds

Investigation of the Cellular Effects of Infrared Electromagnetic Waves and Carbon Nanotubes on HT29 Cell Line

Farshad Lotfollahzadeh [1]

[1] Department of Physics, MAH., Islamic Azad University, Mahabad Iran

Corresponding Author: *naserzadeh_2011@yahoo.com*

Abstract

Colon cancer can occur as small, non-cancerous cell masses called polyps that form in the lining of the colon. Targeted cancer therapy is a method in which substances or drugs are used to target cancer cells without affecting normal cells. This method often uses nanoparticles. Among the nanoparticles that are of great importance are carbon nanotubes, which have many applications in medicine due to their unique properties such as high tensile strength and carbon structure. They are synthesized in the form of nanotubes. They are generally activated by an external agent and increase their effectiveness in dealing with cancer tissue. Infrared radiation is electromagnetic energy that is associated with atomic energy levels. If absorbed by a substance, it stimulates it. It can be used to shrink or eliminate tumors and reduce some of the side effects of cancer, such as bleeding or obstruction and to remove colon polyps or tumors that have caused obstruction of the colon or stomach. The aim of this study is to investigate the synergistic effects of infrared electromagnetic waves, carbon nanotubes, and HT29 cell line. carbon nanotubes were obtained from Merck and the dimensions of the nanoparticles were examined using a SEM microscope to ensure their size. The cytotoxicity effect and damage to the integrity of the lysosomal membrane were evaluated at time. The average diameter of the nanoparticles was in the range of less than 100 nm, and the cytotoxic effect of infrared waves and nanoparticles alone and simultaneously with infrared and nanoparticles on cancer cells showed that the simultaneous effects of nanoparticles with infrared waves were greater than the single case. This study shows that the use of nanoparticles and excitation by an infrared energy source has a great effect on dealing with cancer cells.

Keywords:

Cell Death Signaling, Apoptosis, Nanosructure, Photothermal Therapy

Cellular Toxicity of Laser, Iron Oxide and Manganese Oxide Nanoparticles on the Viability of Breast Cancer Cells Line

Aysan Mansournia [1]

1 Department of Physics, MAH. Islamic Azad University, Mahabad, Iran

Corresponding Author: *parvaneh.naserzadeh1988@gmail.com*

Abstract

Breast cancer is one of the most common cancers among Iranian women, and 7,000 women are diagnosed with this cancer annually. Currently, this technology is used in various medical fields, but one of the most important areas of nanomedicine is related to cancer treatment, because it has had very positive effects on it so far. Iron and manganese oxide nanoparticles are particles in the size range of 100 nanometers. Iron oxide nanoparticles have attracted considerable attention due to their superparamagnetic properties and potential biomedical applications due to their biocompatibility and non-toxicity. Manganese oxide nanoparticles are widely used in the decomposition of hazardous chemicals due to their catalytic properties. Laser therapy uses high-energy light to treat cancer and other diseases. Lasers can also be used to shrink or destroy tumors. Lasers are most commonly used to treat superficial cancers such as basal cell skin cancer, and early stages of some cancers such as cervical, vaginal, and non-small cell lung cancer. The aim of this study was to investigate the synergistic cytotoxic effects of laser, iron oxide, and manganese oxide on a breast cancer cell line. Materials and Methods: Nanoparticles were purchased from Merck, and their dimensions were examined using a scanning electron microscope to ensure their size. The cytotoxicity effect was evaluated by MTT assay and damage to the lysosomal membrane at time. The average diameter of nanoparticles was in the range of less than 100 nm, and the cytotoxicity effect of laser and nanoparticles individually and simultaneously with laser and nanoparticles on cancer cells showed that the simultaneous effects of nanoparticles with laser gave the best response more than the single mode in less time. This study shows that the use of nanoparticles simultaneously with laser has a more effective effect than exposure to a single intervention.

Keywords:

Cell Death Signaling, Apoptosis, Nanostructure, Laser Therapy

Structural Analysis of La-Doped MoO_3 Hole Transport Layers and Their Correlation with Perovskite Solar Cell Performance

Zulfanizam Abdul Wahab [1], Faiz Arith [1], Fauziyah Salehuddin [1]

1 Faculty of Electronics and Computer Technology and Engineering, Universiti Teknikal Malaysia Melaka, Hang Tuah Jaya, Durian Tunggal, 76100, Melaka, Malaysia

Corresponding Author: *p022210003@student.utem.edu.my*

Abstract

The hole transport layer (HTL) is a critical component in perovskite solar cells (PSCs), governing charge extraction efficiency and interfacial stability. Molybdenum trioxide (MoO_3), a wide-bandgap transition metal oxide, offers favorable energy alignment and high work function, yet its performance can be further optimized through controlled doping. In this work, lanthanum (La)-doped MoO_3 thin films were synthesized via spin-coating and systematically characterized using X-ray diffraction (XRD), scanning electron microscopy (SEM), ultraviolet-visible spectroscopy (UV-Vis), and electrical measurements. XRD analysis confirmed the orthorhombic α-MoO_3 phase with high crystallinity and phase purity, while peak broadening revealed microstrain and reduced crystallite size, enhancing surface reactivity and charge transfer dynamics. At 3 mol% La doping, the films exhibited the widest optical bandgap (3.58 eV), minimized defect scattering, and peak electrical conductivity, attributed to improved crystallinity and reduced dislocation density. These structural and electronic improvements translated into enhanced carrier mobility and selective hole transport, reducing recombination losses at the perovskite/HTL interface. The findings establish La-doped MoO_3, particularly at 3 mol% concentration, as a promising HTL candidate for stable, high-performance PSC architectures.

Keywords:

MoO3, Perovskite Solar Cells (PSC), X-Ray Diffraction (XRD), Ultraviolet-Visible Spectroscopy (UV-Vis), Scanning Electron Microscopy (SEM)

Integrated Geophysical, Geochemical and Hydrogeological Methods to Investigation of Groundwater Contamination: A Case Study of Osubi, and its Environ Southern Nigeria

Wasiu Osisanya [1], Onifade Yemi Sikiru [1], Maruf A Bello [2], Saleh Alhaji Saleh [2], Iduseri O. Murphy [3]

1 Department of Physics, College of Science, Federal University of Petroleum Resources, Effurun, Delta State, Nigeria
2 Department of Petroleum Engineering and Geosciences, Petroleum Training Institute, Effurun, Delta State, Nigeria
3 Department of Physics, Faulty of Physical Science, University of Benin, Benin City, Edo State, Nigeria

Corresponding Author: *wasiu.osisanya@uniben.edu*

Abstract

This study evaluates groundwater vulnerability and contamination in Osubi and surrounding communities, Delta State, Nigeria, using an integrated geophysical, hydrogeological, and geochemical approach. The investigation combined 1D, 2D, and 3D electrical resistivity surveys (21 Wenner–Schlumberger profiles and 38 VES), ten MASW seismic traverses, hydrogeological data from fifty hand-dug wells, and laboratory analysis of eleven water and fifteen soil samples. Geoelectrical parameters—including longitudinal conductance, transverse resistance (TR), longitudinal (PL) and transverse resistivity (PT), coefficient of anisotropy (COA), hydraulic conductivity, and transmissivity—were analyzed to assess aquifer integrity and protective capacity. Longitudinal conductance (9.6×10^{-5}–0.159mhos) indicates predominantly poor to moderate overburden protection, suggesting vulnerability to downward contaminant migration. TR, PL, and PT values reveal largely coarse-grained, resistive lithologies consistent with permeable, hydraulically active aquifer systems. COA (0.12–2.00) reflects a mix of homogeneous sands and heterogeneous sand–clay sequences driven by natural depositional variability. Hydraulic conductivity (0.122–3.481m/day) and transmissivity (0.43–67.18m²/day) further confirm moderate to high groundwater potential, particularly around VES 17–20. Localized low-resistivity zones (<50Ωm) at VES 19, 20, 22, 24, and 35 suggest possible shallow contamination. Inverted 2-D and 3-D resistivity models (RMS error 7.29%) show subsurface resistivities generally above the contamination threshold (<40–50Ωm), indicating an overall uncontaminated groundwater system. MASW results delineate a three-layered sequence comprising a loose topsoil, a semi-compacted transition zone, and a deeper saturated aquifer, with limited confining layers that enhance vertical infiltration and aquifer vulnerability. Geochemical indices indicate low to moderate pollution, with notable hotspots near PTI Skills, WOJ-30, and Government Land. PCA and correlation analyses attribute metal enrichment primarily to anthropogenic activities including vehicle emissions, industrial effluents, waste disposal, and agriculture. While groundwater metal concentrations mostly remain within acceptable limits, health-risk assessments highlight greater susceptibility in children, particularly from Pb-, Cd-, and Cr-exposure. Overall, integrated results underscore vulnerable but largely uncontaminated groundwater system requiring continuous monitoring and targeted mitigation.

Keywords:

Groundwater vulnerability, Electrical Resistivity, MASW, Geochemical assessment, Aquifer integrity

Integrated Electrical Resistivity Investigation of Subsurface Peat and Clay Deposits in Orile Whitesand, Orile–Iganmu, Lagos, Southwestern Nigeria

Wasiu Osisanya [1], Maruf A Bello [2], Saleh Alhaji Saleh [2], Iduseri O. Murphy [3], Ohwoharhohwo Etaoghene [4]

1 Department of Physics, College of Science, Federal University of Petroleum Resources, Effurun, Delta State, Nigeria
2 Department of Petroleum Engineering and Geosciences, Petroleum Training Institute, Effurun, Delta State, Nigeria
3 Department of Physics, Faulty of Physical Science, University of Benin, Benin City, Edo State, Nigeria
4 Department of Geosciences, Faculty of Science University of Lagos, Akoka, Lagos State, Nigeria

Corresponding Author: *wasiu.osisanya@uniben.edu*

Abstract

This study employs electrical resistivity methods—Vertical Electrical Sounding (VES) and 2D Electrical Resistivity Imaging (ERT)—to delineate subsurface peat and clay deposits in Orile Whitesand, Orile–Iganmu, Lagos State, Southwestern Nigeria. A total of twenty-four (24) VES and eight (8) 2D resistivity profiles were acquired using a PASI Terrameter (Model 16GL). The Schlumberger array was utilized for VES and the Wenner array for 2D imaging. Data were processed using WinResist 1.0 and DIPROFWIN software to generate geoelectric sections and resistivity models. Results revealed four to six distinct subsurface layers, notably topsoil, clay, peat, sandy clay, clayey sand, and sand. Peat was identified by its extremely low resistivity values (0.3–9.6 Ωm) and variable thickness (1.7–27.2 m), while clay exhibited resistivity values ranging from 11.1 to 31.9 Ωm with thicknesses of 1.3–27.3 m. In several VES stations (e.g., 10, 12, and 14), current penetration was insufficient to resolve complete peat layers, indicating highly resistive overburden or localized saturation anomalies. The 2D resistivity profiles provided enhanced lateral continuity and confirmed the spatial distribution of low-resistivity peat and clay zones. The presence and distribution of these materials are critical for environmental and hydrogeological planning due to their influence on groundwater flow, contaminant retention, and foundation stability. The study recommends complementary hydrochemical analyses to evaluate groundwater quality in relation to the identified peat and clay zones.

Keywords:

Electrical resistivity survey, vertical electrical sounding, Peat and clay delineation, Overburden, Orile Iganmu Lagos

Improving the Pharmacological Properties of Curcumin by Nanoclay

Shahriyar Karimdoust [1], Yavar Nour Mohammadi Ziba [2], Shahdad Mousavi [3], Abbas Razmi [4], Parisa Nami [5], Mehdi Jafarian [6]

1 Department of Geology, Faculty of Science, Payame Noor University, Ardebil, Iran
2 Department of Chemistry, Faculty of Science, Islamic Azad University, Ardabil Branch, Ardabil, Iran
3 Department of Industry, Ministry of Industry, Trade and Mines, Ardabil, Iran
4 Department of Mechanical Engineering, Engineering Faculty, Ataturk University, Erzurum, Türkiye
5 Department of Geography and Urban Planning, Faculty of Engineering, Payame Noor University, Maragheh, Iran
6 Department of Civil Engineering, Faculty of Engineering, Mohaghegh Ardabili University, Ardabil, Iran

Corresponding Author: *karimdoust_sh@yahoo.com*

Abstract

The synthesis of nanoparticles using plant extracts is a simple, cost-effective, and environmentally friendly method. Medicinal plants have long been valued for their therapeutic properties, and their use continues to increase today. Accordingly, extensive research is being conducted to revisit and revitalize the applications of these natural, non-chemical remedies, with modern technologies playing a major role in enhancing and optimizing their therapeutic potential. Nanoclays are among the valuable mineral materials that, due to their microstructural characteristics, high surface area, and compatibility with the body's metabolism, have become essential tools in recent studies. Curcumin, the main active component of turmeric, possesses effective therapeutic properties, particularly in boosting the immune system and combating inflammatory and infectious agents. However, its extremely low water solubility, poor bioavailability, limited gastrointestinal absorption, rapid metabolism, and fast elimination from the bloodstream pose significant challenges to its clinical use. Modifying mineral nanoclays with curcumin is one of the most effective strategies for increasing the stability, efficiency, and bioavailability of this compound, thereby enabling the development of mineral–herbal drugs with enhanced therapeutic performance. Plant-based medicines formulated with clay minerals through advanced technological methods not only offer combined therapeutic benefits but also lack harmful chemical additives and exhibit minimal side effects. Furthermore, they demonstrate high compatibility with both the environment and human metabolism. These structural features represent key standards in the pharmaceutical and medical industries.

Keywords:

Curcumin, Nanoclay, Pathogens, Bioavailability

An Evaluation of Optimum Inclination Angle for Fixed-angle Solar Panel Installations in Erzurum Province

Emre Koşar [1], Muhammet Kaan Yeşilyurt [1]

1 Faculty of Engineering, Department of Mechanical Engineering, Ataturk University, Erzurum, Türkiye

Corresponding Author: *kaan.yesilyurt@atauni.edu.tr*

Abstract

Whether due to the scarcity of fossil fuels or environmental concerns, humanity is rapidly realizing the importance of renewable energy sources and turning to them. Solar energy, among renewable energy sources, is a type of energy whose importance is rapidly increasing globally due to its environmental sustainability and economic viability. Especially in the fight against climate change, its low carbon emissions place solar energy in a privileged position among other energy sources. Photovoltaic (PV) systems are systems that convert direct solar radiation into electrical energy. However, the efficiency of PV systems depends not only on the panel technology but also directly on environmental factors such as the panel's installation angle (tilt), orientation, climatic conditions, atmospheric density, air temperature, and altitude. Within the scope of our country's energy needs, the main problem for Erzurum province, which has a high altitude and cold climate, is the lack of sufficient academic research in the implementation of solar power plants. In practice, it is observed that solar power plants in Erzurum are installed at a fixed angle. Erzurum province, being one of the highest altitude provinces in Turkey with the most pronounced continental climate characteristics, serves as an ideal example for this type of study. Erzurum has an average annual solar energy potential of 1,650 kWh/m²; however, the long winter season, high snow cover, and low temperatures significantly affect PV efficiency. Therefore, determining the optimum tilt angle for fixed-slope PV panel installations in high-altitude regions like Erzurum is both a scientific and economic necessity to increase energy efficiency. This study aims to determine the optimum installation angles of PV panels in Erzurum province during summer and winter periods, and to examine the effects of seasonal differences on efficiency in the context of physical, atmospheric, and geometric parameters.

Keywords:

Solar Energy, Fixed-angle solar panels, Optimum inclination angle, Erzurum province

Unraveling the Mechanism of TiCN Film-Coated NiTi Substrate Toxicity: Evidence of Mitochondrial Electron Transport Dysfunction in Gingival Cells from Diabetic Rats

Parvaneh Naserzadeh [1]

[1] Colorectal Research Center, Iran University of Medical Sciences, Tehran, Iran

Corresponding Author: *pnnew2011@yahoo.com*

Abstract

In recent years, considerable attention has been directed toward exploring alternative materials for screws used in jawbone tissue replacement. Nevertheless, issues related to the cytotoxicity and biocompatibility of these materials remain subjects of ongoing debate. In this study, we developed a novel implant for jawbone tissue regeneration by depositing a titanium carbonitride (TiCN) film onto a NiTi shape memory alloy substrate using the Cathodic Arc Physical Vapor Deposition (CAPVD) technique. The investigation focused on evaluating the cellular responses of TiCN-coated NiTi substrates in gingival cells derived from diabetic rats over periods of 1, 15, and 30 days. Initially, the research involved characterizing the NiTi alloy and assessing its distribution within the tissue. Subsequently, several biological parameters—including white blood cell (WBC) components, adenosine triphosphate (ATP) levels, oxidative stress markers, cytochrome c release, and lysosomal membrane integrity—were analyzed across all experimental groups. The findings revealed that diabetic rats implanted with the TiCN-coated NiTi substrate exhibited notably reduced oxidative stress markers, alongside enhanced cell viability, increased intracellular glutathione (GSH) and ATP concentrations, and diminished cytochrome c release and lysosomal membrane damage. Overall, the results suggest that the TiCN-coated NiTi screw demonstrates excellent biocompatibility and minimal cytotoxicity, making it a promising candidate for jawbone tissue replacement in diabetic patients.

Keywords:

Cell Death Signaling, Apoptosis, Nanosructure

Functional Nanoparticle Incorporated Bioprinted Scaffolds

Behnaz Ashtari [1], Fatemeh Barati [1], Maryam Khosravi [1], Mohamad Javad Hadi [2]

1 Department of Medical Nanotechnology, Faculty of Advanced Technologies in Medicine, Iran University of Medical Sciences, Tehran, Iran
2 Graduate Student, Iran University of Medical Science, Tehran, Iran

Corresponding Author: *fatemehbarati.h@gmail.com*

Abstract

By incorporating functional and stimuli-responsive nanoparticles, passive bioprinted scaffolds can be transformed into controllable and adaptive material systems. Such particles impart chemical, electrical, magnetic, and light-responsive behavior while reinforcing polymer networks and improving rheology. These nanoparticles create nanoscale domains that convert external stimuli into localized thermal, mechanical, or chemical outputs, enabling conductivity tuning, photothermal heating, magnetic actuation, and sustained ion exchange. Together, these effects shift scaffolds from static structures to dynamic, stimulus-regulated platforms designed for next-generation responsive biomaterials.

Keywords:

3D Bioprinting, Bioinks, Smart Biomaterials, Nanoparticles, Responsive Scaffolds

Mechanistic Insights Into Tissue Regeneration Using Carbon-Based Nanoparticles in 3d Bioprnting

Behnaz Ashtari [1], Fatemeh Barati [1], Maryam Khosravi [1], Mohamad Javad Hadi [2]

1 Department of Medical Nanotechnology, Faculty of Advanced Technologies in Medicine, Iran University of Medical Sciences, Tehran, Iran
2 Graduate Student, Iran University of Medical Science, Tehran, Iran

Corresponding Author: *fatemehbarati.h@gmail.com*

Abstract

Carbon-based nanomaterials are emerging as key modifiers in 3D bioprinting due to their electrical, surface, and biochemical properties. They enhance shear-thinning, print fidelity, and mechanical strength by forming conductive polymer–nanomaterial networks. They also influence ionic flux, Ca^{2+} dynamics, and redox conditions through controlled ROS generation, supporting signaling pathways relevant to bone and cartilage regeneration. Through these combined effects, carbon-nanomaterial-enhanced bioinks create microenvironments that promote structural maturation and tissue development, positioning them as next-generation functional enhancers for regenerative scaffolds.

Keywords:

Tissue Engineering, 3D Bioprinting, Bioinks, Scaffold, Carbon Nanoparticle

Fe-Pt Nanoparticles: Synthesis and Characterization

Zhazgul Kelgenbaeva [1]

[1] Institute of Chemistry and Phytotechnology, National Academy of Sciences of the Kyrgyzstan, 720071, Bishkek, Kyrgyzstan

Corresponding Author: *zhazgul.k@gmail.com*

Abstract

Fe-Pt nanoparticles were synthesized from Fe-Pt alloy electrodes using pulsed plasma in ethanol. As synthesized A1 and annealed L10 type FePt nanoparticles were studied by XRD, HR-TEM analysis and VS-Magnetometer. VSM indicated strong ferromagnetic behavior at room temperature.

Keywords:

Nanoparticles, FePt, Pulsed Plasma in Liquid, Ferromagnetism

Product Innovation and Processing Technologies for Agroforestry Food Products

Jamila Smanalieva [1]

1 Department of Food Chemistry, Faculty of Chemistry and Food Chemistry, Technische Universität Dresden, Germany

Corresponding Author: *jamila.smanalieva@tu-dresden.de*

Abstract

Ensuring food and nutrition security remains a major challenge in Kyrgyzstan, where 40% of the population cannot afford adequate nutrition, 70% of children under five lack minimally diverse diets, and 47% suffer from micronutrient deficiencies, especially iron. Meanwhile, non-communicable diseases account for up to 80% of deaths (WHO, 2019), highlighting the urgent need for healthier dietary options. Sustainable agri-food supply chains, focused on value-added processing rather than export of raw materials, represent a key pathway to improving national nutrition and economic resilience. This research presents advances in product innovation and processing technologies for agroforestry food products with the goal of expanding the range of functional, nutrient-dense foods. Comprehensive analyses were conducted on nutrient composition and bioactive components of dried apricots and kernels, as well as freeze-dried strawberries, blackberries, and apricots. The influence of blanching on macronutrients, total polyphenol content, antioxidant capacity, and microbiological stability of dried plums was also evaluated. New functional foods derived from local forest fruits were developed, including nine types of fruit balls, two formulations of fruit marshmallows, four “Baltalkan” cereal–honey bars, and three “Balmaizhemish” fruit spreads. Technological instructions were prepared for production, two patent applications submitted, and one patent already granted. In addition, improved drying technologies were introduced by substituting sulfur dioxide with organic acids during apricot pre-treatment to enhance product safety, preserve color and texture, and reduce microbiological risks. Overall, the outcomes demonstrate significant potential to strengthen sustainable value chains, enhance the quality and safety of dried fruit products, and contribute to improved nutritional health through increased availability of functional foods in Kyrgyzstan.

Keywords:

Functional Foods, Total Polyphenol Content, Antioxidant Capacity, Microbiological Stability, Dried Fruts

Non-Invasive Marine Monitoring with Baited Remote Underwater Video (BRUV) Systems: Capabilities, Limitations, and Regional Opportunities

Rafet Çağrı Öztürk [1], Ayşe Cebeci [2], Melike Alemdağ [2], Şirin Firidin [2], Yahya Terzi [1]

1 Department of Fisheries Technology Engineering, Faculty of Marine Sciences, Karadeniz Technical University, Trabzon, Türkiye
2 Central Fisheries Research Institute, Trabzon, Türkiye

Corresponding Author: *rafetcagriozturk@gmail.com*

Abstract

Baited Remote Underwater Video (BRUV) systems have emerged as one of the most effective non-invasive tools for assessing marine biodiversity, detecting species presence, and monitoring fish assemblages across a wide range of habitats. By using bait as a controlled attractant and deploying underwater cameras on fixed frames, BRUVs provide standardized, replicable observations of demersal and pelagic species without disturbing the environment or altering natural community structure. BRUV systems overcome many limitations associated with traditional methods such as trawl sampling, gillnets, and diver-based visual censuses, which are depth-restricted, habitat-destructive, or biased by diver presence. Their ability to operate across depth gradients, including remote, hazardous, or low-visibility areas, has made BRUVs central to contemporary marine monitoring and conservation planning worldwide. The method generates quantitative metrics such as MaxN, species richness, biomass proxies, behavioral interactions, and trophic composition, enabling long-term ecological assessments and impact studies related to marine protected areas, invasive species, fisheries pressure, artificial reefs, and aquaculture operations. Technological improvements, such as high-resolution cameras, and emerging AI-based species recognition have expanded the analytical capabilities of BRUV systems. Despite these advances, certain limitations persist, including variability in bait plume dispersion, current-dependent attraction ranges, reduced detectability of highly mobile or non-scavenging species, and the need for substantial video processing. When paired with complementary tools such as environmental DNA, or diver surveys, BRUVs provide a more accurate and comprehensive picture of marine biodiversity.In Türkiye, BRUVs show potential across diverse marine environments, from the low-visibility Black Sea to the species-rich Mediterranean. They enable effective monitoring of rocky reefs, seagrass beds, artificial habitats, and aquaculture zones, and are particularly valuable for tracking invasive species and evaluating marine protected areas.

Keywords:

Non-Invasive, Marine Protected Areas, BRUV

Preserving Genetic Diversity: Why Türkiye Needs a National GenBank

Yahya Terzi [1], Rafet Çağrı Öztürk [1]

1 Department of Fisheries Technology Engineering, Faculty of Marine Sciences, Karadeniz Technical University, Trabzon, Türkiye

Corresponding Author: *rafetcagriozturk@gmail.com*

Abstract

The preservation of genetic diversity is fundamental to effective biodiversity research, conservation planning, and long-term ecosystem management. Türkiye, situated at the junction of major biogeographic regions and home to rich terrestrial, freshwater, and marine biota, remains underrepresented in global biodiversity and genomic datasets. Recent international analyses highlight large "biodiversity blindspots", areas where species are present but missing from digitized records due to inadequate specimen archiving or the absence of coordinated genetic repositories. These gaps hinder accurate species assessments, limit the resolution of ecological monitoring tools, and reduce the reliability of conservation decision-making. Establishing a National GenBank for Türkiye would address these limitations by providing a centralized, long-term repository for DNA, tissues, seeds, gametes, and high-quality genomic reference material across taxonomic groups. A national genbank would function as a scientific and conservation infrastructure that (i) preserves genetic diversity threatened by climate change, habitat degradation, overexploitation, invasive species, and emerging diseases; (ii) supports taxonomic and genomic research by enabling reliable species identification and the development of high-resolution reference libraries for tools such as eDNA metabarcoding; (iii) enhances the quality and reproducibility of biodiversity monitoring programs, including BRUV, UVC, fisheries assessments, and long-term ecological surveys, by linking observational data with verified genetic material; and (iv) strengthens restoration, aquaculture improvement, and species recovery efforts through access to well-curated, traceable biological samples.

Keywords:

Genetic Diversity, National GenBank, Ecosystem Monitoring, Biodiversity Conservation

Chemical Composition, Physico-Chemical Properties and Amino Acid Profile of Muffins Enriched with Cricket Powder (*Acheta Domesticus*)

Akylai Chynalieva [1], Bermet Sultanova [1], Aichurok Mazhitova [1]

[1] Department of Food Engineering, Engineering Faculty, Kyrgyz-Turkish Manas University, Bishkek 720038, Kyrgyzstan

Corresponding Author: *aichurok.mazhitova@manas.edu.kg*

Abstract

The incorporation of insect-based protein into muffins is a growing trend in the food industry due to the demand for sustainable and nutritious options. Insect proteins provide a robust nutritional profile, encompassing high-quality protein, and essential amino acids, making them an appealing substitute for conventional protein sources. This research aimed to analyze the chemical composition, color characteristics, physico-chemical properties, and amino acid profile of muffin recipes developed by substituting wheat flour with cricket powder (*Acheta domesticus*) at levels of 10%, 20%, and 30%. The addition of cricket powder (CP) significantly increased protein content from 9.26% in the control muffins to 14.08% at 30% CP. The initial high fat content (13.00%) in control muffins rose to 20.40% with 30% CP. The ash content, indicating mineral presence, also increased with CP concentration, enhancing the muffins' mineral profile. Muffins with 30% CP had a significantly lower pH than the control and lower-enriched samples. Total titratable acidity increased with CP levels, confirming the pH reduction. CP changed the muffins' color significantly, with greater color differences observed as CP concentration rose. The crust showed a noticeable color change even at 10% CP, and the crumb had the most significant color shift at this level before stabilizing at higher concentrations. Water activity (aw) decreased to 0.65 with 30% CP, indicating improved microbial stability. CP inclusion led to an overall increase in essential and non-essential amino acids, with essential amino acids like histidine, threonine, and leucine rising with CP addition. Glutamic acid remained the most abundant amino acid in all samples. Adding cricket powder to muffins effectively enhances protein content and improves amino acid profiles, making them a better nutritional choice than traditional muffins.

Keywords:

Food with Added Value, Protein Content, Enriched Muffin, Insect Powder, Amino Acid Composition

Innovative Pathways for Circular Economy: Repurposing Coal Mine Waste in Construction Materials

Bishnu Pada Bose [1]

1 Department of Civil Engineering, Haldia Institute of Technology, Haldia, India

Corresponding Author: *bosebishnu@gmail.com*

Abstract

Rapid population growth and urbanization have accelerated waste accumulation, pushing the biosphere beyond its natural regenerative capacity under the prevailing linear "take–make–use–dispose" model. Transitioning to a circular economy is essential for mitigating environmental degradation. This study aims to identify environmentally harmful yet abundantly available waste materials that could be repurposed in civil engineering applications. Based on a systematic evaluation of multiple waste streams, coalmine overburden was selected for comprehensive experimental investigation. The results demonstrate that all components of coal mine waste can be successfully transformed into valuable construction resources. After pulverizing large stones and separating silt and coal particles, the processed stones can be used as coarse and fine aggregates for concrete, bricks, and mortar. Silt, when blended with ordinary clay, is suitable for producing fired bricks, while residual coal particles offer additional energy recovery potential. The mechanical performance of concrete, bricks, and mortar manufactured from mine-derived aggregates is comparable to standard materials. These findings highlight the significant potential of recycling waste to extend material life cycles, prevent uncontrolled dumping, and partially replenish rapidly depleting natural resources. The approach aligns with the traditional 3R framework (Reduce, Reuse, Recycle) while extending it to include Replenish (restoring scarce resources) and Release land (freeing land previously occupied by waste). This expanded framework advances the circular economy from a linear "make–use–dispose" trajectory toward a regenerative "make–use–recycle–replenish" cycle. By reducing environmental harm, relieving pressure on ecosystems, and enabling land reclamation, the process contributes to long-term sustainability. Moreover, entrepreneurial adoption of the technologies developed in this study offers substantial social and environmental benefits. Transforming polluting waste into usable resources can mitigate soil, water, and air contamination, enhance agricultural productivity by reducing heavy metal accumulation, and strengthen local economies, further reinforcing a regenerative, resource-efficient circular economy.

Keywords:

Circular Economy, Waste, Mine Waste, Waste Recycling, Construction Materials

An Integrated Web-Based System for Managing MEDEK, MÜDEK, and YÖKAK Accreditation Processes

Mahmut Yeşilyurt [1]

1 Department of Computer Technologies, İzmir Kavram Vocational School, İzmir, Türkiye

Corresponding Author: *mahmut.yesilyurt@kavram.edu.tr*

Abstract

Accreditation processes in Turkish higher education have become increasingly detailed and demanding under efforts to meet the standards and requirements of MEDEK, MÜDEK, and YÖKAK. Institutions must collect and manage large amounts of data, demonstrate consistent alignment between program outcomes and national frameworks, document assessment and improvement cycles, and prepare periodic reports for internal and external evaluations. These tasks are often carried out manually or through uncoordinated systems, which leads to high workload, loss of time, data inconsistencies, and difficulty in maintaining continuous accreditation readiness. To address these challenges, a web-based software system was developed using C-Sharp to support accreditation process management in a structured and efficient way. The system organizes key components of accreditation—such as outcome mapping, evidence collection, assessment tracking, and report generation—into a single platform. It provides predefined templates that match MEDEK, MÜDEK, and YÖKAK criteria, ensures version control, and allows multiple users to work in parallel. Automated workflows reduce repetitive work, support accurate documentation, and make it easier to monitor progress throughout the accreditation cycle. The software is currently in its beta-testing phase and is being used at İzmir Kavram Vocational School. Early use shows improvements in the clarity, consistency, and accessibility of accreditation data. The platform helps institutions maintain up-to-date documentation, prepare required reports with less effort, and manage the process in a more predictable and organized manner. This study presents a practical digital tool that responds to common problems faced by higher education institutions during accreditation. The system shows that software-supported process management can reduce administrative load, improve data quality, and contribute to a more stable and sustainable approach to meeting MEDEK, MÜDEK, and YÖKAK requirements.

Keywords:

Higher Education Accreditation, YOKAK, MEDEK, MUDEK, Web-Based Software

Network Pharmacology and Machine Learning-Driven Virtual Screening with Dynamics Simulations of Natural Compounds for Glioblastoma

Damilola Omoboyowa [1], Abayomi O. Adelaja [2], Babasola Aiyeku [3], Magdi E. A. Zaki [4], Mohit Agrawal [5], Temitope C. Aribigbola [6]

1 Adekunle Ajasin University, Akungba-Akoko Ondo State, Nigeria
2 Pharmacology Department, Faculty of Basic Medical Sciences, Olabisi Onabanjo University, Ago-Iwoye, Ogun State, Nigeria
3 Northern Lincolnshire and Goole NHS Foundation Trust through Medocho Ltd, Scunthorpe, United Kingdom
4 Chemistry Department, College of Science, Imam Mohammad Ibn Saud Islamic University (IMSIU), Riyadh, Saudi Arabia
5 School of Medical & Allied Sciences, K.R. Mangalam University, Gurugram, 122103, India
6 Faculty of Medicine and Dentistry, Department of Medical Microbiology and Immunology, University of Alberta Edmonton, AB T6G 2E1, Canada

Corresponding Author: *damilola.omoboyowa@aaua.edu.ng*

Abstract

Glioma progression is driven by dysregulated signaling networks, including CDK4-Cyclin D3, PI3K-Akt, and EGFR pathways. Targeting CDK4-Cyclin D3 offers a promising therapeutic strategy. A systems-level computational approach was employed to identify potential CDK4-Cyclin D3 inhibitors from the OTAVA library. Network pharmacology, molecular docking, MMGBSA, AutoQSAR modeling, Density function theory (DFT) calculations, drug-likeness and ADMET profiling, and 200 ns molecular dynamics simulations were performed alongside temozolomide as a reference. Network analysis identified 16 shared glioma targets for vorasidenib and temozolomide, highlighting central pathways regulating metabolism, cell survival, and DNA repair. Docking and MMGBSA analyses revealed Compounds 781, 792, and 2299 as potent CDK4-Cyclin D3 inhibitors, outperforming temozolomide. AutoQSAR predicted higher pIC_{50} values for the hits, with Compound 781 ranked highest. DFT calculations indicated favorable electronic properties for protein-ligand interactions. Drug-likeness and pharmacokinetic profiling demonstrated good oral absorption, moderate blood brain barrier (BBB) permeability, and acceptable cardiotoxicity. Molecular dynamics simulations at 200 ns demonstrated stable binding, minimal structural fluctuations, and strong hydrogen bond, particularly for Compound 781. Compounds 781, 792, and 2299 have higher predicted potency, binding stability, and favorable pharmacokinetic properties than temozolomide, indicating their potential as CDK4-Cyclin D3 inhibitors for glioma treatment. These computational insights provide a strong rationale for experimental validation in vitro and in vivo.

Keywords:

Glioma, CDK4-Cyclin D3, Network Pharmacology; Virtual Screening, MD Simulation

Use of Nanoparticles for Drilling Fluid in Petroleum Industry

Abdollah Esmaeili [1], Afonso Cesar Rodrigues Nogueira [1]

1 Geosciences Institute (IG/UFPA), Faculty of Geology, Universidade Federal do Pará (UFPA), Belém, PA, Brazil

Corresponding Author: *esmailyabdollah@gmail.com*

Abstract

In drilling operations, drilling fluids are used to improve drilling operations and bring drilling cuttings to the surface. The formulation of these fluids, commonly known as drilling mud, is one of the most important factors of a successful drilling operation. Considering that the major part of the costs of drilling a well is related to the supply and pumping of drilling mud, the use of more efficient and better fluids plays an important role in reducing costs and increasing drilling efficiency. A suitable drilling fluid should have a high ability to cool the drill bit, bring the drilling cuttings to the surface, smooth the movement of the rotating drill pipes, control the wall pressure, transfer the hydraulic power of the pump to the drill bit and many other things. Preparation of drilling mud with the best formulation and effective materials is an important factor in increasing the speed of drilling, increasing the productivity of drilling operations, preventing the reduction of flow rate, reducing the cost of drilling a well, and finally increasing the success rate in post-drilling operations. In general, the purpose of using nano additives in drilling mud is to reduce the cost and prepare an optimal fluid by reducing the consumption of materials and improving its properties. Adding nanomaterials to the base fluid creates favorable rheological properties, very good stability of suspension and proper lubrication. The use of nanoparticles in drilling fluid enables petroleum industry engineers to quickly correct the properties of drilling fluid by changing the composition, size and distribution of nanoparticles. Also, in well cementing operations, by using advanced compounds, efficiency and productivity as well as operation costs can be greatly improved by using nanotechnology.

Keywords:

Nanoparticles, Drilling, Fluid, Petroleum, Industry

Towards High-Efficiency $CsPbI_3$ Perovskite Solar Cells: A Computational Pathway to Material and Device Optimization,

Nurul Farina Mohd Nazli [1]

1 Faculty of Electronic and Computer Technology and Engineering (FTKEK), Universiti Teknikal Malaysia Melaka, Hang Tuah Jaya, 76100, Durian Tunggal, Malaysia

Corresponding Author: *m122410008@student.utem.edu.my*

Abstract

The rapid evolution of perovskite photovoltaic technology has positioned cesium lead iodide ($CsPbI_3$) as a promising candidate for next-generation solar cells due to its exceptional thermal stability, suitable bandgap, and long carrier diffusion length. However, achieving practical device efficiencies remains constrained by suboptimal layer configurations, defect-induced recombination, and non-optimized charge transport properties. This study presents a comprehensive computational framework to enhance the performance of $CsPbI_3$-based perovskite solar cells through systematic material and device optimization using SCAPS-1D. Key structural and electrical parameters including layer thicknesses, doping concentrations, and defect densities across the absorber, TiO_2 electron transport layer (ETL), and Spiro-OMeTAD hole transport layer (HTL) were systematically varied and analyzed to determine their influence on open-circuit voltage (Voc), short-circuit current density (Jsc), fill factor (FF), and overall power conversion efficiency (PCE). To effectively address multi-parameter interactions, a hybrid Taguchi–Grey Relational Analysis (GRA) approach employing an L27 orthogonal array was implemented. This statistical configuration enabled simultaneous optimization of multiple device parameters while minimizing the computational burden associated with conventional parametric sweeps. The optimization revealed that precise control of thickness profiles, carrier concentrations, and defect densities within each functional layer significantly reduces recombination losses and enhances charge extraction pathways. Under optimized SCAPS-1D conditions, the device achieved a PCE of 23.83%, accompanied by marked improvements in Voc, Jsc, and FF. Subsequent refinement using the Taguchi–GRA L27 framework further enhanced performance, yielding a PCE of 25.01%, corresponding to a 4.95% improvement over the conventionally optimized structure. This study demonstrates that hybrid statistical optimization offers a robust and data-driven pathway for designing efficient and stable inorganic perovskite solar cells. The proposed computational methodology provides actionable design guidelines that can accelerate the fabrication and commercialization of high-performance $CsPbI_3$ photovoltaic devices within the global renewable energy landscape.

Keywords:

Perovskite Solar Cells, $CsPbI_3$, SCAPS-1D, Taguchi-GRA, Optimization

Evaluation of the Sensitivity and Specificity of the Diagnostic Electrochemical Biosensor Using MicroRNAs Biomarkers Involved in Multiple Sclerosis

Azizeh Shadidizaji [1], Farideh Ghalamfarsa [2], Yousef Fazli [3], Ramin Jannesar [3], Kagan Tolga Cinisli [1], Mahmut Sinan Taşpınar [1], Ahmet Hacımüftüoğlu [4]

1 Research and Innovation Hub, Ostad Aali-Nasab Hospital, Iranian Social Security Organization, Tabriz, Iran
2 Department of Cellular and Molecular, Yasuj University of Medical Sciences, Yasuj, Iran
3 Department of Pathology, Yasuj University of Medical Sciences, Yasuj, Iran
4 Department of Pharmacology, Faculty of Medicine, Atatürk University, Erzurum, Türkiye

Corresponding Author: *ls_shadi@yahoo.com*

Abstract

Multiple sclerosis (MS) is a chronic neurodegenerative disease requiring early diagnosis for effective intervention. Current diagnostic methods, such as MRI and cerebrospinal fluid analysis, are costly, time-consuming, and lack sufficient sensitivity for early detection. MicroRNAs (miRNAs), particularly miR-145 and miR-326, have emerged as promising biomarkers due to their differential expression in MS patients and stability in circulating biofluids. This study aims to develop a novel electrochemical biosensor for the rapid, sensitive, and specific detection of these miRNAs in serum samples. The biosensor is constructed using a glassy carbon electrode modified with multi-walled carbon nanotubes and gold nanoparticles, functionalized with thiolated probes for miR-145 and miR-326. Detection is achieved via hybridization-induced changes in methylene blue redox current. The biosensor demonstrates high sensitivity, detecting target miRNAs at femtomolar concentrations, and excellent specificity in distinguishing miR-145 and miR-326 from homologous miRNAs. Validation in spiked human serum confirms its potential for clinical application. This non-invasive, cost-effective platform offers a significant advancement towards point-of-care MS diagnostics, enabling earlier and more accurate disease monitoring.

Keywords:
Electrochemical Biosensor, Multiple Sclerosis, MicroRNA Biomarkers, Mir-145 and Mir-326, Gold Nanoparticles.

Influence of Low-Temperature Annealing on Copper Iodide as Hole Transporting Layer for Perovskite Solar Cell Applications

Omsri Vinasha Aliyaselvam [1], Faiz Arith [2], Mohd Asyadi Azam [3]

1 Centre for Telecommunication Research & Innovation, Faculty of Electronic and Computer Engineering, Universiti Teknikal Malaysia Melaka, Malaysia
2 Faculty of Electronics and Computer Technology and Engineering, Universiti Teknikal Malaysia Melaka
3 Faculty of Industrial and Manufacturing Technology and Engineering, Universiti Teknikal Malaysia Melaka

Corresponding Author: *p122310011@student.utem.edu.my*

Abstract

Copper Iodide (CuI) thin films synthesized using monoethanolamine (MEA) as a green solvent exhibit high optical transparency and uniform planar morphology, supporting their function as efficient hole transport layers (HTLs) in perovskite solar cells. Using this low-temperature, additive-free method, γ-CuI with a zinc-blende structure was successfully obtained. Despite these promising outcomes, maintaining uniform structural integrity and electrical stability during low-temperature processing remains a key challenge, especially when targeting mechanically flexible perovskite devices. The CuI films were deposited on Indium-doped Tin Oxide (ITO) substrates via solution-processable spin coating and subsequently annealed at temperatures between 60 ℃ and 120 ℃. SEM and XRD analyses indicate that annealing temperature critically governs grain evolution, preferred crystallographic orientation, and structural parameters such as crystallite size, lattice constant, lattice strain, and dislocation density. The film annealed at 80 ℃ displayed a sharp nanoflower-like morphology with favourable conductivity and a stable band gap. These observations confirm that precise annealing optimization is essential for producing structurally robust CuI thin films suitable for high-performing PSC applications.

Keywords:

Annealing Temperature, Copper Iodide; Hole Transporting Layer; Perovskite Solar Cell

Integrated Geophysical and Hydrochemical Assessment of Groundwater Contamination and Aquifer Vulnerability in the Ifewara Area, Southwestern Nigeria

Taiwo Kamorudeen Alasi [1], Charles Olubunmi Ogunkoa [2]

1 Department of Physics with Electronics, Faculty of Sciences, University of Ilesa, Ilesa, Nigeria
2 Department of Physics, Faculty of Sciences, Ajayi Crowther University, Oyo, Nigeria

Corresponding Author: *co.ogunkoya@acu.edu.ng*

Abstract

This study investigates groundwater contamination and aquifer vulnerability in the Ifewara area, Southwestern Nigeria, through an integrated geophysical and hydrochemical approach. Vertical Electrical Sounding (VES) was employed to characterize subsurface stratigraphy, while Atomic Absorption Spectrometry (AAS) analyzed trace metal concentrations in groundwater from five boreholes and five hand-dug wells. Hydrochemical results revealed elevated levels of toxic metals, including manganese (up to 1737 ppm), arsenic, lead, nickel, and copper (up to 94.2 ppm), exceeding WHO permissible limits and posing significant health risks. Health risk assessments using Average Daily Dose (ADD) and Hazard Quotient (HQ) calculations indicated chronic exposure concerns, with manganese exhibiting an ADD of 20.61 mg/kg-day and HQ of 147.22, highlighting neurotoxicity risks. Other metals such as arsenic and lead also showed HQ values far above safe thresholds. Geophysical data delineated four subsurface layers: topsoil, lateritic hardpan, clayey saprolite, and fractured bedrock aquifers. The clayey saprolite acts as a semi-confining yet permeable layer, facilitating contaminant migration, consistent with hydrochemical contamination patterns. Integration of resistivity profiles with hydrochemical data effectively mapped contamination hotspots and elucidated geohydrological controls on contaminant transport. The findings demonstrate that both natural geological factors within the Pan-African schist belt and anthropogenic activities, including mining and agriculture, significantly influence groundwater quality and aquifer vulnerability. The study underscores the urgent need for continuous groundwater quality monitoring, targeted remediation, and community education to mitigate health risks. The multidisciplinary methodology provides a robust framework for groundwater contamination assessment in complex tropical basement terrains, supporting sustainable water resource management and public health protection.

Keywords:

Ground Water, Aquifer, Contamination and Geochemical

Development of AI-Machine Learning with the One Health Framework in the Prevention of Foodborne Disease in the "Program Makanan Bergizi Gratis Indonesia"

I Made Dwi Mertha Adnyana [1], Niken Irfa Nastiti [1], Annissa Delfira [1], Zahra Frizki Asty [1], Artka Zildzia Riawan [2], Ni Luh Gede Sudaryati [3]

1 Department of Microbiology and Parasitology, Faculty of Medicine and Health Science, Universitas Jambi, Jambi, 36122, Indonesia
2 Undergraduate Program of Medicine, Faculty of Medicine and Health Sciences, Universitas Jambi, Indonesia
3 Department of Biology, Faculty of Information Technology and Science, Universitas Hindu, Indonesia

Corresponding Author: *dwikmertha13@gmail.com*

Abstract

Background: Indonesia's Free Nutritious Meals Program (MBG), launched in January 2025, has served more than 40 million recipients through more than 15,000 kitchens throughout Indonesia. As of October 2025, there have been 11,660 cases of food poisoning from 211 incidents in 25 provinces (88 districts/cities), accounting for 48% of all incidents. The massive increase in cases indicates the need for an integrated framework for detection, reporting, and innovative technology-assisted surveillance. Objective: This study proposes an integrated artificial intelligence/machine learning (AI/ML) framework that operationalizes the One Health principle for the prevention of foodborne diseases in the Free Nutritious Meals program. Methods: The designed system is expected to have five main components: machine learning algorithms that can predict which kitchens are at high risk; a data platform that integrates information from various ministries for reporting surveillance results and complaints; a food ingredient tracking system using blockchain and IoT sensors; social media monitoring to detect early signs of outbreaks; and pathogen DNA analysis to quickly trace the source of contamination. Results: Compared with conventional methods, the integration and implementation of AI-machine learning is expected to reduce outbreak detection time from weeks to hours, improve the accuracy of food source attribution, and enable proactive food safety management that integrates human health, animal (animal food sources), and the environment (pathogen sources), as well as integrate the One Health concept into the MBG program policy framework in Indonesia. The government needs to mandate AI-assisted certification and blockchain regulations for risky materials, install IoT sensors in 15,000 kitchens, and train 290,000 food officers to minimize food poisoning as a result of this program. Conclusion: The government and all relevant sectors need to develop an integrated surveillance system from the food source to the completion of the program, which should be carried out daily.

Keywords:

Artificial Intelligence, Machine Learning, One Health Framework, Predictive Surveillance, Outbreak Detection.

Sustainable Nanomaterial Production: Carbon Quantum Dots Synthesized from Biological Waste

Taha Yasin Bayram [1], Mehmet Yılmaz [2], Aslı Yılmaz [3]

1 Department of Molecular Biology and Genetics, Institute of Science, Ataturk University, Erzurum, Türkiye
2 Departmant of Chemical Engineering, University of Michigan, Ann Arbor, MI // Department of Chemical Engineering, Faculty of Engineering, Atatürk University, Erzurum, Türkiye
3 Departmant of Chemical Engineering, University of Michigan, Ann Arbor, MI // Department of Molecular Biology and Genetics, Faculty of Science, Atatürk University, Erzurum, Türkiye

Corresponding Author: *tahayasin.bayram20@ogr.atauni.edu.tr*

Abstract

Carbon quantum dots (CQDs) have garnered significant attention in recent years due to their strong fluorescent properties, high water solubility, and biocompatibility. These characteristics make them valuable in biomedical fields such as sensing, bioimaging, diagnosis, and treatment. Various materials, ranging from pure organic compounds to waste products, have been used as precursors in CQD synthesis. Cell culture studies generate significant amounts of waste, primarily from culture media, which is often discarded without further evaluation. Therefore, innovative approaches are needed to convert culture medium waste into high-value-added products. This study proposes a new procedure for producing CQDs using DMEM-based cell culture medium waste. The aim is to evaluate whether biological waste can be used as a functional precursor in CQD synthesis and to characterize the optical and biological properties of the obtained nanostructures. The synthesis was carried out using an environmentally friendly hydrothermal method under different conditions. The produced CQDs were examined for their absorption properties using UV-vis spectroscopy to determine their absorption characteristics, and their emission behavior was confirmed using fluorescence spectroscopy. Optical stability was monitored for 30 days in dark and light conditions, and no significant decrease in emission intensity was detected. Structural characterization was performed using TEM imaging. For biological evaluation, cytotoxicity studies were performed on different cell lines using the MTT assay. Cell viability was measured at varying concentrations, and the results indicated no significant toxicity at low and moderate doses. These findings point to the potential for safe use of waste-based CQDs in biomedical applications. Overall, the findings demonstrate that CQDs with strong optical stability and low cytotoxicity can be successfully synthesized from cell culture waste. This approach contributes to sustainable nanomaterial production by reducing material costs, minimizing waste, and decreasing environmental impact.

Keywords:

Carbon Quantum Dots, Cell Culture Waste, Fluorescence, Cytotoxicity, Sustainable Nanomaterials.

Optical and Biological Properties of Carbon Quantum Dots Synthesized from Daucus Carota Ssp. Sativus Var. Atrorubens Extract

Aslı Yılmaz [1], Ezo Palavan [2], Mehmet Yılmaz [3]

1 Departmant of Chemical Engineering, University of Michigan, Ann Arbor, MI // Department of Molecular Biology and Genetics, Faculty of Science, Atatürk University, Erzurum, Türkiye
2 Department of Molecular Biology and Genetics, Faculty of Science, Atatürk University, Erzurum, Türkiye
3 Departmant of Chemical Engineering, University of Michigan, Ann Arbor, MI // Department of Chemical Engineering, Faculty of Engineering, Atatürk University, Erzurum, Türkiye

Corresponding Author: *ezo.palavan19@ogr.atauni.edu.tr*

Abstract

Carbon quantum dots (CQDs) are carbon-based new class of fluorescence materials with a particle size of less than 10 nm. CQDs represent strong fluorescence properties, chemical inertness, high solubility in water, and biocompatibility. With these unique properties, they have been employed in various applications including the bioimaging, biosensing, diagnosis and treatment. A myriad of materials, from pure organic compounds to waste products, have been utilized as initiators in the synthesis of CQDs. Despite the recent progress, novel initiators and procedures are highly demanded fort he fabrication of CQDs. Daucus carota ssp. sativus var. atrorubens is the botanical name for the black carrot, commonly known as “purple carrot” or “black/purple cultivar of the edible carrot.” This variety is especially rich in anthocyanins, giving it the deep purple/black color. It is nutritionally superior to typical carrots due to high anthocyanin content and strong antioxidant properties. The black carrot provides unique characteristics in cardiovascular, anti-inflammatory, anti-diabetic, neuroprotective, and anticancer applications. The primary objective of this study is to evaluate the extract obtained from the black carrot plant, a natural and sustainable resource, as a carbon source in CQD synthesis. The aim is to thoroughly investigate the optical properties and interaction with biological systems of the CQD obtained through the green synthesis process using the hydrothermal method. The structural and optical properties of the CQD synthesized within the scope of the study were determined using characterization techniques such as UV-vis spectroscopy, TEM, fluorescence spectroscopy, and zeta potential measurements. Subsequently, the biocompatibility, cytotoxic effect, and intracellular localization potential of these particles were evaluated through cell culture studies. CQDs demonstrated high fluorescence activity with high biocompatibility and low cytotoxicity. In conclusion, black carrot-based CQDs via an environmentally friendly green synthesis provided high potential in the biological applications

Keywords:

Carbon Quantum Dot, Black Carrot, Green Synthesis, Biological Applications

Synthesis and Characterization of Ni-Doped ZnO Nanorods for Potential Use in Solar Cells

Thanies Murugan [1], Faiz Arith [2]

1 Graduate Student, Universiti Teknikal Malaysia Melaka
2 Faculty of Electronics and Computer Technology and Engineering, Universiti Teknikal Malaysia Melaka, Hang Tuah Jaya, Durian Tunggal, 76100, Melaka, Malaysia

Corresponding Author: *thaniesscout@gmail.com*

Abstract

Perovskite solar cells (PSCs) are a leading candidate for next-generation photovoltaic technology, offering high-power conversion efficiency (PCE) and cost-effective fabrication. While is conventionally used as the electron transport layer (ETL), its required high-temperature crystallization (450) severely limits its integration into flexible devices built on heat-sensitive substrates. The growing demand for flexible and wearable energy harvesters necessitates the development of alternative low-temperature ETL materials. Zinc oxide nanorods (ZnO NRs) are a promising substitute due to their low-cost, low-temperature synthesis, high electron mobility, and aligned nanostructure. However, pristine ZnO often suffers from intrinsic defect states that hinder charge extraction and reduce PCE. To address this, we investigated nickel (Ni) doping as a strategy to modify the electrical and structural properties of ZnO. In this study, Ni-doped ZnO NRs were synthesized via a low-temperature hydrothermal growth method with varying Ni concentrations (0, 1, 3, and 5 mol%) and growth durations (5 and 9 hours) at 100C. Their structural, morphological, and optical properties were thoroughly analyzed using XRD, EDX, FESEM, and UV–Vis spectroscopy. Photovoltaic performance was assessed via current–voltage (I–V) characterization. The results demonstrate that controlled Ni incorporation successfully improved crystallinity, suppressed defect density, and significantly enhanced electron transport. This led to a marked increase in PCE compared to devices utilizing undoped ZnO. This research establishes Ni-doped ZnO NRs as a promising, low-temperature, and cost-effective ETL material for high-efficiency flexible PSCs. These findings offer valuable insights for developing scalable and energy-efficient photovoltaic devices critical for advancing flexible electronics and sustainable energy applications.

Keywords:

Nickel, Zinc Oxide, Nanorods, Nanowalls, Nanoflower, Nanostrctrue, Hydrothermal

Zinc Oxide Nanostructure Buffer Layers for Improved Charge Transport and Efficiency in DSSC

Juraina Md Yusof [1], Suhaidi Shafie [2], Mohd Ali Mat Nong [1], Ismayadi Ismail [3], Yusnita Yusuf [1]

1 Functional Nanotechnology Devices Laboratory (FNDL), Institute of Nanoscience and Nanotechnology Universiti Putra Malaysia, Serdang, Selangor, Malaysia
2 Department of Electrical and Electronics, Faculty of Engineering, Universiti Putra Malaysia, Serdang, Selangor, Malaysia
3 Nanotechnology Synthesis and Characterization Laboratory, Institute of Nanoscience and Nanotechnology, Universiti Putra Malaysia, Serdang, Selangor, Malaysia

Corresponding Author: *juraina@upm.edu.my*

Abstract

Dye-sensitized solar cells (DSSCs) are among the most promising low-cost alternatives to silicon-based solar cells, offering substantial power conversion efficiency due to their compact size, ease of preparation, and high resistance and sensitivity to weather changes. Recent technological advancements have shifted toward flexible, versatile, and portable electronics, as well as simpler device fabrication. A DSSC consists of a photoanode that includes a transparent conducting material and a semiconducting layer. The semiconducting layer, which adsorbs dye molecules, plays a crucial role in determining the power conversion efficiency. Its efficiency strongly depends on optimal charge transport and sufficient surface area for dye adsorption within the photoanode. One of the key challenges is engineering zinc oxide (ZnO) nanostructured buffer layers that simultaneously enhance electron mobility, increase dye-loading capability, and reduce recombination losses. In this work, zinc oxide nanorods (ZNRs) were synthesized using buffer layer patterning times of 4 and 8 minutes to investigate the influence of deposition duration on the resulting morphology, crystallinity, and photovoltaic performance of DSSCs. The growth of the nanorods was mediated by a plasma induced buffer layer for growth patterning. The ZNRs exhibit excellent properties such as high porosity, large surface area, surface roughness, and high electrical conductivity which are suitable for improving dye adsorption and enhancing charge transfer mobility. Current and voltage measurements under 1000 W/m² illumination show that the DSSC fabricated with the 4 minutes ZnO buffer layer achieves a higher efficiency than the 8 minutes sample. These results demonstrate that optimizing the ZnO buffer layer deposition time, particularly through shorter durations, can significantly improve charge transport and overall DSSC performance.

Keywords:

Dye Synthesized Solar Cells, Zinc Oxide Nanostructures, Semiconductive Layer, Solar Cell Photoanode

Traditional Arts and Mathematics

Aydan Akkök [1], Fatma Yavuz Takım [2]

1 Department of Traditional Handicrafts, Vocational School of Technical Sciences, Atatürk University, Erzurum, Türkiye
2 Department of Envıronmental and Protection Technologies, Vocational School of Technical Sciences, Atatürk University, Erzurum, Türkiye

Corresponding Author: *aydan.akkok@atauni.edu.tr*

Abstract

When we look at traditional arts, we see that throughout history, they have been shaped not only by aesthetic concerns but also by specific mathematical principles and ratio systems, creating a unique field of expression where science and art intertwine. The concepts of rhythm, repetition, symmetry, proportion, and order seen in T u r k i s h -Islamic arts such as calligraphy, illumination, miniature, tile-making, marbling, and geometric ornamentation are concrete examples of the invisible yet decisive influence of mathematics on the visual field. The purpose of this paper is to uncover the mathematical structure underlying traditional arts and to evaluate the aesthetic and technical functions of these structures in artistic production. In calligraphy, the measurements, angles, and line arrangement of letters are based on strict rules. The proportions between letter lengths, particularly in Thuluth and Naskh script, are created according to a specific geometric system. In illumination art, the construction of hatai, rumi, penç, and geometric interlaced motifs is shaped by the Golden Ratio, axes of symmetry, and polygonal-based divisions. Circle, star, and polygonal arrangements are transformed into repetitive surfaces that evoke a sense of infinity through digital multiplication methods. The concept of multiple perspective used in miniature art is created by placing figures and spatial distributions within a mathematical order. In tile art, octagonal, decagonal, and hexagonal interlaces create geometric systems that provide surface continuity through a fractal-like growth logic. The techniques of division, folding, symmetry transformations, and proportioning used in the creation of traditional patterns parallel contemporary design mathematics. Consequently, mathematics in our traditional arts is not only a creator of order but also an aesthetic and visual language. This study aims to reveal the scientific structure behind artistic production by evaluating the fundamental formations of traditional arts and mathematics from an interdisciplinary perspective.

Keywords:

The Art, Aesthetics, Harmony, Golden Ratio, the Mathematics

Effect of Temperature on the Structural and Thermal Properties of Perna Viridis Shells

Rosnah Nawang [1], Mohd Zobir Hussein [2]

1 Nanomaterial Syntesis and Characterization Laboratory, Institute of Nanoscience and Nanotechnology, Universiti Putra Malaysia, Serdang Selangor, Malaysia
2 Faculty of Dentistry, Brawijaya University, Malang, Indonesia

Corresponding Author: *rnawang@upm.edu.my*

Abstract

This study investigates the structural, compositional, and thermal transformations of Perna viridis (PVS) shells heated at 100, 500, and 1000 ℃ using FTIR, XRD, and TGA/DTG analyses. The FTIR spectra of the raw shell reveal the presence of adsorbed water, organic matrix components, and calcium carbonate in the aragonite form. Heating at 500 ℃ induces a clear phase transition from aragonite to calcite. Calcination at 1000 ℃ results in the appearance of CaO, $Ca(OH)_2$, and residual $CaCO_3$, reflecting the decomposition of $CaCO_3$ followed by the rapid rehydration and re-carbonation of CaO upon exposure to atmospheric moisture and CO_2. XRD patterns corroborate these observations, showing predominantly aragonite in the raw sample, calcite at 500 ℃, and portlandite as the major phase at 1000 ℃, with a minor amount of calcite. TGA/DTG analysis reveals three main weight-loss events corresponding to the release of adsorbed water, the decomposition of organic components, and the major thermal decomposition of $CaCO_3$ between 531–916 ℃. Overall, the combined FTIR, XRD, and TGA findings demonstrate significant mineralogical transformations in Perna viridis shells upon high-temperature treatment, highlighting their potential as a biogenic precursor for CaO production and related calcium-based material applications.

Keywords:

Perna Viridis; Calcium Carbonate; Phase Transformation; FTIR; XRD; Thermogravimetric Analysis

Classification of Biomaterials and Their Biomedical Applications

Abbas Razmi [1]

[1] Independent Researcher, Erzurum, Türkiye

Corresponding Author: *abbasrazmi@hotmail.com*

Abstract

Biomaterials are extensively employed in medical implants owing to their remarkable biocompatibility and resistance to corrosion. These materials offer a robust foundation for various coating applications, among which hydroxyapatite is particularly notable due to its close chemical similarity to natural bone tissue, ensuring superior biocompatibility. A wide array of materials is currently developed or utilized as biomaterials for tissue regeneration and replacement in the human body. For instance, metal-based biomaterials such as stainless steel, titanium, and cobalt alloys are widely applied for bone restoration. Similarly, ceramic biomaterials are used in dental applications, including crowns, cements, and dentures. Synthetic polymers such as PEG, PLGA, and PMMA are employed in soft biomaterial applications, ranging from facial prostheses and tracheal tubes to contact lenses and medical adhesives. Moreover, natural polymers including collagen, fibrinogen, hyaluronic acid, and elastin demonstrate high efficacy in soft tissue engineering due to their specific amino acid sequences that interact with host cells, thereby initiating biochemical signals responsible for cell migration, proliferation, and differentiation that facilitate tissue repair and integration. Additionally, composite materials, such as fiber-reinforced and carbon nanotube-polymer composites, are increasingly explored for their lightweight nature and customizable mechanical properties, making them ideal for applications at the hard-soft tissue interface. The primary consideration in selecting suitable biomaterials lies in their compatibility with human physiology, ensuring long-term functionality without inducing adverse immune responses. Thus, biomaterials must be free from harmful effects such as injury, cytotoxicity, genotoxicity, mutagenicity, carcinogenicity, or immunogenicity, while effectively fulfilling their intended therapeutic role and eliciting a favorable cellular or tissue response.

Keywords:

Biomaterials, Biocompatibility, Cytotoxicity

Demand Prediction in Textile Production: A Machine Learning-Based Approach

Mucize Beldek Tomuk [1], Şerafettin Alpay [1]

1 Department of Industrial Engineering, Department of Production and Service Systems, Faculty of Engineering and Architecture, Eskisehir Osmangazi University, Eskişehir, Türkiye

Corresponding Author: *mucizebeldek@gmail.com*

Abstract

Demand fluctuations and increasing product variety make production planning a significant challenge in the textile industry. In environments where parallel machines operate with varying capacities and sequence-dependent setup requirements, accurate demand forecasting becomes essential for establishing realistic schedules and improving resource utilization. This study focuses on developing a reliable machine learning–based demand forecasting model to support these planning decisions. The research uses monthly sales data obtained from a textile manufacturer in Türkiye. Several regression algorithms, including Random Forest, Gradient Boosting and CatBoost, were examined to determine the most effective method for predicting future demand. The dataset was enriched through feature engineering by incorporating seasonal indicators, lagged demand variables and trend components. All models were evaluated using repeated cross-validation to ensure stable performance and to prevent overfitting. Model accuracy was assessed through widely used metrics such as RMSE, MAE and R^2. The results indicate that the CatBoost algorithm provides the highest prediction accuracy among the tested models. Its superior performance contributes to clearer demand visibility and supports planners in making more consistent capacity allocations. Improved forecasts also help reduce bottlenecks related to setup times and enable more balanced machine loading. Overall, the proposed model offers a practical, data-driven approach for textile manufacturers to improve production planning. It also lays the groundwork for a broader study, where the demand forecasts will be used as inputs in developing an optimization model for parallel machine scheduling with sequence-dependent setup times. By integrating accurate forecasts into scheduling decisions, this approach helps reduce bottlenecks, ensures more balanced machine utilization, and strengthens overall planning reliability.

Keywords:

Machine Learning, Demand Forecasting, Textile Industry, Regression Models, Production Optimization

Alternative Wing Designs for UAVs

Hüseyin Gündüz [1], Hamit Akbulut [1]

[1] Department of Mechanical Engineering, Faculty of Engineering, Atatürk University, Erzurum, Türkiye

Corresponding Author: *gunduz28huseyin@gmail.com*

Abstract

Composite materials have become increasingly important in aerospace and automotive applications due to their high specific strength, corrosion resistance, superior fatigue properties, and inherent vibration damping capabilities. These advantages make them particularly suitable for lightweight structural components where performance, durability, and efficiency are critical design factors. In unmanned aerial vehicles (UAVs), the use of composite structures is particularly attractive because weight reduction directly contributes to increased flight time, improved maneuverability, and reduced energy consumption. This study investigates the structural behavior of a hybrid composite-metallic UAV wing configuration using finite element analysis in the ANSYS Workbench environment. The wing model integrates carbon fiber reinforced polymer (CFRP) coatings with metallic beams and ribs to provide an optimized balance between stiffness, strength, and manufacturability. Static loading, aerodynamic pressure distributions, and material-specific failure criteria are evaluated to assess the overall structural integrity of the design. Modal analysis is also performed to determine the inherent frequencies and potential resonance risks associated with UAV operational conditions. The results provide information on stress concentration regions, deformation characteristics, and the contribution of composite layers to the overall stiffness increase. Comparisons between fully metallic and hybrid configurations highlight the performance advantages and weight savings achieved through composite integration. The findings demonstrate that the hybrid composite-metallic architecture increases structural efficiency while maintaining rigidity under expected service loads. This study contributes to the development of lightweight, high-performance UAV structures and provides guidance for future design optimization and material selection.

Keywords:

Composite Materials UAV (Unmanned Aerial Vehicle) ANSYS Workbench Structural Analysis Mechanical Behavior

Examination of the Effect of Genistein on CD36 Lipid Receptor and Lipid Profile in Liver Cancer Cell Line

Ebru Kılıç[1], Fatma Betül Özgeriş[1]

1 Faculty of Health Sciences, Department of Nutrition and Dietetics, Atatürk University, Erzurum, Türkiye

Corresponding Author: *ebru.kilic@atauni.edu.tr*

Abstract

This study aimed to evaluate the effects of Genistein, an isoflavone antioxidant found in soy, on liver cancer (HepG2) and healthy (HDF) cells by assessing its influence on antioxidant activity, cell viability, and CD36-mediated lipid transport. Cells were cultured and prepared for treatment. Cell viability was measured using the MTT assay. CD36 levels were quantified with a CD36 ELISA kit. Antioxidant parameters—including SOD, GSH, MDA, MPO, and GPx—were analyzed using corresponding biochemical assays. Genistein treatment (6.25–200 µg/mL, 48 h) showed a dose-dependent reduction in HepG2 cell viability. Although low concentrations (6.25–25 µg/mL) did not reduce viability below 50%, higher concentrations (50–200 µg/mL) demonstrated significant anticancer activity, decreasing viability below 50% (IC50: 35.34 ± 0.924 µg/mL). Methotrexate (MTX), used as a positive control, showed a similar pattern with an IC50 of 24.35 ± 0.681 µg/mL. ELISA results revealed that Genistein more effectively increased CD36 expression in HepG2 cells compared to MTX ($p=0.002$*) and the control ($p<0.001$). MTX also showed increased CD36 expression versus control ($p<0.001$). In HDF cells, both Genistein ($p=0.002$) and MTX ($p=0.048$*) elevated CD36 levels relative to control. Antioxidant analyses showed that MTX significantly elevated MDA levels in HepG2 cells ($p=0.031$*), whereas Genistein significantly increased GPx levels in HDF cells ($p<0.001$*). Genistein exhibits therapeutic potential in HepG2 liver cancer cells. It modulates CD36 and MDA expression, reducing lipid accumulation, while in HDF cells it affects CD36 and GPx activity. These findings suggest that Genistein may contribute to lipid regulation and oxidative balance in both cancerous and healthy cells.

Keywords:

cancer, liver, phenolic compound, CD36, lipids

Purification of Exopolysaccharides from Thermophilic Bacillus licheniformis SO2 Strain by Three-Phase Separation (TPP) System and Determination of Their in Vitro Biological Activities

Afranur Timur [1], Melda Şişecioğlu [2]

1 Graduate Student, Atatürk Üniversity
2 Department of Molecular Biology and Genetics, Faculty of Science, Ataturk University, Erzurum, Türkiye

Corresponding Author: *afranurtimur.uni@gmail.com*

Abstract

Exopolysaccharides (EPS) are macromolecules with structural diversity that play important roles in various biological processes. EPSs obtained from natural sources such as plants, algae, fungi, and bacteria exhibit a broad pharmacological spectrum, including antitumor, immunomodulatory, and antioxidant effects. Microbial polysaccharides offer significant advantages over plant or animal polysaccharides due to their sustainable production, rapid proliferation, controllable fermentation conditions, and high purity. In recent years, three-phase separation (TPP) has gained importance as a faster, more economical, and more effective alternative to traditional purification techniques. In this study, EPSs were extracted from grape waste using TPP with the thermophilic Bacillus licheniformis SO2 strain, which was isolated and identified in our laboratory. The antioxidant properties of the extracted polysaccharides were investigated using DPPH and ABTS analyses. TPP conditions were optimized using Response Surface Method (RSM) to obtain the highest yield. EPS was obtained under the following conditions: 40% ammonium sulfate, a homogenate/tert-butanol ratio of 1.0:1.25, and pH 7. Under these optimal conditions, EPS at a concentration of 1 mg/ml demonstrated 88.7% radical scavenging activity against DPPH radicals and 65.7% against ABTS radicals. Based on these data, it is shown that thermophilic, bacterially produced exopolysaccharides isolated using a TPP-based extraction method possess strong antioxidant potential. It is thought that these biomolecules could be used in future pharmaceutical and nutraceutical applications.

Keywords:

Exopolysaccharide, TPP, Response Surface Method (RSM), Bioactive Compounds

Risk Assessment of Occupational Hazards in Asphalt Production Plants Using the Fine-Kinney Method

Nursu Koyunoğullarından [1], Emine Çoruh [2]

1 Institute of Graduate Education, Gümüşhane University, Gümüşhane, Türkiye
2 Faculty of Health Sciences, Department of Occupational Health and Safety, Gümüşhane University, Gümüşhane, Türkiye

Corresponding Author: *coruhemine@gmail.com*

Abstract

Occupational accidents have long been recognized as a major social issue. This issue becomes even more pronounced in the industrial and construction sectors, where dynamic workflows, heavy equipment, and hazardous materials create inherently elevated levels of risk. Asphalt plants, where hot-mix asphalt is produced, involve multiple hazards such as high temperatures, bitumen fumes, heavy machinery, and noise. The necessity for effective occupational health and safety (OHS) management in this sector is therefore essential. The objective of this study is to ascertain the potential hazards that could result in occupational accidents within asphalt production facilities, to evaluate the risk levels, and to propose control measures that would enhance the safety of workers. For this purpose, risk analyses were conducted in the asphalt production plant of Erzurum Palandöken Inc. The Fine-Kinney method was employed for risk assessment, which is a process that involves identification, evaluation, and management of potential hazards or risks. Using probability, frequency of exposure, and severity, risks are quantified by this method, with a clear prioritization of unacceptable hazards being provided and safety improvements being guided. The findings suggest that specific operational stages and workplace conditions require enhanced control measures due to their potential to cause serious or undesirable outcomes if adequate preventive action is not taken. These situations may cause severe or even fatal injuries during asphalt production processes. The study is expected to contribute to the development of effective risk control strategies and support the establishment of safer working environments for asphalt industry workers.

Keywords:

Asphalt Production, Fine-Kinney Method, Occupational Health and Safety (OHS), Risk Assessment

Bioprinted Scaffolds Incorporated by Functional Nanoparticles

Behnaz Ashtari [1], Fatemeh Barati [1], Maryam Khosravi [1], Parvaneh Naserzadeh [2]

1 Department of Medical Nanotechnology, Faculty of Advanced Technologies in Medicine, Iran University of Medical Sciences, Tehran, Iran
2 Endocrine Research Center, Institute of Endocrinology and Metabolism, Iran University of Medical Sciences, Tehran, Iran

Corresponding Authors: *fatemehbarati.h@gmail.com, ashtaribeh@gmail.com*

By incorporating functional and stimuli-responsive nanoparticles, passive bioprinted scaffolds can be transformed into controllable and adaptive material systems. Such particles impart chemical, electrical, magnetic, and light-responsive behavior while reinforcing polymer networks and improving rheology. These nanoparticles create nanoscale domains that convert external stimuli into localized thermal, mechanical, or chemical outputs, enabling conductivity tuning, photothermal heating, magnetic actuation, and sustained ion exchange. Together, these effects shift scaffolds from static structures to dynamic, stimulus-regulated platforms designed for next-generation responsive biomaterials.

Keywords:
Smart Biomaterials, 3D Bioprinting, Nanoparticles

Harnessing Interface Engineering to Unlock Performance in Lead-Free, ETL-Free Perovskite Solar Cells: a SCAPS-1D Defect Tolerance Study

Nabilah Ahmad Jalaluddin [1], Faiz Arith [1], Fauziyah Salehuddin [1]

1 Faculty of Electronics and Computer Technology and Engineering, Universiti Teknikal Malaysia Melaka, Hang Tuah Jaya, Durian Tunggal, 76100, Melaka, Malaysia

Corresponding Author: *p022220006@student.utem.edu.my*

Abstract

Perovskite solar cells (PSCs) have rapidly advanced in recent years, achieving impressive power conversion efficiencies. However, challenges such as sensitivity to heat, moisture, and the need for high-temperature processing hinder their long-term stability and commercialization. Traditional PSCs typically use electron transport layers (ETLs) alongside hole transport layers (HTLs) to facilitate efficient charge extraction, but these ETLs often require complex and costly fabrication steps. Specifically, the device structure studied, as shown in Figure 1, consists of the following layers: fluorine-doped tin oxide (FTO), formamidinium tin triiodide (FASnI3) as the absorber layer, doped polyanilinine/graphene oxide (PANI/GO) as the hole transport layer (HTL), and silver (Ag). This study focuses on lead-free, ETL-free perovskite solar cells, which simplify device architecture and enable low-temperature, cost-effective manufacturing suitable for large-area applications. Eliminating the ETL and using lead-free absorber materials results in devices that are more environmentally friendly and scalable. SCAPS-1D simulation software was used to analyze the impact of interface defect densities and defect tolerance on device performance. The results highlight the critical importance of interface engineering, especially at the FTO/absorber interface, which has a stronger influence on device parameters than the absorber/HTL interface. Reducing the interface defect density to around 1×1011 cm-2 is essential to minimize charge recombination and energy losses, leading to significant improvements in power conversion efficiency (PCE), fill factor, and stability. This work demonstrates that careful management of interface quality and defect passivation allows ETL-free, lead-free PSCs to achieve performance comparable to more complex architectures without relying on toxic elements or high-temperature processes. These insights pave the way for developing stable, efficient, and eco-friendly perovskite solar cells with simpler fabrication routes, supporting the future of sustainable photovoltaic technology.

Keywords:

Interface Defect, Doped PANI/GO, ETL-Free, Perovskite Solar Cell

The Impact of Multi-Tagger Consistency on Semi-Supervised Natural Language Processing Models: A Bert-Based Tagging Approach

Aleyna Karaosman [1], Yasemin Gültepe [2]

1 Department of Software Engineering, Institute of Science, Atatürk University, Erzurum, Türkiye
2 Department of Software Engineering, Faculty of Engineering, Atatürk University, Erzurum, Türkiye

Corresponding Author: *karaosmanaleyna@gmail.com*

Abstract

Manual annotation of large text datasets is both time- and cost-intensive, leading to a growing need for semi-supervised learning methods. Furthermore, inconsistencies among human labelers directly impact the quality of synthetic label generation due to the sensitivity of semi-supervised models to initial labels. This study examines the impact of multi-labeler consistency on BERT-based semi-supervised learning models and proposes a holistic framework for statistically modeling labeler reliability, establishing a core training set, and optimizing the synthetic labeling process. The proposed approach involves calculating labeler consistency using methods such as Cohen's Kappa and Dawid-Skene, generating a core dataset of reliable examples, training the BERT model on this dataset, generating synthetic labels for unlabeled data, and redirecting low-confidence examples back to the labeler. Furthermore, the process is enhanced with consistency adjustment and noise reduction techniques, and a labeling interface is developed for practical use. In conclusion, the study demonstrates that multi-labeler consistency plays a critical role on the stability and accuracy of semi-supervised BERT models and provides a scalable, reliable and cost-effective automatic labeling infrastructure on large text datasets.

Keywords:

Natural Language Processing, Semi-Supervised Learning, BERT, Multi-Annotator Consistency, Automatic Labeling, Noisy Labels

2.
FULL-TEXT PAPERS

2.1.
KEYNOTE SPEECHES

Modelling Economic Variables in Offshore Oilwell Drilling

Dalmo S. Amorim Jr. [1], Edmilson S. Moutinho[1], Hirdan K. M. Costa[1]

[1] IEE-USP - Institute of Energy and Environment, University of São Paulo, São Paulo, Brazil

*Corresponding author e-mail address: dalmo.amorim@usp.br

Keywords

Petroleum Engineering

Modeling

Drilling Cost

Environmental Preservation

Abstract

Drilling costs and CO2 emissions in oilwell drilling are direct functions of the time spent on drilling operations, as the energy used during drilling operations is generated on-site by diesel-electric systems. The longer the operations take, the greater the diesel consumption, and the higher are costs and emissions. However, drilling time varies significantly from one well to another. These variations stem from differences in rock properties, drilling equipment, operational conditions, and drilling efficiency. Due to this complexity, traditional statistical methods are not sufficient to adequately analyze the operational results. In this study, we present regression models that can capture these complex relationships, providing a more accurate representation of the results in a field or sedimentary basin. The results offer new and valuable insights for technical, operational, economic, and contractual decision-making. An immediate application is supporting the assessment of testing new technologies and remunerating Turn-Key contracts. The conclusions of this work provide relevant and original contributions to the enterprise at the intersection of drilling engineering and environmental sustainability.

1. Introduction

Drilling operations are the most expensive part of the oil and gas exploration process [1]. To reduce their costs, an optimization process is required, beginning by understanding the boundary conditions and the dynamic phenomena involved in the oilfield's drilling operations. The environment must be well understood to be modeled, so that the optimization processes become less intuitive and less influenced by marketing forces, and more based on lessons learned from analyzing statistical results.

However, the oilwell environment is so complex that building a model to predict the behavior of the drilling operations is almost impossible, once all-encompassing models embed very low coefficients of determination (R^2) [2]. Additionally, most information about drilling operations cannot be verified directly, and it is necessary to infer drilling status based on indirect information provided by sensors, or to perform a full trip of the drill string to check, at the surface, the conditions of the bit or drill string elements. Examples: sharpening of cutters, dimensions of gage stabilizers, condition of bearings, etc. The cost of a round trip is so high that some elements are replaced as they reach the surface, minimizing the non-productive time spent in inspections to check for conditions.

This paper aims to disseminate the Amorim curve methodology, which is designed to optimize offshore oilwell drilling costs. A summary of its numerous outputs is provided to facilitate a desirable extension of a congress paper. The full description is available for open access, allowing researchers with validated drilling data to replicate charts, benchmarks, formulas, and tables using Microsoft Excel [3].

2. Literature review

Predicting involves making an estimation based on a model, along with an associated error. More precise predictions are made by the good models, where total errors are expected to be nearly zero [4]. As the environment of drilling operations involves numerous elements interacting simultaneously, the result is a complex and interdependent reality, making it almost impossible to produce a universal model that predicts the results of drilling operations. In the authors' vision, the deterministic parameter for modeling oilwell drilling should be the vertical depth, as rock compaction, abrasiveness, friction of the drill string, drilling harmonics and temperature all increase with depth. The contour conditions explain the numerous research efforts on the subject in the literature.

Most are directed towards modelling rates of penetration (ROP) using uneven deterministic parameters or strict geological conditions [5]. Research efforts have progressively used more complex analyses, as the variations of Artificial Neural Network, to treat the database [6-15]. More recently, well depth has been introduced as a deterministic variable of the model, assuming that higher errors of the modeled predictions are expected [16, 17] and [18].

The Amorim curve methodology adopts the well depth as the deterministic parameter modelling due to a practical reason: systematically converting the coordinates of all well trajectories of a researched oilfield into vertical depth requires information at a level not yet practiced by the industry. It means that every well should have X-Y-Z coordinates for every bit run found in the database for its whole trajectory.

3. Methodology

This section describes the basic concepts of the Amorim curve methodology, which statistically fits drilling data from oil fields as a function of depth out of the drilling bits. Benchmarks of the fits provide unique insights into naturally dispersed results, offering predictions with a more reliable predictability than those supplied by averages of selected data, typically chosen while disregarding existing sets of positive and negative results from a drilling campaign [19]. The methodology is useful for providing predictions for well programs, generating outputs that reflect the influence of key performance indexes (KPIs) systematically collected in all wells, including bit type, technology, hydraulics, rig type, bit diameter and well inclination, among others.

3.1. Cost of drilling operations

The cost per meter is a unique, non-linear, and non-stochastic event, whose value is influenced by the complex aspects involved in drilling a segment of rock using the available technologies and operational practices [20]. Calculated by Equation 1, **CM** continuously decreases as the operation progresses, as shown in Figure 1. At some point, **CM** stabilizes and slowly begins to increase until a decision is made to pull the bit from the well. Ideally, bits should be pulled at the minimum **CM** of the bit run.

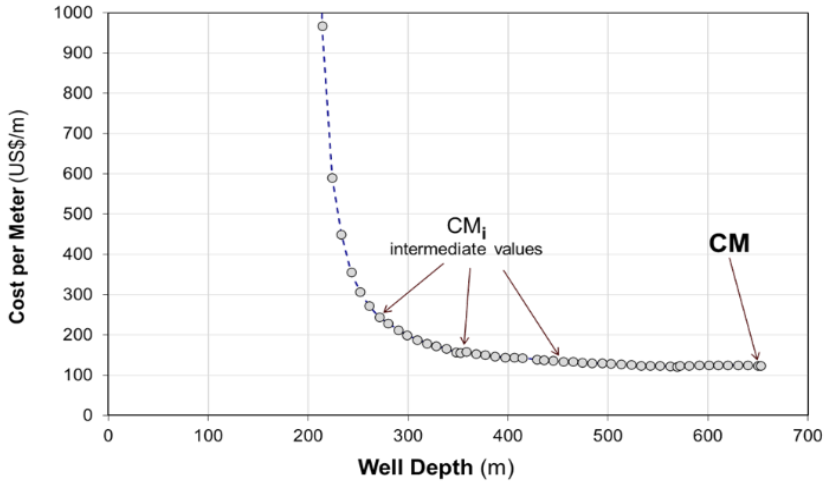

Figure 1 Evolution of CM for any bit run [3]

The final value of **CM** for a bit run becomes tied, in the database, to **MD**, **HR**, and depth out.

Equation 1 - Cost per Meter

$$CM = (CB + CH \times (TT + HR))/MD, \text{ where:}$$

- **CM** - cost per meter of the section drilled **MD** ($/m)
- **CB** - cost of the drilling bit ($)
- **CH** - total cost of rig + special tools + infrastructure + logistics ($/h)
- **TT** - time to remove a bit from the well, change it and lower the string to resume drilling (h)
- **HR** - time spent to drill the section **MD** (h)
- **MD** - length drilled during the period of time **HR** (m)

3.2. The optimization process

The objective of the optimization process is to minimize drilling costs, directly proportional to the time spent, a variable dependent on the efficiency of the drilling operations. This reasoning applies integrally to the CO_2 emissions of the rig, which is indispensable to the enterprise as all the electric energy used must be generated using diesel at the rig location [21]. To drill each section entirely with one bit, to avoid intermediate trips, bits must last the expected lifespan necessary to drill their extension, expressed by Equation 2:

Equation 2 - Optimization of the length drilled

$$Max_{\boldsymbol{MP}} = f(Max_{\boldsymbol{HR}})$$

The next step in the optimization is to drill every section using the least total time, achieved by maximizing the rate of penetration, where **ROP** = **MD**/**HR**. The research question is which set of KPIs results in the minimum time, expressed by Equation 3, which translates into finding the most efficient technical conditions for each bit run.

Equation 3 - Optimization of the drilling time

$$Max_{\boldsymbol{ROP}} = f(Min_{\boldsymbol{HR}})$$

The following actions are adjusting the energy levels applied to maximize ROP and life span [22], and mitigate drill string vibrations and friction using FEA [23], as in Equation 4. That will presumedly lead to achieving the minimum **CM** values after each run.

Equation 4 - Maximum drilling performance

$$Max_{performance} = f(Max_{ROP}, Min_{HR})$$

In summary, the drilling optimization is finding the best set of decisions based on the findings of the research, which should result in drilling every section of the well in the minimum time, expressed by Equation 5:

Equation 5 - Objective of the optimization method

$$Min_{\boldsymbol{CM,CO_2}} = f(Max_{\boldsymbol{MP}}, Min_{\boldsymbol{HR}})$$

The objective in Equation 5 is achieved when the **CM** value is minimized, as shown in Figure 1, which represents the ideal moment to pull the string, provided that the bit does not reach the end of the section [3]. Therefore, the objective of the research is to identify the set of conditions, as defined in Equation 5, focused on determining the lowest CM values within each depth range.

3.3. Benchmarking drilling data

The *Amorim curve* methodology employs an exponential regression of **CM** values *versus* well depth, resulting in a trend line. It represents the benchmark of all **CM** values achieved by the exploration campaign, making it possible to predict **CM** values in future wells under the set of KPIs used in Equation 6.

Equation 6 - Exponential benchmark of CM

$$CM_i = k1 \times e^{k2 \times D}, \text{where:}$$

- $\mathbf{CM_i}$ = value of the benchmark of **CM** at depth **D**, ($/m)
- **D** = measured depth of the trajectory, (m)
- **k1** = value of the theoretical point where the trend curve meets the **y**-axis, ($/m)
- **k2** = variable that reflects the variation of **y** values with the increase of **D**

Determining the sets of KPIs that result in **Minimum** (**CM**, $\mathbf{CO_2}$) is very complex, as there are no standards for the design of trajectories, selection of drill string components or bits, energy levels, mud type etc. Geological conditions change with every meter drilled, adding friction between the string and the wellbore, and providing continuous changes in drilling harmonics with every new pipe added. It occurs simultaneously with a decrease in efficiency, caused by the wear of bit cutters, resulting in an increased overall energy demand from the rig. As so, within any depth range in the oilfield, a myriad of uneven results is produced, presenting very statistical variability.

CM benchmark trends are naturally expected to increase, as shown in Figure 2. As oilfields are explored, the typical initial **CM** values decrease provided by optimized bit runs and higher ROPs. Progress can be observed in the benchmark trends, which slowly become less inclined and decrease, indicated by reductions in **k2**.

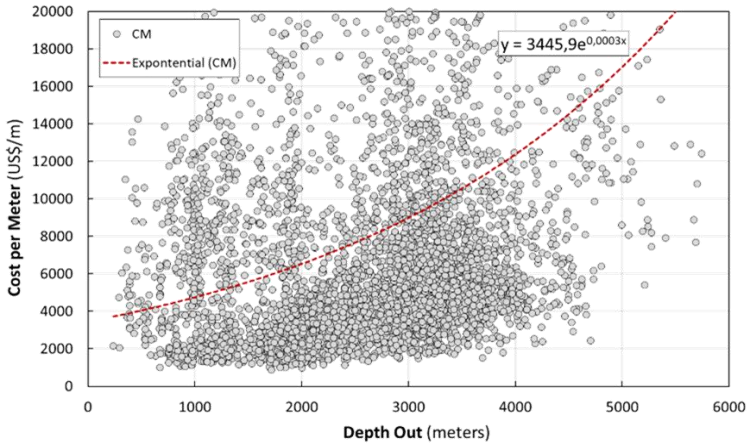

Figure 2 Benchmark of CM for a dataset of 5296-bit runs

3.4. Gains provided by optimization

The methodology allows for research KPIs which have resulted in **CM** values sitting at the lowest part of the chart. It is done by filtering the database to isolate the KPI, like when researching the performances of 12.¼" bits. A new benchmark validates the findings, which can be replicated or improved in future wells in the area.

Positive results represent financial savings, calculated by using Equation 7, resulting from reduced rig time costs and savings achieved through efficient performance, compared to the surrounding wells in the same oilfield. The savings are the gap between $\mathbf{CM_i}$ and the predicted $\mathbf{CM_{benchmark}}$ (**ΔCM**), multiplied by the length drilled. The reasoning applies to losses when $\mathbf{CM_i} > \mathbf{CM_{benchmark}}$, as less efficient drilling results in more time to drill a determined segment.

Equation 7 - Financial savings gap between values predicted and achieved

$$Fin_{sav} = MP \times DCM = MP \times \{CM_{benchmark} - CM_i\}$$

- $\mathbf{CM_{benchmark}}$ - cost per meter predicted by the benchmark, ($/m)

The time saved by the optimization process (**TS**) is a direct calculation in Equation 8:

Equation 8 - Time saved by more efficient drilling

$$TS = Fin_{sav} \div CH$$

- **TS** = lapse of rig time saved, (day)

The cost of drilling any segment of the trajectory between **D1** and **D2** is estimated by integrating Equation 6, which results in Equation 9. The estimation uses factors **k1** and **k2** extracted from benchmark formulas.

Equation 9 - Cost to drill any interval of the trajectory

$$CS = \int_{D1}^{D2} CM \; dD = \int_{D1}^{D2} k_1 \times e^{k_2 \times D} \; dD$$

$$CS = k_1 \times \{(e^{k_2 \times D_2}) - (e^{k_2 \times D_1})\} \div k_2$$

- **CS** = cost of drilling a segment **D1** to **D2**, ($)

The reasoning also applies to the reduction in $\mathbf{CO_2}$ mass achieved through more efficient operations. Similar to the drilling costs, it is directly proportional to the time drilling, with saved mass estimated by Equation 10:

Equation 10 - CO_2 mass reduced by more efficient drilling

$$M_{CO2} = TS \times Rig_{CO2}$$

- **RigCO_2** - daily emissions of CO_2/day of the rig, (ton/day)

4. Case Study

The sedimentary basins along the eastern coast of Brazil were formed during the rifting of the Gondwana Supercontinent, which led to the formation of the South Atlantic Ocean, and the separation of the African and American continents. The evaporites of the pre-salt sequence are the result of sedimentation in shallow waters and a semi-arid climate, shown in Figure 3, which created an extensive package of salts deposited in a lagoon environment under relatively stable tectonic conditions, likely connected to southern oceanic waters [24].

The petroleum habitat of the Campos Basin lies within the Lagoa Feia-Carapebus system, sourced from saline lacustrine shales that charge turbidite reservoirs, such as the Carapebus Formation. It led to thermal history and biodegradation, essential for the prolific, rift-related petroleum system linked to the Gondwana breakup. The main reservoir is composed of turbidite sandstones of the Carapebus Formation. The petroleum system focuses on the interconnected source (shale) and reservoir systems, characterized by effective generation and migration [26].

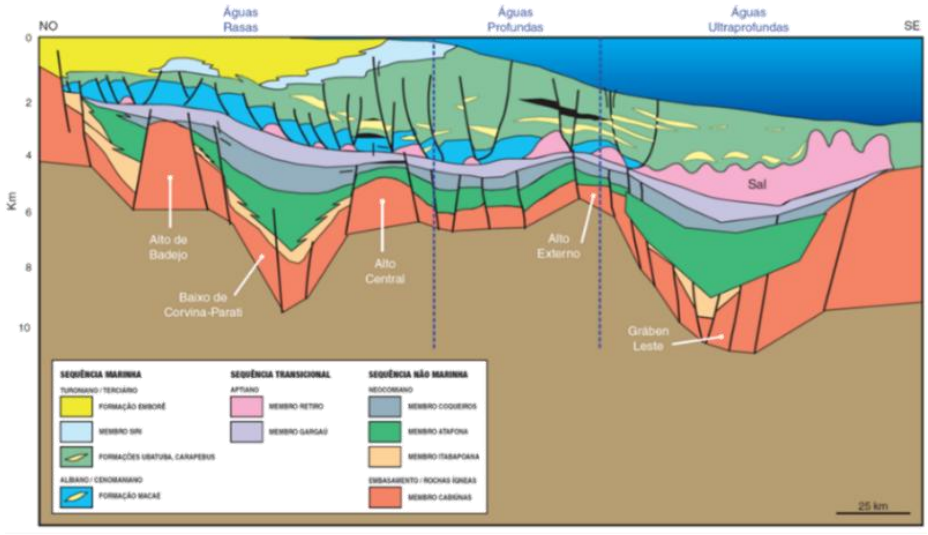

Figure 3 Geological section of the Espirito Santo Basin [25]

Since the first well was spudded in 1971, the offshore part of the basin has been explored from waters as shallow as 12 m, down to the country's record of 3022 m, set in ultra-deep waters. A total of 3584 wells were drilled in the basin as of December 2025 [27], where Petrobras drilled a single onshore dry well. This case study utilizes a robust dataset from 1098 wells of seven oilfields, representing a total of 3584 wells drilled in the basin [27]. The analysis used 5296 validated bit runs. Disregarding minor inaccuracies in the lines that define the regional structures in Figure 4, most wells of the seven fields were drilled within a distance of 50 km at an average water depth of approximately 1000 m.

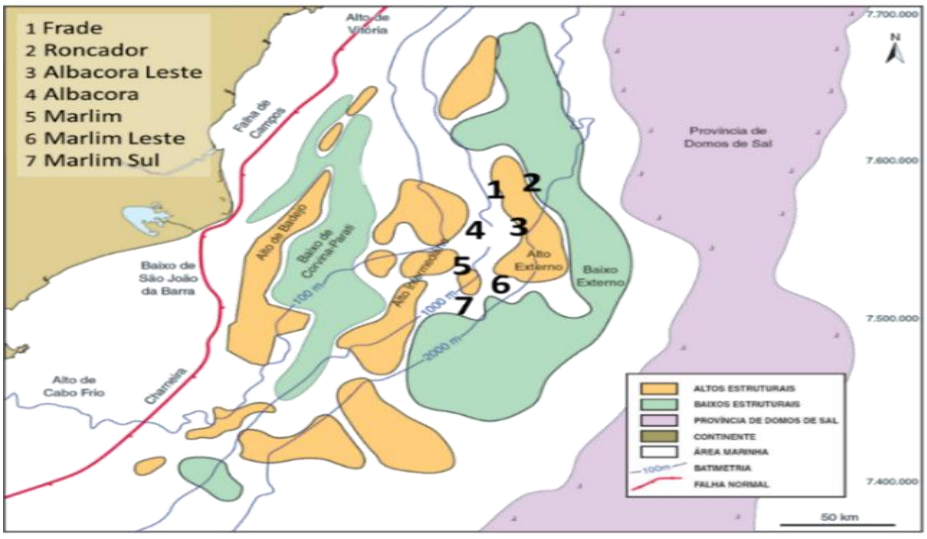

Figure 4 Main structures of the Campos basin, adapted from [25]

4.1. Drilling performances

The case study begins by plotting performance *versus* depth for the main elements of Equation 1: the length drilled (**MD**) and the time drilling per bit run (**HR**), as shown in Figure 5. The charts indicate a high vertical distribution in all depth ranges, a common finding in any oilfield where this methodology is applied.

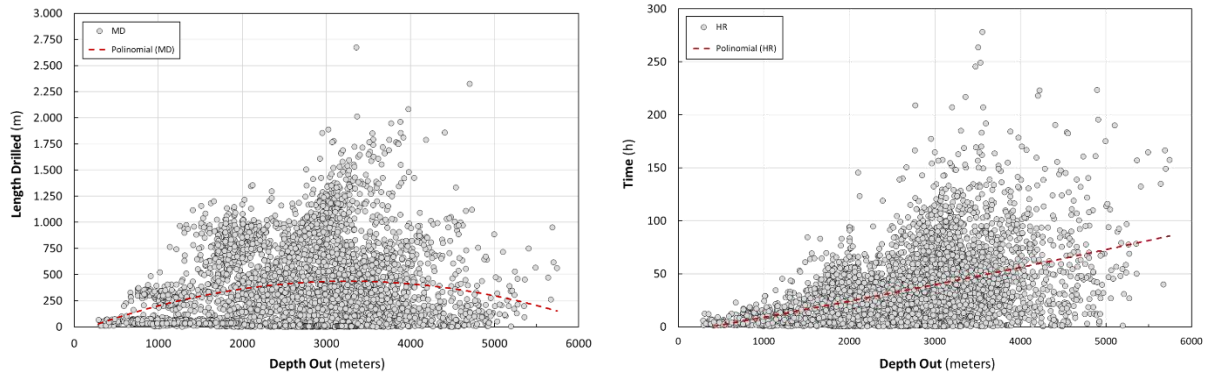

Figure 5 Case study of MD and HR for the seven fields

The remarkable vertical dispersion of results across any depth range renders the development of universal models an arduous task, posing a challenge in producing reliable predictions. Modelling such an environment is challenging and does not yield simple answers. The statistical fits use polynomials for **MD** and **HR**. The benchmarks in Figure 5 were expected to reflect a natural decline in performance as wells become deeper, rocks become harder, more abrasive, and bits wear out faster. However, this is not found in either chart. One reason is the length of the different sections, which progressively reduced to isolate different formations, being set intermediate casing. Performances can be filtered by bit diameter, providing specific additional charts.

A logarithmic fit is used for **ROP**, seen in Figure 6. A first conclusion is that the chart does not provide insights or present logical connections with the previous charts. However, it shows what is naturally expected: **ROP** declining with the well depth. Analyses can also be filtered by bit diameter, providing specific estimations for each diameter.

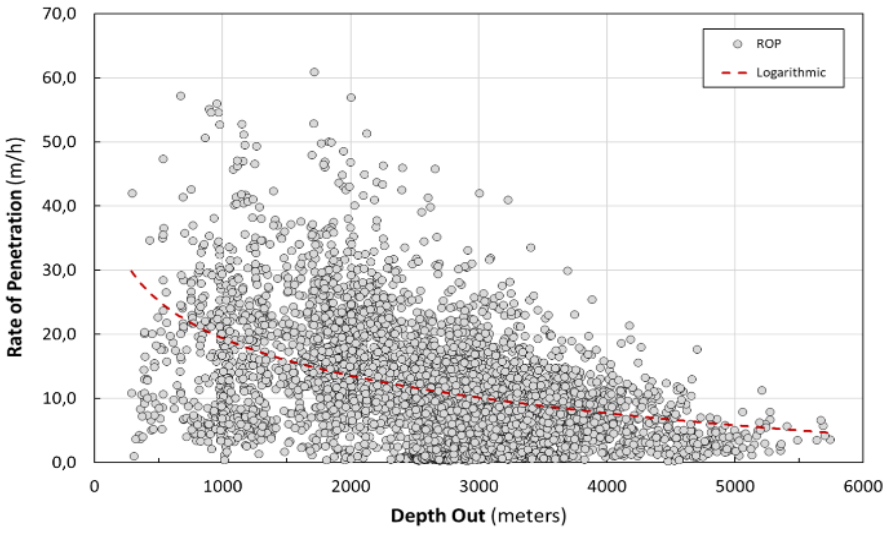

Figure 6 Case study of ROP for the seven fields

However, the findings necessary to solve Equation 5 are not yet available at this stage of the research. To optimize drilling costs, it is essential to determine the contour conditions of the lowest values of **CM** among the reported data, revisiting this step to refine the findings, as described below.

4.2. The Area Fingerprint

The set of decisions taken during the planning and exploration of an oilfield is reflected in *each* of the **CM** results found in a database. As such, plotting all **CM** values *versus* depth produces a unique chart: the *area fingerprint*, a starting point for searching for optimum conditions for each section. The area fingerprint for the seven fields is seen in Figure 7. There is a lack of results at the bottom left, due to the water depth.

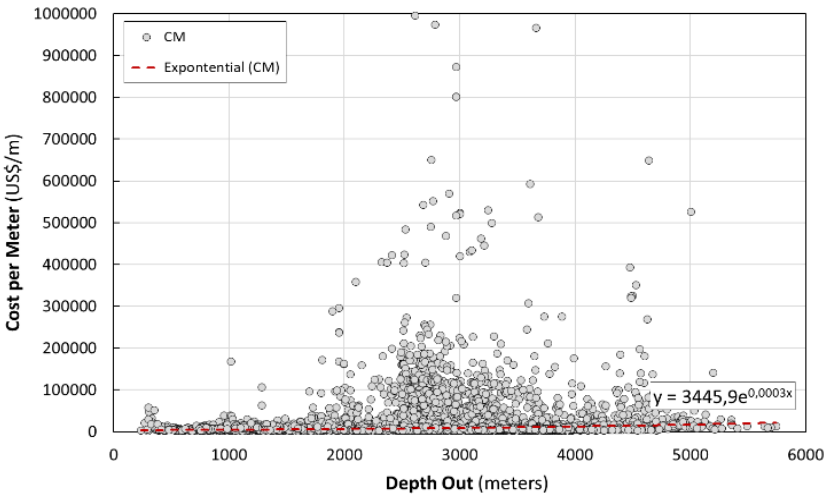

Figure 7 Fingerprint of the seven fields of the case study

The vertical dispersion of **CM** results is also remarkable. A high concentration of high costs per meter in the mid-sections, at approximately 2500-3000 m, requires using the first data filter: **CM** *versus* bit technology. The finding is that coring operations are the origin of most of the high costs per meter, verified in the red dots plotted in Figure 8.

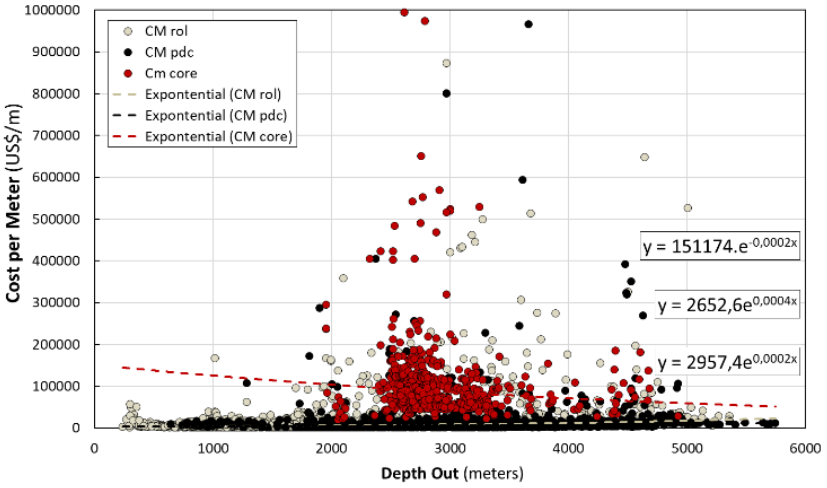

Figure 8 Benchmark of CM for drilling technology

Zooming down the Y-axis to $60000/m produces Figure 9, providing a clearer vision of the benchmark formulas for the drilling technologies. Drilling with PDC bits is expected to cost approximately 50% of the cost with rollercone bits *at this stage of the exploration* (1984 to 2019), due to a 1:2 ration between the two **k2** factors.

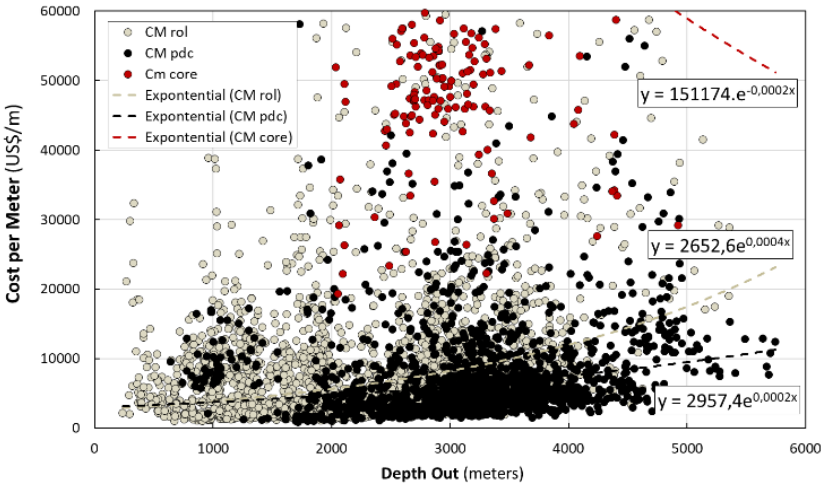

Figure 9 Benchmarks for CM and drilling technology

Next step: filter out the 496 coring operations and zoom in to $20000/m, as shown in Figure 10. The findings are that rollercone bits are predominant in shallow sections. PDC bits are more economical in mid- and deeper sections, providing a benchmark that sits below the rollercone bit benchmark.

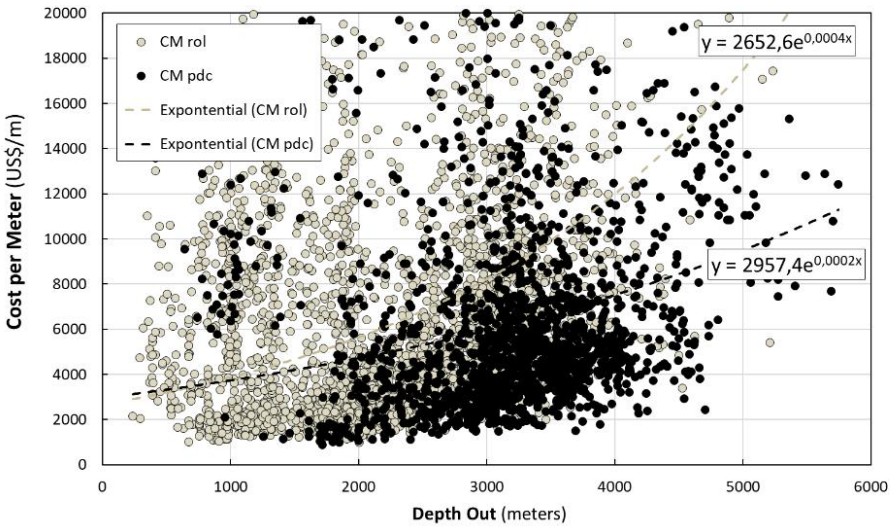

Figure 10 Benchmarks for CM, PDC and rollercone bits

Next filters: hide the rollercone bits, filter bit diameter of the PDC bits. Figure 11 presents a densely populated chart, with 28” bits in black (3 runs), 17.½” in green, ¼” in brown and 8.½” in light blue; benchmarks were not included to avoid image congestion. Analyses be further refined by filtering PDC cutter size, number of blades etc.

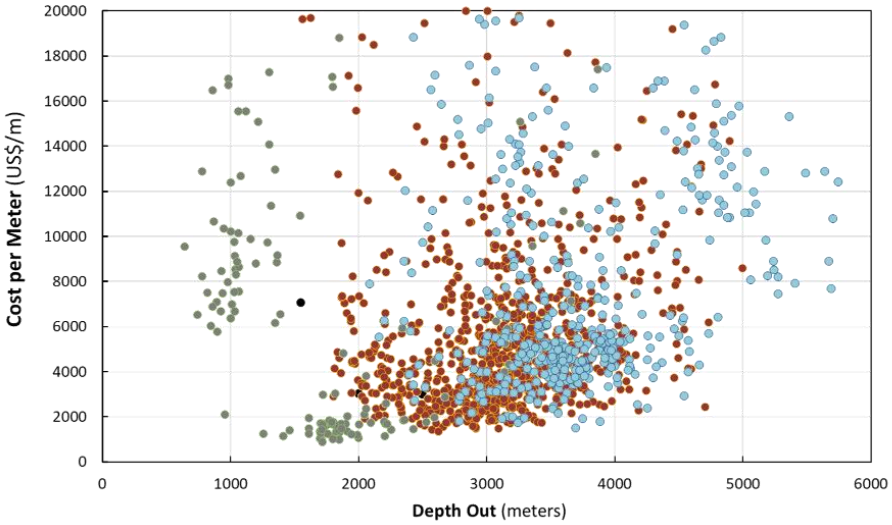

Figure 11 Area fingerprint of CM for PDC bits and diameter

Further analyses can filter bit manufacturer, HSI (hydraulic horsepower per square inch), well inclination range, mud type, and usage of downhole motors or rotary steerable systems in directional wells, among other factors. Analyses might investigate rollercone bits by establishing filters for rollercone IADCs [28], for extra protection at the gage, stabilizers or roller reamers in the BHA, total RPM when using motors, and others. Filtering KPIs and modeling results provide more consistent predictions than those obtained by averaging selected data. The process is completed by reverse engineering, which involves identifying the depth out of the best runs and examining the contour conditions in the database. Each set of filtered KPIs provides different formulas, so the most relevant analyses can be tracked over time, with **k1** and **k2** recorded in a table for the researched KPI.

5. Results

The cost of drilling a segment of the trajectory from depths **D1** to **D2**, calculated using Equation 9, is represented at the bottom right of Figure 12. The concept can be applied to predict the cost of a whole well. In this case, the factors **k1** and **k2** used for the calculations are extracted from the benchmark equation for the filtered KPIs.

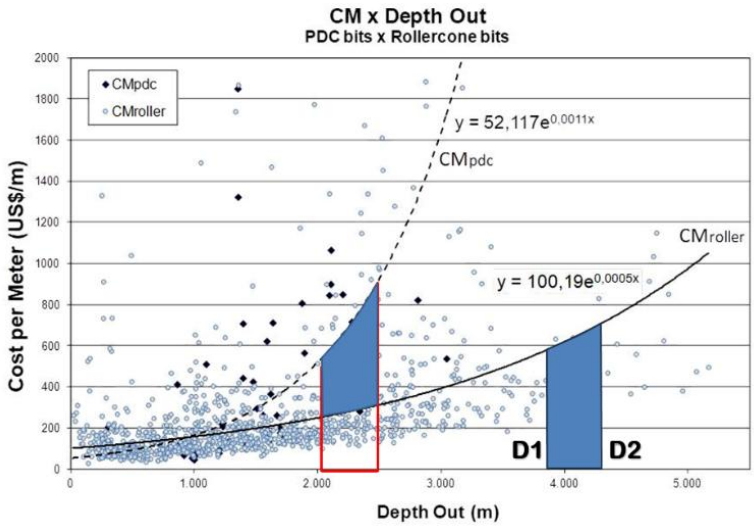

Figure 12 Financial gaps

During any period of exploration of an oilfield, as new bits are run, the area fingerprint becomes more populated, and the benchmarks slowly change. The trend of increasing or decreasing **k2** factors demonstrates improvements or setbacks resulting from the decisions made. The trends of increasing or decreasing **k2** factors demonstrate the improvements or setbacks resulting from the optimization processes and decisions made.

In this sense, it is possible to document the evolution of technologies as a function of time, comparing the factor **k2** of analyses made in different years of exploration. By considering time as a KPI, the financial impact between two periods of exploration phases can be provided, similar to the area represented by the other blue area in Figure 12, which is achieved by comparing benchmarks and calculating the resulting financial impact.

6. Conclusion

The article demonstrated applications using the *Amorim curve* methodology, which can be replicated by any researcher with verified data using Excel. The status of optimization processes can be evaluated in economic terms, revealing notable achievements by filtering different KPIs. The savings resulting from using available technologies are determined by comparing the overall oilfield benchmark with those resulting from a predefined KPI. Details and additional applications of the methodology are provided at the dissertation of the author.

A case study demonstrated the typical high variability of oilfield exploration performances, which makes modeling such environments into a very complex mission. By using the cost per meter as the primary source of analysis, rather than drilling performance, a KPI systematically collected for all wells in the oilfield can narrow down the findings, detecting the most efficient combination of factors for each well segment.

With the subject of carbon credits undergoing legal regulations worldwide, the methodology also serves as a starting point for measuring environmental savings in more efficient drilling operations. The methodology introduces new metrics, serving as benchmarks for operators to claim carbon credits when developing more efficient technologies. The action benefits society by reducing the enterprise's cost and its environmental impact.

References

[1] Rostamsowlat, Iman, Brian Evans, and Hyock J. Kwon. "A review of the frictional contact in rock cutting with a PDC bit." Journal of Petroleum Science and Engineering, 2022: 17 p.

[2] Devore, Jay L. Probability & Statistics for Engineering and the Sciences. Eigth edition. San Luis Obispo, CA: CENGAGE Learning, 2010.

[3] S. Amorim Jr., Dalmo. "Modelling Economic and Environmental Variables in Offshore Oilwell Drilling." 2025. 321 p. https://doi.org/10.11606/T.106.2025.tde-24112025-101817

[4] MathWorks. Parametric Fitting. 2024. https://www.mathworks.com/help/curvefit/parametric-fitting.html.

[5] Payne, M. L., and F. Abbassian. "Advanced Torque and Drag Considerations in Extended-Reach Wells." IADC/SPE Drilling Conference. New Orleans, 1996.

[6] Wiktorski, Ekaterina, Artem Kuznetcov, and Dan Sui. "ROP Optimization and Modeling in Directional Drilling Process." Edited by Society of Petroleum Engineers. SPE Bergen One Day Seminar. Bergen, Norway, 2017. 14 p.

[7] Oyedere, Mayowa, and Ken Gray. "ROP and TOB optimization using machine learning classification algorithms." Journal of Natural Gas Science and Engineering, 02 25, 2020: 13 p.

[8] Guo, Ying, Guangying Ren, Yang Fei, Yong Yang, Dmitry O. Bokov, and Irina N. Fardeeva. "An analytical method to select appropriate linear and non-linear correlations on the effectiveness of penetration rate parameter towards mechanical specific energy." Energy Reports, 2021. P. 3647-3654.

[9] A. Jabbar, Ahmad, Ahmed A. Mahmoud, Salaheldin Elkatatny, and Mahmoud Abughaban. "Artificial neural networks-based correlation for evaluating the rate of penetration in a vertical carbonate formation for an entire oil field." Journal of Petroleum Science and Engineering, 2022.
[10] Shaygan, Kaveh, and Saeid Jamshidi. "Prediction of rate of penetration in directional drilling using data mining techniques." Journal of Petroleum Science and Engineering, 11 2022.
[11] Wan, Youwei, Xiangjun Liu, Jian Xiong, and Lixi Liang. "Intelligent Prediction of Drilling Rate of Penetration Based on Method-Data Dual Validity Analysis." SPE Journal, 10 2023.
[12] Miah, Mohammad I., Mohammad T. Reza, Mizanur Rahman, and Maruf Alam. "Extended Genetic Algorithm-Based Improved Model for Drilling Rate of Penetration Using Mud Logging Data." 8th International Conference on Engineering Research, Innovation and Education. 2025. 9 p.
[13] Han, Xue Yin, Zhen Xin Zhang, Peng Fei Cheng, Xue Sen Qian, Yu Ming Liu, and Bo Tao Lin. "Application and analysis of the shapley additive explanations in predicting the rate of penetration." Petroleum Science and Technology, 11 2025: 20 p.
[14] Meng, Han, Zhen Xin Zhang, Xue Yin Han, and Bo Tao Lin. "Research on rate of penetration prediction method integrating bit wear and pretraining mechanism." Petroleum Science Bulletin, 2025.
[15] Nabavi, Zahra, et al. "Prediction of Rotary Drilling Rate of Penetration in Surface Mines Using Machine Learning Techniques." Rock Mechanics and Rock Engineering, 2025.
[16] Mantegazini, Diunay Zuliani, Andreas Nascimento, Mauro Hugo Mathias, Oldrich J. R. Guzman, and Matthias Reich. "Optimization of Rate of Penetration and Mechanical Specific Energy Using Response Surface Methodology and Multi-Objective Optimization." Applied Sciences, 2024.
[17] Hallai, Said, Abdelmadjid Dobbi, and Rabah Kechiched. "Modeling rate of penetration using hybridization of Artificial Neural Network and Artificial Fish Swarm algorithm." Petroleum Science and Technology, 2024: 19 p.
[18] Ma, Zheng Chao, et al. "Intelligent prediction of rate of penetration through meta-learning and data augmentation synergy under limited sample." Geoenergy Science and Engineering, 2025.
[19] S. Amorim Jr., Dalmo, Edmilson S. Moutinho, Otto L. A. Santos, José Umberto A. Borges, João H. Rittershaussen, and Milena A. R. Amorim. "CO2 Reduction in Oilwell Drilling: Methodology and Case Study." IGRC 2024. Banff, CA, 2024. 12 p.
[20] Van Kampen, N. G. Stochastic Processes in Physics and Chemistry. Fourth Edition. Oxford, EN: Elsevier, 1992.
[21] S. Amorim Jr., Dalmo, Otto L. Santos, J. Umberto A. Borges, and Edmilson S. Moutinho. "CO2 Footprint of the Deepest Oilwell in Brazil." Journal of Petroleum Exploration and Production Technology, 2025.
[22] Amorim Jr., Dalmo S., Otto L.A. Santos, and Ricardo C. Azevedo. "New Industry Standards to Increase the Reliability of Drilling Operations." Holos (IFES), 2019.
[23] Amorim Jr., Dalmo S., Chris Hanley, and Daltro J. Leite. "Parameter Definition Using Vibration Prediction Software Leads to Significant Drilling Performance Improvements." Edited by SPE. Latin American and Caribbean Petroleum Engineering Conference. Ciudad de México, 2012.
[24] Ávila, Ronan, and Ariely Luparelli. "Bacia do Espírito Santo." Brasil 13a Rodada, ANP, 2015, 96 p.
[25] Castro, Ricardo D., e J. P. Picolini. “Principais aspectos da geologia regional da Bacia de Campos.” Geologia e Geomorfologia, 2014: 12 p.
[26] BPS. The Petroleum Habitat of the Campos Basin based on detailed Geological, Geochemical and 2D Petroleum System Modeling. 2025. https://brazilpetrostudies.com.br/multiclient/campos/the-petroleum-habitat-of-the-campos-basin-based-on-detailed-geological-geochemical-and-2d-petroleum-system-modeling/.
[27] ANP. Data. 2025. https://www.gov.br/anp/pt-br/assuntos/exploracao-e-producao-de-oleo-e-gas/dados-tecnicos/ad/tabela-de-pocos.xlsx.
[28] McGehee, D.Y. et al. "The IADC Roller Bit Classification System." IADC/SPE Louisiana, USA: Society of Petroleum Engineers, 801 - 818.

2.2.
ATTENDED POSTER PRESENTATIONS

Copper-Based Metal-Organic Framework Cu(BDC) as a Reusable Heterogeneous Catalyst for Efficient *N*-Arylation of NH-Heterocycles

Yagoub Mansoori [1,2,*] Abbas Jahanbani [2,] Somayeh Fekri [2]

[1] Department of Applied Chemistry, Faculty of Science, University of Mohaghegh Ardabili, Ardabil, Iran, 56199-Tel: +98 45 Fax: +98 45
[2] Nanoscience and Nanotechnology Research Group, University of Mohaghegh Ardabili, Ardabil, Iran, 56199-11367.

* *Corresponding author E-mail: ya_mansoori@uma.ac.ir*

Keywords

N-Arylation

Metal organic framework

Cu(BDC)

Heterogeneous catalyst

Abstract

The copper-based metal-organic framework Cu(BDC) was examined as a heterogeneous catalyst for the *N*-arylation of *NH*-heterocycles with aryl halides under Ullmann-type conditions. Reaction parameters including solvent, base, temperature, and catalyst loading were optimized to promote efficient C–N bond formation with iodo-, bromo-, and chloroarenes. The catalyst exhibited good catalytic activity and demonstrated reusability over multiple cycles, with copper leaching measured at 2 percent after the first cycle. Characterization of the recovered catalyst by FT-IR and WXRD indicated that the framework structure remained largely intact. Hot-filtration experiments confirmed that product formation ceased upon removal of the catalyst, supporting a heterogeneous reaction pathway. These results indicate that Cu(BDC) is an effective and reusable catalyst for *N*-arylation reactions involving *NH*-heterocycles and aryl halides.

1. Introduction

N-Arylimidazoles have become a significant focus in synthetic organic chemistry due to their frequent presence in biologically active compounds [1]. The Ullmann reaction is a well-established method for copper-catalyzed coupling between aryl or alkyl groups [2]. Cu-based MOFs have garnered significant research interest due to their distinctive structural properties, setting them apart from others. Cu-based MOFs are highly efficient heterogeneous catalysts, providing a viable alternative to homogeneous ones and a cost-effective substitute for noble metals like Pd and Rh in organic synthesis [3]. In this study, we present the coupling of *NH*-heterocycles with aryl halides using Cu(BDC) as a highly efficient and recyclable catalyst. The catalyst was easily recovered by centrifugation and reused in subsequent cycles with no significant loss of activity or detectable metal leaching. This study constitutes the first documented application of Cu(BDC) as a catalytic system for the direct *N*-arylation of *NH*-heterocycles with haloarenes.

2. Materials and Methods

Solvents used in the experiments were dried using standard procedures reported in the literature. All additional reagents were obtained from Sigma and employed in their original form without further treatment.

2.1. Preparation of Cu(BDC)

Copper nitrate trihydrate (4.00 mmol, 1.053 g) and terephthalic acid (4.35 mmol, 0.724 g) were dissolved in DMF (87 mL). The resulting solution was transferred to a sealed Teflon-lined hydrothermal autoclave and was heated at 110 °C for 36 h. Upon cooling, blue crystals began to form and were fully developed after one week. The product, Cu(BDC), was filtered and subsequently was refluxed in methanol for 24 h, separated via centrifugation, and washed with acetone three times. Finally, the Cu(BDC) was calcined at 195 °C for 6 h, resulting in a yield of 78%.

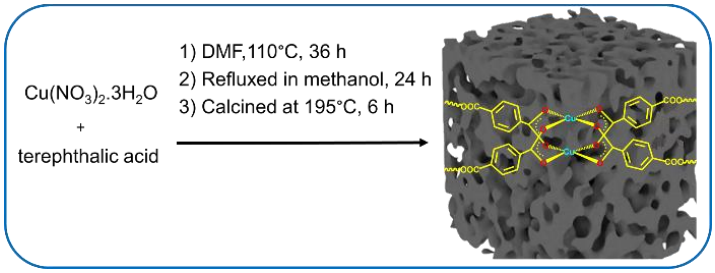

Figure 1 Synthesis Cu(BDC).

3. Results and Discussion

Fig 2a displays the characteristic bands for the asymmetric and symmetric stretching vibrations of the carboxylate group at 1586 cm^{-1} and 1390 cm^{-1}, respectively. Fig 2b presents the surface morphology of Cu(BDC) as characterized by SEM imaging. The micrograph reveals a cubic multilayered structure. Fig 2c displays the wide angle X-ray diffraction pattern (WXRD) of Cu(BDC).

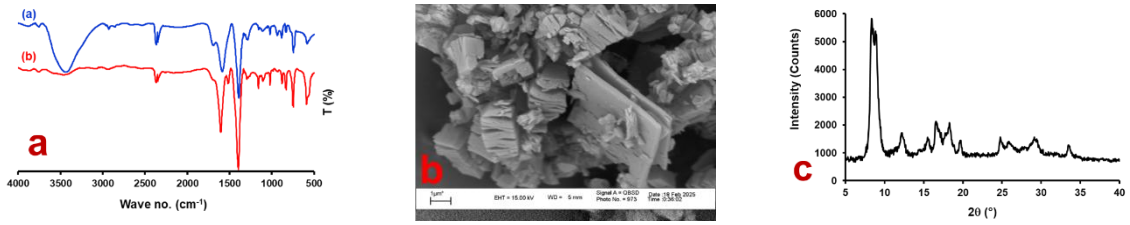

Figure 2 a) FT-IR spectrum (KBr) of a) Cu(BDC), b) terephthalic acid b) SEM image, and c) WXRD pattern of Cu(BDC).

Fig 3a shows the N_2 adsorption-desorption isotherm and BJH pore size distribution of Cu(BDC). The material has a specific surface area of 710 m^2 g^{-1}, Langmuir surface area of 753 m^2 g^{-1}, micropore volume of 0.78 cm^3 g^{-1}, and average pore size of 4.4 nm, matching literature values. Figure 3b illustrates the TGA profile of Cu(BDC), showing a 26% weight loss occurring between 200°C and 280°C, which is attributed to the removal of coordinated DMF molecules. A second weight loss stage, observed between 285°C and 345°C, corresponds to the pyrolysis of terephthalate linkers.

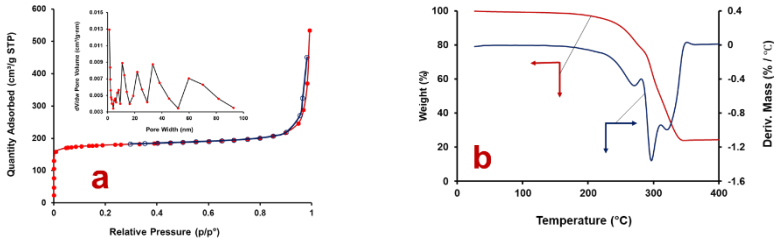

Figure 3 a) N_2 Adsorption (filled circles)-desorption (empty circles) isotherms,b) TGA and DTG curves of (under N_2 atmosphere, scan rate of 10°C/min) of Cu(BDC).

Cu(BDC) was used as a catalyst in the coupling reaction of imidazole and bromobenzene, which was chosen as a representative example. The results are illustrated in Figures 2a-c. The effects of solvent, base, reaction temperature, and catalyst loading on the reaction yield were investigated. The highest yield was obtained using DMSO as the solvent, 2.0 equivalents of NaOH as a base, 7.8 mol% copper (30 mg) at 120°C.

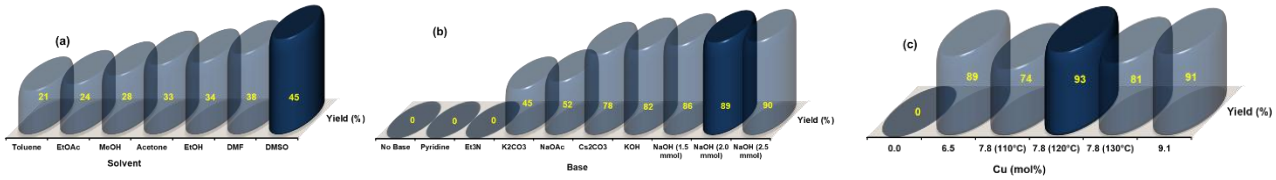

Figure 4 Optimization of the *N*-arylation reaction conditions: Imidazole (1.5 mmol), Ph-Br (1.0 mmol), K_2CO_3 2.0 mmol, solvent (1.5 mL), Catalyst 25 mg (Cu mol% 6.5), and reaction time 15 h.; a) Solvent; b) Base; c) reaction temperature and the catalyst dosage.

The MOF was applied as the catalyst in the coupling reaction of *NH*-heterocycles with chloro-, bromo-, and iodoarenes, with results summarized in Table Products were purified by thin-layer chromatography on silica gel-

coated glass plates. Iodo- and bromoarenes exhibited high reactivity, whereas chloroarenes were less reactive. Imidazole and benzimidazole demonstrated superior activity compared to 2-methylbenzimidazole.

Table 1 Cu(BDC) catalyzed N-arylation of NH-heterocycles with aryl halides a,b.

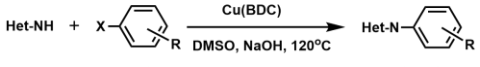

1a-1c 2a-2g 3a-3K

Entry	Het-NH	R	X	Time (h)	Yield (%) /TOF (h^{-1}) × 100
1	 1a	H	I	10	98/125
2		H	Br	15	93/79
3		H	Cl	24	18/10
4		4-CH_3	Br	19	88/59
5		3-CH_3O	Br	17	91/68
6		2-Br-pyridine	Br	13	94/92
7		1-Br-Naphthalene	Br	16	77/61
8	 1b	H	I	21	22/13
9		H	Br	23	5/2
10		H	Cl	26	-/-
11		4-CH_3	Br	23	-/-
12		1-Br-Naphthalene	Br	24	-/-
13	 1c	H	I	19	81/54
14		H	Br	20	61/39
15		H	Cl	22	9/5
16		3-CH_3O	Br	20	89/56
17		2-Br-pyridine	Br	14	91/83

[a] Reaction conditions: Het-NH (1.50 mmol), (hetero)aryl halide (1.00 mmol), NaOH (2.00 mmol), DMSO (1.5 ml), Cu(BDC) 30 mg (Cu 7.8 mol%). [b] Isolated yields.

The efficiency and reusability of the catalyst were assessed over multiple catalytic cycles using the reaction between imidazole and bromobenzene as a model. After each cycle, the catalyst was recovered through centrifugation, dried, and reused in the next reaction. As shown in Figure 3, the efficiency remained nearly constant during the first three cycles, followed by a gradual reduction in later cycles.

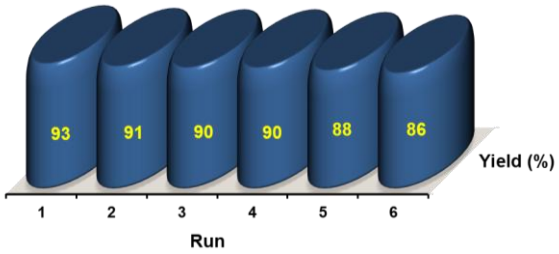

Figure 5 Recycling of the Cu(BDC) in the coupling of imidazole and bromobenzene.

4. Conclusion

This study has successfully demonstrated the catalytic potential of Cu(BDC) as an efficient and versatile material for copper-catalyzed C-N bond formation. Proin pharetra nonummy pede. Mauris et orci. Aenean nec lorem. In porttitor. Donec laoreet nonummy augue. Suspendisse dui purus, scelerisque at, vulputate vitae, pretium mattis, nunc. Mauris eget neque at sem venenatis eleifend. this catalytic system include its operational simplicity, high stability, and recyclability.

References

[1] R. Rossi, F. Bellina, M. Lessi, C. Manzini, L.A. Perego, Synthesis of Multiply Arylated Heteroarenes, Including Bioactive Derivatives, via Palladium-Catalyzed Direct C–H Arylation of Heteroarenes with (Pseudo)Aryl Halides or Aryliodonium Salts, Synthesis 46(21) (2014) 2833-2883.

[2] S. Mondal, Recent advancement of Ullmann-type coupling reactions in the formation of C–C bond, ChemTexts 2(4) (2016) 17.

[3] S. Kousik, S. Velmathi, Engineering Metal– Organic Framework Catalysts for C−C and C−X Coupling Reactions: Advances in Reticular Approaches from 2014–2018, Chem. - Eur. J. 25(72) (2019) 16451-16505.

2.3.
ORAL PRESENTATIONS

Design and Manufacture of PLC Controlled Laboratory Wear Device for in Vitro Biomedical Applications

Efe Çetin Yılmaz[1*], İbrahim Elebeyd[1]

[1] Department of Control Systems Electrical and Electronic Engineering, Engineering and Architecture Faculty, Kilis 7 Aralık University, Kilis, Türkiye

* *Corresponding author E-mail: efecetinyilmaz@msn.com*

Keywords

PLC

Wear Device

Robotic

In Vitro Test

Abstract

This study aims to design and manufacture a Programmable Logic Controller (PLC) controlled wear device with high accuracy and precision that can simultaneously move in two axes through the wear process. Within the scope of the study, synchronous step motors that can provide lateral and vertical axis motion drive and a PLC controller that can provide real-time control were used through the wear test process. The designed and manufactured laboratory device will enable various wear testing methods in the biomedical field. The device will model the wear mechanisms occurring on living tissue over time and can be performed in vitro in a laboratory environment. In addition, the wear and fatigue mechanisms caused by the mechanical movements of the designed and produced wear device were modelled using the finite element method, and the mathematical modelling of the test method was carried out through the wear test process. In this way, test methods that are performed on living tissue for long periods of time will be modelled in a laboratory environment, and results will be obtained in a short time. These data will guide the developments in material engineering and will make a great contribution to the selection of materials for a satisfactory treatment process. In addition, the flexible design structure of the device for modelling different parts of the human body with different modules will contribute to the impact area in research. Finally, by incorporating different modules into the designed and manufactured wear device, fatigue and corrosion mechanisms can be simultaneously analysed through the wear process. This will enable the continuous and complex damage mechanisms occurring in the human body to be simulated in a laboratory environment.

1. Introduction

Today, the rapid advancement of technology has led to significant transformations in many areas, from industrial production processes to scientific research [1]. Automation technologies and control systems, at the heart of these transformations, play a critical role in increasing efficiency, minimizing human error, and ensuring more precise process management. In this context, Programmable Logic Controllers (PLCs) have become one of the fundamental building blocks of modern automation systems thanks to their flexible structures, high reliability levels, and ease of integration. In laboratory-scale experimental systems in particular, precise control and data reliability are of paramount importance. In experimental studies in the field of materials science, wear tests are one of the fundamental methods that provide information about the service life and durability of materials. However, wear tests performed using traditional methods have limitations such as uncontrolled environmental variables, operator errors, and low repeatability. At this point, PLC-based systems make it possible to conduct experiments in a more controlled, systematic, and reliable manner.

In recent years, the mechanical and aesthetic properties of restorative and ceramic materials have emerged as an important concept in dentistry. In intraoral tribology, ceramic and restorative materials are subjected to various mechanical loading and wear mechanisms during chewing. This environment significantly affects the aesthetic and mechanical properties of the materials. For a long time, numerous in vitro experiments have been developed in the literature to determine these properties of materials in a laboratory environment [2-4] However, due to the very complex nature of intraoral tribology, these developed in vitro test methods have never been able to fully simulate the

process. Nevertheless, in vitro studies are always needed in dentistry because in vivo (tests on living tissue) tests are very time-consuming and costly. Evaluations obtained after in vitro studies have led to a more satisfactory treatment process. In intraoral tribology, it is possible to say that four basic wear mechanisms occur during chewing. These are: wear occurring between the mating material and the tooth (two-body wear); the presence of a third abrasive medium between the mating material and the tooth, which is generally considered to be food particles during chewing (three-body wear); fatigue wear caused by subsurface cracks in the material due to repeated loading; and corrosive wear caused by changes in pH and temperature values in the oral environment due to ingested food. These wear mechanisms can occur individually or simultaneously in intraoral tribology. The complex and constantly changing nature of intraoral tribology negatively affects the mechanical and aesthetic properties of restorative and implant materials.

Many researchers in the literature are developing various wear testing mechanisms [3, 5-13]. The design and material selection of these abrasion testing devices can significantly affect the accuracy of tests in a laboratory environment. For example, in chewing test experiments, vibrations can occur due to direct or indirect contact between the test material and the biting force generated by the movement of the upper jaw. If these vibrations cannot be dampened during the testing process, they will affect the wear resistance of the test material. This can weaken the validity of the test results.

2. Materials and Methods

This study focuses on the fabrication of a PLC-controlled wear testing device designed to simulate the wear mechanisms experienced by biomaterials in a real-world environment within a laboratory setting. This biaxial laboratory wear testing device, based on Programmable Logic Control (PLC), aims to provide an innovative contribution to the field of materials engineering. The study will consist of four phases: device design, analysis using the finite element method (ANSYS), fabrication and assembly (SOLIDCAM), and calibration according to international standards. The device aims to contribute to the development of clinical treatment methods by enabling life and performance testing of biomaterials. Thus, it will be possible to predict the behavior of biomaterials within living organisms. The device designed and manufactured in this study is expected to make a significant contribution to the fields of biomedical engineering and materials science by analyzing the wear properties of biomaterials.

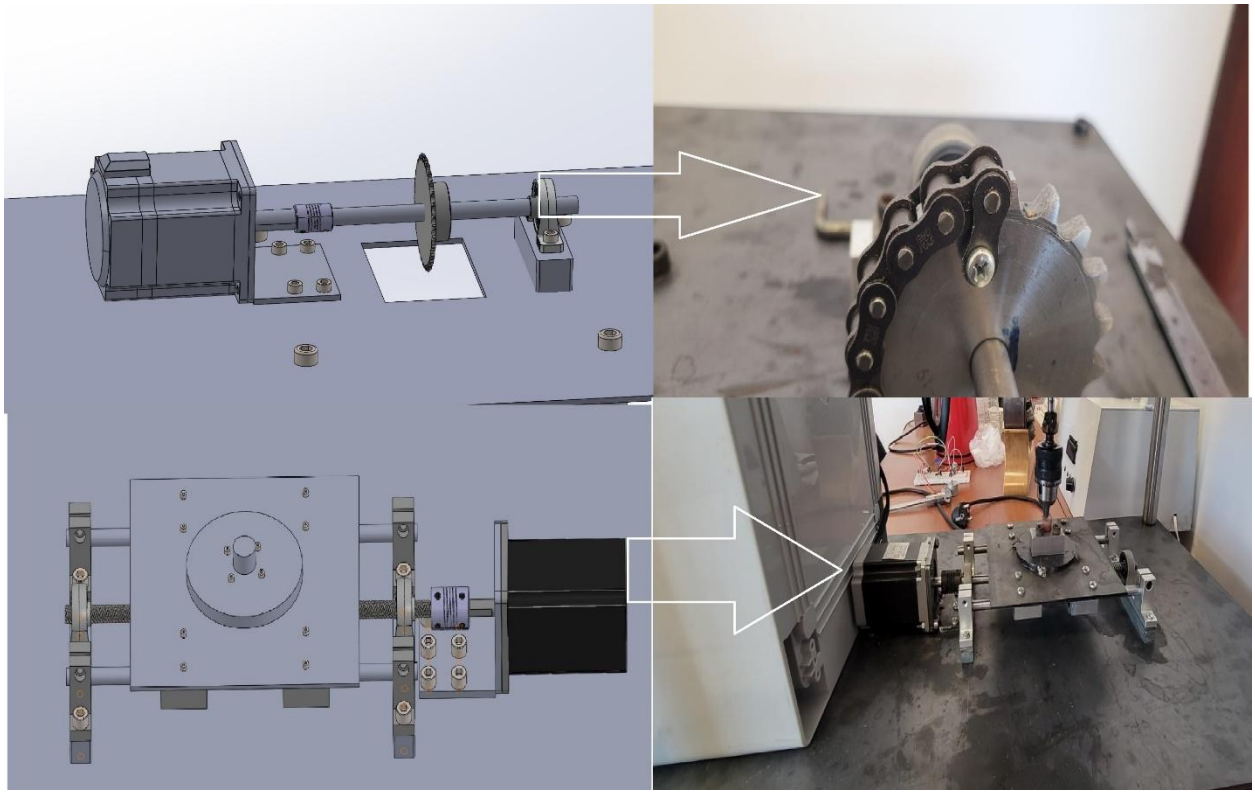

Figure 1 The schematic design of the wear device designed within the scope of this study

Within the scope of this project, various options were evaluated for the selection of a suitable control unit. While a wide range of alternatives exist, from the simplest manual control techniques to more advanced automation systems, Programmable Logic Controllers (PLCs) have become the most commonly preferred solution in industrial applications. The main reasons for this include low cost, ease of programming, and high reliability in industrial environments.Considering the local market and usage conditions in Turkey, Delta brand PLCs were determined to be

the most suitable solution in terms of performance and cost balance. Since our project needs did not require more than 5 digital outputs and 8 digital inputs, the Delta DVP-14SS2T model PLC was chosen.This model has 8 digital inputs and 6 digital outputs. The outputs are transistor type, providing superior performance in applications requiring fast switching. Additionally, the device includes 4 high-speed outputs, making it suitable for applications requiring precise timing. The Delta PLC DVP-14SS2T boasts excellent processing speed, executing basic commands in approximately 0.35 to 1 microsecond. It supports eight high-speed inputs, two at up to 100 kHz and six at 10 kHz, while A/B phase counting can reach up to 50 kHz. In terms of outputs, the DVP-14SS2T offers four high-speed pulse output points for motor control, each operating at a maximum frequency of 10 kHz, making it suitable for many control applications requiring fast response. These features make the selected PLC ideal for controlling the stepper motor drivers used in the project. Each driver requires one high-speed output (Pulse) to determine the number of steps of movement and one standard digital output (Direction) to determine the direction of rotation. The Delta DVP-14SS2T model meets both the technical requirements and allows for future system expansion. Furthermore, it offers a solution that fits within the project budget.

The schematic design of the wear device designed within the scope of this study is shown in Figure The use of two independent stepper motors in this design has increased the wear mechanism capability of the device. The stepper motors have the ability to communicate with each other in 0.2-second periods. This indicates that it can achieve a 5 Hz capability in wear mechanisms using the formula f=1/T (T: period).

In industrial systems requiring high precision, problems such as step loss frequently occur in applications using conventional stepper motors; this can lead to deviations from the target position or potential operational failures. To overcome this problem, encoder stepper motors are used in the designed system. These motors offer more reliable and precise control by providing continuous feedback on the movement thanks to their closed-loop control system. In this structure, an optical encoder disc and reader unit, each with 1000 pulses, are integrated into the rear of the motor. The encoder checks whether the motor takes each step correctly. If step loss is detected, the system increases the current applied to the relevant winding, increasing the motor torque and thus ensuring the completion of the movement. However, if the movement cannot be completed despite this correction, the drive unit automatically activates the alarm mode and stops the motor from operating. In this way, the system is protected from possible failures or damage such as burning. Thanks to the interactive operation of encoder-equipped stepper motors and intelligent drive units, the following advantages are achieved in critical applications:

3. Results and Discussion

The tribological process within the oral cavity is quite complex and variable. Unlike materials in the external environment, implanted materials interact with numerous parameters such as body fluids, varying ambient temperature, fluctuating pH levels, and mechanical stresses along various axes. This interaction significantly affects the mechanical and aesthetic behavior of implanted materials. For example, extreme temperature changes from ice cream (0°C) to hot coffee (90°C) lead to compatibility problems such as thermal expansion, changes in mechanical properties, or failure of bonding [14]. Significant advancements have been made in implantable materials in recent years. These advancements have been achieved by altering the microstructure chemistry of the material or by applying coatings to the material. The most important aspect of these advancements is considered to be the material's ability to be fully compatible with the body and to exhibit the expected aesthetic and mechanical properties throughout its lifespan. In recent years, due to the time-consuming nature, high cost, and ethical concerns associated with experiments on living tissue, there has been a shift towards in vitro laboratory experiments. The ability of in vitro laboratory experiments to simulate, in very short periods of time, the changes a material undergoes in living tissue over a long period of time is considered their greatest advantage. However, the continuous and complex nature of the process in living tissue makes simulating living tissue quite challenging.

4. Conclusion

The process of producing the project prototype involved carefully planning a production schedule to ensure performance accuracy and rapid completion while minimizing the possibility of errors in all stages of the work. The plan began with a comprehensive review of the project idea and an analysis of the requirements of the proposed machine. The motion principle was evaluated, and the necessary mechanical and electrical requirements were determined to ensure efficient operation. After ensuring the realism and effectiveness of the idea, we proceeded to the 3D design phase using SolidWorks software and created a digital model for the main components. During this phase, we conducted numerous experiments on virtual prototypes to simulate motion and examine the mechanical interactions between the parts. Thus, we aimed to achieve a complete prototype reflecting the final engineering design of the system. Simulation tools helped us uncover some design problems. For example, it was determined that the thickness of the top base needed to be increased and that an auxiliary base needed to be added to prevent vertical axis deviation. After these adjustments were made, production files were prepared with accurate dimensions using

materials (such as aluminum and stainless steel) selected to suit the acting forces and operating conditions. After the engineering drawings were completed, a detailed plan was prepared for the parts to be manufactured. First, the shaft parts, which were produced using a lathe, were determined. These shaft parts were carefully manufactured to ensure smooth movement. On the other hand, the parts placed under the ball bearing were produced with a CNC milling machine to ensure precision.

References

[1] Rashid, A.B. and M.D.A.K. Kausik, AI revolutionizing industries worldwide: A comprehensive overview of its diverse applications. Hybrid Advances, **7**: p. 100277.

[2] Souza, J.C.M., et al., *Abrasive and sliding wear of resin composites for dental restorations.* Tribology International, **102**: p. 154-160.

[3] Yilmaz, E.Ç., *Chewing simulation parameters and mechanical properties of composites as used in dental bio-materials.* Proceedings of the Institution of Mechanical Engineers, Part H: Journal of Engineering in Medicine, **239**(11-12): p. 1087-1097.

[4] Yilmaz, E., *Investigating the Effect of Chewing Force and an Abrasive Medium on the Wear Resistance of Composite Materials by Chewing Simulation.* Mechanics of Composite Materials, **56**(2): p. 261-268.

[5] Santos, R.L.P., et al., *Tribological behavior of zirconia-reinforced glass-ceramic composites in artificial saliva.* Tribology International, **103**: p. 379-387.

[6] Yilmaz, E.C. and R. Sadeler, *Investigation of Two- and Three-Body Wear Resistance on Flowable Bulk-Fill and Resin-Based Composites*. Mechanics of Composite Materials, **54**(3): p. 395-402.

[7] Lawson, N.C., et al., *Characterization of third-body media particles and their effect on in vitro composite wear*. Dental Materials, **28**(8): p. E118-E126.

[8] Faria, A.C.L., et al., *Wear resistance of experimental titanium alloys for dental applications.* Journal of the Mechanical Behavior of Biomedical Materials, **4**(8): p. 1873-1879.

[9] Yilmaz, E.Ç., *Effect of Sliding Movement Mechanism on Contact Wear Behavior of Composite Materials in Simulation of Oral Environment.* Journal of Bio- and Tribo-Corrosion, **5**(3): p. 63.

[10] Injeti, V.S.Y., et al., *A comparative study on the tribological behavior of Ti-6Al-4V and Ti-24Nb-4Zr-8Sn alloys in simulated body fluid.* Materials Technology, 2018: p. 1-15.

[11] Yilmaz, E.Ç., *Investigation of three-body wear behavior and hardness of experimental titanium alloys for dental applications in oral environment.* Materialwissenschaft und Werkstofftechnik, **51**(1): p. 47-53.

[12] Yilmaz, E.Ç., *Effect of axial Bruxism bite force on titanium alloys biomaterials experimental chewing test and 3D finite element simulation.* Computer Methods in Biomechanics and Biomedical Engineering, 2024: p. 1-10.

[13] Yilmaz, E.Ç., *Analyzing the Effect of Thermal Change on Test Biomaterials in Chewing Test Experiments.* Journal of Preventive, Diagnostic and Treatment Strategies in Medicine, **4**(2).

[14] St John, K.R., *Biocompatibility of dental materials.* Dent Clin North Am, **51**(3): p. 747-60, viii.

Investigation Contact- and Contact-Free Wear Resistance of Titanium for Biomedical Applications: Correlation with Wear Depth and Volume Loss

Efe Çetin Yılmaz[1*]

[1] Department of Control Systems Electrical and Electronic Engineering, Engineering and Architecture Faculty, Kilis 7 Aralık University, Kilis, Türkiye

* *Corresponding author E-mail: efecetinyilmaz@msn.com*

Keywords

Biomaterials
Wear
Titanium
Volume Loss
In Vitro Study

Abstract

Commercially pure titanium is often preferred in biomedical applications due to its high biocompatibility behaviour. However, the inadequate wear, fatigue, and corrosion resistance of titanium limit its use as a biomaterial in the human body. The purpose of the present study was to investigate contact- and contact-free wear resistance and hardness of titanium for biomedical applications. In this study, pure titanium specimen was exposed to contact- and contact-free wear tests using a computer-controlled chewing simulator with a steatite ball as antagonist (100 N bite force loads, 1.0 Hz chewing frequency, 1.000 and 2.000 chewing cycles immersed air and poppy seed ambient. The maximum wear depth and the volume loss of the worn surfaces were measured with a 3D profilometer. The interactions between the titanium test specimen and the maximum depth of wear and volume loss were found to be significant through the wear test process..

1. Introduction

Commercially pure titanium and its alloys are frequently preferred as biomaterials in the human body due to their superior fatigue behavior, corrosion resistance, and low elastic modulus. However, pure titanium is known to exhibit poor wear resistance, particularly in wear mechanisms involving abrasive metallic countermaterials [1]. Biomaterials placed in the human oral cavity are inevitably subject to various fatigue, corrosion, and wear factors during mastication. To ensure satisfactory long-term treatment, it is crucial to understand the wear and fatigue properties of biomaterials placed in the human oral cavity for varying periods of time. Due to the lengthy and expensive nature of in vivo experiments, as well as the associated ethical concerns, researchers have turned to in vitro testing methods. Laboratory in vitro testing methods allow for the evaluation of the wear and fatigue properties of biomaterials, which can remain in living tissue for years, in a very short period of time (e.g., 10–20 days of testing). Another important advantage of this method is the ability to determine the mechanical and chemical properties of newly developed biomaterials for the human body in a very short time, without using them on living tissue. However, the human body is a continuous and extremely complex structure. It is known that biomaterials placed in the human oral cavity can be continuously and complexly subjected to various wear and fatigue factors. Four main wear mechanisms have been reported that occur during chewing movement mechanism [2-4].These wear mechanisms can be defined as direct contact wear (two-component wear), the presence of a third abrasive medium (three-component wear), subsurface cracks formed in the material under cyclic loading (fatigue wear), and wear caused by corrosion (corrosive wear). In direct contact wear (two-component wear), contact between the base material and the substrate occurs through direct contact, which transfers forces of varying magnitudes between the two materials. In three-component wear, third abrasive particles (e.g., food particles during chewing) become trapped between the abrasive material and the substrate, preventing direct contact. The literature reports that direct contact wear and abrasive wear are the primary wear mechanisms occurring during chewing movement mechanism [4]. The intraoral tribological process has a continuous and complex structure that has dynamics that can show different behaviors in the time band. Therefore, in literature, researchers have modeled different wear mechanisms in the intraoral tribological process [3, 5, 6].

2. Materials and Methods

The process environment in which wear tests were carried out in this study is shown in Figure The effect of bite force during chewing behavior was determined using dead weights (e.g., approximately 7 kg was chosen for 70 N). The

lower table on which the test sample was fixed was controlled by the Programmable Logic Controller (PLC) structure according to the test parameters determined by the stepper motor drive. Cylinder balls with a diameter of 6 mm were used as abrasive material in each chewing test. Pure titanium test specimen was produced with a diameter of 12 mm and a thickness of 2 mm. The surface hardness value of pure titanium material was determined using the Vicker's Hardness (HV) method before the wear test. The wear depths of the pure titanium test material after the wear test procedures were determined with then 3D non-contact profilometer device.

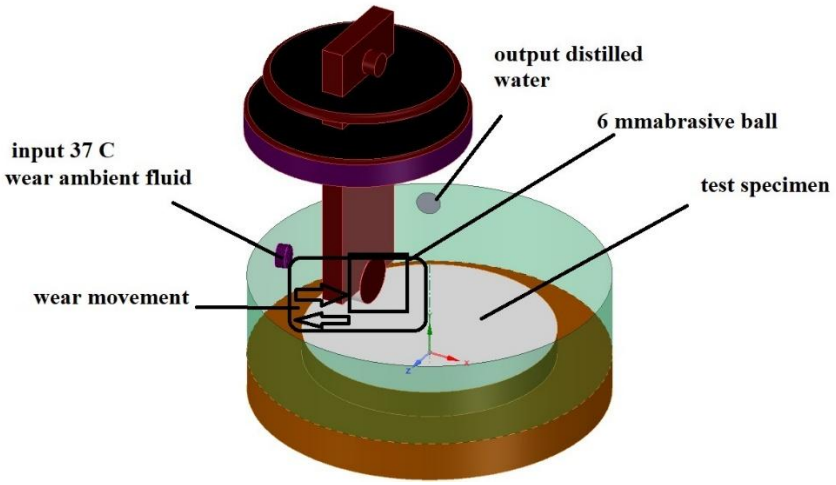

Figure 1 Systematic representation of the chewing wear process

3. Results and Discussion

The hardness value of the pure titanium material tested in this study before the wear test was determined to be approximately 230 Vicker's Harddness (HV). The analysis of the wear depth on the surface of the pure titanium test material after the wear test procedure is shown in Figure 2.

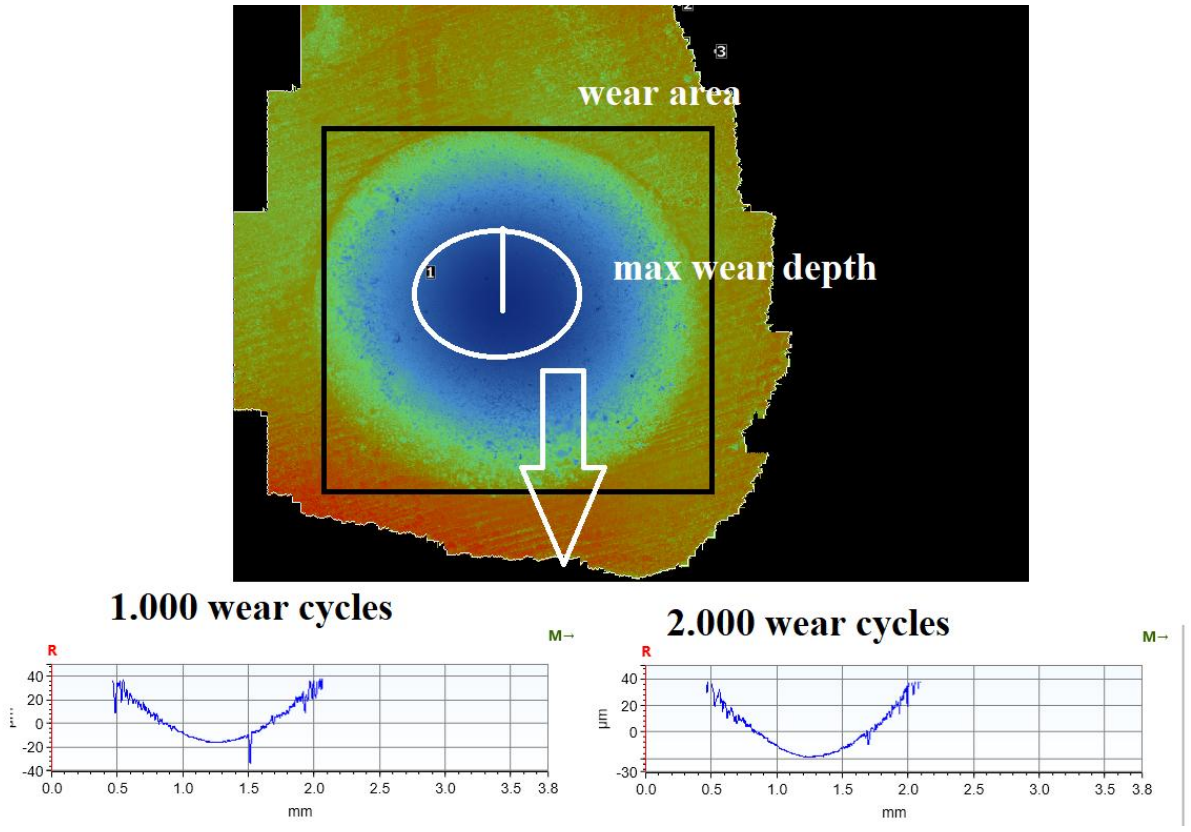

Figure 2 The analysis of the wear depth on the surface of the pure titanium test material after the wear test procedure

In vitro wear analysis of biomaterials used in the human body can be assessed using various methods, including contact or non-contact profilometers, digital microscopes, optical sensors, and laser scanning. These methods may have their own advantages and disadvantages. One study published in the literature assessed biomaterial volume loss and wear depth using various methods, including profilometers, optical sensors, and laser scanning [7]. Consequently, it was found that both wear depth and wear surface area volume loss along the transverse axes were significantly correlated. In this study, wear analysis was performed using a 3D non-contact profilometer, and wear depth and wear area along the transverse axes were correlated through wear test procedures. It can be said that the wear mechanisms of pure titanium and titanium alloys placed in the human oral cavity during laboratory chewing tests essentially occur in two stages. In the first stage, the biomaterial exhibits elastic-plastic properties when chewing forces are applied. In the second stage, wear marks form on the wear surface due to chewing movements. The wear patterns along the transverse axes were correlated through wear test procedures.

The intraoral tribological process has a complex and continuous structure. It is crucial to determine the mechanical and aesthetic behavior of biomaterials placed in this structure over time. Accurately predicting the mechanical and aesthetic behavior of biomaterials placed in the oral cavity over time will significantly contribute to the development of a satisfactory treatment process. Numerous in vivo and in vitro testing methods for predicting the mechanical and aesthetic behavior of biomaterials have been described in the literature [8-14]. However, due to the labor-intensive nature of in vivo studies, high costs, and ethical considerations, researchers tend to focus on in vitro testing methods. It is crucial to be able to model the complex and continuous nature of the human intraoral tribological process using in vitro test parameters. For example, the bite force generated during chewing is a continuously changing and continuous parameter. Numerous studies presented in the literature focus on the mechanisms of in vitro wear testing for direct contact (two-component) and abrasive (three-component) wear of various biomaterials [15-19].Furthermore, given the intraoral tribological process, the occurrence of heat exchange cycles during chewing tests is inevitable.

4. Conclusion

The data obtained within the scope of this study showed that the wear depth in pure titanium material increased with the increase in the number of wear cycles. This situation can be explained by the increase in the number of particles breaking off on the wear surface and the increase in the resulting wear volume loss. The fact that the maximum wear area in the wear depth occurs in the direct contact region of the biting force can be explained by the plastic deformation mechanism of the pure titanium test material. In future studies, conducting fatigue wear and corrosive wear tests on titanium alloys will contribute to determining the mechanical behavior of biomaterials on living tissue. Consequently, the in vitro test data obtained in this study are expected to contribute to the development of a more satisfactory treatment process on living tissue.

References

[1] Cvijovic-Alagic, I., et al., Wear and corrosion behaviour of Ti-13Nb-13Zr and Ti-6Al-4V alloys in simulated physiological solution. Corrosion Science, 53(2): p. 796-808.
[2] Yilmaz, E.Ç., Investigation of Bruxism wear behavior of titanium alloy biomaterials; experimental and 3D finite element simulation. Computer Methods in Biomechanics and Biomedical Engineering, 28(11): p. 1771-1782.
[3] Yilmaz, E.C. and R. Sadeler, Effects of Contact-Stress on Wear Behavior of Zirconia-Reinforced Lithium Silicate Glass-Ceramic. Biomedical and Biotechnology Research Journal (BBRJ), 4(1): p. 51-54.
[4] Lazaridou, D., et al., Are resin composites suitable replacements for amalgam? A study of two-body wear. Clinical Oral Investigations, 19(6): p. 1485-1492.
[5] Yilmaz, E., Investigating the Effect of Chewing Force and an Abrasive Medium on the Wear Resistance of Composite Materials by Chewing Simulation. Mechanics of Composite Materials, 56(2): p. 261-268.
[6] Yilmaz, E.Ç. and R. Sadeler, Effect of Artificial Aging Environment and Time on Mechanical Properties of Composite Materials. Journal of Dental Research and Reviews, 5(4): p. 111-115.
[7] Heintze, S.D., How to qualify and validate wear simulation devices and methods. Dental Materials, 22(8): p. 712-734.
[8] Santos, R.L.P., et al., Tribological behavior of zirconia-reinforced glass-ceramic composites in artificial saliva. Tribology International, 103: p. 379-387.
[9] Yilmaz, E.C. and R. Sadeler, Investigation of Two- and Three-Body Wear Resistance on Flowable Bulk-Fill and Resin-Based Composites. Mechanics of Composite Materials, 54(3): p. 395-402.
[10] Lawson, N.C., et al., Characterization of third-body media particles and their effect on in vitro composite wear. Dental Materials, 28(8): p. E118-E126.
[11] Faria, A.C.L., et al., Wear resistance of experimental titanium alloys for dental applications. Journal of the Mechanical Behavior of Biomedical Materials, 4(8): p. 1873-1879.
[12] Yilmaz, E.Ç., Effect of Sliding Movement Mechanism on Contact Wear Behavior of Composite Materials in Simulation of Oral Environment. Journal of Bio- and Tribo-Corrosion, 5(3): p. 63.
[13] Injeti, V.S.Y., et al., A comparative study on the tribological behavior of Ti-6Al-4V and Ti-24Nb-4Zr-8Sn alloys in simulated body fluid. Materials Technology, 2018: p. 1-15.
[14] Yilmaz, E.Ç., Investigation of three-body wear behavior and hardness of experimental titanium alloys for dental applications in oral environment. Materialwissenschaft und Werkstofftechnik, 51(1): p. 47-53.
[15] Yilmaz, E.C. and R. Sadeler, Investigation of three-body wear of dental materials under different chewing cycles. Science and Engineering of Composite Materials, 25(4): p. 781-787.
[16] Ghazal, M., et al., Two-body wear of resin and ceramic denture teeth in comparison to human enamel. Dental Materials, 24(4): p. 502-507.
[17] Hahnel, S., et al., Two-body wear of dental restorative materials. J Mech Behav Biomed Mater, 4(3): p. 237-44.

[18] Souza, J.C.M., et al., Abrasive and sliding wear of resin composites for dental restorations. Tribology International, 102: p. 154-160.

[19] Yilmaz, E.Ç., Effect of Artificial Saliva on the Mechanical and Tribological Behavior of Nano-/Micro-Filled Biocomposite Materials for Biomedical Applications. Journal of Dental Research and Review, 7(2): p. 37-41.

Effect of Sliding Wear Mechanism of Titanium Biomaterials: 3D Finite Element Analysis

Efe Çetin Yılmaz[1*], Muhammet Kaan Yeşilyurt[2]

1 Department of Control Systems Electrical and Electronic Engineering, Engineering and Architecture Faculty, Kilis 7 Aralık University, Kilis, Türkiye

2 Department of Mechanical Engineering, Faculty of Engineering, Ataturk University, Erzurum, Türkiye

* *Corresponding author E-mail: efecetinyilmaz@msn.com*

Keywords

Finite Element Analysis

Wear Simulation

Biomaterial

Titanium

Sliding Wear

Abstract

This study aims to analyze the effect of the lateral movement mechanism occurring during the chewing movement on the pure titanium material-based implant body using the Finite Element Analysis (FEA) method. In this study, a pure titanium-based dental implant material designed to international standards was subjected to 0.5 mm lateral movement mechanisms under a 70 N bite force. The force distribution generated within the implant body was analyzed using the FEA method. The obtained data showed that the load distribution generated by the lateral movement mechanism of the implant body and the bite force was distributed in the direction of movement. Additionally, it was observed that some residual loads occurred in the implant body upon completion of the chewing period. This suggests that residual stresses may be generated in the implant structure and may lead to various damage mechanisms depending on the parameters of the chewing movement. The ability of researchers to observe these data, which can be obtained over long periods of time in living tissue studies, through in vitro and FEA-method analysis, will make a great contribution to material development. In future studies, modeling the lateral wear movement mechanism in vitro with the FEA method and analyzing it on different materials will greatly contribute to the understanding of this mechanism.

1. Introduction

Titanium and its alloys have been used as biomaterials in living organisms due to their superior mechanical and esthetic properties. However, researchers have discovered through various studies that titanium and its alloys may exhibit poor mechanical and esthetic behavior [1, 2]. In vivo, in vitro and Finite Element Analysis method test models developed in the literature can analyze the mechanical and esthetic behavior of titanium and titanium alloys, which are preferred as biomaterials, in the environment to which they are exposed living environmet . However, these test methods have advantages and disadvantages depending on the experimental conditions and selected parameters. Researchers need to be able to choose these test methods depending on the dynamics of the experimental system. Structures that can be formed by different deformation mechanisms can occur simultaneously in different parts of the living structure.

Biomaterials placed in the human mouth are inevitably subjected to various fatigue, corrosion, and wear mechanisms during chewing. To ensure long-term satisfactory treatment, it is crucial to understand the wear and fatigue behavior of biomaterials placed in the human mouth over various periods. Due to the time-consuming, expensive nature of experiments conducted on living tissue (in vivo), and the ethical challenges involved, researchers have turned to in vitro testing methods. Laboratory (in vitro) testing methods allow the wear and fatigue behavior of a biomaterial that can remain on living tissue for years to be assessed in very short periods (such as 10-20 days of testing). Another major advantage of this method is that the mechanical and chemical behavior of recently developed biomaterials for the human body can be determined in very short periods of time without being used on living tissue. However, the human body is a continuous and highly complex structure. It is known that biomaterials placed in the human body can be subjected to various wear and fatigue mechanisms in a continuous and complex manner. Four basic wear mechanisms have been reported to occur during chewing movement mechanism [3, 4]. These wear mechanisms can

be defined as direct contact wear (two-body wear), the presence of a third abrasive medium (three-body wear), subsurface cracks in the material caused by repeated loading (fatigue wear), and corrosion (corrosive wear). In direct contact wear (two-body wear), the contact between the backing material and the substrate occurs through direct contact, which transfers forces of varying magnitudes between the two materials. In three-body wear, a third abrasive particle (such as food particles during chewing) is introduced between the abrasive material and the backing material, preventing direct contact. Direct contact wear and abrasive medium wear mechanisms have been reported in the literature as the primary wear mechanisms during chewing [5].

2. Materials and Methods

In this study, a finite element chewing test simulation of titanium bio-material was carried out using the ANSYS 19 workbench academic version program. For this reason, the mesh amount is set to a maximum of 30.000 which this ratio is in a range of values sufficient for the analysis performed finite element chewing test analyses. The material was chosen as a titanium alloy from the general material library of the ANSYS program. The mechanical properties of pure titanium, test samples, mesh test samples, and counter-abrasive materials tested in this study are shown in Figure 1.

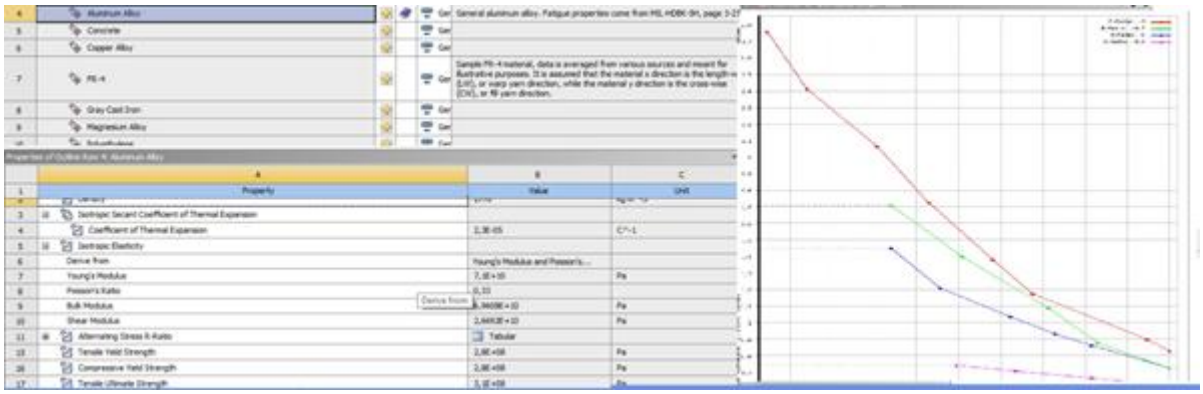

Figure 1 The mechanical properties of pure titanium, test samples, mesh test samples, and counter-abrasive materials tested in this study

In this study, an dental implant material was designed using pure titanium base material in international standard sizes in show Figure The designed dental implant material was subjected to a 0.5 mm lateral movement mechanism under a 70 N bite force. The stress distributions occurring in the implant body during horizontal movement were analyzed throught one chewing cycle.

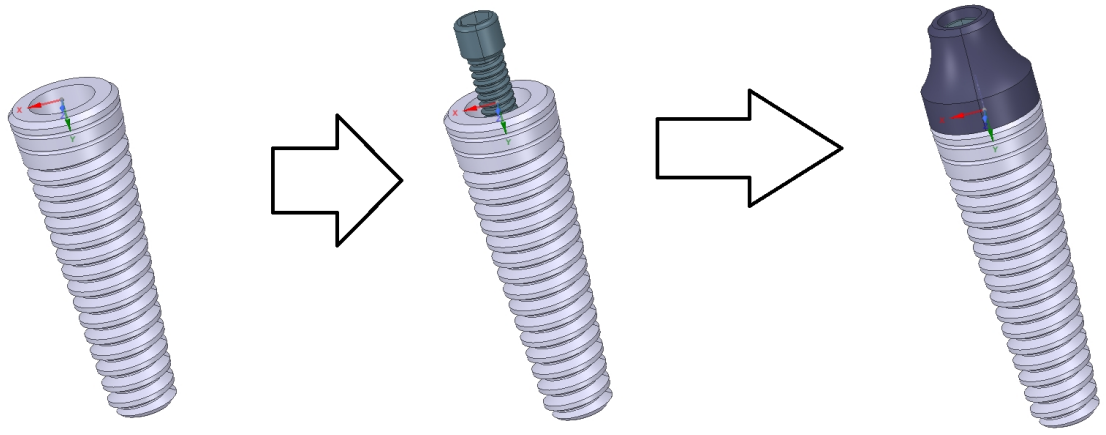

Figure 2 Example of dental implant material was designed using pure titanium base material in international standard sizes

3. Results and Discussion

The stress distribution on the pure titanium dental implant material structure after the experimental process determined within the scope of this study is shown in Figure 2.

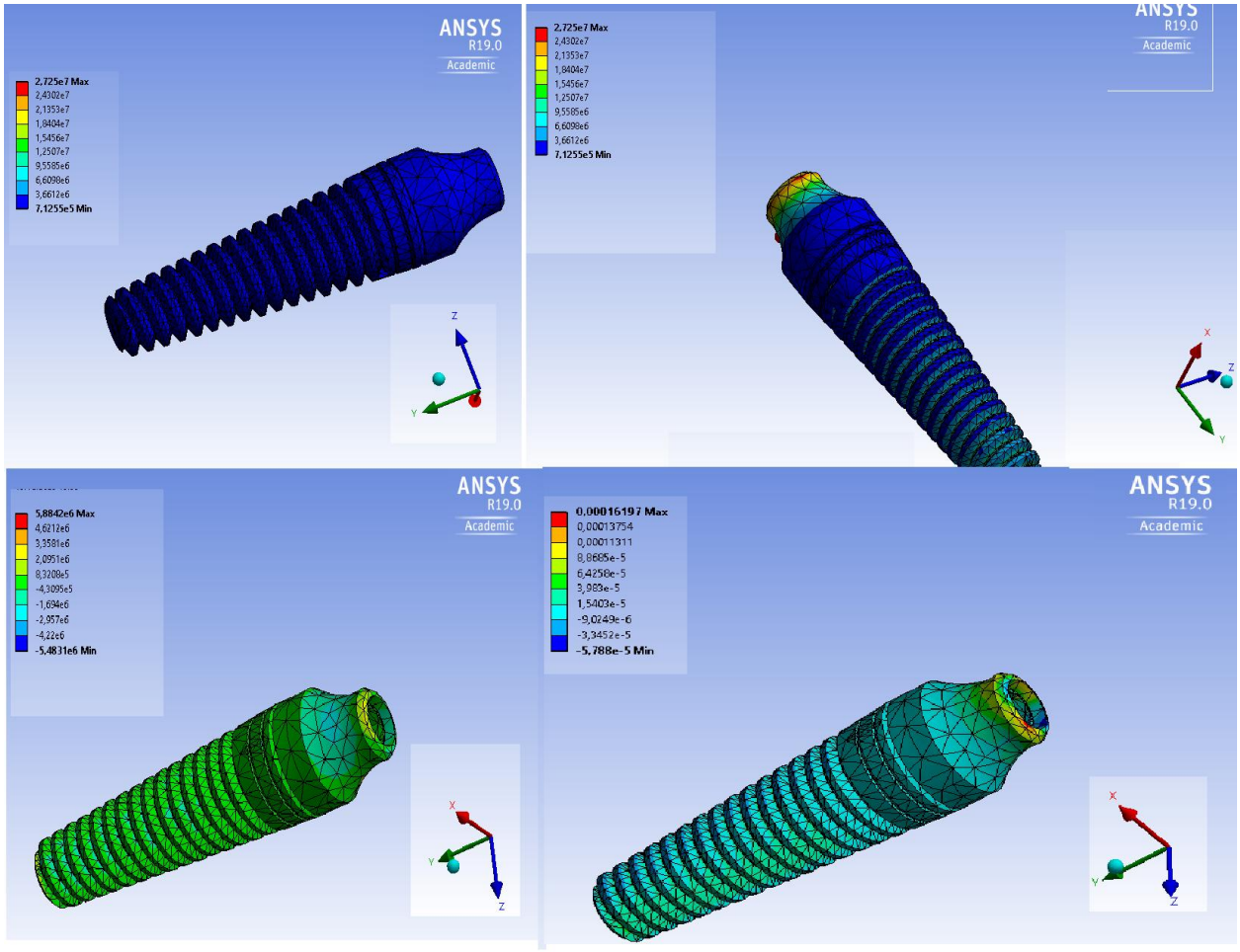

Figure 3 The stress distribution on the pure titanium dental implant material structure after the experimental process

In the experiment, during the defined wear process, it was assumed that in step 1, no load was applied to the implant material under ideal conditions. In step 2, a 70N biting force was applied to the crown portion of the implant through upper jaw movement. During this process, a maximum stress zone was created in the implant body. In step 3, the maximum stress zones in the crown region were distributed across the implant area using a horizontal movement mechanism. In this study, since the experimental parameters were modeled in an ideal environment, the stress distribution resembled a homogeneous structure. However, in laboratory tests, the stress distribution will not be homogeneous depending on the sample and environmental conditions. This process time was measured as approximately 0.6 seconds in an experimental setting. Therefore, it is possible to say that the wear frequency is 1.7 Hz using the formula f=1/T.

It is not always possible to fully model the damage mechanisms occurring in the human body at a 1:1 scale. Therefore, researchers in the literature have developed many different testing methods [6-10]. Due to their internal dynamics, these test methods may have advantages over each other depending on the experimental conditions, such as long time, complexity of repetition, and difficulty of modeling living tissue parameters. To give an example of a general understanding of the wear mechanism, it occurs when the abrasive material comes into direct contact with the test material. While it is possible to model this wear process in a laboratory setting alone, mathematically modeling the wear process can significantly contribute to the validity of the test results. Therefore, applying wear process tests simultaneously with different testing methods will increase the similarity of the obtained results to live samples. In wear tests, the counter abrasive material has a significant effect on the wear resistance of the test materials. This is because the mechanical and chemical behavior of the counter material can determine the type of wear mechanism. In the literature, researchers have made various choices regarding different abrasive materials in dental wear tests [11-13].

Mathematical modeling of a laboratory environment significantly simplifies the interpretation of experimental results, as the experimental value of a selected parameter reflects changes in the material being studied in real time. However, mathematical modeling of a laboratory environment may not always be possible, for example, due to improper selection of experimental conditions, a lack of researcher experience, or the inadequacy of the chosen modeling

program. Therefore, the creation of experimental systems for testing the laboratory environment and obtaining results by the researcher will significantly contribute to mathematical modeling.

4. Conclusion

The obtained data showed that the load distribution generated by the lateral movement mechanism of the implant body and the bite force was distributed in the direction of movement. Additionally, it was observed that some residual loads occurred in the implant body upon completion of the chewing period. This suggests that residual stresses may be generated in the implant structure and may lead to various damage mechanisms depending on the parameters of the chewing movement. The ability of researchers to observe these data, which can be obtained over long periods of time in living tissue studies, through in vitro and FEA-method analysis, will make a great contribution to material development. In future studies, modeling the lateral wear movement mechanism in vitro with the FEA method and analyzing it on different materials will greatly contribute to the understanding of this mechanism

References

[1] Tkachenko, S., et al., Wear and friction properties of experimental Ti-Si-Zr alloys for biomedical applications. Journal of the Mechanical Behavior of Biomedical Materials, 39: p. 61-72.

[2] Yilmaz, E.Ç., Investigation of three-body wear behavior and hardness of experimental titanium alloys for dental applications in oral environment. Materialwissenschaft und Werkstofftechnik, 51(1): p. 47-53.

[3] Yilmaz, E.Ç., Effect of Artificial Saliva on the Mechanical and Tribological Behavior of Nano-/Micro-Filled Biocomposite Materials for Biomedical Applications. Journal of Dental Research and Review, 7(2): p. 37-41.

[4] Yilmaz, E.C. and R. Sadeler, Effects of Contact-Stress on Wear Behavior of Zirconia-Reinforced Lithium Silicate Glass-Ceramic. Biomedical and Biotechnology Research Journal (BBRJ), 4(1): p. 51-54.

[5] Lazaridou, D., et al., Are resin composites suitable replacements for amalgam? A study of two-body wear. Clin Oral Investig, 19(6): p. 1485-92.

[6] Yilmaz, E.C. and M. Polat, Design and Manufacture of Computer-controlled Wear Device for Biomedical Material: A Different Ambient pH Experimental Application. Biomedical and Biotechnology Research Journal (BBRJ), 7(4): p. 558-562.

[7] Alecrim, L., et al., Wear behavior of conventional and spark plasma sintered Al2O3-NbC nanocomposites. International Journal of Applied Ceramic Technology, 15(2): p. 418-425.

[8] Yilmaz, E.Ç., Chewing simulation parameters and mechanical properties of composites as used in dental bio-materials. Proceedings of the Institution of Mechanical Engineers, Part H: Journal of Engineering in Medicine, 239(11-12): p. 1087-1097.

[9] Yılmaz, E.Ç., Effect of Antagonist Material Geometry on Titanium Biomaterials Two-Body Wear Behavior: Finite Element Analysis Study. International Journal of Innovative Research and Reviews, 9(1): p. 22-27.

[10] Yılmaz, E.Ç., Dynamic thermal cycle ambient simulation under mouth motion; a finite element analysis. NanoEra, 5(1): p. 16-21.

[11] Wassell, R.W., J.F. McCabe, and A.W. Walls, A two-body frictional wear test. J Dent Res, 73(9): p. 1546-53.

[12] Heintze, S.D., et al., Influence of the antagonist material on the wear of different composites using two different wear simulation methods. Dental Materials, 22(2): p. 166-175.

[13] Hahnel, S., et al., Two-Body Wear of Artificial Acrylic and Composite Resin Teeth in Relation to Antagonist Material. Journal of Prosthetic Dentistry, 101(4): p. 269-278.

Electrochemical Synthesis of CoBi2O4 Nanostructures

Hülya Öztürk Doğan[1,2,*], Pınar Anlar Daldal[3], Neslihan Çelebi[1,2], Arzu Kavaz Yüksel[2,3]

[1] Department of Chemical Technology, Vocational School of Technical Sciences, Atatürk University, Türkiye
[2] Department of Nanoscience and Nanoengineering, Atatürk University, Türkiye
[3] Department of Food Technology, Vocational School of Technical Sciences, Atatürk University, Türkiye

* *Corresponding author E-mail: hdogan@atauni.edu.tr*

Keywords

Electrochemical Synthesis

$CoBi_2O_4$

Nanomaterial

Abstract

Spinel metal oxides have the general formula AB_2O_4 (A, B = Co, Cu, Mn, Ni, etc.) and exhibit high thermal and chemical stability compared to single metal oxides. Therefore, spinel metal oxide structures have attracted greater attention than single-metal oxides in recent years. Traditional noble metal materials have strong catalytic properties and are used in a wide range of applications. In this study, the one-pot electrochemical synthesis of cobalt bismuthate ($CoBi_2O_4$) nanostructures, $Co(NO_3)_2.6H_2O$ and $Bi(NO_3)_3$ solutions were mixed at a 1:2 ratio. O2 gas was passed through the solution at a constant flow rate. A cyclic voltammogram (CV) was recorded with the cleaned pencil graphite electrode (PGE). This determined the deposition potential at which $CoBi_2O_4$ nanostructures could be deposited. The produced $CoBi_2O_4$ nanostructures were characterized using various techniques, including XRD, XPS, Raman, and SEM.

1. Introduction

Various semiconductor metal oxides, such as TiO_2, CeO_2, ZnO, and Cu_2O, are promising photocatalysts due to their favorable band gaps, non-toxicity, and remarkable affinity for morphology control, all of which are essential for a good photocatalyst. Recent studies have shown that binary and ternary metal oxides are more stable and electroactive than single metal oxides. Among all ternary metal oxides, spinel and inverse spinel oxides have attracted attention due to their ease of preparation, low cost, and tunability [1-2].

Traditional noble metal materials have good catalytic properties and can be used in a wide range of applications. However, their high cost is a major drawback for practical applications. Therefore, in recent years, metals, oxides, alloys, or hydroxides such as Ni, Co, Fe, Cu, Bi, Ti, and Mn, which are abundant in the earth, have been shown to be the most potential catalysts due to their abundant reserves and low cost. Bismuth and cobalt-based oxides/hydroxides are potential candidates for electrochemical applications, including energy applications such as supercapacitors, due to their diverse properties, chemical stability and broad oxidation states, strong redox behavior in alkaline electrolytes, and cheap and abundant sources [2-3]. The first cobalt-bismuth binary compound was prepared by Schwarz and his group at high pressure (5–10 GPa) and high temperature (370–1200 ◦C) [4]. Cobalt-bismuth oxide (CBO) nanoneedles with an average diameter of 10 nm were produced by a simple and cost-effective hydrothermal method followed by heat treatment. The unique morphology of CBO nanoneedles provides an interconnected 1D network for the rapid transport of electrons and ions and can tolerate volume changes. To successfully fabricate nanostructured electrodes, electroplating is a versatile technique that can be used for thin film production on electrode substrates. In this study, CBO nanostructures were produced on the pencil graphite electrode (PGE) surface using electrochemical technique.

2. Materials and Methods

An electrolyte mixture containing Co^{2+} and Bi^{3+} ions was used in the electrochemical synthesis of cobalt bismuthate ($CoBi_2O_4$) nanostructures. For this purpose, 5 mM $Co(NO_3)_2.6H_2O$ and 10 mM $Bi(NO_3)_3$ (in 0.1 M HCl) solutions were mixed at a 1:1 volume ratio. O_2 gas was passed through the solution at a constant flow rate. Cyclic voltammogram (CV) was recorded with the cleaned PGE electrode. The produced $CoBi_2O_4$ nanostructures were characterized using various techniques, including XRD, XPS, Raman, and SEM.

3. Results and Discussion

The cyclic voltammogram (CV) of the PGE electrode was recorded in a solution of 5 mM $Co(NO_3)_2.6H_2O$ and 10 mM $Bi(NO_3)_3$ (in 0.1 M HCl) (Figure 1). When the CV graph shown in Figure 1 was examined, a strong peak was observed at approximately -200 mV due to the presence of O_2 gas in the solution. As the potential was moved to a more negative value, a reduction peak resulting from the reduction of the species in the solution was detected. The CV graph shown in Figure 1 indicated that electrochemical deposition could be achieved in the region of approximately -800 mV.

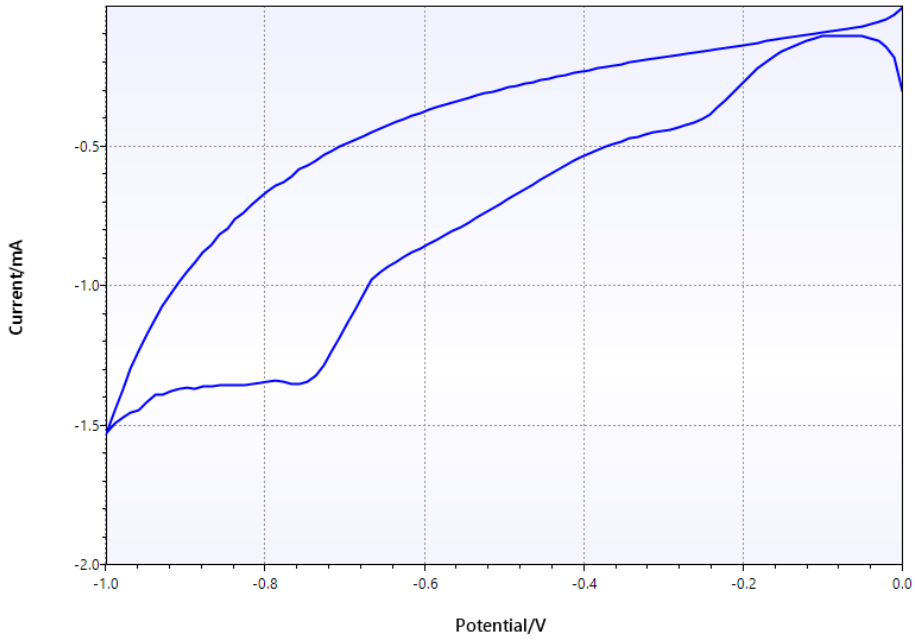

Figure 1 CV graph of PGE electrode in electrolyte medium containing 5 mM $Co(NO_3)_2.6H_2O$ and 10 mM $Bi(NO_3)_3$.

SEM images were recorded for morphological characterization of the CBO nanostructures. Figure 2 shows that the PGE surface was completely covered with CBO nanostructures.

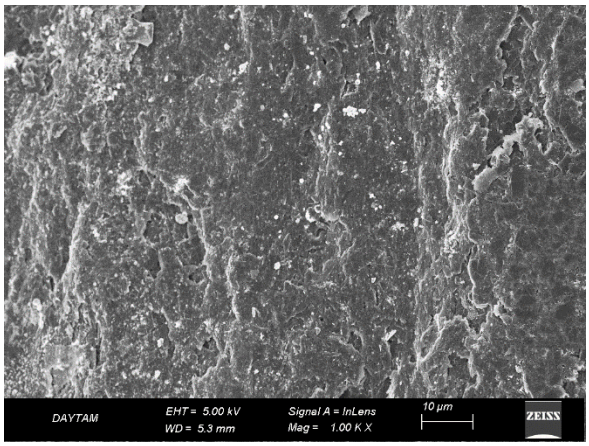

Figure 2 SEM image of $CoBi_2O_4$ nanostructures

4. Conclusion

In this study, PGE electrodes modified with $CoBi_2O_4$ nanostructures were successfully synthesized using a one-pot, single-step electrochemical deposition technique. For the synthesis of CBO electrodes, a constant potential of -800 mV was applied to Ag/AgCl for 30 minutes. The produced nanomaterial was thermally annealed at 350 °C for 1 hour in an air atmosphere. Analytical and morphological characterizations revealed that the synthesized CBO nanostructures contained both Co and Bi.

Acknowledgments

We would like to thank Atatürk University's Scientific Research Projects Unit for their support of this study (Project No: FBA-2024-14249)

References

[1] Sun, J., Xue, H., Zhang, Y. F., Zhang, X. L., Guo, N., Song, T., Dong, H., Kong, Y., Zhang, J., Wang, Q. Unraveling the Synergistic Effect of Heteroatomic Substitution and Vacancy Engineering in CoFe2O4 for Superior Electrocatalysis Performance. Nano Lett., 22 (8), 3503– 3511.

[2] Zhang, Y., Chen, Z., Tian, J., Sun, M., Yuan, D., Zhang, L. Nitrogen Doped CuCo2O4 Nanoparticles Anchored on Beaded-like Carbon Nanofibers as an Efficient Bifunctional Oxygen Catalyst toward Zinc-Air Battery. J. Colloid Interface Sci., 608, 1105– 1115.

[3] Rajan K.D., Mondal S., Ganesh V., Rathinam M. Cobalt (II/III) Bismuth Oxide Nanosheets as Photocatalysts for Peroxide-Assisted Tetracycline Degradation. J. Phys. Chem. C, 128, 3, 1368–1376.

[4] Schwarz U., Tence S., Janson O., Koz C., Krellner C., Burkhardt U., Rosner H., Steglich F., Grin Y. CoBi3: A Binary Cobalt-Bismuth Compound and Superconductor. Angew. Chem. Int. Ed., 52, 9853-9857

Removal of Heavy Metals in Ice Tea Beverages Using Electrochemically Synthesized Glutathione Modified Electrodes

Ayşenur Şuvak[1], Fatma Bayrakçeken [2]

[1] Department of Chemistry, Faculty of Science, Atatürk University, Erzurum, Türkiye
[2] Department of Chemistry, Faculty of Science, Atatürk University, Erzurum, Türkiye

* *Corresponding author E-mail: * aysenur.suvak19@ogr.atauni.edu.tr*

Keywords

L-glutathione
Electrodeposition
Nanofabrication
Heavy Metals

Abstract

Electrodes with enhanced active surface area were successfully synthesized by electrochemical methods using excellent L-glutathione nanostructured materials, prepared with the aim of eliminating heavy metals that may endanger human health, particularly in beverages. Most importantly, through these electrochemical methods, high-performance L-glutathione nanostructured electrodes can be directly fabricated at room temperature and atmospheric pressure, in a cost-effective manner, without the need for additional steps or extensive processing. Furthermore, with this method, L-glutathione nanostructures of desired composition, structure, and size could be easily synthesized by controlling electrochemical parameters such as potential and time. The nanostructured layers of the electrodes not only provide higher and more stable structural properties but also demonstrate significant morphological effects on electrode performance. Since this thin film formation is carried out electrochemically directly on ITO, interfacial defects and other contact-related problems are minimized. The surface morphology of the prepared three-dimensional (3D) electrodes was characterized using scanning electron microscopy (SEM). The functional groups and optical properties of L-glutathione thin nanostructured films were analyzed by Fourier transform infrared spectroscopy (FTIR) and UV-VIS spectroscopy. In addition, in the application stage, inductively coupled plasma mass spectrometry (ICP-MS) was employed to determine the heavy metal removal capacities of these electrodes.

1. Introduction

Glutathione (GSH) is a natural tripeptide composed of glutamic acid, cysteine, and glycine, and its heavy metal binding property mainly arises from the thiol (-SH) group of the cysteine residue [1]. This group forms covalent or coordinative bonds with heavy metals such as lead (Pb^{2+}), cadmium (Cd^{2+}), mercury (Hg^{2+}), and arsenic (As^{3+}), resulting in chelate complexes. In this way, the biologically active and toxic forms of metals are neutralized, their intracellular accumulation is reduced, and the formed glutathione–metal complexes are expelled from the cell, providing detoxification [2]. Moreover, glutathione plays a role in conjugation reactions with metals and other toxic compounds through the enzyme glutathione S-transferase. With these properties, glutathione is both a crucial biomolecule that protects cells against heavy metal–induced oxidative stress and a valuable component in environmental remediation and biosensor applications, where it is used to selectively capture metal ions when immobilized on electrode surfaces [3, 4].

1.1. Experimental Studies

A BAS 100B/W electrochemical workstation connected to a three-electrode cell (C3 Cell Stand, BAS) was used for the electrochemical experiments. The morphological analysis and elemental composition determination L-Glutathione nanostructures were carried out by a ZEISS system coupled to the scanning electron microscope.

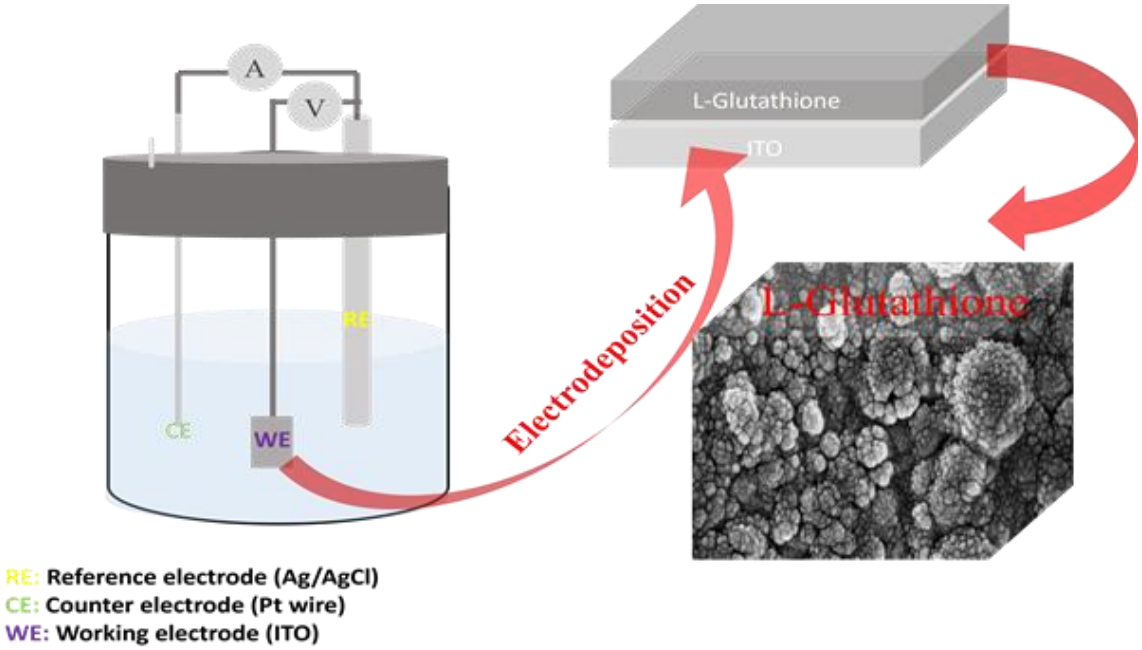

Figure 1 Electrochemical synthesis of ITO/L-Glutathione nanostructured thin films

This ability continues for L- Glutathione thin film electrodes; in a solution containing 8 mM L- Glutathione, pH:5 acetate buffer at a -460 mV constant potential at 25oC for different electrodeposition time. The schematic representation given in Figure 1 shows L- Glutathione thin film electrodes in the room (40 minutes electrodeposition time) were analyzed electrochemically.

2. Results and Evaluatıon

The SEM images of L-glutathione nanostructures are shown in Figure 2, indicating that the nanostructures exhibit aggregated formations with an approximate diameter of 50 nm. Moreover, as the electrodeposition time of the L-glutathione nanostructures increases, the surface area and pore volume of the nanomaterials are enhanced, providing more active sites for charge storage on the electrode surfaces and more pathways for the diffusion of charge species during electrochemical reactions. Consequently, a greater adsorption of heavy metals on the surface is achieved. The formation of a charged monolayer and interfacial electronic interactions effectively facilitates the rapid adsorption/desorption processes of catalytic intermediate reactions.

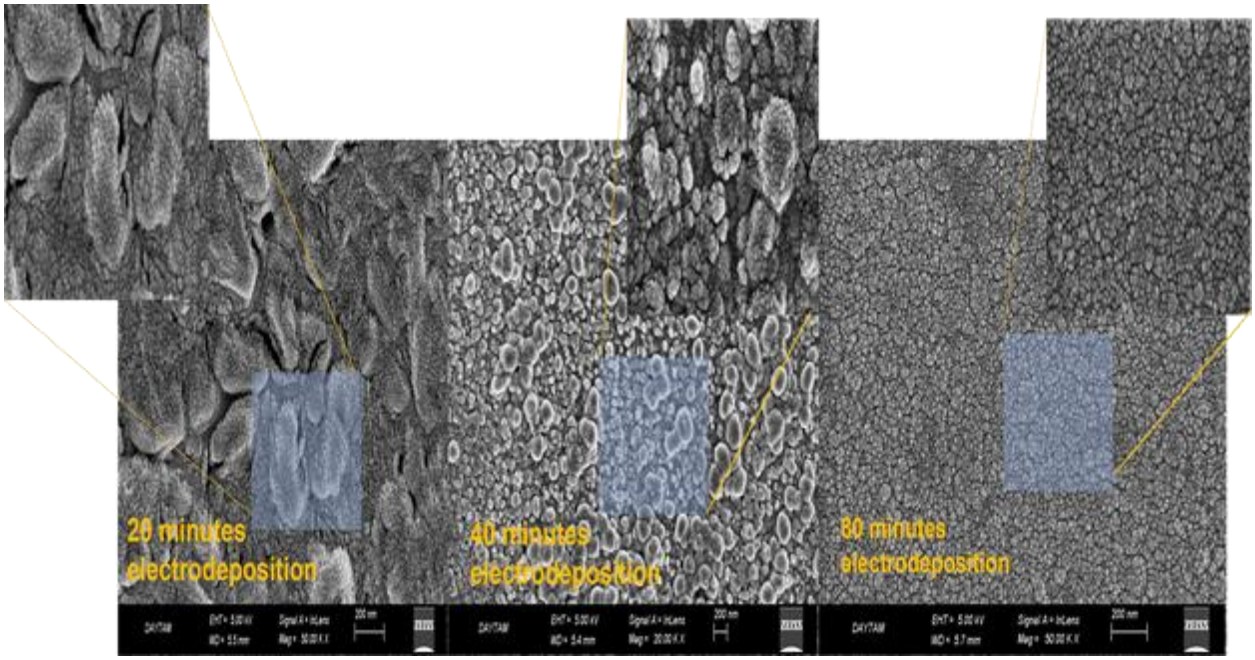

Figure 2 SEM images of L-Glutathione nanostructures on ITO electrodes.

3. General Evaluation and Conclusion

In summary, the structure of L-glutathione nanostructures was successfully characterized by controlling simple preparation parameters in the electrochemical method. The experiments further revealed that the size of L-glutathione nanostructures can be easily tuned by adjusting the deposition time. SEM, FTIR, and UV measurements demonstrated a lower defect concentration and improved optical quality in the enlarged L-glutathione nanostructures. Studies conducted with the fabricated L-glutathione electrodes on commercial iced tea samples, supported by ICP-MS data results, showed that a high level of heavy metal removal was achieved.

References

[1] Ukirade, N., Jagtap, S., Rane, S. (2023). Recent progress in electrochemical detection of glutathione. Hybrid Advances, 3, 100042. https://doi.org/10.1016/j.hybadv.2023.100042

[2] Dhanalakshmi, N., Priya, T., Thennarasu, S., Sivanesan, S, Thinakaran, N. (2021). Synthesis and electrochemical properties of environmental free Lglutathione grafted graphene oxide/ZnO nanocomposite for highly selective piroxicam sensing. Journal of Pharmaceutical Analysis, 11, 48e56. https://doi.org/10.1016/j.jpha.2020.02.001

[3] Forman, H. J., Zhang, H., & Rinna, A. (2009). Glutathione: Overview of its protective roles, measurement, and biosynthesis. Molecular Aspects of Medicine, 30(1-2), 1–12. https://doi.org/10.1016/j.mam.2008.08.006

[4] Anchidin-Norocel, L., Gutt, G., Tătăranu, E., Amariei, S. (2024). Effective tools for detecting heavy metals in water and food. International Journal of Electrochemical Science, 19(8), 100643. https://doi.org/10.1016/j.ijoes.2024.100643

Efficient *N*-Arylation of *NH*-Heterocycles Catalyzed by the Copper-Based Metal-Organic Framework Cu(BDC): A Reusable Heterogeneous Catalyst

Yagoub Mansoori [1,2,*] Maryam Fathinejad [2,] Somayeh Fekri [2]

[1] Department of Applied Chemistry, Faculty of Science, University of Mohaghegh Ardabili, Ardabil, Iran, 56199-Tel: +98 45 Fax: +98 45
[2] Nanoscience and Nanotechnology Research Group, University of Mohaghegh Ardabili, Ardabil, Iran, 56199-11367.

* *Corresponding author E-mail: ya_mansoori@uma.ac.ir*

Keywords

Carbonylation
Palladium catalyst
SBA-15@PHEN-Pd(II)
Heterogeneous
1,10-phenanthroline

Abstract

A heterogeneous palladium catalyst (SBA-15@PHEN-Pd(II)) was prepared by immobilizing a 1,10-phenanthroline-Pd(II) complex onto mesoporous SBA-15 via CPTES silylation and subsequent ligand grafting atomic absorption spectroscopy determined a Pd content of 0.16 mmol g-The catalytic performance of SBA-15@PHEN-Pd(II) was evaluated in the carbonylation of haloarenes using formic acid/DCC as a CO surrogate. Optimization identified DMF as the preferred solvent, NaOH (1.5 eq.) as the optimal base, and 120 °C as the ideal temperature, affording up to 66% yield at 0.63 mol% Pd. The catalyst retained activity over six cycles with minimal deactivation. Leaching tests, hot filtration, and control experiments indicated that the reaction proceeds via surface-immobilized Pd species.

1. Introduction

In recent decades, transition metal-catalyzed carbonylation reactions have emerged as a central focus within the field of organic chemistry.Carboxylic acid derivatives represent pivotal intermediates in the synthesis of dyes, pharmaceuticals, agrochemicals, and a broad spectrum of industrially relevant compounds [1]. CO surrogates offer a convenient and safer approach to carbonyl compounds, avoiding the use of gaseous CO.Formic acid has emerged as an efficient carbonyl donor in palladium-catalyzed reactions [2]. Heterogeneous catalysts have been developed to improve catalyst recoverability and reusability while minimizing waste in accordance with green chemistry principles [3]. we present a carbon monoxide-free carbonylation of haloarenes catalyzed by SBA-15@PHEN-Pd(II). The rigid bidentate ligand 1,10-phenanthroline (PHEN), comprising three fused aromatic rings and two nitrogen atoms, forms stable complexes with transition metals.

2. Materials and Methods

Solvents used in the experiments were dried using standard procedures reported in the literature. All additional reagents were obtained from Sigma and employed in their original form without further treatment.

2.1. Preparation of SBA-15@PHEN-Pd(II)

A heterogeneous palladium catalyst (SBA-15@PHEN-Pd(II)) was prepared by immobilizing a 1,10-phenanthroline-Pd(II) complex onto mesoporous SBA-15 via CPTES silylation and subsequent ligand grafting. 5-nitro-1,10-phenanthroline was synthesis from nitration of 1,10-Phenanthroline in concentrated H_2SO_4/HNO5-amino-1,10-phenanthroline was prepared by reducing of 5-nitro-1,10-phenanthroline with Hydrazine hydrate and Pd/C. 5-amino-1,10-phenanthroline (0.200 g, 1.02 mmol) was supported on as-prepared chloro silylated SBA-15 in NMP and Et_3N as base to give SBA-15@PHEN. Palladium(II) chloride was complexed with SBA-15@PHEN in methanol to give SBA-15@PHEN-Pd(II), Figure The palladium content of the final material, determined by atomic absorption spectroscopy, was 0.16 mmol g^{-1}.

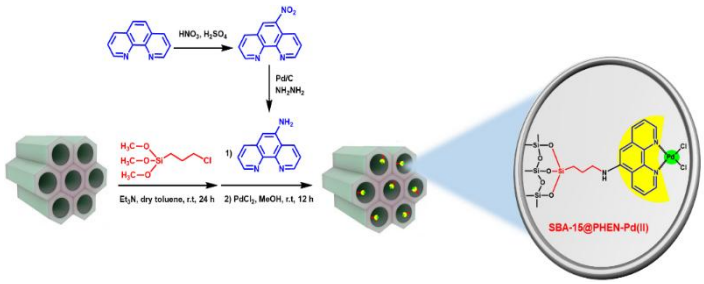

Figure 1 **Synthesis of SBA-15@PHEN-Pd(II).**

3. Results and Discussion

The FT-IR spectra of the synthesized materials are presented in Figures 2Aa-c. The FT-IR spectrum of 5-amino-1,10-phenanthroline (Figure 2Ac) displays a characteristic C=N stretching band at 1638 cm^{-1}, associated with the aromatic phenanthroline core. A comparable band at 1664 cm^{-1} is detected in SBA-15@PHEN (Figure 2Ab).

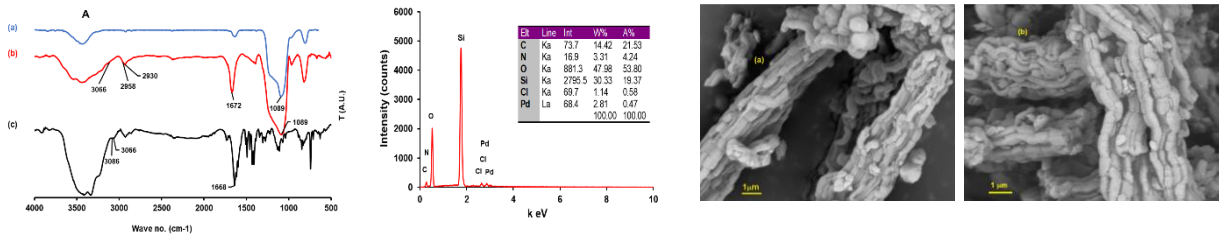

Figure 2 A) FT-IR (KBr) spectra of a) SBA-15, b) SBA@PHEN, and c) 5-amino-1,10-phenanthroline, B) EDAX spectrum of SBA@PHEN-Pd(II), C) SEM image of a) SBA-15 and b) SBA@PHEN-Pd(II).

Energy-dispersive X-ray (EDAX) analysis of the synthesized catalyst, in conjunction with qualitative elemental data, confirms the presence of C, N, O, Si, Cl, and Pd within the material matrix, as presented in Figure 2B. Well-ordered tubular channels are visible in the SEM micrograph (Figure 2Ca). As presented in Figure 2Cb, the ordered tabular architecture of the mesoporous silica is preserved for SBA-15@PHEN-Pd(II).

The nitrogen adsorption-desorption isotherms and pore size distribution profiles of the synthesized mesoporous materials are displayed in Figures 3a-b. The BET surface area, total pore volume, and mean pore radius of SBA-15 are 698 $m^2 g^{-1}$, 0.88 $cm^3 g^{-1}$, and 6.12 nm, respectively. After functionalization with the Pd(II)-PHEN complex, these values decrease significantly to 290 $m^2 g^{-1}$, 0.56 $cm^3 g^{-1}$, and 3.15 nm, respectively.

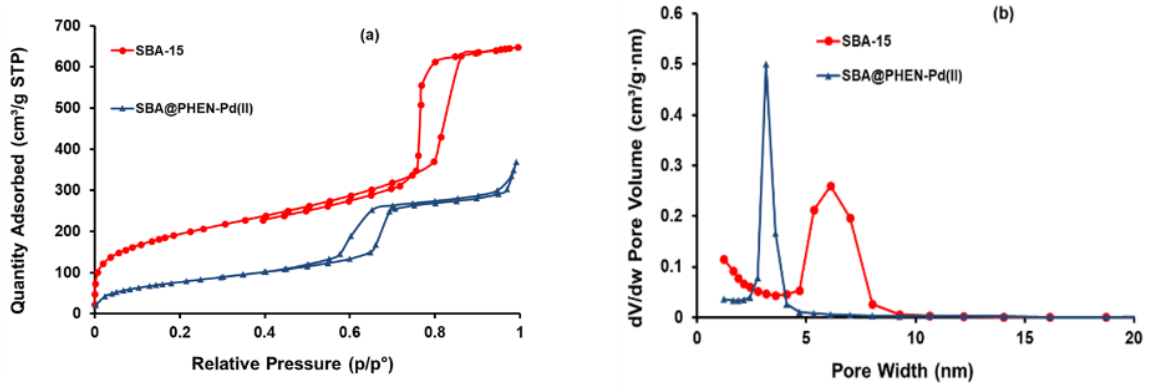

Figure 3 a) N_2 absorption-desorption, b) pore size distribution of SBA-15 , SBA@PHEN-Pd(II)

The SBA-15@PHEN-Pd(II) catalytic system was employed to mediate the carbonylation of haloarenes into the corresponding carboxylic acids, utilizing formic acid/DCC as the CO source. The reaction parameters were rigorously optimized, and are graphically delineated in Figures 4a-d. The effects of HCOOH/DCC, temperature, base and the catalyst dosage on the reaction yield were investigated. The highest yield was obtained using DMF as the solvent, 1.5 equivalents of NaOH as a base, 0.63 mol% palladium (40 mg), HCOOH 3.0 mmol, DCC 3.0 mmol at 120°C.

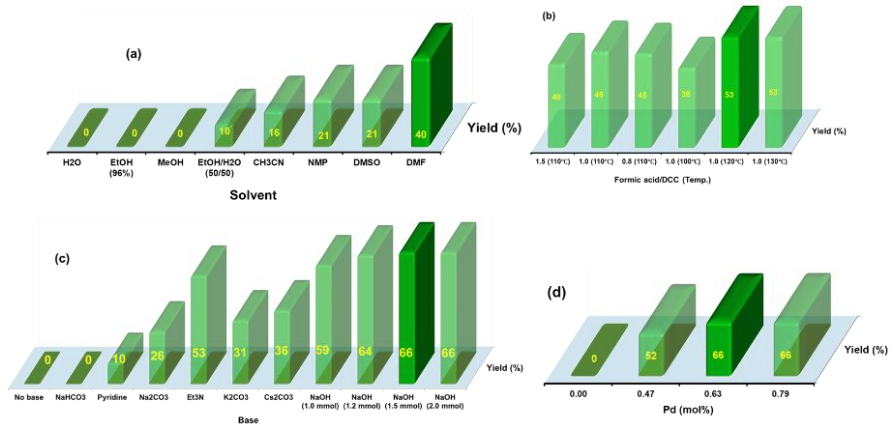

Figure 4 Optimization of the carbonylation reaction conditions: *p*-bromotoluene (1.0 mmol); Solvent (1.0 mL); and reaction time 24 h; a) Solvent: Pd(II) 0.79 mol%, reaction temperature 110°C, Et_3N: 1.2 mmol, formic acid: 3 mmol, DCC: 2 mmol; b) HCOOH/DCC and temperature: Pd(II) 0.79 mol%, Et_3N 1.2 mmol; c) Base: Pd(II) 0.79 mol%; and d) The catalyst dosage.

SBA-15@PHEN-Pd(II) catalyzed the carbonylation of chloro-, bromo-, and iodoarenes using formic acid/DCC as the CO source, Table 1.

Table 1 Carbonylation of aryl halides and synthesis of the corresponding acids catalyzed by SBA-15@PHEN-Pd(II)

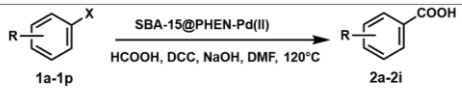

Entry	R	X	Product	Time (h)	Yield (%)[b]	m.p.(°C) (Lit.)
1	H	I **(1a)**	**2a**	24	70	119-121 (Lit. 120-121 [47])
2		Br **(1b)**		24	66	
3		Cl **(1c)**		24	50	
4	4-COOH	Br **(1d)**	**2b**	26	42	298-300 (Lit. 300 [48])
		Cl **(1e)**		26	33	
5	4-NH_2	Br **(1f)**	**2c**	24	60	180-183 (Lit. 182-185 [49])
6		Cl **(1g)**		24	55	
7	4-NO_2	Cl **(1h)**	**2d**	20	76	235-237 (Lit. 235-236 [50])
8	4-CH_3	Br **(1i)**	**2e**	26	60	182-184 (Lit. 181-182 [51])
9	4-OH	Br **(1j)**	**2f**	24	55	214-217 (Lit. 214-217 [51])
10	2-NH_2	Br **(1k)**	**2g**	24	50	142-144 (Lit. 142-145 [52])
11	3-CH_3	Br **(1l)**	**2h**	26	60	108-110 (Lit. 108-111 [51])
12	2-Pyridyl	Br **(1m)**	**2i**	26	49	135-137 (Lit. 136-138 [53])
13	4-NO_2-2-COOH	Cl **(1n)**	**2j**	24	0	-
14	4-CH_3-2-NH_2	Cl **(1o)**	**2k**	24	0	-
15	4-Ac	Cl **(1p)**	**2l**	24	0	-

[a]Reaction conditions: Arylhalide 1.0 mmol; NaOH 1.5 mmol; Pd 0.63 mol% (0.040 g), DMF 1.0 mL. HCOOH 3. mmol, DCC 3.0 mmol. [b] Isolated yields.

As illustrated in Figure 5, the catalytic activity remained unchanged for the first two cycles, while a gradual decline in the yield of approximately 10% was observed after six cycles. These results confirm that SBA-15@PHEN-Pd(II) retains both stability and catalytic activity in haloarene carbonylation over multiple cycles.

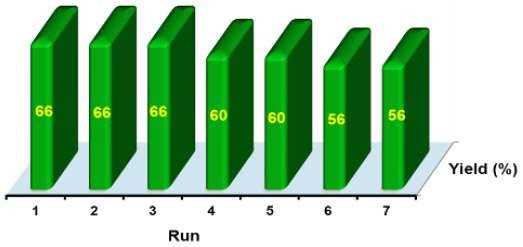

Figure 5 Recycling of SBA@PHEN-Pd(II) in carbonylation of 4-bromotoluene.

4. Conclusion

A heterogeneous palladium catalyst, SBA-15@PHEN-Pd(II), was prepared by immobilizing a 1,10-phenanthroline-Pd(II) complex onto mesoporous SBA-The catalyst promoted the carbonylation of various haloarenes using formic acid/DCC as the carbonyl source. Electron-withdrawing substituents increased the reaction efficiency, whereas steric

effects or coordinating substituents reduced product yields.The catalyst retained its activity over multiple reaction cycles, demonstrating its stability under the applied conditions.

References

[1] N. Hussain, A.K. Chhalodia, A. Ahmed, D. Mukherjee, Recent Advances in Metal-Catalyzed Carbonylation Reactions by Using Formic Acid as CO Surrogate, ChemistrySelect 5(36) (2020) 11272-11290.

[2] R. Sang, P. Kucmierczyk, K. Dong, R. Franke, H. Neumann, R. Jackstell, M. Beller, Palladium-catalyzed selective generation of CO from formic acid for carbonylation of alkenes, J. Am. Chem. Soc. 140(15) (2018) 5217-5223.

[3] A. Neyyathala, F. Flecken, F. Rang, C. Papke, S. Hanf, Support Engineering for the Stabilisation of Heterogeneous Pd3P-Based Catalysts for Heck Coupling Reactions, Chem. Eur. J. 30(1) (2024) e202302825.

Application of Dynamic Light Scattering Method in Nanofluids

Bahman Rahmatinejad *[1], Farzin Azimpour Shishevan [1],Hadi Ghasemi Zavaragh [1]

1 Department of Mechanical Engineering, Technical and Vocational University (TVU), Tehran, Iran.

*Corresponding Author E-mail: brahmati@tvu.ac.ir

Keywords

Nanofluids; DLS; Particle Size Distribution; Colloidal Stability; Thermophysical Properties

Abstract

Dynamic Light Scattering (DLS), also known as photon correlation spectroscopy or quasi-elastic light scattering, is a widely used technique for characterizing nanoparticle size, size distribution, and aggregation behavior in dispersions, making it essential for nanofluid research engineered colloidal suspensions of nanoparticles in base fluids such as water, ethylene glycol, or oils. The thermophysical properties of nanofluids, including thermal conductivity, viscosity, optical characteristics, and stability, are strongly influenced by particle size and dispersion quality, with minor variations potentially causing aggregation or sedimentation. DLS measures fluctuations in scattered light intensity due to Brownian motion, from which the diffusion coefficient is obtained and converted to a hydrodynamic diameter via the Stokes–Einstein equation. This hydrodynamic size accounts for primary particles, aggregates, solvation layers, and surfactant coatings, providing insight into real dispersion conditions. DLS is widely applied to assess colloidal stability, detect aggregation, monitor zeta potential, and perform time-dependent studies under storage or operational stresses, guiding the optimization of surfactants, pH, ionic strength, and preparation methods. It also evaluates the effectiveness of nanofluid synthesis techniques such as ultrasonication, high-shear mixing, and one-step versus two-step approaches. Correlating DLS-derived particle size distributions with thermophysical properties enables the design of nanofluids with predictable performance. Modern instruments allow in-situ monitoring under controlled temperature, flow, or shear conditions, simulating practical operating environments. Despite its advantages, DLS has limitations for highly polydisperse, concentrated, or non-spherical particle systems, necessitating complementary techniques like TEM, SEM, AFM, or nanoparticle tracking analysis for validation. Overall, DLS serves as a critical diagnostic tool, linking nanoscale particle behavior to the macroscale performance of nanofluids.

1. Introduction

Experimental studies by Tyndall on light scattering from airborne particles were conducted in 1869, and the early theoretical work of Rayleigh on light scattering for examining various physical phenomena was carried out between 1871 and in 1871, Rayleigh explained the blue color of the sky and the influence of atmospheric particles, reporting one of the significant effects of light scattering by particles smaller than the wavelength of light. In his 1881 paper, he presented an approximate theory for particles of any shape and size whose relative refractive index is equal to one. In the following years, Rayleigh's scattering theory was further developed by Mie, Smoluchowski, Einstein, and Debye. For example, in 1915, Debye expanded Rayleigh's theory and extended the calculations to particles with non-spherical shapes [1].

Recent advancements in optical instruments have made it possible to measure very small changes in the frequency and intensity of light scattered from a sample. Moreover, due to the high intensity of the laser source focused at a single point, even weak scattered light can be detected [2]. The dynamic light scattering (DLS) method, also known as photon correlation spectroscopy (PCS), is one of the suitable techniques for determining particle size distribution. In the DLS method, the particle size distribution in a solution can be determined from the Brownian motion of particles in the fluid phase. Measurement of Brownian motion is achieved by calculating the fluctuations in the intensity of light beams scattered by small and large particles [3].

1.1. Brownian Motion

In a solution, collisions between particles and small molecules with the molecules of the solvent lead to random motion of the molecules. This effect was first discovered in 1827 by a microbiologist named Robert Brown, who observed it while examining a living organism under an optical microscope. The motion of small particles in a fluid is called Brownian motion. The French mathematician Louis Bachelier was the first to present a theory of Brownian motion in his doctoral dissertation. In 1905, Albert Einstein successfully explained this random motion using a probabilistic model.

1.2. Rayleigh Scattering Theory and Mie Scattering

In 1871, Rayleigh proposed his theory on the scattering of sunlight by gas molecules in the atmosphere, thereby explaining the color of the sky. More generally, Rayleigh scattering describes the elastic scattering of light by particles that are much smaller than the wavelength of the incident light. Rayleigh scattering arises from the electric polarizability of the particles. When such a small particle is exposed to electromagnetic waves, the oscillating electric field of the light wave acts on the charges within the particle, causing them to become polarized so that the negative charges are displaced from the positive nucleus. As a result of this charge separation, the particle acquires an instantaneous dipole moment, (p).

The characteristics of light scattering depend on the ratio of particle size to the wavelength of the incoming light. To theoretically analyze light scattering from fine particles, the dimensionless size parameter is used. If we define the size parameter (x) as follows [4]:

$$x = \frac{2\pi r}{\lambda} \tag{1}$$

In this expression, (r) is the particle radius and (λ) is the wavelength of the incident light. If this parameter is approximately 0.1, Rayleigh scattering applies; for a size parameter close to one where the particle diameter is comparable to the wavelength of the incident light the Mie scattering theory is used. When particle sizes are on the order of, or slightly larger than, the wavelength of the incident light, the Rayleigh approximation is no longer valid. For particles larger than the wavelength, Mie developed a theory by solving Maxwell's equations under defined boundary conditions to describe light scattering from particles, taking into account the particle shape and the difference in refractive index between the particles and the surrounding medium. Compared to small particles, larger particles scatter light at smaller angles relative to the incident beam [5]. In Mie theory, the user must know the refractive index of the particle and the medium, or the relative refractive index. The intensity of light scattered by the particles is a function of the wavelength of the incident light, the scattering angle, the particle size, and the relative refractive index of the particle and the medium. In other words, in a scattering pattern, the intensity of scattered light at various angles depends on the particle's size, shape, and optical properties.

1.3. Conditions for Using Mie Theory:

The incident light used to determine particle size must be monochromatic; in other words, all incoming light rays must have the same wavelength and frequency.

The particle must be spherical, because particle shape affects the scattering pattern.

The particles must be isotropic; if a particle is anisotropic, its optical properties will differ in various directions.

The incident light must consist of planar (flat) waves.

Both scattering and absorption must be taken into account.

The refractive index of both the medium and the particle must be known.

The system must be homogeneous, since inhomogeneity affects the scattering pattern.

1.4. Principle of Dynamic Light Scattering

Every particle in a suspension is constantly in motion, and its movement is independent of other particles. Observing larger particles compared to smaller ones shows that, at a given temperature, larger particles move much more slowly. In this method, a laser beam is directed at the suspension, and the scattering of the laser light is recorded by an optical detector. Particles of different sizes scatter light in different ways. Larger particles scatter light at smaller angles, whereas smaller particles scatter light over a wider angular range (Figure 1).

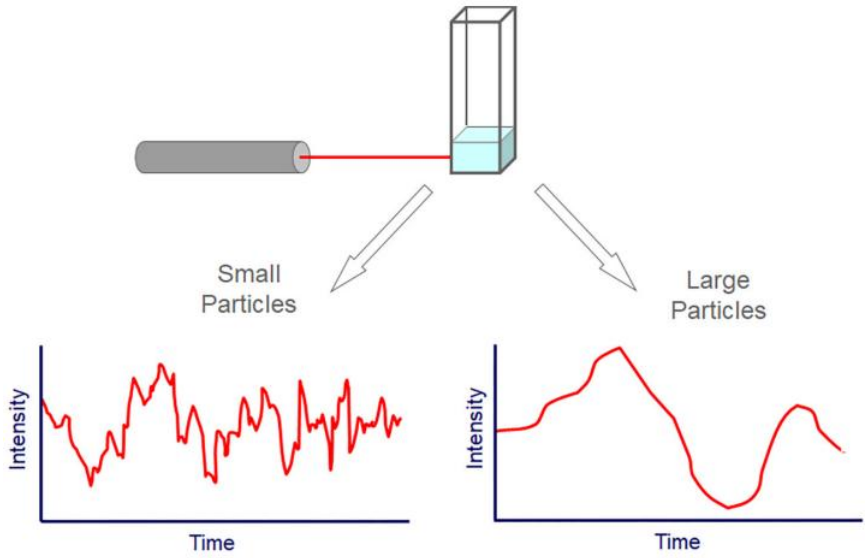

Figure 1 Mechanism of laser light interaction with particles [6].

Light scattering by solid particles creates a pattern of bright and dark spots on the detector. These patterns change as the particles move, causing the resulting pattern to vary over time. When a laser beam of a specific frequency interacts with moving particles, the scattered light emerges with a different frequency, producing fluctuations in the phase of the scattered light. The amount of frequency shift in the scattered light is related to particle size and is used to determine particle dimensions [7]. At higher average velocities, smaller particles produce greater changes in the frequency of the scattered light.

The intensity of scattered-light fluctuations can be measured using a suitable detector, such as a photon-counting photomultiplier. The fluctuation intensity is directly related to the diffusion rate of the particles in the solvent, and with knowledge of the medium's viscosity, these fluctuations are used to determine the particle diameter. The diameter measured by this method is known as the hydrodynamic diameter (Figure 2).

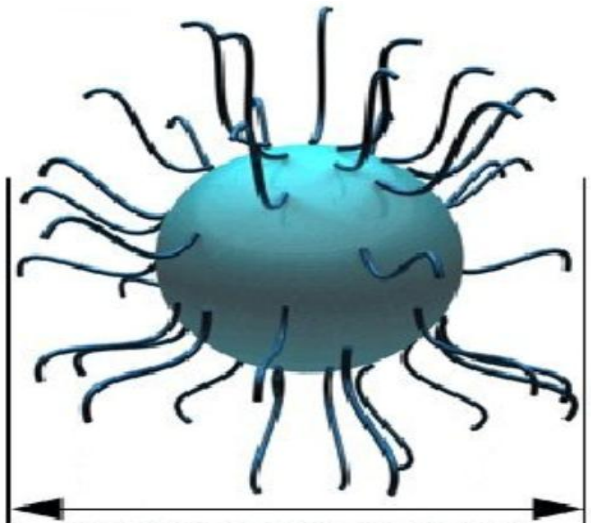

Figure 2 Representation of the hydrodynamic diameter of a particle [8].

The relationship between particle size and the rate of Brownian motion is expressed by the Stokes–Einstein equation (Equation 2).

$$d_H = \frac{KT}{3\pi\eta\ \mathrm{D}} \tag{2}$$

Here, d_H is the hydrodynamic diameter of the particle; (K) is the Boltzmann constant; (η) is the dynamic viscosity of the solvent, which depends on temperature but is not related to the density or pressure of the system; (T) is the absolute temperature; and (D) is the diffusion coefficient [9].

The hydrodynamic diameter represents the diameter of an equivalent hypothetical sphere that has the same diffusion coefficient or viscosity response as the particle under investigation. Therefore, a sphere with this hydrodynamic diameter would diffuse at the same rate as the actual particles being measured. Although the hydrodynamic diameter is relatively easy to determine, it can differ significantly from the particle's true physical size [10].

The DLS instrument software can determine the particle size distribution by analyzing the time-dependent changes in this scattering pattern. Larger particles move more slowly in the solution compared to smaller particles. Therefore, the changes in the scattering pattern in a suspension containing larger particles occur more slowly than in a suspension containing smaller particles [11]. If the signal intensity obtained from DLS at a moment (t) is compared with the signal intensity at a slightly later time (t + δt), the similarity or close correlation between the two signals can be evaluated. Continued comparison of the initial signal at later times (t + 2δt) shows a decrease in the correlation function. If correlation measurements continue at later times, the correlation eventually reaches zero (Figure 3).

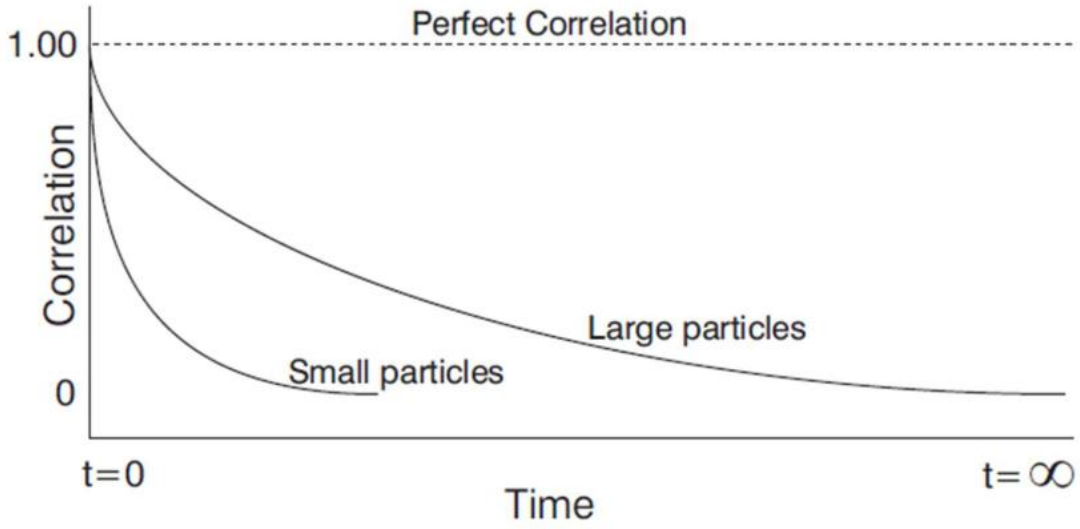

Figure 3 Correlation function curves for large and small particles

By comparing signal intensities at relatively long-time intervals, the lack of correlation becomes observable. For this reason, the DLS method operates over short time intervals. Typically, it takes about one to ten milliseconds for the correlation function to reach zero. Note that perfect correlation is represented by the value one, and no correlation by the value zero.

The rate at which the correlation function decays depend on particle size. The decay rate is faster for smaller particles than for larger ones. Information obtained from measuring the correlation function is then used to determine the particle size distribution. An example of a particle size distribution plot is shown in Figure In this plot, the horizontal axis indicates the particle size distribution, and the vertical axis represents the relative intensity of the scattered light.

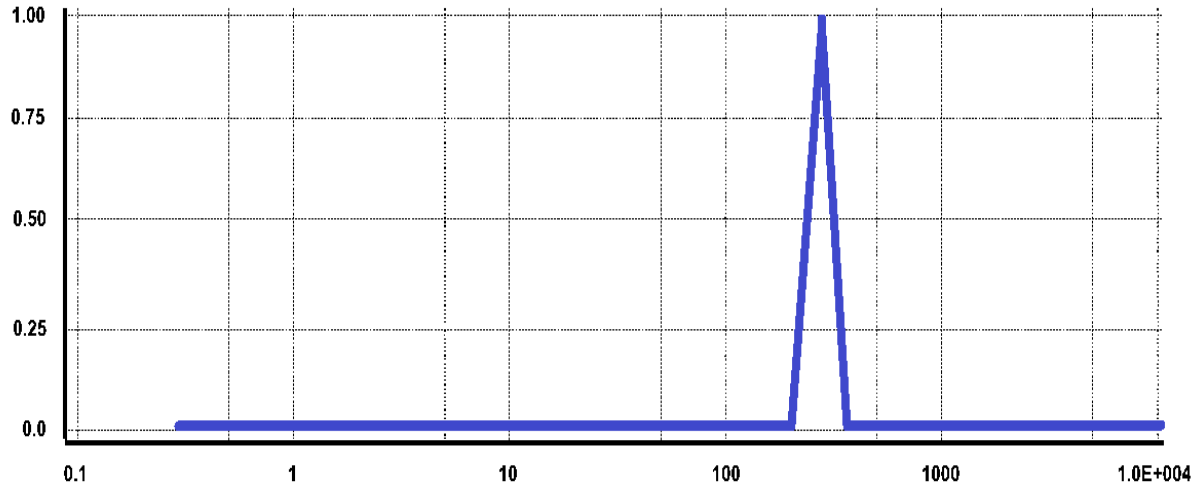

Figure 4 Particle size distribution chart

1.5. Components of a DLS Instrument

All DLS instruments used for measuring particle size distribution consist of several main components, and a simplified schematic of the device layout is shown in Figure 5.

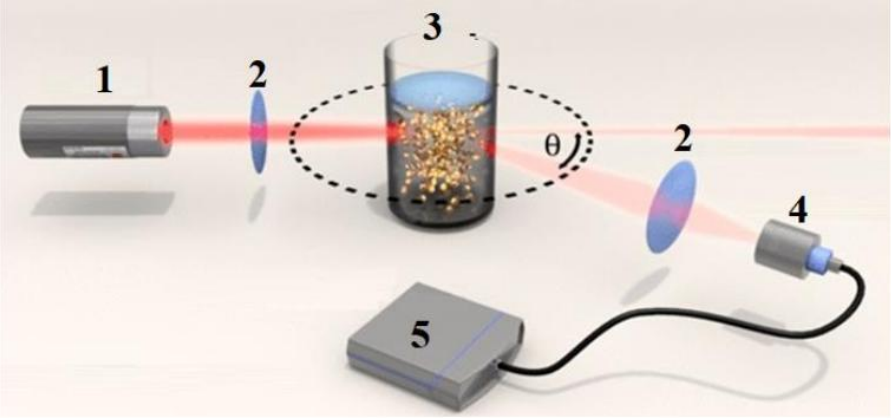

Figure 5 Schematic layout of DLS instrument components [1].

The components of a DLS-based nanoparticle size measurement system, as shown in Figure 5, include:

1 – Laser,
2 – Lens,
3 – Sample,
4 – Detector,
5 – Correlator.

The light emitted from the DLS laser source must pass through a section called the attenuator before reaching the sample. The function of the attenuator is to adjust the laser intensity depending on the type of sample being tested. The attenuator can vary the incident light intensity from 0% to 100% transmission. When the intensity of scattered light from the sample is too high, making measurement impossible such as in highly concentrated samples or samples with high scattering or when the scattering is too low, the attenuator reduces the incident light to an appropriate level, optimizing the scattered light intensity and creating ideal conditions for measurement. After passing through the attenuator, the laser beam reaches the sample, which is injected as a suspension or emulsion into a cuvette. The cuvette (or cell) is one of the main components of the DLS system where the sample is placed. Most of the light entering the cuvette passes straight through without changing direction. However, the portion of the light that interacts with the sample particles becomes scattered. This scattered light, at a specific angle, is then received by the detector another key component of the device (Figure 6). The detector's function is to measure and record the intensity of the scattered light. By comparing the scattered light intensity at different time intervals, the rate of intensity fluctuation can be calculated. Finally, the collected data are transferred to a computer, where specialized software analyzes the information and displays the particle size distribution.

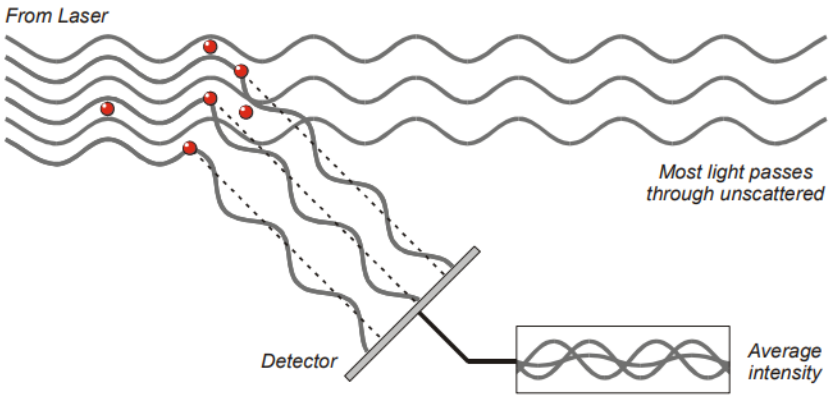

Figure 6 Laser waves after interacting with a particle

1.6. Limitations of the DLS Method

The DLS technique has the following limitations:

Variations in results due to changes in temperature and viscosity

Need for sample preparation

Requirement for knowledge of the relative refractive index

Particles must be dispersed in liquids

Due to physical and chemical interactions between particles and the liquid, finding a suitable dispersing medium can be challenging

2. Application of DLS

Dynamic Light Scattering (DLS), also known as photon correlation spectroscopy or quasi-elastic light scattering, is one of the most widely used techniques for characterizing nanoparticle size and size distribution in dispersions. In the field of nanofluids engineered colloidal suspensions of nanoparticles in base fluids such as water, ethylene glycol, or oils DLS plays a central role in understanding particle behavior, stability, and overall thermophysical performance. The following are some of the applications of this method in nanofluids.

2.1. Importance of Particle Size in Nanofluids

DLS plays a crucial role in understanding the importance of particle size in nanofluids, as the performance and stability of these engineered fluids are highly dependent on the dimensions and distribution of suspended nanoparticles. In nanofluid systems, particle size directly influences key thermophysical properties such as thermal conductivity, viscosity, and heat transfer efficiency. DLS enables precise, real-time measurement of the hydrodynamic diameter of nanoparticles dispersed in a base fluid, providing insight into whether the particles remain well-dispersed or tend to agglomerate over time. Even slight aggregation can significantly alter the effective particle size, reducing surface area availability and diminishing the potential enhancements nanofluids are known for. By accurately characterizing particle size and size distribution, DLS helps researchers optimize synthesis methods, select appropriate surfactants, and ensure long-term stability, all of which are essential for maintaining consistent performance in practical applications. Additionally, particle size data from DLS aids in predicting rheological behavior, as larger or aggregated particles tend to increase viscosity, potentially compromising pumping efficiency and system reliability. Overall, the use of DLS in studying particle size allows for the systematic design, control, and quality assurance of nanofluids, ensuring that their enhanced thermal and functional properties are fully realized in industrial, biomedical, and energy-related applications.

2.2. Principle of DLS in Nanofluid Characterization

The principle of DLS relies on analyzing the Brownian motion of particles in a suspension. In a nanofluid, nanoparticles are in constant random motion due to collisions with the surrounding fluid molecules. When a coherent laser beam is directed at the nanofluid, the nanoparticles scatter the incident light. The scattered light intensity fluctuates over time, and these fluctuations are directly related to the speed of the Brownian motion, which in turn depends on particle size. Larger particles move more slowly, resulting in slower fluctuations in scattered light, while smaller particles move faster, producing more rapid fluctuations. By using a correlator to measure the temporal autocorrelation function of the scattered light, the DLS instrument can determine the diffusion coefficient of the particles. Applying the Stokes–Einstein equation then allows the calculation of the hydrodynamic diameter of nanoparticles, which represents the effective size of a particle as it moves through the fluid. This method is particularly useful in nanofluid research because the particle size distribution significantly influences the fluid's thermophysical properties, such as thermal conductivity, viscosity, and stability. Accurate measurement of particle size and size distribution using DLS helps in optimizing nanofluid formulation, preventing aggregation, and ensuring uniform dispersion, which are essential for reliable performance in applications such as heat transfer, cooling systems, and energy storage. Overall, the DLS method provides a non-invasive, rapid, and precise approach for monitoring and controlling nanoparticle characteristics in nanofluids, making it indispensable in both research and industrial applications.

2.3. Assessing Stability of Nanofluids

DLS is an essential technique for assessing the stability of nanofluids, as the long-term performance of these fluids is highly dependent on maintaining a uniform dispersion of nanoparticles. Nanofluid stability is primarily influenced by factors such as particle aggregation, sedimentation, and changes in particle size over time. DLS provides a non-invasive and highly sensitive method to monitor these changes by analyzing the Brownian motion of suspended nanoparticles. In a stable nanofluid, nanoparticles exhibit consistent Brownian motion, resulting in a steady pattern of scattered light intensity. Conversely, in an unstable nanofluid, particle aggregation or sedimentation alters the movement of particles, which leads to variations in the scattering pattern over time. By measuring the autocorrelation function of the scattered light, DLS can detect even subtle shifts in particle size distribution, offering quantitative

information about aggregation rates and the onset of instability. This allows researchers to evaluate the effectiveness of surfactants, stabilizing agents, or other formulation strategies aimed at enhancing nanofluid stability. Moreover, DLS can monitor temporal changes in hydrodynamic diameter, providing insight into whether nanoparticles remain uniformly dispersed or begin forming clusters, which can negatively affect thermal conductivity and viscosity. The ability to rapidly and accurately assess particle size distribution and detect early signs of aggregation makes DLS an invaluable tool in both laboratory studies and industrial applications of nanofluids. By enabling precise monitoring of stability, DLS helps ensure consistent performance in heat transfer systems, cooling devices, and other technologies that rely on the enhanced thermophysical properties of nanofluids.

2.4. Optimization of Nanofluid Preparation Methods

Dynamic light scattering (DLS) is a crucial tool for optimizing nanofluid preparation methods by providing precise information on particle size and distribution immediately after synthesis. By using DLS, researchers can quickly evaluate whether the chosen preparation method, including dispersion techniques, sonication time, or surfactant use, produces nanoparticles with the desired size and minimal aggregation. DLS allows the monitoring of hydrodynamic diameter and particle size distribution, making it possible to detect even slight clustering or irregular dispersion that could compromise fluid stability or heat transfer efficiency. Furthermore, DLS can assess the effect of different solvents, stabilizing agents, and preparation parameters, enabling systematic optimization to achieve a well-dispersed, stable nanofluid. This rapid feedback loop helps in refining synthesis protocols, reducing trial-and-error experimentation, and ensuring that nanofluids meet the required performance standards for industrial, energy, and cooling applications.

2.5. Thermophysical Property Correlation

The thermal conductivity, viscosity, and heat transfer performance of a nanofluid are closely linked to the size, distribution, and stability of its suspended nanoparticles. DLS enables precise measurement of the hydrodynamic diameter and particle size distribution, providing critical data that can be directly related to these macroscopic properties. For instance, smaller, well-dispersed nanoparticles typically enhance thermal conductivity more effectively due to the larger surface area available for heat transfer, while large aggregates can increase viscosity and reduce flow efficiency. By monitoring particle size over time, DLS can also assess the impact of aggregation or sedimentation on thermophysical behavior, allowing researchers to establish quantitative relationships between nanoparticle characteristics and fluid properties. This correlation is essential for optimizing nanofluid formulations, predicting performance in heat transfer systems, and designing fluids with tailored properties for specific industrial or energy applications. Overall, DLS provides a fundamental link between microscopic particle behavior and the macroscopic thermophysical performance of nanofluids.

2.6. Real-Time Monitoring Under Environmental Conditions

Dynamic light scattering (DLS) is an effective tool for real-time monitoring of nanofluids under various environmental conditions, allowing researchers to study how factors such as temperature, pH, and ionic strength affect particle behavior and stability. Nanoparticles in a fluid are highly sensitive to environmental changes, which can induce aggregation, sedimentation, or changes in particle mobility, ultimately altering the nanofluid's thermophysical properties. By continuously measuring the scattered light intensity and calculating the autocorrelation function, DLS provides instantaneous information on particle size, distribution, and dynamics as conditions vary. This capability enables the detection of early signs of instability, such as the formation of clusters or changes in Brownian motion, before they significantly impact fluid performance. Real-time monitoring is particularly valuable for applications where nanofluids are exposed to fluctuating conditions, such as in cooling systems, energy devices, or chemical reactors. Using DLS, researchers can optimize formulation strategies, adjust stabilizing agents, and predict long-term behavior under operational conditions.

2.7. Limitations and Considerations

DLS is highly sensitive to environmental factors such as temperature and viscosity, which can influence particle Brownian motion and, consequently, the calculated hydrodynamic diameter. Accurate measurements also require knowledge of the relative refractive index of the nanoparticles and the dispersing medium, as incorrect values can lead to errors in size determination. Additionally, the method assumes that particles are spherical, monodisperse, and well-dispersed in the fluid; deviations from these assumptions, such as particle aggregation or anisotropic shapes, can distort scattering data and reduce reliability. High particle concentrations or highly scattering samples may also cause multiple scattering effects, which complicate data interpretation. Careful sample preparation, including proper dilution and stabilization, is essential to minimize these issues. Despite these limitations, understanding the constraints of DLS allows researchers to optimize experimental conditions and interpret data correctly, ensuring that measurements of particle size, distribution, and stability in nanofluids are meaningful and reproducible.

3. Conclusion

Dynamic Light Scattering (DLS) has proven to be an indispensable technique for the characterization and optimization of nanofluids, providing critical insights into nanoparticle size, aggregation, and dispersion quality. Its ability to measure hydrodynamic diameter, monitor stability over time, and assess the effectiveness of preparation methods allows researchers to directly correlate nanoscale particle behavior with macroscale thermophysical properties such as thermal conductivity, viscosity, and optical performance. Furthermore, advancements in in-situ and real-time DLS measurements enable the evaluation of nanofluid behavior under practical operating conditions, including elevated temperatures, shear, and chemical exposure. While limitations exist, particularly for polydisperse, concentrated, or non-spherical systems, these can be mitigated through complementary techniques like TEM, SEM, AFM, or nanoparticle tracking analysis. Overall, DLS serves as a vital diagnostic and optimization tool, bridging the gap between nanoparticle characteristics and the reliable, high-performance behavior of nanofluids, and thereby facilitating the development of advanced fluids for thermal, optical, and energy applications.

References

[1] Berne, B. J., & Pecora, R. (2000). Dynamic light scattering: with applications to chemistry, biology, and physics. Courier Corporation.

[2] Hallaj Jahani, A., & Shirazian, S. (2019). Introduction to Dynamic Light Scattering. Journal of New Approaches in Iranian Scientific Laboratories, 3(3), 13-18.

[3] Rahmatinejad, B., Abbasgholipour, M., & Mohammadi Alasti, B. (2021). Investigating thermo-physical properties and thermal performance of Al2O3 and CuO nanoparticles in Water and Ethylene Glycol based fluids. International Journal of Nano Dimension, 12(3), 252-271.

[4] He, G. S., Qin, H. Y., & Zheng, Q. (2009). Rayleigh, Mie, and Tyndall scatterings of polystyrene microspheres in water: Wavelength, size, and angle dependences. Journal of Applied Physics, 105(2).

[5] Pecora, R. (2000). Dynamic light scattering measurement of nanometer particles in liquids. Journal of nanoparticle research, 2, 123-131.

[6] Mehtala, J. G., & Jones, H. J. (2020, April). Measuring the Concentration of Adeno-Associated Virus (AAV) with Multi-Angle Dynamic Light Scattering (MADLS) Using the New Zetasizer (TM) Ultra. In MOLECULAR THERAPY (Vol. 28, No. 4, pp. 586-587). 50 HAMPSHIRE ST, FLOOR 5, CAMBRIDGE, MA 02139 USA: CELL PRESS.

[7] Atahar, A., Mafy, N. N., Rahman, M. M., Mollah, M. Y. A., & Susan, M. A. B. H. (2019). Aggregation of urea in water: Dynamic light scattering analyses. Journal of Molecular Liquids, 294, 111612

[8] Williams, P. M., Oatley-Radcliffe, D. L., & Hilal, N. (2017). Feed solution characterization. Membrane Characterization, Elsevier, 379-404.

[9] Pecora, R. Dynamic Light Scattering. Applications of Photon Correlation Spectroscopy. Springer.

[10] Bhattacharjee, S. (2016). DLS and zeta potential–what they are and what they are not?. Journal of controlled release, 235, 337-351.

[11] XU R., Particle Characterization:Light Scattering Methods. Kluwer Academic Publishers, 2002.

[12] Rahmati Nejad, B., Abbasgholipour, M., & Mohammadi Alasti, B. (2022). Experimental Evaluation of Heat Transfer of MF 285 Tractor Radiator, using Nano-fluid AL2O3+ Water. Journal of Agricultural Machinery, 12(3), 281-299.

The Effect of Fractal Phenomena on the Thermal Conductivity of Nanofluids

Bahman Rahmatinejad [*1], Hadi Ghasemi Zavaragh [1]

[1] Department of Mechanical Engineering, Technical and Vocational University (TVU), Tehran, Iran.

*Corresponding Author E-mail: brahmati@tvu.ac.ir

Keywords

Nanofluid,
Thermal conductivity,
Nanoparticles,
Fractal dimension,
Heat transfer enhancement,
Nanoparticle aggregation

Abstract

The thermal conductivity of nanofluids, suspensions of nanoparticles in base fluids, can be significantly influenced by the fractal nature of nanoparticle aggregates. Fractal structures, characterized by self-similarity across multiple scales, determine how nanoparticles cluster and form conductive pathways within the fluid. This study investigates the effect of fractal phenomena on the thermal conductivity of nanofluids by integrating theoretical models, computational simulations, and experimental observations. The fractal dimension of aggregates, a measure of their structural complexity, is found to play a critical role: low-fractal-dimension aggregates, which are open and chain-like, promote continuous heat transfer pathways and enhance effective thermal conductivity, while high-fractal-dimension aggregates, which are more compact, disrupt connectivity and reduce thermal transport efficiency. Factors such as nanoparticle concentration, temperature, and interparticle forces significantly influence aggregation behavior and fractal dimension, thereby modulating thermal performance. Experimental studies on copper oxide and silicon dioxide nanofluids confirm that fractal clustering creates low-resistance conductive networks, validating the predictive capabilities of fractal-informed models. Understanding the fractal characteristics of nanoparticles enables the optimization of nanofluid formulations for enhanced heat transfer, improved cooling efficiency, and greater operational stability. Overall, the integration of fractal theory with nanofluid research offers a robust framework for predicting and tailoring thermal properties, opening pathways for the design of high-performance thermal fluids and advanced energy management systems. This approach provides fundamental insights into the interplay between microstructure and heat transport in nanofluids, highlighting the critical role of fractal aggregation in thermal enhancement.

1. Introduction

Nanofluids, as one of the most advanced developments in the field of materials science and engineering, have attracted significant attention in recent years. These compounds consist of a base fluid and suspended nanoparticles, which typically measure less than 100 nanometers. The nanoparticles used in these fluids are usually made of various materials such as metal oxides, carbon, and silicon. By adding them to liquids, the thermal, electrical, and mechanical properties of the fluid undergo remarkable changes. Nanofluids have gained special attention due to their ability to enhance heat transfer, reduce viscosity, and improve performance in thermal and cooling systems particularly in industries such as automotive, electronics, and renewable energy [1,2]. Additionally, their increased surface contact area compared to traditional liquids commonly used as heat transfer fluids is another advantage of these new materials. One of the interesting phenomena observed in the study and application of nanofluids is the fractal phenomenon. A fractal is a complex geometric shape that contains similar details within its structure at different scales, and its irregularity remains the same whether viewed from near or far. Nanoparticles in nanofluids can form fractal structures, which may enhance heat distribution and increase the contact surface between the nanoparticles and the fluid, ultimately leading to better heat transfer. The fractal dimensions of nanoparticles and nanoparticle clusters can have a direct impact on the thermal properties of nanofluids. Fractals can play a role in determining how nanoparticles aggregate and distribute within the fluid, as well as influence the overall thermal conductivity of the nanofluid. The use of mathematical models to analyze and predict the properties of nanofluids can provide a better understanding of the effect of fractality on their thermal behavior. For example, mathematical models can incorporate fractal dimensions and simulate the most probable heat transfer scenarios. The fractal dimension is a metric that quantifies the complexity of a fractal structure. In the case of nanofluids, it describes how nanoparticles cluster as they disperse within a base

fluid. Nanofluids with fractal structures can be used in industrial and engineering applications, particularly in cooling systems, heat exchangers, and renewable energy systems. These materials can enhance heat transfer efficiency and improve system performance. Researchers have increasingly used fractal geometry to describe nanoparticle aggregation in nanofluids. The fractal dimension provides information about the size and shape of clusters formed during aggregation, which ultimately affects the thermal conductivity and viscosity of the nanofluid [3]. Studies have shown that factors such as temperature, concentration, and interaction forces (van der Waals forces, electrostatic charges) can significantly influence the fractal nature of nanoparticle clusters and subsequently alter the properties of nanofluids [3].

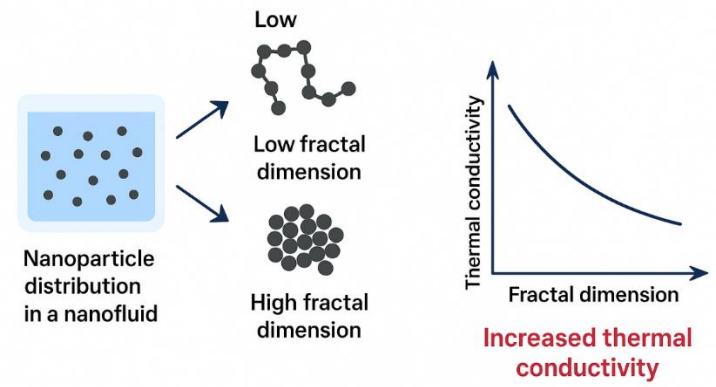

Figure 1 Effect of fractal phenomena on the thermal conductivity on nanofluids

Only a limited number of researchers have investigated the effect of the fractal phenomenon on the thermal conductivity coefficient of nanofluids, some of whom will be mentioned in the following sections.

Skouras, E. D., et al. (2024); This computational/analytical study on hybrid nanofluids shows that aggregate morphology (number of primary particles per aggregate and the aggregate fractal dimension) strongly controls the formation of continuous conductive pathways: lower fractal-dimension (more open, tenuous) aggregates form long-range conductive chains and increase effective thermal conductivity compared with more compact (higher fractal-dimension) aggregates at the same particle loading [4]. Zhang, W. (2024) Using numerical experiments and analysis, the author demonstrates that thermal conductivity of a nanofluid decreases as the fractal dimension of aggregates increases (i.e., as aggregates become more compact); the study quantifies the change and reports a measurable drop in conductivity when fractal dimension grows from ~1 to ~2, attributing the effect to reduced continuous conductive paths and decreased liquid-layering effectiveness around more compact clusters [5]. Madhu, A. K., et al. (2023) This study focuses explicitly on the role of nanoparticle aggregate fractal dimension: it reports that low-fractal-dimension aggregates (open, chain-like) enhance thermal transport through increased liquid layering at cluster surfaces and by forming percolating conductive paths; by contrast, compact aggregates reduce these mechanisms and lower effective conductivity [6]. Rahman, M. A., et al. (2024) A broad review of nanofluid preparation and properties which emphasizes that aggregation and fractal-like clustering are among the dominant microstructural variables controlling thermal conductivity; the review synthesizes experimental and modeling work showing that both the fractal dimension and degree of aggregation must be accounted for in predictive models [7]. Arif, M. S., et al. (2024) This numerical study models mixed convective flows of nanofluids with fractal-like structure and reports that fractal-based formulations for the nanoparticle distribution (used in the transport equations) affect bulk heat transfer predictions; the paper highlights that correctly representing fractal aggregation in closure models changes local temperature fields and predicted thermal conductivity [8]. Murshed, S. M. S. (2025) A recent synthesis on thermal properties of nanofluids that highlights new computational and experimental results where fractal aggregation and nanolayering are combined in models: the article argues that both the fractal geometry of aggregates and the thermal conductivity profile of the solid–liquid interfacial layer must be included to match experimental conductivity enhancements [9]. Yu, H. (2025) Develops a fractal-based predictive model combining fractal geometry with radiative/continuum conduction principles; while focused on porous/fractal media broadly, the methodology and conclusions are applicable to porous aggregate networks in nanofluids, showing how fractal metrics can be integrated into closed-form thermal conductivity predictions [10]. Raza, Q. (2025) Examines heat and mass transfer for fractal interfacial structures and shows that fractal interfacial roughness/layering alters both local transport coefficients and the effective thermal conductivity; the paper presents a combined high-conductivity model with fractal interfacial theory that predicts larger enhancements under certain fractal parameter ranges [11]. Ali, B., et al. (2025) A multidisciplinary paper (recently posted) that links nanoparticle aggregation (and thus fractal-like microstructure) to thermal conductivity increases in rotating/complex flows, highlighting that aggregation-induced conductive networks can dominate thermal transport even when other enhancement mechanisms (Brownian motion, interfacial layering) are present [12].

Advanced methods such as sol–gel and hydrothermal techniques have been employed to synthesize and produce nanoparticles with controlled fractal properties. This ability to customize the size and shape of nanoparticles helps optimize their distribution and aggregation behavior in nanofluids. Research in this field seeks to answer questions regarding how fractal-featured nanoparticles can be used to enhance thermal conductivity and how to identify the most optimal compositions and nanoparticle ratios. This combination of fractals and nanofluids holds great potential for advancements in thermal technologies and nanotechnology, and it may help solve more complex challenges in the design of materials and thermal systems.

2. Materials and methods

2.1. Fractal Theory

Fractal theory was first introduced by the French mathematician Benoît Mandelbrot. This theory, also known as the theory of chaos, is considered a mathematical concept that cannot be precisely defined, but it can be described as a form of randomness accompanied by determinism. Its deterministic nature arises from the fact that disorder has internal causes and does not occur due to external disturbances. Its randomness, however, stems from the irregular and unpredictable behavior of chaotic systems. This theory, which has entered fields such as experimental sciences, mathematics, behavioral studies, management, sociology, and more, has transformed the way humans approach the solution of unpredictable problems. The key idea behind chaos theory is that within every disorder lies a hidden order. This means that order should not be sought only at a single scale; a phenomenon that appears completely random and unpredictable at a local scale may, at a larger scale, be entirely stable and predictable. In the context of predicting the thermal conductivity of nanofluids, this theory effectively describes the chaotic process of nanoparticle agglomeration and polarization within the intermediate-scale range [13]. For the first time, Pechoumani and Yao applied this theory in studying the thermal conductivity of unidirectional fiber composites and determined their fractal characteristics [13]. However, limited research has been conducted on using fractal theory to describe nanoparticle agglomeration in suspensions for predicting thermal conductivity coefficients.

2.2. Fractal Indices

Yu and his colleagues proposed that the Bruggeman model together with fractal theory can be used to predict the thermal conductivity of nanoparticle agglomerates. Using fractals, Havlin and Ben-Avraham demonstrated that both the radial distribution of nanoparticles and their distribution in a suspension exhibit a form of self-similarity. Scaling theory is commonly used to quantitatively describe a fractal system. However, before applying it, several fractal indices must be defined. The fractal dimension, D_f, is one of the fundamental variables used to characterize a fractal and is defined by a scalar ε. If the fractal volume (surface area, particle number, etc.) is denoted by $F(\varepsilon)$, then the fractal dimension can be obtained from the following relation [14].

$$F(\varepsilon) = C_{\varepsilon}^{D_f} \tag{1}$$

Where C (the shape factor) is independent of ε. For describing complex fractals, different indices are required. The anomalous diffusion index, D_w, represents the self-similarity of particle diffusion within the host system and is estimated using D_w and D_{wf} [14].

$$\frac{2D_f}{D_w} = D_s = 1.33 \tag{2}$$

In the above equation, D_s is the fractal sub-dimension and represents the self-similarity of the spatial density distribution of the fractals. Therefore, the anomalous diffusion index D_w can be determined using the calculated fractal dimension D_f. It should be noted that the fractal dimension of agglomerates, D_{f1}, differs from the fractal dimension related to the spatial distribution of agglomerates, D_{f2}. Both of these can be determined experimentally.

2.3. Effect of Fractals on Nanofluids

Nanoparticles can be distributed fractally within a fluid, and this distribution influences the fluid's thermal properties and mass transfer behavior. Fractal structures typically possess a larger surface area relative to their volume, which can help enhance heat transfer in nanofluids. The behavior of nanofluids may become nonlinear due to the presence of fractal structures, causing their properties to change in unexpected ways.

2.3.1. Xu, J et al. Model [15]

Traditional models often oversimplify the interactions used to determine thermal conductivity in nanofluids. The aim of this new model is to account for the complex fractal distributions of nanoparticles to provide a more accurate prediction of thermal conductivity in nanofluids. Using fractal geometry allows us to describe the irregular and self-similar nature of nanoparticle distributions in fluids. Instead of assuming a uniform distribution, this model considers

how nanoparticles cluster and interact at different scales, which has a significant impact on thermal conductivity. The relationship between effective thermal conductivity and the fractal characteristics of nanoparticle distribution can be modeled using Equation 3.

$$keff = kf + \phi \cdot (kp - kf) \cdot f(D) \quad (3)$$

where:

*k*eff is the effective thermal conductivity of the nanofluid,

kf is the thermal conductivity of the base fluid,

kp is the thermal conductivity of the nanoparticles,

ϕ is the volume fraction of the nanoparticles,

f(*D*) is a function that accounts for the fractal dimension D and adjusts the effective conductivity based on the fractal distribution.

A proposed form for f(D) can be expressed as Equation 4.

$$f(D) = a.D^b \quad (4)$$

where (a) and (b) are constants that can be adjusted based on experimental data. This model provides improved predictive capabilities for thermal conductivity in nanofluids because it takes fractal organizations into account. This leads to better design of thermal systems using nanofluids. Customized nanofluid formulations By understanding how distributions affect thermal properties, engineers can adjust the type and concentration of nanoparticles for specific applications and optimize thermal conductivity.

2.3.2. Anwar, T., & Kumam, P. Model [16]

A fractal model was proposed to analyze the thermal behavior of hybrid nanofluid flow in a channel, taking shape effects into account. The governing equations for the flow of the hybrid GO-NaAlg-Gr nanofluid in a channel are expressed as follows:

Continuity equation:

$$\frac{\partial \rho}{\partial t} + \nabla.(\rho u) = 0 \quad (5)$$

Momentum equation:

$$\frac{\partial (\rho u)}{\partial t} + \nabla.(\rho u u) = -\nabla p + \nabla.\mu(\nabla u) + F \quad (6)$$

Energy equation (considering fractality):

$$\frac{\partial T}{\partial t} + \mathrm{u}.\nabla T = \frac{K_{eff}}{\rho c_p}\nabla^2 T + \mathrm{Q} + D^r(D)T \quad (7)$$

where $D^r(D)$ represents a fractional derivative operator that depends on the fractal dimension (D). The effective thermal conductivity, keff, for the hybrid GO-NaAlg-Gr nanofluid can be modeled using Equation 8.

$$keff = kf + \phi \cdot (kp - kf) \cdot f(D) \quad (8)$$

where:

*k*eff is the effective thermal conductivity of the nanofluid,

kf is the thermal conductivity of the base fluid,

kp is the effective thermal conductivity of the hybrid nanoparticles,

ϕ is the volume fraction of the nanoparticles,

$f(D)$ is a function that accounts for the effect of the fractal dimension on thermal conductivity.

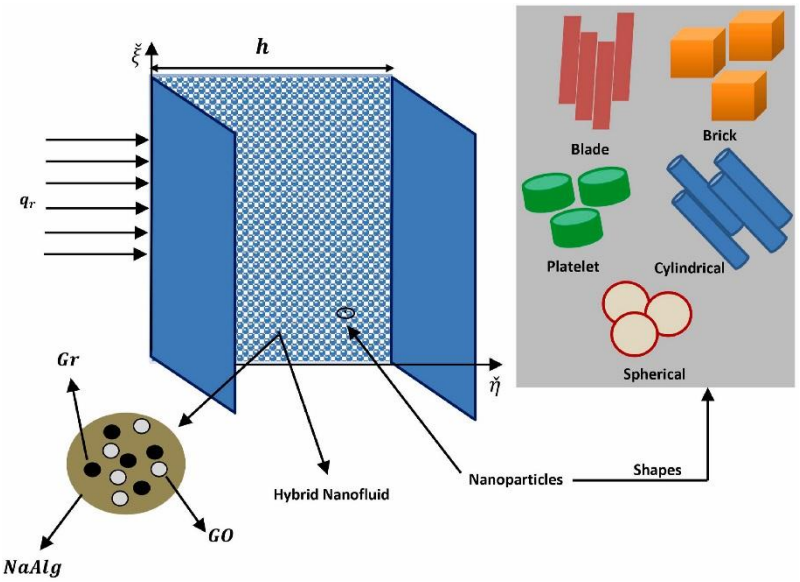

Figure 2 Geometrical configuration of the model [16]

The shape of nanoparticles can significantly influence heat transfer properties. In this model, spherical, cylindrical, and plate-like shapes were considered for analysis. By incorporating fractal dimensions and the effects of nanoparticle shapes, this model provides more accurate predictions of thermal conductivity and fluid behavior in channels. The insights gained from this study can lead to improved efficiency in various engineering applications that utilize hybrid nanofluids.

2.3.3. Wang et al. Model [17]

Various fractal models have been developed to predict the thermal conductivity of nanofluids. These models take into account the fractal dimensions of nanoparticles and their distribution within the base fluid. By incorporating fractal characteristics, researchers can provide more accurate predictions of heat transfer phenomena.Wang and colleagues, based on fractal theory and utilizing the Bruggeman model, proposed a model for predicting nanofluid thermal conductivity. They also developed a model for a fully dispersed nanoparticle by considering the interfacial layer. They synthesized silicon dioxide nanofluids with a particle size of 25 nanometers and, by examining scanning tunneling microscope images, observed that the clusters have a significant effect on increasing thermal conductivity. These researchers employed a steady-state method to measure thermal conductivity [17].

$$K_{eff} = \frac{(1-\phi) + 3\phi \int_0^{\infty} \frac{K_{CL(r)} n(r)}{K_{CL(r)} + 2K_f} dr}{(1-\phi) + 3\phi \int_0^{\infty} \frac{K_{CL(r)} n(r)}{K_{CL(r)} + 2K_f} dr} K_f \quad (9)$$

This equation is derived from the fractal model for predicting the effective thermal conductivity of fluids containing nanoparticles. In this equation, K_f is the thermal conductivity of the base fluid, $K_{CL(r)}$ is the thermal conductivity of the particle clusters, and n(r) is the particle radius distribution function. This model shows good agreement with experimental data for copper oxide nanoparticle suspensions with a particle diameter of 50 nm in ionized water and a nanoparticle volume fraction below 25%. Regarding the particle clusters, it has been shown that they form by creating pathways with lower thermal resistance. Since heat can move very rapidly within such clusters, the volume fraction of the conductive phase that is, the solid particles can significantly increase the thermal conductivity. $K_{CL(r)}$ in the above equation represents this very phenomenon [17].

2.4. Factors Affecting Fractal Dimension and Thermal Conductivity

Nanoparticle concentration: Higher concentrations can lead to more extensive aggregation, thereby altering the fractal dimension and affecting the effective thermal conductivity.

Temperature effects: Temperature can influence the stability and interactions between nanoparticles, affecting their aggregation behavior and consequently changing the fractal dimension of the resulting structures.

Interparticle forces: The type and strength of interparticle forces (such as van der Waals forces and electrostatic charges) can significantly affect how nanoparticles aggregate and the resulting fractal dimension.

2.5. Applications

Predict Thermal Conductivity More Accurately: Fractal-based models capture the self-similar and irregular distribution of nanoparticles, leading to more precise predictions of effective thermal conductivity compared to classical models that assume uniform dispersion.

Optimize Nanofluid Formulations: Knowledge of fractal structures allows engineers to tailor nanoparticle types, shapes, and concentrations to achieve desired thermal properties for specific applications.

Improve Cooling System Efficiency: Nanofluids with controlled fractal distributions enhance heat transfer performance in industrial cooling systems, electronics thermal management, and energy systems.

Design Advanced Composite Materials: Incorporating nanofluids with fractal characteristics into composites can improve mechanical and thermal properties, benefiting applications in aerospace, automotive, and renewable energy technologies.

Understand Aggregation and Interactions: Fractal analysis helps quantify how nanoparticle clusters form, interact, and create low-resistance heat transfer pathways, providing insights into the mechanisms governing thermal conductivity enhancement.

3. Results and Discussion

The analysis of fractal-based models demonstrates that the fractal dimension of nanoparticle aggregates significantly influences the thermal conductivity of nanofluids. Computational and experimental studies [4–12, 17] consistently show that low-fractal-dimension aggregates, which are open and chain-like, facilitate the formation of continuous conductive pathways, leading to higher effective thermal conductivity. Conversely, more compact aggregates with higher fractal dimensions reduce the continuity of conductive paths and decrease thermal transport efficiency.

Using the model proposed by Xu et al. [5], the effective thermal conductivity $k$eff was calculated as a function of nanoparticle volume fraction, base fluid conductivity, and the fractal function $f(D) = a.D^b$. Incorporating fractal characteristics yielded more accurate predictions compared with classical models assuming uniform nanoparticle dispersion. In hybrid nanofluids, such as the GO-NaAlg-Gr system analyzed by Anwar and Kumam [16], considering both nanoparticle shape (spherical, cylindrical, and plate-like) and fractal dimensions further enhanced thermal conductivity predictions, capturing clustering effects and the increased surface area inherent to fractal structures.

The Bruggeman-based fractal model by Wang et al. [17] also confirmed that particle clustering forms low-resistance heat transfer pathways. Experimental data for copper oxide nanofluids (50 nm particles, volume fraction <25%) showed excellent agreement with model predictions. Here, $K_{CL(r)}$, representing the conductivity of nanoparticle clusters, highlighted the contribution of cluster-mediated heat transfer. Factors such as nanoparticle concentration, temperature, and interparticle forces were found to alter fractal dimensions and, consequently, thermal conductivity. Higher concentrations promote extensive aggregation, while temperature influences particle interactions and cluster stability. Interparticle forces, including van der Waals and electrostatic interactions, determine aggregation behavior and the resulting fractal structure.

Overall, the results indicate that fractal phenomena provide a fundamental explanation for the non-linear thermal behavior of nanofluids. Open, low-fractal-dimension aggregates enhance thermal transport via increased surface contact and the formation of continuous conductive paths, whereas compact clusters hinder heat transfer. Fractal-based models integrate these microstructural features, enabling more precise predictions and optimized design of nanofluids for applications in cooling systems, electronics, energy systems, and composite materials. Future work should focus on extending fractal-based predictive models to a wider range of nanofluid compositions and validating them under varying operating conditions, thereby enabling the rational design of high-performance thermal fluids with tailored fractal characteristics.

4. Conclusion

Recent studies indicate that the fractal dimensions of nanoparticle clusters play a crucial role in determining the thermal conductivity of nanofluids. Higher fractal dimensions correspond to more open and complex cluster structures, which create effective pathways for heat transfer and enhance the overall thermal conductivity of the

nanofluid. These structures also influence particle–fluid interactions, facilitating efficient energy transport from the nanoscale to the macroscopic level. Experimental investigations and numerical modeling approaches, including molecular dynamics and Monte Carlo simulations, have demonstrated that incorporating fractal parameters into predictive models allows for more accurate estimations of the thermal and physical properties of nanofluids. This fractal-based approach has led to the development of nanofluids with significantly improved thermal performance, making them suitable for applications in cooling systems, heat exchangers, and energy storage technologies. Furthermore, understanding the effect of fractal clustering on particle stability enables the design of nanofluids with minimal sedimentation and extended operational lifetimes. Overall, integrating fractal theory with nanofluid research provides innovative pathways for enhancing thermal performance and energy management. With continued advancements in this field, it is expected that nanofluids with optimized thermal properties and stability will be developed for diverse industrial applications and advanced thermal technologies.

References

[1] Rahmatinejad, B. (2022). Investigating thermophysical properties and thermal performance of Al2O3 nanoparticles in water and ethylene glycol based fluids. Journal of Nanostructures, 12(3), 642-659.

[2] Rahmatinejad, B., Azimpour Shishevan, F., & Ghasemi Zavaragh, H. (2025). Analysis of thermophysical properties of CuO nanoparticles in Water and Ethylene Glycol Based Fluids. Journal of Engineering and Applied Research, 2(2), 86-108.

[3] Cai, J., Hu, X., Xiao, B., Zhou, Y., & Wei, W. (2017). Recent developments on fractal-based approaches to nanofluids and nanoparticle aggregation. International Journal of Heat and Mass Transfer, 105, 623-637.

[4] Skouras, E. D., Karagiannakis, N. P., & Burganos, V. N. (2024). Thermal conduction in hybrid nanofluids and aggregates. Nanomaterials, 14(3), 282.

[5] Zhang, W., Zhu, C., Chen, S., Wang, S., Jing, Z., & Cui, L. (2024). Effect of Morphological Characteristics of Aggregates on Thermal Properties of Molten Salt Nanofluids. Energies, 17(5), 1080.

[6] Madhu, A. K., Jayadeep, U. B., & Sobhan, C. B. (2023). Effect of the fractal dimension of nanoparticle aggregates on enhanced thermal transport in nanofluids–a molecular dynamics study. Molecular Simulation, 49(7), 690-700.

[7] Rahman, M. A., Hasnain, S. M., Pandey, S., Tapalova, A., Akylbekov, N., & Zairov, R. (2024). Review on nanofluids: preparation, properties, stability, and thermal performance augmentation in heat transfer applications. ACS omega, 9(30), 32328-32349.

[8] Arif, M. S., Abodayeh, K., & Nawaz, Y. (2024). Numerical modeling of mixed convective nanofluid flow with fractal stochastic heat and mass transfer using finite differences. Frontiers in Energy Research, 12, 1373079.

[9] Murshed, S. S. (2025). Thermal Properties and Features of Nanofluids. Nanomaterials, 15(5), 334.

[10] Yu, H., Li, M., Guo, N., Chen, A., Zhang, H., & Du, M. (2025). Fractal-Based Thermal Conductivity Prediction Modeling for Closed Mesoporous Polymer Gels. Gels, 11(6), 391.

[11] Raza, Q., Wang, X., Qureshi, M. Z. A., Chamkha, A. J., & Ghanzwani, H. A. (2025). Heat and mass transfer phenomena for fractal interfacial layer model on metallic-nanomaterials nanofluids flow with chemical reaction effect. Numerical Heat Transfer, Part A: Applications, 86(11), 3640-3663.

[12] Ali, B., Hussain, M., Awan, A.U. et al. Influence of coriolis force and nanoparticle aggregation on entropy generation and thermal conductivity in dusty nanofluid flow: a numerical investigation. Sci Rep 15, 42278 (2025). https://doi.org/10.1038/s41598-025-27894-x

[13] Lee, S., Choi, S. S., Li, S. A., & Eastman, J. A. (1999). Measuring thermal conductivity of fluids containing oxide nanoparticles.

[14] Eastman, J. A., Choi, S. U. S., Li, S., Yu, W., & Thompson, L. J. (2001). Anomalously increased effective thermal conductivities of ethylene glycol-based nanofluids containing copper nanoparticles. Applied physics letters, 78(6), 718-720.

[15] Xu, J., Yu, B., Zou, M., & Xu, P. (2006). A new model for heat conduction of nanofluids based on fractal distributions of nanoparticles. Journal of Physics D: Applied Physics, 39(20), 4486.

[16] Anwar, T., & Kumam, P. (2022). A fractal fractional model for thermal analysis of GO− NaAlg− Gr hybrid nanofluid flow in a channel considering shape effects. Case Studies in Thermal Engineering, 31, 101828.

[17] Wang, X., Xu, X., & Choi, S. U. (1999). Thermal conductivity of nanoparticle-fluid mixture. Journal of thermophysics and heat transfer, 13(4), 474-480.

Design and Thermodynamic Analysis of a Geothermal-Based Tri-Generation System for Simultaneous Production of Power, Fresh Water, and Domestic Hot Water

Yaser Shokri[1], Hadi Ghasemi Zavaragh[2], Bahman Rahmatinejad [3], Omid Khanmohammadi [4], Abolfazl Taghavi [5]

PhD Student, Department of Mechanical Engineering, University of Tabriz, Tabriz, Iran
Department of Mechanical Engineering, Technical and Vocational University (TVU), Tehran, Iran
Department of Mechanical Engineering, Technical and Vocational University (TVU), Tehran, Iran
B.s student, Department of Mechanical Engineering, Technical and Vocational University (TVU), Tehran, Iran
B.s student, Department of Mechanical Engineering, Technical and Vocational University (TVU), Tehran, Iran

* *Corresponding author E-mail: Yaser_shokri@tabrizu.ac.ir*

Keywords

Geothermal energy,
Thermodynamic analysis,
Humidification
Dehumidification process,
Energy efficiency

Abstract

In recent years, there has been a growing emphasis on the use of sustainable energy resources to reduce carbon emissions and improve energy efficiency. In this study, an energy and exergy analysis of a trigeneration system consisting of a double-flash geothermal cycle, a Domestic Water Heater (DWH) system, and a humidification dehumidification (HDH) desalination unit has been investigated. This system, powered by a renewable geothermal energy source, produces three distinct outputs: electrical power, domestic hot water, and potable water. The results of the analysis indicate that under baseline conditions, the net power output, freshwater production rate, energy efficiency, and exergy efficiency of the proposed system are 49.06 kW, 0.2392 kg/s, 47.6%, and 58.06%, respectively. In addition, the thermal power of the domestic hot water was found to be 329.6 kW. The exergy analysis also reveals that the highest share of exergy destruction occurs in components subjected to high temperature differences and irreversible conversion processes. These findings suggest that optimizing thermal design and reducing exergy losses can enhance the overall performance and promote more sustainable utilization of geothermal energy resources.

1. Introduction

One of the fundamental challenges associated with non-renewable energy resources is their instability and the impossibility of replenishing them after consumption. The continuous growth of the global population, the expansion of industrial processes, the increasing dependence on energy, and the excessive consumption of fossil fuel resources have motivated researchers to seriously seek sustainable alternative sources to meet humanity's energy demands [1]. Among these options, geothermal energy—recognized as a clean, environmentally safe, reliable, and economically viable renewable resource—has played a significant role in reducing dependence on fossil fuels [2]. The use of this resource has nearly doubled over the past five years [3]. In general, geothermal resources can be classified according to their reservoir temperature into three categories: high-temperature resources above 150 °C, which are primarily used for electricity generation [4]; medium-temperature resources in the range of 90–150 °C, which are suitable for direct applications such as industrial processes, heating, cooling, and greenhouse heating; and low-temperature resources below 90 °C, which are applied in small-scale heating systems and domestic uses [5]. Given the intensifying global water crisis, the production of freshwater from abundant saline seawater has attracted considerable attention as a key solution for addressing water scarcity [6]. In this regard, desalination technologies are recognized as effective options for alleviating concerns arising from the limited availability of freshwater sources. Although numerous desalination methods are currently available, most of these technologies require extensive infrastructure and rely on energy derived from fossil fuels; therefore, their economic feasibility is generally limited to large-scale industrial applications. Considering the aim of the present study, the humidification–dehumidification (HDH) desalination system, due to its simple structure and suitability for small-scale applications, represents an appropriate option for meeting freshwater demand. The humidification dehumidification process is a type of thermal desalination that essentially mimics the natural cycle of water evaporation and condensation. This method is based on the ability of air

to absorb and retain water vapor; in other words, as the air temperature increases, its capacity to carry moisture also rises [7].

HDH systems are classified into four main categories based on whether the water and air streams operate in open or closed loops:

(a) closed-water/open-air,

(b) open-water/closed-air,

(c) open-water/open-air, and

(d) closed-water/closed-air.

Additionally, in terms of thermal energy supply, these systems are categorized into two types: water-heated systems and air-heated systems.

Sen et al. [8] introduced a hybrid system consisting of a double-loop geothermal power plant and a parabolic solar collector. This system produced a total power output of 2900 kW, of which the geothermal section with a source temperature of 130 °C and a mass flow rate of 85 kg/s contributed the major share of 2693 kW, while the solar section generated only 207 kW. Yüksel et al. [9] also developed a trigeneration system capable of producing freshwater, electricity, hydrogen, domestic hot water, and ammonia. Performance evaluation of this system showed that its energy and exergy efficiencies were 75.07% and 76.26%, respectively. The parametric analysis revealed that the mass flow rate of the fluid exiting the geothermal reservoir, within the range of 30–50 kg/s, had the greatest impact on the energy and exergy indicators. Moreover, the geothermal source temperature, as a key factor, caused significant variations in system performance. Liu et al. [10] conducted a comparative study from thermodynamic and exergoeconomic perspectives on four different configurations of geothermal systems. Based on the conducted analyses, system (d) consisting of a double-flash geothermal system, an HDH desalination system, and two thermoelectric generators—was identified as the best option among the four systems examined. The output variables, including total product cost, net power output, system energy efficiency, and exergy efficiency, were found to be 4.532 $/GJ, 106.8 kW, 45.83%, and 51.53%, respectively. Deymi et al. [11] analyzed a trigeneration system for producing heating, power, and water for a building in Saint Petersburg, Russia. The results showed that the proposed system could cover up to 70% of the electricity demand and 57.9% of the heating demand without any auxiliary system.

Numerous studies have been conducted on the performance and optimization of HDH systems. The earliest research was reported in the early 1990s in Tunisia, Malaysia, and Jordan [12–13]. Goosen et al. [14] demonstrated that the commercial production of solar HDH desalination systems is economically viable and exhibits high operational efficiency. Farid et al. [15] investigated an open-water/closed-air system and found that increasing the mass flow rate of the inlet water enhanced the system efficiency up to an optimal point, beyond which it declined. Similarly, Dai et al. [16] studied a closed-air circulation system with water heating and reported that the amount of freshwater produced strongly depends on the inlet temperatures of water and air as well as their mass flow rates in the system loop. Majidi et al. [17], in a thermoeconomic-exergy analysis of various system components, found that the heating section with approximately 88% of the total exergy losses played the most significant role in reducing system efficiency; therefore, improving the heating section performance can markedly enhance the overall system efficiency. Mahdizade et al. [18], based on the first law of thermodynamics, showed that in a semi-open water/open-air system, heating from the water side increases the overall efficiency, whereas heating from the air side has negligible impact. Hosseini et al. [19] examined the performance of an HDH system coupled with solar collectors and found that for specific values of saline water and air flow rates, there exists an optimal combination that maximizes the system's energy efficiency. Ashrafizadeh et al. [20], using the concept of driving forces, performed an exergy analysis and demonstrated that heat transfer has no effect on the total exergy losses, while the heater contributes the largest share to system irreversibility.

In the present study, an innovative trigeneration system simultaneously producing electricity, domestic hot water, and freshwater based on geothermal energy has been designed and analyzed. The proposed configuration integrates the three main processes into a single thermal cycle, offering a novel approach to utilizing renewable resources and enhancing energy conversion efficiency. A key feature of this system is the simultaneous management of energy and exergy across all subsystems, enabling more effective use of thermal energy and reducing thermodynamic losses.

2. System Description

The proposed system for the present study comprises a double-flash geothermal system, a humidification dehumidification (HDH) desalination unit, and a domestic water heater (DWH) system. A schematic of the proposed system is presented in Figure The following sections describe the operation of each of the subsystems that constitute the proposed system.

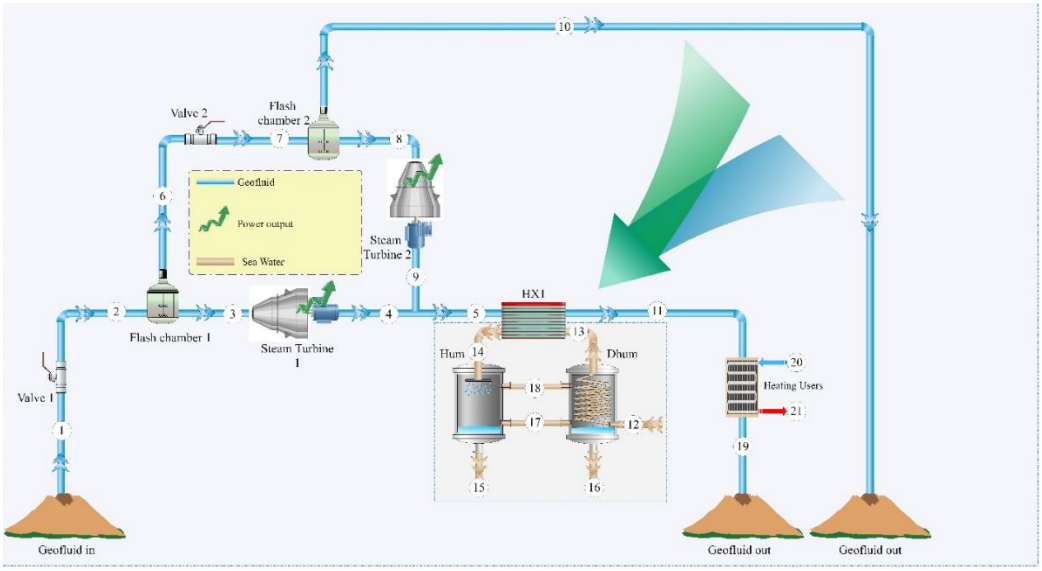

Figure 1 Schematic of the proposed system for the simultaneous production of electricity, freshwater, and domestic hot water

2.1. Double-Flash Geothermal System

The energy required for operating the proposed system is supplied from a renewable geothermal energy source. In this process, the working fluid, after absorbing heat from the geothermal reservoir, enters the first throttling valve at state (1) as a saturated liquid and becomes two-phase due to the pressure drop. The fluid then passes through the first flash chamber and enters the first steam turbine at state (3) as saturated vapor, and subsequently, at state (6), it reaches the second throttling valve as saturated liquid. In this study, a double-flash geothermal system is employed; therefore, the separation of saturated liquid and vapor exiting the throttling valves is carried out in two distinct stages. Accordingly, after passing through the second flash chamber, the working fluid enters the second steam turbine at state (8) as saturated vapor, while its saturated liquid portion is discharged at state (10). The outlet streams of both steam turbines are combined at state (5) and directed toward Heat Exchanger 1, where the required energy for the humidification dehumidification desalination unit is supplied. Finally, the residual heat leaving Heat Exchanger 1 enters the water heater to provide domestic hot water and is ultimately discharged.

2.2. Humidification–Dehumidification (HDH) Desalination System

The humidification dehumidification desalination system consists of three main components: a humidifier, a dehumidifier, and a heating unit. Using the incoming air and saline water as working streams, the system performs the freshwater production process. In operation, the feedwater from the external environment enters the dehumidifier at state (12), where it absorbs heat from the moist air stream at state (18). After being warmed, it flows toward Heat Exchanger 1 at state (13). Following the temperature increase, the water enters the humidifier at state (14). In this section, through direct contact with the dry air stream at state (17), part of the water evaporates and transfers moisture to the air. Subsequently, the resulting humid air stream exits the humidifier at state (18) and enters the dehumidifier, where its moisture condenses, producing freshwater at state (16). The remaining concentrated brine is discharged from the humidifier at state (15), and finally, the dried air at state (17) is returned to the equipment to repeat the process cycle.

3. Thermodynamic Modeling of the Proposed System

In this section, the simulation procedure of the present study is described according to Fig. All calculations associated with this simulation have been carried out using the EES engineering software. First, the thermodynamic assumptions employed in the study are introduced. Then, the modeling of the proposed system including energy and exergy analyses is examined in detail and presented in the following subsections. Finally, the proposed system is validated using reference studies available in the literature.

3.1. Research Assumptions

The following assumptions have been considered in the present study:

- The system analysis is performed under steady-state conditions.
- The ambient temperature is assumed to be 25 °C and the ambient pressure 100 kPa.

- Pressure drops in pipes and heat exchangers are negligible.
- The turbines operate with isentropic efficiency.
- The temperature and mass flow rate of the geothermal source outlet are assumed constant.
- Kinetic and potential energy effects are neglected.
- The fluid passing through the throttling valves undergoes an isenthalpic process.
- The relative humidity of the air at the outlet of the humidifier and dehumidifier is assumed to be 0.9 [21].

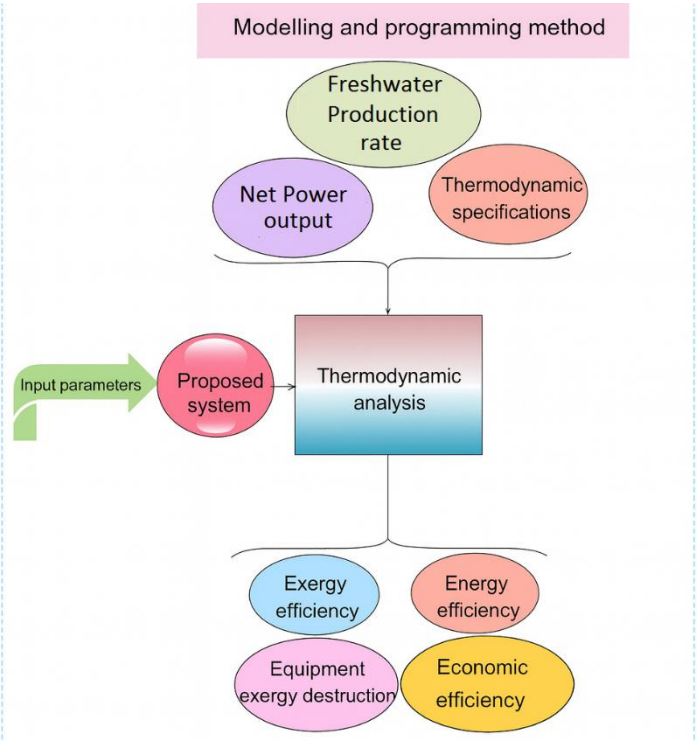

Figure 2 Modeling Method of the Proposed System

The input parameters for performing the simulation under the baseline condition are also presented in Table 1.

Table 1 Input Parameters for Simulation of the Proposed System [22] and [10]

Parameter	Value
$P_0\ (kPa)$	100
$P_2\ (kPa)$	1000
$P_7\ (kPa)$	600
$P_9\ (kPa)$	100
$T_0\ (K)$	298.15
$T_{18}\ (K)$	335
$\dot{m}_{12}\ (\frac{kg}{s})$	5.237
$\dot{m}_r\ (\frac{kg}{s})$	2.33
$\eta_{ST1,2}$	0.7
ϵ_{DH}	0.8
ϵ_H	0.8
ϵ_{HX1}	0.5

3.2. Energy and Exergy Analysis

The mass, energy, and exergy balances for each control volume under steady-state conditions, with negligible changes in kinetic and potential energies, are expressed as follows [23]:

$$\sum \dot{m}_{in} = \sum \dot{m}_{out} \tag{1}$$

$$\dot{Q} - \dot{W} = \sum(\dot{m}h)_{out} - \sum(\dot{m}h)_{in} \tag{2}$$

$$\dot{E}x_{heat} - \dot{W} = \sum_{out} \dot{E}x_{out} - \sum_{in} \dot{E}x_{in} + \dot{E}x_D \tag{3}$$

In the above relations, ṁ is the mass flow rate of the fluid, Q̇ is the net heat input rate, Ẇ is the net output work rate, h is the enthalpy, and the subscripts in and out denote the inlet and outlet, respectively. $\dot{E}x_D$, The exergy destruction rate arises from irreversibilities. Furthermore, the net exergy transfer rate by heat at temperature T is obtained from the following relation.

$$\dot{E}x_{heat} = \sum(1 - \frac{T_0}{T})\dot{Q} \tag{4}$$

In this expression, T is the temperature at which the heat transfer occurs, and T_0 is the dead-state (ambient) temperature. The specific flow exergy and the total exergy rate are defined as follows, respectively [24].

$$e = (h - h_0) - T_0(S - S_0) \tag{5}$$

$$\dot{E} = \dot{m}e \tag{6}$$

In the above relations, the subscript 0 denotes the dead (ambient) state, T_0 is the dead-state temperature, h is the enthalpy, and S is the entropy. The mass flow ratio is defined as the ratio of the mass flow rate at the humidifier inlet to the mass flow rate of dry air in the humidifier.

$$\dot{m}_r = \frac{\dot{m}_w}{\dot{m}_{da}} \tag{7}$$

The resulting output ratio is equal to the ratio of the product of the latent heat of evaporation and the mass flow rate of the produced pure water to the heat input rate to the system. In fact, this parameter represents the efficiency of the system and also serves as a good indicator for determining the amount of recovered energy [22].

$$GOR = \frac{\dot{m}_{fw} * h_{fg}}{\dot{Q}_{HX1}} \tag{8}$$

The energy efficiency and exergy efficiency are defined as follows [23].

$$\eta_{energy} = \frac{\text{energy in products}}{\text{total energy inputs}} \tag{9}$$

$$\eta_{\text{exergy}} = \frac{\text{exergy in products}}{\text{total exergy inputs}} \tag{10}$$

The mass and energy balance equations, as well as the relations for fuel and product exergy, are presented in Tables 2 and 3 for each component of the proposed system.

Table 2 Mass and energy balance equations for the components of the proposed system.

Equipment	Equations
EV1	$h_1 = h_2$
EV2	$h_6 = h_7$
FCH1	$\dot{m}_2 h_2 = \dot{m}_3 h_3 + \dot{m}_6 h_6$ $\dot{m}_2 = \dot{m}_3 + \dot{m}_6$
FCH2	$\dot{m}_7 h_7 = \dot{m}_8 h_8 + \dot{m}_{10} h_{10}$ $\dot{m}_7 = \dot{m}_8 + \dot{m}_{10}$
ST1	$\dot{W}_{ST1} = \dot{m}_3(h_3 - h_4)$
ST2	$\dot{W}_{ST2} = \dot{m}_8(h_8 - h_9)$

HX1	$\dot{Q}_{HX1} = \dot{m}_5(h_5 - h_{11})$ $\dot{Q}_{HX1} = \dot{m}_{13}(h_{14} - h_{13})$
DHUM	$\dot{Q}_{DH} = \dot{m}_{13}(h_{13} - h_{12})$ $\dot{Q}_{DH} = \dot{m}_{18}h_{18} - \dot{m}_{17}h_{17} - \dot{m}_{16}h_{16}$ $\dot{m}_{16} = \dot{m}_{da}(\omega_{18} - \omega_{17})$
HUM	$\dot{Q}_H = \dot{m}_{14}(h_{14} - h_{15})$ $\dot{m}_{14}h_{14} + \dot{m}_{17}h_{17} = \dot{m}_{15}h_{15} + \dot{m}_{18}h_{18}$ $\dot{m}_{15} = \dot{m}_{14} - \dot{m}_{da}(\omega_{18} - \omega_{17})$
MIX1	$\dot{m}_5h_5 = \dot{m}_4h_4 + \dot{m}_9h_9$ $\dot{m}_5 = \dot{m}_4 + \dot{m}_9$
DWH	$\dot{Q}_{DWH} = \dot{m}_{11}(h_{11} - h_{19})$ $\dot{Q}_{DWH} = \dot{m}_{20}(h_{21} - h_{20})$

Table 3 Relations for fuel and product exergy for the components of the proposed system.

Equipment	Fuel	Exergy Equations	Product
EV1	$\dot{E}x_1$		$\dot{E}x_2$
EV2	$\dot{E}x_6$		$\dot{E}x_7$
FCH1	$\dot{E}x_2$		$\dot{E}x_3 + \dot{E}x_6$
FCH2	$\dot{E}x_7$		$\dot{E}x_8 + \dot{E}x_{10}$
ST1	$\dot{E}x_3 - \dot{E}x_4$		$\dot{W}_{ST1}$
ST2	$\dot{E}x_8 - \dot{E}x_9$		$\dot{W}_{ST2}$
HX1	$\dot{E}x_5 - \dot{E}x_{11}$		$\dot{E}x_{14} - \dot{E}x_{13}$
DHUM	$\dot{E}x_{18} - \dot{E}x_{17}$		$\dot{E}x_{13} - \dot{E}x_{12} + \dot{E}x_{16}$
HUM	$\dot{E}x_{14} - \dot{E}x_{15}$		$\dot{E}x_{18} - \dot{E}x_{17}$
MIX1	$\dot{E}x_4 + \dot{E}x_9$		$\dot{E}x_5$
DWH	$\dot{E}x_{11} - \dot{E}x_{19}$		$\dot{E}x_{21} - \dot{E}x_{20}$

3.3. Validation of Results

The validity of the thermodynamic simulation results has been verified using key and reliable references. In Fig. 3, the comparison chart related to the validation of the double-flash geothermal system is presented. Moreover, Fig. 4 comparatively illustrates the simulation results for the humidification–dehumidification desalination system under different inlet mass flow rate conditions.

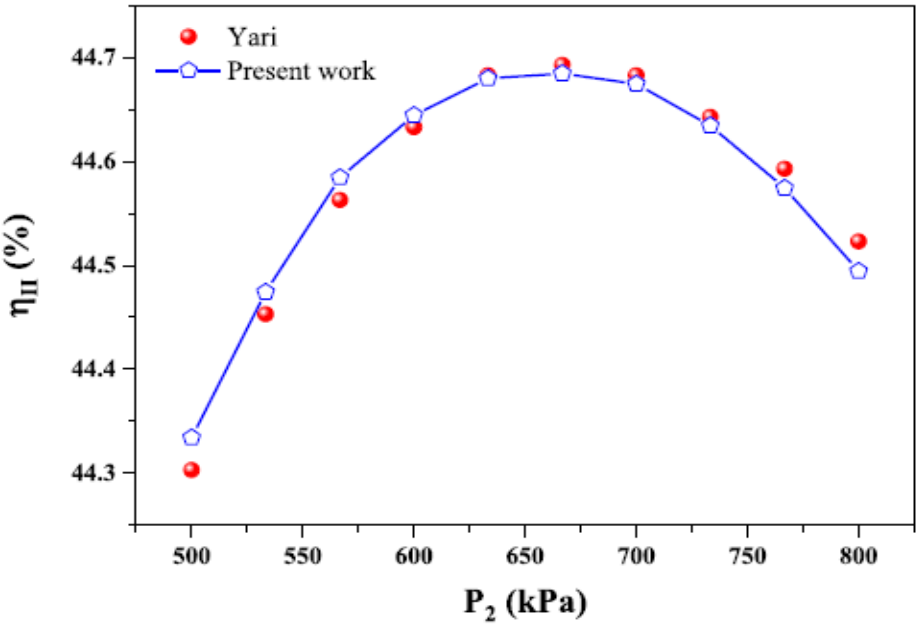

Figure 3 Validation results of the double-flash geothermal system in the present study compared with Ref [23].

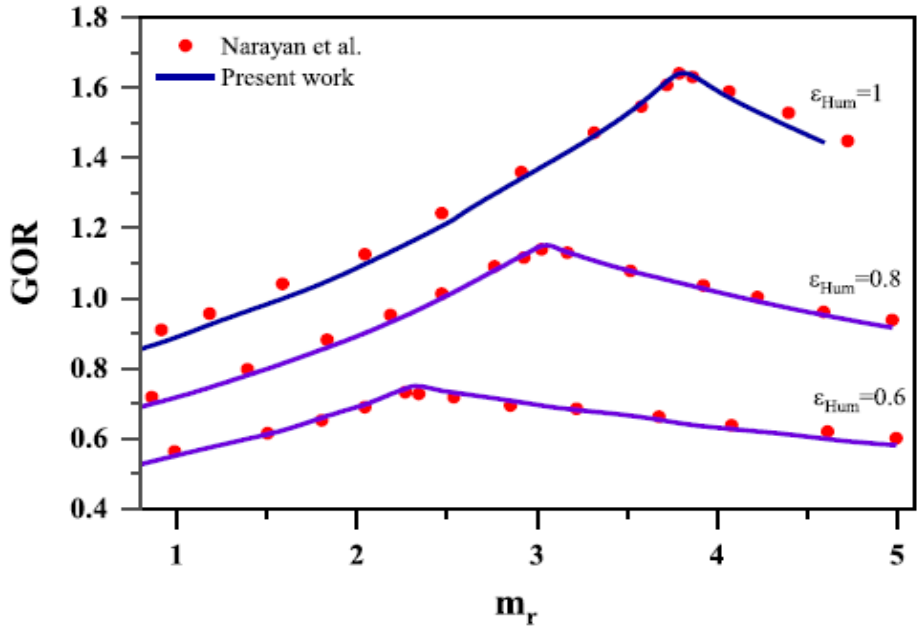

Figure 4 Validation results of the desalination system in the present study compared with Ref [25].

4. Results and Discussion

4.1. Parametric Analysis

4.1.1. Effect of Geothermal Fluid Temperature on the Output Variables of the Proposed System

The impact of increasing the geothermal source temperature on the key system variables was examined. As shown in Fig. 5, with the rise in temperature, the net output power increases steadily, while the obtained output ratio (GOR) gradually decreases. This behavior is due to the higher evaporation rate and increased specific energy consumption at elevated temperatures. On the other hand, Fig. 6 illustrates the variation of energy efficiency and exergy efficiency with respect to the geothermal energy source temperature. Both efficiency indicators decrease gradually as the temperature rises, which results from the growth of thermodynamic irreversibilities and the reduction in energy quality during the conversion process. Overall, although increasing the geothermal fluid temperature improves the system's output power, the overall thermodynamic performance experiences a relative decline due to intensified exergy losses and higher specific energy consumption.

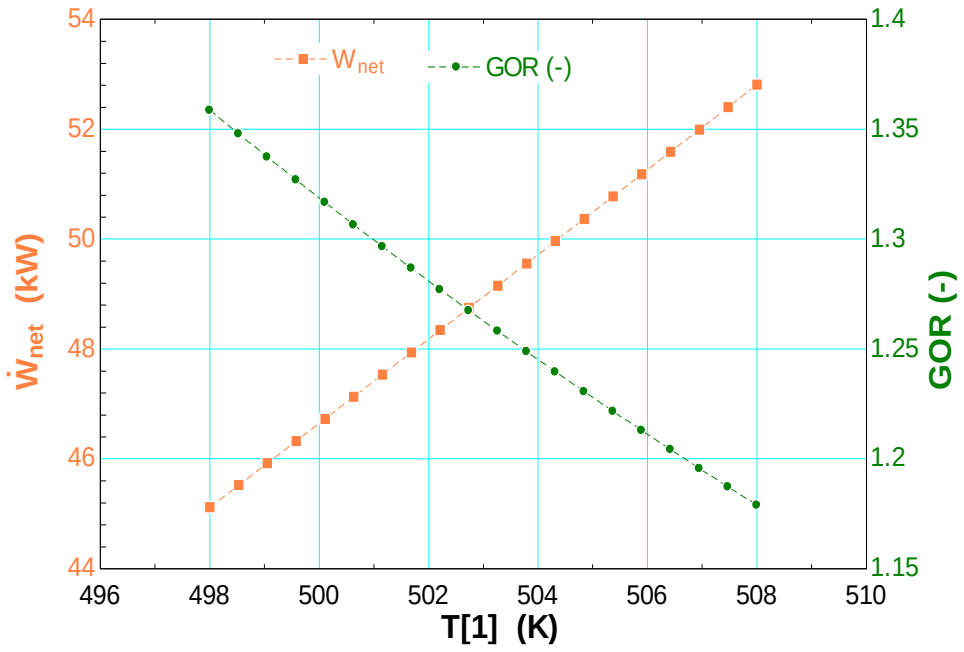

Figure 5 Effect of geothermal fluid temperature on net output power and GOR.

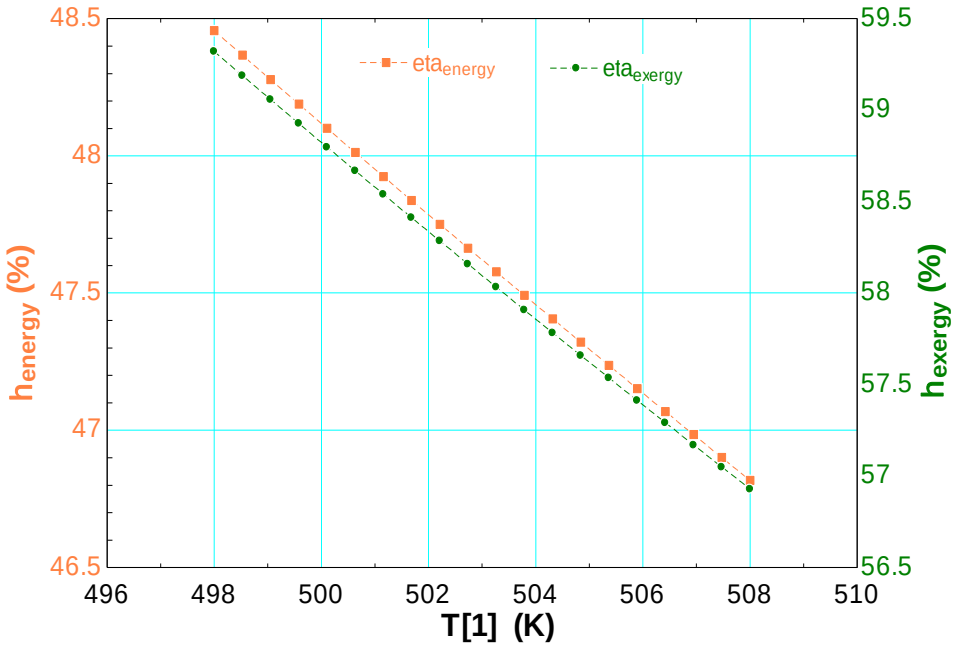

Figure 6 Effect of geothermal fluid temperature on energy and exergy efficiencies.

4.1.2. Effect of Geothermal Fluid Mass Flow Rate on the Output Variables of the Proposed System

The impact of increasing the geothermal fluid mass flow rate on system performance is shown in Fig. An increase in mass flow rate leads to a higher net output power; however, this increase is accompanied by a direct reduction in GOR. This occurs because, with a higher inlet mass flow rate, there is insufficient time for optimal heat exchange in the heat exchangers. As a result, more thermal energy from the geothermal fluid is not fully extracted and is lost as waste heat from the system. This greater loss causes a reduction in the desalination system's efficiency. In Fig. 8, the effect of mass flow rate on efficiency indicators is examined. It is observed that as the mass flow rate increases, both the energy efficiency and exergy efficiency of the system continuously decrease. This decline in efficiency reflects increased thermal and exergetic losses per unit volume of fluid and the suboptimal matching between the inlet flow rate and the capacity of the heat exchangers at higher flow rates.

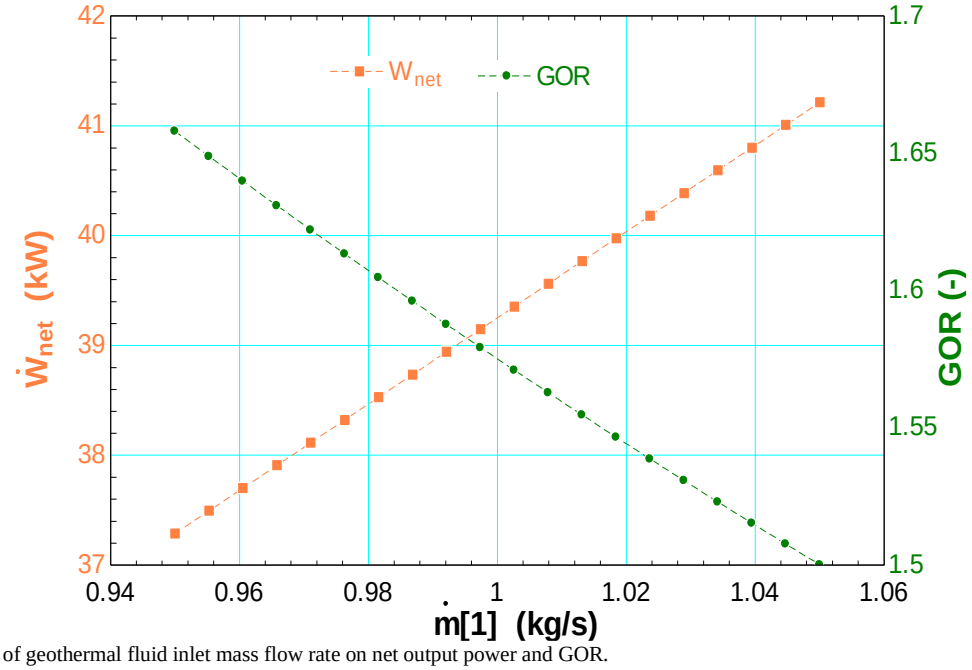

Figure 7 Effect of geothermal fluid inlet mass flow rate on net output power and GOR.

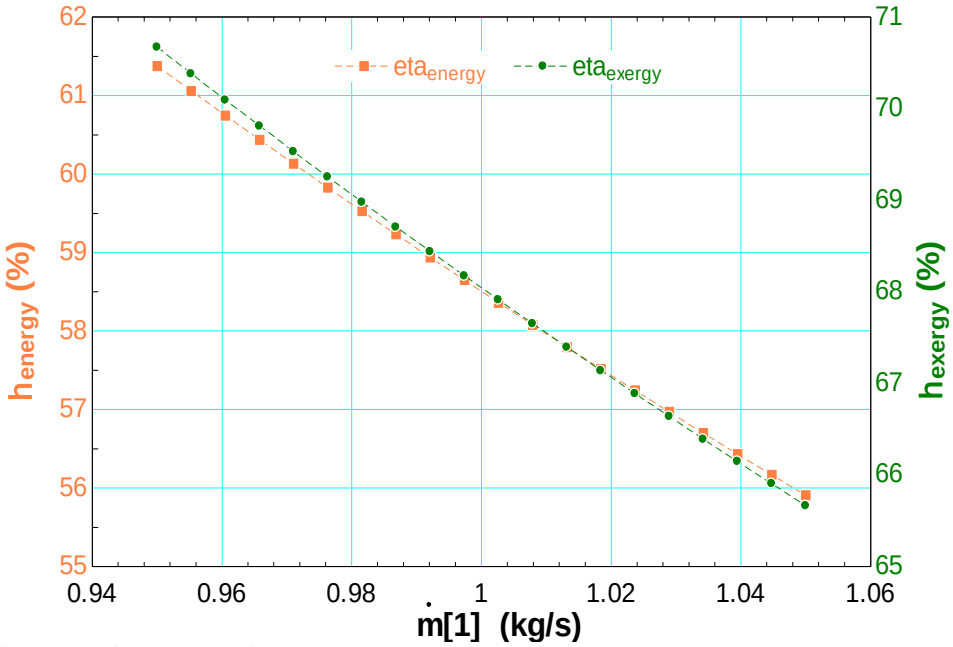

Figure 8 Effect of geothermal fluid inlet mass flow rate on energy and exergy efficiencies.

4.1.3. Effect of Expansion Valve 1 Pressure on the Output Variables of the Proposed System

Figure 9 shows the trend of changes, indicating that with an increase in pressure P2, the net power output initially rises and, after reaching a maximum at around 1400 kPa, begins to decrease. This behavior is due to improved power generation at intermediate pressures, followed by increased pressure drop and reduced mass flow rate at higher pressures. On the other hand, the GOR decreases uniformly, indicating a decline in thermal efficiency in the evaporation and condensation processes as the pressure increases. Therefore, the optimal operating point of the cycle is determined within the medium-pressure range, where both power and efficiencies are simultaneously at their best. As observed in Figure 10, with increasing P2, both energy and exergy efficiencies initially show an upward trend and then decrease after reaching their optimal values around 1300–1500 kPa. The initial increase is due to improved thermodynamic conditions and reduced thermal losses in the cycle, whereas the decrease at higher pressures results from increased exergy losses and reduced component efficiency. Overall, the maximum energy and exergy efficiencies are achieved within the medium-pressure range.

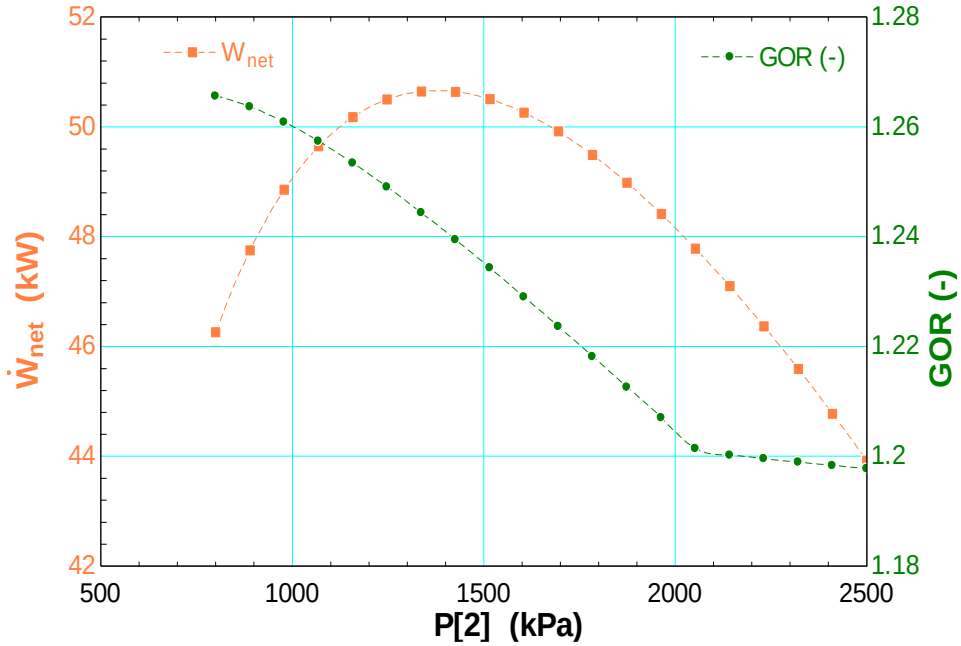

Figure 9 Effect of Expansion Valve 1 Pressure on Net Power Output and GOR

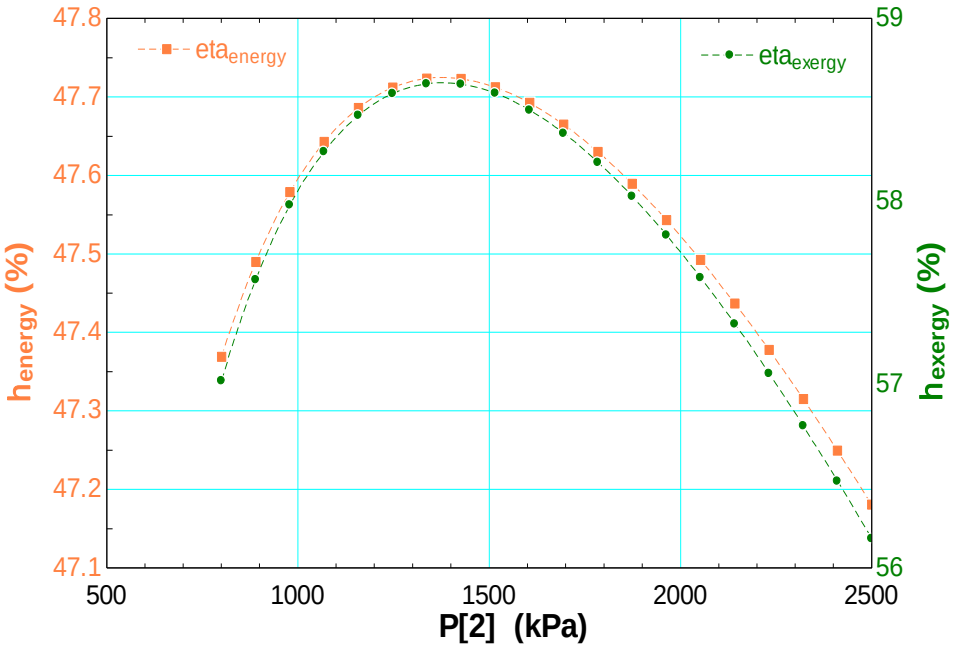

Figure 10 Effect of Expansion Valve 1 Pressure on Energy and Exergy Efficiencies

4.1.4. Effect of Expansion Valve 2 Pressure on the Output Variables of the Proposed System

Figure 11 shows the trend of increasing P7 in relation to net power output and GOR. With an increase in Expansion Valve 2 pressure, the net power output exhibits a decreasing trend, while GOR increases. This behavior is due to the fact that a higher pressure at the expansion point reduces the pressure difference across the valve, thereby lowering the recoverable energy available for power generation. Conversely, it improves the evaporation process in the thermal loop and allows better utilization of the input heat, which in turn increases the GOR. Therefore, Expansion Valve 2 pressure plays a key role in balancing power generation and heat recovery.

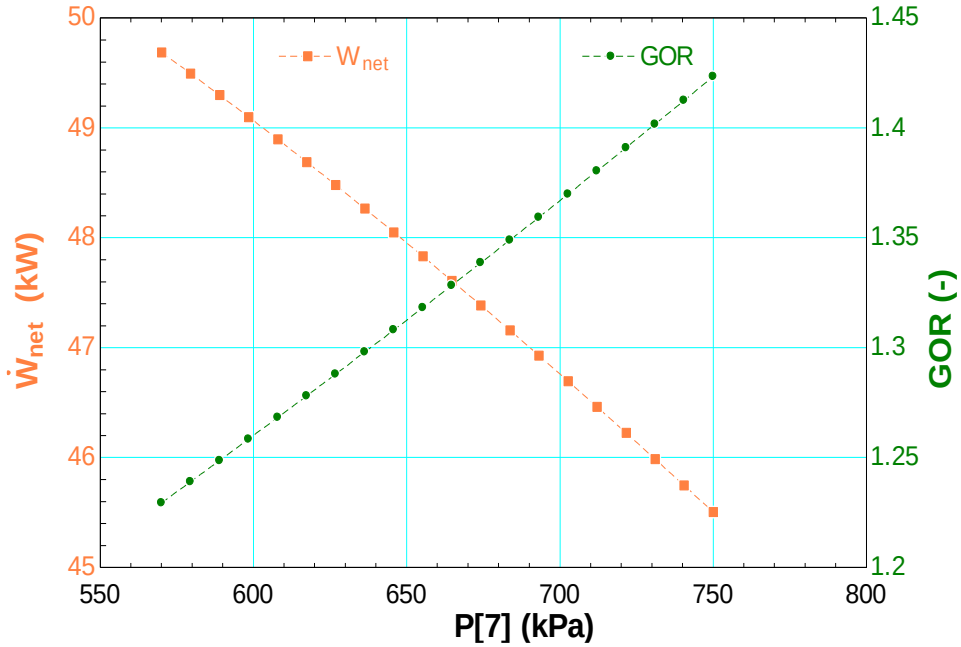

Figure 11 Effect of Expansion Valve 2 Pressure on Net Power Output and GOR

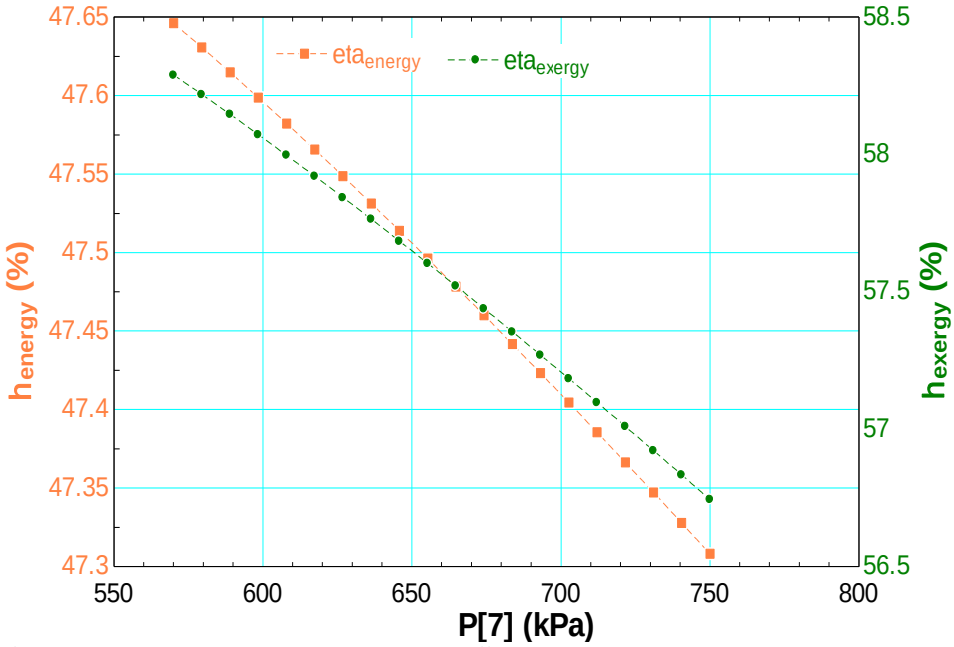

Figure 12 Effect of Expansion Valve 2 Pressure on Energy and Exergy Efficiencies

4.1.5. Effect of Feed Water Mass Flow Rate to the Desalination Unit on the Output Variables of the Proposed System

Figure 13 shows the variations of net power output and GOR with respect to the mass flow rate entering the desalination unit. With an increase in the mass flow rate to the humidification–dehumidification section, both net power output and GOR show an increasing trend. A higher feed mass flow rate leads to greater heat transfer in the evaporator and condenser, increased vapor mass generated by the cycle, and consequently higher power production in the turbine. In addition, the increased hot water flow improves the thermal energy recovery process, and the rise in GOR indicates better thermal efficiency of the cycle. As observed in Figure 14, both energy and exergy efficiencies also increase with the increase in feed mass flow rate. Increasing the mass flow rate to the desalination section allows more effective utilization of the heat source and reduces relative losses in system components. Specifically, at constant pressure and temperature, this increase improves the heat balance and enhances the quality of energy conversion throughout the humidification dehumidification process. Therefore, the feed mass flow rate to the desalination unit is considered one of the key parameters affecting the improvement of energy and exergy performance of the proposed system.

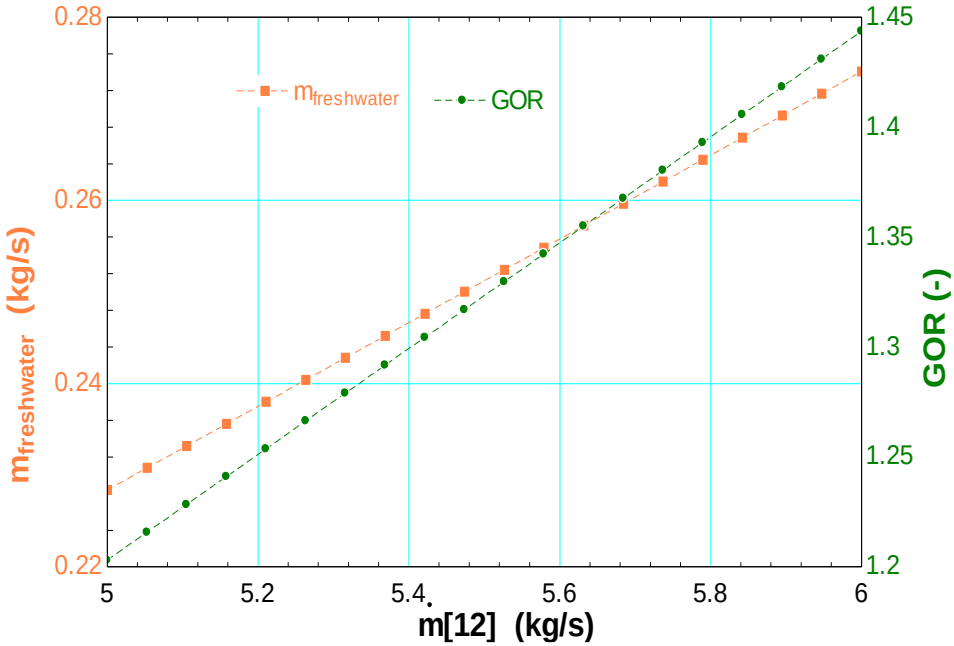

Figure 13 Effect of Desalination Unit Feed Mass Flow Rate on Net Power Output and GOR

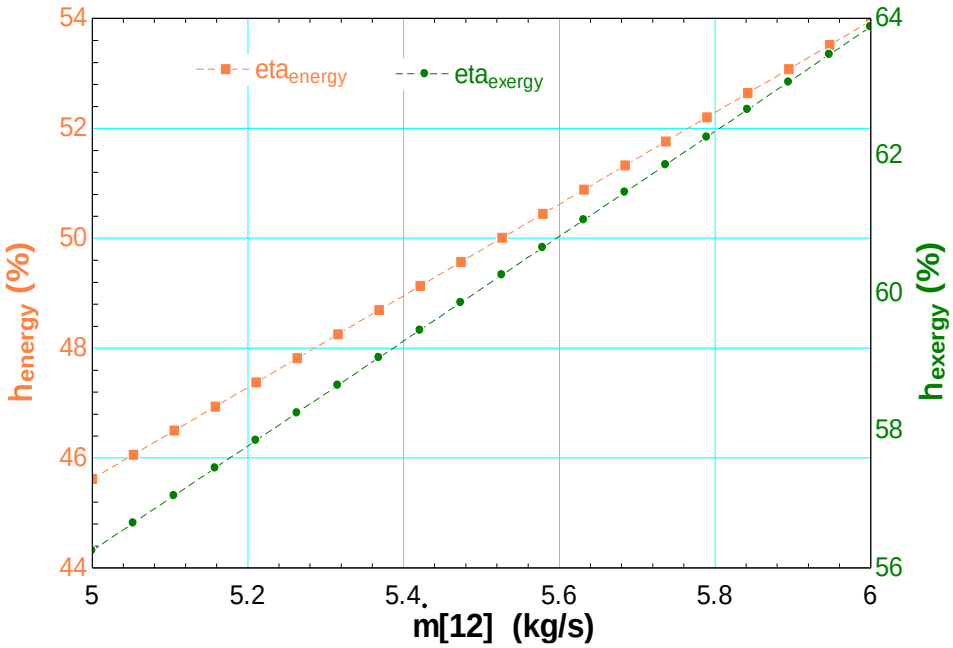

Figure 14 Effect of Desalination Unit Feed Mass Flow Rate on Energy and Exergy Efficiencies

5. Conclusion

In this study, the performance of a geothermal-based cogeneration system, including a double-flash cycle, domestic hot water production, and a humidification–dehumidification desalination unit, was investigated. Energy and exergy analyses showed that the proposed system, utilizing renewable geothermal energy, is capable of simultaneously providing three key products: electricity, hot water, and potable water. Under baseline conditions, the net power output was 49.06 kW, the freshwater production rate was 0.2392 kg/s, the energy efficiency was 47.6%, the exergy efficiency was 58.06%, and the thermal power required for hot water was 329.6 kW. Overall, the results indicate that using geothermal energy in a cogeneration structure integrated with a desalination unit not only reduces energy losses and improves the overall system efficiency but also plays an effective role in achieving sustainable development goals and mitigating environmental impacts.

References

[1] Kabeyi MJ, Olanrewaju OA. Sustainable energy transition for renewable and low carbon grid electricity generation and supply. Frontiers in Energy research. 2022 Mar 24;9:1032.

[2] Moya D, Aldás C, Kaparaju P. Geothermal energy: Power plant technology and direct heat applications. Renewable and Sustainable Energy Reviews. 2018 Oct 1;94:889-901.

[3] Li K, Liu C, Jiang S, Chen Y. Review on hybrid geothermal and solar power systems. Journal of cleaner production. 2020 Mar 20;250:119481.

[4] Basaran A, Ozgener L. Investigation of the effect of different refrigerants on performances of binary geothermal power plants. Energy Conversion and Management. 2013 Dec 1;76:483-98.

[5] Al-Zyoud S. Geothermal energy utilization in jordanian deserts. International Journal of Geosciences. 2019 Oct 21;10(10):906.

[6] N. Ghaffour et al., “Renewable energy-driven innovative energy-efficient desalination technologies,” Appl. Energy, Vol. 136, pp. 1155–1165, 2014.

[7] Seeking energy efficient solutions for clean water supplies. http://lienhard.scripts.mit.edu/research/.

[8] O. Sen, O. F. Guler, C. Yilmaz, and M. Kanoglu, "Thermodynamic modeling and analysis of a solar and geothermal assisted multi-generation energy system," Energy Conversion and Management, vol. 239, p. 114186, 2021.

[9] Y. E. Yuksel, M. Ozturk, and I. Dincer, "Development and assessment of a novel geothermal power-based multigenerational system with hydrogen and ammonia production options," Energy Conversion and Management, vol. 243, p. 114365, 2021.

[10] Z. Liu, S. Zhanguo, A. M. Abed, R. Chaturvedi, M. Feyzbaxsh, and A. K. Salavat, "A comparative thermodynamic and exergoeconomic scrutiny of four geothermal systems with various configurations of TEG and HDH unit implementations," Applied Thermal Engineering, vol. 216, p. 119094, 2022.

[11] M. Deymi-Dashtebayaz, A. Nikitin, V. Davoodi, V. Nikitina, M. Hekmatshoar, and V. Shein, "A new multigenerational solar energy system integrated with near-zero energy building including energy storage–A dynamic energy, exergy, and economic-environmental analyses," Energy Conversion and Management, vol. 261, p. 115653, 2022.

[12] Nawayseh N. K. N., Farid M. M. M., Al-Hallaj S., Al- Timimi A. R., Solar desalination based on humidification process - I. Evaluating the heat and mass transfer coefficients, Energy Convers. Manag., Vol. 40, No. 13, pp. 1423–1439, 1999.

[13] Farid M. M. et al., A simulation study to improve the performance of a solar humidification-dehumidification desalination unit constructed in Jordan, Desalination, Vol. 109, No. 3, pp. 277–284, 1997.

[14] Goosen, M. F. A., Sablani, S. S., Shayya, W. H., Paton, C. & Al-Hinai, “Thermodynamic and economic considerations in solar desalination, Elsevier, Vol. 129, pp. 63–89, 2000.

[15] Farid M. M., Parekh S., Selman J. R. and Al-Hallaj S., Solar desalination with a humidification-dehumidification cycle: mathematical modeling of the unit, Desalination, Vol. 151, No. 2, pp. 273–280, August 1998.

[16] Dai Y. J. and Zhang H. F., Experimental investigation of a solar desalination unit with humidification and dehumidification, Desalination, Vol. 130, No. 2, pp. 169–175, Nov. 2000.
[17] Majidi G. and Hosseinnezhad F., "Thermoexergy Analysis of Components of a Solar Desalination Cycle with Humidification and Dehumidification." First International Conference on New Technologies in Sciences, September 7, 2017.
[18] Mahdizade, E., & Ameri, M. (2017). Thermodynamic Analysis of Humidification-Dehumidification Desalination System with Semi-open Air Circulation. Amirkabir Journal of Mechanical Engineering, 49(3), 643-652.
[19] Hosseini, S. A. and Sarhaddi, F. (2017). Performance Assessment of a Humidification Dehumidification Desalination Unit Connected to Photovoltaic Thermal Collectors. Amirkabir Journal of Mechanical Engineering, 49(3), 653-
[20] Ashrafizadeh S. A. S., Desalination M. A., and Amidpour M., Exergy analysis of humidification-dehumidification desalination systems using driving forces concept, Desalination, Vol. 285, pp. 108–116, 2012.
[21] Zubair M. I., Al-Sulaiman F. A., Antar M. A., Al-Dini S. A. and Ibrahim N. I., Performance and cost assessment of solar driven humidification dehumidification desalination system, Energy Convers. Manag., Vol. 132, pp. 28–39, Jan. 2017.
[22] Feili M, Ghaebi H, Parikhani T, Rostamzadeh H. Exergoeconomic analysis and optimization of a new combined power and freshwater system driven by waste heat of a marine diesel engine. Thermal Science and Engineering Progress. 2020 Aug 1;18:100513.
[23] Yari M, Exergetic analysis of various types of geothermal power plants. Renew. Energy 35(1):112–2010.
[24] Bejan, A., Tsatsaronis, G., and Moran, M. J., 1995, Thermal design and optimization, John Wiley & Sons.
[25] Narayan, G. P., John, M. G. S., and Zubair, S. M., "Thermal design of the humidification dehumidification desalination system: An experimental investigation," International Journal of Heat and Mass Transfer, 58 (1-2), pp. 740-2013.

Effect of Using a Vertical Heat Exchanger on Performance in a Vapor Compression Heat Pump Using R417a Gas as an Alternative to R22

Fadime Şimşek [1]

[1] Department of Mechanical Engineering, Faculty of Engineering, Atatürk University, Erzurum, Türkiye

Corresponding Author: *fadimesimsek@atauni.edu.tr*

Keywords

Classification

R417A,

Shell Type Heat Exchanger,

COP

Abstract

In this study, a vertical shell-type heat exchanger was used as the superheating-cooling unit in a vaporcompression heat pump. R417A gas was selected as the refrigerant, requiring no additional modifications to the system. The ambient temperatures of the condensers and evaporators used in the system were 22°C and 15°C, respectively, and the airflow velocities were 3.7 m/s and 4.6 m/s, respectively. After the system stabilized, the calculated COP values from the obtained data were examined. It was observed that using a vertical heat exchanger with a 6 mm finned spaced evaporator increased system performance by 16.43% compared to using a vertical heat exchanger with an 8 mm finned spaced evaporator..

1. Introduction

Although renewable energy sources are being used more and more every day, carbon dioxide emissions are rapidly increasing because fossil fuels still play a significant role in meeting the world's energy needs.

With rising fuel prices and increasing concerns about global warming, many researchers are working on heat pumps as an effective energy conversion device[1].

Heat pumps are devices that can extract low-level heat energy from the air, water, or ground. Air-source heat pumps are the most commonly used type and have been the subject of numerous studies, including performance, development, energy, exergy, and economic analyses.

In this study, two evaporators of approximately equal capacity were connected in parallel to the system so that they would operate separately in a heat pump using R417A as an alternative to R22 refrigerant. To achieve superheating-cooling in the system, a vertical body type heat exchanger was used instead of the concentric heat exchanger commonly used. Although there are studies using concentric double-pipe heat exchangers in heat pump systems, a different study from the literature was conducted based on testing the vertical body type heat exchanger.

In this study, where excessive heating-cooling was desired in a vapor compression heat pump system using a vertical body type heat exchanger, the system performance of R417A was experimentally evaluated in two evaporators with approximately equal capacity and 6 mm and 8 mm fin spacing. The results indicate that the use of the vertical heat exchanger is more efficient in the evaporator with 6 mm fin spacing.

2. Experimental Studies

2.1. Introduction to the System

The vapor compression heat pump system consists of four main components: the compressor, condenser, evaporator, and throttle valve, as well as auxiliary components such as the heat exchanger, liquid tank, sight glass, filter, and refrigerant flow meter.

The experimental setup shown in Figure 1 illustrates the subject of this study, which involves cooling the refrigerant flowing from the condenser to the expansion valve in the heat pump and heating the refrigerant flowing from the evaporator to the compressor using a heat exchanger.

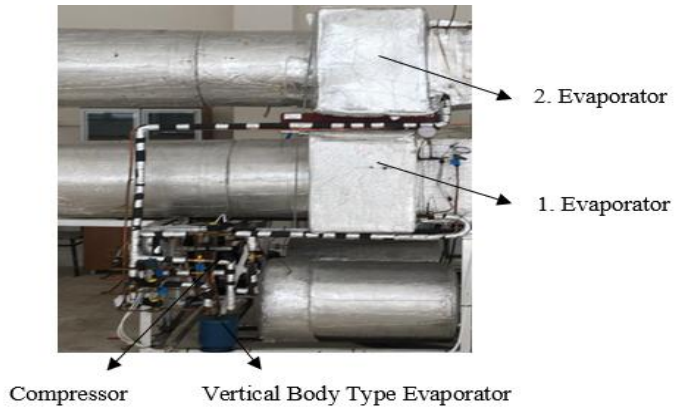

Figure 1 Side view of the experimental system

The visual representation of the vertical body type heat exchanger used in the test system is shown in Figure 2 [2], while the characteristics of the evaporators used in the heat pump are given in Table 1 [3].

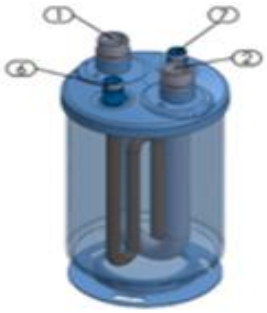

(1) Evaporator Arrival (Heat Exchanger Inlet) 5/8" ODS

(2) Compressor Outlet (Heat Exchanger Outlet) 5/8" ODS

(6) Coming from Condenser (Heat Exchanger Inlet) 3/8" ODS

(7) Return to Expansion Valve (Heat Exchanger outlet) 3/8" ODS

Figure 2 Vertical body type heat exchanger

Table 1 Input Parameters for Simulation of the Proposed System [22] and [10]

Lamella spacing (mm)	Evaparatör Tipi	Capacity	Surface Area	Pipe Volume	Air Flow	Fan Diameter	Blowing Distance	Links	
		Watt	m^2	dm^3	m^3/h	mm	m	Input	Exit
8	8 GNE 40.1.5	4000	16,1	5,7	3500	1x400	13	12	22
6	6 GNE 40.1.5	4600	20,8	5,7	3300	1x400	13	12	22

2.2. Experimental Procedure

In the study using R417A refrigerant, whose thermal and physical properties are given in Table 2, the condenser air inlet temperature was 22°C, the evaporator air inlet temperature was 15°C, the condenser volumetric flow rate was 0.74 m³/s, and evaporator volumetric flow rates of 0.92 m³/s. After ensuring the system reached a steady state, the COP values of the system under the specified operating conditions were determined using the temperature and pressure data obtained from the inlet and outlet of the main components. The average of the COP values obtained from the experiments, which were repeated 6 times, was calculated.

Table 2 Thermal and physical properties of R417A refrigerant [4]

Chemical Formula	**R125/R134a/R600(%46.6/50/3.4)**
Molecular Weight (kg/kmol)	106.8
Critical Temperature (^{0}C)	87.1
Boiling Point (^{0}C)	-39.1
ODP	0
GWP (Year)	2346

K-type chromium-nickel thermocouples were used for the condenser, evaporator, and inlet and outlet temperatures at specified points in the heat pump system, while Bourdon-type pressure gauges were used for the pressures. The air velocity through the condenser and evaporator, which are based on the air-to-air transfer principle, was controlled using switches capable of providing speed control adjustment. The flow rate of the refrigerant was measured with a gas flow meter. The energy consumed by the compressor was calculated by recording the voltage, current, and power factors from the compressor measurement panel. The measurement data, which stabilized after approximately 20 minutes, was calculated by substituting it into the following equations.

Heat removed by the condenser;

$$\dot{Q}_{kon} = \dot{m}_{ref}\left(h_{con,out} - h_{con,in}\right) = \dot{m}_{air}\left(h_{con,out} - h_{con,in}\right) \quad (1)$$

Heat absorbed by the evaporator;

$$\dot{Q}_{ev} = \dot{m}_{ref}\left(h_{ev,in} - h_{ev,out}\right) = \dot{m}_{air}\left(h_{ev,in} - h_{ev,out}\right) \quad (2)$$

Input power to the compressor,

$$\dot{W}_{comp} = \sqrt{3}.\text{Cos}\varphi.\,U.\,I \quad (3)]$$

Where U, I, and Cosφ are voltage (V), current (A), and power factor, respectively.

Coefficient of performance of the heat pump,

$$COP_{IP} = \frac{\dot{Q}_{kon}}{\dot{W}_{comp}} \quad (4)$$

3. Results and Discussion

In this study, which investigates the effect of a vertical shell-and-tube heat exchanger used to cool the refrigerant flowing from the condenser to the expansion valve and to heat the refrigerant flowing from the evaporator to the compressor on the heat pump performance, the COP values under specified conditions were calculated when evaporators connected to the system to operate separately were used, as shown in Figure 5.

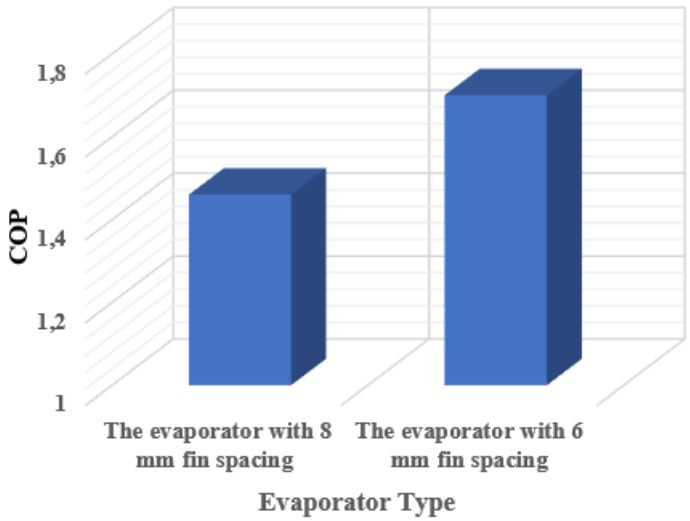

Figure 3 Measured COP values in a system using a vertical heat exchanger with two evaporators connected in parallel to the heat pump system

When using a vertical heat exchanger with a 6 mm fin spacing evaporator, a 16.43% increase in system performance was observed compared to using a vertical heat exchanger with an 8 mm fin spacing evaporator.

In another study conducted on the existing heat pump system, it was determined that under the same specified conditions, when R417A was used as an overheating-cooling unit with a horizontal heat exchanger, the COP value increased in the evaporator with 6 mm fin spacing compared to the evaporator with 8 mm fin spacing [5].

4. Conclusion

In experiments conducted on an air-to-air heat pump system, where the condenser air ambient temperature was 22 °C and the evaporator air ambient temperature was 15°C, COP values were determined when a vertical body type heat exchanger was used.

- In experiments using R417A refrigerant, a 16.43% increase in COP was achieved with an evaporator with 6 mm fin spacing compared to an evaporator with 8 mm fin spacing.
- It was noted that the effect on system performance could also be investigated if the capacity of the cylindrical vertical heat exchanger used in the current system were to be changed.

References

[1] Chen, H., Wang, Y., Li, J., Cai, B., Zhang, F., Lu, T., Yang, J., Jiang, L., Zhang, Y., Zhou, J., 2020. Experimental research on a solar air-source heat pump system with phase change energy storage. Energy Build. 228, 110451 https://doi.org/10.1016/j.enbuild.2020.110451.

[2] https://www.elektronika-sa.com.pl/en/products/refrigeration/suction-line-accumulators/sla-e/SLA.E.30b.16.10.2.5 (Access Date:15.05.2025)

[3] GEMAK, General Refrigeration Machinery Industry and Trade Inc. Product Catalog (Access Date: May 15, 2025)

[4] Katırcıoğlu F., Cingiz Z., Çay F., Gürel A.E., Sarıdemir S. and Kolip A. (2020). Investigation of refrigeration system performance using infrared image processing techniques for R22 and its alternatives, R438A and R417A refrigerants., Academic Platform Journal of Engineering and Science, 8-3, 500-513.

[5] Şimşek F., Akkoca M., Effect of using evaporators with different fin spacing on the performance of air-to-air heat pumps using R417A and R407C gases, 11th International Conference on Applied Sciences, Proceedings Book, 85-92, JUNE 1 – 3, 2024 - Izmir.

Cauliflower Disease Classification Using Vision Transformer Architecture

Rabiye Kılıç [1,*], Ahmed N. Nusari [2], Emin Argun Oral[2], İbrahim Yücel Özbek[2,3]

[1] Department of Computer Engineering, Faculty of Engineering, Atatürk University, Erzurum, Türkiye
[2] Department of Electrical and Electronics Engineering, Faculty of Engineering, Atatürk University, Erzurum, Türkiye
[3] Department of Artificial Intelligence and Data Engineering, Faculty of Engineering, Atatürk University, Erzurum, Türkiye

* *Corresponding author E-mail: rabiyekilic@atauni.edu.tr*

Keywords

Classification
Cauliflower Disease
Vision Transformer
VegNet

Abstract

In this study, a deep learning model based on Vision Transformer (ViT-B/16) was used to automatically classify cauliflower leaf diseases from images. The VegNet dataset was used in the study, and the images were divided into training, validation, and test subsets. Data augmentation was applied to the training and validation data, and the test data was evaluated in its raw form. The pre-trained ViT model on ImageNet was refactored to classify four classes (Black Rot, Downy Mildew, Bacterial Spot Rot, and Healthy). The model achieved 99.05% accuracy on the test data and demonstrated high consistency. The results demonstrate that the Vision Transformer architecture is a powerful alternative for plant disease classification.

1. Introduction

Early and accurate detection of plant diseases is critical for maintaining agricultural productivity and reducing crop losses [1]. Leaf diseases, particularly common in vegetable production, both reduce quality and lead to economic losses for producers. Today, deep learning-based image processing methods have become powerful tools that achieve high accuracy in automatically recognizing such diseases [2]. While classical approaches generally utilize Convolutional Neural Networks (CNN), Transformer-based architectures have emerged as an important alternative in image classification problems in recent years [3]. Vision Transformer (ViT) models, in particular, can more effectively represent complex visual details thanks to their ability to directly learn global context relationships through the self-attention mechanism [4]. This study aims to automatically classify diseases using the Vision Transformer (ViT-B/16) architecture on the VegNet dataset containing cauliflower leaf diseases. The dataset includes four different cases (Downy Mildew, Black Rot, Bacterial Spot Rot and No Disease) and was obtained under real field conditions [5]. The model was retrained with a transfer learning approach and high accuracy was achieved on the test set, demonstrating that Transformer-based methods offer a powerful and effective solution for agricultural image analysis.

2. Materials and Methods

In this study, a Vision Transformer-based deep learning approach was applied to automatically classify cauliflower leaf diseases. The VegNet cauliflower disease dataset was used for training and evaluation of the model. The images were processed according to a specific training-validation-testing scheme, and model performance was analyzed. This section details the dataset, preprocessing steps, model architecture, and training process.

2.1. Dataset

The VegNet dataset [5] used in this study consists of four classes of cauliflower leaf diseases (Bacterial Spot Rot, Black Rot, Downy Mildew, and No Disease) and contains a total of 656 original images. Figure 1 shows sample images from the dataset. The dataset was divided into training, validation, and test subsets. The training set consisted of 454 images (123 Bacterial Spot Rot, 67 Black Rot, 120 Downy Mildew, and 144 No Disease), the validation set consisted of 97 images (26 Bacterial Spot Rot, 13 Black Rot, 30 Downy Mildew, and 28 No Disease), and the test set consisted of 105 images (24 Bacterial Spot Rot, 20 Black Rot, 27 Downy Mildew, and 34 No Disease). All images were obtained under real field conditions, and to increase the generalizability of the training process, data augmentation was applied only to the training and validation sets; the test data was preserved in its original form for use in performance evaluation.

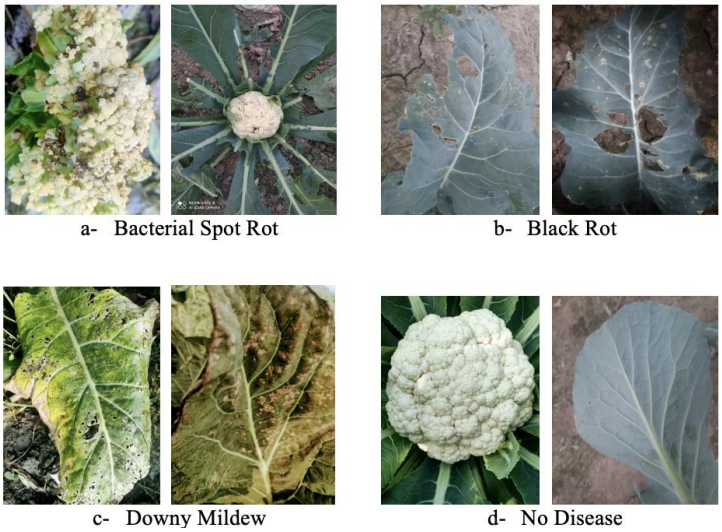

Figure 1 Dataset image

2.2. Preprocessing and Augmentation

To ensure compliance with the input size required by the model, all images in the dataset were rescaled to 224×224 pixels. During the training process, data augmentation was applied only to the training and validation data to increase the generalizability of the model and reduce the risk of overfitting. Random horizontal translation, random rotation within ±15°, and normalization (mean = 0.5, std = 0.5) were used. Only rescaling and normalization were applied to the test set to accurately measure the model's performance on the true distribution. All preprocessing steps were performed using the standard transformation functions of the PyTorch library.

2.3. Vision Transformer Architecture

In this study, the Vision Transformer Base/16 (ViT-B/16) architecture [6], pre-trained on ImageNet, is used as the base classification model. In the ViT-B/16 model, input images are divided into 16×16 pixel patches, which are linearly embedded and transferred to Transformer layers along with positional information. This structure enables global relationships in the image to be learned via a self-attention mechanism. In this study, the classification layer of the pre-trained model is removed and reconstructed with a new fully connected layer suitable for the four classes of the VegNet dataset. Thus, the model is optimized to adapt to the target dataset using a transfer learning approach, and all weights are retrained for this task.

2.4. Training Procedure

The model was trained using the PyTorch deep learning library. The loss function used during the training process was Cross-Entropy Loss, suitable for multi-class problems, and the optimization was carried out using the Adam algorithm. During the training phase, the learning rate was set to 1×10^{-4}, the batch size was set to 16, and the number of epochs was set to All training steps were run on GPU-supported hardware to increase computational efficiency. Throughout the training process, model performance was regularly monitored on the validation set, and hyperparameters were kept constant to ensure consistent model learning on the dataset. At the end of the training process, the best-performing model weights were recorded, and the final evaluation was performed on the test dataset.

3. Results and Discussion

The results obtained in this study demonstrate significant differences and significant performance advantages compared to previous studies conducted on the VegNet dataset. The trained Vision Transformer (ViT-B/16) model achieved 99.05% accuracy on the VegNet test dataset, demonstrating a highly successful performance in classifying cauliflower leaf diseases. Confusion matrix and class-based ROC analyses revealed that the model classified all classes with high discrimination power, with AUC values close to Figure 2 shows confusion matrix.These results demonstrate that, despite the similarities between classes, the ViT architecture minimizes the error rate.The obtained performance significantly exceeds literature [3]. The balanced application of data augmentation and the advantages of transfer learning increased the generalizability of the model and achieved higher accuracy. These findings confirm that the Vision Transformer architecture is a more robust and stable alternative to traditional CNN approaches in agricultural image classification.

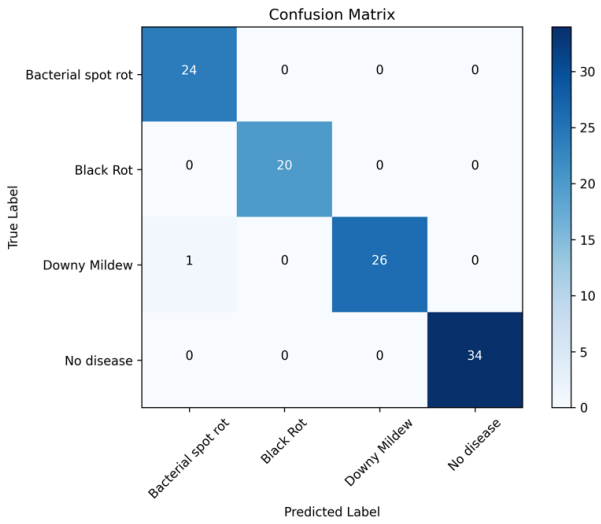

Figure 2 Confusion matrix

4. Conclusion

In this study, a comprehensive evaluation was conducted on the VegNet dataset using the Vision Transformer (ViT-B/16) architecture to classify cauliflower leaf diseases. The model demonstrated a high classification accuracy of 99.05% on the test set and effectively distinguished subtle textural differences between classes. The obtained results exceed the accuracy rates reported by CNN-based models in the original VegNet study, demonstrating that the Transformer architecture offers a more powerful and generalizable alternative in agricultural image analysis. These findings demonstrate that Vision Transformer-based approaches can provide an effective solution for the early detection of plant diseases and can be successfully applied to diverse agricultural datasets in the future.

References

[1] Liu, Z., Li, X. (2024). An improved YOLOv5-based apple leaf disease detection method. Scientific Reports, 14(1), 17508.

[2] Girmaw, D.W., Salau, A.O., Mamo, B.S., Molla, T.L. (2024). A novel deep learning model for cabbage leaf disease detection and classification. Discover Applied Sciences, 6(10), 521.

[3] Arnob, A.S., Kausik, A.K., Islam, Z., Khan, R., Rashid, A.B. (2025). Comparative result analysis of cauliflower disease classification based on deep learning approach VGG16, Inception V3, ResNet, and a custom CNN model. Hybrid Advances, 10, 100440.

[4] Huo, Y., et al. (2023). Vision transformer (ViT)-based applications in image classification. Proceedings of the 2023 IEEE 9th Intl Conference on Big Data Security on Cloud (BigDataSecurity), HPSC and IDS, IEEE.

[5] Sara, U., Rajbongshi, A., Shakil, R., Akter, B., Uddin, M.S. (2022). VegNet: an organized dataset of cauliflower disease for a sustainable agro-based automation system. Data Brief, 43, 108422. https://doi.org/10.1016/j.dib.2022.108422

[6] Appati, J.K., Ziamah, B., Akrofi, H.A., Dodoo, A.A. (2025). SARS detection in chest CT scan images using the bootstrapped ViT-B/16 model. Iran Journal of Computer Science, 8(2), 537–551.

Experimental and Numerical Investigation of the Thermo-Hydraulic Performance of Mini-Channel Graphite Foam and Aluminum Heat Sinks

Zekeriya Kutlu[1], Beytullah İsmet Toprak[1*], Ercan Doğan[1], İsmail Solmaz[1]

[1] Atatürk University, Department of Mechanical Engineering, Erzurum, Türkiye

* *Corresponding author E-mail: bismet.toprak@atauni.edu.tr*

Keywords

Heat sink

Graphite foam

Heat transfer

Mini channel

Numerical study

Abstract

Effective thermal management is crucial for improving the performance and reliability of electronic devices with increasing power densities. In this study, a novel modification approach was proposed by introducing cylindrical mini-channels along the flow direction of block graphite foam material. For comparison, an aluminum heat sink with the same mini-channel configuration was also developed, as aluminum is commonly used in heat transfer applications. Both heat sinks with a mini-channel diameter of 2 mm were numerically investigated. Subsequently, parametric studies were conducted within a Reynolds number (Re) range of 163–1862 using COMSOL Multiphysics by varying the the number of channels (41, 50, and 59). The influence of these parameters on the Nusselt number (Nu), pressure drop (ΔP), and thermal performance factor (η) were systematically evaluated. The results indicate that Nu and ΔP increase with Re for both heat sinks. Increasing the number of channels improves Nu without causing a significant rise in ΔP, resulting in a moderate increase in η. A comparison between aluminum and graphite foam heat sinks reveals that, although the porous structure of graphite foam ensures consistently lower ΔP, Nu values remain comparable due to the balance between its high specific surface area and the high thermal conductivity of aluminum with added surface area from mini-channels.

1. Introduction

Rapid advancements in science and technology have led to increasing performance demands on electronic devices across numerous application domains. As a result, these devices generate significant amounts of heat during operation, and the inability to dissipate this heat efficiently and promptly may adversely affect the performance of electronic components and, in the long term, lead to system failures [1, 2]. Therefore, developing new and innovative thermal management solutions capable of effectively removing heat from electronic devices and dispersing it into the surrounding environment has become essential [3]. Among the widely adopted thermal management strategies, heat sinks play a crucial role in dissipating heat generated by electronic components [4, 5]. Conventional heat sinks commonly employ extended surfaces such as micropins [6, 7], cylindrical fins [8, 9], plate fins [10–12], and triangular fins [13, 14], all of which have been extensively investigated by numerous researchers. As an alternative, open-cell porous materials with high thermal conductivity have attracted considerable attention due to their large surface-area-to-volume ratios and their ability to promote flow mixing, thereby enhancing heat transfer [15, 16], making them promising candidates for high-performance heat sink applications [1, 17].

Another widely explored approach to enhance thermal performance involves the use of porous heat sinks. Among the various porous media, metallic foams constitute a particularly important category, and numerous studies have examined their use as block-type heat sinks. Li et al. [18] numerically analyzed flow and heat transfer in a channel containing staggered porous blocks, demonstrating that the presence of porous blocks significantly improves heat transfer, although at the expense of increased pressure drop—an increase deemed acceptable given the thermal benefits. Leong and Jin [19], in an experimental study investigating the effect of oscillating flow frequency on the thermal performance of aluminum-foam heat sinks with varying pore densities, reported that oscillatory flow substantially enhances heat transfer in metal foams, thereby enabling innovative heat-sink designs. In another study, Jeng and Tzeng [20] numerically evaluated the impingement cooling performance of porous graphite-foam heat sinks. Their findings revealed that graphite foams exhibit approximately 30% lower thermal resistance and two to three times

higher heat-transfer performance compared to conventional plate-fin heat sinks, demonstrating their high potential for electronic cooling applications.

Existing literature highlights that the unique thermophysical properties of graphite foam materials make them highly attractive candidates for various engineering applications. However, due to their relatively low permeability, graphite foams can introduce significant flow resistance when used as block structures within a channel, thereby limiting their applicability in heat-sink designs. To overcome this limitation and minimize pressure drop, the graphite-foam block used in this study was modified by drilling cylindrical mini-channels of 2 mm diameter along the flow direction. For comparative evaluation, an aluminum heat sink—commonly employed in thermal applications—was modelled with the same mini-channel geometry. Within this framework, the thermal performance of graphite-foam and aluminum heat sinks enhanced with circular mini-channels was numerically investigated in COMSOL Multiphysics for Reynolds numbers ranging from 163 to 1862, considering mini-channel count as a key design parameter. This approach aims to increase heat-transfer surface area, reduce pressure drop, and lower overall heat-sink weight, thereby enabling a more efficient thermal management design.

2. Numerical Analysis

In this study, numerical analyses based on the finite element method were carried out using CFD simulations performed with the COMSOL Multiphysics software. The analyses were performed in three-dimensional and steady-state conditions. Before conducting parametric studies with diversified structural properties, a numerically developed model was obtained in the COMSOL Multiphysics.

2.1. 2.1 Description of the problem

In the system using air as the cooling fluid, a constant heat flux was applied to the bottom surface of the test section. The side and upper surfaces were thermally insulated for modeling purposes. It was assumed that the forced air flow entered the test section with a uniform distribution of constant velocity and temperature under fully developed conditions, passing through the graphite foam and aluminum heat sinks before exiting the test section. Thus, the heat generated beneath the test plate within the horizontal channel is dissipated to the external environment at the channel's outlet through the cooling fluid.

2.1.1. 2.2 Numerical model

The mathematical model of the test section of the system was developed in three dimensions using the COMSOL Multiphysics software. The 3D representations and front view of the created CFD models for the graphite foam and aluminum are provided in Figure 1.

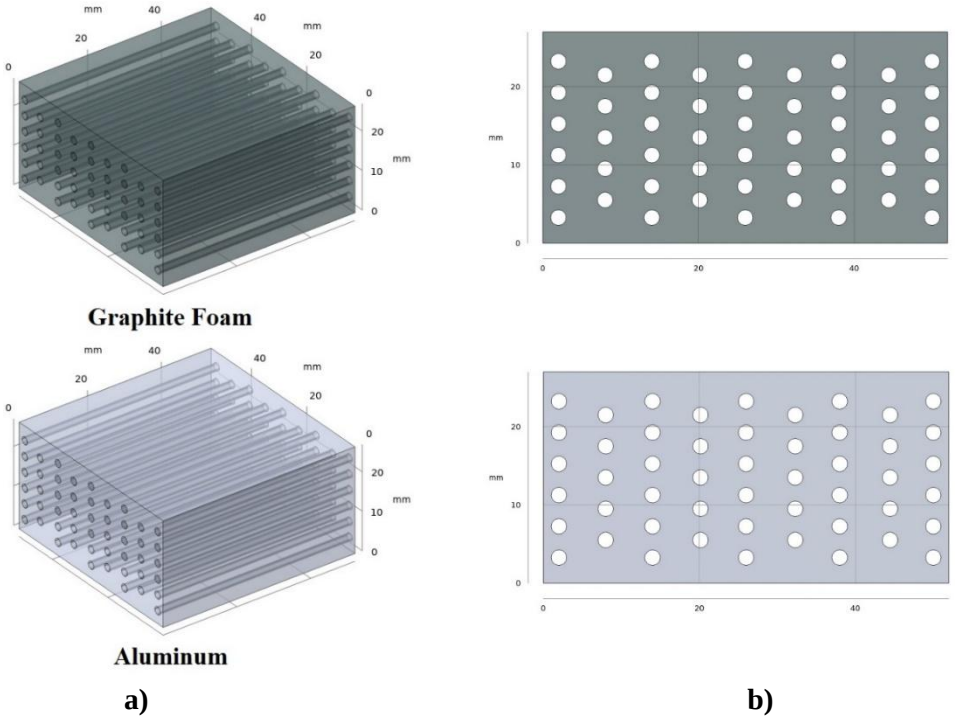

Figure 1 a) 3D view and b) Front view of the modeled heat sinks.

In the analyses for both heat sink conducted, the "Heat Transfer in Solids and Fluids" heat transfer model was utilized. In the analyses for graphite foam heat sink, "Free and Porous Media Flow" flow model, which solves the Navier-Stokes equations for fluid regions without solid materials and the Brinkman equation for porous domain, in conjunction with the continuity equation. The coupling between the heat transfer and fluid flow was simulated using the "Conjugate Heat Transfer" module with "Laminar Flow" multiphysics interface when analyzing aluminum heat sink. Since the flow occurs inside the mini channels, it was modeled as laminar because Re number is less than Additionally, the "Nonisothermal Flow Multiphysics" module was incorporated into the fluid flow and heat transfer physics modules for both heat sinks, allowing for their simultaneous operation.

The following assumptions were made in the simulations conducted:

It was assumed that there is a steady-state local thermal equilibrium (LTE) between the aluminum foam and the cooling air at each point when analyzing graphite foam heat sink.

The porosity value for the open-cell graphite foam was considered constant and uniform in dimensional terms.

The flow was assumed to be steady, laminar, and incompressible.

Heat transfer due to radiation and natural convection, viscous dissipation, and work done by pressure changes were neglected.

In all analyses, the thermophysical properties of the solid and gas phases were assumed to be constant.

The conservation equations for mass, momentum, and energy for the solid, fluid, and porous domains are as follows;

The continuity equation is expressed by Eq. (1).

$$\nabla.(u) = 0 \tag{1}$$

The momentum and energy equations for laminar free flow are given by Eqs. (2) and (3), respectively.

$$\rho(u.\nabla)u = \nabla.[-pI + \mu\nabla u] + F \tag{2}$$

$$\left(\rho c_p\right)_f u.\nabla T = \nabla.\left(k_f \nabla T\right) \tag{3}$$

The momentum and energy equations for the porous domain are expressed by Eqs. (4) and (5), respectively.

$$\frac{\rho_f}{\varepsilon^2}(u.\nabla)u = \nabla.\left[-pI + \frac{\mu}{\varepsilon}\nabla u\right] - \left(\frac{\mu}{K} + \beta_F|u|\right)u + F \tag{4}$$

$$\left(\rho c_p\right)_f u.\nabla T = \nabla.\left(k_{eff} \nabla T\right) \tag{5}$$

where, $k_{eff} = (1-\varepsilon)k_s + \varepsilon k_f$

2.2. Boundary conditions

The boundary conditions accepted during the numerical analyses are specified in Table The inlet air flow was maintained at a constant temperature (T = 25 °C), while the velocity value was varied in the range of U_0= 0.14-1.6 m/s for the analysis.

Table 1 The considered boundary conditions.

Boundary (*x, y, z*)	Condition
Inlet (*0, y, 0:t*)	Insulated
Inlet (*0, y, t:H*)	Inflow (T=25 ^{o}C and P=1 atm, U= 0.14- 1.6 m/s)
Right (*x, 0, z*)	Insulated and No-slip
Left (*x, W, z*)	Insulated and No-slip
Top (*x, y, H*)	Insulated and No-slip
Bottom (*x, y, t*)	No-slip
Bottom (*x, y, 0*)	Constant heat flux (8000 W/m^2)
Outlet (*L, y, 0:t*)	Insulated
Outlet (*L, y, t:H*)	Outflow (P=0)

2.3. Parametric analysis

To conduct parametric numerical analyses, the heat transfer and flow characteristics of the for both graphite foam and solid aluminum heat sinks were numerically investigated independently for various Reynolds numbers (*Re*) with different mini channel number (41, 50, 59), constant mini channel diameters (2 mm) and constant heat sink heights

(27 mm). The numerical analyses were performed for Re_{Dh} in the range of 163 to 1862 under a constant heat flux of 8000 W/m². The base conditions examined for each of the two heat sinks are shown in Figure 2.

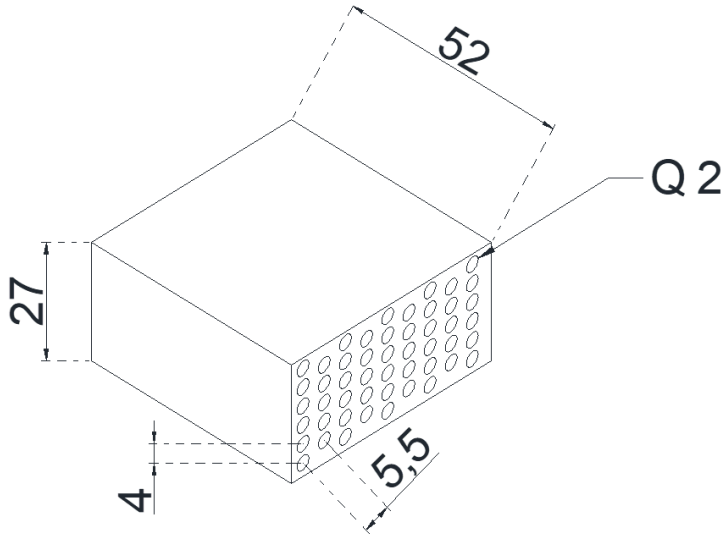

Figure 2 Isometric technical drawing of an artificial aluminum heat sink.

During the numerical analyses conducted, while the number of mini channels were changed, the distance between mini channels and their arrangement remained unchanged. This approach allowed for the examination of how different Mini Channel Number affect heat transfer and pressure drop while using the same mini channel arrangement. Finally, the physical properties of graphite foam, such as permeability, PPI and porosity values are $7.9243*10^{-10}$, 20 and 0.75, respectively.

2.4. Data reduction and uncertainty analysis

In the analyses conducted, the Reynolds number defined based on the hydraulic diameter (Re_{Dh}) was calculated as follows: $D_H = 2*W*H/(W+H)$ ρ_f, U ve μ_f

$$Re = \frac{\rho_f U D_H}{\mu_f} \tag{6}$$

Here, ρ_f, U and μ_f represent the density, average flow velocity, and dynamic viscosity of the air fluid, respectively. The hydraulic diameter is calculated using the formula: $D_H = 2*W*H/(W+H)$. The average Nusselt number used in the numerical analyses was calculated along the test section as follows:

$$Nu = \frac{q_{net} D_H}{(T_w - T_i) k_f} \tag{7}$$

Here, T_i represents the inlet temperature of the fluid, while T_w is the average temperature of the bottom surface, k_f is the thermal conductivity of the air.

To evaluate the enhancement of heat transfer at the surface within the channel, it is important to analyze the Thermal Performance Factor (TEF) which uses both Nu and ΔP.

$$\eta = \frac{Nu/Nu_o}{(\Delta P/\Delta P_0)^{1/3}} \tag{8}$$

It is calculated using the formula, where subscript of '0' indicates the base condition considered as the reference.

2.5. Mesh independency analysis

A mesh independence test was carried out to ensure the reliability of the simulation results. In this study, the tetra hedral geometry mesh generation of COMSOL Multiphysics v5.4 was utilized to create the numerical model's mesh structure. To evaluate the effect of mesh density on the average Nu, simulations were run with sample meshes of coarser, coarse, normal, and fine solution densities for sample of solid aluminum heat sink with 2 mm diameter holes. In the conducted trials, analyses were performed at the smallest (163) and largest (1862) Re values with domain

element number of 1195399, 2123207, 3557550, 4160210, respectively, and the results of the mesh independence tests are listed in Table

Table 2 Results of the mesh independence test.

		Re_{Dh}=163		Re_{Dh}=1862		
Mesh Size	**No. of D. E.**	**Nu**	**E_{Nu} (%)**	**Nu**	**E_{Nu} (%)**	**Computation Time**
Coarser	1195399	103.58	-	1187.3	-	17 min
Coarse	2123207	98.259	5.4153	1245.31	4.65828	21 min
Normal	3557550	93.224	5.401	1032.52	20.6088	24 min
Fine	4160210	93.24	0.0172	1130.75	8.68715	47 min

Based on the conducted analyses, the lowest error value of 0.0172% for Nu at the lowest Re_{Dh} value was considered acceptable for CFD analyses, especially when considering the analysis durations. At the highest Re_{Dh} value, an error value consistent with this situation was obtained for the same mesh density. From this perspective, it was anticipated that using a normal density mesh would be sufficient for the numerical accuracy of the simulations.

3. Results and Discussion

3.1. Effect of Number of Mini Channel on Heat Transfer and Pressure Drop

The effects of the number of drilled mini-channels on the heat-removal and pressure-drop characteristics of the heat sinks were numerically investigated while keeping the heat-sink length and height constant. The resulting findings are presented in Figures 3 and 4.

As shown in Figure 3, for both heat-sink models analyzed, an increase in Reynolds number (Re) leads to an increase in both the Nusselt number (Nu) and the pressure drop (ΔP). For a fixed number of mini-channels, increasing flow velocity results in a higher Re, which strengthens convective heat transfer and thereby increases the Nu number. At higher Re values, the mixing behavior of the flow is enhanced, improving the coolant's heat-removal capability. However, the increase in velocity also intensifies the hydrodynamic resistance encountered by the fluid as it passes through the mini-channels or the porous structure, giving rise to larger pressure drops (ΔP). Thus, an increase in Reynolds number simultaneously enhances heat transfer while also increasing pressure losses.

Furthermore, Figure 3 clearly shows that increasing the number of mini-channels leads to higher Nu values for both heat sinks, whereas the corresponding ΔP values exhibit no significant variation. For the highest mini-channel count tested (N = 59), the Nu value increases by up to 1.54 and 1.53 times for the graphite-foam and aluminum heat sinks, respectively, compared with the lowest channel count (N = 41). This behavior can be explained as follows: when Re—defined based on mini-channel hydraulic diameter—is kept constant within the range of 163–1862, increasing the number of mini-channels raises the overall mass flow rate. Consequently, the air velocity within the flow domain increases, strengthening convective heat transfer and resulting in higher Nu numbers. However, because the number of channels does not affect the velocity within each individual mini-channel, no notable change in pressure drop is observed.

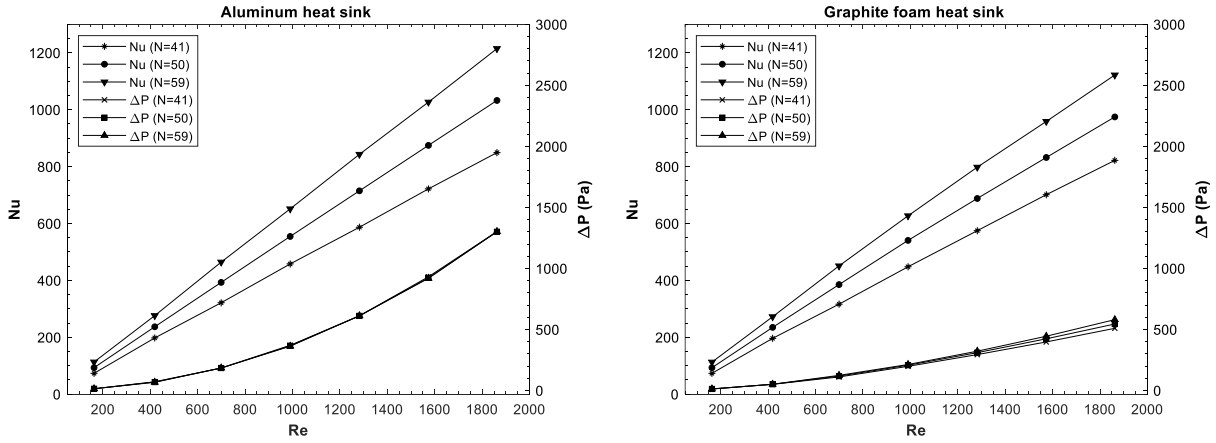

Figure 3 The variation of Nu and ΔP with ReDh for various mini channel counts of the heat sinks

When comparing graphite-foam and aluminum heat sinks under identical Re values and identical mini-channel counts, the graphite-foam configuration exhibits lower pressure losses due to its porous nature. Nevertheless, no substantial

difference in Nu is observed between the two materials. The Nu values obtained for both heat sinks with the same number of mini-channels are nearly identical, with the aluminum heat sink exhibiting at most a 1.03-fold higher Nu. This outcome can be attributed to the balancing of two competing effects: the high specific surface area of the graphite foam, which enhances heat transfer, and the high thermal conductivity of aluminum combined with the increased surface area provided by the drilled mini-channels. As a result, the distinct heat-transfer advantages of the two materials counteract each other, leading to comparable Nu values.

Figure 4 illustrates the influence of the number of drilled mini-channels on the thermal performance factor (η) of both graphite-foam and aluminum heat sinks across the examined Re range. As evident from the graph, η—which depends directly on both Nu and ΔP—increases with mini-channel count (N = 41, 50, and 59) at a fixed Reynolds number. This trend primarily stems from the enhancement in heat transfer, and consequently in Nu, as the number of mini-channels increases for both heat-sink structures. However, when comparing identical mini-channel counts, no significant change in η is observed with increasing Re for either material. This is because, with rising Re, the relative rates of increase in Nu and ΔP (both used in calculating η) remain nearly identical. In the configurations containing 59 and 41 channels, the change ratios of Nu and ΔP relative to the reference case (50 channels) are very similar, resulting in negligible variation in η despite increasing Reynolds number.

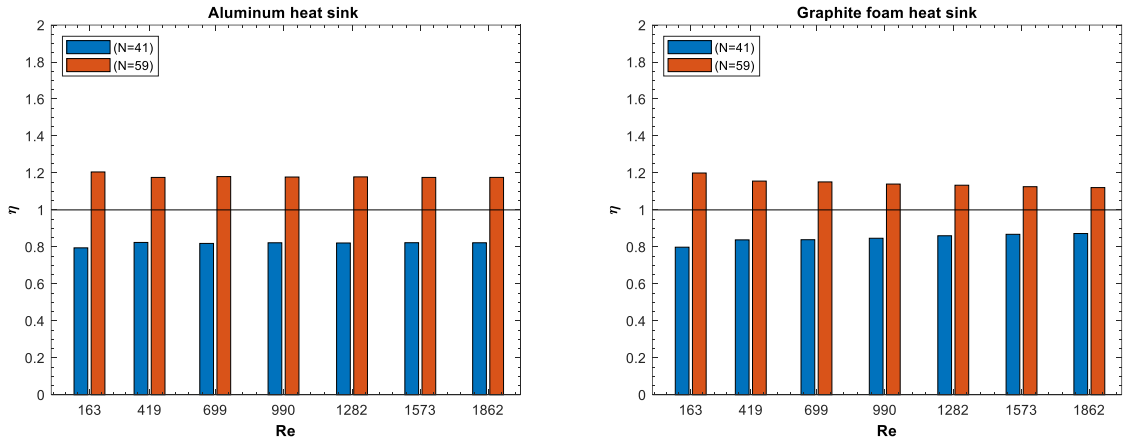

Figure 4 The variation of η with ReDh for various mini channel counts of the heat sinks

4. Conclusions

In this study, the thermal and hydraulic performance of modified heat sinks modelled by introducing cylindrical mini-channels with a diameter of 2 mm into block graphite foam and aluminum materials was investigated numerically. To ensure a fair comparison, both materials were subjected to identical channel modifications, and their thermo-hydraulic characteristics were analyzed under a range of Reynolds numbers from 163 to The parametric study numerically considered the effects of number of mini channels on thermal performance, pressure drop. The key findings of this study can be summarized as follows:

As the Reynolds number increased, both the Nusselt number (Nu) and the pressure drop (ΔP) increased for aluminum and graphite foam heat sinks.

Increasing the number of mini-channels resulted in higher Nu for both samples. For the maximum channel number (N = 59) compared to the minimum (N = 41), Nu increased up to 1.54 times for the graphite foam and 1.53 times for the aluminum heat sink. At constant Re values, since the flow velocity inside each channel remained nearly constant, ΔP showed no significant variation with channel number. As a result, η also improved with channel number, though less prominently than with channel diameter.

When comparing aluminum and graphite foam, the ΔP values were consistently lower in graphite foam due to its porous structure. However, the Nu values were relatively similar for both materials under the same conditions. This behavior can be explained by the compensation of advantages: the high specific surface area of graphite foam promoting heat transfer versus the high thermal conductivity and increased surface area of aluminum with mini-channels. Consequently, both materials exhibited comparable Nu values despite their different mechanisms of thermal enhancement.

References

[1] F. T. Bayrak, B. İ. Toprak, İ. Solmaz, and Ö. Bayer, "The influence of slotted solid cylindrical fin with aluminum foam insert on the thermal and hydraulic characteristics of air-cooled pin-fin heat sink," Int. Commun. Heat Mass Transf., vol. 162, no. January, 2025, doi: 10.1016/j.icheatmasstransfer.2025.108595.

[2] X. Zhang, Z. Ji, J. Wang, and X. Lv, "Research progress on structural optimization design of microchannel heat sinks applied to electronic devices," Appl. Therm. Eng., vol. 235, no. August, p. 121294, 2023, doi: 10.1016/j.applthermaleng.2023.121294.

[3] J. Wang, H. Kong, Y. Xu, and J. Wu, "Experimental investigation of heat transfer and flow characteristics in finned copper foam heat sinks subjected to jet impingement cooling," Appl. Energy, vol. 241, no. January, pp. 433–443, 2019, doi: 10.1016/j.apenergy.2019.03.040.

[4] M. Wong, I. Owen, C. J. Sutcliffe, and A. Puri, "Convective heat transfer and pressure losses across novel heat sinks fabricated by Selective Laser Melting," Int. J. Heat Mass Transf., vol. 52, no. 1–2, pp. 281–288, 2009, doi: 10.1016/j.ijheatmasstransfer.2008.06.002.

[5] H. GHALY, K. YAKUT, and M. H. OSTA, "Experimental Investigation of Cube Cavity Synthetic Jet Performance on Heat Sinks," Heat Transf. Res., vol. 56, no. 18, pp. 21–39, 2025, doi: 10.1615/heattransres.2025058034.

[6] K. Kim et al., "A machine learning approach for predicting heat transfer characteristics in micro-pin fin heat sinks," Int. J. Heat Mass Transf., vol. 194, 2022, doi: 10.1016/j.ijheatmasstransfer.2022.123087.

[7] D. E. Metzger, C. S. Fan, and S. W. Haley, "Effects of Pin Shape and Array Orientation on Heat Transfer and Pressure Loss in Pin Fin Arrays," [Online]. Available: http://www.asme.org/about-asme/terms-of-use.

[8] L. Chen, A. Yang, Z. Xie, and F. Sun, "Constructal entropy generation rate minimization for cylindrical pin-fin heat sinks," Int. J. Therm. Sci., vol. 111, pp. 168–174, 2017, doi: 10.1016/j.ijthermalsci.2016.08.017.

[9] M. Ismail, "Experimental and numerical analysis of heat sink using various patterns of cylindrical pin-fins," Int. J. Thermofluids, vol. 23, no. June, p. 100737, 2024, doi: 10.1016/j.ijft.2024.100737.

[10] X. Yu, J. Feng, Q. Feng, and Q. Wang, "Development of a plate-pin fin heat sink and its performance comparisons with a plate fin heat sink," Appl. Therm. Eng., vol. 25, no. 2–3, pp. 173–182, 2005, doi: 10.1016/j.applthermaleng.2004.06.016.

[11] P. Kamma, K. Loksupapaiboon, J. Phromjan, M. Promtong, and C. Suvanjumrat, "Optimization of plate-fin heat sink configurations for enhanced thermal performance and manufacturability," Case Stud. Therm. Eng., vol. 73, no. May, p. 106529, 2025, doi: 10.1016/j.csite.2025.106529.

[12] M. H. Osta, K. Yakut, and H. Köksal, "Experimental performance assessment of two-stage thermoelectric system in a closed-cycle drying process," Appl. Therm. Eng., vol. 278, no. April, 2025, doi: 10.1016/j.applthermaleng.2025.127451.

[13] D. Hithaish, V. Saravanan, C. K. Umesh, and K. N. Seetharamu, "Thermal management of Electronics: Numerical investigation of triangular finned heat sink," Therm. Sci. Eng. Prog., vol. 30, no. May 2021, p. 101246, 2022, doi: 10.1016/j.tsep.2022.101246.

[14] V. Saravanan, D. Hithaish, C. K. Umesh, and K. N. Seetharamu, "Numerical investigation of thermo-hydrodynamic performance of triangular pin fin heat sink using nano-fluids," Therm. Sci. Eng. Prog., vol. 21, no. November 2020, p. 100768, 2021, doi: 10.1016/j.tsep.2020.100768.

[15] G. Gürüf, İ. Solmuş, K. Bilen, and Ö. Bayer, "Experimental based numerical approach for determination of volumetric heat transfer coefficients of modified graphite foams," Appl. Therm. Eng., vol. 174, no. April, 2020, doi: 10.1016/j.applthermaleng.2020.115310.

[16] I. Kurtbas and N. Celik, "Experimental investigation of forced and mixed convection heat transfer in a foam-filled horizontal rectangular channel," Int. J. Heat Mass Transf., vol. 52, no. 5–6, pp. 1313–1325, Feb. 2009, doi: 10.1016/j.ijheatmasstransfer.2008.07.050.

[17] K. S. Al-Athel, "A computational methodology for assessing the thermal behavior of metal foam heat sinks," Appl. Therm. Eng., vol. 111, pp. 884–893, 2017, doi: 10.1016/j.applthermaleng.2016.10.014.

[18] H. Y. Li, K. C. Leong, L. W. Jin, and J. C. Chai, "Analysis of fluid flow and heat transfer in a channel with staggered porous blocks," Int. J. Therm. Sci., vol. 49, no. 6, pp. 950–962, 2010, doi: 10.1016/j.ijthermalsci.2010.01.006.

[19] K. C. Leong and L. W. Jin, "Effect of oscillatory frequency on heat transfer in metal foam heat sinks of various pore densities," Int. J. Heat Mass Transf., vol. 49, no. 3–4, pp. 671–681, 2006, doi: 10.1016/j.ijheatmasstransfer.2005.08.015.

[20] T. M. Jeng and S. C. Tzeng, "Numerical study of confined slot jet impinging on porous metallic foam heat sink," Int. J. Heat Mass Transf., vol. 48, no. 23–24, pp. 4685–4694, 2005, doi: 10.1016/j.ijheatmasstransfer.2005.06.032.

Performance Assessment of Thermoelectric Cooling Applied to Photovoltaic Panels

Muhammet Harun Osta[1,*]

[1] Department of Mechanical Engineering, Faculty of Engineering, Atatürk University, Erzurum, Türkiye

* *Corresponding author E-mail: harun.osta@atauni.edu.tr*

Keywords

Thermoelectric cooling

Photovoltaic panel

Heat sink

PV Power

Wasted heat

Abstract

This study experimentally investigates the performance of a finned thermoelectric cooling structure designed to mitigate power losses in photovoltaic (PV) panels caused by temperature rise, as well as the effect of forced airflow applied to enhance heat dissipation from its hot side. Under standard test conditions, PV panels generate maximum power at a cell temperature of 25 °C, and any increase beyond this value leads to power degradation. Accordingly, the effects of the finned thermoelectric cooling system on panel temperature and power output were evaluated over 18-minute test periods. The results indicate that cooling provided by the thermoelectric module and fins can only delay the onset of power loss, while the addition of forced airflow over the fins offers a limited further improvement by enhancing heat rejection. Nevertheless, the overall cooling capacity remained insufficient to fully counteract the thermal load on the PV panel, and the power loss could not be completely prevented. These findings demonstrate that thermoelectric-based cooling alone is inadequate for PV applications and highlight the need for further optimization of fin geometry and airflow conditions.

1. Introduction

Electric energy plays a critical role in modern societies, supporting applications that range from residential use to industrial operations and advanced technological systems [1]. Rising global energy demand and increasing environmental concerns make the development of sustainable production technologies essential, and photovoltaic (PV) systems have become one of the most prominent renewable energy solutions [2, 3]. The performance of PV panels, which convert solar radiation directly into electricity, is highly sensitive to operating temperature [4, 5]. As the cell temperature increases, the electrical resistance of semiconductor materials rises, leading to efficiency losses and accelerated material degradation. This situation negatively affects the electrical output of the panel. To address these thermal challenges, a wide variety of cooling strategies have been proposed in the literature. Passive techniques such as heat sinks and phase change materials are commonly used, while active cooling methods that rely on forced air or liquid flow have also been widely implemented [6]. Among the active methods, thermoelectric cooling (TEC) attracts attention because it operates in a solid state, contains no moving components, has a compact structure, and is capable of providing both cooling and electricity generation through the Seebeck effect. When an electrical current is supplied, TEC modules create a temperature difference between their two sides, allowing heat on the PV panel surface to be transferred to the surroundings [7]. Experimental studies have shown that integrating thermoelectric cooling structures into PV panels can reduce operating temperature, thereby improving power output and the overall stability of the system. Building on these findings, the present study examines the performance of a hybrid cooling approach in which thermoelectric modules are combined with finned heat sinks and forced airflow applied at two different air flow rates. The effects of this finned TEC structure and its airflow supported heat dissipation on power reduction in a PV panel were evaluated through experimental tests conducted over an eighteen minute period.

2. Materials and Methods

In this study, a thermoelectric (TE) based cooling structure was designed and experimentally tested to reduce the temperature rise on a photovoltaic panel. The system incorporates TE modules together with finned heat sinks and forced airflow supplied at two different volumetric flow rates. The experimental setup consists of fifty-four TEC1-12706 modules connected in series and mounted on the rear surface of the PV panel, with thermal paste applied between the modules and the fins to ensure effective heat transfer. Forced airflow of 2.5 and 5 cubic meters per hour was directed across the fins to enhance heat removal. Solar irradiation was generated in a controlled laboratory

environment using five halogen lamps rated at 500 watts each, and the irradiation intensity was measured with a pyranometer. The temperatures on the rear side of the PV panel were recorded using five thermocouples, while electrical power data were collected with a PCE-PVA 100 power analyzer. All temperature, irradiation and electrical measurements were gathered and processed through a data logger. To evaluate the cooling performance, the experiments were conducted over an eighteen minute period, and the temporal variation of PV power output was compared for the configurations involving TE modules with fins and TE modules with fins combined with forced airflow.

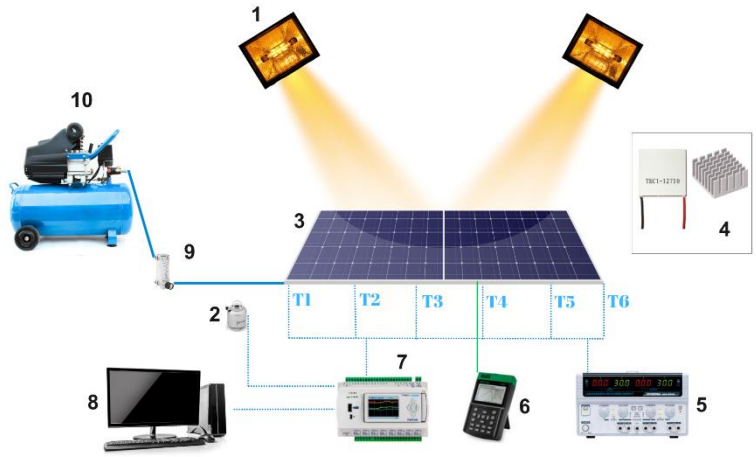

Figure 1. Schematic diagram of the experimental setup

Figure 1 provides a schematic representation of the experimental setup, where the main components are labeled as follows: (1) halogen lamps, (2) pyranometer, (3) photovoltaic panel, (4) thermoelectric modules with finned heat sinks, (5) power supply, (6) power analyzer, (7) data logger, (8) computer, (9) airflow meter and (10) compressor.

3. Results and Discussion

In this study, three different test conditions were comparatively examined to reduce the power loss associated with the rise in operating temperature of a photovoltaic panel. These conditions include a baseline case without cooling, a configuration using TEC modules combined with finned heat sinks, and a configuration using TEC modules supplied with twelve volts together with forced airflow applied over the fins at two volumetric flow rates of 2.5 and 5 cubic meters per hour. All experiments were carried out for eighteen minutes, during which the panel temperature and PV power output were recorded simultaneously. In the first test, where no cooling was applied, the PV panel temperature increased from twenty five degrees Celsius to eighty degrees Celsius, and the power output decreased steadily as a direct consequence of this temperature rise.

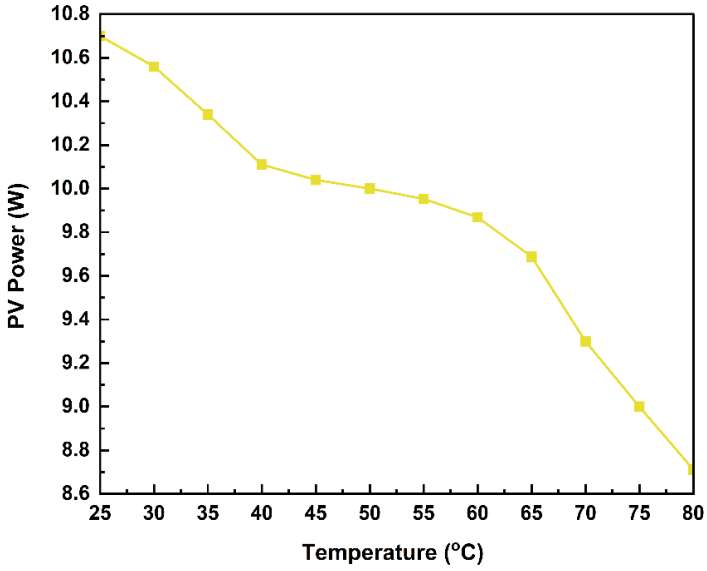

Figure 2. Temperature dependent variation of PV panel power output under the no cooling condition

Figure 2 shows that power generation decreases markedly as the PV panel temperature increases, with a noticeably sharper decline occurring at temperatures above sixty-five degrees Celsius. This trend clearly illustrates the high sensitivity of PV panels to temperature rise. In the second test, the thermoelectric modules were operated together with finned heat sinks at voltage levels of five, eight and twelve volts. As the applied voltage increased, the cooling effect became stronger, although the panel temperature continued to rise over time.

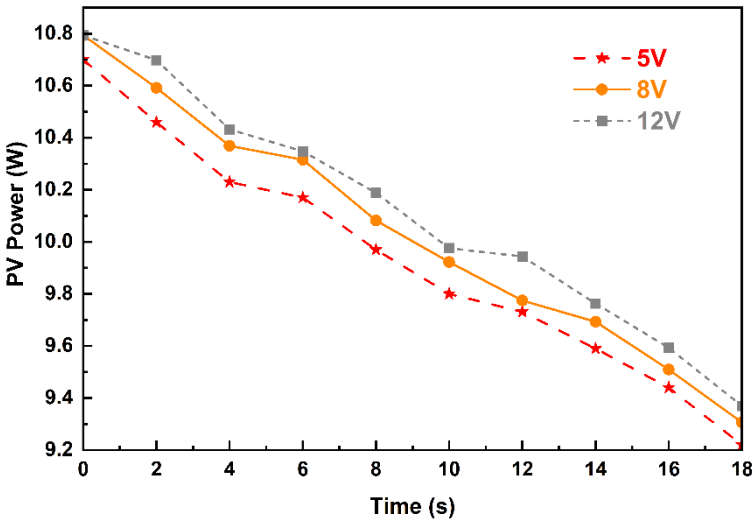

Figure 3. Time dependent variation of PV power output under finned thermoelectric cooling operated at voltage levels of five, eight and twelve volts

Figure 3 presents the time dependent variation of PV power output for three different voltage levels. The graph clearly shows that the power reduction curve under the twelve-volt condition decreases more slowly compared with the other two voltage levels. Nevertheless, the increase in panel temperature could not be fully prevented, and the loss in power was only delayed. These findings indicate that although the finned thermoelectric cooling structure contributes to mitigating power degradation, it is not sufficient on its own to maintain the panel at a stable operating temperature. In the third test, forced airflow at volumetric flow rates of 2.5 and 5 cubic meters per hour was applied over the finned structure while the thermoelectric modules operated at twelve volts. The aim was to enhance heat dissipation through the fins and thereby strengthen the cooling effect provided by the thermoelectric system.

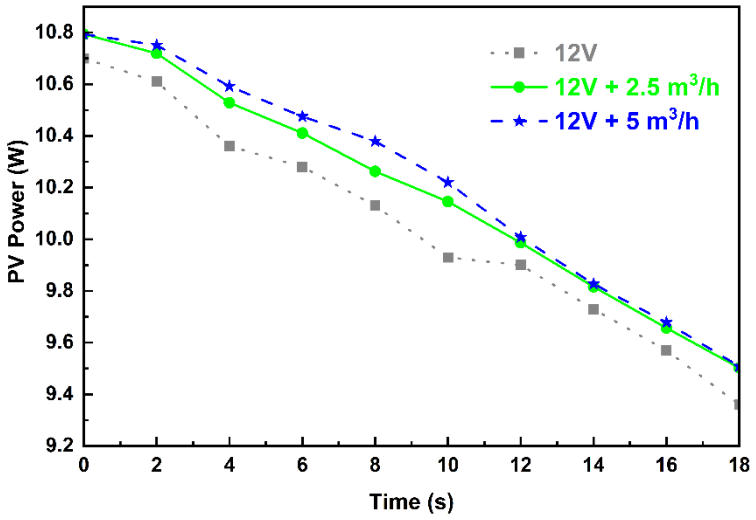

Figure 4. Effect of different airflow rates of 2.5 and 5 cubic meters per hour on the PV panel power output under finned cooling driven by a twelve-volt thermoelectric module

Figure 4 illustrates the temporal variation of PV panel power output and shows that forced airflow at both flow rates delays the power reduction to a certain extent. As the airflow rate increases, the enhancement in heat dissipation becomes more evident, leading to a slower decline in the power curve. However, even at the highest flow rate, the power loss could not be fully prevented, and the system was unable to sufficiently suppress the rise in panel temperature. In addition, the electrical generation obtained from the thermoelectric modules remained at very low levels in all tests, providing no meaningful contribution to overall system performance. These findings indicate that

although finned TE cooling and airflow assisted operation offer the greatest improvement compared with the no cooling condition, they remain insufficient to fully mitigate the substantial thermal load on the PV panel. It is therefore considered that system performance may be enhanced through more advanced fin geometries, optimized airflow channels and the use of higher efficiency thermoelectric modules.

4. Conclusion

In this study, thermoelectric modules, finned heat sinks and forced airflow were evaluated together to reduce the power loss caused by temperature rise in photovoltaic panels. The main findings obtained from the experiments are summarized as follows:

In the absence of cooling, the PV panel temperature increased from twenty five degrees Celsius to eighty degrees Celsius, resulting in a pronounced reduction in power output.

The finned TE cooling structure did not fully prevent power loss, although it delayed the decline to a certain extent.

Increasing the voltage supplied to the TE modules, particularly the twelve volt condition, enhanced the cooling effect but was still insufficient to keep the panel temperature within safe operating limits.

Forced airflow applied across the fins at flow rates of 2.5 and 5 cubic meters per hour improved heat dissipation and produced a slower decrease in the power output curve.

Even at the highest airflow rate, the rise in panel temperature could not be fully controlled and the power reduction continued.

Overall, the results show that thermoelectric based cooling is effective in delaying PV power degradation but remains insufficient to maintain a stable panel temperature under high thermal loads. For future work, the design of more advanced fin geometries, optimization of airflow channels, integration of thermoelectric modules with higher coefficients of performance and the implementation of a more comprehensive thermal management strategy are recommended.

References

[1] H. Ghaly, K. Yakut, and M. H. Osta, “EXPERIMENTAL INVESTIGATION OF CUBE CAVITY SYNTHETIC JET PERFORMANCE ON HEAT SINKS,” Heat Transf Res, vol. 56, no. 18, 2025, doi: 10.1615/HEATTRANSRES.2025058034.

[2] G. Deepak, K. Aggarwal, N. Dineshbabu, R. Sowndharya, B. Manimaran, and B. J. Job Karuna Sagar, “Thermodynamic analysis of a novel concentrated solar power plant with integrated thermal energy storage,” Thermal Science and Engineering Progress, vol. 56, Dec. 2024, doi: 10.1016/j.tsep.2024.103055.

[3] A. Mwesigye and İ. H. Yılmaz, “Thermal and thermodynamic optimization of the performance of a large aperture width parabolic trough solar collector using gaseous and supercritical CO2 as heat transfer fluids,” Thermal Science and Engineering Progress, vol. 37, Jan. 2023, doi: 10.1016/j.tsep.2022.101543.

[4] J. G. Hernandez-Perez, J. G. Carrillo, A. Bassam, M. Flota-Banuelos, and L. D. Patino-Lopez, “A new passive PV heatsink design to reduce efficiency losses: A computational and experimental evaluation,” Renew Energy, vol. 147, pp. 1209–1220, Mar. 2020, doi: 10.1016/J.RENENE.2019.09.088.

[5] M. H. Osta and K. Yakut, “EXPERIMENTAL AND NUMERICAL ANALYSIS OF SPRAY COOLING IN PHOTOVOLTAIC SYSTEMS,” Heat Transf Res, vol. 56, no. 12, pp. 81–94, 2025, doi: 10.1615/HEATTRANSRES.

[6] I. O. Harmailil, S. M. Sultan, C. P. Tso, A. Fudholi, M. Mohammad, and A. Ibrahim, “A review on recent photovoltaic module cooling techniques: Types and assessment methods,” Results in Engineering, vol. 22, Jun. 2024, doi: 10.1016/J.RINENG.2024.102225.

[7] M. H. Osta, K. Yakut, and H. Köksal, “Experimental performance assessment of two-stage thermoelectric system in a closed-cycle drying process,” Appl Therm Eng, p. 127451, Jul. 2025, doi: 10.1016/j.applthermaleng.2025.127451.

Investigation of Erzurum Ilıca District Liquefaction Potential With Different Methods

Hamit Çakıcı [1*], Koray Babadan[2]

[1] Department of Architecture and Urban Planning, Pasinler Vocational School, Ataturk University, Erzurum, Türkiye
[2] Graduate Student

* *Corresponding author E-mail: hamitcakici@atauni.edu.tr*

Keywords

SPT

Consistency Limits Liquefaction

Liquefaction Potential

Erzurum

Abstract

Soil liquefaction is the sudden loss of strength and stiffness in water-saturated, loose, and cohesionless (non-clayey) granular soils (especially sandy and silty soils) due to cyclic dynamic loading (vibrations) during an earthquake. As a result, the soil, instead of behaving like a solid, temporarily becomes fluid, like a viscous liquid. When liquefaction occurs, the soil loses its bearing capacity, causing foundations to sink, tilt, or topple. Permanent deformations such as sand volcanoes, horizontal spreading (lateral spreading), and excessive settlement occur on the ground surface. Within the scope of the thesis study, it was aimed to determine the liquefaction potential to be obtained as a result of examining the liquefaction potential of Erzurum Ilıca District with the methods given by Iwasaki et al. and Sönmez and Gökçeoğlu. In the study, Standard Penetration Test (SPT) was performed in the boreholes drilled in the field. Consistency limits, natural and saturated unit volume weight, sieve analysis and hydrometer tests were carried out in the laboratory on the samples taken from the research pits. Using data obtained from field and laboratory experiments, Iwasaki et al. and Sönmez and Gökçeoğlu the liquefaction potential was examined. As a result of field and laboratory tests, the average values were SPT-N 12.3, Natural unit volume weight 11.53 (kN⁄m^3), Saturated unit volume weight 12.70 (kN⁄m^3), Plasticity Index 23.63, Clay Content % 20.13, fine grain content was determined to be 75.9%. Depending on these values, liquefaction potential analyzes were made according to Iwasaki et al. and Sönmez-Gökçeoğlu. As a result of the field and laboratory studies, it was determined that liquefaction was expected in SK-1 and SK-5, while the liquefaction potential was very low in SK-2, SK-3, SK-4 and SK-6.

1. Introduction

Earthquake hazards, particularly in loose, water-saturated sandy soils, carry the risk of soil liquefaction. Liquefaction manifests itself during earthquakes when increased pore water pressure in granular soils causes a temporary decrease in soil strength and a fluid-like behavior [1]. This can lead to serious engineering problems such as settlement, lateral displacement, or lateral spreading of building foundations.

Assessing soil liquefaction is a critical engineering issue. Traditional analysis methods include stress-based liquefaction analyses, and these methods are also included in current regulations. For example, Dağdeviren [2] discusses the use of stress-based analyses and soil improvement strategies within the scope of the New Turkish Building Earthquake Code [3].

The controlling factors affecting liquefaction span a wide spectrum. In a study by Durmaz and Soyaslan [4], the role of parameters such as groundwater level, soil particle structure, and density on liquefaction mechanics was examined in detail, and the effects of these parameters on potential deformations (settlement, lateral slide, etc.) were analyzed. Furthermore, field studies demonstrate that liquefaction is important not only in theory but also in practice. For example, geotechnical investigations conducted in the Düzce city center determined that the groundwater level was very close to the surface and the ground had an alluvial and sandy structure. Liquefaction potential maps were created based on possible earthquake scenarios through Liquefaction Potential Index (LPI) and Liquefaction Severity Index (LSI) analyses conducted under these conditions [5]. Recently, new theoretical approaches have emerged in the literature that go beyond the traditional pore water pressure increase mechanism. Clément, Toussaint, and Aharonov [6] demonstrated through theoretical and experimental studies that liquefaction is not solely due to excess pore water

pressure; gravity (buoyancy) can also trigger liquefaction under drained conditions. This finding may necessitate a reevaluation of liquefaction risk models in engineering applications.

Liquefaction risk is a significant engineering challenge in our country. The presence of active fault zones and high groundwater levels in some regions increase the potential for soil liquefaction [7]. Therefore, both the precision of liquefaction analyses and the development of effective ground improvement techniques against liquefaction are vital for reducing earthquake risk.

2. Materials and Methods

Field and laboratory studies were carried out in terms of materials and methods.

2.1. Field Studies

Drilling and exploration pits were carried out as field work in the study area. Drilling was carried out by Eras Engineering using a TSM-750 rotary drilling machine, operating in six boreholes, totaling 96.5 m [8]. Additionally, a 24 m land pit was opened in six research pits in the study area (Figure 1).



Figure 1 Satellite image of borehole locations and research pits (Google Earth) 2022.

2.2. Laboratory Studies

Disturbed and undisturbed samples taken from 6 research pits in the field were brought to the laboratory environment and sieve analysis, consistency limits, hydrometer, natural and saturated unit volume weight tests were performed.

Sieve Analysis is a test performed using sieves with different mesh sizes to determine the grain size distribution of soils. As a result of this test, the classification of the soils and their fines content (%) were determined [9].

The Consistency Limits test is used to determine the limits of water content. These limits are determined as solid, semi-solid, plastic, and liquid states [6].

The hydrometer test is a sedimentation analysis performed to determine the grain size of soils consisting of very small sized particles (fine grained) and the analysis method is based on Stokes' law [9].

Natural unit volume weight, defined as the amount of soil in a natural state within a unit volume, and saturated unit volume weight, expressed as the amount of soil in a unit volume whose voids are completely filled with water, were tested [10].

3. Results and Discussion

The study area is located within the borders of the Aziziye district of Erzurum province. Soil conditions were examined in the study area through geological mapping, drilling, and laboratory testing of field samples. Based on this data, a liquefaction analysis was conducted to determine whether liquefaction would occur in the soil. A program called "liquefaction potential analysis," developed by the Chamber of Geological Engineers, was used to determine the liquefaction analysis [11]. The data used in the program and its results are presented below and evaluated.

3.1. General Geology

The most widespread units within the study area are the Quaternary-aged recent alluvium and the Quaternary-aged old alluvium. Old and new alluvial units overlie the underlying older units with a thick sequence. The entire Erzurum basin is covered by alluvial units. Basalt, andesite, tuff, agglomerate, and pyroclastic volcanic deposits, generally formed in the Upper Miocene-Pliocene period, are observed on the foothills and slopes as the slope increases. East of Erzurum city center, sedimentary units consisting of Pliocene-aged conglomerate, sandstone, and mudstone intercalations are observed [12]. Fan-shaped talus units are also observed on the foothills of mountains and hills to the south and southeast of the study area. In addition, faults located in the study area were retrieved from a geological map viewer website and added to the geological map [13].

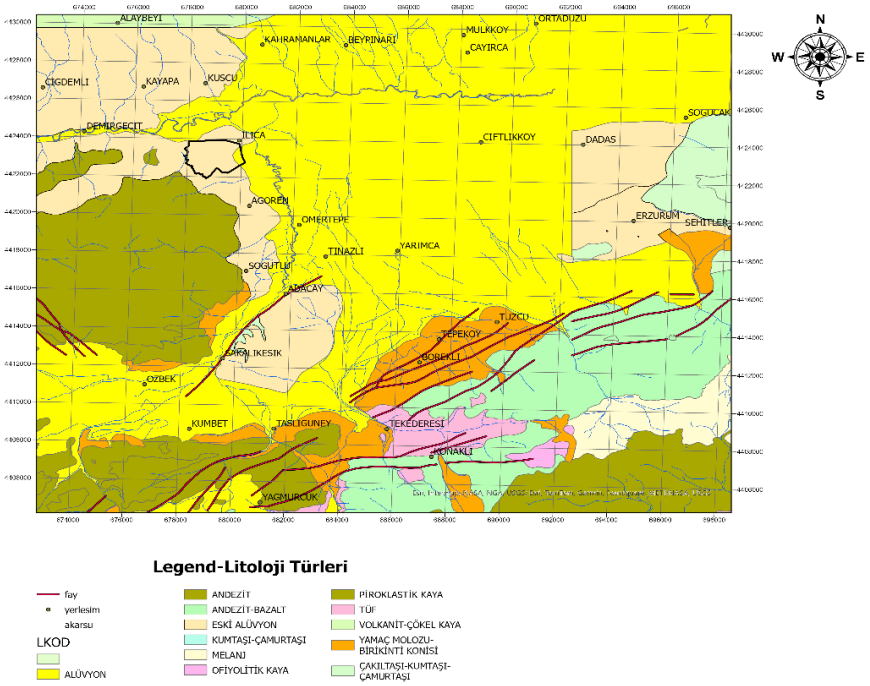

Figure 2 Geological map of the study area and its surroundings.

The study area consists of generally light gray siltstone, occasionally containing green clayey silt, and fractured and fissured siltstone between 7.50 and 19.50 m. The area between 3.00 and 7.50 m consists of light brown, light gray, and light cream colored clayey silt, occasionally dark brown. Decomposed siltstone is also observed. The area between 0.50 and 3.00 m consists of poorly sorted gray gravel-sand mixture and clayey silt. The geological map of the study area is shown in Figure 2.4.

3.2. SPT-N Values

Eras Engineering carried out the work using a TSM-750 model rotary system, a truck-mounted drilling rig. Six boreholes, each with a depth of 96.5 m, were drilled in the field. The coordinates, drilling depths, elevations, underground water levels, and (N_60) 30 values obtained from the Standard Penetration Test (SPT) for the six boreholes drilled in the study area are listed in Table 1 below.

Table 1 Data obtained from 6 drilled wells

Drill number	Drilling Well Coordinates		Depth (m)	Altitude(m)	UWL (m)	$(N_{60})_{30}$
	Y	X				
SK1	422063,235	4423309,686	18	1773	7	9,33
SK2	421748,397	4422774,550	12	1798	-	14
SK3	422309,743	4422150,057	12	1820	7	11,16
SK4	422584,533	4422724,932	16,5	1794	14	16,16
SK5	423124,951	4422315,811	18,5	1791	9	12,71
SK6	423437,045	4422696,228	19,5	1769	7	10,43

According to TBDY 2018, the $(N_{60})_{30}$ value obtained as a result of the standard penetration test (SPT) performed during drilling was used to determine the local soil class. The $(N_{60})_{30}$ values given in Table 1 were evaluated according

to the TBDY (2018) local soil classification given in figure When the $(N_{60})_{30}$ values given in Table 1 were examined, it was determined that the local soil class of SK-1, SK2, SK-3, SK-5 and SK-6 was ZE, while SK-4 was ZD.

Yerel Zemin Sınıfı	Zemin Cinsi	Üst 30 metrede ortalama		
		$(v_s)_{30}$ $[m/s]$	$(N_{60})_{30}$ $[darbe/30\ cm]$	$(c_u)_{30}$ $[kPa]$
ZA	Sağlam, sert kayalar	> 1500		-
ZB	Az ayrışmış, orta sağlam kayalar	760 - 1500		-
ZC	Çok sıkı kum, çakıl ve sert kil tabakaları veya ayrışmış, çok çatlaklı zayıf kayalar	360 - 760	> 50	> 250
ZD	Orta sıkı-sıkı kum, çakıl veya çok katı kil tabakaları	180 - 360	15 - 50	70 - 250
ZE	Gevşek kum, çakıl veya yumuşak-katı kil tabakaları $PI > 20$ ve $w > \%\ 40$ koşullarını sağlayan toplamda 3 metreden daha kalın yumuşak kil tabakası (cu < 25 kPa) içeren profiller.	< 180	< 15	< 70
ZF	Sahaya özel araştırma ve değerlendirme gerektiren zeminler: 1) Deprem etkisi altında çökme ve potansiyel göçme riskine sahip zeminler (sıvılaşabilir zeminler, yüksek derecede hassas killer, göçebilir zayıf çimentolu zeminler vb.), 2) Toplam kalınlığı 3 metreden fazla turba ve/veya organik içeriği yüksek killer, 3) Toplam kalınlığı 8 metreden fazla olan yüksek plastisiteli ($PI > 50$) killer, 4) Çok kalın (> 35 m) yumuşak veya orta katı killer.			

Figure 3 Local Ground Classification According to Türkiye Building Earthquake Code [3].

3.2.1. Short Period Design Spectral Acceleration Coefficient [dimensionless] (Sds)

Short-period design spectral acceleration coefficient (Sds) values were calculated using the Turkey Earthquake Hazard Maps Interactive Web application on the Disaster and Emergency Management Presidency (AFAD) website [14]. The resulting short-period design spectral acceleration coefficient (Sds) values are given in Table 2.

Table 2 Short Period Design Spectral Acceleration Coefficient [Dimensionless] Values

Drill Number	Short Period Design Spectral Acceleration Coefficient (dimensionles, S_{ds})
SK 1	0,971
SK 2	0,972
SK 3	0,974
SK 4	0,891
SK 5	0,975
SK 6	0,974

3.2.2. Sieve Analysis

The sieve analysis test was conducted according to TSE 17892-4 standards. The coordinates and depths of the samples taken from the research pits in the study area are given in and The values obtained from the grain diameter distribution tests are given in Table According to the USCS classification, AÇ-1 was classified as Ml, AÇ-2 as SM, AÇ-3 as MH, AÇ-4 as CH, AÇ-5 as ML, and AÇ-6 as CL. When Table 3 is examined, it is seen that the gravel material is between 0.2% and 23.6%, the sand material is between 7.0% and 30.2%, and the fine material is between 46.2% and 88.0%.

Table 3 Coordinates and depths of research wells

Research Pit	Drilling Well Coordinates		Depth (m)	Sieve Analysis Results				
	Y	X		Block%	Gravel%	Sand%	Thin%	Total %
RP -1	421941.513	4423134.259	4	0,0	11,9	16,0	72,1	100,0
RP -2	421747.654	4422777.117	4	0,0	23,6	30,2	46,2	100,0
RP -3	422306.254	4422151.652	4	0,0	6,1	7,0	86,9	100,0
RP -4	422580.782	4422725.863	4	0,0	3,8	10,7	85,5	100,0
RP -5	423125.399	4422317.810	4	0,0	0,2	11,8	88,0	100,0
RP -6	423440.116	4422695.536	4	0,0	3,5	19,8	76,7	100,0

3.2.3. Hydrometer Experiment

Hydrometer tests were carried out in accordance with TS EN ISO 17892-The clay ratios obtained as a result of the hydrometer test are given in Table 4 and were found to be 8.9% in AC-1, 7.2 in AC-2, 25.1 in AC-3, 37.1 in AC-4, 5.2 in AC-5 and 37.3 in AC-6.

Table 4 Grain Distribution Clay-Silt Ratio

Research Pit	Rate Passing Through 0,002 mm % (amount of clay)	Amount of silt % (0.075-0.002 mm between)
RP -1	8,9	63,2
RP -2	7,2	39,0
RP -3	25,1	61,8
RP -4	37,1	48,4
RP -5	5,2	82,8
RP -6	37,3	39,4

3.2.4. Natural and Saturated Unit Weights

Experiments were conducted in accordance with TS 1900 1:2006 standards. The values determined for natural and saturated unit weights are given in Table When Table 5 is examined, it is seen that the natural unit volume weight is between 9.09-13.90 kN⁄m^3 and the saturated unit volume weight is between 10.36-14.90 kN⁄m^3.

Table 5 Natural Unit and Saturated Unit Weight Results

Research Pit	Natural unit volume weight (kN/m^3)	Saturated unit volume weight (kN/m^3)
RP -1	13,90	14,90
RP -2	9,70	10,63
RP -3	11,00	12,25
RP -4	12,52	13,71
RP -5	9,09	10,36
RP -6	12,98	14,38

3.2.5. Consistency Limits Test

The results of the consistency limits test, conducted according to TSE 1900-1 standards, are given in Table 6.

Table 6 *Atterberg Limits Experiment Results*

Research Pit	Liquid Limit %	Plastic Limit %	Plasticity index
RP-1	NP	NP	NP
RP -2	NP	NP	NP
RP -3	54,3	30,1	24,2
RP -4	53,4	25,3	28,1
RP -5	NP	NP	NP
RP -6	43,6	25,0	18,6

An examination of Table 6 reveals that LL values in the research pits varied between 54.3% and non-plastic, PL values varied between 30.1% and non-plastic, and PL values varied between 28.1% and non-plastic. Using sieve analysis, hydrometer, and consistency limit tests, soil classification was performed according to the unified soil classification system shown in Figure 3, and is presented in Table 7.

Table 7 Soil Type According to Sample Points (USCS)

Research Pit	Classification	Explanation
RP -1	ML	Inorganic silts, inorganic silty or fine sands (low plasticity)
RP -2	SM	Silty sand
RP -3	MH	Inorganic silts (high plasticity)
RP -4	CH	Inorganic clays (high plasticity)
RP -5	ML	Inorganic silts, inorganic silty or clayey fine sands (low plasticity)
RP -6	CL	Inorganic clays, Inorganic silty clays (low plasticity)

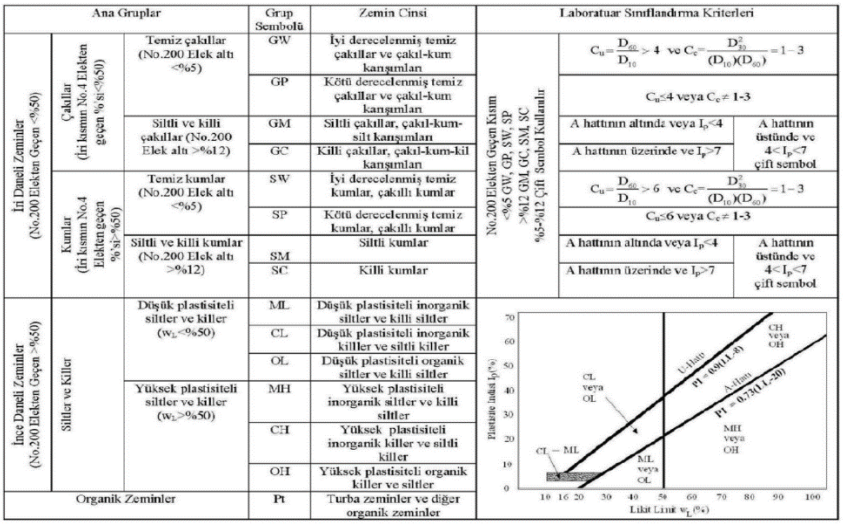

Figure 4 Unified Soil Classification [15]

3.2.6. Assessment of Liquefaction Potential

The methods of Iwasaki et al. [16] and Sönmez and Gökçeoğlu [17] were used to assess liquefaction potential. The Iwasaki et al. method, one of the most widely used indices in earthquake engineering, was developed to calculate the liquefaction potential of a vertical soil column comprising multiple layers at a drilling location, up to 20 m below the ground surface. The liquefaction potential index was calculated using the equation given below.

$$LPI = \int_0^{20} F(z) * W(z) * dz \tag{1}$$

$$F(z) = 1 - FS\ (for\ FS < 1.0)$$
$$F(z) = 0\ (for\ FS \geq 1.0)$$
$$W(z) = 10 - 0{,}5z\ (for\ z \leq 20\ m) \tag{2}$$
$$W(z) = 0\ (for\ z > 20\ m)$$

The value of the liquefaction potential graded according to the calculated total liquefaction potential index value is given in Table 8.

Table 8 Liquefaction Potential (L_I) Classification (Iwasaki et al., 1982)

Liquefaction index (L_I)	**Liquefaction potential**
0	Very low
$0 < L_I \leq 5$	Low
$5 < L_I \leq 15$	High
$15 < L_I$	Very high

Calculated liquefaction potential index (L_I) values are given in Table 9.

Table 9 Liquefaction Potential Index (L_I) Values

Drill number	**Depth (m)**	**liquefaction potential index (L_I) values**	**Liquefaction potential**
SK-5	10,50	21,08	Very high

An examination of Table 9 reveals that the liquefaction potential index (L_I) value for SK-5 is 21.This indicates that the liquefaction potential is very high in the SK-5 well. It was not calculated at other depths because it remains above the groundwater table.

The liquefaction potential index defined by LPI is calculated with the help of equation (1) depending on the changes in the safety coefficient (F) and weight constant (W) values, which change with depth, from the surface to a depth of 20 m.

Sönmez and Gökçeoğlu [17] recognized some limitations of the LPI and developed a more sensitive intensity index. The liquefaction intensity index (Ls), developed to calculate the liquefaction potential of a vertical soil column forming multiple layers up to 20 m below the surface, was calculated using the following equation.

$$L_s = \int_0^{20} P_l(z) * W(z) * dz \tag{3}$$

$$P_L(z) = \frac{1}{1 + \left(\frac{F_L}{0{,}96}\right)^{4{,}5}} \; (for\ F_L \leq 1{,}411) \tag{4}$$

$$P_L(z) = 0 \; (for\ F_L > 1{,}411) \tag{5}$$

The values of liquefaction potential graded according to the calculated total liquefaction severity index value are given in Table 10.

Table 10 Liquefaction Severity (LS) Index Classification [18

Liquefaction index (L_s)	**Liquefaction potential**
$85 \leq L_S \leq 100$	Very high
$65 \leq L_S \leq 85$	High
$35 \leq L_S \leq 65$	Middle
$15 \leq L_S \leq 35$	Low
$0 \leq L_S \leq 15$	Very low
$L_S = 0$	Does not liquefy

Liquefaction severity index (L_S) values were found using the Liquefaction Potential Analysis program developed by the Chamber of Geological Engineers and the results are given in Table When Table 11 is examined, it is seen that the liquefaction intensity index values according to this method are 3.07 and 41. This indicates that the liquefaction potential is very low in the SK-1 well and moderate in the SK-5 well.

Table 11 *Liquefaction Severity Index (L_S) Values*

Drill number	**Depth (m)**	**Liquefaction Severity Index (L_S) Values**	**Liquefaction potential**
SK-1	7,50	3,07	Very low
SK-5	10,50	41,95	middle

4. Conclusion

The results obtained in the light of field and laboratory data within the scope of this study are presented below.

The average N values of the SPT (Standard Penetration Test) carried out in the study area were found to be 9.33 in SK-1, 14 in SK-2, 11.16 in SK-3, 16.16 in SK-4, 12.71 in SK-5, and 10.43 in SK-According to the average N values of the SPT (Standard Penetration Test) carried out in the study area, it was determined that the local soil class of SK-1, SK2, SK-3, SK-5 and SK-6 was ZE, while SK-4 was ZD.

As a result of the consistency limits tests, it was found to be NP in AC-1, AC-2 and AC-Liquid limit values were 54.3% in AC-3, 53.4% in AC-4 and 43.6% in AC-6; plastic limit values were 30.1% in AC-3, 25.3% in AC-4 and 25.0% in AC-6; platicity index values were found to be 24.2% in AC-3, 28.1% in AC-4 and 18.6% in AC-Clay content values were determined to be 8.9% in AC-1, 7.2% in AC-2, 25.1% in AC-3, 37.1% in AC-4, 5.2% in AC-5 and 37.3% in AC-6.

According to the material passing through the 0.075 mm aperture sieve, the fine particle content was found to be 72.1% in AC-1, 46.2% in AC-2, 86.9% in AC-3, 85.5% in AC-4, 88% in AC-5 and 76.7% in AC-6.

The natural unit weight values on undisturbed samples taken from research pits were 13.90 kN⁄m^3 in AÇ-1, 9.70 kN⁄m^3 in AÇ-2, 11.00 kN⁄m^3 in AÇ-3, 12.52 kN⁄m^3 in AÇ-4, 9.09 kN⁄m^3 in AÇ-5, 12.98 kN⁄m^3 in AÇ-6, and the saturated unit weight values were 14.90 kN/m^3 in AÇ-1, 10.63 kN⁄m^3 in AÇ-2, 12.25 kN⁄m^3 in AÇ-3, 13.71 kN⁄m^3 in AÇ-It was determined that it was 10.36 kN⁄m^3 and 14.38 kN⁄m^3 in AC-As a result of the sieve analysis performed on the samples

taken from the research pits, it was determined that the soil class according to USCS was Ml in AC-1, SM in AC-2, MH in AC-3, CH in AC-4, ML in AC-5 and CL in AC-6.

According to the method of Iwasaki et al. (1982), the liquefaction potential index (L_1) value was found to be 21.08 in SK-According to the method of Sönmez and Gökçeoğlu [14], the liquefaction severity index (L_S) value was found to be 3.07 in SK-1 and 41.95 in SK-5.

According to the JMO liquefaction calculation program, liquefaction is expected in wells SK-1 and SK-According to the method of Iwasaki et al. (1982), the liquefaction potential is very low in wells SK-1, SK-2, SK-3, SK-4, and SK-6, while the liquefaction potential is expected to be very high in well SK-According to the method of Sönmez and Gökçeoğlu (2005), while very low is expected in well SK-1, it is not expected in wells SK-2, SK-3, SK-4, and SK-6, and it is expected to be moderate in well SK-5.

This study indicates that all drilled wells have a liquefaction potential ranging from low to very high. Considering all of this data, it is recommended that any potential development in the study area be carefully considered to minimize liquefaction risks and take the necessary precautions.

References

[1] Sarıgül, Tuba. (2017).Toprak Sıvılaşması Nedir?,Tübitak Bilim Genç.

[2] Dağdeviren, Uğur. (2019). Yeni Türkiye Bina Deprem Yönetmeliğine Göre Zeminlerin Sıvılaşma Analizi ve Sıvılaşmaya Karşı İyileştirilmesi. Artvin Çoruh Üniversitesi Doğal Afetler Uygulama ve Araştırma Merkezi Doğal Afetler ve Çevre Dergisi. 5(1): 153-165.

[3] Türkiye Bina Deprem Yönetmeliği. 2018.

[4] Durmaz, S. Gül., Soyaslan, İ. İskender. (2023). Zemin Sıvılaşmasını Denetleyen Koşulların ve Sıvılaşma Nedenli Deformasyonların İncelenmesi. Mehmet Akif Ersoy Üniversitesi Fen Bilimleri Enstitüsü Dergisi. 14(2): 401-411.

[5] Akın, Müge K. (2019). Düzce Kent Merkezi Zeminlerinin Sıvılaşma Potansiyelinin Değerlendirilmesi. Jeoloji Mühendisliği Dergisi. 43, 39-56,

[6] Clement, Cecile., Toussaint, Renaud., Aharanov, Einat. (2018). Journal of Geophysical Research. Liquefaction Without Pressurization. arxiv:1802.04391.

[7] Ülker, M. Barışcan. (2021-2024). Sıvılaşabilen Zeminlerin Deprem Etkisi Altında Dinamik Davranışlarını Modelleyen Yeni Nesil Akıllı Bir Bünye Modeli Geliştirilmesi. Tübitak Projesi

[8] Eras Mühendislik Harita Planlama Jeoloji İnşaat Taahhüt TİC ve SAN. LTD. ŞTİ.(2022). Erzurum İli, Aziziye İlçesi, Ilıca Mahallesi 1/5000 Ölçekli I46A07B ve I46A08A Paftaların Nazım İmar Planı ve 1/1000 Ölçekli I46A07B3D, I46A07B4B, I46A07B3A, I46A07B2C, I46A07B3B, I46A07B3C, I46A07B2A, I46A07B2D, I46A07B1B, I46A07B2B, I46A07B1C, I46A08A1D, I46A08A4A, I46A08A4D, I46A08A4B, I46A08A1A ve I46A08A1C Paftalar 10003 Ada 66-72-73-74 Parsellerin Uygulama İmar Planına Esas Jelojik ve Jeoteknik Etüt Raporu.

[9] Türk Standartları Enstitüsü. (2016). 17892-4 Zemin Mekaniği Labaratuvar deneyleri.

[10] Türk Standartları Enstitüsü. (2006).1900-1 Zemin Mekaniği Labaratuvar deneyleri

[11] Jeoloji Mühendisleri Odası. (2021). Türkiye Bina Deprem Yönetmeliği İle Uyumlu Basitleştirilmiş Zemin Sıvılaşma Potansiyeli Analizi ve Sıvılaşma Sonrası Oturma, Yanal Defarmasyon, Kayma Dayanımı Kaybı ve Kapak Tabakası Etkisi Hesap Cetveli ve Kullanım Kılavuzu (v.2).

[12] MTA, (1988). 1:100 000 Ölçekli Açınsama Nitelikli Türkiye Jeoloji Haritaları Serisi Erzurum F 32 Paftası

[13] https://www.mta.gov.tr/v3.0/sayfalar/hizmetler/doc/diri fay haritalari/erzurum.pdf

[14] https://www.afad.gov.tr/turkiye-deprem-tehlike-haritasi

[15] Unified Soil Classification System(USCS).https: ://www.researchgate.net/figüre/ Unified-Soil-Classification-System-USCS-of-coarse-grained-soils-ASTM-D2487-11_fig5_312036169

[16] Iwasaki, T., Tokida, K., Tatsuoka, F., vd. (1982). Microzonation for soil liquefaction potential using simplified methods. In: Proceedings of the 3rd International Conference on Microzonation. Seattle. 3, 1319- 1330.

[17] Sönmez, H., Gökçeoğlu, C. (2005). "A liquefaction severity index suggested for engineering practice". Environmental Geology. 48: 81–91.

[18] Babadan, K. (2023). Erzurum ılıca mahallesi sıvılaşma potansiyelinin farklı yöntemlerle araştırılması tezi. Atatürk Üniversitesi, Fen Bilimleri Enstitüsü.

Hydrogeochemistry, Petrography, and Groundwater Quality in the Waru–Apo Area (Abuja FCT, Nigeria)

Hairat Banaru*[1], Jatau B.S[1], Tanko I.Y[1], Sadiq Abdulmaliqq[1]

[1] Department of Geology and Mining, Nasarawa State University, Keffi, Nigeria

* *Corresponding Author: hairatbanaru@hotmail.com* | *+2348078129000*

Keywords

Groundwater quality;
Hydrogeochemistry;
Petrography;
Heavy metals;
Pollution indices;
Waru; Abuja

Abstract

This study presents an integrated geologic, petrographic and hydrogeochemical assessment of groundwater resources in the Waru area of Apo (FCT), Abuja, North-Central Nigeria. The objective was to characterize lithological units, evaluate groundwater chemistry, determine heavy metal concentrations and assess potential environmental and health implications. Field mapping and petrographic analyses established four rock types in the study area which are: migmatite, granite gneiss, biotite gneiss and anatectic granite as the dominant basement lithologies, with deformation features such as joints, folds and quartz veins promoting groundwater. Twenty-two groundwater samples obtained from streams, hand-dug wells and boreholes were analysed using Atomic Absorption Spectroscopy in order to quantify major cations, anions, heavy, and trace metals. The concentrations of chromium (0.046–0.236 mg/L), cadmium (0.034–0.121 mg/L) and lead (0.003–0.023 mg/L) exceed World Health Organization (WHO) and Nigerian Standard for Drinking Water Quality statutory limits in several locations, indicating localized contamination. Hydrochemical evaluation revealed Na–SO_4 and Na–Mg–SO_4 water types, which reflect dominant ion-exchange processes, sulphate dissolution and contributions from rock weathering. Application of Nemerow's Pollution Index, Contamination Factor and Pollution Load Index indicated low-to-moderate pollution levels in most samples, although localized anomalies were observed particularly in areas proximal to abattoir and domestic waste zones. Elevated trace-metal values correlate with both geogenic release from basement rock weathering and anthropogenic inputs associated with abattoir effluent. The health implications of observed Cr, Cd and Pb levels include carcinogenic and neurotoxic risks, especially for vulnerable populations dependent on shallow wells. The study underscores the need for improved groundwater monitoring, stricter regulation of abattoir waste disposal and the provision of safer potable-water.

1. Introduction

Groundwater is a critical source of potable water in Nigeria, yet it faces increasing threats from both natural geological processes and anthropogenic activities such as abattoir operations, agriculture, and urbanization. Abattoirs, in particular, discharge effluents rich in organic matter and heavy metals, which infiltrate soils and aquifers, compromising water quality [1, 2].

In the Federal Capital Territory (FCT), Abuja, the Waru abattoir is a major slaughterhouse, but little is documented about its impact on local geology and hydrochemistry. This study addresses this gap by combining geological, petrographic, and hydrochemical analyses to evaluate groundwater quality and assess its implications for public health and sustainable resource management.

The specific objectives of this study are to:

- Characterize the lithological and structural framework of the Waru area.
- Assess groundwater and soil quality using hydrochemical and pollution indices.
- Evaluate implications for environmental health and sustainable groundwater management.

2. Materials and Methods:

2.1. Study Area

The Waru area is underlain by basement complex rocks including migmatite, granite gneiss, biotite gneiss, and anatectic granite. These lithologies and their weathering products exert strong control on groundwater quality.

2.2. Sample Collection:

A total of 22 groundwater samples were collected from streams, hand-dug wells, and boreholes. 10 Soil samples were also collected at different depths to determine heavy metal concentrations.

2.3. Analytical Methods:

Atomic Absorption Spectroscopy (AAS): Used to measure Cr, Cd, and Pb concentrations.

Hydrochemical Analysis: Major cations (Na, Mg, Ca) and anions (SO_4, HCO_3, Cl) were analyzed to classify water types.

2.4. Pollution Indices

Nemerow's Pollution Index (NPI), Contamination Factor (CF), and Pollution Load Index (PLI) were calculated to determine contamination levels.

2.5. Statistical and Graphical Analysis:

Hydrochemical plots including Schoeller, Gibbs, and Durov diagrams were used to identify processes influencing water chemistry.

3. Results and Discussion:

3.1. Geological and Petrographic Findings:

Field mapping revealed migmatite, granite gneiss, biotite gneiss, and anatectic granite as dominant lithologies. Structural features including folds, joints, and quartz veins trending NE–SW and NW–SE provide pathways for groundwater flow and enhance aquifer vulnerability.

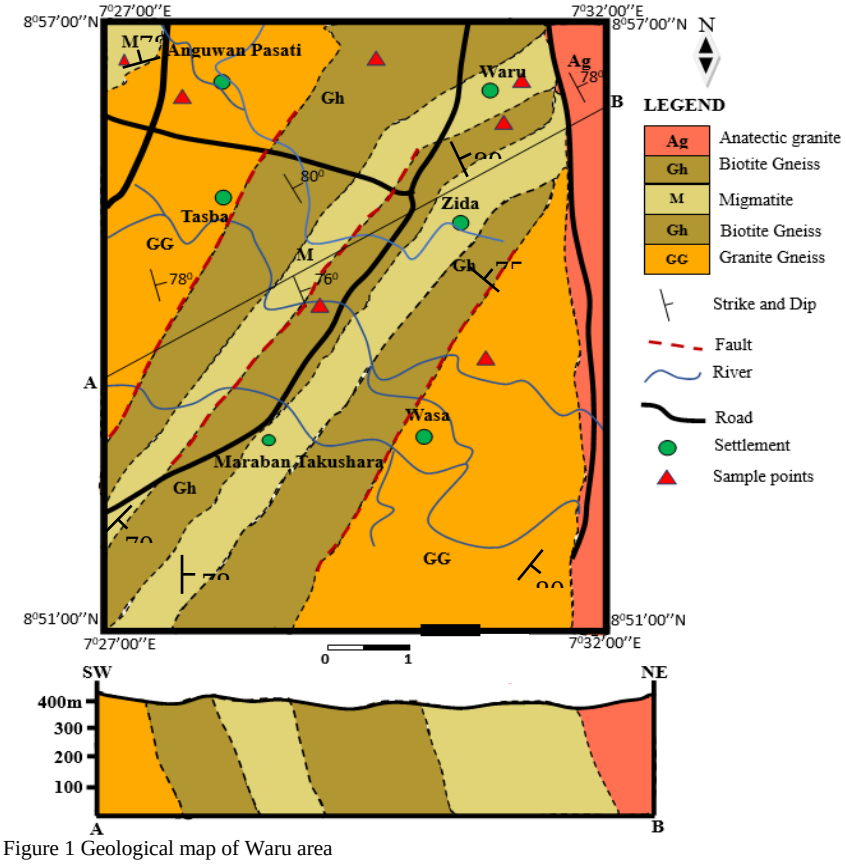

Figure 1 Geological map of Waru area

3.2. Hydrochemical Characteristics:

Water pH ranged from slightly acidic (5.48–6.86) to slightly alkaline (7.4–8.11). Two major water facies were identified: Na–SO_4, and Na–Mg–SO_4, indicating ion exchange and dissolution/mixing processes as dominant geochemical controls.

Table 1 Summary of hydrochemical parameters of groundwater samples. Physical Parameters Data for Groundwater Samples in Waru and surrounding areas.

S/N	PH	TDS	TEMP	E.C
1	8.11	62	24	132
2	7.4	72	27	154
3	6.2	15	26	33
4	5.56	36	27	78
5	5.6	66	27	137
6	6.14	92	26	195
7	6.36	33	25	66
8	6.2	52	27	104
9	5.48	100	27	200
10	6.86	106	27	211
11	6.3	70	26	138
WHO (2012)	**8.5**	**600**	**25**	**3000**
NSDWQ (2007)	**8.5**	**500**		**1000**
SUM	**70.21**	**704**	**289**	**1448**
MEAN	**6.382727**	**64**	**26.27273**	**131.6364**
STDEV.	**0.805209**	**28.70888**	**1.00905**	**57.64941**
VARIANCE	**0.648362**	**824.2**	**1.018182**	**3323.455**
MINIMUM	**5.48**	**15**	**24**	**33**
MAXIMUM	**8.11**	**106**	**27**	**211**

3.3. Heavy Metal Concentrations:

Chromium: 0.046–0.236 mg/L

Cadmium: 0.034–0.121 mg/L

Lead: 0.003–0.023 mg/L

These values exceed WHO and NSDWQ permissible limits in several locations, indicating localized contamination. Soil analyses revealed similar enrichment, suggesting that both natural weathering and anthropogenic activities contribute to heavy metal presence.

Table 2 Heavy metal concentrations in groundwater

S/N	Mn	Cr	Cd	Fe	Zn	Cu	Pb
1	0.055	0.046	0.096	0.121	0.026	0.009	0.005
2	0.08	0.179	0.087	0.018	0.043	0.006	0.006
3	0.129	0.114	0.041	0.013	0.121	0.012	0.007
4	0.014	0.054	0.067	0.007	0.075	0.023	0.009
5	0.031	0.077	0.063	0.022	0.041	0.013	0.003
6	0.099	0.095	0.04	0.04	0.062	0.037	0.017
7	0.053	0.049	0.079	0.015	0.079	0.037	0.023
8	0.032	0.048	0.121	0.004	0.257	0.007	0.007
9	0.045	0.075	0.034	0.005	0.039	0.007	0.019
10	0.033	0.236	0.053	0.019	0.038	0.013	0.003
11	0.135	0.077	0.115	0.006	0.092	0.009	0.004
SUM	**0.706**	**1.05**	**0.796**	**0.27**	**0.873**	**0.173**	**0.103**
Maximum	**0.135**	**0.236**	**0.121**	**0.121**	**0.257**	**0.037**	**0.023**
Minimum	**0.014**	**0.046**	**0.034**	**0.004**	**0.026**	**0.006**	**0.003**
Mean	**0.03715789**	**0.05526**	**0.04189**	**0.01421**	**0.04595**	**0.00911**	**0.00542**
Stdv	**0.0410897**	**0.06062**	**0.02999**	**0.03362**	**0.06538**	**0.01151**	**0.00699**
WHO(2012)	0.4	0.05	0.003	0.3	5	1	0.01
NSDWQ(2007)	0.2	0.05	0.003	0.3	3	1	0.01

3.4. Contamination Indices:

Nemerow's Pollution Index (NPI): Many samples showed NPI > 1 for Cr and Cd.

Contamination Factor (CF): Indicated low-to-moderate contamination.

Pollution Load Index (PLI): Classified the Waru area as largely unpolluted.

Table 3 Contamination Factor (CF) of Heavy Metals in the water samples.

S/N	Mn	Cr	Cd	Fe	Zn	Cu	Pb
1	0.000119826	0.000645	0.32	0.025636	0.000275	0.00033	0.000168
2	0.000174292	0.002511	0.29	0.003814	0.000456	0.00022	0.000202
3	0.000281046	0.001599	0.136667	0.002754	0.001282	0.00044	0.000236
4	3.05011E-05	0.000757	0.223333	0.001483	0.000794	0.000842	0.000303
5	6.75381E-05	0.00108	0.21	0.004661	0.000434	0.000476	0.000101
6	0.000215686	0.001332	0.133333	0.008475	0.000657	0.001355	0.000572
7	0.000115468	0.000687	0.263333	0.003178	0.000837	0.001355	0.000774
8	6.97168E-05	0.000673	0.403333	0.000847	0.002722	0.000256	0.000236
9	9.80392E-05	0.001052	0.113333	0.001059	0.000413	0.000256	0.00064
10	7.18954E-05	0.00331	0.176667	0.004025	0.000403	0.000476	0.000101
11	0.000294118	0.00108	0.383333	0.001271	0.000975	0.00033	0.000135
SUM	**0.0015381**	**0.01473**	**2.65333**	**0.0572**	**0.00925**	**0.00634**	**0.00347**
Maximum	**0.0002941**	**0.00331**	**0.40333**	**0.02564**	**0.00272**	**0.00136**	**0.00077**
Minimum	**3.05E-05**	**0.00065**	**0.11333**	**0.00085**	**0.00028**	**0.00022**	**0.0001**
Mean	**8.095E-05**	**0.00078**	**0.13965**	**0.00301**	**0.00049**	**0.00033**	**0.00018**
Stdv	**8.952E-05**	**0.00085**	**0.09997**	**0.00712**	**0.00069**	**0.00042**	**0.00024**
Product	**4.35225E-44**	**4.91E-33**	**6.47E-08**	**2.3E-28**	**1.35E-35**	**2.42E-37**	**2.23E-40**

Table 4 Pollution Load Index (PLI) of Heavy Metals in the water samples.

S/N	PLI
1	0.001374
2	0.001376
3	0.00155
4	0.001058
5	0.001052
6	0.002062
7	0.001776
8	0.001141
9	0.000969
10	0.001177
11	0.001303

Table 5 Nemerow's Pollution Index (NPI) of Heavy Metals in the water samples.

S/N	Mn	Cd	Cr	Cu	Fe	Pb	Zn
1	0.1375	32	0.92	0.009	0.403333	0.5	0.0052
2	0.2	29	3.58	0.006	0.06	0.6	0.0086
3	0.3225	13.66667	2.28	0.012	0.043333	0.7	0.0242
4	0.035	22.33333	1.08	0.023	0.023333	0.9	0.015
5	0.0775	21	1.54	0.013	0.073333	0.3	0.0082
6	0.2475	13.33333	1.9	0.037	0.133333	1.7	0.0124
7	0.1325	26.33333	0.98	0.037	0.05	2.3	0.0158
8	0.08	40.33333	0.96	0.007	0.013333	0.7	0.0514
9	0.1125	11.33333	1.5	0.007	0.016667	1.9	0.0078
10	0.0825	17.66667	4.72	0.013	0.063333	0.3	0.0076
11	0.3375	38.33333	1.54	0.009	0.02	0.4	0.0184
SUM	1.765	265.3333	21	0.173	0.9	10.3	0.1746
Maximum	0.3375	40.33333	4.72	0.037	0.403333	2.3	0.0514
Minimum	0.035	11.33333	0.92	0.006	0.013333	0.3	0.0052
Mean	0.092895	13.96491	1.105263	0.009105	0.047368	0.542105	0.009189
Stdv	0.102724	9.996969	1.212448	0.011507	0.112065	0.69896	0.013077

3.5. Hydrogeochemical Processes:

Gibbs plots placed most samples in the rock-weathering dominance field, confirming that basement complex weathering significantly governs water chemistry. However, elevated Cr, Cd, and Pb point to additional anthropogenic inputs from abattoir activities and local waste disposal.

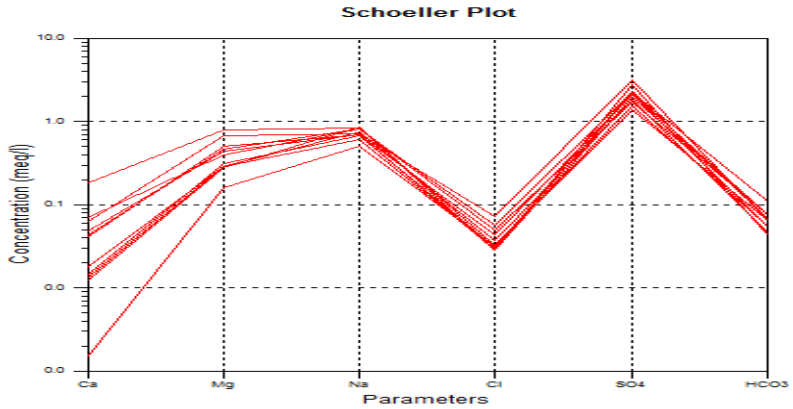

Figure 2 Schoeller diagram of ionic composition]

Schoeller plot showing average chemical composition of groundwater.

Schoeller plot shows the average chemical composition of the groundwater samples in the area. The relative trend for the cations shows that Na > Mg > Ca, and that of the anions showed that SO_4> HCO_3> Cl.

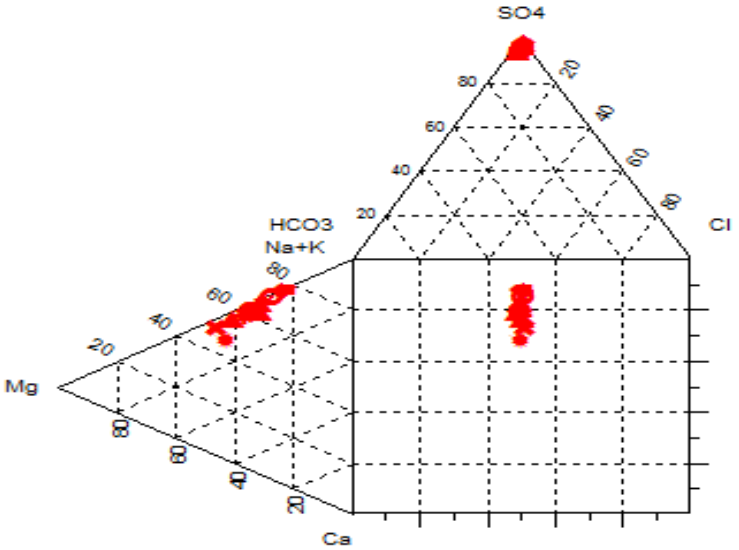

Figure 3 Durov plot of major ions in the water samples.

The Durov plot shows that the water samples collected for the study plot in fields 2 and 5, with majority of the samples plotting in field Water samples in field 2 indicate an important ion exchange (with significant sodium ions). Samples in field 5 indicate fresh recent recharge water exhibiting simple dissolution or mixing.

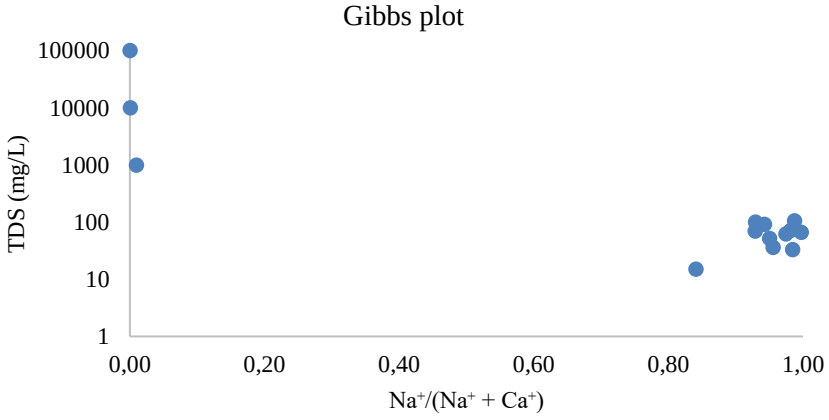

Figure 4 Gibbs plot

3.6. Environmental and Health Implications:

The presence of heavy metals above WHO standards poses risks such as kidney damage, neurological disorders, and carcinogenic effects (WHO, 2017; IARC, 2020). Children and vulnerable populations are at higher risk due to bioaccumulation and long-term exposure.

Table 6 Standards for drinking water (maximum permitted limit, in mg/L) and health impact.

S/N	Parameter	NSDWQ (2007)	WHO (2018)	Health impact (SON, 2007)
1.	Aluminium	0.2	0.2	Potential neuro-degenerative disorders
2.	Arsenic	0.01	0.01	Cancer
3.	Barium	0.7	0.7	Hypertension
4.	Cadmium	0.003	0.003	Toxic to the kidney
5.	Chloride	250	250	None
6.	Chromium	0.05	0.05	Cancer
7.	Conductivity	1000µS/cm	2500µS/cm	None
8.	Copper	1	2.0	Gastro-intestinal disorder
9.	Hardness (as $CaCO_3$).	150	500	None
10.	Iron	0.3	0.3	None
11.	Lead	0.01	0.01	Cancer, toxic to central nervous system, affects mental development in infants and interferes with vitamin D metabolism.
12.	Magnesium	0.20	None specified	Consumer acceptability
13.	Manganese	0.2	0.4	Neurological disorder
14.	Mercury	0.001	0.006	Affects the kidney and central nervous system
15.	Nickel	0.02	0.07	Possible carcinogenic
16.	Nitrate	50	50	Cyanosis and asphyxia
17.	pH	6.5-8.5	8.5	None
18.	Sodium	200	200	None
19.	TDS	500	1000	None
20.	Sulphate	100	250	None
21.	Zinc	3	5	None
22.	Calcium	-	150	
23.	Temperature (℃)	-	25	
24.	Potassium	-	10	
25.	Selenium	-	0.04	

3.7. Conclusion

This study establishes that groundwater quality in the Waru area is influenced by both geological controls and anthropogenic activities. Elevated levels of Cr, Cd, and Pb in some samples, though localized, highlight significant public health concerns.

Recommendations

Regular groundwater monitoring to track contamination hotspots.

Enforcement of abattoir waste treatment and disposal standards.

Provision of safe alternative water supplies for the local population.

Seasonal studies to capture hydrochemical variability and pollution dynamics.

These interventions align with SDG 6 (Clean Water and Sanitation) and will protect both environmental and public health.

References

[1] Abiola, O. O., Adewumi, J. R., & Hassan, T. (2022). Impact of abattoir effluent on groundwater quality in urban Nigeria. Environmental Monitoring and Assessment, 194(3), https://doi.org/10.1007/s10661-022-09764-5

[2] Adewumi, J. R., Olanrewaju, O. O., & Ogunlaja, O. (2020). Hydrochemical assessment of groundwater around abattoirs in southwestern Nigeria. Heliyon, 6(11), ehttps://doi.org/10.1016/j.heliyon.2020.e05412

[3] Nwankwoala, H. O., & Amadi, A. N. (2019). Hydrogeochemical implications of abattoir operations on groundwater in Nigeria. Applied Water Science, 9(4), https://doi.org/10.1007/s13201-019-0987-9

[4] Olobaniyi, S. B., & Owoyemi, F. B. (2016). Environmental hydrogeology of basement aquifers in Nigeria. Journal of African Earth Sciences, 120, 123– https://doi.org/10.1016/j.jafrearsci.2016.04.005

[5] Suleiman, Y. A., Ibrahim, A. S., & Mohammed, A. A. (2021). Assessment of abattoir waste impact on water resources in Nigeria. Environmental Challenges, 5, https://doi.org/10.1016/j.envc.2021.100301

[6] World Health Organization. (2017). Guidelines for drinking-water quality (4th ed.). World Health Organization. https://www.who.int/publications/i/item/9789241549950

[7] International Agency for Research on Cancer. (2020). Monographs on the identification of carcinogenic hazards to humans. World Health Organization. https://monographs.iarc.who.int

Oxidation Mechanism in Vegetable Oils and Methods for Enhancing Oxidative Stability

Büşra Aydın [1], Saliha Erentürk [2]

1 Department of Chemical Engineering, Faculty of Engineering, Atatürk University, Erzurum, Türkiye

* *Corresponding author E-mail: serenturk@atauni.edu.tr*

Keywords

Natural antioxidants,
lipid oxidation,
oxidative stability,
Rancimat,
edible oils.

Abstract

Vegetable oils are important components of human nutrition, not only as a primary source of energy but also for the transport of fat-soluble vitamins and their contribution to sensory quality. However, all vegetable oils—particularly corn oil, which is rich in polyunsaturated fatty acids—are highly susceptible to oxidation. Oxidation consists of chain radical reactions that lead to deterioration in taste, odor, and color, as well as a reduction in nutritional value. The aim of this study is to present, on a literature-based approach, the oxidation mechanisms in vegetable oils, the methods used to determine oxidative stability, and the natural and technological strategies developed to enhance stability. Within the methodological framework, the chemical basis of the initiation, propagation, and termination stages of the oxidation process is explained, and analytical methods used for the evaluation of oxidative stability are defined. According to findings reported in the literature, certain approaches delay oxidation by chelating metal ions and interrupting chain reactions. Studies demonstrate that natural antioxidants significantly improve oxidative stability, particularly in oils with a high degree of unsaturation, as evidenced by prolonged induction periods and reduced reaction rates. In conclusion, the literature indicates that both natural and synthetic antioxidants effectively enhance the oxidative stability of oils, contributing to extended shelf life, preservation of sensory quality, and improved consumer safety. In this context, the study contributes to a better understanding of oxidation processes in vegetable oils and to the development of strategies aimed at improving their stability.

1. Introduction

Fats and oils are among the fundamental components of human nutrition and play vital roles in sustaining life. Vegetable and animal fats not only provide energy but also contribute to the transport of fat-soluble vitamins such as A, D, E, and K, supply essential fatty acids required by the human body, prolong satiety and support appetite control, and impart characteristic taste and aroma properties to foods [1]. The increasing demand for vegetable oils has made it more important to preserve their chemical and sensory qualities throughout production, storage, and consumption processes [2].

One of the most important causes of quality deterioration in edible oils is lipid oxidation [3]. Lipid oxidation leads to undesirable changes in sensory properties such as taste, odor, color, and texture, and also reduces nutritional value through the degradation of fat-soluble vitamins [4]. Uncontrolled oxidation can be slowed by the action of antioxidants and synergistic compounds. Antioxidants enhance oil stability by inhibiting the formation of harmful compounds during oxidative degradation, while synergists act as auxiliary components that enhance antioxidant effectiveness [5].

The inhibitory effects of both natural and synthetic antioxidants on lipid oxidation are well established. However, toxicological concerns associated with synthetic antioxidants have led consumers to favor natural antioxidant sources. This trend has accelerated research into the antioxidant potential of plant materials rich in phenolic compounds [6, 7]. In particular, extracts obtained from plant sources such as thyme, rosemary, sage, olive leaf, green tea, and sesame have been reported to exhibit strong antioxidant properties and, in many oil systems, to provide higher efficacy than synthetic antioxidants [8, 9, 10].

In the food industry, extending the shelf life of oils, preserving sensory quality, and delaying oxidative deterioration are among the primary objectives. Considering the formation of off-flavors, toxic by-products, and nutritional losses

resulting from lipid oxidation, natural antioxidants are regarded as safer alternatives for the stabilization of food products.

Within this context, the oxidative stability of hazelnut oil and corn oil will be evaluated using natural plant materials, including bay leaf, olive leaf, and willow leaf. The oxidation process will be monitored using the Rancimat method, and kinetic parameters such as induction period, activation energy, and reaction rate constant will be determined. In this way, the potential of these natural materials to extend the shelf life of oils will be quantitatively assessed.

2. Research and Findings

The conceptual framework of this study is based on understanding the mechanisms affecting lipid oxidation, the role of natural antioxidants in preventing oxidative deterioration, and the factors determining the oxidative stability of edible oils. This framework comprehensively addresses the stages of lipid oxidation, antioxidant activity, and the interactions between plant-derived bioactive compounds and oil matrices.

2.1. Lipid Oxidation Mechanism

Lipid oxidation is a complex deterioration process that predominantly occurs in unsaturated fatty acids and proceeds through chain reactions. This process takes place in three main stages: initiation, propagation, and termination. During the initiation stage, free radicals are formed as a result of the removal of a hydrogen atom from lipid molecules. These radicals react with oxygen to form peroxyl radicals, which subsequently attack other lipid molecules, thereby sustaining the chain reaction. In the termination stage, two radicals combine to form more stable compounds, effectively ending the reaction. Lipid oxidation leads to quality losses such as aroma deterioration, nutrient degradation, pigment changes, and the formation of undesirable volatile compounds. Therefore, understanding the chemistry of oxidation is essential for developing strategies aimed at improving oil stability.

2.2. Factors Affecting Oxidative Stability

The oxidative stability of oils is influenced by both intrinsic and extrinsic factors. Intrinsic factors include fatty acid composition (Table 1), degree of unsaturation, presence of metal ions, and natural antioxidant content. Extrinsic factors consist of temperature, light exposure, oxygen availability, and storage conditions. Oils rich in polyunsaturated fatty acids, such as linoleic and linolenic acids, are more susceptible to oxidation. The Rancimat test, which measures the induction period under accelerated conditions, is widely used as a scientific method for evaluating the oxidative resistance of oils.

Table 1 Fatty Acid Composition of Some Vegetable Oils [11]

Oil Name	C12:0 Lauric	C14:0 Myristic	C16:0 Palmitic	C16:1 Palmitoleic	C18:0 Stearic	C18:1 Oleic	C18:2 Linoleic	C18:3 Linolenic	C20:1 Gadoleic
Olive oil	–	–	13.0	1.0	3.0	71.0	10.0	1.0	1.0
Palm oil	0.3	1.0	45.0	0.3	4.0	40.0	10.0	0.2	–
Coconut oil	47.0	18.0	9.0	–	3.0	6.0	2.0	–	–
Peanut oil	–	–	11.0	0.1	2.0	48.0	32.0	–	2.0
Rice bran oil	–	0.4	20.0	0.3	1.4	39.0	37.0	1.0	0.5
Canola oil	–	0.1	4.1	0.3	2.0	62.0	22.0	10.0	1.5
Rapeseed oil	–	0.1	4.0	0.3	1.0	19.0	15.0	11.0	7.0
Corn oil	–	–	11.0	0.1	2.0	28.0	58.0	1.0	0.2
Soybean oil	–	0.1	11.0	0.1	4.0	24.0	54.0	7.0	0.2
Safflower oil	–	0.1	7.0	0.1	2.0	13.0	78.0	0.1	0.2
Sunflower oil	–	0.1	7.0	0.1	5.0	19.0	68.0	1.0	0.4

2.3. Role of Antioxidants in Lipid Stabilization

Antioxidants are compounds that inhibit or delay lipid oxidation and exert their effects through various mechanisms. These mechanisms include scavenging free radicals, chelating metal ions, decomposing hydroperoxides, and providing synergistic interactions with other antioxidants. Although synthetic antioxidants such as BHA, BHT, and TBHQ are effective, toxicological concerns associated with their use have increased interest in natural antioxidants. Consequently, plant-derived natural antioxidants have gained greater preference in recent years.

2.4. Plant-Derived Natural Antioxidants

Natural antioxidants consist of phenolic compounds, flavonoids, and other bioactive substances found in plants. Bay leaf, olive leaf, and willow leaf—commonly examined in the literature—are rich in phenolic compounds and exhibit strong potential to delay oxidative deterioration. These compounds stabilize free radicals by donating hydrogen atoms, inhibit the formation of new radicals through resonance stabilization, and interrupt the oxidation chain reaction. Antioxidant effectiveness varies depending on the chemical structure of the compound, its concentration, and its resistance to temperature.

2.5. Interaction of Plant Extracts with Oil Matrices

The effectiveness of natural antioxidants is closely related to their solubility, polarity, and thermal stability within the oil matrix. While some plant-derived compounds exhibit higher efficiency in bulk oils, others perform better in emulsion systems. A proper understanding of oil–antioxidant interactions is essential for accurately evaluating the performance of natural compounds under conditions of high temperature and oxidative stress.

2.6. Kinetic Evaluation of Oxidative Stability

Kinetic analyses enable the quantitative evaluation of the oxidation process. Parameters such as the reaction rate constant (k), activation energy (Ea), and induction period provide a scientific basis for comparing the oxidative behavior of oils. These kinetic parameters can be calculated using accelerated oxidation systems such as the Rancimat method, allowing the extent to which natural antioxidants delay oxidative degradation to be clearly determined.

3. Materials and Methods

The primary objective of studies reported in the literature is to evaluate the oxidative stability of different vegetable oils and to elucidate the effects of natural plant-based materials on the oxidation process of oils. In this context, research is generally structured around the preparation of materials, the performance of oxidation analyses, and the evaluation of the obtained results using kinetic approaches. In particular, oxidative stability comparisons are commonly conducted based on parameters such as induction period, reaction rate constant, and activation energy, which are determined using the Rancimat method.

3.1. Oil Samples

Studies employing the Rancimat method typically use commonly consumed vegetable oils such as hazelnut oil, corn oil, olive oil, sunflower oil, and soybean oil. It is reported that these oils are selected in fresh and refined forms, with particular attention paid to ensuring that they have not undergone oxidative deterioration. Prior to analysis, the oils are stored in dark-colored containers to minimize exposure to light and oxygen. It is emphasized that storage conditions can significantly influence Rancimat results; therefore, maintaining standardized storage conditions is considered essential.

3.2. Plant-Derived Antioxidants

The direct addition of natural antioxidants to oils is a widely applied approach in the literature. Studies report that plant materials or their extracts are incorporated into oils at specific concentrations, and mechanical or magnetic stirring is used to ensure homogeneous distribution. In addition, oil samples without antioxidant addition are evaluated as control groups, and the results are reported on a comparative basis.

3.3. Addition of Antioxidants to Oils

Each plant-based material is added to the corresponding oil sample at predetermined amounts, followed by mixing for a defined period using a magnetic stirrer to achieve homogeneity. To establish control groups, oil samples without any antioxidant addition are prepared under the same conditions.

3.4. Methods for Determining Oxidative Stability

In the determination of oxidative stability of vegetable oils, classical chemical methods such as peroxide value and anisidine value are widely used, in addition to the Rancimat test. The Rancimat method evaluates oxidative resistance by determining the induction period of oils under accelerated oxidation conditions. Studies have reported that Rancimat results generally show consistent trends with peroxide and anisidine values; therefore, this method is considered to reliably reflect the oxidative behavior of oils.

4. Conclusion and Discussion

Numerous studies have focused on improving the oxidative stability of vegetable oils such as hazelnut oil, corn oil, and similar edible oils. In particular, increasing toxicological concerns regarding the long-term use of synthetic antioxidants have intensified interest in the evaluation of natural plant-based materials as alternative antioxidant

sources in the food industry. In this context, phenolic-rich plant materials such as bay leaf, olive leaf, and willow leaf have been frequently investigated for their effects on the oxidation processes of oils.

Experimental studies reported in the literature indicate that the oxidation behavior of oils is commonly evaluated using the Rancimat method following the addition of plant leaves or their extracts. The induction periods obtained have been reported to increase with the incorporation of natural antioxidants, demonstrating that these compounds can significantly enhance the oxidative stability of oils. The extension of the induction period is attributed to the ability of natural antioxidants to slow down the lipid oxidation chain reaction. This effect is explained by mechanisms such as free radical scavenging, metal ion chelation, and suppression of hydroperoxide formation [9, 12].

Kinetic evaluations reported in the literature indicate that the addition of natural antioxidants reduces the oxidation reaction rate constant while increasing the activation energy. An increase in activation energy suggests that a higher amount of energy is required to initiate oxidative degradation, indicating enhanced thermal stability of oils. These findings are consistent with previous studies reporting the protective role of natural antioxidants, particularly in oils rich in unsaturated fatty acids [10].

Comparative studies among different plant materials emphasize that antioxidant effectiveness may vary depending on the type of leaf used. These differences are associated with variations in phenolic compound profiles, total phenolic content, and antioxidant activity levels of the plants. In particular, several studies have reported that bay leaf and olive leaf, owing to their rich phenolic composition, are more effective in delaying oxidation processes [13].

Overall, the literature indicates that natural plant-based materials can effectively enhance oxidative stability in oils with high unsaturated fatty acid content. This provides a significant advantage in terms of extending shelf life, preserving sensory quality, and maintaining nutritional value. The use of natural antioxidants is regarded as a safer, more sustainable, and economically viable approach in the food industry. Future studies comparing different plant species, extraction methods, and oil matrices are expected to contribute to the development of more comprehensive strategies for the application of natural antioxidants.

References

[1] Gül, V., Öztürk, E., Polat, T., (2016), The importance of sunflower in closing the vegetable oil deficit in today's Turkey, Journal of Agricultural Sciences, 30(B), 70-76

[2] Bodoira, R.M., Penci, M.C., Ribotta, P.D., Martínez, M.L., (2017), Chia (Salvia hispanica L.) oil stability: Study of the effect of natural antioxidants, LWT - Food Sci. Technol. 75 107-113.

[3] Da Silva, A., & Jorge, N. (2014). Influence of Lentinus edodes and Agaricus blazei extracts on the prevention of oxidation and retention of tocopherols in soybean oil. Journal of Food Science and Technology, 51, 1208–1212.

[4] Gallego, M. G., Gordon, M., Segovia, F., Skowyra, M., & Almajano, M. (2013). Antioxidant properties of rosemary, thyme, and lavender in oil-in-water emulsions. Journal of the American Oil Chemists' Society, 90, 1559–1568.

[5] Keskin, H. (1981). Food chemistry (Vol. 1). Istanbul University Press.

[6] Sherwin, E.R., (1990), Food Additives. Ed. by L. Branen, Marcel Dekker, New York, 139–193.

[7] Fernández-López, J., Zhi, N., Aleson-Carbonell, L., Pérez-Alvarez, J. A., & Kuri, V. (2005). Antioxidant and antibacterial activities of natural extracts: Application in beef meatballs. Meat Science, 69(3), 371–380.

[8] Balasundram, N., Sundram, K., & Samman, S. (2006). Phenolic compounds in plants and agri-industrial by-products: Antioxidant activity, occurrence, and potential uses. Food Chemistry, 99, 191–203

[9] Taghvaei, M., & Jafari, S. M. (2013). Application and stability of natural antioxidants in edible oils in order to substitute synthetic additives. Journal of Food Science and Technology, 52(3), 1272–1282.

[10] Kozlowska, M., & Gruczyńska, E. (2018). Comparison of the oxidative stability of soybean and sunflower oils enriched with herbal plant extracts. Chemical Papers, 72(10), 2607–2615.

[11] Can, N. (2019). The importance of oxidative stability in the preservation of vegetable oils and analytical methods used for determining oxidative stability. ABMYO Journal, (54), 107–124.

[12] Balasundram, N., Sundram, K., & Samman, S. (2006). Phenolic compounds in plants and agri-industrial by-products: Antioxidant activity, occurrence, and potential uses. Food Chemistry, 99(1), 191–203.

[13] Sevim, D. (2011). Antioxidants and olive oil. Olive Science, 2(1), 43–47.

Optical Properties of a Novel Pyrazoline Derivative in Diverse Micelle Systems

Ebru Bozkurt[1,2*], Halise İnci Gül[3], Cem Yamalı[4], Turgut Seçkin Gül[5]

[1] Program of Occupational Health and Safety, Vocational College of Technical Sciences, Atatürk University, Erzurum, Türkiye
[2] Department of Nanoscience and Nanoengineering, Graduate School of Natural and Applied Sciences, Atatürk University, Erzurum, Türkiye
[3] Department of Pharmaceutical Chemistry, Faculty of Pharmacy, Ataturk University, Erzurum, Türkiye
[4] Department of Basic Pharmaceutical Sciences, Faculty of Pharmacy, Çukurova University, Sarıçam, Adana, Türkiye
[5] Department of Pharmacology, Faculty of Medicine, Ataturk University, Erzurum, Türkiye

Corresponding author E-mail: ebrubozkurt@atauni.edu.tr

Keywords

Pyrazoline
CTAB
SDS
T80
Fluroscence

Abstract

In this study, a novel pyrazoline derivative, 4-(5-phenyl-3-(thiophen-2-yl)-4,5-dihydro-1H-pyrazol-1-yl) benzenesulfonamide (**TP1**), was synthesized and its optical behavior was investigated in different micelle structures. For this purpose, micelles were prepared using cationic (Cetyltrimethylammonium bromide, CTAB), anionic (Sodium dodecyl sulfate, SDS), and nonionic (Tween 80, T80) surfactants at different concentrations. Absorbance and fluorescence measurements of **TP1** were performed in all micelle structures prepared at room temperature. It was observed that in the fluorescence band maxima of **TP1** shifted to blue region at critical micelle concentration (CMC) values of CTAB, SDS, and T80 surfactants. The binding constants were found to be 1.35, 0.14, and 44.42 mM^{-1} for CTAB, SDS, and T80, respectively. It has been determined that **TP1** can be used as a probe to determine the critical micelle concentration (CMC) of CTAB, SDS, and T80 surfactants.

1. Introduction

Pyrazoline is an important heterocyclic compound containing two adjacent nitrogen atoms and an endocyclic double bond (Figure 1). These derivatives possess a broad spectrum of biological activity, including antibacterial, anticancer, antitumor, anti-HIV, and anti-inflammatory activities. Currently, pyrazoline systems are attracting increasing interest among biomolecules due to their remarkable pharmacological properties. They generally exhibit blue fluorescence with high quantum yield in solution due to their intramolecular charge transfer properties. These strong fluorescence properties have led to their widespread use in materials science applications such as hole transfer materials, organic light-emitting diodes, dye-sensitized solar cells, electroluminescence, and optical limiters [1].

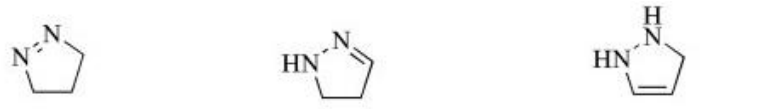

Figure 1 General structure of pyrazoline

Micelles are supramolecular structures formed by the spontaneous aggregation of surfactant molecules, particularly in aqueous environments. In a typical micelle structure, hydrophilic head groups interact with water, while hydrophobic tails are located in the interior, leading to the formation of nano-aggregates of various sizes and morphologies (Figure 2). These aggregates are mostly spherical, but ellipsoidal, cylindrical, or bilayer structures are also observed. Micelle formation is determined by parameters such as molecular geometry, concentration, pH, temperature, and ionic strength. In general, micelle systems are microheterogeneous two-phase colloidal systems and appear macroscopically homogeneous due to their colloidal dimensions. Aggregation occurs only under critical micelle concentration (CMC) and Kraft temperature conditions. In this process, hydrophobic interactions are

considered the primary driving force, and these effects arise from the competition between hydrogen bonds of the interface and bulk water [2].

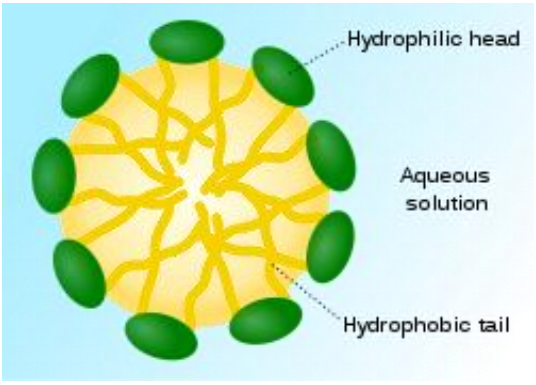

Figure 2 Structure of normal spherical micelle

In this study, the optical behavior of a newly synthesized pyrazoline derivative compound (4-(5-Phenyl-3-(thiophen-2-yl)-4,5- dihydro-1H-pyrazol-1-yl)benzenesulfonamide (**TP1**)) was investigated in different micelle environments obtained using anionic, cationic, and nonionic surfactants. Micelle structures were prepared at different concentrations of cationic surfactant (cetyltrimethylammonium bromide, CTAB), anionic surfactant (sodium dodecylsulfate, SDS), and nonionic surfactant (Tween 80, T80). Absorbance and fluorescence measurements of **TP1** were performed at room temperature in all prepared micelle structures. It was observed that the fluorescence band maxima of **TP1** shifted to blue region at critical micelle concentration (CMC) values of CTAB, SDS, and T80 surfactants.

2. Materials and Methods

2.1. Materials

Ethanol and surfactants including those from Sigma and Merck, as well as quinine sulfate (Fluka) and sulfuric acid (H_2SO_4, Sigma), were used as received without further purification. The stock solution of **TP1** was prepared in ethanol. The stock solutions of surfactants (0.1 M for CTAB, 0.5 M for SDS, 0.1 M for T80) were prepared in water. A certain amount of fresh probe samples in different solution was obtained from this stock solution by evaporating the solvent. For all measurements, the concentrations of **TP1** were 7 µM. All the experiments were performed at room temperature.

2.2. UV-vis. absorption and fluorescence spectroscopy

The UV-vis. absorption and fluorescence spectra of the samples were recorded using Shimadzu UV-1800 spectrophotometer and Agilent Technologies Cary Eclipse Fluorescence spectrophotometer. respectively. For the steady-state fluorescence measurements, all the samples were excited at 350 nm and fluorescence intensities were recorded between 360-650 nm. The fluorescence quantum yield values of all samples were determined using the Parker-Rees method, as described by the following equation 1.

$$\Phi_s = \Phi_r \left(\frac{D_S}{D_r}\right)\left(\frac{\eta_s^2}{\eta_r^2}\right)\left(\frac{1-10^{-OD_r}}{1-10^{-OD_s}}\right) \quad (1)$$

Quinine sulfate (Φ_f = 0.55 in 0.5 M H_2SO_4) was used as the reference material for the calculations. In this context, D denotes the integrated area under the corrected fluorescence spectrum, n represents the refractive index of the solution, and OD corresponds to the optical density at the excitation wavelength (λ_{exc} = 350 nm). The subscripts s and r refer to the sample and reference solutions, respectively [3].

2.3. Synthesis of 4-(5-Phenyl-3-(thiophen-2-yl)-4,5- dihydro-1H-pyrazol-1-yl)benzenesulfonamide (TP1)

2-Acetylthiophene (2 g) and benzaldehyde (1.7 g) were dissolved in ethanol (10 ml), and an aqueous solution of potassium hydroxide (10 ml, 40% w/v) was added dropwise into the reaction flask. Reaction mixtures were stirred for at room temperature, and reactions were followed by thin layer chromatography (TLC) using dichloromethane:methanol (4.8:0.2) solvent system. After completion of the reaction, the reaction mixture was poured into the water (25 ml) and then acidified with hydrochloric acid solution (10%) to pH 3–The solid obtained was filtered, washed with water and ethanol for several times. The purity of the chalcone was checked by TLC, and then, they were used in the synthesis of pyrazoline without further purification. At the second step, a solution of the chalcone (0.5 g, 2 mmol) in ethanol (30 ml) with glacial acetic acid (0.1 ml) was heated until chalcone dissolved and then p-

hydrazinobenzene sulfonamide hydrochloride (0.5 g, 2 mmol) was added into the reaction mixture, and finally, the mixture was refluxed. The reactions were monitored by TLC plates using chloroform:methanol (5 ml:2 drops) as solvent system. After completion of the reaction, the mixture was poured into the water (50 ml). The solid compounds obtained were filtered and dried. The compound was purified by crystallization from ethanol (Figure 3) [4].

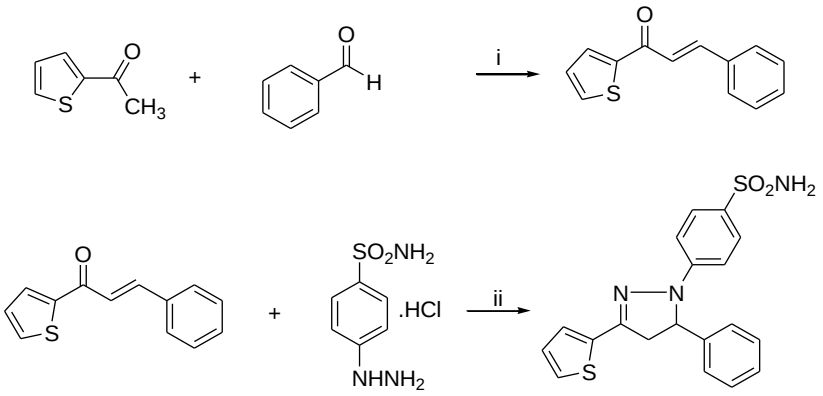

Reagents: i) Ethanol, potassium hydroxide solution (40% w/v), rt

ii) Ethanol, glacial acetic acid, reflux

Figure 3 Synthesis of the compound TP1

3. Results and Discussion

The effects of cationic, anionic, and nonionic surfactants such as CTAB, SDS, and T80 on the optical properties of **TP1** were investigated. Absorption and fluorescence measurements of TP1 were taken in the presence and absence of these surfactants. When the absorption spectra of **TP1** were examined, peaks corresponding to characteristic π→π* transitions resulting from intramolecular charge transfer in water were observed around 260-270 nm, while peaks corresponding to n→π* transitions resulting from conjugation in the pyrazolin ring were observed around 370 nm [5].

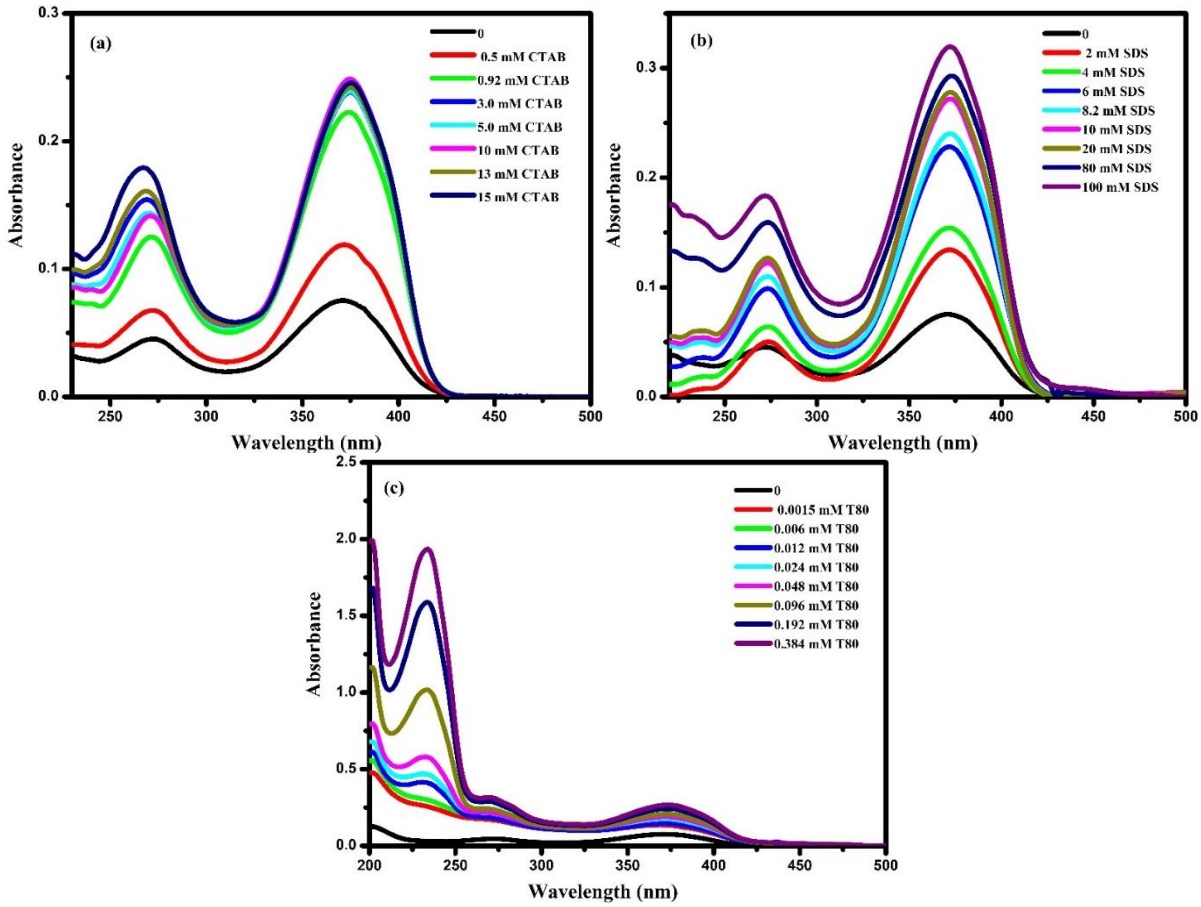

Figure 4 Absorption spectra of TP1 (7 µM) in different concentrations of (a) CTAB (b) SDS (c)T80

It was determined that these peaks were also observed in the presence of the studied surfactants, and that the absorption peaks of **TP1** increased as the surfactant concentration increased (Figure 4).

The fluorescence emission spectrum of **TP1** was also measured in the presence and absence of CTAB, SDS, and T80 (Figure 5). On gradual addition of CTAB, SDS and T80 in aqueous solution of **TP1**, an enhancement of the fluorescence intensity with major blue shift (in CTAB, SDS and T80) of spectral maxima from 466 nm (in aqueous solution) was observed (Table 1).

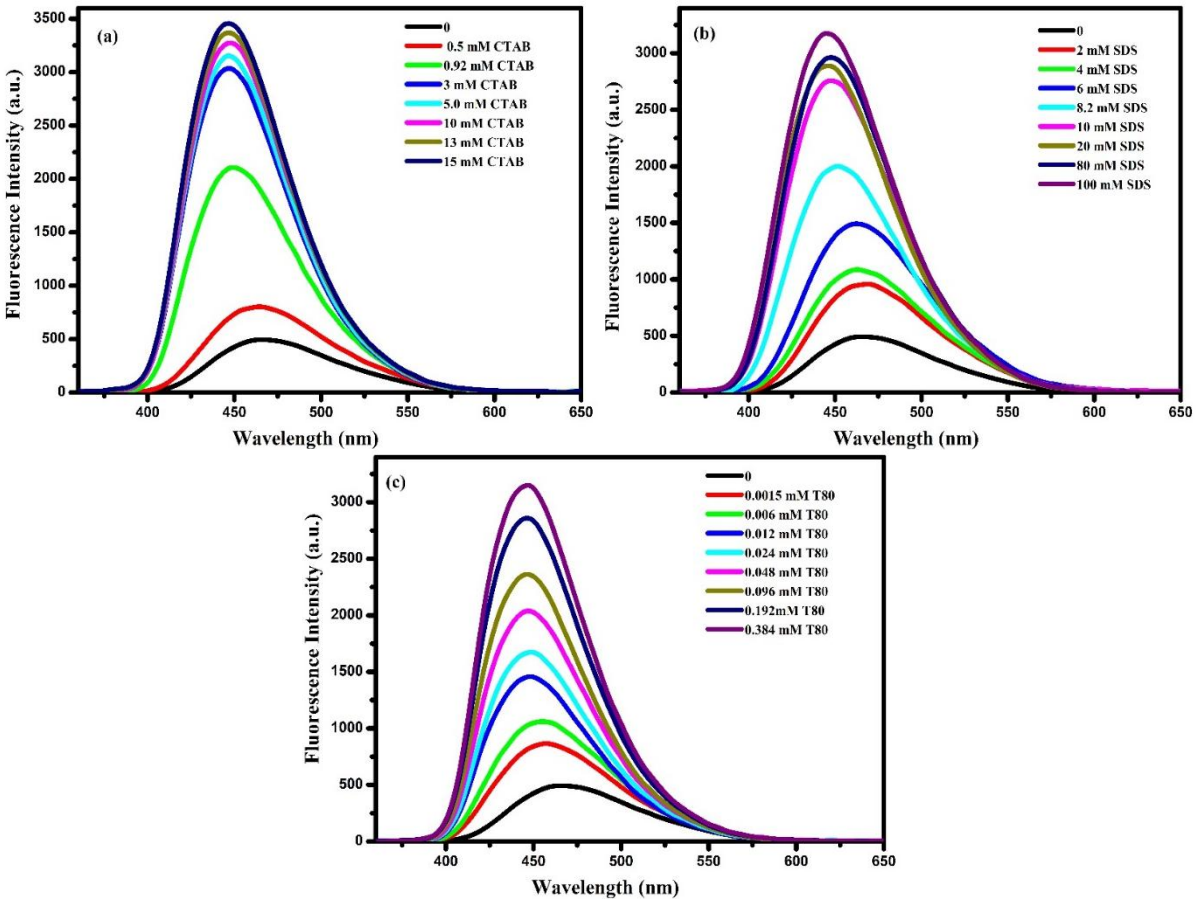

Figure 5 Fluorescence spectra of TP1 (7 µM) in different concentrations of (a) CTAB (b) SDS (c)T80

The quantum yield values of the synthesized **TP1** in all studied micelle environments were also calculated. As shown in Table 1, the quantum yield of **TP1** increased as the micelle concentration increased.

Table 1 The photo-physical parameters of **TP1** in different micelles

CTAB (mM)	λ_{max}	**Φ**
0.0	466	0.11
0.5	465	0.12
0.92	449	0.18
3	447	0.24
5	447	0.25
10	447	0.25
13	447	0.27
15	447	0.27
SDS (mM)	λ_{max}	Φ
0	466	0.11
2	469	0.14
4	463	0.13
6	462	0.13
8.2	452	0.16
10	448	0.20
20	446	0.20
80	448	0.20

100	445	0.19
T80 (mM)	λ_{max}	Φ
0	466	0.11
0.0015	457	0.09
0.006	455	0.10
0.012	448	0.14
0.024	449	0.14
0.048	447	0.16
0.096	446	0.17
0.192	446	0.19
0.384	447	0.19

The increase in fluorescence intensity observed in both ionic and non-ionic micelle systems of **TP1** is attributed to the interaction of the probe with the micelle structures. The strength of this interaction can be defined by calculating the probe-micelle binding constant K. Binding constants were obtained from fluorescence data using the method (Equation 2) developed by Almgren et al. [6], and the graphs are presented in Figure 6.

$$\frac{I_\infty - I_0}{I - I_0} = 1 + \frac{1}{K[M]} \tag{2}$$

where I_0, I, and I_∞ are the fuorescence intensities of **TP1** in absence of surfactant, in presence of micelles (micellar concentration [M]), and at maximum micellar concentration, respectively.

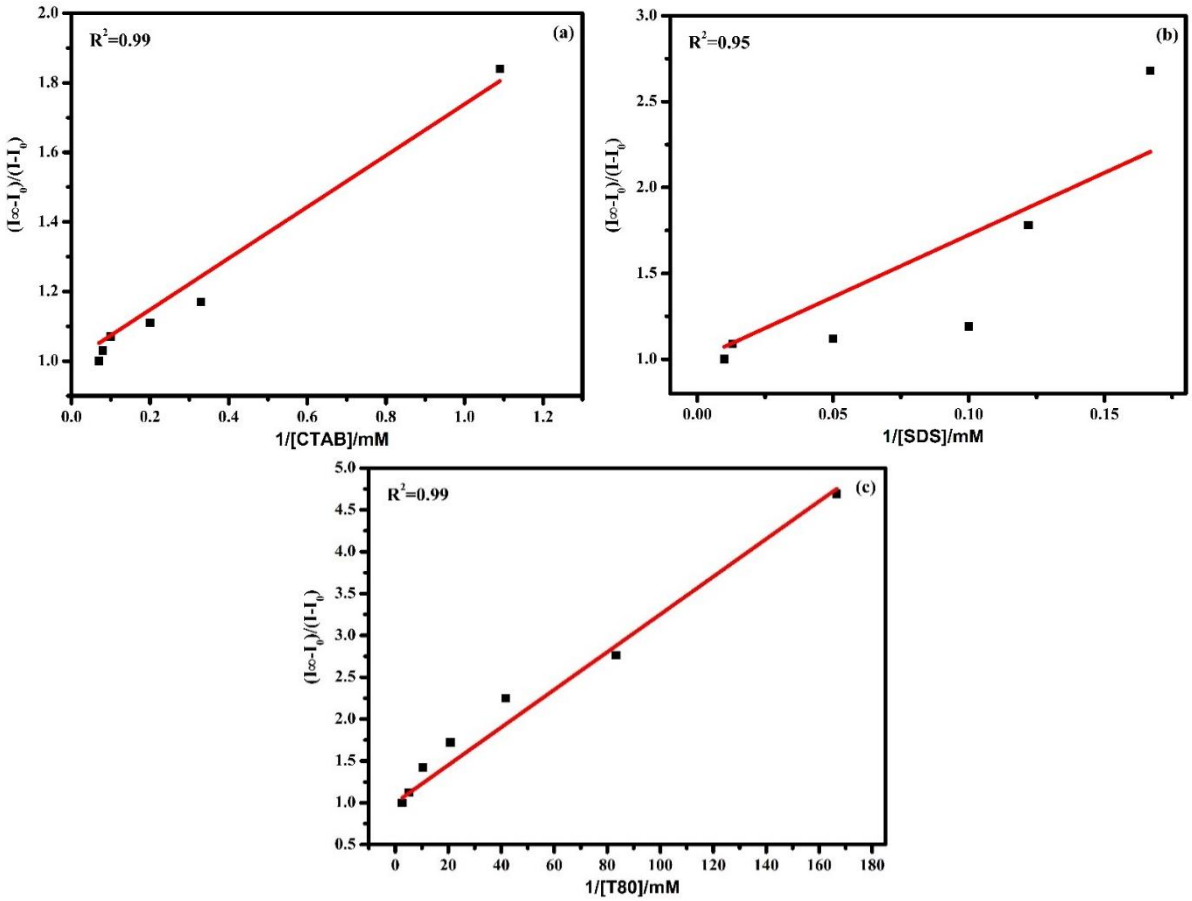

Figure 6 Binding plots of TP1 for (a) CTAB (b) SDS and (T80).

The graphs plotted using the Almgren method were found to be highly linear, and the binding constants were calculated from the slopes of the graphs. The binding constants were found to be 1.35, 0.14, and 44.42 mM^{-1} for CTAB, SDS, and T80, respectively. In the nonionic T80 micelle, the probe's higher binding constant with the micelle is due to its stronger stabilization in the micelle environment compared to ionic micelles. Compared to the Stern layer of CTAB and SDS micelles, the higher microviscosity of **TP1** in T80 is related to the denser packing of surfactant chains. Among ionic micelles, although the thickness of the Stern layer is similar, the binding constant of **TP1** with

CTAB is higher than with SDS. This can be explained by the fact that the head group of SDS is more hydrated than that of CTAB, and consequently, the Stern layer remains less hydrated in the CTAB micelle [7].

4. Conclusion

The optical properties of pyrazoline derivative **TP1** were studied in different micelles by using UV-Vis absorption and fluorescence spectroscopy techniques. UV–Vis absorption and fluorescence measurements were monitored as a function of surfactant (CTAB, SDS and T80) concentration. Blue shifts in the fluorescence band maxima of **TP1** occurred at critical micelle concentration (CMC) values of CTAB, SDS, and T80 surfactants, which are 0.92, 8.2, and 0.012 mM, respectively. The binding constants were found to be 1.35, 0.14, and 44.42 mM^{-1} for CTAB, SDS, and T80, respectively. It has been determined that **TP1** can be used as a probe to determine the critical micelle concentration (CMC) of CTAB, SDS, and T80 surfactants.

References

[1] Khan, S. A. (2020). Multi-step synthesis, photophysical and physicochemical investigation of novel pyrazoline a heterocyclic D- π -A chromophore as a fluorescent chemosensor for the detection of Fe3+ metal ion. Journal of Molecular Structure, 1211, 128084.

[2] Wani, M. M., Bhat, B. A. (2025). Micelle-driven organic synthesis: an update on the synthesis of heterocycles and natural products in aqueous medium over the last decade. RSC Advances, 15, 25586-25607.

[3] Bozkurt, E., Gul, H. I., Ozgun, DO. (2018). Pyrazoline derived new “off-on-off” fluorescent pH sensors. Optical Materials, 84,550-555.

[4] Yamali, C., Gul, H. I., Ece, A. Taslimi, P. Gulcin, I. (2018). Synthesis, molecular modeling, and biological evaluation of 4-[5-aryl-3-(thiophen-2-yl)-4,5-dihydro-1H-pyrazol-1-yl] benzenesulfonamides toward acetylcholinesterase, carbonic anhydrase I and II enzymes. Chemical Biology and Drug Design, 91, 854–866.

[5] Zayed, M. E. M., Kumar, P. (2021). Microwave-assisted synthesis, physicochemical, and optical properties of extended pi (π) bond pyrazoline derivative. Polycyclic Aromatic Compounds, 41(4), 685–697.

[6] Almgren, M., Grieser, F., Thomas, J. K. (1979). Dynamic and static aspects of solubilization of neutral arenes in ionic micellar solutions. Journal of the American Chemical Society, 101, 279-291.

[7] Banerjee, P., Pramanik, S., Sarkar, A., Bhattacharya, S. C. (2008). Modulated photophysics of 3-pyrazolyl-2-pyrazoline derivative entrapped in micellar assembly. The Journal of Physical Chemistry B, 112, 7211–7219.

Therapeutic Effect of the SN-38–Fe2O3 Nanoparticle Combination Targeting Dopamine Receptors in Colorectal Cancer Cells

Ozlem Ütme [1], Sıdıka Genç [1*], Ali Taghizadehghalehjoughi [1]

[1] Department of Medical Pharmacology, Faculty of Medicine, Şeyh Edebali University, Bilecik, Türkiye

* *Corresponding author E-mail: sidika.genc@bilecik.edu.tr*

Keywords

Anticancer,

CaCo-2,

Dopaminergic receptors,

Fe_2O_3 nanoparticles,

SN-38

Abstract

Introduction: In recent years, the link between cancer pathogenesis and neurotransmitter systems has gained increasing attention, particularly the regulatory role of dopamine in tumor biology. Dopamine, a monoamine neurotransmitter, can enhance antitumor responses through dopamine receptors (DRs). The Caco-2 colorectal adenocarcinoma cell line serves as a suitable model for studying DR-mediated signaling and anticancer agents interacting with these pathways. Among therapeutic molecules, SN-38 (the active metabolite of irinotecan) exerts strong cytotoxicity via DNA topoisomerase I inhibition. At the same time, iron oxide nanoparticles (Fe_2O_3 NPs) exhibit anticancer activity through ROS generation, modulation of intracellular stress responses, and selective uptake by cancer cells. This study evaluated the anticancer effects of SN-38 and Fe_2O_3 NPs on Caco-2 cells, exploring the potential involvement of dopaminergic signaling in these responses. Materials and Methods: Caco-2 cells were cultured under standard cell culture conditions. Once optimal conditions were achieved, the SN-38 anticancer agent encapsulated within nanoparticles was administered at defined doses (SN-38 10 nM + Fe_2O_3 25 µg/mL and SN-38 10 nM + Fe_2O_3 50 µg/mL). After 24 hours of treatment, cells and media were collected for analysis. Cell viability was assessed by MTT assay; oxidative stress parameters were evaluated using TAS and TOS assays; and the gene expression levels of dopamine receptor 1 and dopamine receptor 2 were examined. Results: The findings showed that the combined application of both molecules significantly reduced cell viability (approximately 25–40%) and disrupted oxidative stress balance to the detriment of tumor cells. The increase in TOS levels and decrease in TAS levels supported the conclusion that the treatment combinations enhanced pro-oxidant activity. Conclusion: This study demonstrates that the combination of SN-38 and iron oxide nanoparticles produces a pronounced anticancer effect in Caco-2 cells. The SN-38/ Fe_2O_3 nanoparticle combination appears to be a promising therapeutic approach for colorectal cancer.

1. Introduction

Colorectal cancer (CRC) affects a tissue that is renewed every five days by the division of colon epithelial stem cells. It targets the epithelial lining of the colon and is reported as the second leading cause of cancer-related deaths in both sexes. The primary approach for localized colorectal tumors is surgical resection; adjuvant therapies such as chemotherapy, radiotherapy, and targeted/immunotherapy are also considered depending on the tumor stage [1, 2]. However, chemotherapy agents often have serious side effects that can bother patients even after treatment is finished. These side effects include fatigue, nausea, and a weakened immune system [3]. Because of these side effects, researchers are seeking alternative treatment methods. Nanotechnology, aiming to provide molecular imaging, drug delivery, targeted therapy, etc., is offering promising results in cancer detection and treatment. Precisely targeting cancerous tissues using nanoparticles has been associated with promising successes. This approach could increase the effectiveness of treatment and minimize its side effects [4]. Due to their small size, nanoparticles can easily penetrate host tissues, reach cancerous tissues, and enter target cells. Iron nanoparticles (Fe_2O_3 NPs) exhibit anticancer activity through mechanisms such as reactive oxygen species (ROS) production, modulation of intracellular stress responses, and selective uptake by cancer cells [5-8].

In recent years, the relationship between cancer pathogenesis and neurotransmitter systems has become an increasingly important focus of interest, with the regulatory role of dopamine in tumor biology gaining particular prominence [1]. Dopamine (DA) is one of the major catecholamine neurotransmitters found in the central nervous

system (CNS). Based on their biochemical and pharmacological properties, dopamine is divided into two subfamilies: D1 and D2-like. It exerts its effects by binding to specific membrane receptors (DA-Rs) [9]. DA acts via multiple brain pathways. Two receptors, called D1 and D2, are distinguished from each other by their different binding affinities to a group of agonists and antagonists, different mechanisms of action, and different distribution regions in the central nervous system [9, 10]. It can also act as an antagonist, inhibiting tumor cell growth and leading to cell death. The expression levels of dopamine receptors vary in different tumor types and tumor development. In neuronal systems, dopamine is found to induce cell cycle regulation, DNA degradation, and apoptosis. Many effective dopamine inhibitors suppress angiogenesis, leading to tumor breakdown, and this process is a crucial part of its management [10].

7-Ethyl-10-hydroxycamptothecin, also known as SN-38, has been reported to have an active effect in irinotecan and exhibit strong inhibitory effects against DNA topoisomerase I [11].

Considering this information, our study aimed to evaluate the anticancer effects of the cytotoxic drug SN-38, encapsulated with Fe2O3, on dopaminergic signaling in CaCO-2 cells.

2. Materials and Methods

2.1. Cell Culture

CaCo-2 cells were obtained from the Department of Medical Pharmacology, Bilecik Şeyh Edebali University (Bilecik, Türkiye). Cell growth and development were achieved using Dulbecco's Modified Eagle Medium supplemented with 10% Fetal Bovine Serum (Euroclone, Milan, Italy) and F12 medium containing 0.1% Penicillin/Streptomycin (Euroclone, Milan, Italy). The cells were grown at 37 °C in a medium containing 5% CO_2 [12].

2.2. Cellular Therapy

After the cells reached sufficient density, they were passaged and seeded into 96-well plates. CaCO-2 cells that reached 100% density were treated with specific concentrations of Fe_2O_3 NP (10, 25, and 50 µg/mL) and SN-38 10 nM [13].

2.3. MTT Analyses

A commercial kit from Sigma-Aldrich (USA) was used to perform the MTT test. 10 µL of MTT (5 mg/ml) was added to each well, and the mixture was incubated at 37 °C with 5% CO_2 for 4 hours. DMSO was then applied to each well to dissolve the formazan crystals. Optical density (OD) measured at 570 nm using a spectrophotometer was used to determine the percentage of viable cells. The OD of the control group was set to 100, and the viability rate of the other groups was calculated [12].

2.4. TAC (Total Antioxidant Capacity) & TOS (Total Oxidative Stress)

Total Antioxidant Capacity (TAC) and Total Oxidative Status (TOS) levels were measured using the Rel Assay Total Antioxidant Capacity (Rel Assay Diagnostics, Gaziantep, Türkiye) commercial kit. Antioxidant capacity was assessed by preventing the formation of the 2,2'-azinobis(3-ethylbenzothiazoline-6-sulfonate) (ABTS+) radical. In summary, the supernatant was used and added according to the reagent production protocol. Color change was evaluated by measuring at a wavelength of 660 nm for TAC and 530 nm for TOS. TAC results were expressed in mmol Trolox Equivalent/L, and TOS results were expressed in µmol H_2O_2 Equivalent/mg protein [12].

2.5. Gene Analysis

D1 and D2 gene levels were measured by RNA isolation using the EcoPURE RNA isolation kit (EcoTECH Biotechnology, Erzurum, Türkiye). cDNA synthesis was measured using a cDNA synthesis kit (EcoScript) with a fixed amount of RNA from each sample. Each experiment was repeated independently three times, and the results were statistically evaluated [14].

2.6. Statistical Analysis

The statistical evaluation of the obtained findings was carried out using one-way analysis of variance (ANOVA). Statistical comparisons between groups were performed using the SPSS 20 test, and data with a significant level of $p<0.05$ were considered statistically significant.

3. Results and Discussion

3.1. MTT Results

The MTT results regarding cell viability are shown in Figure In this study, the 24-hour exposure results of the control, Sn-38 10 nM, Sn-38 10 nM + Fe_2O_3 25 µg/mL, and Sn-38 10 nM + Fe_2O_3 50 µg/mL groups were evaluated. The

control group was rated as 100, and the treatment groups were compared with the Sn-38 10 nM control group. The Sn-38 10 nM control group showed approximately a 15% reduction compared to the control group. Among the combined treatment groups, Sn-38 10 nM + Fe_2O_3 25 µg/mL, Sn-38 10 nM + Fe_2O_3 50 µg/mL, and Sn-38 10 nM showed significantly reduced cell viability compared to the control group (*p<0.05). The most effective reduction was observed in the Sn-38 10 nM + Fe_2O_3 50 µg/mL dose groups compared to the Sn-38 control group (**p<0.01).

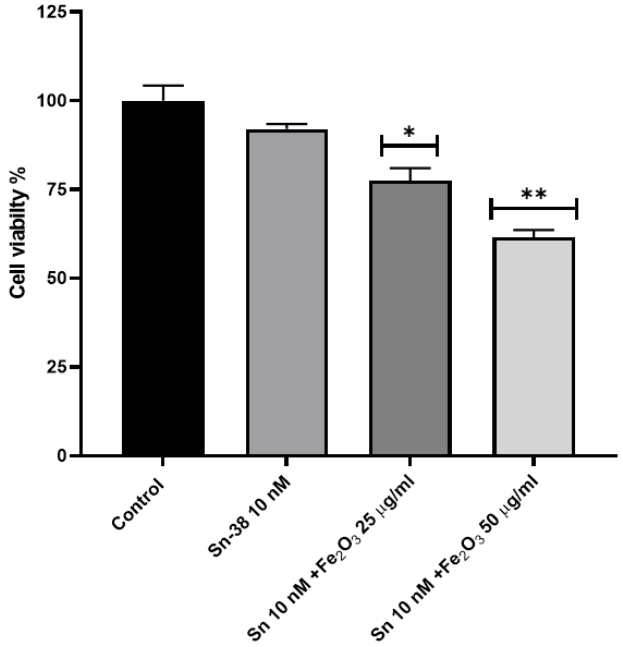

Figure 1 MTT analysis results show that SN-38 reduces cell viability, but combinations of SN-38 + Fe_2O_3 NPs significantly enhance this effect. Specifically, the combination group containing 50 µg/mL Fe_2O_3 NPs shows an increased cytotoxic effect and decreased cell viability (*p<0.05, **p<0.01).

3.2. TAS and TOS Analyses Results

The evaluation results regarding TAS and TOS outcomes are shown in Figures 2A and B. While TAC decreased significantly when SN-38 was applied alone, this effect was even more significant in combinations of SN-38 and Fe_2O_3 NP. In particular, the Sn-10 nM + Fe_2O_3 NP 50 µg/mL group showed a significantly lower TAC compared to the Sn-38 control group (#p<0.05). SN-38 alone increases oxidative stress. However, in the combined treatments, a statistically significant increase occurred in the SN-38 10 nM + Fe_2O_3 50 µg/mL NP group compared to the SN-38 control group (*p<0.05).

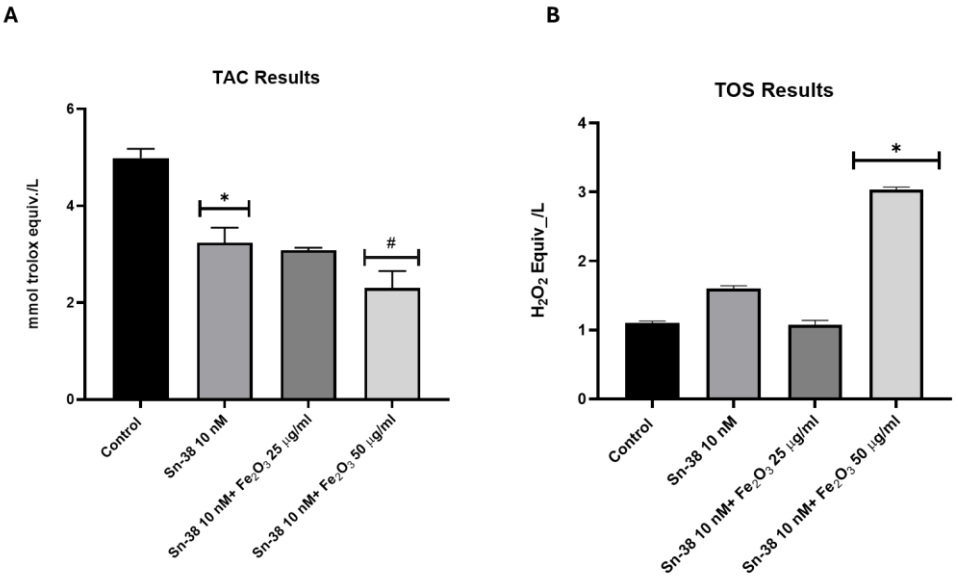

Figure 2 TAS and TOS analysis results. A: According to TAS results, the Sn-38 10 nM control group showed approximately a 2-fold decrease compared to the control group. The most effective decrease occurred in the Sn-38 10 nM + Fe2O3 combined treatment group. B: According to

TOS results, Sn-38 10 nM showed approximately a 2-fold increase compared to the control group. Among the treatment groups, Sn-38 10 nM + Fe2O3 50 µg/mL, Sn-38 increased significantly compared to the control group (*p<0.05, #p<0.05).

3.3. Gene Results

When the gene expression levels of D1 and D2 dopamine receptors were evaluated in the CaCo-2 cell line, it was observed that the applied treatment produced different regulatory effects specific to the receptors (Figure 3A and B). According to the results obtained, it was determined that D1 receptor gene expression increased with treatment, while D2 receptor gene expression decreased compared to the control group. This increase in D1 receptor expression suggests that the treatment may activate dopaminergic pathways associated with proliferation, cellular signal transduction, and survival mechanisms in CaCo-2 cells. On the other hand, the decrease in D2 receptor gene levels indicates that D2-mediated signaling, which is mostly associated with suppression of cell growth and pro-apoptotic processes, was inhibited after treatment. The obtained gene expression results support the idea that the treatment may exert biological effects on colorectal cancer cells via dopaminergic signaling.

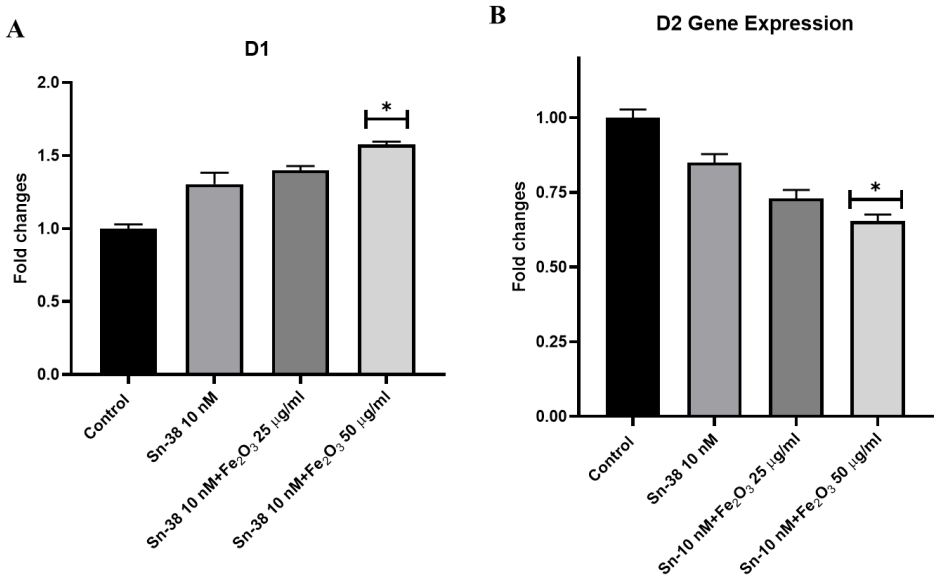

Figure 3 Gene Analysis Results. A: D1 expression gradually increases in treatment groups. The significant increase, especially in the SN-38 + Fe_2O_3 NP 50 µg/mL group, suggests that the dopaminergic D1 pathway is activated in relation to oxidative stress. B: D2 expression tends to decrease in the SN-38 and combination groups. A significant decrease occurred in the Fe_2O_3 NP 50 µg/mL group (*p<0.05).

SN-38, a chemical compound developed as an analogue of irinotecan, is one of the agents used in chemotherapy [8]. Iron oxide nanoparticles exhibit unique properties such as superparamagnetism, biocompatibility, and tunable surface chemistry. Furthermore, due to their low cost, biocompatibility, and distinctive characteristics, iron oxide nanoparticles have found applications in pharmaceutical fields such as cancer treatment and targeted drug delivery [15]. Therefore, in our study, the anticancer effect of the Fe_2O_3 NPs + SN-38 combination on colorectal cancer via dopamine receptors was investigated. When the findings were examined, it was observed that the Fe_2O_3 NPs + SN-38 combination produced a cytotoxic effect. In particular, the approximately 10% decrease in viability at the 50 µg/ml combination and the 45% decrease at the 25 µg/ml combination indicate the presence of a dose-dependent interaction. Many studies show that surface modifications significantly affect the biocompatibility, intracellular uptake kinetics, and selective toxicity of Fe_2O_3 NPs [16]. However, different synthesis methods (chemical, biological, thermal) and coating strategies lead to differences in results between studies; some reports indicate significant antitumor effects through strong ROS (reactive oxygen species) production and triggering of apoptosis mechanisms, while other studies have shown limited efficacy due to uncertainties in cell line-specific sensitivity and in vivo toxicity data [17]. This situation can be explained by possible mechanisms such as Fe_2O_3 NPs facilitating the uptake of Sn-38 into cells, increasing DNA alkylation efficiency, or lowering the oxidative stress threshold in tumor cells [18]. Dopamine alone is known to be effective in slowing the growth of these tumors by inhibiting tumor angiogenesis. Studies have shown that when dopamine is used in combination with anticancer drugs, it significantly inhibits tumor growth compared to treatment with dopamine alone or with anticancer drugs alone. The antiangiogenic effect of dopamine inhibits the proliferation and migration of tumor endothelial cells through the suppression of VEGF receptor-2, mitogen-activated protein kinase, and focal adhesion kinase phosphorylation [19].

The strong correlation between oxidative damage parameters and viability outcomes supports the idea that combination therapy induces cellular death largely through increased ROS production. Literature reports that Fe_2O_3

NPs increase ROS production, disrupting mitochondrial function, causing DNA damage, and triggering apoptosis [20]. This study shows that the Sn-38+ Fe_2O_3 NP combination leads to higher ROS levels compared to Sn-38 application alone, revealing that Fe_2O_3 NPs exhibit pro-oxidant properties and enhance the cytotoxicity of Sn-While Sn-38, as a known alkylating agent, causes cytotoxicity through DNA methylation, Fe_2O_3 NPs can disrupt the oxidative balance in tumor cells, leading to mitochondrial stress. The combination approach (Fe_2O_3 NP) can be considered a resistance-breaking strategy [13, 21].

In conclusion, the fact that the Sn-38 + Fe_2O_3 NP combination both increases ROS production and causes a significant decrease in cell viability indicates that this combination creates a synergistic anticancer effect [22]. These findings suggest that Fe_2O_3 NPs could be used as adjunct agents in Sn-38-based therapies and have therapeutic potential, particularly in tumors where Sn-38 resistance is a significant clinical problem. However, molecular-level confirmation of this effect and evaluation of safety and efficacy parameters in vivo models will be critical for future studies.

4. Conclusion

Our findings show that Sn-38 10 nM + Fe_2O_3 conjugation induces apoptosis in CaCo-2 cells. Specifically, it was determined that Sn-38 10 nM + Fe_2O_3 25 µg/ml and Sn-38 10 nM + Fe_2O_3 50 µg/ml doses activated the ROS mechanism in CaCo-2 cells, leading to cell death. However, these findings need to be supported by further mechanistic studies at the molecular level and in vivo models in different cancer cell lines for clinical validation.

References

[1] Narayana, S., et al., Inorganic nanoparticle-based treatment approaches for colorectal cancer: recent advancements and challenges. Journal of nanobiotechnology, 22(1): p. 427.

[2] Cuevas, S., et al., Renal dopamine receptors, oxidative stress, and hypertension. International journal of molecular sciences, 14(9): p. 17553-17572.

[3] Xiong, G., et al., Albumin-based nanoparticles encapsulating SN-38 demonstrate superior antitumor efficacy compared to irinotecan. Drug Delivery, 32(1): p. 2545519.

[4] Moura, C. and N. Vale, The role of dopamine in repurposing drugs for oncology. Biomedicines, 11(7): p. 1917.

[5] Ahmadzadeh Chaleshtori, M.A., A. Salehzadeh, and M. Peymani, Identification of oncogenes associated with colorectal cancer mortality and the effect of cinnamon-conjugated magnetic nanoparticles on their expression. Scientific Reports, 15(1): p. 17467.

[6] Elfiky, A.M., et al., Production of novel theranostic nano-vector based on superparamagnetic iron oxide nanoparticles/miR-497 targeting colorectal cancer. Scientific Reports, 15(1): p. 4247.

[7] Jijo, H., et al., Harnessing the potential of iron oxide nanoparticles: A comprehensive review on their synthesis, functionalization and pharmaceutical innovations. Next Nanotechnology, 8: p. 100270.

[8] Qi, Q.-r., et al., Research progress of SN38 drug delivery system in cancer treatment. International Journal of Nanomedicine, 2024: p. 945-964.

[9] Ozdemir, E., I. Bagcivan, and S. Gursoy, Role of D1/D2 dopamin receptors antagonist perphenazine in morphine analgesia and tolerance in rats. Bosnian journal of basic medical sciences, 13(2): p. 119.

[10] Sayın, A., Dopamin Reseptörleri ve Sinyal İletim Özellikleri. Klinik Psikiyatri Dergisi, 11(3).

[11] Bataille Backer, P., et al., Development of a Targeted SN-38-Conjugate for the Treatment of Glioblastoma. ACS omega, 9(2): p. 2615-2628.

[12] Genç, S., et al., Hydrocortisone and vitamin B12 protect SHSY-5Y cells against glutamate excitotoxicity by altering VIP and GAL levels. Journal of Anatolian Environmental and Animal Sciences. 9(4): p. 754-761.

[13] Genc, S., et al., New Anti-Cancer Impact of Cerium Oxide, Lithium, and Sn-38 Synergy via DNA Methylation-Mediated Reduction of MMP-2 and Modulation of the PI3K/Akt/mTOR Pathway. Pharmaceuticals, 18(11): p. 1725.

[14] Cicek, B., et al., AuNPs with Cynara scolymus leaf extracts rescue arsenic-induced neurobehavioral deficits and hippocampal tissue toxicity in Balb/c mice through D1R and D2R activation. Environmental Toxicology and Pharmacology, 107: p. 104417.

[15] Pankhurst, Q.A., et al., Applications of magnetic nanoparticles in biomedicine. Journal of physics D: Applied physics, 36(13): p. R167.

[16] Vallabani, N.S. and S. Singh, Recent advances and future prospects of iron oxide nanoparticles in biomedicine and diagnostics. 3 Biotech, 8(6): p. 279.

[17] Lamichhane, N., et al., Iron oxide-based magneto-optical nanocomposites for in vivo biomedical applications. Biomedicines, 9(3): p. 288.

[18] Mojica Pisciotti, M.L., et al., In vitro and in vivo experiments with iron oxide nanoparticles functionalized with DEXTRAN or polyethylene glycol for medical applications: magnetic targeting. Journal of Biomedical Materials Research Part B: Applied Biomaterials, 102(4): p. 860-868.

[19] Lud Cadet, J., et al., Dopamine D1 receptors, regulation of gene expression in the brain, and neurodegeneration. CNS & Neurological Disorders-Drug Targets (Formerly Current Drug Targets-CNS & Neurological Disorders), 9(5): p. 526-538.

[20] Singh, A., et al., Leaf extract mediated green synthesis of iron-oxide nanoparticles (FeO-NPs) by using Hibiscus rosa-sinensis (China rose): A potential approach and its biological application. Orbital: The Electronic Journal of Chemistry, 2024: p. 271-278.

[21] Kannupaiyan, J., et al., Facile Green Synthesis of Inorganic FeO NPs from Azima tetracantha for Organic Dye Degradation and Multifunctional Biological Applications. Journal of Inorganic and Organometallic Polymers and Materials, 2025: p. 1-18.

[22] Panneerselvam, C., et al., Green synthesis of Abutilon indicum (L) derived iron oxide (FeO) nanoparticles with excellent biological, anticancer and photocatalytic activities. Polyhedron, 257: p. 117022.

Therapeutic Potential of Ginseng Against Cancer Exosome–Induced Toxicity in Neuronal and Endothelial Cells

Yunus Emre Aydın[1], Ali Taghizadehghalehjoughi[1], Sıdıka Genç[1*]

[1] Department of Medical Pharmacology, Faculty of Medicine, Bilecik Şeyh Edebali University, Bilecik, Türkiye

* *Corresponding author E-mail: sidika.genc@bilecik.edu.tr*

Keywords

Exosome

HUVEC

SH-SY5Y

Oxidative damage

Abstract

Introduction: Cancer-induced exosomes cause toxicity in the recipient due to the oncogenic miRNAs, pro-inflammatory proteins, tumor-specific metabolites, and DNA/RNA fragments they carry. These exosomes, through their formation and endothelial application, trigger apoptosis by increasing oxidative stress and treatment, and consequently, essentially ensure viability. Current treatments are insufficient in mitigating this difficulty. Recent studies on Panax Ginseng have revealed significant effects, particularly in suppressing oxidative stress and apoptosis. Furthermore, studies show that it suppresses temperature-induced pro-inflammatory molecules, such as IL-6 and TNF-α, triggered by exosomes, and exhibits anti-inflammatory effects by reducing intracellular NF-κB activation. A more comprehensive evaluation of the power and therapeutic effects of exosome-mediated therapy is being attempted through co-culture models that mutually alter broader endothelial communication. Materials and Methods: The study included cocultures containing HUVEC and SH-SY5Y cell lines. After incubation, cancer exosomes (40 ng/mL) from the T98G cell line were added to the coculture, resulting in exosome-induced damage. Subsequently, Ginseng was applied as a therapeutic agent at doses of 200 ng/mL and 400 ng/mL. Viability analysis (MTT) and oxidative stress markers (TAC and TOS) were evaluated throughout the process. Results: The data obtained showed that 400 ng/mL of Ginseng sustained oxidative stress and increased plant viability by approximately 30% compared to exosome control groups. Conclusion: In conclusion, our study successfully demonstrated that Ginseng can be used as a therapeutic agent against the harmful effects of cancer exosomes that cause damage to cell length and endothelial stability.

1. Introduction

Cells secrete various extracellular vesicles (EVs) in response to specific stimuli or as part of normal physiological conditions. One of these is exosomes [1]. With diameters of 30–150 nm, exosomes constitute the smallest subgroup of EVs and are of endosomal origin. They are formed by budding from the plasma membrane [2]. Exosomes widely function as carriers of molecular information in intercellular communication and facilitate the movement of cargo molecules from donor cells to recipient cells, playing a role in both physiological and pathological processes [3]. Exosomes can be classified according to their size and cellular origin [4].

For example, exosomes released from cancer cells are more numerous than those from normal cells and contain oncogenic miRNAs, mutated DNA fragments, and tumor-specific proteins [5]. Through the molecules they contain, they promote angiogenesis and migration of cancer, particularly inflammation that supports tumor development [6]. Furthermore, cancer cells that ingest exosomes produced by cancer cells activate pathways such as EGFR, downregulating genes that increase ROS (reactive oxygen species) production and making them resistant to chemotherapy [7]. However, it has been shown that cancer-derived exosomes have significant toxic effects on cell groups outside of cancer cells, such as neuronal cells. These exosomes have been reported to increase oxidative stress in neurons, suppress antioxidant defense mechanisms, and consequently trigger apoptosis, reducing cellular viability. It has also been reported that these effects are increased depending on the exosome concentration, with higher doses causing greater disruption of oxidative balance and more pronounced neuronal loss [8]. Exosomes also cause inflammation in ECs by activating the NF-Kβ transcription factor in endothelial cells and subsequently increasing the production of pro-inflammatory cytokines such as IL-6 and Tumor Necrosis Factor-α (TNF-α) [9].

Current treatments are insufficient to prevent this toxicity and the pathways that cause inflammation. Recent studies on Panax ginseng and its organic phenolic compounds have shown that this plant exhibits suppressive effects on oxidative stress, inflammation, and apoptosis [10]. Panax ginseng is a plant that has gained significant importance in Asian medicine, especially in China. Initially used for mild symptomatic diseases, its applications expanded after the discovery of its phenolic content [11]. It has been reported in various in vitro and in vivo models to reduce mitochondrial damage by decreasing ROS production, thereby increasing cellular viability [12]. Furthermore, ginseng administration has been shown to reduce pro-inflammatory cytokine expression (TNF-α, IL-1β, and IL-6) and enzyme expression (iNOS and COX-2), thus suppressing the inflammatory response [13, 14].

Monoculture in vitro models, used to assess oxidative stress and inflammation caused by exosomes, are useful in demonstrating the direct effects of exosomes on target cells, but they are insufficient to reflect physiological cell-cell interactions and the complexity of the microscopic environment [15, 16]. However, in vivo, exosomes affect not just a single cell type, but all cells in that microenvironment simultaneously. This effect leads to a greater increase in oxidative stress and inflammation [17]. Therefore, the aim is to overcome the shortcomings of monoculture by using co-culture models [18, 19].

In this study, a co-culture model consisting of SH-SY5Y neuron-like cells and HUVEC (Human Umbilical Cord Endothelial Cells) endothelial cells was created to evaluate intercellular interactions under more realistic physiological conditions. A toxic microenvironment was created in the co-culture system using exosomes isolated from the T98G glioblastoma cell line, and the oxidative stress and inflammatory effects of tumor-derived exosomes on neuronal and endothelial cells were investigated. Furthermore, the study investigated whether cellular damage caused by exosomes released by tumor cells in individuals with glioblastoma, affecting surrounding neuronal and endothelial cells, could be modulated by Panax ginseng application. In this context, it is predicted that Panax ginseng may reduce cellular toxicity by suppressing exosome-mediated oxidative stress and inflammation, thus contributing to the development of more effective therapeutic approaches against exosome-induced damage.

2. Materials and Methods

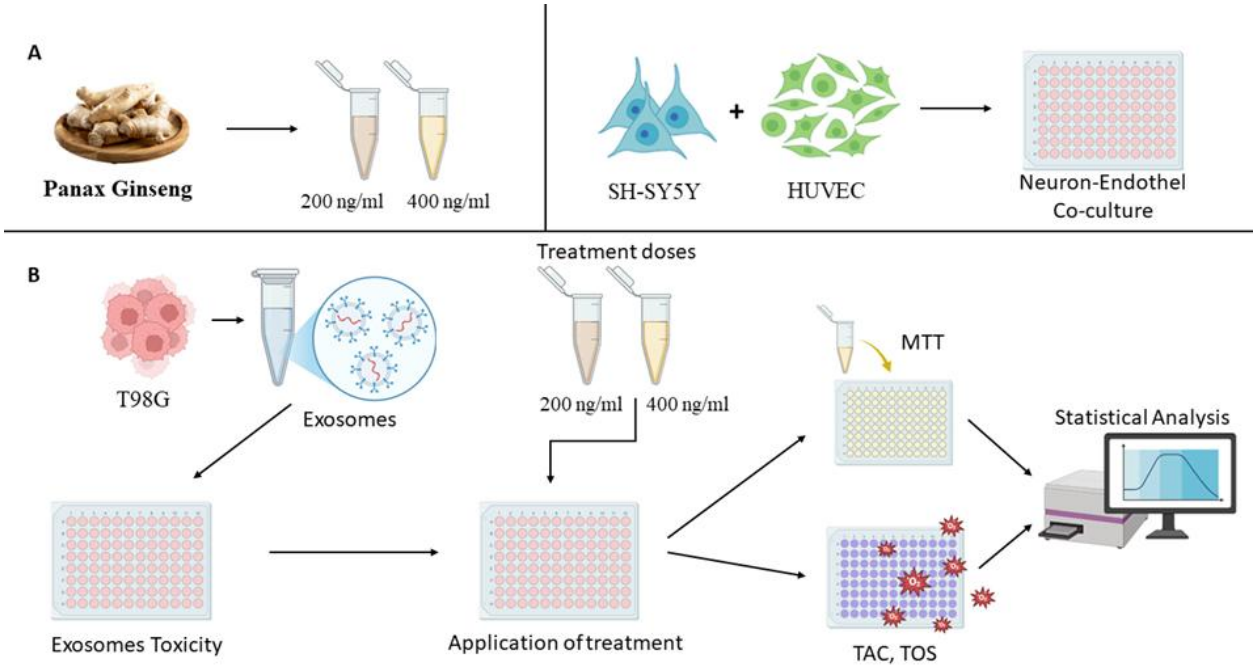

Figure 1 Graphical abstract

2.1. Cell Culture

SH-SY5Y (ATCC: CRL-2266) and HUVEC (ATCC: CRL-1730) cells were obtained from the Department of Medical Pharmacology, Faculty of Medicine, Bilecik Şeyh Edebali University (Bilecik, Türkiye). The cells were passaged and plated in a 96-well plate when they reached 90% confluence.

2.2. Creating Neuronal and Endothelial Co-Culture

A cell-contactless Transwell co-culture system was used to model paracrine communication between neuronal and endothelial cells. For this purpose, 0.4 µm pore size Transwell inserts (Corning) were selected. HUVEC cells were seeded in endothelial growth medium (~70–80% confluence) in the lower compartment and, after fixation, SH-SY5Y

cells were placed in the upper inserts at the same ratio. Both cell lines were cultured under standard incubation conditions (37 °C, 5% CO). This arrangement allowed for intercellular signal transduction and exosome interaction without direct contact. Co-cultures were prepared for experimentation after 24 hours, and cancer-derived exosomes and therapeutic agents were applied. This system is a frequently used approach in the literature to study paracrine interactions between different cell types, and Transwell-based co-culture models provide reliable results in toxicity and therapeutic effect studies [20].

2.3. T98G Exosome Production and Toxicity Generation

T98G cells were seeded into cell culture medium and, after reaching 80% confluence, the flask was washed three times with Hanks Balanced Salt Solution (HBSS) to remove residual fetal bovine serum (FBS). The cells were incubated in FBS-free medium for 48 hours. At the end of 48 hours, the liquid in the flask was collected. The supernatant was then centrifuged at 300g for 10 minutes, followed by centrifugation at 2000g and 10000g for 10 minutes each. Subsequently, exosomes were obtained by performing the steps according to the exosome isolation kit procedure [8].

2.4. Experimental Groups and Dosage Application

After inducing exosome toxicity in co-culture, cells were treated with Panax Ginseng (at concentrations of 200 ng/ml and 400 ng/ml). Cell groups were defined as follows:

Table 1 Experimental Groups

Control
Exosome Control
Panax Ginseng 200 ng/ml
Panax Ginseng 400 ng/ml

After treatment, the cells were incubated for 24 hours. At the end of 24 hours, oxidative damage markers (TAC and TOS) and viability analysis (MTT) were measured and evaluated.

2.5. MTT (3-(4,5-Dimethylthiazol-2-yl)-2,5-Diphenyltetrazolium Bromide) Assay

After 24 hours of treatment, 10 µL of MTT was added to each well of the 96-well plate, and the plate was incubated in a CO2 incubator for 4 hours. After 4 hours, 100 µL of DMSO (Dimethyl Sulfoxide) solution was added (to liquefy the formazan crystals). Data were obtained by reading at 570 nm with a spectrophotometer reader [21].

2.6. TAC (Total Antioxidant Capacity) Assay

TAC (Rel Assay Total Antioxidant Capacity (Rel Assay Diagnostics, Gaziantep, Türkiye)) levels were measured using a Multiskan™ GO microplate spectrophotometer. Color intensity was obtained by performing procedures on the samples according to the commercial kit instructions. TAC levels were determined by measuring absorbance at 660 nm, and antioxidant-related data were obtained. TAC results were expressed as µmol Trolox Equiv/L [21].

2.7. TOS (Total Oxidative Status) Assay

TOS (Rel Assay Total Oxidant Status (Rel Assay Diagnostics, Gaziantep, Türkiye)) levels were measured using a Multiskan™ GO microplate spectrophotometer. Color intensity was obtained by performing procedures on the samples in accordance with the commercial kit instructions. TOC levels were determined by measuring absorbance at 530 nm, providing oxidant-related data. TOS results were expressed as µmol H_2O_2 Equiv per mg protein [22].

2.8. Statistical Analysis

The results were analyzed using SPSS 20.0 (IBM SPSSCorp., Armonk, NY, USA) Windows program, and mean and standard error values were obtained. Statistical comparisons were made between groups using the One Way ANOVA test, and data with a significance level of $p<0.05$ were considered statistically significant.

3. Results and Discussion

3.1. MTT Result

The control group was compared with the exosome control group. The exosome control group was compared with the Panax ginseng (200 and 400 ng/mL) groups (Figure 2). Cells treated with ginseng were subjected to the MTT assay

to determine cell viability after 24 hours of incubation. As a result of the assay, cell viability decreased by 40% in the group exposed to cancer-derived exosomes (Ex, 40 ng/mL) compared to the control group. In contrast, a dose-dependent increase in cell viability was observed in the ginseng-treated groups (200 and 400 ng/mL), with viability increasing by 30–35% and approaching control levels (*p < 0.05). Notably, treatment with 400 ng/mL ginseng most effectively reversed the exosome-induced reduction in cell viability.

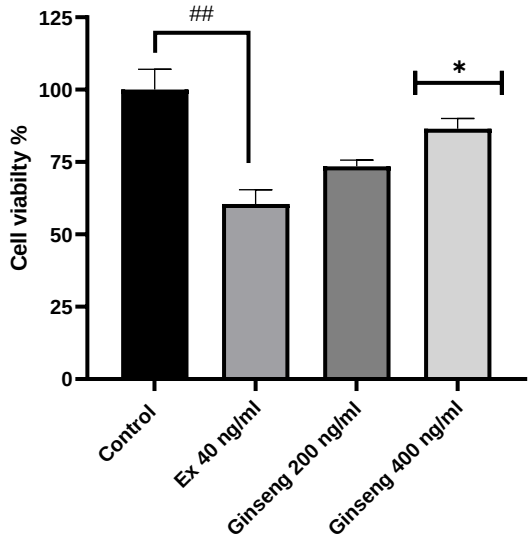

Figure 2 MTT analysis result. Ex 40 ng/mL Control: T98G exosomes 40 ng/mL; Ginseng: Panax ginseng; ng/mL: nanogram/milliliter; (##p < 0.01, *p < 0.05).

3.2. TAC Result

The control group was compared with the exosome control group. The exosome control group was compared with the Panax ginseng (200 and 400 ng/mL) groups (Figure 3). To evaluate antioxidant levels in the cells, TAS values were analyzed after 24 hours of incubation. According to the results, TAS levels in the T98G exosome control group decreased by approximately 50% compared to the control group, whereas treatment with ginseng at doses of 200 and 400 ng/mL resulted in an approximately 60% increase in TAS levels compared to the exosome control groups.

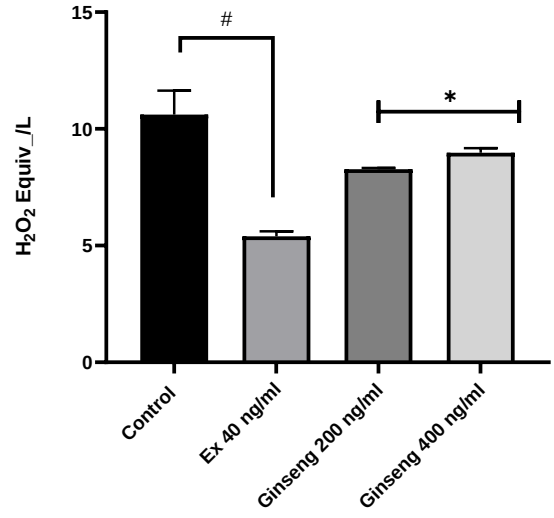

Figure 3 TAC (Total Antioxidant Capacity) analysis result. Ex 40 ng/mL Control: T98G exosomes 40 ng/mL; Ginseng: Panax ginseng; ng/mL: nanogram/milliliter; (#p < 0.05, *p < 0.05).

3.3. TOC Result

The control group was compared with the exosome control group. The exosome control group was compared with the Panax ginseng (200 and 400 ng/mL) groups (Figure 4). To evaluate oxidant levels in the cells, TOS values were analyzed after 24 hours of incubation. According to the results, TOS levels in the T98G exosome control group showed a fourfold increase compared to the control group, whereas in the groups treated with ginseng at doses of 200 and 400

ng/mL, TOS levels decreased compared to the exosome control groups, with an approximately 20% reduction observed at 200 ng/mL ginseng and a 55% reduction observed particularly at 400 ng/mL ginseng.

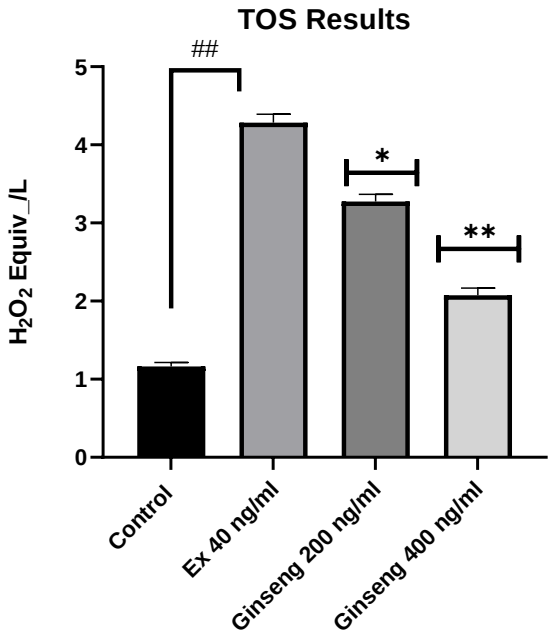

Figure 4 TOS (Total Oxidant Status) analysis result. Ex 40 ng/mL Control: T98G exosomes 40 ng/mL; Ginseng: Panax ginseng; ng/mL: nanogram/milliliter; (*p < 0.05, **p < 0.01, ##p < 0.01).

Exosomes derived from cancer cells enhance tumor development and cause toxicity in cells within the tumor microenvironment [23]. Much of the current literature on the pathobiology of cancer cell-derived extracellular vesicles focuses on the fact that these exosomes enhance tumor formation or transform other cells by transporting oncogenic material to nearby or even far from their origin. On the other hand, it has been shown that cancer cells secrete extracellular vesicles containing tumor suppressor and proapoptotic proteins such as P53, DKK4, PTEN, and maspin [24]. For example, studies by Genç et al. (2022) showed that cancer exosomes produced from T98G and U373 glioblastoma-derived cells increased LDH release in neurons. This dose-dependent increase in oxidative stress levels has been shown to lead to neuronal damage and consequently death [25].

The findings revealed a significant decrease in viability in neuronal and endothelial cells treated with exosomes released from the T98G cell line. MTT analysis results show that glioblastoma-derived exosomes exert a cytotoxic effect on recipient cells, causing a significant decrease in cell viability.

Furthermore, tumor cell-derived exosomes induce tumor angiogenesis by carrying angiogenic stimulants including vascular endothelial growth factor (VEGF), fibroblast growth factor (FGF), and transforming growth factor-β (TGF-β), and can increase vascular permeability by targeting endothelia, which leads to tumor cells disrupting the endothelial barrier of blood vessels, creating opportunities for metastasis [26]. In this context, the therapeutic potential of natural compounds targeting oxidative stress, inflammation, and abnormal angiogenesis processes triggered by exosomes in the tumor microenvironment is gaining increasing importance. Panax ginseng, with its phenolic compounds, possesses immunomodulatory, antioxidant, and anti-inflammatory properties [27]. Looking at the studies, Wang et al. (2015) showed that the phenolic compound of ginseng improved endothelial dysfunction caused by oxidative stress by upregulating the Nrf2-ARE pathway via AKT activation [28]. Hwang et al. (2010) found that it reduced and protected against 6-hydroxydopamine (6-OHDA)-induced oxidative damage in SH-SY5Y cells via the PI3K/Akt/Nrf2 signaling pathway [29].

In our study, increased oxidative stress and inflammation due to T98G-derived exosomes were observed, and a significant increase in antioxidant potential was seen in neuron and endothelial cells after ginseng treatment. In parallel, Total Oxidant Status (TOS) analysis showed a reverse trend; TOS significantly decreased after ginseng treatment, a result supporting the literature.

4. Conclusion

To strengthen the findings of this study, it is recommended that the underlying molecular mechanisms by which Ginseng reduces exosome-induced inflammation and oxidative stress, particularly via pathways such as NF-κB and

Nrf2, be validated in more detail. Additionally, studies in different cell types, at wider dose ranges, and using 3D/co-culture models will increase the generalizability of the results. Finally, validation in in vivo models will provide a clearer perspective on the therapeutic potential of Ginseng.

References

[1] Van der Pol, E., et al., Classification, functions, and clinical relevance of extracellular vesicles. Pharmacological reviews, 64(3): p. 676-705.

[2] McGough, I.J. and J.-P. Vincent, Exosomes in developmental signalling. Development, 143(14): p. 2482-2493.

[3] Bang, C. and T. Thum, Exosomes: new players in cell–cell communication. The international journal of biochemistry & cell biology, 44(11): p. 2060-2064.

[4] Hessvik, N.P. and A. Llorente, Current knowledge on exosome biogenesis and release. Cellular and Molecular Life Sciences, 75(2): p. 193-208.

[5] Kalluri, R., The biology and function of exosomes in cancer. The Journal of clinical investigation, 126(4): p. 1208-1215.

[6] Kok, V.C. and C.-C. Yu, Cancer-derived exosomes: their role in cancer biology and biomarker development. International Journal of Nanomedicine, 2020: p. 8019-8036.

[7] Li, F., et al., EGFR-rich extracellular vesicles derived from highly metastatic nasopharyngeal carcinoma cells accelerate tumour metastasis through PI3K/AKT pathway-suppressed ROS. Journal of extracellular vesicles, 10(1): p. e12003.

[8] Yeni, Y., et al., Glioblastoma cell-derived exosomes induce cell death and oxidative stress in primary cultures of olfactory neurons. Role of redox stress. Molecular Biology Reports, 50(5): p. 3999-4009.

[9] Nikdoust, F., et al., Exosomes: potential player in endothelial dysfunction in cardiovascular disease. Cardiovascular Toxicology, 22(3): p. 225-235.

[10] Zhang, B.-Z., et al., Panax Ginseng Root Extract Exhibits Antioxidant and Anti-Inflammatory Properties by Diminishing Oxidative Stress Levels and Modulating the NF-κB Signaling Pathway at Both the Cellular and Tissue Levels in the Skin. Natural Product Communications, 20(9): p. 1934578X251364582.

[11] Kiefer, D. and T. Pantuso, Panax ginseng. American family physician, 68(8): p. 1539-1542.

[12] Liu, P., et al., Panax ginseng alleviates diabetic peripheral neuropathy by suppressing mitochondrial dysfunction and oxidative stress via modulation of the RAGE, NF-κB, and Nrf2 pathways. Journal of Ginseng Research, 2025.

[13] Im, D.-S., Pro-resolving effect of ginsenosides as an anti-inflammatory mechanism of panax ginseng. Biomolecules, 10(3): p. 444.

[14] Jang, W.Y., J.Y. Hwang, and J.Y. Cho, Ginsenosides from Panax ginseng as key modulators of NF-κB signaling are powerful anti-inflammatory and anticancer agents. International Journal of Molecular Sciences, 24(7): p. 6119.

[15] McKee, T.J. and S.V. Komarova, Is it time to reinvent basic cell culture medium? 2017, American Physiological Society Bethesda, MD. p. C624-C626.

[16] Tkach, M. and C. Théry, Communication by extracellular vesicles: where we are and where we need to go. Cell, 164(6): p. 1226-1232.

[17] da Costa, V.R., et al., Exosomes in the tumor microenvironment: From biology to clinical applications. Cells, 10(10): p. 2617.

[18] Shimasaki, T., S. Yamamoto, and T. Arisawa, Exosome research and co-culture study. Biological and Pharmaceutical Bulletin, 41(9): p. 1311-1321.

[19] Lee, H., et al., Detection of micro-plasma-induced exosomes secretion in a fibroblast-melanoma co-culture model. Analytica Chimica Acta, 1281: p. 341910.

[20] Monteiro, A.R., et al., Co-culture models: Key players in in vitro neurotoxicity, neurodegeneration and BBB modeling studies. Biomedicines, 12(3): p. 626.

[21] Genç, S., et al., Amygdalin (Vitamin B17) Effect on Glioblastoma: Focus on Oxidant Capacity and Antioxidant Status. Recent Trends in Pharmacology, 2(2): p. 75-78.

[22] Genç, S., et al., Evaluation of Bee Venom Induced Toxicity: Toxicity and Management. Journal of Anatolian Environmental and Animal Sciences, 10(4): p. 514-520.

[23] Wang, X., et al., Exosomes and cancer-Diagnostic and prognostic biomarkers and therapeutic vehicle. Oncogenesis, 11(1): p. 54.

[24] D'Asti, E., et al., Extracellular vesicles in brain tumor progression. Cellular and molecular neurobiology, 36(3): p. 383-407.

[25] Genc, S., et al., Potential neurotoxic effects of glioblastoma-derived exosomes in primary cultures of cerebellar neurons via oxidant stress and glutathione depletion. Antioxidants, 11(7): p. 1225.

[26] Li, M., et al., The recent progress of tumor cell-derived exosomes in the pathogenesis, diagnosis and therapeutic strategies of tumors. Journal of Translational Medicine, 23(1): p. 925.

[27] Morshed, M.N., et al., Antioxidant activity of Panax ginseng to regulate ROS in various chronic diseases. Applied Sciences, 13(5): p. 2893.

[28] Wang, X., et al., Ginsenoside Rg3 antagonizes adriamycin-induced cardiotoxicity by improving endothelial dysfunction from oxidative stress via upregulating the Nrf2-ARE pathway through the activation of akt. Phytomedicine, 22(10): p. 875-884.

[29] Hwang, Y.P. and H.G. Jeong, Ginsenoside Rb1 protects against 6-hydroxydopamine-induced oxidative stress by increasing heme oxygenase-1 expression through an estrogen receptor-related PI3K/Akt/Nrf2-dependent pathway in human dopaminergic cells. Toxicology and applied pharmacology, 242(1): p. 18-28.

Perceptions of Artificial Intelligence in Türkiye: A Descriptive Analysis of TGSS Data

Esra Çelik[1,*]

[1] Department of Industrial Engineering, Faculty of Engineering, Atatürk University, Erzurum, Türkiye

* *Corresponding author E-mail: esraaclk64@gmail.com*

Keywords

Artificial intelligence
Perception
Statistical analysis
TGSS

Abstract

This study examined public perception of artificial intelligence across Türkiye using open-access data from the 2024 Turkish General Social Survey (TGSS). To this end, the increasing role of artificial intelligence in every field was addressed, and studies on artificial intelligence perception across the country were reviewed. In this context, the analysis and presentation of the data used with a large sample distinguishes the study from other studies. The study then provides information about the participants, dependent, and independent variables, utilizing the TGSS platform and the Veri Analiz Okulu (Data Analysis School) lecture notes where the data is shared. To evaluate the results, firstly frequency and percentage distributions were analyzed, then variance analysis, chi-square analysis, t-test, post hoc, and Tukey tests were conducted to examine how perceptions of artificial intelligence varied across independent variables and whether significant differences emerged. Based on the results, the general trend in perceptions of artificial intelligence and its differences across independent variables were interpreted. Accordingly, significant differences in perceptions of artificial intelligence were observed across demographic variables. Finally, suggestions were made to address these differences and for future studies.

1. Introduction

Artificial intelligence (AI), as defined by Gursoy and Cai (2025) [1], involves machines performing cognitive tasks traditionally associated with humans, such as learning, problem-solving, and interacting with the environment. Day by day, AI continues to increase its role in every aspect of daily life, including the economy, education, and public services. AI is actively used in all areas of daily life, from devices equipped with smart technology and digital assistants to personalized services. Applications like Google Assistant and Siri on smartphones, providing directions, finding content similar to watched series/movies or listened to music on platforms based on user experiences, presenting new alternatives based on preferences on shopping sites, and leading to early diagnosis by analyzing MRI or X-ray images clearly demonstrate the extent to which artificial intelligence is integrated into daily life [2].

AI has a significant impact on productivity, efficiency, the labor market, and financial systems in the economy. By automating routine tasks, productivity is increased, and the workforce is redirected to more strategic tasks. This leads to reduced costs and increased productivity [3].With AI, the need for human labor in low- and medium-skill jobs has decreased. On the other hand, new job opportunities have emerged in fields such as information processing and data analysis, brought about by high technology [4]. Furthermore, AI algorithms enable the detection of fraud, optimization of trade strategies, and analysis of credit risk [5]. Adapting the content of education systems to artificial intelligence and tailoring them to student needs has made learning processes more personalized and efficient. This has ensured equal opportunities in education [2]. AI also transforms the public sector into a more responsive and solution-oriented structure addressing the needs of society. This is achieved through increased efficiency, the use of effective decision support systems, citizen satisfaction, security and emergency management, transparency and accountability, and cost and resource savings [6]. In his study, Karataş (2025) stated that in order for AI to be used effectively in the public sector, the ethics mechanism should be strengthened, data infrastructures should be strengthened, and human resources should be transformed. He also noted that the use of artificial intelligence in the public sector is not a "magic wand," but it can be an effective "tool" if used correctly [7]. AI will become even more widespread in the public sector in the coming years. However, human rights, justice, and equality principles should not be ignored in this process.

The societal perception of AI-driven technologies, the trust felt, and ethical and cultural dimensions determine the speed and shape of the diffusion of AI systems [8]. For example, the study stated that for technology to be accepted

in healthcare, it should be developed with a human-centered design [9]. Ecer (2025) stated that for technology to be accepted, it must be adopted by society before individual benefit. He exemplified this by saying that individuals make decisions based on social norms as well as budget constraints in their consumer choices [10]. Moore (1991) argued that an individual's acceptance of a technology is due more to the social status it brings than to the functional benefits it provides [11]. In a similar study, Venkatesh (2000), based on the Unified Technology Acceptance and Use Theory model, experimentally proved that an individual's use of technology depends not only on the convenience or benefit offered to the individual but also on the influence and perceived image of their environment [12]. This is similar to Rogers' (2003) emphasis that technology adoption is not entirely an individual decision but an observable process within a social system [13]. AL Athmay *et al.* (2016) showed that individuals' acceptance of e-government services is influenced by the usage patterns and attitudes of those around them [14].

In Türkiye, the perception, acceptance, and use of artificial intelligence have gained momentum in recent years compared to other countries. For example, Saka (2025) systematically examined the perception, awareness, perspective, and applications of AI in Türkiye between 2020 and According to this, both students and teachers in the field of education have a positive view of AI and are aware of the potential benefits of AI applications [15]. Yalçın (2024) analyzed AI-based applications developed by public institutions for the benefit of society, such as the Ministry of National Education's "MEB Assistant," the Ministry of Foreign Affairs' "Hızır," and the Ministry of Interior's "ASENA." He stated that with the widespread use of such applications, society is interacting more with AI in daily life, which has increased societal perception, acceptance, trust, and ease of use of AI [16]. However, according to the latest data from the Turkish Statistical Institute (TÜİK) (2025), the low societal perception of artificial intelligence is attributed to the low adoption rates of AI in various sectors for solving real-life problems. Specifically, it is stated that only an average of 7.5% of businesses in Türkiye use AI [17]. Factors such as budget and expert shortages are highlighted as reasons for this (Packworld Türkiye, 2024). Furthermore, Sönmez (2025) also noted in his study that the possibility of information spreading rapidly in an inaccurate, dangerous, and unethical manner leads society to be cautious towards AI [19].

Studies measuring AI perception in Türkiye using descriptive analysis have focused on a single city/region, age group, time period, or occupational group. For example, a study measuring the impact of AI perception on occupational anxiety among university students focused on a single young generation group, and comparative analysis with graduates or working groups was not possible. Another study measured the attitudes of public employees towards artificial intelligence and their acceptance levels in service delivery only among public employees in a single region. Furthermore, studies generally prefer large city centers, and the perceptions and attitudes towards AI in rural areas, medium-density cities, or the elderly population have not been examined in sufficient depth.

This study measures and descriptively analyzes the perception of AI in Turkish society using the chosen sampling method, sample size, and analysis methods. The perception levels of different independent variable groups are presented comparatively. Subsequently, an in-depth examination is conducted on the groups where significant differences were found.

2. Materials and Methods

This section includes information on the data source, the dependent and independent variables examined, how the sample was selected, the research participants, and the analytical methods used.

2.1. Data Source

The data used in this study were obtained from the TGSS (Türkiye General Social Field Survey) platform and the lecture notes of the Data Analysis School, with open access permission [20]. TGSS is a social research project planned to monitor and analyze the changes over time in individuals' attitudes and opinions on many social issues, depending on parameters such as different demographic structures, social relationships, education, and family structures. From the many themes provided on the TGSS analysis platform, the theme "Perceptions of Artificial Intelligence" was selected. Six questions specific to this theme were posed to the participants. The content of the questions included interest and curiosity about the concept of artificial intelligence. Each question was formulated using different Likert scales. The first question was a binary answer (1=Yes, 2=No), the second a six-point frequency scale (1=Never, 2=Approximately once a month, 3=A few times a month, 4=A few times a week, 5=Once a day, 6=Many times a day), the third a five-point attitude scale (1=Strongly disagree, 2=Disagree, 3=Neither agree nor disagree, 4=Agree, 5=Strongly agree), the fourth a five-point knowledge level scale (1=No knowledge at all, 2=Very little knowledge, 3=Moderate knowledge, 4=Quite knowledge, 5=Very knowledgeable), the fifth question (1=Very negative, 2=Negative, 3=Neither positive nor negative, 4=Positive, 5=Very positive), and the sixth question a five-point attitude scale (1=No trust at all, 2=Very little trust, 3=Some trust, 4=Mostly trust). It is structured as follows: I trust, 5=I completely trust).

Ölçek soruları, ulusal ve uluslararası çalışmaların anket sorularının oluşturduğu bir soru havuzundan araştırmanın amacına en uygun ve en etkili soruların seçilmesi ile elde edilmiştir. Anket hem uluslararası kıyaslamalara uygun hem de yerel gerçekliğe duyarlı bir yapı halene getirilmiştir [21].

2.2. Variables

The content of the dependent and independent variables examined in the study is given below.

Dependent Variables: These are questions developed to examine society's perception of artificial intelligence. These are:

Have you ever heard of the concept of artificial intelligence before? (A1)

How often do you use AI-powered applications or programs? (A2)

How much do you agree with the statement, 'Artificial intelligence and automation will create more jobs than they will eliminate'? (A3)

How much do you think you know about artificial intelligence? (A4)

How positive or negative do you think the impact of artificial intelligence on society is? (A5)

How much do you trust the decisions that artificial intelligence will make about things that will affect your life? (A6)

Independent Variables: Gender, education level, age group, urbanization, region, and occupational group variables were selected as independent variables.

2.3. Participants

TGSS initially considered a minimum sample size of 2400 individuals to obtain reliable results with a 95% confidence interval and a ±2% margin of error. However, the sample size was later increased by 50% to account for potential data loss. Thus, between May 17, 2024, and June 2, 2024, 3600 surveys were conducted among all individuals aged 18 and over residing in Türkiye. However, after the data control process, the number of surveys deemed valid was The surveys were conducted through face-to-face interviews and self-completion by the participants.

To increase the representativeness of the research, ensure manageability, and obtain statistically generalizable results, the Multistage Stratified Clustered Probability Sampling method was used. Accordingly, the research population was divided into groups, and data was collected from randomly selected clusters within each group. As shown in the Figure 1, a five-stage sampling process was applied. First, based on the Turkish Statistical Regional Units Classification (NUTS-1), Türkiye's 12 statistical geographic regions were defined. Then, in the second stage, grouping was done according to settlement type based on the NUTS Level 2 classification. For this purpose, 26 provinces, namely Istanbul, Tekirdağ, Balıkesir, İzmir, Aydın, Manisa, Bursa, Kocaeli, Ankara, Konya, Antalya, Adana, Hatay, Kırıkkale, Kayseri, Zonguldak, Kastamonu, Samsun, Trabzon, Erzurum, Ağrı, Malatya, Van, Gaziantep, Şanlıurfa, and Mardin, were selected as the second sample unit. In the third stage, based on TÜİK 2023 data, settlement areas were divided into three main categories according to population density. In the fourth stage, cluster locations were designed as blocks consisting of approximately 500 household addresses. Finally, in the fifth stage, individuals were randomly selected from each cluster using systematic sampling [22].

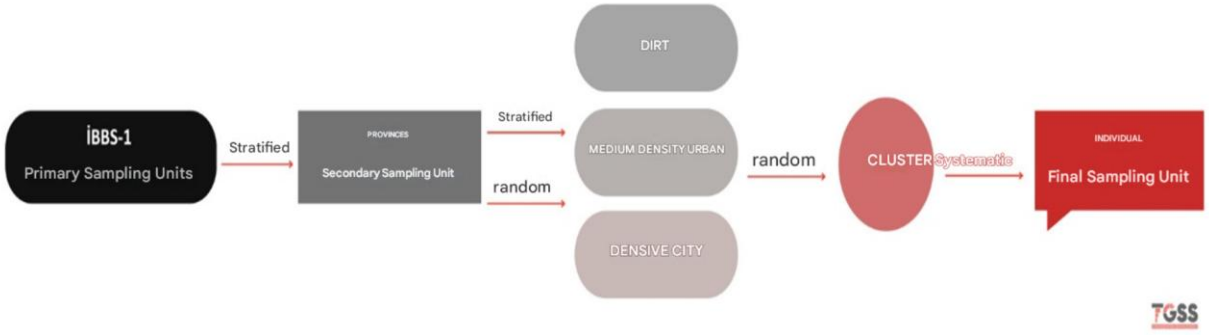

Figure 1 Multistage Stratified Clustered Probability Sampling (TGSS, 2024c)

The individuals participating in the study were statistically analyzed according to gender, education level, age group, urbanization, region, and occupational group variables.

Of the total 2615 people who participated in the survey, 1331 were male and 1284 were female. The percentage distribution is shown in the Figure 2.

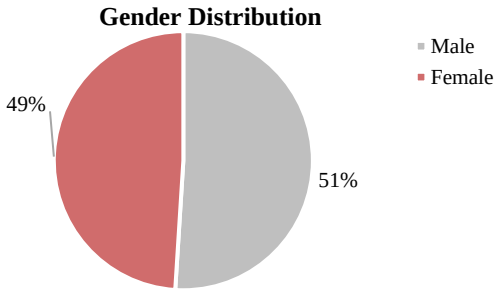

Figure 2 Percentage gender distribution of individuals participating in the survey

The data shows that out of 2615 individuals who participated in the survey, 64 were illiterate and had not completed any schooling, 49 were literate but had not completed any schooling, 492 had completed primary school, 395 had completed middle or elementary school, 862 had completed high school, 255 had completed a 2 or 3-year vocational college, 427 had completed a 4-5-6 year faculty or a 4-year higher education institution, 61 had a master's degree, and 10 had a doctorate. The percentage distribution of this situation is shown in Figure 3.

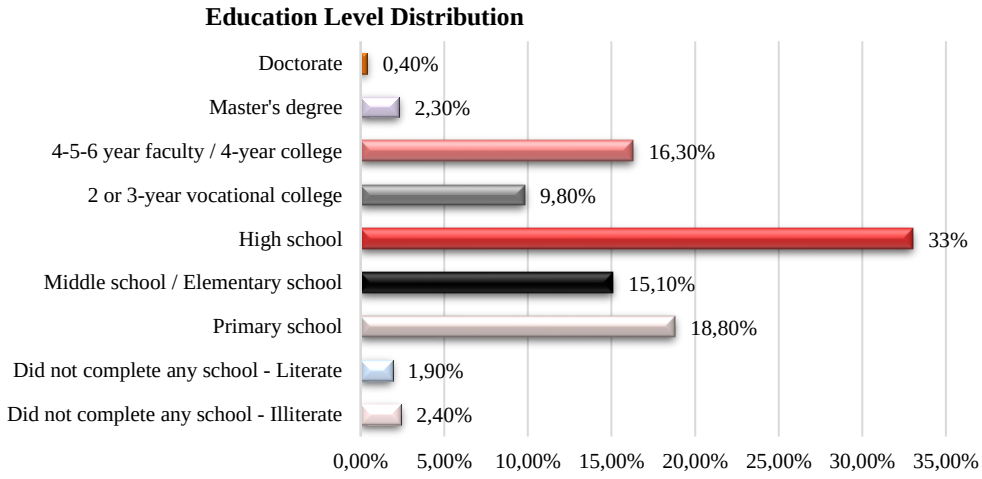

Figure 3 Percentage distribution of education level among individuals participating in the survey

The age distribution of individuals was grouped according to the most commonly used meaningful age range. Accordingly, 491 individuals were in the 18-24 age range (young adults or university age), 588 individuals were in the 25-34 age range (early adulthood), 562 individuals were in the 35-44 age range (early middle adulthood), 454 individuals were in the 45-54 age range (middle age), 316 individuals were in the 55-64 age range (late middle age), and 204 individuals were in the 65 and over age range (old age). The distribution of participants according to age ranges is visually presented in Figure 4.

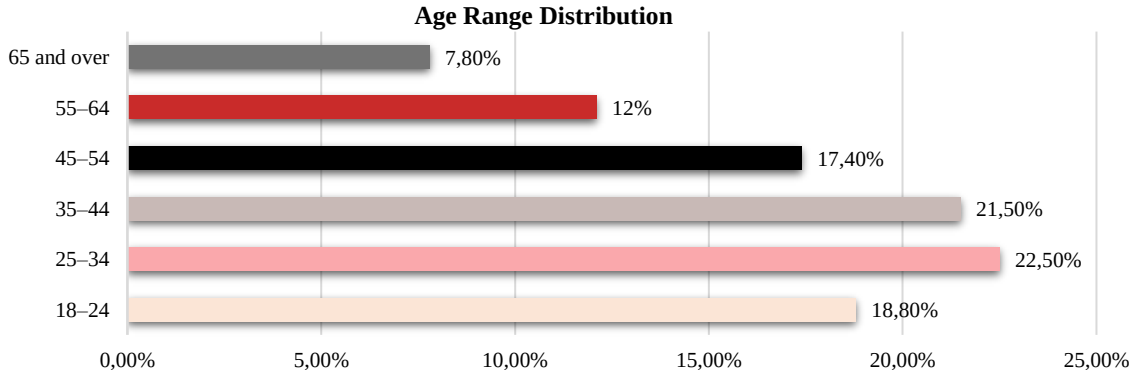

Figure 4 Percentage distribution of survey participants according to age range

It was stated that 426 individuals lived in rural areas, 436 in moderately dense urban areas, and 1753 in densely populated urban areas. The percentage distribution of this situation is given in the Figure 5.

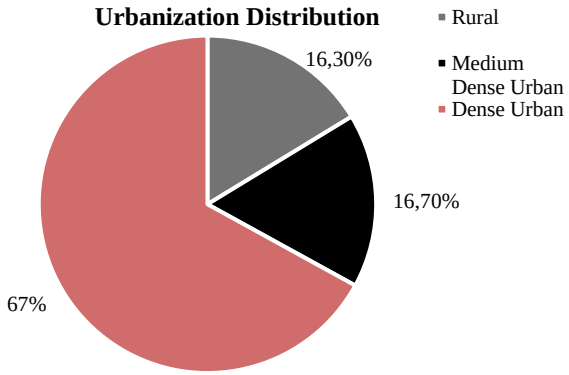

Figure 5 Percentage distribution of individuals participating in the survey according to their level of urbanization

The regional distribution of participants is as follows: 421 from the Istanbul Region, 333 from the Mediterranean Region, 328 from the Aegean Region, 304 from the Southeastern Anatolia Region, 265 from the Western Anatolia Region, 245 from the Eastern Marmara Region, 165 from the Western Black Sea Region, 149 from the Central Anatolia Region, 134 from the Eastern Anatolia Region, 115 from the Western Marmara Region, 85 from the Eastern Black Sea Region, and 71 from the Northeastern Anatolia Region. The percentage distribution of these participants is visually shown in the Figure 6.

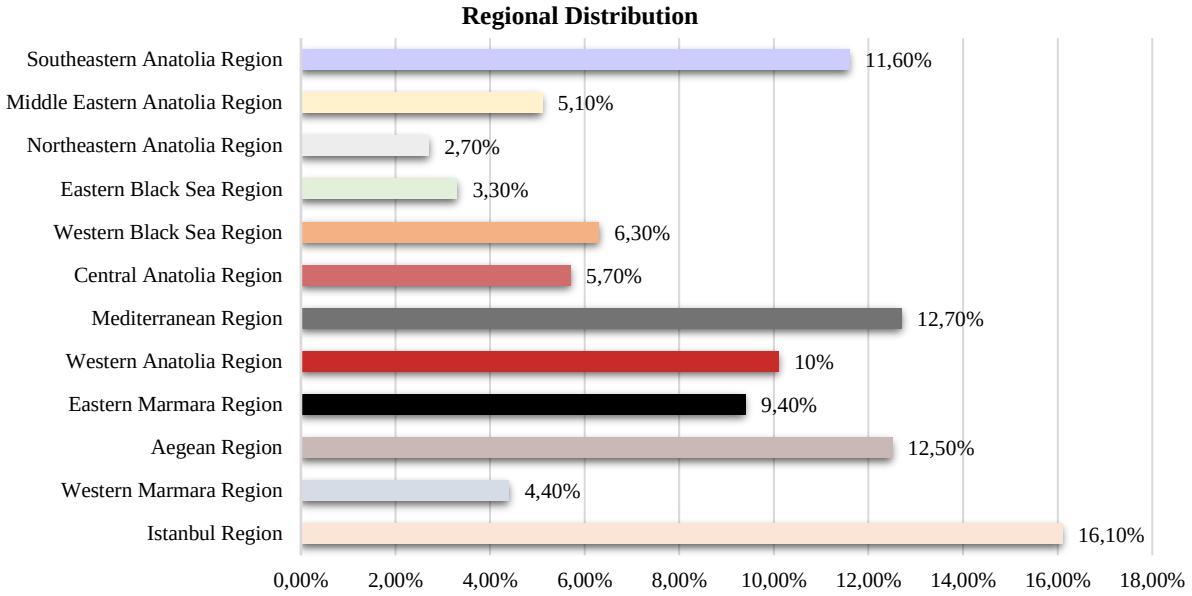

Figure 6 Percentage distribution of individuals participating in the survey according to their level of urbanization

The perceptions of artificial intelligence among individuals participating in the survey were measured by grouping their occupations. This is listed and presented in Table 1 below.

Table 1 Classification of occupations

Occupational Group	**Occupations**
Professional, technical occupations	Doctor, teacher, engineer, artist, accountant, etc.
High-level management occupations	Senior manager in large businesses, bureaucrat, union leader, etc.
Office occupations	Secretary, clerk, office manager, cashier, etc.
Sales service occupations	Sales manager, shop owner, salesperson, insurance agent, etc.
Service sector occupations	Restaurant owner, barber, cashier, waiter, officer, police officer, etc.
Skilled labor occupations	Electrician, plumber, foreman, printer, furniture worker, auto mechanic, etc.
Semi-skilled labor occupations	Bricklayer, bus driver, canning factory worker, carpenter
Unskilled labor occupations	Construction worker, factory worker, textile worker, daily wage worker, day laborer, cleaner
Farming	Self-employed or family-working farmer

Paid workers employed in agricultural activities	Farm worker, daily wage or seasonal agricultural worker

According to the data, the participation of individuals according to occupational groups is as follows: 231 people in the professional, technical occupations group, 30 people in the senior management occupations group, 94 people in the office occupations group, 155 people in the sales service occupations group, 222 people in the service sector occupations group, 113 people in the skilled labor occupations group, 77 people in the semi-skilled labor occupations group, 143 people in the unskilled labor occupations group, 52 people in the farming group, and 17 people in the group of wage laborers engaged in agricultural activities. The percentage distribution of this situation is visually presented in Figure 7.

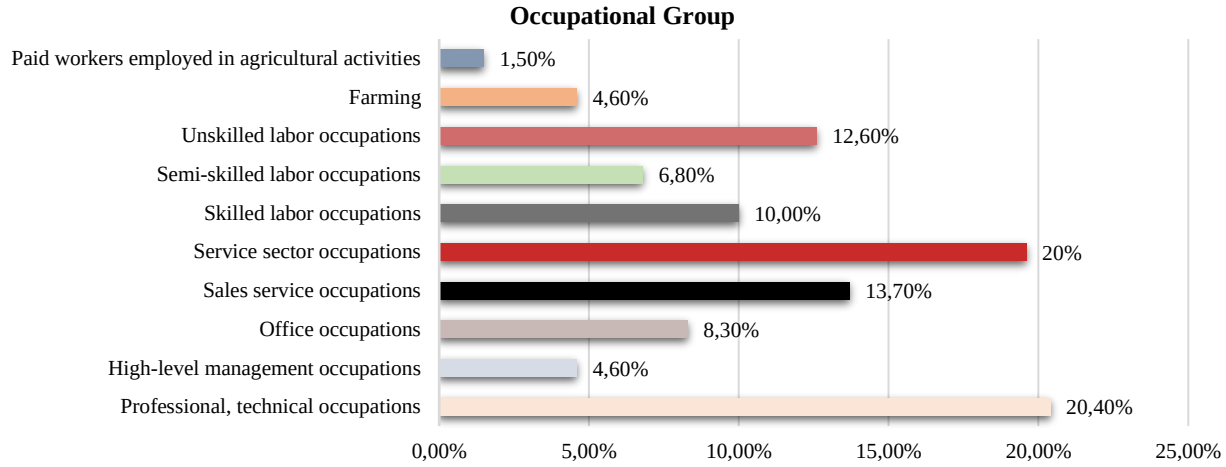

Figure 7 Percentage distribution of survey participants according to their regions

2.4. Analysis Methods

The study employed a scientific method called retrospective analysis, where data collected or recorded in the past are analyzed. This method involves the researcher obtaining data from existing sources, databases, or surveys [24, 25]. Furthermore, to obtain meaningful results from the data, a quantitative research method was used, involving statistical analysis of objectively collected numerical data [23].

To interpret the data, descriptive analysis methods such as frequency (number of responses), percentage distributions, mean, and standard deviation were used. T-tests, one-way analysis of variance (ANOVA), and Chi-Square tests were conducted to determine the relationships between independent variables. Additionally, post hoc tests and Tukey tests were performed to identify differences after determining the significance level.

3. Findings

This section presents the findings related to the dependent and independent variables used to measure perceptions of artificial intelligence in the research. For this purpose, the data, processed in the SPSS program, were analyzed using the SPSS software package.

3.1. Descriptive Results

Descriptive analysis of each question administered in the survey was performed, and the number of responses (N), the mean ($\bar{X}$) for the overall distribution of responses, the deviation from the mean, the standard deviations (S) to show participant agreement, and the minimum and maximum values are given in Table 2. Additionally, responses such as "I don't know," "I don't want to answer," or blank answers were considered missing values.

The percentage distribution of responses to each question is shown in the figures. Figure 8'de indicates that 79% of the participants had heard of the concept of artificial intelligence before.

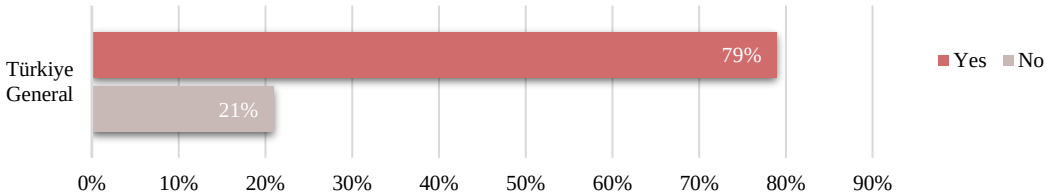

Figure 8 Distribution of responses to the question, "Have you ever heard of the concept of artificial intelligence?"

Table 2 Descriptive analysis results regarding the survey questions

Question	N		$\bar{X}$	S	Min.	Max.	Comments
	Valid	**Missing Value**					
A1	1724	891	1.21	0.41	1	2	The participants' responses were quite similar, and it appears that the vast majority had heard of the concept of artificial intelligence before.
A2	1026	1589	2.44	1.74	1	6	The participants' average frequency of using AI-powered applications or programs is approximately once a month. However, the high standard deviation indicates a wide distribution of usage frequency among participants, meaning some participants use the applications or programs very frequently while others do not use them at all.
A3	951	1664	3.02	1.05	1	5	The statement, "AI and automation will create more jobs than they will eliminate," received little response from the majority of participants, and those who did respond were largely undecided.
A4	1335	1280	2.42	0.97	1	5	Participants perceived their knowledge of artificial intelligence to be below average.
A5	1050	1565	3.14	0.98	1	5	The study shows that the majority of participants were undecided about whether artificial intelligence would have a positive or negative impact on society.
A6	1011	1604	2.2	1.06	1	5	It has become clear that there is very little trust in artificial intelligence when it comes to making decisions that will affect life.

Figure 9 shows the distribution of how frequently participants use AI-powered applications or programs. According to this, half of the participants have never used AI.

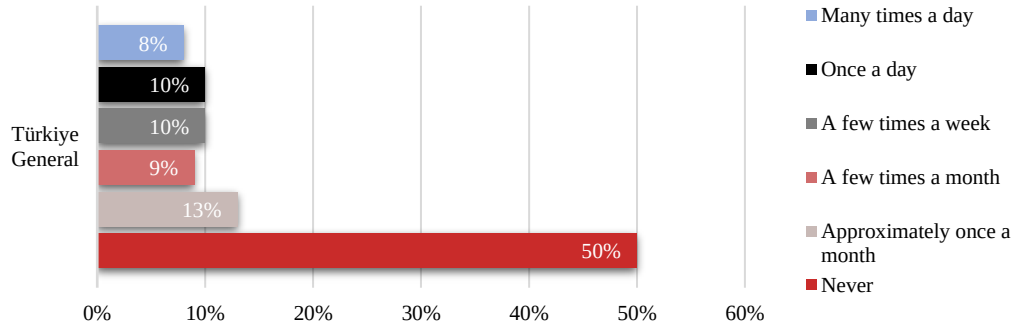

Figure 9 Distribution of responses to the question, "How often do you use AI-powered applications or programs?"

The percentage distribution of participants' responses to the question, "How much do you agree with the statement, 'Artificial intelligence and automation will create more jobs than they will eliminate'?" is given in Figure According to this, it is seen that the majority of participants are undecided on this issue, but those who agree or disagree are also close to this percentage. Overall, the participants' attitude is moderate (31%), indicating that they are undecided.

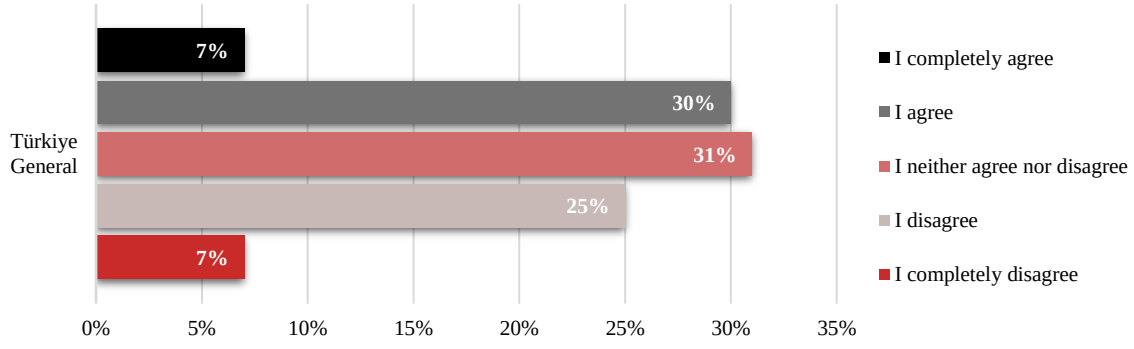

Figure 10 Distribution of responses to the question, "How much do you agree with the statement, 'Artificial intelligence and automation will create more jobs than they will eliminate'?"

Figure 11 shows the percentage distribution of participants according to how much they think they know about artificial intelligence. Accordingly, participants think they have either very little (36%) or a moderate level (36%) of knowledge about artificial intelligence.

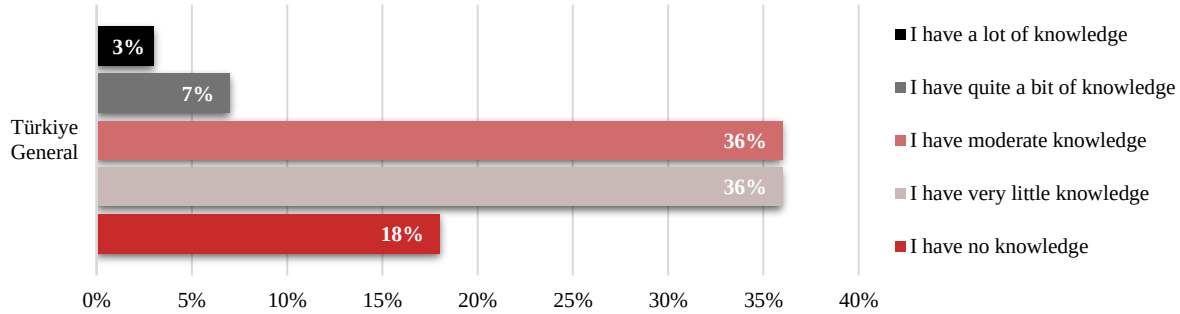

Figure 11 Distribution of responses to the question, "How much do you think you know about artificial intelligence?"

Participants responded to questions about how positive the impact of artificial intelligence is on society as shown in Figure The majority of participants (35%) were undecided on this issue. Another majority (39%) believe that the impact of artificial intelligence on society is positive.

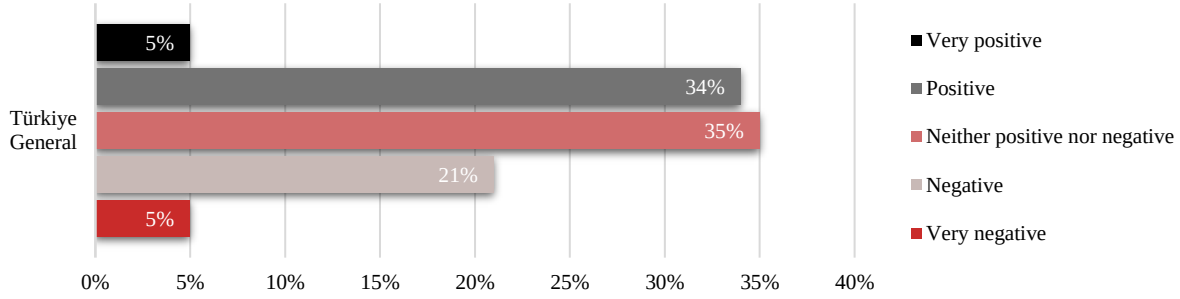

Figure 12 The distribution of responses to the question, "In your opinion, how positive or negative is the impact of artificial intelligence on society?"

The percentage distribution of participants' trust in the decisions that artificial intelligence will make regarding things that will affect their lives is given in Figure Accordingly, it was revealed that 33% of the participants had some trust, while 30% had no trust at all.

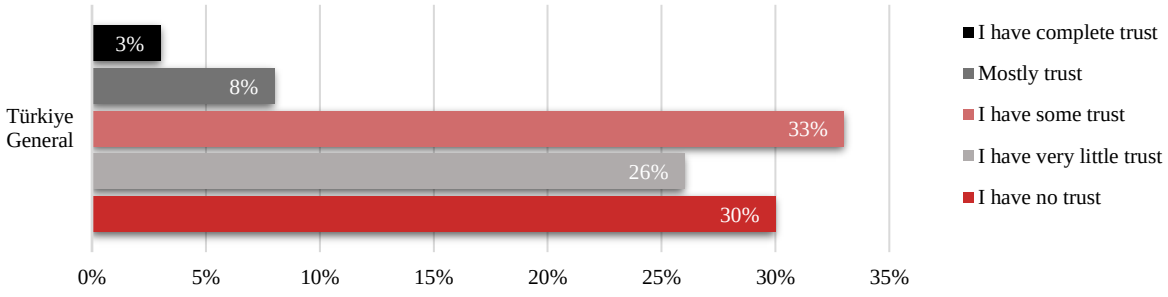

Figure 13 Distribution of responses to the question, "How much trust do you place in the decisions that artificial intelligence will make about things that will affect your life?"

Overall, based on the information obtained from the research, it can be said that individuals' perceptions of artificial intelligence in Türkiye are moderately low.

3.2. Differences in Perception of Artificial Intelligence Based on Gender

Table 3 presents the results of an independent samples t-test conducted on the responses of male and female participants to the questions asked to measure their perception of artificial intelligence. Additionally, Figure 14 shows the average of the responses to the survey questions by gender.

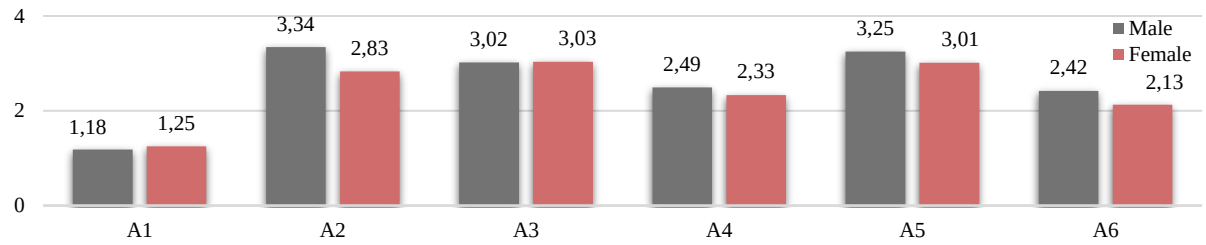

Figure 14 Average of responses to survey questions by gender

Table 3 Independent samples t-test results on responses to AI perception questions by gender

Perception of Artificial Intelligence	Gender	N	$\bar{X}$	S	χ^2	sd	*p
A1	Male	875	1.18	0.01	3.094	1722	0.002*
	Female	849	1.25	0.02			
A2	Male	551	3.34	2.64	3.177	1024	0.002*
	Female	475	2.83	2.54			
A3	Male	517	3.02	1.12	-0.183	949	0.855
	Female	434	3.03	0.96			
A4	Male	710	2.49	1.03	3.070	1333	0.002*
	Female	625	2.33	0.89			
A5	Male	558	3.25	1.03	3.982	1048	0.000*
	Female	492	3.01	0.90			
A6	Male	547	2.42	1.12	4.340	1009	0.000*
	Female	464	2.13	0.97			

As seen in the Figure 14 and Table 3, the significant differences in the average responses of male and female participants to questions A1, A2, A4, A5, and A6, with a $p<0.05$ value, indicate that this difference is significant. The results show that women have heard of the concept of artificial intelligence more than men (A1), but for the other questions, men have heard of it more than women;

They use AI-powered applications or programs more frequently (A2),

They think they know more about AI (A4),

They think more that AI has a positive impact on society (A5),

They trust AI more in the decisions it will make about things that will affect their lives (A6).

No significant difference was observed in the responses of male and female participants to the statement, 'Artificial intelligence and automation will create more jobs than they will eliminate.' (A3).

3.3. Differences in Perception of Artificial Intelligence Based on Education Level

The research expects that perceptions of artificial intelligence will increase with rising education levels. To this end, the average of the responses to the survey questions according to education level is given in Figure Then, to examine the relationship between education level and perception of artificial intelligence, the Chi-Square test for question A1 is presented in Table 4, and the one-way analysis of variance for the other questions is also presented in Table 4.

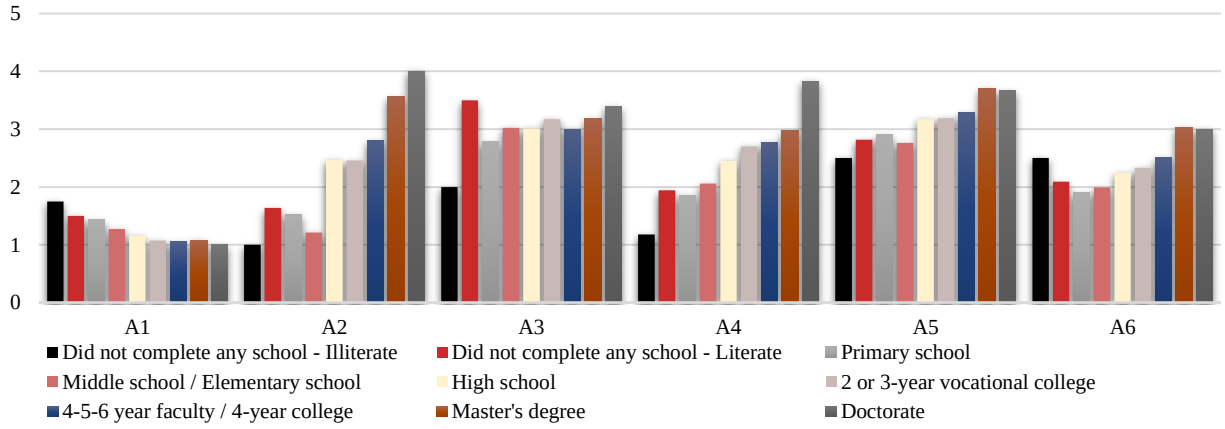

Figure 15 Average of responses to survey questions according to education level.

Table 4 Chi-Square test results for answers to question A1 according to education level

Perception of Artificial Intelligence	Education Level	N	$\bar{X}$	S	χ^2	sd	* p
A1	**(1)**	44	1.75	0.44	278,824	8	<0,001*
	(2)	36	1.50	0.51			
	(3)	327	1.43	0.50			
	(4)	251	1.27	0.44			
	(5)	553	1.14	0.35			
	(6)	170	1.08	0.27			
	(7)	297	1.05	0.21			
	(8)	40	1.08	0.27			
	(9)	6	1.00	0.00			
Did not complete any school – Illiterate (1), Did not complete any school – Literate (2), Primary school (3), Middle school / Elementary school (4), High school (5), 2 or 3-year vocational college (6), 4-5-6 year faculty /4-year college (7), Master's degree (8), Doctorate (9)							

As shown in Table 4, a significant relationship was found between education level and the responses to the question "Have you heard of artificial intelligence before?" (A1) (χ^2=278.824, sd=8, p<0.001). Analysis of the Standardized Residuals revealed that illiterate, literate, and primary school graduates gave significantly more "No" answers than expected. High school, vocational school, and especially university graduates gave significantly more "Yes" answers. Therefore, as expected, the number of "Yes" answers to question A1 increased significantly with increasing education level.

Table 5 Results of ANOVA analysis regarding responses to AI perception questions according to education level

Perception of Artificial Intelligence		Education Level									F	p
		(1)	**(2)**	**(3)**	**(4)**	**(5)**	**(6)**	**(7)**	**(8)**	**(9)**		
A2	**N**	2	11	103	115	371	140	246	32	6	8.929	<0.001*
	$\bar{X}$	1.00	1.64	1.52	1.21	2.47	2.46	2.80	3.56	4.00		
	S	0	1.5	1.21	2.05	1.73	1.72	1.78	1.92	1.27		
A3	**N**	1	10	94	98	348	127	240	28	5	1.511	0.149
	$\bar{X}$	2.00	3.50	2.78	3.02	3.01	3.17	3.00	3.18	3.40		
	S	-	1.18	1.17	1.07	1.04	0.99	1.03	1.19	0.89		
A4	**N**	11	18	181	179	466	155	282	37	6	26.221	<0.001*
	$\bar{X}$	1.18	1.94	1.86	2.06	2.45	2.70	2.77	2.97	3.83		
	S	0.41	1.06	0.9	2.06	2.45	2.7	0.94	1.07	0.75		
A5	**N**	2	11	105	115	387	141	252	31	6	5.788	<0.001*
	$\bar{X}$	2.50	2.82	2.90	2.76	3.17	3.19	3.28	3.71	3.67		
	S	0.71	1.25	1.13	0.93	0.92	0.96	0.97	0.86	0.52		
A6	**N**	2	11	97	114	372	135	245	30	5	6.658	<0.001*
	$\bar{X}$	2.50	2.09	1.90	1.99	2.24	2.33	2.51	3.03	3.00		
	S	0.71	1.14	1.14	0.98	1.01	1.07	1.02	1.22	0.71		
Did not complete any school – Illiterate (1), Did not complete any school – Literate (2), Primary school (3), Middle school / Elementary school (4), High school (5), 2 or 3-year vocational college (6), 4-5-6 year faculty / 4-year college (7), Master's degree (8), Doctorate (9)												

Table 5 shows whether there is a significant difference in the average perceptions of artificial intelligence across education levels through ANOVA analysis. The p-value for question A3 is 0.149, which is above the 0.05 significance level, indicating no significant difference across education levels. Participants' opinions did not change according to their education level. However, for all other questions, the p-value is below the 0.05 significance level, indicating a significant difference between education levels and the questions. A Tukey test was conducted to determine the source of this difference. According to this test, as the education level increases:

Frequency of using AI-supported applications or programs increases significantly (A2),

Individuals believe they have more knowledge about artificial intelligence (A4),

Individuals believe more that the impact of artificial intelligence on society is positive (A5),

Individuals have more confidence in the decisions that artificial intelligence will make regarding things that will affect their lives (A6).

3.4. Differences in Perception of Artificial Intelligence According to Age Groups

It is expected that the perception of artificial intelligence will decrease as age increases among participants. For this purpose, the average of the responses to the survey questions according to age groups is first presented in Figure Then,

in order to examine the relationship between age groups and the perception of artificial intelligence, the Chi-Square test for question A1 is presented in Table 6, and the one-way analysis of variance (ANOVA) for the other questions is presented in Table 7.

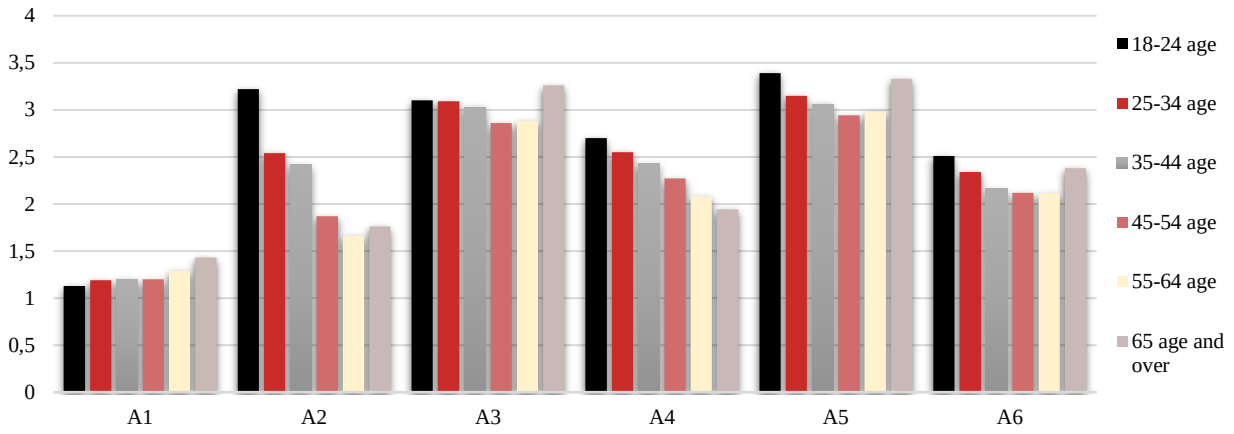

Figure 16 Average of responses to survey questions by age group

Table 6 Chi-Square test results for the answer to question A1, categorized by age group

Perception of Artificial Intelligence	Age Groups	N	$\bar{X}$	S	χ^2	sd	*p
A1	**(1)**	317	1.13	0.34	57.817	5	<0.001*
	(2)	375	1.19	0.40			
	(3)	381	1.20	0.40			
	(4)	313	1.20	0.40			
	(5)	210	1.29	0.45			
	(6)	128	1.43	0.50			
18–24 age (1), 25–34 age (2), 35–44 age (3) 45–54 age (4), 55–64 age (5), 65 age and over (6)							

As shown in the table, a significant relationship was observed between age groups and the responses to the question "Have you heard of artificial intelligence before?" (A1) (χ^2=57.817, sd=5, p<0.001). Examination of the Standardized Residuals revealed significant differences, particularly in the 18–24, 55–64, and 65+ age groups. In the 18-24 age group, awareness of artificial intelligence ("Yes" response) was higher than expected. This indicates that artificial intelligence is well-known among young people. In the 55–64 and 65 age and over groups, awareness of artificial intelligence was much lower than expected ("No" response). Overall, awareness of artificial intelligence decreased significantly with increasing age.

Table 7 Results of ANOVA analysis regarding responses to AI perception questions by age group.

Perception of Artificial Intelligence		Age Groups						F	p
		(1)	**(2)**	**(3)**	**(4)**	**(5)**	**(6)**		
A2	N	231	245	233	178	97	42	20.087	<0.001*
	$\bar{X}$	3.22	2.54	2.42	1.87	1.66	1.76		
	S	1.72	1.72	1.82	1.46	1.32	1.64		
A3	N	218	226	211	166	92	38	1.971	0.081
	$\bar{X}$	3.10	3.09	3.03	2.86	2.88	3.26		
	S	0.93	1.02	1.11	1.10	1.15	1.06		
A4	N	270	301	298	248	146	72	14.719	<0.001*
	$\bar{X}$	2.70	2.55	2.43	2.27	2.08	1.94		
	S	0.89	0.99	0.96	0.94	0.95	0.96		
A5	N	241	251	240	181	97	40	5.843	<0.001*
	$\bar{X}$	3.39	3.15	3.06	2.94	2.98	3.33		
	S	0.85	0.93	1.03	1.01	1.07	0.94		
A6	N	236	240	231	168	94	42	4.455	<0.001*
	$\bar{X}$	2.51	2.34	2.16	2.12	2.11	2.38		
	S	0.98	1.07	1.09	0.99	1.06	1.32		
18–24 age (1), 25–34 age (2), 35–44 age (3) 45–54 age (4), 55–64 age (5), 65 age and over (6)									

The ANOVA analysis performed in the table shows whether there is a significant difference in the average perception of artificial intelligence across age groups. The p-value for question A3 is 0.081, which is above the 0.05 significance level, indicating no significant difference between age groups. Participants' opinions did not vary according to their age groups. However, for all other questions, the p-value is below the 0.05 significance level, indicating a significant difference between age groups and questions. A Tukey test was conducted to determine the source of this difference. Accordingly:

Individuals in the 18-24 and 25-34 age groups have a higher frequency of use (A2) and a higher level of knowledge (A4) regarding artificial intelligence compared to other age groups. They also evaluate its impact on society more positively (A5) and find it more reliable (A6).

Individuals in the 35-44 age group have a moderate perception of artificial intelligence compared to other groups.

Individuals aged 45 and over, unlike younger groups, have lower frequencies of artificial intelligence use, lower levels of knowledge, lower positive attitudes, and lower levels of trustworthiness.

3.5. Differences in Perception of Artificial Intelligence According to Urbanization

It is expected that participants' perception of artificial intelligence will increase according to the density of the city they live in. To examine this, the average of the responses to the survey questions according to urbanization is first presented in Figure Then, to examine the relationship between urbanization and the perception of artificial intelligence, the Chi-Square test for question A1 is presented in Table 8, and the one-way analysis of variance (ANOVA) for the other questions is presented in Table 9.

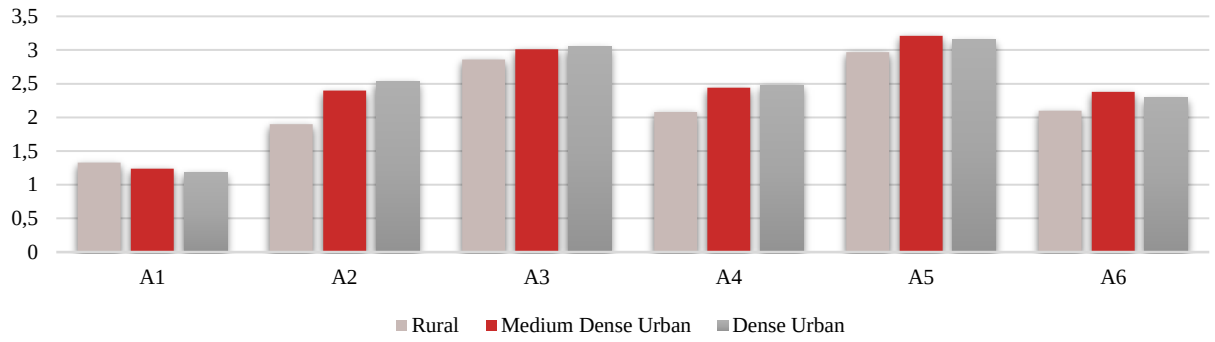

Figure 17 Average of responses to survey questions according to urbanization

Table 8 Chi-Square test for question A1

Perception of Artificial Intelligence	Urbanization	N	$\bar{X}$	S	χ^2	sd	*p
A1	**Rural**	278	1.33	0.47	31.163	2	<0.001*
	Medium Dense Urban	300	1.24	0.43			
	Dense Urban	1146	1.18	0.38			

As shown in the table, a significant relationship (χ^2=31.163, sd=2, p<0.001) was observed between urbanization and the responses to the question "Have you heard of artificial intelligence before?" (A1). Analysis of the Standardized Residuals revealed that individuals living in rural areas have less awareness of artificial intelligence than expected ("Yes" response). Results were as expected in moderately dense cities. Conversely, individuals living in densely populated cities showed a higher level of awareness of artificial intelligence than anticipated.

Table 9 Results of ANOVA analysis regarding responses to artificial intelligence perception questions according to urbanization

Perception of Artificial Intelligence		Urbanization			F	p
		Rural	Medium Dense Urban	Dense Urban		
A2	N	118	171	737	6.820	0.001*
	$\bar{X}$	1.90	2.40	2.53		
	S	1.63	1.65	1.76		
A3	N	103	161	687	1.400	0.247
	$\bar{X}$	2.86	3.01	3.05		
	S	1.03	1.04	1.06		

A4	N	181	222	932	13.265	<0.001*
	$\bar{X}$	2.08	2.44	2.48		
	S	0.93	0.94	0.97		
A5	N	119	179	752	2.410	0.090
	$\bar{X}$	2.97	3.21	3.15		
	S	1.04	0.94	0.97		
A6	N	115	170	726	2.563	0.978
	$\bar{X}$	2.10	2.38	2.29		
	S	1.07	1.00	1.07		

The ANOVA analysis performed in the table shows whether there is a significant difference in the average perceptions of artificial intelligence with urbanization. The p-values for questions A3, A5, and A6 are 0.247, 0.090, and 0.978 respectively, which are above the 0.05 significance level, indicating no significant difference with urbanization in these questions. Participants' opinions did not change according to urbanization. However, for questions A2 and A4, the p-value is lower than the 0.05 significance level, indicating a significant difference between urbanization and these questions. A Tukey test was conducted to determine the source of this difference. Accordingly:

The frequency of use (A2) and knowledge level (A4) are lower in individuals living in rural areas compared to other regions. • The level of knowledge about artificial intelligence has increased with urbanization (A4).

The frequency of use is higher in moderate and dense urbanization, and there is no significant difference between them (A2).

4. Differences in Perception of Artificial Intelligence by Region

To examine participants' perception of artificial intelligence according to their region of residence, the average of the answers given to the survey questions according to the region of residence is first presented in Figure Then, to examine the relationship between urbanization and the perception of artificial intelligence, the Chi-Square test for question A1 is presented in Table 10, and the one-way analysis of variance (ANOVA) for the other questions is presented in Table 11 and

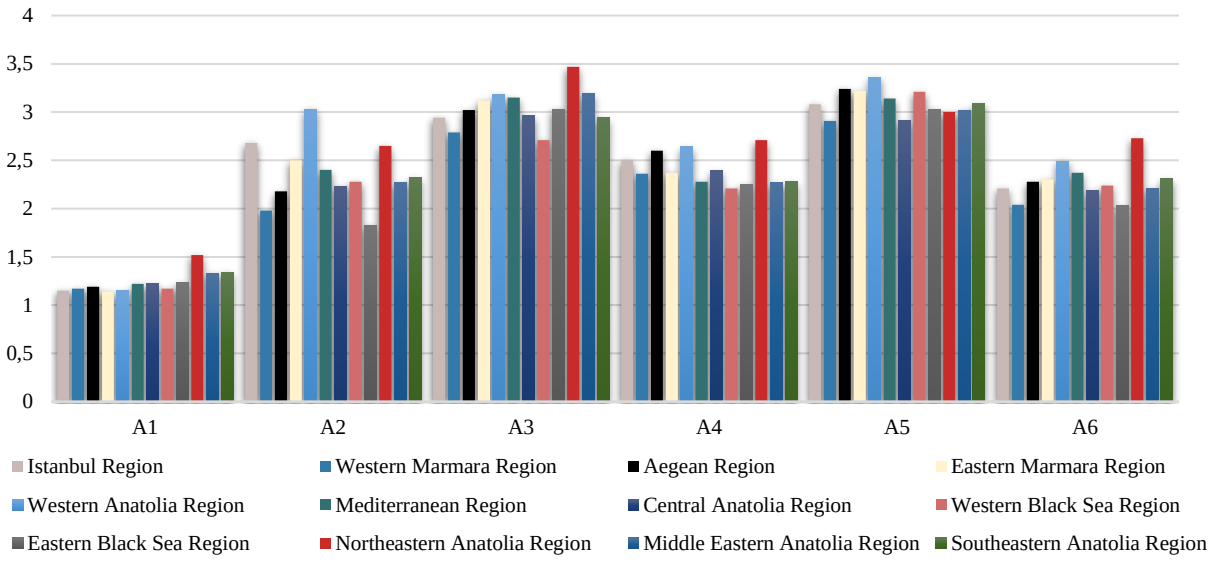

Figure 18 Average of responses to survey questions by region

Table 10 Chi-Square test results for the answer to question A1, by region.

Perception of Artificial Intelligence	Region	N	$\bar{X}$	S	χ^2	sd	*p
A1	**(1)**	265	1.15	0.35	73.139	11	<0.001*
	(2)	82	1.17	0.38			
	(3)	218	1.19	0.40			
	(4)	160	1.14	0.35			
	(5)	174	1.15	0.36			

	(6)	214	1.22	0.41			
	(7)	96	1.22	0.42			
	(8)	102	1.17	0.37			
	(9)	66	1.23	0.42			
	(10)	48	1.52	0.50			
	(11)	91	1.33	0.47			
	(12)	208	1.34	0.48			
Istanbul Region, (1), Western Marmara Region (2), Aegean Region (3), Eastern Marmara Region(4), Western Anatolia Region(5), Mediterranean Region(6), Central Anatolia Region(7), Western Black Sea Region(8), Eastern Black Sea Region(9), Northeastern Anatolia Region(10), Middle Eastern Anatolia Region(11), Southeastern Anatolia Region(12)							

As shown in the table, a significant relationship (χ^2=73.139, sd=11, p<0.001) was observed between the region and the responses to the question "Have you heard of artificial intelligence before?" (A1). Analysis of the Standardized Residuals revealed that awareness of artificial intelligence is higher than expected, particularly in Istanbul, Western Anatolia, and Eastern Marmara regions. However, awareness is even lower than expected in Northeastern Anatolia and Southeastern Anatolia regions. This indicates that awareness of artificial intelligence is directly related to the region's level of development and access to technology.

Table 11 Results of ANOVA analysis regarding responses to questions on perception of artificial intelligence by region.

Perception of Artificial Intelligence	A2			A3			A4		
Region	N	$\bar{X}$	S	N	$\bar{X}$	S	N	$\bar{X}$	S
(1)	180	2.68	1.86	175	2,94	1,14	224	2,50	0,91
(2)	54	1.98	1.49	47	2,79	1,02	66	2,36	0,91
(3)	141	2.18	1.60	134	3,02	1,08	173	2,60	1,04
(4)	107	2.50	1.77	102	3,12	1,07	136	2,37	0,92
(5)	119	3.03	1.83	111	3,18	1,11	146	2,64	1,04
(6)	107	2.40	1.65	104	3,15	0,96	163	2,28	0,98
(7)	56	2.23	1.73	48	2,96	1,01	75	2,39	0,82
(8)	60	2.28	1.66	55	2,71	0,90	85	2,21	1,00
(9)	39	1.82	1.30	34	3,03	0,94	51	2,25	0,87
(10)	17	2.65	1.87	15	3,47	0,83	21	2,71	1,15
(11)	44	2.27	1.78	36	3,19	1,19	60	2,27	1,07
(12)	102	2.32	1.75	90	2,94	0,96	135	2,28	0,94
F	2.962			1.612			2.804		
p	<0,001*			0.090			0.001*		

Table 12 Results of ANOVA analysis regarding responses to AI perception questions by region – Continued

Perception of Artificial Intelligence	A5			A6		
Region	N	$\bar{X}$	S	N	$\bar{X}$	S
(1)	184	3.08	1,02	177	2,21	1,09
(2)	55	2.91	0,95	51	2,04	0,98
(3)	142	3.24	0,97	140	2,28	1,07
(4)	108	3.22	1,04	105	2,30	1,14
(5)	120	3.36	0,92	121	2,49	1,05
(6)	118	3.14	0,94	114	2,37	1,07
(7)	57	2.91	0,91	54	2,19	0,93
(8)	62	3.21	0,93	58	2,24	1,01
(9)	40	3.03	1,05	36	2,03	0,94
(10)	18	3.00	0,84	15	2,73	1,28
(11)	42	3.02	1,05	43	2,21	0,97
(12)	104	3.09	0,94	97	2,31	1,07
F	1.576			1.319		
p	0.100			0.208		

The ANOVA analysis performed in the table shows whether there is a significant difference in the average perception of artificial intelligence based on region. The p-values for questions A3, A5, and A6 are 0.090, 0.100, and 0.208 respectively, which are above the 0.05 significance level, indicating no significant difference between regions in these questions. Participants' opinions did not vary according to region. However, for questions A2 and A4, the p-value is lower than the 0.05 significance level, indicating a significant difference between regions and the questions. A Tukey test was conducted to determine the source of this difference. Accordingly:

Individuals living in Western Anatolia, Istanbul, and Northeastern Anatolia regions show a higher tendency to use artificial intelligence more frequently than those in other regions (A2).

Individuals living in Northeastern Anatolia, Western Marmara, Aegean, and Istanbul regions believe they are more knowledgeable about artificial intelligence (A4) than those in other regions.

Overall, the frequency of use is low in all regions, varying from approximately once a month to several times a month. The level of perceived knowledge about artificial intelligence is below average in all regions.

4.1. Differences in Perception of Artificial Intelligence According to Occupational Group

To examine participants' perceptions of artificial intelligence according to their occupational groups, the average of the responses to the survey questions is first presented in Figure Then, to examine the relationship between occupational group and perception of artificial intelligence, the Chi-Square test for question A1 is presented in Table 13, and the one-way analysis of variance (ANOVA) for the other questions is presented in Tables 14 and 15.

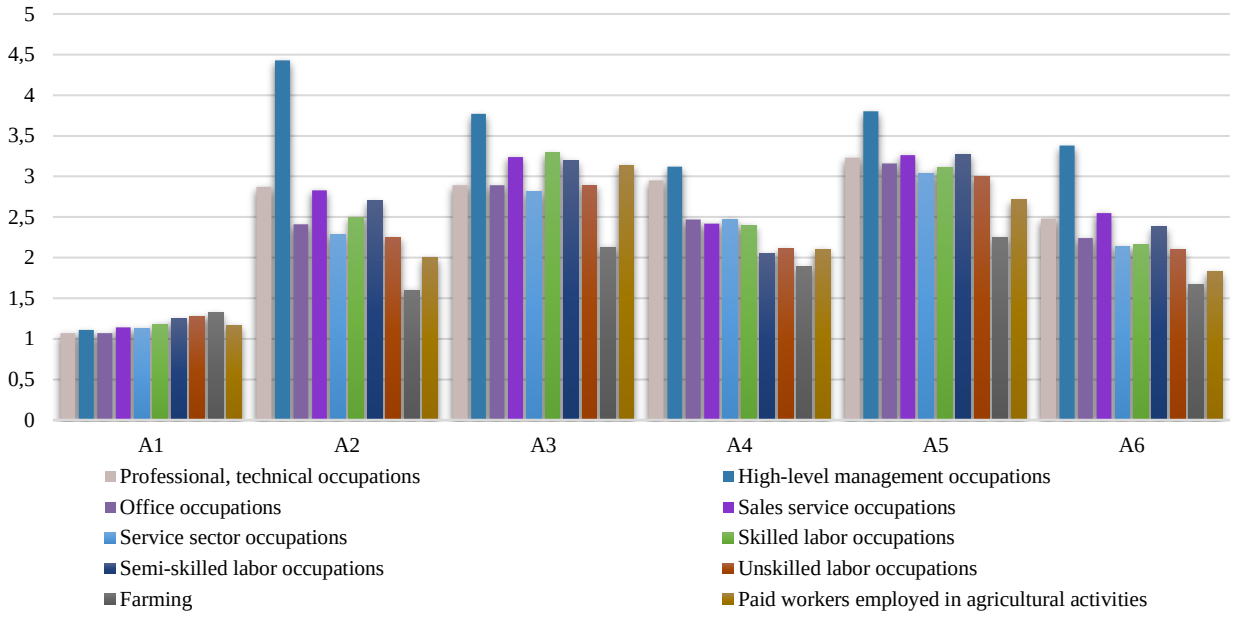

Figure 19 Average of responses to survey questions according to occupational group

Table 13 Chi-Square test results for the response to question A1 according to occupational group

Perception of Artificial Intelligence	Occupational group	N	$\bar{X}$	S	χ^2	sd	*p
A1	(1)	151	1.07	0.25	35.837	9	<0.001*
	(2)	19	1.11	0.32			
	(3)	61	1.07	0.25			
	(4)	100	1.14	0.35			
	(5)	157	1.13	0.33			
	(6)	71	1.18	0.39			
	(7)	53	1.25	0.43			
	(8)	101	1.28	0.45			
	(9)	28	1.32	0.48			
	(10)	12	1.17	0.39			
Professional, technical occupations (1), High management occupations (2), Office occupations (3), Sales service occupations (4), Service sector occupations (5), Skilled labor occupations (6), Semi-skilled labor occupations (7), Unskilled labor occupations (8), Farming (9), Wage workers employed in agricultural activities (10)							

As shown in Table 13, a significant relationship (χ^2=35.837, sd=9, p<0.001) was observed between occupational groups and the responses to the question "Have you heard of artificial intelligence before?" (A1). Analysis of the Standardized Residuals revealed that the level of awareness of artificial intelligence was significantly higher than expected, particularly among skilled laborers and farmers. Conversely, awareness of artificial intelligence was higher than expected among professional and technical occupational groups.

Table 14 Results of ANOVA analysis regarding responses to AI perception questions by occupational group

Perception of Artificial Intelligence	**A2**			**A3**			**A4**		
Occupational group	**N**	$\bar{X}$	**S**	**N**	$\bar{X}$	**S**	**N**	$\bar{X}$	**S**
(1)	130	2.87	1.70	123	2,89	1,11	140	2,95	0,88
(2)	14	4.43	1.40	13	3,77	1,01	17	3,12	1,32
(3)	51	2.41	1.63	47	2,89	1,05	57	2,47	0,85
(4)	70	2.83	1.74	66	3,24	1,07	86	2,42	1,00
(5)	108	2.28	1.70	104	2,81	1,10	137	2,47	0,88
(6)	44	2.50	1.80	41	3,29	1,03	58	2,40	1,02
(7)	23	2.70	1.99	21	3,19	0,98	39	2,05	1,07
(8)	53	2.25	1.76	44	2,89	1,04	73	2,11	0,83
(9)	10	1.60	1.58	8	2,13	1,36	18	1,89	1,13
(10)	7	2.00	1.53	7	3,14	1,46	10	2,10	0,88
F	3,495			2.696			8.016		
p	<0,001*			0.005*			<0.001*		

Table 15 Results of ANOVA analysis regarding responses to AI perception questions by occupational group Continued

Perception of Artificial Intelligence	**A5**			**A6**		
Occupational group	**N**	$\bar{X}$	**S**	**N**	$\bar{X}$	**S**
(1)	130	3.23	1,00	126	2,48	1,08
(2)	15	3.80	0,77	13	3,38	1,33
(3)	51	3.16	0,99	50	2,24	0,98
(4)	69	3.26	0,98	64	2,55	1,15
(5)	114	3.04	1,02	109	2,14	1,04
(6)	45	3.11	1,01	45	2,16	0,90
(7)	22	3.27	0,94	21	2,38	0,97
(8)	54	3.00	0,82	52	2,10	0,93
(9)	8	2.25	1,28	9	1,67	1,32
(10)	7	2.71	1,11	6	1,83	0,75
F	2,183			3.495		
p	0,022*			<0.001*		

The ANOVA analysis performed in the table shows whether there is a significant difference in the average perceptions of artificial intelligence among occupational groups. The p-values of questions A2, A3, A4, A5, and A6 are <0.001, 0.005, <0.001, 0.022, and <0.001, respectively, and are below the 0.05 significance level, indicating a significant difference between occupational groups and the questions. A Tukey test was conducted to determine the source of the difference. There is no significant difference in artificial intelligence perception across all questions among occupations. However, a significant difference is observed, particularly between individuals in the senior management occupational group and farmers. Accordingly, compared to farmers, individuals in the senior management occupational group showed:

Higher frequency of artificial intelligence use (A2),

Agreement that artificial intelligence and automation will perform more tasks (A3),

Higher level of knowledge (A4),

More positive perception of its impact on society (A5), and

More trustworthiness (A6).

5. Conclusion and Recommendations

The general assessment of the responses to the questions posed to examine the public's perception of artificial intelligence can be summarized as follows:

Have you ever heard of the concept of AI before? (A1): Considering that 79% of those who answered this question said yes, it can be said that 4 out of 5 people in Türkiye are aware of the concept of AI. Furthermore, individuals in the following groups have heard of artificial intelligence more frequently than others: "men," "those with undergraduate and postgraduate education," "those in the 18-34 age group," "those living in densely urbanized areas," "those living in Istanbul, Western Anatolia, and the Eastern Marmara region," and "those with professional, technical occupations."

How often do you use AI-supported applications or programs? (A2): Approximately half of the individuals answered "never" to this question. Turkish Statistical Institute (TÜİK) data (2025) shows that the reason given by those who do not use AI is generally that they do not need it [18]. A small majority stated that they either do not know how to use it or are unaware of its existence. Furthermore, individuals in the "men," "those living in densely populated cities," "those living in Western Anatolia, Istanbul, and Northeastern Anatolia regions," and "service sector" groups use AI-supported applications or programs more frequently than other individuals. Additionally, increased education levels and a younger age range have increased the frequency of use.

How much do you agree with the statement, "AI and automation will create more jobs than they will eliminate"? (A3): Approximately 31% of participants were undecided on this point, while 30% agreed. The idea that AI and automation will create more jobs did not show a statistically significant difference for any independent variable. Agreement with this statement was similar across all groups.

How much do you think you know about AI? (A4): The general perception of having knowledge is at a moderately low level. Furthermore, individuals, particularly those in the "men," "those living in densely populated cities," "those living in Western Anatolia, Northeastern Anatolia, and the Aegean region," and "service sector professions," believe they possess more knowledge about AI compared to other individuals. Additionally, it appears that knowledge levels increase with higher education levels and towards younger age groups.

How positive or negative do you think the impact of artificial intelligence on society is? (A5): 34% of participants viewed the impact of AI on society positively, while 35% saw it as neither positive nor negative. In terms of independent variables, it was observed that individuals in the "men" and "high-level managerial professions" groups found the opinion more positive than other individuals. At the same time, an increase in education level increased the "positive" opinion, while an increase in age increased the "negative" opinion. However, no significant difference was observed in urbanization and regional variables regarding the question, and neither the positive nor the negative opinion was dominant for individuals in all groups.

How much do you trust the decisions that artificial intelligence will make about things that will affect your life? (A6): The level of trust among participants is particularly high among male individuals, in medium-density cities, in the northeastern Anatolia region, and among individuals with high-level managerial professions. In addition, an increase in education level and a decrease in age also increase the level of trust in AI.

According to the findings of the research, independent variables such as gender, age range, education level, urbanization, region, and occupational group show significant differences in perceptions of artificial intelligence. To reduce or prevent these differences:

Programs can be organized to increase social awareness, especially targeting specific groups. For individuals with low education levels, those working in unskilled jobs or in the agricultural sector, and those living in rural areas, the relationship between AI and life should be demonstrated through concrete scenarios rather than abstract technologies.

Basic digital literacy training programs should be organized to increase the level of knowledge about AI. This will also equip individuals with the skills to use AI critically and consciously.

Increasing age and education levels have led to lower perceptions of AI. Therefore, awareness of AI can be increased through age- and education-level appropriate training models and learning materials.

Access to technology should be increased in socioeconomically underdeveloped regions, investments in education should be made, and awareness campaigns supported by the public sector should be conducted. • Individuals working in professional and technical fields with high levels of AI knowledge and perception can be introduced to sectoral examples demonstrating the practical contributions of AI to individuals working in low-skilled jobs or in agriculture.

Future Research

The level of societal perception of artificial intelligence can be examined dimensionally, including usage level, purpose of use, perceived knowledge, societal impact, and concerns.

Due to the continuous development of AI technology and the changing perceptions of individuals, perceptions of AI should be measured over time.

Similar to this study conducted throughout Türkiye, studies in different countries can be used to comparatively measure perceptions of AI in a regional or cultural context.

References

[1] Gursoy, D., & Cai, R. (2025). Artificial intelligence: An overview of research trends and future directions. International Journal of Contemporary Hospitality Management, 37(1), 1–https://doi.org/10.1108/IJCHM-03-2024-0322

[2] Emektar, M. B. (2025). Yapay zekâ günlük yaşamımızda nerelerde kullanılıyor? TÜBİTAK Bilim Genç. https://bilimgenc.tubitak.gov.tr/makale/yapay-zeka-gunluk-yasamimizda-nerelerde-kullaniliyor

[3] Haliç University. (2024). Yapay zekânın zararları, tehditleri ve faydaları nelerdir? https://halic.edu.tr/tr/haberler/yapay-zekanin-zararlari-tehditleri-ve-faydalari-nelerdir

[4] Murat, G., & Şengül, B. (2023). Yapay zekânın istihdama yönelik etkileri: Bir sosyal politika önlemi olarak evrensel temel gelir. Sosyal Siyaset Konferansları Dergisi, (85), 199–https://doi.org/10.26650/jspc.2023.85.1331159

[5] Bayram, O. (2024). Yapay zekânın ekonomik etkileri. İstanbul Gedik Üniversitesi Yayınları (ss. 45–67). https://doi.org/10.61150/gedikyay.240403

[6] Türkiye Bilişim Derneği. (2024). Kamuda yapay zekâ uygulamaları: Kamu BİB Çalışma Grubu raporu. https://www.tbd.org.tr/pdf/kamubib-calisma-grubu/kamuda-yapay-zeka-uygulamalari-2024.pdf

[7] Karataş, A. (2025, 22–23 February). Yapay zekânın kamu kurumlarının idari kapasitesine etkisi: Ulusal ve uluslararası literatür çerçevesinde bir analiz. 2nd International Colosseum Scientific Researches and Innovation Congress, İtalya. https://www.wosconkongreleri.com/

[8] https://www.milliirade.com/yapay-zeka-hayatimizi-nasil-degistiriyor-gunluk-yasantimiza-etkileri-ve-gelecegi

[9] Akbaş, A. (2024). Yapay zekâ ile toplumsal dönüşüm: Sosyolojik perspektif. İnsan ve Toplum Bilimleri Araştırmaları Dergisi, 10(22), 151–https://doi.org/10.59304/ijhe.1477203

[10] Solmaz, G., Doğan Merih, Y., & Arga, K. Y. (2020). Sağlığın dijital dönüşümünde kamu projeleri ve akademi ile ortaklığın önemi. A. S. Fak (Ed.), Kardiyolojide dijital dönüşüm: Bugün ve yarın (baskı, ss. 32–38). Türkiye Klinikleri.

[11] Ecer, S. (2025). Yapay zekâ ile ilişkili gelişmelere sosyal bilimler ve özellikle ekonomi bilimi açısından bakış. İTÜ Vakfı. https://www.ituvakif.org.tr/yapay-zeka-ile-iliskili-gelismelere-sosyal-bilimler-ve-ozellikle-ekonomi-bilimi-acisindan-bakıs

[12] Moore, G. C., & Benbasat, I. (1991). Development of an instrument to measure the perceptions of adopting an information technology innovation. Information systems research, 2(3), 192-222.

[13] Venkatesh, V., & Davis, F. D. (2000). A theoretical extension of the technology acceptance model: Four longitudinal field studies. Management science, 46(2), 186-204.

[14] Rogers, E. M. (2003). Diffusion of innovations (5th ed.). Free Press.

[15] AL Athmay, A. A. A., Fantazy, K., & Kumar, V. (2016). E-government adoption and user's satisfaction: an empirical investigation. EuroMed Journal of Business, 11(1), 57-83.

[16] Saka, A. (2025). Türkiye'de eğitimde yapay zekâ çalışmalarının sistematik derlemesi (Master's thesis). Bursa Uludağ University, Institute of Educational Sciences.

[17] Yalçın, A. (2024). Türkiye'de Kamu Kurumlarinin Toplum İçin Geliştirdiği Yapay Zekâ Uygulamalari. İstanbul Aydın Üniversitesi Sosyal Bilimler Dergisi, 16(2), 185-215.

[18] Türkiye İstatistik Kurumu. (2025, 1 Ekim). Yapay zeka istatistikleri, 2025 (Haber Bülteni No. 57945). https://data.tuik.gov.tr/Bulten/Index?p=Yapay-Zeka-Istatistikleri-2025-57945

[19] Packworld Türkiye. (2024). Türkiye yapay zeka kullanımında %5,5'te kaldı: Uzman ve bütçe eksikliği belirleyici. https://www.packworldturkiye.com/haber/turkiye-yapay-zeka-kullaniminda-55te-kaldi-uzman-ve-butce-eksikligi-belirleyici.html

[20] Sönmez, G. (2025). Türkiye'de iletişim alanında yapay zekâ kullanımı: Sorunlar ve çözümler. İletişim ve Diplomasi Araştırmaları Dergisi, 9(2), 309–https://doi.org/10.30692/sisad.1628299

[21] Türkiye Genel Sosyal Saha Araştırması (TGSS). (2024a). Yapay Zekaya Dair Algılar. Erişim tarihi: 1 Aralık 2025, https://analiz.tgss.org.tr

[22] Türkiye Genel Sosyal Saha Araştırması (TGSS). (2024b). Genel bakış. Erişim tarihi: 1 Aralık 2025, https://www.tgss.org.tr/sayfa/genelbakis

[23] Türkiye Genel Sosyal Saha Araştırması (TGSS). (2024c). Örneklem. Erişim tarihi: 1 Aralık 2025, https://www.tgss.org.tr/sayfa/orneklem

[24] Awwad, M. Y. H. (2024). The power of C-reactive protein biomarker in detecting the severity progress of COVID-19 patients' illness (Master's thesis). Al-Quds University, Faculty of Public Health

[25] Field, A. (2013). Discovering statistics using IBM SPSS statistics. Sage.

[26] Portney, L. G. (2020). Foundations of clinical research: applications to evidence-based practice. FA Davis.

Analysis of the RL Circuit Using the Physics-Informed Neural Network (PINN) Method

Peruzet Aydın [1], Bilal Usanmaz[2]

[1] Department of Computer Engineering, Institute of Science, Atatürk University, Erzurum, Türkiye
[2] Department of Computer Engineering, Faculty of Engineering, Atatürk University, Erzurum, Türkiye

* *Corresponding author E-mail: peruzetaydin@gmail.com*

Keywords

RL Circuit,

Physics-Informed Neural Networks,

Neural Networks

Abstract

In this study, the time-dependent current behavior of an RL circuit, which is a basic electrical circuit, is investigated using the Physics-Informed Neural Networks (PINN) approach. The first-order differential equation governing the RL circuit is incorporated into the training process of the neural network as a physical constraint. Analytical solutions and simulation data are used as reference solutions. The obtained results shows that the PINN model can accurately predict the current-time behavior and that the loss function decreases steadily during training. These findings demonstrate that the PINN approach is an effective alternative to classical methods for modeling electrical circuits.

1. Introduction

Due to the limitations of conventional methods in solving differential equations of electrical circuits, interest in alternative approaches has been increasing. In this study, the performance of Physics-Informed Neural Networks (PINNs) in solving the differential equation of an RL circuit was investigated. Neural networks are computational models inspired by the information-processing structure of neurons in the human brain. In these structures, patterns are learned from data through interconnected artificial neurons, allowing complex relationships to be represented. In recent years, this structure has also begun to be used in modeling physical systems. Raissi et al. (2019) defined PINNs as a method that integrates the differential equations of a system into the training of a neural network, producing consistent results by considering both data and physical constraints. Karniadakis et al. (2021) noted that PINNs can provide highly accurate solutions even with limited data and offer a data-efficiency advantage compared to classical numerical methods. Moreover, PINNs provide the flexibility to combine data and physical knowledge by enabling applicability to complex geometries and high-dimensional problems without the need for mesh generation (Jagtap et al., 2024). PINNs offer high accuracy, especially when working with limited data. Considering the data requirements of conventional methods, PINNs deliver much more efficient solutions (Lu and Karniadakis, 2021). By taking physical constraints into account, PINNs achieve faster and more accurate results, which presents a significant advantage for engineering applications. Additionally, by integrating both data and physical knowledge, generate robust solutions. With these characteristics, PINNs offer a suitable approach for real-time simulations and modeling dynamic systems. They can also provide effective solutions for complex structures such as advanced power systems and communication networks (Zhu and Zhang, 2023).

One of the fundamental structures that can be considered as an example of such dynamic systems is the RL circuit. An RL circuit, consisting of a resistor and an inductor, is a basic circuit structure in which the steady-state and transient currents' changes over time are analyzed mathematically (Coufal, 2025). Transient analysis of RL circuits is an important tool for determining how the current in the circuit changes over time, as well as for assessing the inductor's energy storage capacity. This feature plays a critical role in understanding the circuit's responses to sudden changes (Smith and Zhang, 2024). Furthermore, studies on the frequency response and time delays of RL circuits particularly investigate the reactions of inductive loads to high-frequency sinusoidal voltages (Novák and Hrubý, 2025). Accurate modeling of such dynamic behaviors is crucial for evaluating the performance of the developed methods. Therefore, the dynamic behavior of the RL circuit is aimed to be modeled and analyzed using the Physics-Informed Neural Networks (PINN) approach.

2. Mathematical Model and Analytical Solution of the RL Circuit

An RL circuit is a basic electrical circuit consisting of a resistor (R) and an inductor (L). Due to the inductor's energy storage, the current in the circuit changes over time, and this behavior is described by a first-order differential equation. When a voltage V*(t)* is applied to a series RL circuit, the time-dependent variation of the current

$$L\frac{di}{dt} + Ri(t) = V(t) \tag{1}$$

is defined by the following equation. Here, $i(t)$ represents the current, R the resistance, L the inductance, and V*(t)* the applied voltage. Under a constant DC voltage and the initial condition $i(0) = 0$, Equation (1) can be solved analytically, and the resulting solution shows that the current approaches a steady state over time. This analytical solution has been used as a reference for validating both the simulation and PINN results.

Under a constant direct current (DC) voltage V*(t)*=V and the initial condition $i(0)=0$ the analytical solution of Equation (1) is obtained as follows.

$$i(t) = \frac{V}{R}\left(1 - e^{-\frac{R}{L}t}\right) \tag{2}$$

This expression indicates that the current in the circuit starts from zero and exponentially approaches the steady-state value of V/R over time. The obtained analytical solution has been used as a reference to evaluate the accuracy of the simulation and PINN results.

3. Physics-Informed Neural Networks

Physics-Informed Neural Networks (PINNs), unlike classical artificial neural networks, are a machine learning approach that directly incorporates the differential equations describing physical systems into the training process of the network (Raissi et al., 2019). Figure 1 schematically illustrates the general working principle of the PINN approach.

In this approach, the input variables are fed into the neural network, and the network predicts the unknown solution of the system. The neural network output is then substituted into the differential equations using automatic differentiation, yielding the physical residual terms.

The total loss function consists of a combination of the physical residuals and the losses associated with the initial and boundary conditions, and the network parameters are updated to minimize this loss. In this way, the PINN method produces physically consistent solutions by simultaneously utilizing both data and physical knowledge.

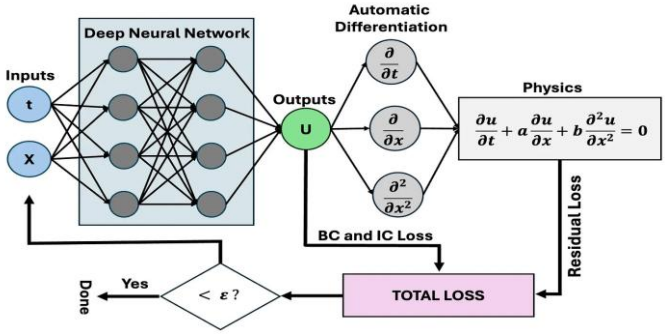

Figure 1 General structure of Physics-Informed Neural Networks (Loveland and Dent, 2024)

4. Method

In this study, the time-dependent current behavior of the RL circuit was modeled using Physics-Informed Neural Networks (PINNs). First, the RL circuit was set up using a circuit simulation program, and data on the time-dependent variation of the current were obtained. These data were used for the training and validation of the PINN model.

In the PINN model, the input to the neural network was chosen as the time variable, and the output was defined as the predicted value of the circuit current. The predicted current from the network was differentiated with respect to time using automatic differentiation and substituted into the differential equation of the RL circuit. In this way, the model

was forced to produce solutions that are not only consistent with the data but also comply with physical laws. During the training process, the model parameters were first brought to a suitable initial region using the Adam optimization algorithm, and then more precise optimization was performed using the LBFGS method. This two-stage optimization approach ensured that the model produced more stable and accurate results.

4.1. PINN Loss Function

The total loss function of the PINN model consists of three main components: the physical equation loss, the initial condition loss, and the data loss. The total loss function is defined in Equation (3) as follows:

$$L_{total} = L_{PDE} + L_{IC} + L_{DATA} \tag{3}$$

Here, L_{PDE} represents the residual error obtained from the physical differential equation, L_{IC} denotes the error associated with the initial condition, and L_{DATA} corresponds to the difference between the model output and the available measurement or simulation data.

4.2. Training Process

The neural network parameters were updated using gradient-based optimization algorithms to minimize the total loss function. During the training process, it was observed that the loss value decreased with the number of epochs. At the end of the training, the resulting PINN model was able to predict the time-dependent current response of the RL circuit with high accuracy. The model's performance was evaluated by comparing it with the analytical solution.

5. Result

In this section, the results obtained using the Physics-Informed Neural Networks (PINN) method are presented and compared with the analytical solution. Additionally, the accuracy of the model was evaluated based on the absolute error and the loss function during the training process.

5.1. Current-Time Graph

Figure 2 shows the comparison of the time-dependent variation of the current predicted by the PINN model at different training stages with the analytical solution of the RL circuit. As the training progresses, it can be seen that the PINN outputs approach the analytical solution, accurately representing both the transient and steady-state behaviors.

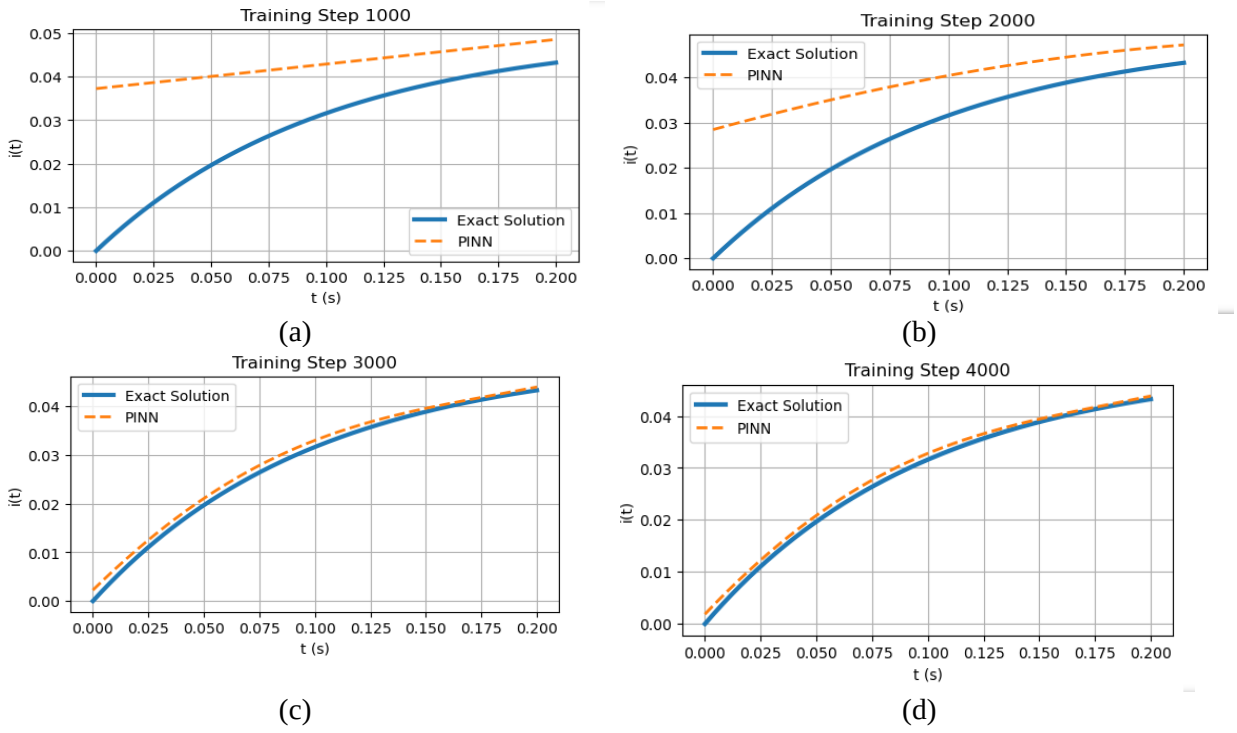

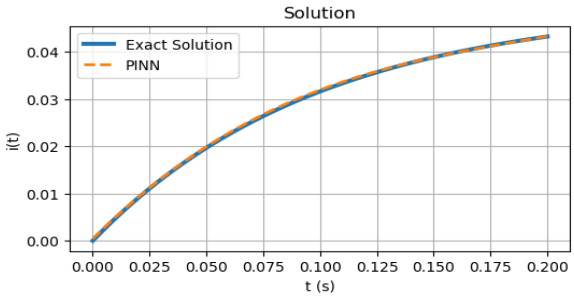

(e)

Figure 2 Comparison of the PINN model and the analytical solution at different training stages.

5.2. Loss Graph

It was observed that the total loss value steadily decreased with the number of epochs during the training process, and the model reached a stable state (Figure 3).

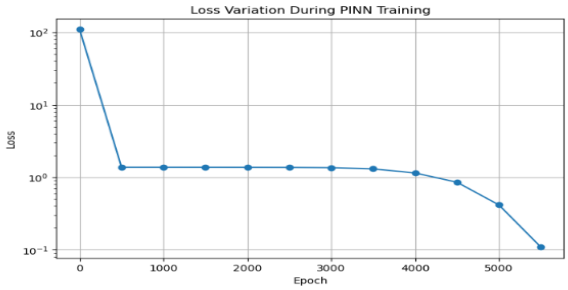

Figure 3 Absolute error between the analytical solution and the PINN outputs.

5.3. Absolute Error Graph

To evaluate the accuracy of the PINN model, the absolute error between the analytical solution and the PINN outputs was calculated (Figure 4). The results indicate that the PINN model closely approximates the analytical solution with high accuracy.

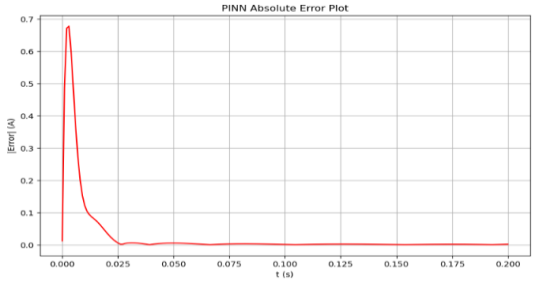

Figure 4 Time-dependent variation of the absolute error between the analytical solution and the PINN outputs.

The obtained findings demonstrate that the PINN method can model the dynamic behavior of the RL circuit with high accuracy. In this context, the overall evaluation and conclusions derived from the study are presented in the next section.

6. Conclusion

In this study, the time-dependent current behavior of the RL circuit was investigated using the Physics-Informed Neural Networks (PINN) method. The developed PINN model produced highly accurate results when compared with the analytical solution and data obtained from circuit simulations.

The steady decrease of the total loss value with increasing epochs during the training process indicates that the model successfully learned both the physical differential equation and the data consistency. Additionally, the absolute error analyses demonstrated that the PINN outputs rapidly approached the analytical solution.

The findings indicate that the PINN method offers a strong alternative to classical numerical methods and can be effectively used for the analysis of electrical circuits, particularly under conditions of limited data.

Future Work

In future studies, the proposed PINN approach is planned to be tested on different circuit types (RC, RLC) and real measurement data. Additionally, the model's performance under noisy data conditions will be investigated.

References

[1] M. Raissi, P. Perdikaris, and G. E. Karniadakis, "Physics-informed neural networks: A deep learning framework for solving forward and inverse problems involving nonlinear partial differential equations," Journal of Computational Physics, vol. 378, pp. 686–707, 2019.

[2] Loveland, M., & Dent, S. (2024). *Quantum physics-informed neural networks*. Entropy, 26(8), https://doi.org/10.3390/e26080649

[3] Karniadakis G.E., Kevrekidis I.G., Lu L. ve diğerleri, "Physics-informed machine learning". *Nature Reviews Physics*, 3:422–440, 2021.

[4] Jagtap, A.D., Kharazmi, E., Karniadakis, G.E., "Physics-informed neural networks for PDE problems: a comprehensive review", *Artificial Intelligence Review*, 2024.

[5] Coufal, O. (2025). *Transient and steady currents in a parallel RL circuit*. Journal of Electrical Engineering, 76(2), 145–158.

[6] Novák, J., & Hrubý, P. (2025). *Lagrangian for RLC circuits using analogy with the classical mechanics concepts*. International Journal of Circuit Theory, 92(4), 123-135.

[7] Lu, L., & Karniadakis, G. E. (2021). Physics-informed neural networks for nonlinear systems. *Journal of Computational Physics*, 432, 109544.

[8] Zhu, J., & Zhang, Y. (2023). Real-time system analysis in power electronics using physics-informed neural networks. *IEEE Access*, 11, 50512–50521.

[9] Zhang R., Xu N., Zhang K., Wang L. ve Lu G.(2023). A Parametric Physics-Informed Deep Learning Method for Probabilistic Design of Thermal Protection Systems. Energies.16.3820.

[10] Smith, J., & Zhang, L. (2024). *Analysis of Transient Behavior in RL Circuits*. Journal of Electrical Engineering, 42(3), 124-135.

The Impact of Amorphous Boron Waste on the Long-Term Mechanical Properties of Steel Fiber-Reinforced

Meral Oltulu[1]*, Emrah Turan[1]

[1] Department of Civil Engineering, Faculty of Engineering, Atatürk University, Erzurum

* *Corresponding author E-mail: mroltulu@atauni.edu.tr*

Keywords

Steel Fiber Concrete
Boron
Compressive Strength
Splitting Tensile
Long Term

Abstract

This study investigates the long-term mechanical performance of high-strength steel fiber-reinforced concrete (SFRC) incorporating calcined boron waste with increased amorphous content. Calcined waste was used as a partial cement replacement at ratios of 5%, 10%, and 15% to prepare the mixtures. The mechanical behavior was monitored over a three-year period through compressive, flexural, and splitting tensile strength tests. Results indicate that calcined boron waste significantly enhances long-term mechanical properties, with the 5% replacement ratio yielding the highest strength values. Consequently, calcined boron waste is identified as a high-potential additive for improving SFRC characteristics.

1. Introduction

Boron minerals and the wastes generated during their processing offer considerable potential for the sustainable production of construction materials within the construction industry. Turkey, which holds approximately 73% of the world's boron reserves, generates between 500,000 and 1,000,000 tons of boron waste annually, and the improper disposal of these wastes causes serious environmental concerns [1, 2]. Numerous studies have investigated the incorporation of borogypsum, colemanite, and other boron-containing wastes into cement and concrete composites, demonstrating that these materials may exhibit pozzolanic behavior and enhance the mechanical performance of concrete when used at appropriate replacement levels.

Topçu and Boğa reported that the incorporation of boron-containing clay waste as a cement additive had a limited effect on workability; however, it resulted in a significant reduction in strength values [1]. Similarly, Sevim et al. found that the use of borogypsum in mortar influenced both mechanical properties and durability performance [3]. Conversely, Koumpouri and Angelopoulos examined the feasibility of utilizing boron waste in the production of low-energy belite cement and reported that while boron addition delayed the setting time due to its retarding effect on cement hydration, it contributed to improved long-term strength development [4].

The use of boron wastes in construction materials has not been limited to concrete and cement alone, but has also been evaluated in lightweight aggregate production, radiation shielding applications, asphalt mixtures, and ceramic products. Kavas et al. demonstrated that different types of boron-containing wastes (sieve waste, dewatering waste, thickener waste) could be used in lightweight aggregate production, achieving aggregates with unit weights ranging from 0.9 to 1.2 g/cm³ [5]. Aldakshe et al. reported that the use of boron wastes as a replacement for pumice aggregate in lightweight concrete production improved physical and mechanical properties, with 9% replacement providing optimum results [2].

Regarding radiation protection applications, Çelen et al. and Binici et al. revealed that colemanite-containing concretes provided effective protection against neutron and gamma radiation [6, 7]. Öztürk et al. determined that boron-containing wastes significantly improved the electromagnetic properties and radiation shielding effectiveness of concrete [8]. In road construction applications, Zhang et al. demonstrated that boron waste could be used as a road base material with lime–cement stabilization, achieving frost resistance indices above 70% [9]. Gürer and Selman investigated the usability of boron wastes as mineral filler material in asphalt concrete and reported that Marshall stability values met the standards [10]. Finally, in ceramic and brick applications, Uslu and Arol and Christogerou et al. determined that the use of boron wastes in red brick and tile production improved physical properties and particularly increased frost resistance [11, 12].

Calcination significantly enhances the pozzolanic activity and reactivity of boron wastes by increasing the B_2O_3 content and inducing structural transformations. Previous studies have shown that calcined boron wastes improve

compressive strength and regulate cement hydration, whereas the direct use of uncalcined wastes negatively affects early-age strength and setting time [13]. Moreover, thermally treated boron wastes contribute to improved long-term durability and more stable hydration products in cementitious systems [14]. From an environmental perspective, the calcination of boron wastes has also been reported as a sustainable approach in belite cement production due to reduced CO_2 emissions [15].

In light of the literature, the primary aim of this study is to reduce energy consumption by utilizing heat-treated boron derivative wastes in the production of steel fiber-reinforced concrete, while simultaneously providing a solution to environmental problems stemming from waste storage. Boron waste was subjected to a calcination process at 600 °C for 2 h and incorporated into the concrete at replacement ratios of 5%, 10%, and 15% by weight of cement. The specimens were cured for a long term (three years), and late-age compressive and splitting tensile strength tests were conducted.

2. Materials and Methods

2.1. Materials

CEM I 42.5 R ordinary Portland cement (OPC) was used to prepare the mixture specimens. Chemical compositions and physical characteristics of OPC are presented in Table 1.

Table 1 Chemical Composition and Physical Properties of Binders.

Chemical Composition	**%**	**Physical Properties**	**Value**
SiO_2	19,84	45 micron sieve (%)	5,27
Al_2O_3	4,91	Specific Surface Area (Blaine) (cm^2/g)	3625
Fe_2O_3	3,52	Specific Gravity (g/cm^3)	3,12
CaO	61,65	Initial Setting Time	155
MgO	1,33	Final Setting Time	230
SO_3	2,70	Water Requirement(%)	27,5
Loss in Ignition	2,73	Volume Expansion (mm)	0,55
Na_2O	0	2-Day Compressive Strength (MPa)	24,75
K_2O	0	28-Day Compressive Strength (MPa)	57,70
CI	0,007		

A polycarboxylate-based superplasticizer was incorporated at a dosage of 1.5% of the cement weight. The admixture is green in color and has a specific gravity of 1.045±0.02 g/cm^3.The boron waste was obtained from the Eti Maden Bigadiç Bor Works. Figure 1 presents the images of the boron wastes before and after calcination.



Figure 1 Boron waste (before and after calcination)

Figure 2 illustrates the aggregate particle size distribution curve, including sieve sizes and the cumulative percent passing

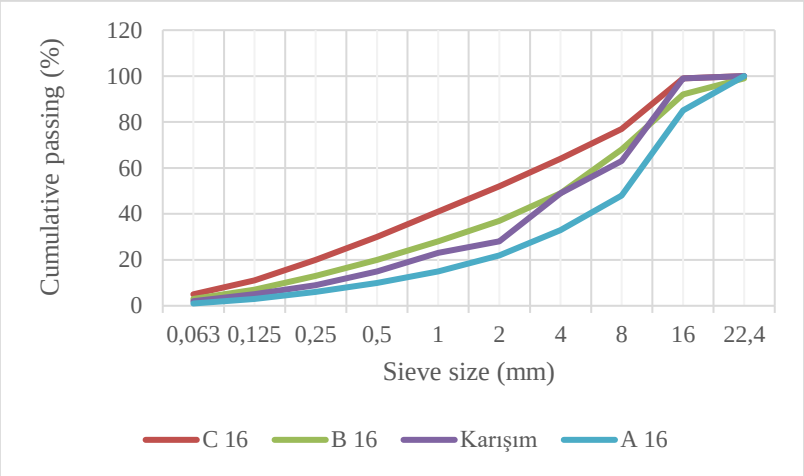

Figure 2 Granulometric curve of aggregates.

Low-carbon, hooked-end steel fibers with dimensions of 35/0.35 were used in the research at a ratio of 1% by volume of the concrete. The technical properties of the steel fibers are presented in Table 2.

Table 2 Fiber properties

Property	**Value**
Fiber Type	Hooked-end steel fiber
Length (mm)	35
Diameter (mm)	0,35
Aspect Ratio	100
Tensile Strength (GPa)	1,15
Elastic Modulus (GPa)	200
Specific Gravity (g/cm³)	7,48
Number of Fibers per 1 kg (pieces)	13000

2.2. Mix Proportions and Specimen Designation

Table 3 presents the mix proportions of the steel fiber–reinforced concrete and the mixtures containing 5%, 10%, and 15% calcined boron waste (KBA5, KBA10, and KBA15).

Table 3 Concrete Mix Proportions (kg/m³).

Materials	**Amount by weight in mix (kg)**			
	S	**KBA5**	**KBA10**	**KBA15**
Cement	400	400	400	400
Water	181.4	181.4	181.4	181.4
Süperplasticizer	4.8	4.8	4.8	4.8
0-2 mm aggregate	510.26	510.26	510.26	510.26
2-4 mm aggregate	264.65	264.65	264.65	264.65
4-8 mm aggregate	331.14	331.14	331.14	331.14
8-16 mm aggregate	381.7	381.7	381.7	381.7
16-25 mm aggregate	165.94	165.94	165.94	165.94
Steel Fiber	74,8	74,8	74,8	74,8
Calcine boron waste	-	90,5	181,0	271,5

2.3. Mixing and Curing Regime

In this study, the specimens were weighed using a sensitive electronic balance with a precision of 0.01 g, and their densities were calculated by dividing the mass by the volume. To ensure homogeneity in the mixtures, the dry materials were first placed into the mixer and mixed for 1 minute. Half of the mixing water was added to the dry mixture and mixed for 2 minutes. The superplasticizer was added to the remaining half of the mixing water, and this solution was slowly poured into the mixer, followed by mixing for an additional 2 minutes.

2.4. Testing Procedure

Compressive and splitting tensile strength tests were conducted in accordance with TS EN 12390-3 (2019) and TS EN 12390-5 (2010) standards [16,17], respectively. A constant loading rate of 0.6 MPa/s was applied for the compressive strength test, and 0.05 MPa/s for the splitting tensile strength test. The test results for each group were calculated by taking the average of 3 specimens.

3. Results and Discussion

Table 4 presents the splitting tensile and compressive strengths of steel fiber-reinforced concrete specimens incorporating calcined boron waste at the end of three years, as well as their variations relative to the steel fiber-reinforced control specimen.

Table 4 Table Experimental Results

Groups	Compressive Strength, MPa (Change, %)	Splitting Tensile MPa (Change, %)
Steel Fiber	54,47	7,4
KBA5	83,05 (52)	8,9 (20)
KBA10	76,77 (41)	9,01 (22)
KBA15	61,31 (13)	7,2 (3)

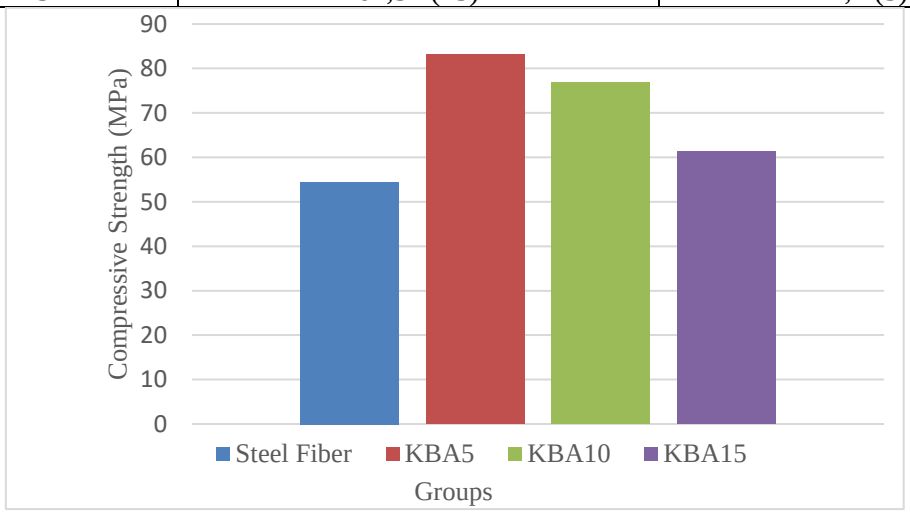

Figure 3 Compressive strength of groups

The incorporation of KBA significantly enhanced the compressive performance across all replacement ratios (Fig. 3). The maximum compressive strength was recorded for the KBA5 mixture at 83.05 MPa, which corresponds to a 52% increase compared to the reference. However, further increasing the KBA content resulted in a gradual reduction in strength gains; the KBA10 and KBA15 mixtures exhibited increases of 41% and 13%, respectively.

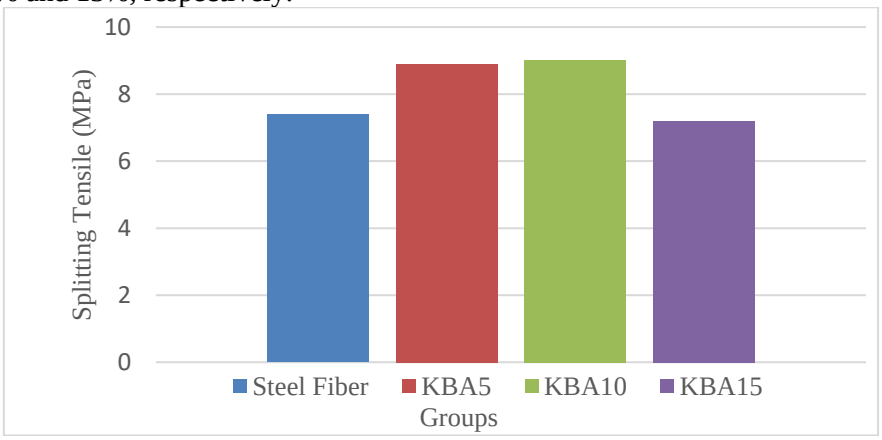

Figure 4 Splitting tensile strength of groups.

Regarding the splitting tensile strength, the results followed a slightly different trend compared to compressive strength (Fig. 4). The highest performance was observed in the KBA10 mixture, which reached 9.01 MPa (22% increase). The KBA5 mixture also showed a significant improvement with 8.9 MPa (20% increase). Conversely, increasing the KBA content to 15% (KBA15) caused the splitting tensile strength to decrease to 7.2 MPa, falling below the reference value. This indicates that excessive amounts of KBA (15%) may adversely affect the fiber-matrix bond or the tensile behavior of the composite.

In conclusion, the experimental data reveals that KBA replacement ratios between 5% and 10% provide the most favorable mechanical properties. While KBA5 is ideal for compressive strength, KBA10 offers the peak performance for splitting tensile strength.

There is a strong correlation between compressive strength and splitting tensile strength, with a coefficient of determination (R^2) of 0.86.

4. Conclusion

In this study, the late-age compressive and splitting tensile strengths were investigated following the addition of calcined boron waste at ratios of 5%, 10%, and 15% to fiber-reinforced concrete. The main conclusions drawn from these experimental results are summarized below:

- The optimum replacement ratio for maximizing compressive strength is 5% boron waste.

- Splitting tensile strength showed a different trend than compressive strength, with the highest value at KBA10, while 15% KBA reduced the strength below the reference level.

- KBA contents of 5–10% yield optimal mechanical performance, with KBA5 maximizing compressive strength and KBA10 maximizing splitting tensile strength.

-It is thought that the boron waste improves the strength by densifying the structure via filler and pozzolanic actions. Consequently, we can conclude that this material has significant potential for application in cementitious composites.

-It is advisable to support the mechanical findings with instrumental analysis and microstructure imaging methods. Additionally, future research may focus on observing durability effects in other special concrete types.

References

[1] Topçu, İ. B., & Boğa, A. R. (2010). Utilization of boron-containing wastes as cement additives. Construction and Building Materials, 24, 165–170.

[2] Aldakshe, A. M., et al. (2020). Use of boron wastes as pumice aggregate replacement in lightweight concrete. Construction and Building Materials, 246, 118420.

[3] Sevim, Ö., et al. (2019). Effects of borogypsum on mechanical and durability properties of mortar. Journal of Building Engineering, 25, 100821.

[4] Koumpouri, D., & Angelopoulos, G. N. (2016). Utilization of boron waste in low-energy belite cement production. Cement and Concrete Composites, 68, 1–8.

[5] Kavas, T., et al. (2011). Production of lightweight aggregates from boron wastes. Ceramics International, 37, 53–58.

[6] Çelen, Y., et al. (2019). Radiation shielding properties of colemanite-containing concrete. Construction and Building Materials, 210, 382–390.

[7] Binici, H., et al. (2014). Neutron and gamma radiation shielding characteristics of colemanite-added concrete. Annals of Nuclear Energy, 63, 440–449.

[8] Ozturk, S., et al. (2020). Electromagnetic and radiation shielding properties of boron-containing concretes. Materials Chemistry and Physics, 247, 122857.

[9] Zhang, Y., et al. (2016). Application of boron waste as stabilized road base material. Construction and Building Materials, 122, 384–392.

[10] Gürer, C., & Selman, E. (2016). Use of boron waste as mineral filler in asphalt concrete. Construction and Building Materials, 123, 104–111.

[11] Uslu, T., & Arol, A. İ. (2004). Use of boron waste in brick production. Waste Management, 24, 217–222.

[12] Christogerou, A., et al. (2021). Utilization of boron-containing wastes in ceramic tiles. Ceramics International, 47, 10245–10253.

[13] Demirbaş, A., & Karslıoğlu, A. (1995). Effect of boric acid sludge on cement hydration and setting time. Cement and Concrete Research, 25, 1381–1386.

[14] Bullerjahn, F., et al. (2019). Influence of boron compounds on hydration of belite-based cements. Cement and Concrete Research, 116, 191–201.

[15] Kavas, T., et al. (2015). Sustainable belite cement production using boron wastes. Construction and Building Materials, 90, 108–115.

[16] Turkish Standards Institution. (2010). Testing hardened concrete—Part 5: Flexural strength of test specimens (TS EN 12390-5). Turkish Standards Institution.

[17] Turkish Standards Institution. (2019). Testing hardened concrete—Part 3: Compressive strength of test specimens (TS EN 12390-3). Turkish Standards Institution..

The Critical Role of Rare Elements in Renewable Energy Systems and Türkiye

Hüseyin Güllüce[1*]

[1] Department of Machine, Technical Sciences Vocational School, Ataturk University, Erzurum, Türkiye

* *Corresponding author E-mail: hgulluce@atauni.edu.tr*

Keywords

Renewable Energy
Rare Earth Elements
Critical Raw Materials
Energy Transition
Sustainable Mining

Abstract

The global transition toward renewable energy depends not only on the rapid deployment of solar, wind, geothermal, hydroelectric, and bioenergy technologies but also on advanced materials with highly specific functional properties. Rare earth elements (REEs) are central to this transition due to their unique magnetic, optical, and electronic characteristics. Elements such as neodymium, praseodymium, and dysprosium enable high-performance permanent magnets used in wind turbines and electric vehicle powertrains, while gallium, indium, and germanium are key to high-efficiency photovoltaic devices. Lanthanum and cerium further contribute to hydrogen-storage alloys, catalytic systems, and solid oxide fuel cells, reinforcing the technological backbone of low-carbon energy systems. However, the geographic concentration of REE supply chains introduces strategic vulnerabilities, price volatility, and geopolitical risks. Addressing these challenges requires diversified sourcing, circular material utilization, and environmentally responsible extraction technologies. Turkey holds notable potential in this context, supported by its major boron reserves and emerging REE-rich deposits in regions such as Eskişehir-Kızılcaören and Malatya-Hekimhan. Strengthening domestic processing capacity, advancing research and development, and integrating recycling infrastructure into national energy strategies will be essential to reducing dependency and enhancing competitiveness. Sustainable and strategic REE management is therefore vital for secure and resilient renewable energy systems aligned with global transition goals.

1. Introduction

The global transition toward low-carbon and sustainable energy systems has significantly increased the strategic importance of rare elements, particularly rare-earth elements (REEs). Comprising the lanthanide series together with scandium and yttrium, these elements exhibit unique magnetic, optical, electrical, and catalytic properties that cannot be easily substituted by conventional materials. These characteristics underpin the performance of numerous renewable-energy components, including high-strength permanent magnets for wind turbine generators, traction motors for electric vehicles, advanced battery systems, and energy-efficient lighting technologies [1, 2].

Over the past two decades, the rapid expansion of wind and solar energy, the electrification of transportation, and the digitalization of energy systems have sharply increased global REE demand. Elements such as neodymium, praseodymium, dysprosium, and terbium are essential constituents of Nd–Fe–B permanent magnets, offering superior magnetic energy density and thermal stability for high-efficiency applications. Likewise, lanthanum and cerium play key roles in battery alloys, catalytic processes, and polishing materials across clean-energy supply chains [3, 4, 5].

Despite their technological significance, REE supply remains constrained by geological, technological, and geopolitical factors. Economically viable REE deposits are limited, and the chemical similarity among individual elements makes extraction and separation technically challenging. Consequently, many national and international bodies classify REEs as “critical materials” due to their high economic importance and vulnerability to supply disruptions [1, 6]. Additionally, conventional REE processing routes are energy-intensive and generate environmentally sensitive wastes, including radioactive by-products associated with thorium and uranium [2].

In response to these challenges, recent research has focused on enhancing resource efficiency and developing alternative recovery pathways. Advances in mineral flotation, hydrometallurgical separation, adsorption-based recovery, bioleaching, and the recycling of industrial waste and end-of-life products demonstrate significant potential for improving supply security while reducing environmental impacts [4], 7, 8, 9]. These approaches align with

circular-economy principles and are increasingly recognized as essential for the long-term sustainability of renewable-energy systems.

In conclusion, understanding the critical role of rare elements in renewable-energy technologies requires an integrated perspective connecting material properties, technological applications, resource availability, and processing challenges. This study aims to provide such a perspective by examining the roles of REEs in key renewable-energy technologies, the limitations associated with their supply and processing, and emerging strategies supporting a secure, sustainable, and environmentally responsible REE value chain.

2. Materials and Methods

This study aims to examine the role of rare elements in renewable energy systems not only from a technological perspective but also through the lenses of materials science, supply chain dynamics, and sustainability principles. Such a comprehensive approach is essential for understanding the multilayered impacts of rare elements on modern energy technologies.

2.1. Materials Required in Renewable Energy Technologies

Solar, wind, hydrogen, and energy storage technologies rely on advanced semiconductors, high-performance magnetic materials, and efficient catalytic structures to achieve optimal performance. Elements such as gallium (Ga), indium (In), neodymium (Nd), praseodymium (Pr), and dysprosium (Dy) play a particularly significant role in enhancing the efficiency of photovoltaic systems, wind turbines, and other energy conversion components.

2.1.1. Technical Characteristics of Rare Elements

Rare earth elements (REEs) comprise a group of 17 elements, including the 15 lanthanides in the periodic table (atomic numbers 57–71), as well as scandium (Sc) and yttrium (Y), which exhibit comparable chemical and physical behaviors [10, 11, 12]. Their classification typically relies on atomic number, electron configuration—especially the occupancy of the 4f orbitals—and ionic radii. The most commonly adopted approach in the literature categorizes REEs into two primary groups: Light Rare Earth Elements (LREEs) and Heavy Rare Earth Elements (HREEs); however, in some cases, an intermediate group is also proposed [4]. The general properties of rare earth elements are summarized in Table 1 [13].

Table 1 The general properties of rare elements

Element	Symbol	Atom Number	Atomic Weight (g/mol)	Density (g/cm³)	Melting Point (°C)	Vickers Hardness* (kg/mm²)
Scandium	Sc	21	44.95	2.989	1541	85
Yttrium	Y	39	88.90	4.469	1522	38
Lanthanum	La	57	138.90	6.146	918	37
Cerium	Ce	58	140.11	6.160	798	24
Praseodymium	Pr	59	140.90	6.773	931	37
Neodymium	Nd	60	144.24	7.008	1021	35
Promethium	Pm	61	145.00	7.264	1042	—
Samarium	Sm	62	150.36	7.520	1074	45
Europium	Eu	63	151.96	5.244	822	17
Gadolinium	Gd	64	157.25	7.901	1313	57
Terbium	Tb	65	158.92	8.230	1356	46
Dysprosium	Dy	66	162.50	8.551	1412	42
Holmium	Ho	67	164.93	8.795	1474	42
Erbium	Er	68	167.26	9.066	1529	44
Thulium	Tm	69	168.93	9.321	1545	48
Ytterbium	Yb	70	173.04	6.966	819	21
Lutetium	Lu	71	174.97	9.841	1663	77
* Vickers hardness: Measured under a load of 10 kg.						

2.1.1.1 Light Rare Earth Elements (LREE – Cerium Group)

Light rare earth elements (LREE), also referred to as the Cerium Group, encompass elements with relatively lower atomic numbers. The boundaries of this group vary slightly across the literature. Some studies define LREEs as the elements between lanthanum (La) and samarium (Sm)—namely La, Ce, Pr, Nd, Pm, and Sm (Dent, 2012). Other classifications extend the group by including europium (Eu) (Bashiri et al., 2022) or gadolinium (Gd), expanding the series to eight elements: La, Ce, Pr, Nd, Pm, Sm, Eu, and Gd [2, 4].

From an electronic standpoint, LREEs are characterized by the gradual filling of the 4f orbitals and an increasing number of unpaired electrons [2]. In terms of natural abundance, LREEs are significantly more common in the Earth's crust compared to heavy rare earth element [12].

Below is a summary of the principal technical properties and applications of individual LREEs:

Scandium (Sc): Scandium is primarily used as a strengthening agent in aluminum alloys. Aluminum-scandium alloys are widely employed in aerospace applications requiring a combination of low density and high strength. It is also used in lighting technologies and electron-beam tubes [1, 3, 10].

Lanthanum (La): Lanthanum is an important component of optical glasses and camera lenses due to its high refractive index and colorless nature. Up to 40% lanthanum oxide may be incorporated to improve corrosion resistance. It is also a key component in Ni-MH batteries used in hybrid vehicles due to its high hydrogen absorption capacity. Additionally, lanthanum plays a major role as a catalyst in fluid catalytic cracking (FCC) processes in petroleum refining [1, 3, 10].

Cerium (Ce): Cerium is the most abundant rare earth element and is widely used in automotive catalytic converters for emission control. In the glass industry, cerium oxide acts as a polishing agent for LCD screens, optical surfaces, and mirrors due to its combined chemical and mechanical action. It is also used for decolorizing glass and absorbing UV radiation [3, 10, 14].

Praseodymium (Pr): Praseodymium is utilized with neodymium in didymium mixtures for manufacturing high-strength permanent magnets. It serves as a yellow pigment in ceramics and glass and is used in welding goggles to filter UV and IR radiation [1, 3, 10].

Neodymium (Nd): Neodymium is the key component of NdFeB (Neodymium-Iron-Boron) magnets, known as the strongest permanent magnets available. These magnets are essential in electric vehicle motors, wind turbine generators, hard disk drives, and headphones. Nd is also used in Nd:YAG laser systems and as a coloring agent in glass [1, 3, 10, 12].

Promethium (Pm): Promethium is a radioactive element that does not occur naturally. It is used in miniature nuclear batteries and pacemakers as a long-lasting power source. Additionally, it has applications in phosphorescent paints [3, 10].

Samarium (Sm): Samarium is alloyed with cobalt to produce Sm-Co magnets, which maintain high magnetic stability under elevated temperatures (up to 300°C) and exhibit high corrosion resistance. These characteristics make them valuable for defense technologies, radar systems, and high-temperature motors. Samarium is also employed as a neutron absorber in nuclear reactor control rods [1, 3, 10, 12].

Europium (Eu): Europium is essential for the production of red phosphors. It provides the bright red emission used in LCD and LED screens and is incorporated into energy-efficient lighting and anti-counterfeiting markers in banknotes [1, 3, 10].

2.1.1.2 Heavy Rare Earth Elements (HREE – Yttrium Group)

Heavy rare earth elements (HREE), which include lantanides with higher atomic numbers as well as yttrium (Y), constitute a classification based on shared chemical and ionic characteristics. This group generally spans the elements from terbium (Tb) to lutetium (Lu)—namely Tb, Dy, Ho, Er, Tm, Yb, and Lu—and incorporates yttrium due to its strong chemical affinity with heavy lanthanides [2, 11]. Some classifications also include europium (Eu) and gadolinium (Gd) among the HREEs [12].

Although yttrium lacks a 4f electron, it is categorized as an HREE because its ionic radius and chemical behavior closely resemble those of heavy lanthanides such as holmium (Ho) [2, 4]. In terms of electronic structure, the number of unpaired electrons in the 4f shell decreases gradually across the HREE series, influencing their magnetic and optical properties. Due to their low crustal abundance, HREEs are generally more economically valuable than LREEs [1].

A summary of the key technical characteristics and applications of major HREEs is provided below:

Gadolinium (Gd): Due to its paramagnetic properties, gadolinium is widely used as a contrast agent in magnetic resonance imaging (MRI). Its high neutron capture cross-section also makes it valuable in nuclear reactor shielding and magnetic refrigeration technologies [3, 10, 15].

Terbium (Tb): Terbium is essential for the production of green phosphors in lighting and display technologies. It is also added to NdFeB magnets to improve coercivity and high-temperature stability [3, 6, 10, 12].

Dysprosium (Dy): Dysprosium is a crucial dopant in NdFeB magnets, enabling them to maintain magnetic properties at elevated temperatures. This makes dysprosium indispensable for electric vehicle motors and wind turbine generators. It is also used in control rods in nuclear reactors [3, 10, 12].

Holmium (Ho): Holmium possesses one of the highest magnetic moments among all elements, making it useful for high-field magnetic applications. It is also used in medical laser systems and nuclear reactor control rods [3, 10].

Erbium (Er): Erbium is a key dopant in fiber-optic amplifiers, reducing signal attenuation in long-distance data transmission. It is also used in medical lasers and as a coloring agent in specialty glasses [1, 3, 10].

Thulium (Tm): Thulium is used as a radiation source in portable X-ray devices and has additional applications in laser systems and microwave ferrite components. Its high scarcity limits its use [3, 10].

Ytterbium (Yb): Ytterbium plays a significant role in fiber-optic communication systems and high-power lasers. In metallurgy, it is employed to refine the grain structure of stainless steels. It is also being explored for enhancing solar cell efficiency [1, 3, 10].

Lutetium (Lu): Lutetium is a preferred scintillation material in PET scanners due to its high density and efficiency. It is also used as a catalyst in hydrocarbon cracking during petroleum refining [1, 10].

Yttrium (Y): Despite not being a lanthanide, yttrium is classified among the HREEs because of its ionic and chemical compatibility with heavy lanthanides. It is used in red phosphor production, YAG lasers, superconductors, and in stabilizing zirconia coatings for jet engine components [1, 3, 6, 10].

2.1.1.3 Alternative Classification Approaches (MREE and Sc)

In addition to the two commonly accepted categories of rare earth elements—Light Rare Earth Elements (LREE) and Heavy Rare Earth Elements (HREE)—some sources propose a third subgroup known as the "Medium Rare Earth Elements" (MREE) (Marion et al., 2020). Although the boundaries of this classification are not clearly defined in the literature, elements such as samarium (Sm), europium (Eu), and gadolinium (Gd) are sometimes included within this intermediate group. The MREE classification has gained particular relevance in economic frameworks, such as China's resource taxation policies, as it can influence market valuation and supply chain strategies for rare earth elements [4].

Furthermore, scandium (Sc), while formally recognized as a rare earth element, exhibits structural and chemical properties that differ significantly from both LREEs and HREEs. As a result, several studies treat scandium as a distinct and independent category outside the traditional two-group system [4]. This unique classification has become increasingly important due to scandium's rising technological relevance, particularly in aerospace alloys and advanced materials engineering.

2.2. Procurement and Preparation of Materials

Rare earth elements (REEs) are obtained from two primary sources: (i) primary geological mineral deposits and (ii) secondary waste streams evaluated within the framework of the circular economy. Primary resources are extracted through direct mining operations, whereas secondary sources include industrial residues, electronic waste, spent magnets, and other process by-products.

2.2.1. Primary Mineral Sources

The recovery of primary rare earth elements is a multi stage and complex process that varies depending on the geological nature of the ore (hard rock deposits, placer deposits, or ion adsorption clays). The process typically consists of mining, physical beneficiation, and subsequent chemical separation.

- Mining and Ore Preparation: Hard rock deposits—such as carbonatites and alkaline intrusions—are usually mined by open pit operations, followed by comminution (crushing and grinding) to liberate REE bearing minerals such as bastnäsite and monazite [2, 4]. Ion adsorption clay deposits, in contrast, do not require blasting or intensive comminution and are typically processed using in situ or heap leaching techniques. Placer (mineral sand) deposits are exploited using dredging, gravity separation, and screening methods [2].

- Physical Beneficiation: Physical and chemical differences between minerals are exploited to increase ore grade and remove gangue minerals.

- Gravity and Magnetic Separation: Gravity separation is frequently applied in placer sediments and some hard rock ores. Magnetic separation—using both low and high intensity systems—is employed to remove strongly magnetic minerals while concentrating paramagnetic REE minerals [2].

- Electrostatic Separation: Based on differences in electrical conductivity, this technique is used to separate conductive minerals (e.g., ilmenite, rutile) from non conductive minerals (e.g., monazite, zircon) [2].

- Froth Flotation: Flotation is the most common technique for hard rock REE ores. Collectors such as fatty acids or hydroxamic acids render the surface of bastnäsite and monazite hydrophobic, allowing these minerals to attach to air bubbles and separate from gangue materials The efficiency of flotation is strongly governed by zeta potential and mineral surface chemistry . [4, 16].

• Hydrometallurgical Processing: Cracking and Leaching: The concentrates produced from beneficiation (typically containing 50–60% REEs) are often refractory and do not dissolve readily in acids. Thus, thermal or chemical decomposition ("cracking") steps are required before leaching.

• Acid or Alkali Cracking: Concentrates are treated at 200–600°C (sometimes above 650°C) using sulfuric acid (acid bake) or sodium hydroxide (alkali cracking). These treatments remove fluorine and convert REEs into water soluble sulfates or chlorides [2].

• Leaching: The cracked material is leached with water or dilute acids to transfer REEs into solution, forming the Pregnant Leach Solution (PLS). Ion adsorption clays, however, are processed through ammonium based electrolytes that displace REEs through ion exchange mechanisms [2].

• Separation and Purification (Solvent Extraction – SX): Because REEs have closely similar chemical properties, separating individual elements from mixed solutions is highly challenging. Solvent extraction is the most widely applied method. The aqueous PLS is contacted with an organic phase containing specific extractants (e.g., phosphonic acid derivatives such as P507) [2, 11]. Achieving ultra high purities (up to 99.99%) requires hundreds of extraction–stripping–scrubbing cycles. The purified REEs are precipitated as oxalates or carbonates and subsequently calcined into rare earth oxides (REOs). For metal production, electrolysis or thermal reduction processes are employed [2].

2.2.2. Secondary Sources and Industrial Wastes

The recovery of rare earth elements (REEs) from secondary sources—also known as "urban mining"—is becoming increasingly significant for environmental sustainability and raw material security. Secondary sources are broadly categorized into (i) end-of-life products (Waste Electrical and Electronic Equipment, WEEE) and (ii) industrial by-products such as phosphogypsum and coal fly ash. Despite their relatively low grades, these sources hold substantial potential due to their high volumes and strategic value within circular economy frameworks.

2.2.2.1 Recovery from End-of-Life Products (WEEE)

Recycling REEs from end of life products primarily targets high technology components such as permanent magnets, nickel metal hydride (Ni MH) batteries, and fluorescent lamps.

• Permanent Magnets: NdFeB (Neodymium Iron Boron) and Sm Co (Samarium Cobalt) magnets are widely used in hard disk drives, air conditioning compressors, and electric vehicle motors. Their recovery is challenging due to their embedded position within devices, protective coatings (e.g., nickel), and mechanical brittleness [12]. Hydrometallurgical routes are predominantly used, where magnets are dissolved through leaching and separated via solvent extraction or hollow fiber supported liquid membrane systems to recover Nd, Pr, Dy, and other REEs [11, 12].

• Batteries and Lighting Products: Ni MH batteries, used in hybrid electric vehicles, contain high concentrations of lanthanum (La), cerium (Ce), neodymium (Nd), and praseodymium (Pr). Recovery of REEs from these batteries is achieved through acid leaching and hydrometallurgical separation [10, 14]. Fluorescent lamp phosphors are another significant secondary source, especially for yttrium (Y), europium (Eu), and terbium (Tb). Recovery typically involves sulfuric or nitric acid leaching followed by solvent extraction, yielding oxide purities up to 99.9% [14].

2.2.2.2 Recovery from Industrial By-Products

Although industrial by products contain low REE concentrations, their large volumes make them strategically important secondary sources.

• Phosphogypsum: Produced during phosphoric acid and fertilizer manufacturing, phosphogypsum may contain 0.3–0.7% rare earth oxides depending on the geological origin of the processed phosphate rock (Kiegiel et al., 2018). REE recovery is achieved through leaching with sulfuric or nitric acid. Studies indicate that nitric acid leaching can yield recovery efficiencies of around 90%, although it poses additional environmental and waste management challenges [14].

• Coal Fly Ash (CFA): Fly ash generated from coal fired power plants is a technologically enriched secondary source of REEs. Bioleaching processes have been developed using sulfur oxidizing acidophilic microorganisms such as Acidithiobacillus and Sulfobacillus, which oxidize elemental sulfur to generate sulfuric acid in situ, promoting REE dissolution. Under optimized conditions (45°C, pH 2.0, 10% pulp density), recovery rates of 50–60% have been reported for scandium (Sc), yttrium (Y), and lanthanum (La) [8]. Furthermore, membrane technologies such as micelle enhanced ultrafiltration (MEUF) and nanofiltration have been successfully used to recover REEs from coal fly ash leachates [11].

2.2.3. Sample Preparation and Purification

Sample preparation and purification of rare earth elements (REEs) involve multi stage hydrometallurgical and physical processes due to the complex mineralogical and chemical structures of both primary ores and secondary sources. These processes are generally carried out in three sequential steps: (i) dissolution and leaching, (ii) separation and purification of mixed REE ions, and (iii) production of the final solid product through precipitation and calcination.

- Ore Preparation and Leaching: Before purification, ore concentrates or secondary samples must be conditioned for chemical processing. Refractory minerals such as bastnäsite and monazite do not dissolve directly in acids and thus require a preliminary "cracking" step. Cracking is performed either through high temperature acid baking (200–600°C) using sulfuric acid, or through caustic cracking using sodium hydroxide These treatments remove fluoride and convert REEs into water soluble sulfates or chlorides. Subsequent leaching with water or dilute acids produces a Pregnant Leach Solution (PLS) containing the dissolved REE ions [2]. In laboratory scale studies, sample preparation also involves grinding in ball mills, sieving to a desired particle size (e.g., −150 +38 μm), magnetic purification, and verification of mineralogical purity using X ray diffraction (XRD) [4].

- Purification by Solvent Extraction (SX): Solvent extraction is the most widely utilized industrial method for separating and purifying REEs from PLS. In this method, metal ions in the aqueous phase are transferred to an organic phase containing selective extractants such as phosphonic acid derivatives (e.g., P507) dissolved in kerosene [11, 2]. The SX process consists of: (1) Extraction, (2) Scrubbing (removal of impurities), (3) Stripping (back extraction of REEs into an aqueous phase) Due to the very similar chemical behaviors of REEs, achieving high purity levels (>99.99%) requires hundreds of extraction–scrubbing–stripping cycles in mixer settler batteries [2].

- Ion Exchange and Membrane Technologies: Ion exchange resins offer an effective alternative for recovering REEs from dilute solutions [14]. Advanced membrane systems—including Polymer Inclusion Membranes (PIM) and Supported Liquid Membranes (SLM)—combine extraction and stripping in a single step, providing high selectivity and reduced chemical consumption. Hollow fiber supported membrane systems have demonstrated promising separation efficiencies for neodymium and dysprosium[11]. Adsorption-based methods are also widely employed due to their simplicity and low cost. Parameters such as pH, contact time, and adsorbent dosage strongly influence recovery efficiency [7].

- Final Product Formation: Precipitation and Calcination: After separation, the dissolved rare earth elements (REEs) are converted into solid form, most commonly by precipitating them as oxalates using oxalic acid [2]; the resulting precipitates are then filtered, washed, and calcined at about 900 °C to obtain rare earth oxides (REOs). For producing metallic REEs, molten salt electrolysis or metallothermic reduction may be employed, while achieving ultra-high purity levels (≥99.99%) requires advanced refining techniques such as vacuum distillation or zone melting; additionally, redox-selective precipitation can be applied to elements like Ce and Eu [14].

3. Results and Discussion

3.1. Results

The results of the analyses clearly demonstrate that rare earth elements (REEs) used in renewable energy technologies are not merely auxiliary components but fundamental elements that determine the structural functionality of these systems. Across a wide range of applications—including wind turbines, electric vehicle (EV) motors, energy storage systems, photovoltaic technologies, and hydrogen production—REEs directly influence critical performance metrics such as efficiency, durability, thermal and magnetic stability, and operational reliability. Consequently, the use of REEs in technologies at the core of the global energy transition has evolved into a technical necessity rather than an optional enhancement.

The most pronounced manifestation of this necessity is observed in wind energy systems. The development of modern direct-drive wind turbines, characterized by high efficiency and low maintenance requirements, relies heavily on the exceptional magnetic energy density provided by neodymium–iron–boron (Nd–Fe–B) permanent magnets. Existing literature consistently indicates that alternative magnet technologies have not yet reached comparable performance levels, particularly in meeting the high-torque, low-speed operational requirements of large-scale turbines. This demonstrates that REE dependence in wind energy is not only quantitative but also structural, shaping the technological limits of efficiency, quality and scalability.

Similarly, electrification processes and energy storage technologies stand out as other domains in which REE dependence is rapidly increasing. Nd–Fe–B magnets have become the industry standard in EV traction motors due to their high torque output, high power density, and superior energy efficiency. Hybrid vehicles, on the other hand, widely employ nickel-metal hydride (NiMH) batteries that contain significant amounts of lanthanum (La), cerium (Ce), and other REEs. This reveals a strong correlation between the pace of the renewable energy transition in the

transportation sector and the global demand for REEs, indicating that REE consumption will continue to grow in parallel with technological advancement.

In photovoltaic technologies, although the mass fraction of REEs is relatively small, their functional contribution is critical. REEs are used in high-purity glass, phosphors, optical coatings, and advanced semiconductor layers, directly affecting light absorption, transmission, panel stability, and overall system efficiency. Thus, REEs play an indispensable yet indirect role in achieving high-efficiency photovoltaic performance.

Hydrogen technologies and advanced energy systems provide further evidence that global REE demand will continue to accelerate. REEs are used extensively in electrolyzers, fuel cells, high-temperature ceramics, and catalytic components due to their unique magnetic, electrochemical, and thermal properties. Their crucial role in power electronics and high-performance energy converters also suggests sustained long-term demand as hydrogen-based energy infrastructures expand globally.

Taken together, these findings indicate that renewable energy technologies are highly dependent on rare earth elements in terms of performance, reliability, and scalability. Moreover, this technical dependence is closely intertwined with the global supply structure, geographical concentration of production, and geopolitical factors. Therefore, assessing the global and national position of REEs—particularly for countries such as Türkiye—is essential for developing coherent energy policies, strengthening supply security strategies, and guiding long-term planning in a more holistic framework.

3.2. Discussion

The findings clearly indicate that the renewable energy transition is, at its core, also a materials transition. Rare earth elements define the upper limits of efficiency, durability, magnetic performance, and compact system design across modern energy technologies. Although substitution efforts continue in various applications, most available alternatives lead to significant decreases in system performance, reduced energy efficiency, or unfavorable economic feasibility. This situation highlights a growing risk of technological lock-in and increases the vulnerability of global supply chains.

The limited availability of heavy rare earth elements (HREEs) has emerged as a critical factor that may constrain the scalability of wind power technologies and electric mobility systems. Furthermore, while renewable energy technologies are low-carbon during operation, the extraction, separation, and refining of rare earth elements impose a substantial upstream environmental burden. Mining and processing stages generate significant waste, require intensive chemical use, and consume considerable energy, thereby raising important environmental sustainability concerns.

For these reasons, the literature strongly emphasizes the necessity of integrating recycling, secondary resource utilization, and circular economy strategies into rare earth supply chains. However, the current technological maturity and economic feasibility of recycling methods remain insufficient to replace primary mining at a meaningful scale. This underscores the need for innovative, high-efficiency, and scalable recycling solutions to ensure long-term supply security and reduce environmental impact.

4. Türkiye’s Position and Strategic Approach

Türkiye’s significance in the context of rare earth elements (REEs) stems not only from the potential size of its reserves but also from its strategic role in enhancing global supply security and diversifying the geographical structure of the energy transition. Currently, the global REE supply chain is heavily concentrated in China across mining, processing, and separation stages, making renewable energy technologies increasingly vulnerable to geopolitical disruptions. In this framework, Türkiye’s high-potential deposits—particularly the Eskişehir–Beylikova district—represent an important alternative for supply diversification, especially for the European Union. Türkiye therefore holds the potential to emerge as a strategic actor not only for its national energy goals but also within the broader context of regional and global energy security [2, 17, 18].

A key factor strengthening Türkiye’s strategic position is its ability to conceptualize REEs not merely as raw materials but as inputs for high-value industrial production, including renewable energy technologies, defense systems, and advanced material manufacturing. Considering Türkiye’s expanding domestic markets in wind power, electric mobility, and energy efficiency, the integration of REEs into local magnet production, electric motor manufacturing, and high-performance materials offers a substantial opportunity to reduce import dependence and build a value-added industrial ecosystem. With appropriate technology, industrial, and R&D policies, Türkiye has the potential to transform REEs from a passive natural resource into an active competitive advantage.

The technical role of REEs in energy technologies cannot be dissociated from the global supply structure and geopolitical context. Evaluating Türkiye’s national potential together with global supply dynamics reveals that REEs occupy a critical position not only in economic planning but also in policy-making and national security strategies.

At the core of Türkiye's REE strategy lies the defense industry, where REEs are indispensable in a wide range of high-technology systems, including laser platforms, target designation units, precision-guided munitions, military communication infrastructure, electronic warfare equipment, radar systems, avionics, and night-vision technologies. In particular, Samarium–Cobalt (Sm-Co) and Neodymium–Iron–Boron (NdFeB) magnets play essential roles due to their high-temperature stability and magnetic durability. For instance, Sm-based components used in advanced radar systems such as the Aegis Spy-1 are capable of maintaining performance for decades, illustrating their strategic importance. Similarly, REE-based materials used in TWTA focusing magnets and high-torque electric motors are indispensable for the sustainability and performance of modern defense technologies [10].

In alignment with Türkiye's long-term goals, establishing a fully integrated national supply chain—ranging from extraction to value-added end products—is of critical importance. China's dominance in global REE markets and its periodic export restrictions [12] further highlight the necessity of a self-sufficient production ecosystem. Beyond defense, REE usage is expanding rapidly across civilian sectors including electric and hybrid vehicles, satellite communication systems, clean energy technologies, and advanced medical devices. Türkiye's strategic orientation centers on converting REEs into high-value technological products, even when used in small quantities, thereby contributing to national economic development and technological sovereignty. In this regard, the development of domestically produced electric motors, wind turbine generators, and advanced industrial components represents a crucial milestone for both economic progress and the enhancement of national strategic capacity [10].

5. Conclusion

Rare earth elements (REEs) constitute essential components of low-carbon technologies such as wind turbines and electric vehicles, and the demand for magnet-critical elements—particularly neodymium (Nd) and dysprosium (Dy)—is expected to increase exponentially in the coming decades [1, 10, 12]. Analyses of global reserves and processing capacities indicate that China maintains a dominant position in both primary production and separation/refining technologies, which poses substantial supply risks for other countries and introduces a significant geopolitical vulnerability to the renewable energy sector [2, 17].

Evaluations of ore preparation and beneficiation processes demonstrate that froth flotation is the most widely used technique for processing primary REE minerals such as bastnäsite and monazite. However, flotation performance is highly dependent on mineral surface chemistry and the selectivity of reagents—particularly hydroxamic acid collectors [4]. Additionally, lesser-studied fluorocarbonate minerals such as parisite exhibit zeta potential characteristics similar to bastnäsite, suggesting that deposits with complex mineralogy may be processed using analogous flotation schemes [16].

Within hydrometallurgical processing, the adoption of membrane technologies—including supported liquid membranes and polymer inclusion membranes—has gained increasing attention due to their low energy requirements, high selectivity, and potential for process intensification [11]. Nonetheless, the management of radioactive by-products such as thorium and uranium, generated during the processing of primary REE ores, remains one of the most significant challenges for environmental sustainability and regulatory compliance [2].

Ensuring supply security necessitates the strategic utilization of secondary sources. Recovery of REEs through bioleaching of coal fly ash [8], hydrometallurgical extraction from phosphogypsum wastes [14], and recycling of end-of-life permanent magnets [9] represent key "urban mining" opportunities with both economic and environmental benefits. For developing countries such as Türkiye, exploiting domestic secondary resources is crucial for reducing dependence on external suppliers, particularly in defense technologies and high-value industrial applications [10].

Future research should prioritize the development of environmentally benign reagents for processing low-grade and complex ores, the industrial-scale advancement of membrane technologies, and the enhancement of recovery efficiencies from secondary sources.

References

[1] Drobniak A, Mastalerz M. Rare Earth Elements: A brief overview. Indiana J Earth Sci [Internet]. 07 Ocak 2022 [a.yer 17 Aralık 2025];4. Erişim adresi: https://scholarworks.iu.edu/journals/index.php/IJES/article/view/33628

[2] McNulty T, Hazen N, Park S. Processing the ores of rare-earth elements. MRS Bull. Mart 2022;47(3):258-66.

[3] Duchna M, Cieślik I. Rare Earth Elements in New Advanced Engineering Applications. Içinde: T. Aide M, editör. Rare Earth Elements - Emerging Advances, Technology Utilization, and Resource Procurement [Internet]. IntechOpen; 2023 [a.yer 17 Aralık 2025]. Erişim adresi: https://www.intechopen.com/chapters/85395

[4] Marion C, Li R, Waters KE. A review of reagents applied to rare-earth mineral flotation. Adv Colloid Interface Sci. Mayıs 2020;279:102142.

[5] Gulluce H. Using of Nanotechnology for Photovoltaic Solar Energy Systems. NanoEra. Aralık 2021; Volume 1(Issue 2):39-44.

[6] Ku AY, Dosch C, Grossman TR, Herzog JL, Maricocchi AF, Polli D, vd. Addressing Rare-Earth Element Criticality: An Example from the Aviation Industry. JOM. Kasım 2014;66(11):2355-9.

[7] Anastopoulos I, Bhatnagar A, Lima EC. Adsorption of rare earth metals: A review of recent literature. J Mol Liq. Eylül 2016;221:954-62.

[8] Muravyov MI, Bulaev AG, Melamud VS, Kondrat'eva TF. Leaching of rare earth elements from coal ashes using acidophilic

chemolithotrophic microbial communities. Microbiology. Mart 2015;84(2):194-201.
[9] Gerasimova LG, Nikolaev AI, Maslova MV, Okhrimenko RF. Utilization of waste containing rare-earth elements. Theor Found Chem Eng. Ekim 2010;44(5):818-21.
[10] Aslan N, Say Y. NADİR TOPRAK ELEMENTLERİNİN UYGULAMA ALANLARI. Kırklareli Üniversitesi Mühendis Ve Fen Bilim Derg. 30 Haziran 2022;8(1):148-78.
[11] Bashiri A, Nikzad A, Maleki R, Asadnia M, Razmjou A. Rare Earth Elements Recovery Using Selective Membranes via Extraction and Rejection. Membranes. 11 Ocak 2022;12(1):80.
[12] Dent PC. Rare earth elements and permanent magnets (invited). J Appl Phys. 01 Nisan 2012;111(7):07A721.
[13] Walters A, Lusty P. Rare earth elements. 2011;
[14] Kiegiel K, Miśkiewicz A, Herdzik-Koniecko I, Gajda D, Zakrzewska-Kołtuniewicz G. Perspective of Obtaining Rare Earth Elements in Poland. Içinde: S. Awwad N, T. Mubarak A, editörler. Lanthanides [Internet]. IntechOpen; 2019 [a.yer 17 Aralık 2025]. Erişim adresi: https://www.intechopen.com/books/lanthanides/perspective-of-obtaining-rare-earth-elements-in-poland
[15] Ascenzi P, Bettinelli M, Boffi A, Botta M, De Simone G, Luchinat C, vd. Rare earth elements (REE) in biology and medicine. Rendiconti Lincei Sci Fis E Nat. Eylül 2020;31(3):821-33.
[16] Owens CL, Nash GR, Hadler K, Fitzpatrick RS, Anderson CG, Wall F. Zeta potentials of the rare earth element fluorcarbonate minerals focusing on bastnäsite and parisite. Adv Colloid Interface Sci. Haziran 2018;256:152-62.
[17] He Y. Reregulation of China's rare earth production and export. Alon, Julian Chang, Christoph Latte I, editör. Int J Emerg Mark. 14 Nisan 2014;9(2):236-56.
[18] Rare Earth Elements - Republic of Turkey Ministry of Energy and Natural Resources [Internet]. [Accessed December 28, 2025]. Available at: https://enerji.gov.tr/bilgimerkezi-tabiikaynaklar-nadirtoprakelementleri

Eco-Friendly Synthesis of Carbon Quantum Dots (CQDs) and Their Use in the Detection of Mycotoxins

Hatice Yüncü[1*], Hayrunnisa Nadaroğlu[1,2]

1 Department of Nano-Science and Nano-Engineering, Institute of Science, Ataturk University, 25240 Erzurum, Türkiye
dincarslanhatice@gmail.com
2 Department of Food Technology, Vocational College of Technical Sciences, Ataturk University, 25240 Erzurum, Türkiye

* *Corresponding author E-mail: hnisa25@atauni.edu.tr*

Keywords

Plant waste (BA),

Carbon quantum dots (CQDs),

Mycotoxin, Aflatoxin (AF),

Fluorescent probe.

Abstract

Food contaminants are substances that are not naturally present in food products and can enter food through various means. Mycotoxins, one of these, are chemical compounds produced by fungi such as Fusarium, Penicillium, and Aspergillus, and can have carcinogenic effects on humans. Aflatoxin (AF) contamination, in particular, significantly impacts the economic value of crops. The presence of food contaminants is one of the most critical threats to food safety and human health. In this context, biosensors and environmental monitoring technologies, especially the synthesis and use of carbon quantum dots (CQDs), have increased interest in nanotechnology. Thanks to their small size (less than 10 nm) and large surface area, CQDs can be used for precise measurement of chemical and biological processes in food; they exhibit new optical and electrical properties with enhanced reactivity. Due to their exceptional physical and chemical properties, CQDs have emerged as promising materials in rapidly developing food safety research worldwide in recent years. CQDs with different surface functional groups can detect contaminants such as additives in processed foods, drug residues in honey, and mycotoxins in beer and flour using IFE, PET, and FRET-based detection mechanisms. In this study, stable, water-soluble, and biocompatible green fluorescent CQDs were synthesized from plant waste using a novel approach via pyrolysis synthesis. The fluorescence quantum yield of the CQDs was measured as 0. Furthermore, CQDs are highly effective in detecting aflatoxin using a fluorescence resonance energy transfer (FRET) mechanism, with a clear fluorescence emission peak observed at 448.02 nm. The photoluminescence properties of CQDs were evaluated under different pH conditions and temperatures, showing the highest fluorescence intensity at pH 7; this suggests their potential use in pH-sensitive sensor applications. This environmentally friendly and cost-effective synthesis method offers a promising alternative for AFB1 detection in food samples by using waste material to create valuable analytical tools. The results of this study demonstrate the usability of CQDs synthesized from plant waste as fluorescent probes for aflatoxin detection. By leveraging the unique properties of CQDs, a sensitive, fast, and economical detection platform has been developed that can be integrated into food safety monitoring systems. Thus, this not only contributes to the synthesis of carbon dots from sustainable sources but also addresses a significant need in the fields of food safety and environmental monitoring.

1. Introduction

Carbon quantum dots (CQDs) constitute the newest class of fluorescent nanoparticles with sizes ranging from 1-10 nm and are considered a new member of the quantum dot family [1]. They are nanoparticles whose fluorescence emission properties vary with their size and dimensions, and they are carbon materials with many functional groups on their surface [2, 3].

These semiconductor nanocrystals are superior to other fluorescent molecules in terms of their ability to modify fluorescence emission properties, provide better luminescence brightness, have excellent biocompatibility, and are resistant to photodegradation. The superior properties of quantum dots stem from quantum size limitation [4, 5].

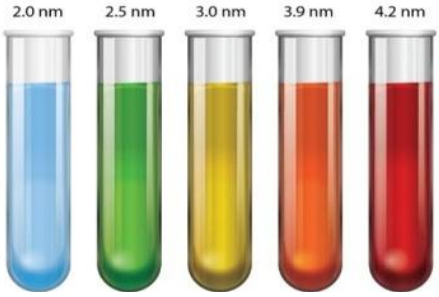

Figure 1 Illustration of the radiation properties of CQDs of different sizes.

The wavelength of the electromagnetic radiation emitted by carbon quantum dots is redshifted as they grow (Figure 1). This allows for the preparation of quantum dots that absorb and emit light at the desired wavelength, as needed [5, 6].

Carbon quantum dots, with their ultra-fine dimensions, have been considered promising materials for the detection of foodborne pathogens [7]. This is because CQDs are equipped with good chemical stability, low toxicity, excellent electron transfer efficiency, and photo-induced redox properties, along with strong fluorescence intensity [8].

Some Application Areas of Quantum Dots; Quantum dots find applications in optoelectronics, solar cells, medicine, biology, and industry [6, 9]. It is known that quantum dots can be widely used in biotechnological applications, bioimaging for cells, nanomedicine applications, drug and gene targeting, and nano-biosensor applications.

Biosensors: Biosensors essentially consist of two main components: bioreceptors and transducers. The bioreceptor recognizes the analyte, while the transducer transmits the signal into an electrical field. These devices are systems that can detect other biological molecules, directly or indirectly, using biological recognition compounds (Figure 2).

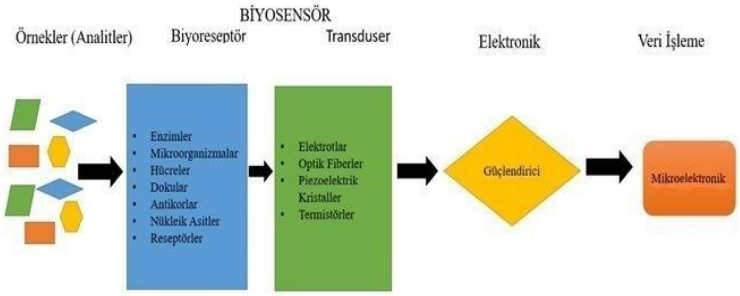

Figure 2 Schematic representation of the biosensor [10]

The use of carbon-based quantum dots in sensor applications has become quite widespread. In these applications, quantum dots prepared against the target molecule or ion are used. The reaction of these prepared quantum dots to the target molecule is interpreted by the device and converted into meaningful data. In this way, it is possible to perform quantitative or qualitative analysis of the molecule or ion.

Aflatoxins: Food products undergo some changes when conditions are suitable, by microorganisms that are both found in their natural flora and that can be contaminated later due to inadequate hygienic conditions. Molds constitute a large part of these changes. These molds have the ability to produce chemical substances that have toxic effects on humans and animals. These substances are mycotoxins. They are the main food contaminants that change the appearance, smell, taste and other properties of foods.

Mycotoxins can be named with their chemical names, as well as (deoxynivalenol), whose name can also be derived from the mold that produces it (Aflatoxin) [8, 11]. Aflatoxins (AFs) are one of the main causes of food contamination and have a high carcinogenic effect. AFs are low molecular weight secondary metabolites that can be widely produced by Aspergillus in a wide variety of agricultural food products such as milk, corn, peanuts, fruits, cereals, etc. They consist mainly of six types: Aflatoxin B1, B2, G1, G2, M1, and M2 [12]. Aflatoxin B1 (AFB1) is a dominant mycotoxin produced by several Aspergillus species. For this reason, our study will focus on the investigation of AFB1 detection, different types of nanomaterials such as AuNPs, CQDs, and GOs can be used as fluorescent quenchers. AFB1 has the ability to directly quench or reduce fluorescence intensity. The investigation of AFs in different food samples is carried out using fluorescence spectrophotometry techniques.

2. Results

CQDs were obtained using the pyrolysis method. The basis of the synthesis is the reduction of the plant sample at 200ºC in the presence of ammonium citrate. The advantages of pyrolysis synthesis are; it is a rapid synthesis method for COD formation, the yield is high, inexpensive reactants are used, the cost is low, and the reactants are easily accessible. In this study, CQDs were synthesized by pyrolysis synthesis, a rapid and environmentally friendly method, and these points were used in nanobiosensor applications for the detection of mycotoxins. The high solubility, stability, and high biocompatibility of CQDs in water made them suitable candidates for food safety applications. In particular, CQDs obtained from agricultural wastes provide great advantages in terms of both sustainability and low cost. The quantum yield of CQDs (0.05) is in a suitable range compared to other CQDs reported in the literature. However, the stability of CQDs and their suitability for biosensor applications make them highly effective in practical applications. Previous studies have highlighted that nitrogen doping improves the optical properties and sensitivity of CQDs in AFB1 detection [13, 14]. Sustainable and environmentally friendly approaches to nanomaterial synthesis are attracting increasing attention due to their environmental and economic advantages. Thanks to the use of waste products, the cost is almost negligible, and the contribution to the economy cannot be ignored. In addition, the abundance of CQDs allows them to be considered as a sustainable resource and contributes to the reduction of environmental pollution. The synthesized CQDs showed strong photoluminescence properties, high stability, and water solubility. These properties make CQDs extremely suitable for biosensor applications. The quantum efficiency (%QY) was calculated as 0.05, and this value reveals the optical efficiency of the obtained nanomaterials. pH and temperature-dependent studies revealed the sensitivity that can be used for the detection of the mycotoxin aflatoxin in food samples. The nitrogen and oxygen-containing functional groups on the surface of BA-CQDs played a significant role in enhancing their interaction with AFB1, providing a sensitive and selective detection platform. These findings demonstrate that CQDs derived from agricultural wastes can be used in the development of cost-effective and efficient biosensors for food safety monitoring.

3. Conclusion

In this study, carbon quantum dots (CQDs) were successfully synthesized from plant waste using a pyrolysis method, a sustainable and low-cost approach. The chemical and photoluminescence properties of the synthesized CQDs clearly demonstrate their potential for use in food safety applications. The quantum yield (%QY ≈ 0.05) of the synthesized CQDs was found to be consistent with similar studies reported in the literature and offered sufficient optical performance for practical sensor applications. In conclusion, it has been proven that CQDs obtained from agricultural/plant wastes offer a significant alternative in terms of sustainable nanomaterial synthesis and can be used as effective fluorescent probes in food safety monitoring systems. This study contributes to the transformation of wastes into high value-added nanomaterials and offers a sustainable, fast, and low-cost solution for detecting contaminants such as aflatoxins, which pose serious risks in food. The findings indicate that CQDs-based biosensors can be widely used in food safety and environmental monitoring in the future.

Acknowledgements

The study received funding from the Ataturk University, Scientific Research Projects Commission with grant number FDK-2022-10569. The authors want to thank Ataturk University for its assistance, through the Scientific Research Projects initiative.

References

[1] Kamal, A.; Hong, S.; Ju, H. Carbon Quantum Dots: Synthesis, Characteristics, and Quenching as Biocompatible Fluorescent Probes. Biosensors 2025, 15, 99, doi:10.3390/bios15020099.

[2] Wang, Y.; Hu, A. Carbon quantum dots: synthesis, properties and applications. Journal of Materials Chemistry C 2014, 2, 6921, doi:10.1039/C4TC00988F.

[3] Huang, H.-Y.; Wang, M.-C.; Chen, Z.-Y.; Chiu, W.-Y.; Chen, K.-H.; Lin, I.-C.; Yang, W.-C.V.; Wu, C.-C.; Tseng, C.-L. Gelatin–epigallocatechin gallate nanoparticles with hyaluronic acid decoration as eye drops can treat rabbit dry-eye syndrome effectively via inflammatory relief. International Journal of Nanomedicine 2018, Volume 13, 7251–7273, doi:10.2147/IJN.S173198.

[4] Ozyurt, D.; Kobaisi, M. Al; Hocking, R.K.; Fox, B. Properties, synthesis, and applications of carbon dots: A review. Carbon Trends 2023, 12, 100276, doi:10.1016/j.cartre.2023.100276.

[5] Varmazyarı, A. Kadmiyum Sülfür (CQDS) Kuantum Noktaların Biyosentezi, Yapısal Karakterizasyonu ve Toksisitesinin Araştırılması, Atatürk Üniversitesi, Fen Bilimleri Enstitüsü Tezi. 2018, 129.

[6] Liu, L.; Peng, Q.; Li, Y. Preparation of CdSe Quantum Dots with Full Color Emission Based on a Room Temperature Injection Technique. Inorganic Chemistry 2008, 47, 5022–5028, doi:10.1021/ic800368u.

[7] Zhou, Y.; Xiong, S.; Zhang, K.; Feng, L.; Chen, X.; Wu, Y.; Huang, X.; Xiong, Y. Quantum bead-based fluorescence-linked immunosorbent assay for ultrasensitive detection of aflatoxin M1 in pasteurized milk, yogurt, and milk powder. Journal of Dairy Science 2019, 102, 3985–3993, doi:10.3168/jds.2018-16109.

[8] Yuncu, H.; Nadaroglu, H.; Bozkurt, E. Eco-friendly synthesis of Carbon Quantum Dots (CQDs) from hazelnut husk for sensitive Aflatoxin B1 (AFB1) detection. Toxicology Reports 2024, 13, 101824, doi:10.1016/j.toxrep.2024.101824.
[9] Wang, X.; Wu, X.; Lu, Z.; Tao, X. Comparative Study of Time-Resolved Fluorescent Nanobeads, Quantum Dot Nanobeads and Quantum Dots as Labels in Fluorescence Immunochromatography for Detection of Aflatoxin B1 in Grains. Biomolecules 2020, 10, 575, doi:10.3390/biom10040575.
[10] Velasco-Garcia, M.N.; Mottram, T. Biosensor Technology addressing Agricultural Problems. Biosystems Engineering 2003, 84, 1–12, doi:10.1016/S1537-5110(02)00236-2.
[11] Yuncu, H., Bozkurt, E., Nadaroglu, H. Investigation of the use of carbon dots from Euphorbia amygdaloides for the detection of aflatoxin B1. Arabian Journal of Chemistry 2025, In press.
[12] Gong, Y.Y.; Watson, S.; Routledge, M.N. Aflatoxin Exposure and Associated Human Health Effects, a Review of Epidemiological Studies. Food Safety 2016, 4, 14–27, doi:10.14252/foodsafetyfscj.2015026.
[13] Serebrennikova, K. V.; Samokhvalov, A. V.; Zherdev, A. V.; Dzantiev, B.B. A Fluorescence Resonance Energy Transfer Aptasensor for Aflatoxin B1 Based on Ligand-Induced ssDNA Displacement. Molecules 2023, 28, 7889, doi:10.3390/molecules28237889.
[14] Hamad, G.M.; Mehany, T.; Simal-Gandara, J.; Abou-Alella, S.; Esua, O.J.; Abdel-Wahhab, M.A.; Hafez, E.E. A review of recent innovative strategies for controlling mycotoxins in foods. Food Control 2023, 144, 109350, doi:10.1016/j.foodcont.2022.109350.

Nature-Based Healing Approach: Horticultural Therapy Gardens

Aslıhan Esringü[1*], Feyza Gündoğdu[2]

[1] Atatürk University, Faculty of Architecture and Design, Department of Landscape Architecture, Erzurum, Türkiye
[2] Independent Researcher, Erzurum, Türkiye

* *Corresponding author E-mail: esringua@atauni.edu.tr*

Keywords

Healthy city
Horticultural therapy garden
Disabled individuals
Nature-based healing
Landscape planning

Abstract

Today, the intense urban life and social isolation brought about by digitalization are causing a rapid increase in physical and mental illnesses. Furthermore, the fact that the proportion of disabled individuals in the world population is approximately 16%, and in Turkey it is 10-13%, indicates that the number of disabled individuals in society is quite high. Innovative, inclusive, and accessible landscape designs are needed to support the physical, cognitive, emotional, and social skills of these individuals. In this context, horticultural therapy gardens (HTGs), as a nature-based healing approach, have an important role to play. Horticultural therapy gardens (HTGs) are applications that utilize the healing power of interaction with nature through a systematic approach, reducing stress levels and increasing psychological resilience, thereby encouraging social participation, through processes such as plant cultivation, contact with soil, interaction with sensory stimuli, and participation in garden activities. It is observed that HTGs are not widely used in many institutions and spatial planning processes today. However, HTGs can be applied in many different areas, from rehabilitation centers and educational institutions to hospitals and elderly care homes. This study aims to reveal the therapeutic effects of horticultural therapy gardens, a nature-based healing approach, on different user groups (individuals with disabilities, the elderly, chronic patients, individuals receiving psychological support, stress-related risk groups, etc.) and to examine the design principles of these gardens on a scientific basis. The findings show that horticultural therapy gardens reduce users' stress levels, increase emotional well-being, and provide significant improvements in motor skills, attention, and social interaction, especially in individuals with disabilities. These results demonstrate that horticultural therapy gardens are not only an aesthetic landscape element but also a nature-based solution that supports physical, mental, and social health in cities. By widespread adoption of this approach, public health can be strengthened, quality of life can be improved, and sustainable and inclusive healing spaces can be created.

1. Introduction

In recent years, with migration from rural areas to cities and the resulting increase in urban population, the amount of green space in cities has decreased, and the people living there have begun to continue their lives in stressful living conditions amidst concrete jungles. However, this situation has also led to an increase in the prevalence of mental disorders among urban people. Spending less time in nature is shown as a reason for the emergence of mental disorders. Throughout history, people have used plants and natural elements to overcome problems such as psychological problems, illnesses, or disabilities resulting from accidents that negatively affect their quality of life. In England, in the 1960s, special "therapeutic garden designs" accessible to disabled individuals were developed and used for educational and therapeutic purposes. These gardens also functioned as social interaction areas for patients [1]. Horticultural therapy gardens are special landscape areas planned to support the physical, psychological, cognitive, and social well-being of individuals through interaction with plants and integrated into the therapy process [2]. Horticultural gardens are urban areas created for therapeutic purposes in various healthcare facilities such as hospitals, nursing homes, retirement homes, and even prisons. These gardens are designed to maximize the positive effects of interaction with nature, especially on individuals experiencing mental and psychological problems [3]. Horticultural therapy gardens support disadvantaged groups in society, including the elderly, people with disabilities, those with mental and psychological health problems, individuals with developmental disabilities, and those struggling with substance abuse [4]. A study indicated that plant landscape applications and horticultural therapy garden applications offer a therapeutic experience by contributing to the health and well-being of stressed and pressured individuals [5]. Horticultural therapy gardens are designed to be safe and accessible and support individuals' sensory

functions by providing sensory stimulation. The design and operation of horticultural therapy gardens require a multidisciplinary approach. Collaboration between landscape architects, therapists, rehabilitation specialists, and other relevant professionals ensures that these special gardens provide maximum benefit and serve the needs of individuals. Horticultural therapy gardens are considered a comprehensive healing and development tool for individuals with moderate special needs, enabling them to participate more actively and independently in society [4]. This study aims to examine the therapeutic effects of horticultural therapy gardens, a nature-based healing approach, on different user groups (individuals with disabilities, the elderly, chronic patients, individuals receiving psychological support, stress-related risk groups, etc.) and to examine the design principles of these gardens on a scientific basis.

2. Materials and Methods

2.1. Material

The material of this study consists of studies related to horticultural therapy gardens.

2.2. Method

A bibliometric analysis was carried out in this study [6]. The research method consists of three stages. These stages are as follows;

First stage; At this stage, publications related to the topic were identified from national and international journals, conference proceedings, theses, and book chapters using keywords such as "Horticultural therapy garden," "effects of horticultural therapy gardens on patients," "principles of horticultural garden landscape design," and "areas of use of horticultural therapy gardens" in national and international databases such as Google Scholar, Scopus, Web of Science, and DergiPark.

Second stage; In this stage, the studies obtained from the first stage were subjected to title and abstract review, and publications that were outside the scope of the topic, duplicate publications, studies whose full text could not be accessed, and studies that were not directly related to horticultural therapy gardens were eliminated.

Third stage; In this final stage, scientific studies that were found suitable as a result of all elimination and suitability evaluations were taken into consideration and articles were written.

3. Results

3.1. The Concept of Horticultural Therapy

The concept of horticulture is derived from the combination of the Latin words "hortus," meaning "garden," and "culture," and includes meanings such as gardening, horticulture, or garden culture. Defined as the art and science of growing plants, horticulture has been considered separately from agricultural activities, especially in Europe since the Middle Ages [7] (Von Baeyer 2014). While therapy is defined as "treatment" in the Turkish Language Association, there are various different definitions of this concept (URL-3 2018). In one study, horticultural therapy was expressed as a controlled and directed therapeutic intervention designed to support a person's mental, physical, and emotional health [8]. "Horticultural Therapy Gardens (HTB)" are gardens designed to suit the patients' treatment goals and using plant materials in the gardens to positively influence the treatment process [9].

3.2. Historical Development of Horticultural Therapy

Health gardens are a concept that reflects the awareness of benefiting from the healing powers of nature throughout human history and is gaining popularity again today. Since prehistoric times, people have used natural environments, and especially gardens, in health and healing processes. Since ancient times, gardens and the plants grown in them have been used in ancient Asian, Greek and Roman cultures to treat both physical and mental ailments of people. In the Middle Ages, monastery gardens served both to preserve the medicinal values of plants and as a therapeutic space for individuals with mental disorders. These gardens, dating back to 2000 BC, were used for health purposes, and in 500 BC, the Persians designed gardens to please all the senses by bringing together elements such as visuals, scent, music and water [10] (AHTA 2012). Similarly, in the Seljuk, Ottoman and generally Islamic civilizations, the positive effects of gardens and nature on human health were well known and therefore integrated into health practices in various ways. During these periods, gardens were important not only for their aesthetic and cultural values but also for their healing properties [11]. Following World War II, HT programs were developed in hospitals in the United States to support the rehabilitation process of returning soldiers. It has been observed that these programs have positive effects on the recovery processes of various mental and psychological illnesses, including schizophrenia. Following World War II, HT programs were developed in hospitals in the United States to support the rehabilitation process of returning soldiers. It has been observed that these programs have positive effects on the recovery processes of various mental and psychological illnesses, including schizophrenia [12] In 1973, the “Horticultural Therapy and

Rehabilitation Council" was established by a group of HT specialists, and this organization was renamed "American Horticultural Therapy Association (AHTA)" in 1988 [13].

3.3. Benefits of Horticultural Therapy Gardens

Horticultural therapy (HT) has been adopted as therapy in many cultures for centuries due to its healing effects on people's health and well-being. This type of therapy is based on interaction with natural materials, and this interaction is known to have positive effects, especially on mental health. The effects of HT on human health are grouped under 3 headings:

- **Physical benefits**

Individuals participating in HT have been observed to have improved hand-eye coordination, strengthened muscles and joints, and stimulated sensory organs [14]. One study indicated that visiting a botanical garden can lower blood pressure and reduce heart rate in people [15].

- **Psychological benefits**

Working with plants in this therapy helps individuals increase their self-esteem, awareness, and sense of responsibility [16].

- **Social benefits**

Therapy gardens offer opportunities for socialization by bringing together people with shared interests. Individuals experience a sense of relaxation by spending their free time in such environments and gain more decision-making skills [17].

3.4. General Design Principles for Horticultural Therapy Gardens

HTB design varies depending on the usability of the garden. The garden's design should incorporate design elements that will encourage patients to participate willingly in programs by increasing the use of resources. For example, the garden's accessibility, visibility, adequate seating and shaded areas, separate areas for staff and patients, accessible pathways, and the inclusion of elements that increase visual interest using flora and fauna are necessary. The basic principles that designers obtain from various sources in garden design and creation can be briefly summarized as follows:

Site Selection: When selecting a location for Horticultural Therapy Gardens, proximity to living areas is an important factor to ensure easy access for users to the garden. Also, the garden's location should be on a relatively flat terrain for ease of movement [4].

Users: The design of therapy gardens should include creating comfortable, safe, and high-quality spaces that respond to the needs of users. When designing therapy gardens, the needs of other users who will benefit from the garden (responsible staff, patient relatives, etc.) as well as the age and disease group that the garden addresses should be taken into consideration [19] [20].

Accessibility: The garden should be safe and comfortable for all users, regardless of age and ability.

Orientation: The garden should be easily understandable by every individual who will enter it. A simple and clear path should be designed, and garden entrances and exits should be supported by directional signs. Unfamiliar or unclear environments can be challenging, especially for individuals with mental illness [21].

Material selection: When selecting materials, a balanced harmony between aesthetics and functionality should be achieved, taking into account the needs and safety of the users. The selected materials should not contain overly monotonous or overly complex designs. [22]

Plant selection: Plants are indispensable parts of therapy gardens. Vegetation can positively affect human psychology. Plants should stimulate all five senses by offering sensory richness, with features such as color, texture, scent, and even the sounds of leaves moving in the wind [23].

Socialization: Areas should be created in gardens where users can spend time individually. In addition to these areas, open and closed seating areas should be designed for group use. Designing private areas for staff who spend most of their time with patients is very important. These private areas should be created in such a way that staff can easily access patients and visitors in any situation requiring intervention.

Security: This is a priority for all users of the garden. Institutions serving different treatment groups should take security measures that vary according to their needs [24].

Sustainability: Sustainable planning should be done in a way that ensures the enjoyable and safe use of structural and plant design elements.

Layout: The garden design should be simple and understandable. Paths and entrances should be planned in a way that is easily perceived [23].

Boundaries: It is essential to protect patients receiving treatment within garden boundaries from external threats and to prevent them from going outside uncontrollably and harming themselves or the environment. Natural boundaries should be created using plant materials in a way that provides a safe environment without creating a feeling of being closed off [24].

Visibility: When designing the garden, the overall visibility of the garden should be such that caregivers can clearly see every point in the garden. There should be no blind spots in the garden where patients can hide from their caregivers. However, a balance between privacy and security should be achieved during the design, and private areas should be created where patients do not feel constantly watched [24].

4. Conclusion

Horticultural gardens, as is known, are plant-based environments specifically designed to facilitate interaction with the healing elements of nature. Garden therapy practices help improve memory, cognitive abilities, language skills, and socialization. Furthermore, in physical rehabilitation, garden therapy helps strengthen muscles and improve coordination, balance, and endurance. In conclusion, the positive effects of gardening activities on humans have been scientifically proven. Therefore, horticultural therapy gardens should be considered an integral component of health and rehabilitation structures; pilot applications should be initiated in hospitals, elderly care centers, and living spaces for people with disabilities. A legal and institutional framework encompassing the fields of health, landscape architecture, and social services should be established to ensure that horticultural therapy is officially recognized as a complementary therapy method. Collaboration models should be developed between municipalities, universities, and health organizations to encourage the scientific monitoring and evaluation of these practices. Accessibility, sensory diversity, and user-centricity should be adopted as fundamental design criteria in therapeutic garden designs. Plant species and design approaches suitable for Turkish conditions should be used. Studies in this field in Turkey are still in their early stages, and there is a frequent need for examples of good practices. If legal decisions are made in state policies regarding horticultural therapy gardens and their applications, they will spread more rapidly, increasing their recognition and use. In conclusion, therapy gardens should be designed according to the different cognitive states of the users and should be accessible to everyone.

References

[1] Pfeffer, J. C., (2007). Horticultural therapy in tennessee. master's thesis, University of Tennessee.
[2] American horticultural therapy association. (2023). *What is horticultural therapy?*
[3] Severtsen, B. (2011). Healing Gardens. https://tr.scribd.com/document/64378688/HealingGardens-by-Betsy-Severtsen .
[4] Cooper-Marcus, C., Sachs, N. A. (2014.) Therapeutic landscapes: An evidence-based approach to designing healing gardens and restorative outdoor spaces. John Wiley.
[5] Söderback, I., Söderström, M., Schälander, E. (2004). *Horticultural therapy: The 'healing garden' and gardening in rehabilitation measures at Danderyd Hospital Rehabilitation Clinic, Sweden.* Pediatric Rehabilitation, 7(4), 245–260.
[6] Zupic, I., Cater, T. (2015). .Bibliometric methods in management and organization. organizational research methods, 18(3), 429–472.
[7] Von Baeyer, E., (2014). The Development and history of horticulture. In M. Agnoletti, E. Johann, and S. Serneri (eds.), World Environmental History. EOLSS Publisher.
[8] Duchemin, E. (2009). Horticultural therapy and mental health: A field of human-nature interactions. Journal of Therapeutic Horticulture, 20, 21-30.
[9] Brown, R.G. (2013). Therapeutic horticulture: horticulture as a medical treatment. Winston Churchill Memorial Trust. West Yorkshire, UK.
[10] American Horticultural Therapy Association. (2012). Definitions and positions.
[11] Gürel, E. (2001). Osmanlı bahçelerinde sağlık ve estetik. Türkiye İş Bankası Kültür Yayınları, İstanbul.
[12] Sempik, J. (2010). Green care and mental health: gardening and farming as health and social care. mental health and social inclusion, 14(3), 15-22.
[13] American Horticultural Therapy Association. (2019). History of horticultural therapy.
[14] Uslu, A., and Shakouri, N. (2012). Zihinsel ve fiziksel engelliler için hortikültürel terapi. Kastamonu üniversitesi, Orman Fakültesi Dergisi, 12(1), 134-143.
[15] Elings, M. (2006). People-plant interaction: The physiological, psychological and sociological effects of plants on people.
[16] Kaiser, M. (1976). Alternative to Therapy: Garden program. journal of clinical child psychology, 5(2), 21-24.
[17] GezondheidsraaD, RMNO. (2004). Natuur en gezondheid: invloed van natuur op sociaal, psychisch en lichamelijk welbevinden. Den Haag: Gezondheidsraad en RMNO
[18] Shamanth, M.G. (2014).Therapeutic Garden, Seminar Credit 2014-2016, Dr. Y.S.R. Horticultural University,
[19] Davis, B. E. (2011). Rooftop hospital gardens for physical therapy: A post-occupancy evaluation. HERD: Health Environments Research and Design Journal, 4(3), 14-43.
[20] Stigsdotter, U. A., Grahn, P. (2002). What makes a garden a healing garden? Journal of Therapeutic Horticulture, 13, 60-69.
[21] Carek, P. J., Laibstain, S. E., Carek, S. M. (2011). Exercise for the treatment of depression and anxiety. International Journal of Psychiatry in Medicine, 41(1), 15–28.
[22] Serez, A. (2011). Tarihsel süreç içinde sağlık bahçeleri. Yüksek Lisans Tezi, İstanbul Teknik Üniversitesi, İstanbul.
[23] Mitchell, L., Burton, E. J., Blackman, T. J., Williams, K. (2003). Making the outside world dementia-friendly: Design issues and considerations. Environment and Planning B: Planning and Design, 30, 605-632.
[24] MPK. (2017). Design guidelines for therapeutic gardens in Singapore. National Parks Board. ISBN: 978-981-11-3632-0.

Urban Water Management Approaches for Resilient Cities

Senanur Seher Ağbaba[1,*], Aslıhan Esringü [1,*]

[1] *Atatürk University, Faculty of Architecture and Design, Department of Landscape Architecture, Erzurum, Türkiye*

* *Corresponding author E-mail: s.seheragbaba@gmail.com*

Keywords

Urban water management

Resilient cities

Sustainable water management

Urban resilience

Climate change adaptation

Abstract

The rapid increase in population in urban areas, dense construction, and the increasing flood events due to climate change are significantly altering the quality and quantity of water resources. Due to these reasons, rainwater management has become a necessary and mandatory urban issue to increase resilience to water resources in cities. Solutions are being developed in cities through green infrastructure applications and rainwater management measures to reduce surface runoff, lower flood risk, and manage rainwater on-site. The aim of this study is to examine nature-based solutions used to increase the resilience of cities against extreme rainfall caused by climate change and to reveal the environmental, social, and economic benefits these solutions will provide. In this context, the effects of nature-based solutions such as rainwater harvesting, green infrastructure systems, permeable surfaces, bio-swales, rain gardens, and urban wetlands on the water cycle have been examined using the literature, and successful national and international applications have been compared. When the findings are evaluated, it is seen that nature-based practices reduce flood risk, improve water quality, contribute to climate adaptation, and increase the long-term resilience of cities, thus offering a holistic solution. Therefore, by widespread adoption of urban green infrastructure systems, water will be retained at its source. In conclusion, rapidly implementing green infrastructure systems to increase urban resilience to water management challenges is not a choice but a necessity. For successful implementation, local governments need to develop mandatory strategic plans, allocate resources for infrastructure investments, and address spatial planning, landscape design, and climate adaptation policies with an integrated approach. Urban water management is not just a matter to be addressed from the perspective of landscape architecture; it is a strategic issue that urgently needs to be tackled in collaboration with various professional disciplines.

1. Introduction

Today, cities face multifaceted environmental problems due to rapidly increasing populations, climate change, dwindling water resources, and the pressures created by intense urbanization. The increase in urban populations globally significantly increases the demand for water, placing a serious pressure on water resources in terms of both quantity and quality. In particular, unplanned urbanization, the increase in impermeable surfaces, and the disruption of the natural water cycle make water management in urban areas more complex [1]

In this context, urban water management stands out as a strategic area encompassing numerous components, not limited solely to the supply of drinking and usable water, but also including wastewater management, stormwater control, water quality protection, and ecosystem sustainability. Cities must simultaneously combat long-term structural problems such as drought, water pollution, and the depletion of surface and groundwater resources, while also being prepared for sudden and unpredictable shocks such as floods, infrastructure collapse, and extreme weather events [1]

Climate Change and Its Impacts on Urban Water Systems

Climate change is a key factor that further increases the pressures on urban water management. Rising temperatures, changing rainfall patterns, and the increased frequency of extreme weather events are straining existing water

infrastructures in cities and exacerbating water-related risks. Prolonged droughts threaten water supply security, while short periods of intense rainfall increase the risk of flooding in urban areas [1]

Under these conditions, traditional, centralized, and rigid infrastructure systems alone are proving insufficient. For cities to withstand climate uncertainties, water systems need to be designed to be flexible, adaptable, and responsive to different scenarios. This necessity has led to the concept of urban resilience gaining increasing importance in the water management literature.

1.1. Urbanization

Urbanization, in its broadest sense, is the process of population movement from rural to urban areas, resulting in the physical, economic, social, and cultural growth and development of urban areas [4]

However, urbanization is not only a concentration of population; it also means the spatial centralization of industries, services, and infrastructure activities, and the reshaping of lifestyles around urban values [5]

This process historically emerged as a result of the transition from an agricultural society to an industrial society, and in the modern era, it has gained different dimensions with globalization, technological developments, and economic restructuring [3]

Reasons for Urbanization

The following stand out as the main reasons for urbanization:

Economic Reasons: More job opportunities in cities compared to rural areas, concentration of industry and service sectors in city centers.

Social Reasons: Ease of access to services such as education, health, culture and transportation.

Migration Dynamics: Unemployment in rural areas, agricultural inefficiency, natural disasters or political reasons leading to migration to cities.

Modernization and Globalization: Technological developments and concentration of international capital in large cities.

1.2. The Effects Of Urbanization On Water Resources

It is predicted that two-thirds of the world's population and 95% of our country's population will live in cities in 2050 [11]

Considering the mostly impermeable surfaces, fossil fuel use, deforestation, and ecosystem degradation caused by urbanization; it is inevitable that these factors will pose a great threat to water resources and the water cycle. [Figure 1.]

Groundwater resources are not being adequately replenished, the rate of transpiration and evaporation is decreasing, and the water cycle is not being completed sufficiently [11]

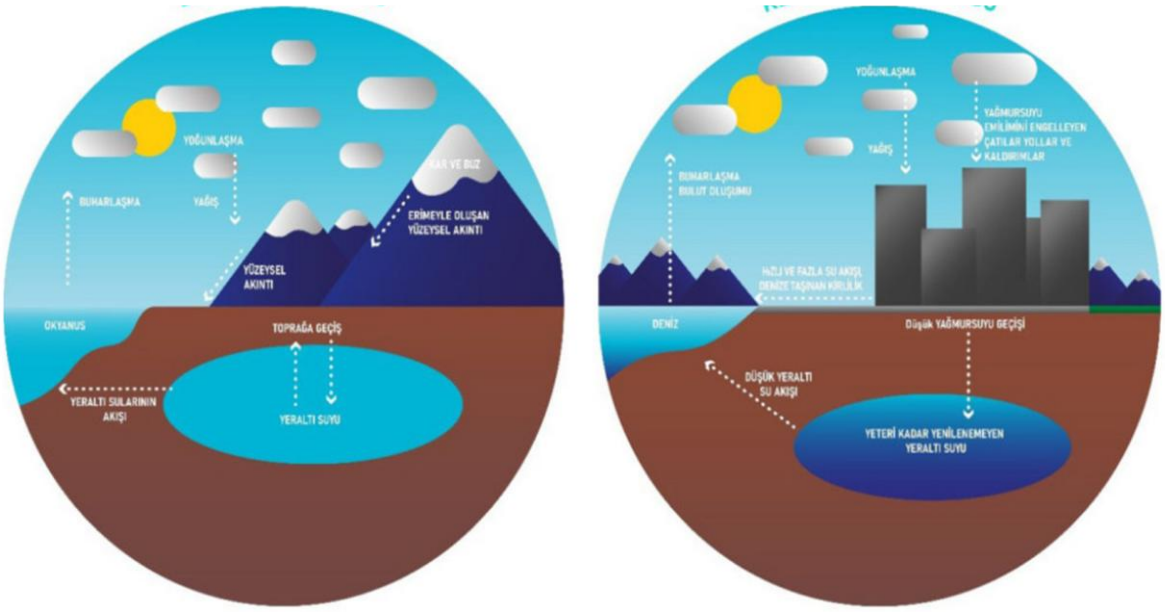

Figure 1 Water cycles

1.3. Urban Water Management

Urban water management is an interdisciplinary field that refers to the holistic management of the planning, supply, distribution, use, wastewater disposal and treatment, and rainwater and flood risk management processes of water resources in a city, according to the principles of sustainability, efficiency and resilience [8] [Figure 2.]

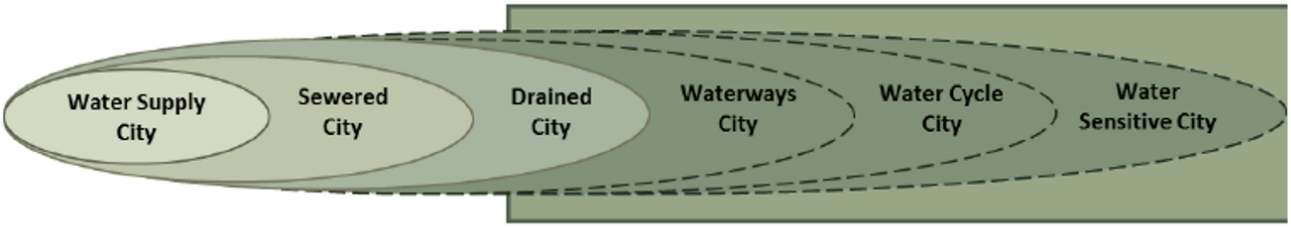

Figure 2 Transitioning towards smart cities with well-managed water management

1.4. The Importance of Urban Water Management

Reduces water scarcity

Prevents infrastructure collapses

Protects public health

Makes cities resilient to flood and drought shocks

Supports ecosystems and biological life

In this context, the city is no longer considered a passive water consumer, but an active system managing the water cycle [10].

1.5. Raingarden Structures Within The Scope Of Urban Water Management

Gardens created in shallow depressions where rainwater is directed directly without any processing and where plants can be grown are called "Rain Gardens". Rain gardens, which are based on the principle of collecting and reusing rainwater, are also called "micro-bioretention areas" [Figure 3].



Figure 3 Rain garden systems

2. Materials and Methods

2.1. Materials

The material for this study consists of research on urban water management approaches for resilient cities.

2.2. Methods

This study involved a bibliometric analysis. The research methodology consisted of three stages:

First stage: In this stage, publications related to the topic were identified from national and international journals, conference proceedings, theses, and book chapters using keywords such as "Urban Resilience," "Urban Water Management," "Urban Water Management Approaches," and "Urban Water Management Approaches in Resilient Cities" in national and international databases such as Google Scholar, Scopus, Web of Science, and DergiPark.

Second stage: In this stage, the studies obtained from the first stage were subjected to title and abstract review. Duplicate publications, studies whose full text was inaccessible, and studies not directly related to urban water management approaches in resilient cities were eliminated.

Third stage: In this final stage, scientific studies deemed suitable after all elimination and suitability assessments were evaluated and the article was written.

3. Conclusion

The findings of this study reveal that urban water management is not only a technical service area for today's cities, but also a strategic policy area directly related to climate change, environmental degradation, and societal vulnerabilities. Increasing population pressure, changing climate conditions, and intense stresses on water resources necessitate a reassessment of current water management approaches in cities. In this context, the concept of urban resilience offers a holistic framework for the planning and implementation of water management.

The literature shows that resilient urban water systems rely not only on infrastructural capacity but also on governance structures, institutional cooperation, community participation, and ecosystem-based approaches. This approach, which emphasizes integrated and nature-based solutions, has the potential to increase cities' capacity to adapt to both sudden shocks and long-term environmental stresses. Accordingly, the conclusion section will evaluate the key implications and policy-related issues for strengthening resilience in urban water management.

In conclusion:

Rapid urbanization increases the risk of flooding, reduces ecosystem services, and disrupts the urban water cycle, increasing vulnerability.

A resilient city approach requires addressing water management holistically with ecological, social, and technical solutions.

Blue-green infrastructure (rain gardens, green roofs, permeable surfaces, wetlands, etc.) ensures water management in situ, reduces floods, and strengthens the urban ecosystem.

However, challenges such as lack of technical knowledge, inter-institutional coordination, and maintenance costs arise during implementation. In general, sustainable, nature-based water management strategies are necessary to achieve a resilient city vision.

Planning and Management

Blue-green infrastructure applications should be integrated into zoning plans.

Urban water management should be coordinated with different disciplines (transportation, landscape, disaster management).

Technical and Design

Rainwater harvesting, permeable surfaces, and green roof applications should be widespread in settlements.

Hybrid systems should be developed by using grey infrastructure and nature-based solutions together.

Ecological and Environmental

Ecological corridors and infiltration areas should be increased.

Natural filtration systems that improve water quality (wetlands, plant-based treatment) should be implemented.

Social and Institutional

Awareness training should be provided for the public and students.

University-municipality-private sector collaborations should be strengthened.

Economic

Structures that harvest rainwater should be encouraged.

Infrastructure maintenance costs should be reduced in the long term through nature-based solutions.

Disaster Risk Management

Flood risk maps should be updated.

Resilient water management systems suitable for climate change scenarios should be designed.

References

[1] Krueger, E. H., Borchardt, D., Jawitz, J. W., Klammler, H., Yang, S., Zischg, J., & Rao, P.

[2] S. C. (2019). Resilience Dynamics of Urban Water Security and Potential for Tipping Points. arXiv preprint [arXiv:1904.07863].

[3] Carramiñana, D., Bernardos, A. M., Besada, J. A., & Casar, J. R. (2025). Towards resilient cities: A hybrid simulation framework for risk mitigation through data driven decision making. arXiv preprint [arXiv:2501.04746].

[4] Hall, P., & Pfeiffer, U. (2013). Urban Future 21: A Global Agenda for Twenty-First Century Cities. Routledge.

[5] Keleş, R. (2016). Kentleşme Politikası. İmge Kitabevi.

[6] Pacione, M. (2009). Urban Geography: A Global Perspective. Routledge.

[7] Ward, P. J., Jongman, B., Aerts, J. C. J. H., et al. (2020). A global framework for future costs and benefits of river-flood protection in urban areas. Nature Climate Change, 10, 642–646.

[8] Wong, T. H. F., & Brown, R. R. (2009). The water sensitive city: principles for practice. Water Science & Technology, 60(3), 673–682.

[9] Mitchell, V. G. (2006). Applying integrated urban water management concepts: A review of Australian practice. Environmental Management, 37, 589–605.

[10] SIWI (Stockholm International Water Institute). (2023). *Water-wise cities: Integrated and resilient urban water management*. Stockholm: SIWI.

[11] Fletcher, T. D., Shuster, W., Hunt, W. F., Ashley, R., Butler, D., Arthur, S., Trowsdale, S., Barraud, S., Semadeni-Davies, A., Bertrand-Krajewski, J. L., & Viklander, M. (2015). SUDS, LID, BMPs, WSUD and more – The evolution and application of terminology surrounding urban drainage. *Urban Water Journal*, **12**(7), 525–542.

[12] Urban Planning Council. (2017). *Commission report on urban planning policies for resilient cities*. Ministry of Land, Infrastructure, Transport and Tourism (MLIT), Japan.

Synthesis and Bioactivities of Zinc Oxide (ZnO) Nanoparticles

Aysu Kırali[1]*, Esen Taşğın[1], Hayrunnisa Nadaroğlu[2], Bülent Çetin[3], Aynur Babagil[2]

[1] Department of of Nutrition and Dietetics, Faculty of Health Sciences, Atatürk University, Erzurum, Türkiye
[2] Department of Nanoscience and Nanoengineering, Technical Sciences Vocational School, Atatürk University, Erzurum, Türkiye
[3]Department of Food Engineering, Faculty of Agriculture, Atatürk University, Erzurum, Türkiye

* *Corresponding author E-mail: aysukrali.98@gmail.com*

Keywords

Postbiotic

Zinc oxide nanoparticles

Green synthesis

Abstract

Postbiotics are components formed as a result of the metabolic processes of probiotic microorganisms and have the capacity to create positive effects on health. Nanoparticles (NPs) are carriers designed at the molecular level, mostly ranging in size from 1 to 100 nm, capable of delivering targeted effects. The food industry uses zinc oxide (ZnO), a source of zinc as a basic micronutrient, and it is listed as a Generally Recognized as Safe (GRAS) material by the Food and Drug Administration (FDA). The aim of this study is to produce zinc oxide (ZnO) nanoparticles using a green synthesis method with a postbiotic, and to determine the antimicrobial and antioxidant activities of the synthesized nanoparticles. In this study, ZnO nanoparticles were synthesized using the hydrothermal green synthesis method with these postbiotics as reducing agents. The obtained nanoparticles were characterized and antimicrobial and antioxidant activities was determined. These study findings demonstrate that postbiotics can be used as effective reducing biocatalysts in ZnO nanoparticle synthesis, and that these resulting nanomaterials hold promise for biomedical applications and functional food fields.

1. Introduction

The microbiota is the community of microorganisms living in our bodies, and numerous studies have helped us to understand more deeply the importance of the microbiota in the digestive system in maintaining or improving health. The gut microbiota, which exists with these microorganisms, is a constantly changing entity throughout every stage of life [1]. At the same time, the microbiota is a highly complex ecosystem that directly affects not only gut health but also overall health. The cyclical processes, functions, and systems in an individual's body are intertwined with the microbiota [2]. The composition and structure of the microbiota, and the microorganisms that make it up, have been the focus of researchers due to their impact on health.

Biobiotics (probiotics, prebiotics, postbiotics), which can be considered functional nutrients for the gut microbiota, are one of the nutritional plans that can positively affect health. Postbiotics, which have various definitions, are innovative components that are formed as a result of the metabolic processes of probiotic microorganisms, recently discovered by modern science, and attracting attention with their potential health benefits [3]. Postbiotics are bioactive compounds derived from probiotic microorganisms and consist of both microbial metabolites and structural cell components (Figure 1). Postbiotics consist of non-viable microorganisms and/or their components produced during fermentation and exert health benefits through antioxidant, immunomodulatory, gut barrier–enhancing, and antimicrobial mechanisms. As illustrated, postbiotic metabolites such as short-chain fatty acids, organic acids, enzymes, and bioactive peptides are produced during fermentation and exert diverse biological effects, including antioxidant, antimicrobial, anti-inflammatory, antiproliferative, and antidiabetic activities [4].

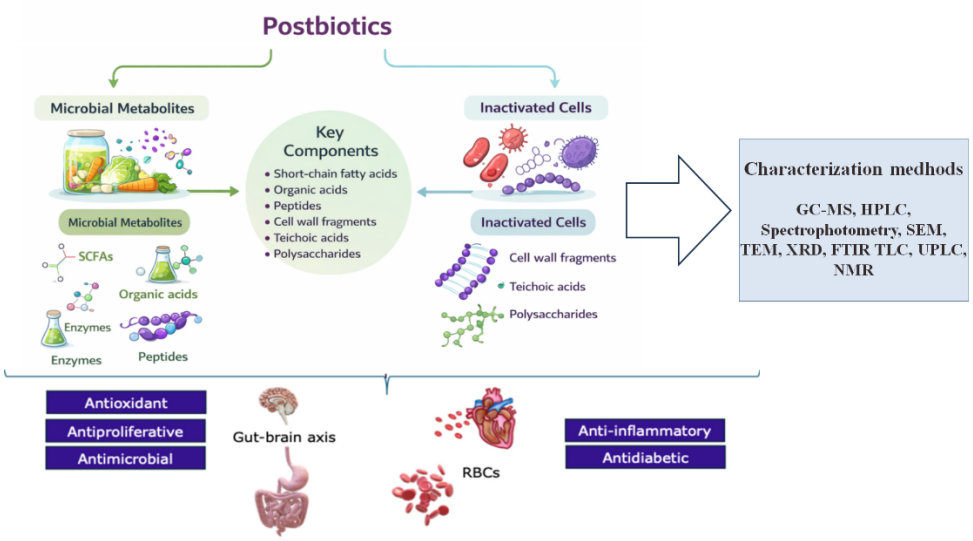

Figure 1 Rain garden systems

In addition to secreted metabolites, non-viable microbial cell components such as polysaccharides, teichoic acids, lipids, and peptidoglycan also contribute significantly to host health by modulating immune responses, improving gut barrier function, and influencing metabolic and cardiovascular pathways, including hypocholesterolemic and antihypertensive effects [5]. Postbiotics can be obtained either from inactivated microorganisms through physical or thermal treatments or from live microorganisms via controlled isolation and purification of metabolites. The resulting postbiotic fractions, which include vitamins, enzymes, organic acids, biosurfactants, and peptides, are subsequently characterized using advanced analytical techniques such as chromatography, spectroscopy, and mass spectrometry. Together, these processes highlight the multifaceted nature of postbiotics and their potential as stable, safe, and functionally versatile bioactive agents for applications in functional foods and biomedical fields [6,7,8,9]. These compounds, which have a wide range of effects from gut health to the immune system, are expected to find more therapeutic applications in the future. However, more research and clinical data are needed to ensure that postbiotics can be used safely and effectively as part of a healthy lifestyle and balanced diet. Nanoscale encapsulated bacterial metabolic byproducts can have targeted biological effects, leading to the emergence of novel terms such as “postbiotic nanoparticles,” and their use in clinical applications and commercial products could represent a new direction in the pharmaceutical and functional food industries in the future [10]. Nanoparticle technology is emerging as a valuable strategic step to enhance the efficacy of postbiotics [11].

Another concept that does not exhibit viability but provides health benefits is the term "postbiotics." In 2021, ISAAP defined postbiotics as "non-viable microorganisms and/or preparations of components of such microorganisms that provide a health benefit to the host" [7,12]. Postbiotics can be directly present in fermented products (yogurt, pickles, pickled vegetables, etc.) or obtained from different types of fungi or bacteria [13]. The most preferred bacteria for obtaining postbiotics are lactic acid bacteria, with Bifidobacterium and Lactobacillus bacteria being frequently used, although postbiotics can also be obtained from Streptococcus and Faecalibacterium strains [14,15]. The most common processes used for microbial inactivation are thermal processes such as pasteurization, sterilization, and ohmic heating, and non-thermal processes such as pulsed electric fields, ultrasound, irradiation, and supercritical carbon dioxide [16]. Nanoparticles are carriers designed at the molecular level, mostly ranging in size from 1 to 100 nm, capable of delivering targeted effects [17]. Oral administration is commonly used for small molecules to facilitate the delivery of biological drugs, drug degradation, and rapid passage through the gastrointestinal tract; however, significant challenges are encountered for macromolecules such as peptides and proteins, resulting in poor bioavailability [18]. Nanoparticles are widely used as drug delivery vehicles in miniaturized forms to enhance the advantages of a co-delivery system. Decades of extensive research have investigated both natural and synthetic materials to improve drug bioavailability, and trials have resulted in successful drug delivery systems [19].

2. Results and Discussion

This study provides an important scientific foundation for future research into postbiotic-based green nanotechnology applications. The usability of postbiotics as bioreducing and stabilizing agents in the synthesis of ZnO nanoparticles with an environmentally friendly approach was investigated. The findings reveal that postbiotics are not only functional bioactive components but also biocatalytic agents that can play an active role in nanotechnology applications. Characterization studies have shown that prebiotics, due to their multifunctional groups, can promote the formation of more homogeneous, spherical nanoparticles by chelating Zn^{2+} ions and limiting uncontrolled growth

[8]. In particular, in green synthesis approaches, postbiotics act as a natural biocatalyst in the reduction of metal ions and form a biocompatible coating on the nanoparticle surface. This reduces the risk of toxicity of the synthesized nanoparticles and makes their biological interactions more controlled [9,20,21]. Postbiotics contain numerous components such as short-chain fatty acids, organic acids, enzymes, exopolysaccharides, cell wall components (peptidoglycan, lipoteichoic acid), proteins, and peptides [15,21]. It is thought that these components contained in postbiotics may have taken on a coating role on the nanoparticle surface. These components show positive effects on health, especially through mechanisms such as supporting intestinal barrier function, modulating the immune response, strengthening antioxidant defense, and protective effects against pathogenic microorganisms [3]. One of the most important advantages of postbiotics is that they have higher stability compared to probiotics and are more predictable in terms of safety due to not containing live microorganisms [13]. These features make postbiotics stand out as suitable biofunctional components, especially for infants, the elderly, and immunocompromised individuals [15]. Nanoparticles obtained using postbiotics have become a noteworthy research area in terms of functional food and biomedical applications. In this approach, the use of postbiotics as bioreducing and stabilizing agents in nanoparticle synthesis is prominent. It has been shown that postbiotics exhibit different antimicrobial activities, and that the antioxidant potential of postbiotics is increased as a result of the nanoencapsulation process. This situation shows that postbiotic-nanoparticle interaction can produce different biological results depending on the application purpose [22].

3. Conclusion

Nanoparticles synthesized with postbiotics offer promising potential for biomedical and functional food applications, especially in terms of their antioxidant properties. However, advanced optimization studies and in vivo-supported research are needed to increase antimicrobial activity and ensure controlled biological effects. In conclusion, although postbiotics have application possibilities in many areas of nanotechnology such as functional foods and nutraceuticals, drug delivery systems, antimicrobial and antioxidant coatings, understanding nanoparticle-postbiotic interactions at the molecular level, increasing bioavailability and toxicity studies, and supporting them with clinical data are necessary for the safe and effective use of these systems.

References

[1] González, S., Fernández-Navarro, T., Arboleya, S., de Los Reyes-Gavilán, C. G., Salazar, N., Gueimonde, M. (2019). Fermented dairy foods: impact on intestinal microbiota and health-linked biomarkers. Frontiers in microbiology, 10: 1046.

[2] Ferreira, R. D. S., Mendonça, L. A. B. M., Ribeiro, C. F. A., Calças, N. C., Guimarães, R. D. C. A., Nascimento, V. A. D., Gielow, K. D. C. F., Carvalho, C. M. E. C., Castro, A. P., Franco, O. L. (2022). Relationship between intestinal microbiota, diet and biological systems: an integrated view. Critical Reviews in Food Science and Nutrition, 62(5): 1166-1186.

[3] Ballini, A., Charitos, I. A., Cantore, S., Topi, S., Bottalico, L., & Santacroce, L. (2023). About Functional Foods: The Probiotics and Prebiotics State of Art. Antibiotics. 12(4), 635.

[4] Aguilar-Toalá, J. E., Garcia-Varela, R., Garcia, H. S., Mata-Haro, V., González-Córdova, A. F., Vallejo-Cordoba, B., & Hernández-Mendoza, A. (2018). Postbiotics: An evolving term within the functional foods field. Trends in Food Science & Technology, 75, 105–114.

[5] Żółkiewicz, J., Marzec, A., Ruszczyński, M., & Feleszko, W. (2020). Postbiotics—A Step Beyond Pre- and Probiotics. Nutrients, 12(8), 2189. https://doi.org/10.3390/nu12082189

[6] Wegh, C. A. M., Geerlings, S. Y., Knol, J., Roeselers, G., & Belzer, C. (2019). Postbiotics and their potential applications in early life nutrition and beyond. International Journal of Molecular Sciences, 20(19), Article 4673.

[7] Salminen, S., Collado, M. C., Endo, A., Hill, C., Lebeer, S., Quigley, E. M. M., Sanders, M. E., Shamir, R., Swann, J. R., Szajewska, H., & Vinderola, G. (2021). The International Scientific Association for Probiotics and Prebiotics (ISAPP) consensus statement on the definition and scope of postbiotics. Nature Reviews Gastroenterology & Hepatology, 18(9), 649–667. https://doi.org/10.1038/s41575-021-00440-6

[8] Alharthi, M. N., Ismail, I., Bellucci, S., Jaremko, M., Abo-Aba, S. E., & Abdel Salam, M. (2023). Biosynthesized zinc oxide nanoparticles using Ziziphus jujube plant extract assisted by ultrasonic irradiation and their biological applications. Separations, 10(2), 78.

[9] Sharifabady, S. M., Shakib, P., Omidi, B., & Zolfaghari, M. R. (2023). Biosynthesis of Zinc Oxide nanoparticles by Lactobacillus spp. and investigation of their antimicrobial effect. Current Drug Discovery Technologies, 20(5), 10-18.

[10] Mohammed, S., & Çon, A. H. (2024). Postbiotic nanoparticles (postbiotics-NPs): a novel strategy for providing probiotics' health advantages through food consumption. Food Science and Biotechnology, 33(12), 2729-2736.

[11] Islam, F., Imran, A., Afzaal, M., Zahoor, T., Amjad, N., Wei, C. R., ... & Asif Shah, M. (2024). Nanotechnology for the improvement of the quality, properties, and safety of food and agriculture: recent and future trends. Cogent Food & Agriculture, 10(1), 2398857.

[12] Vinderola, G., Sanders, M. E., & Salminen, S. (2022). The concept of postbiotics. Foods, 11(8), 1077.

[13] Thorakkattu P, Khanashyam A, Shah K et al. (2022). Postbiotics: Current Trends in Food and Pharmaceutical Industry. Foods, 11(19).

[14] Aggarwal S, Sabharwal V, Kaushik P, Joshi A, Aayushi A and Suri M. (2022) Postbiotics: From emerging concept to application. Front. Sustain. Food Syst. 6:887642. doi: 10.3389/fsufs.2022.887642

[15] Viswanathan K., Muthusamy S. (2022) Review on the current trends and future perspectives of postbiotics for developing healtheir foods. eFood, 3(6).

[16] Pimentel, T. C., Cruz, A. G., Pereira, E., da Costa, W. K. A., da Silva Rocha, R., de Souza Pedrosa, G. T., ... & Magnani, M. (2023). Postbiotics: An overview of concepts, inactivation technologies, health effects, and driver trends. Trends in Food Science & Technology, 138, 199-214.

[17] Nasrollahzadeh, M., Sajadi, S. M., Sajjadi, M., & Issaabadi, Z. (2019). An introduction to nanotechnology. In Interface science and technology (Vol. 28, pp. 1-27). Elsevier.

[18] Subramanian, D. A., Langer, R., & Traverso, G. (2022). Mucus interaction to improve gastrointestinal retention and

pharmacokinetics of orally administered nano-drug delivery systems. Journal of nanobiotechnology, 20(1), 362.

[19] Akiyama, Y., & Nagahara, N. (1999). Novel formulation approaches to oral mucoadhesive drug delivery systems. Drugs and the pharmaceutical sciences, 477-505.

[20] Mohd Yusof, H., Abdul Rahman, N., & Mohamad, R. (2020). Biosynthesis of zinc oxide nanoparticles by cell-biomass and supernatant of Lactobacillus plantarum TA4 and its antibacterial and biocompatibility properties. Sci Rep 10: 19996.

[21] Mahajan, M., Kumar, S., Gaur, J., Kaushal, S., Dalal, J., Singh, G., ... & Ahlawat, D. S. (2025). Green synthesis of ZnO nanoparticles using Justicia adhatoda for photocatalytic degradation of malachite green and reduction of 4-nitrophenol. RSC advances, 15(4), 2958-298.

[22] Gurunathan, S., Thangaraj, P., & Kim, J. H. (2023). Postbiotics: functional food materials and therapeutic agents for cancer, diabetes, and inflammatory diseases. Foods, 13(1), 89.

Use of Metal Oxide Nanoparticles in the Food Industry: Toxicological Risks and Effects on Child Nutrition

Behina Asadoghli[1*], Esen Taşğın[1*]

[1] Department of of Nutrition and Dietetics, Faculty of Health Sciences, Atatürk University, Erzurum, TURKİYE

* *Corresponding author E-mail: behinaasadoghli@gmail.com, esent25@atauni.edu.tr*

Keywords

Metal oxide nanoparticles

Food security

Child health

Toxicology

Abstract

Metal oxide nanoparticles (MONPs) have become increasingly used materials in food Metal oxide nanoparticles (MONPs) are widely used in the food industry, particularly in active and smart packaging technologies. Nanoparticles such as titanium dioxide (TiO_2), zinc oxide (ZnO), and silicon dioxide (SiO_2) provide technological advantages, including antimicrobial activity, reduced oxygen and moisture permeability, and extended food shelf life. However, the migration of these nanoparticles from packaging materials into food raises concerns regarding dietary exposure. Nanoparticle migration from packaging varies depending on factors such as food fat content, pH, temperature, contact duration, and the physicochemical properties of the packaging material. Metal oxide nanoparticles reaching the gastrointestinal tract through oral ingestion may interact with the intestinal epithelial barrier and gut microbiota, and these interactions have been reported to exert indirect effects on oxidative stress, inflammatory responses, and metabolic processes. Evaluating such exposure is particularly important in populations with frequent consumption of packaged and processed foods. Children represent a higher-risk group due to their greater food intake relative to body weight and increased developmental sensitivity. This study aims to examine the use of metal oxide nanoparticles in food packaging, their potential toxicological effects, and the risks they may pose to child nutrition in light of current findings reported in the literature.

1. Introduction

The use of nanotechnology in the food sector has increased significantly in recent years due to its potential to improve the physicochemical properties of foods, extend shelf life, and enhance product stability [1].In this context, metal oxide nanoparticles (MONPs), particularly in forms containing compounds such as titanium dioxide (TiO_2), zinc oxide (ZnO), and silicon dioxide (SiO_2), are widely used in food additives and food contact materials [2]. The size of nanoparticles in the range of 1–100 nm increases their surface area and biological reactivity, leading to different biological behaviors compared to their macro-scale forms [3]. This situation raises new risk assessment requirements regarding the interaction of nanoparticles ingested through food with the gastrointestinal system, their bioavailability, and potential toxic effects [4]. The demonstration that additives long considered “biologically inert” particularly titanium dioxide (E171), can contain nanofractions has led to a reassessment of food safety approaches [3]. In 2021, the European Food Safety Authority (EFSA) stated that TiO_2 could not be considered safe as a food additive because the risk of genotoxicity could not be completely ruled out [5]. From a nutritional science perspective, it is increasingly emphasized that nanoparticle exposure can affect not only toxicological processes but also processes such as gut microbiota, nutrient absorption, metabolic regulation, and immune system development [6,7]. These effects are of particular importance in the developmentally vulnerable child population, as children consume more food relative to their body weight and are more frequently exposed to processed foods [8]. The aim of this study is to evaluate the applications of metal oxide nanoparticles in the food industry from the perspective of the gastrointestinal system, microbiota, and biodiffusion in light of current toxicological findings, and to discuss the potential risks, particularly in terms of child nutrition.

1.1. Applications of Metal Oxide Nanoparticles in the Food Sector

1.1.1. Food Production and Processing

Metal oxide nanoparticles are evaluated in food production not so much for direct use as components, but rather to improve product properties through additives and technological aids [2]. In particular, titanium dioxide (TiO_2–E171)

and silicon dioxide (SiO_2– E551) are among the most frequently used metal oxide nanoparticles to provide color, fluidity, and stability in foods [3,9].

1.1.2. Titanium Dioxide (TiO_2 – E171)

Titanium dioxide has been widely used in the food industry, particularly in confectionery, chewing gum, coated baked goods, and dairy-based products, due to its whitening and opacifying properties [3]. However, the demonstration that food-grade forms of E171 can contain nano-sized fractions has raised concerns about the biological interaction potential of this additive [4]. Experimental studies have shown that TiO_2 nanoparticles can actively interact with the intestinal mucosa, although they can aggregate in the gastrointestinal system after oral ingestion [6]. These interactions have been associated with weakening of intestinal barrier integrity, triggering of inflammatory responses, and changes in microbiota composition [4,7]. High consumption of foods containing TiO_2, especially by children, leads to increased exposure per kilogram [8]. This necessitates a more careful assessment of the potential chronic effects of TiO_2 nanoparticles in long-term and low-dose exposure scenarios [5].

1.1.3. Silicon dioxide (SiO_2 – E551)

Silicon dioxide is a widely used additive in foods as an anti-caking agent, particularly preferred for improving fluidity in powdered products [3]. Studies on the interaction of nano-sized SiO_2 particles with the digestive system have shown that these particles can disrupt intestinal barrier integrity and lead to microbiota-mediated systemic effects. These studies have revealed that oral SiO_2 nanoparticle exposure can trigger neuroinflammation and neurodegenerative-like processes via the gut-microbiota-brain axis. These findings suggest that SiO may be not only a technologically "auxiliary" additive but also a biologically active component [9].

1.2. Food Packaging (Active and Intelligent Packaging)

Metal oxide nanoparticles are currently used as key components of active and smart packaging technologies in food contact packaging materials rather than in food production [2]. These nanoparticles are evaluated for integration into packaging polymer matrices to extend food shelf life, reduce microbial spoilage, and improve physical barrier properties [10]. Titanium dioxide (TiO_2), zinc oxide (ZnO), and silicon dioxide (SiO_2) nanoparticles, in particular, are widely preferred in food packaging due to their functions such as blocking UV light, reducing oxygen permeability, and providing antimicrobial activity [2,11]. While these applications offer technological advantages in terms of preserving food quality, they also raise concerns about the risk of exposure through ingestion due to the migration of nanoparticles from packaging to food [10].

1.3. Antimicrobial Packaging

Antimicrobial packaging containing metal oxide nanoparticles aims to improve food safety by suppressing the growth of microorganisms [2]. ZnO and TiO_2 nanoparticles can damage the cellular structures of bacteria, yeasts, and molds by producing reactive oxygen species (ROS), especially in the presence of light [11]. While this mechanism can extend the shelf life of packaged food by reducing its microbial load, it is noted that the same ROS production capacity can increase the risk of oxidative stress and inflammation when it comes into contact with the human gastrointestinal system [8]. From a nutritional science perspective, this situation necessitates consideration of long-term low-dose nanoparticle exposure, especially in individuals who frequently consume packaged and processed foods [1]. In addition, nanoparticles used in packaging act as fillers within the polymer matrix, extending gas diffusion pathways and thus improving the shelf stability of the food [10].

1.4. From the packaging Migration (Leaching) and Exposure through nutrition

It has been reported that not all nanoparticles used in packaging to improve barrier properties are completely immobilized in the polymer matrix and can be released under certain conditions [11]. It is emphasized that nanoparticle migration can increase, especially in cases of high temperature, long-term storage, and contact with foods with high fat content [2]. Nanoparticle migration from food packaging is considered one of the most important exposure pathways for metal oxide nanoparticles entering the human diet [10]. Nanoparticle migration varies depending on the type of packaging material, the size and surface properties of the nanoparticle, the fat content, pH, temperature, and contact time of the food [2]. It has been reported that foods with high fat content facilitate the separation of metal oxide nanoparticles from the packaging and increase gastrointestinal exposure [11]. The potential for nanoparticles migrating from packaging to reach the digestive system and indirectly affect the gut microbiota, intestinal barrier, and metabolic processes is significant [6,7] (Figure 1). This situation leads to a more pronounced risk of exposure, especially in the child population where the consumption of packaged and ready-to-eat foods is high [10,11].

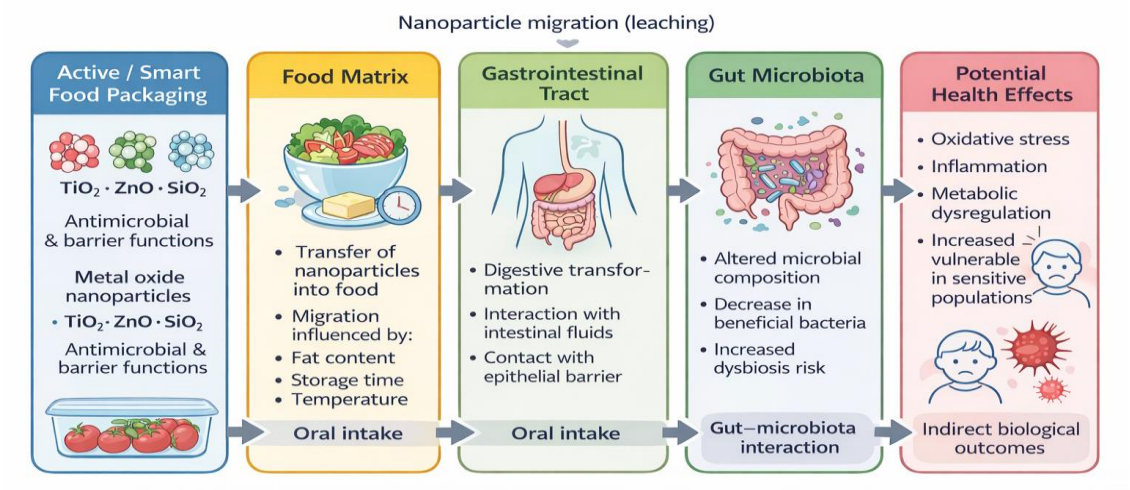

Figure 1 Food packaging, the potential effects of metal oxide nanoparticles.

2. Nano-encapsulation Applications

Nano-encapsulation technologies are attracting increasing interest in food production to enhance the stability of bioactive components, ensure controlled release, and improve bioavailability [1]. However, it is emphasized that nanoparticle exposure may occur as a result of the degradation of nano-carrier systems in the digestive environment or their interaction with the intestinal epithelium, and this should be taken into account in safety assessments [1].

2.1. Metal Oxide Nanoparticles (MONPs) The Toxicology of Profile — Current Results

The toxicological effects of MONPs depend not only on their chemical composition but also on particle size, surface area, surface charge, crystal structure, and aggregation status [3]. MONPs ingested through food can produce local effects following initial contact with the gastrointestinal tract and, under certain conditions, can enter systemic circulation, albeit to a limited extent [4]. Recent experimental studies have shown that TiO_2, ZnO, and SiO_2 nanoparticles are not “biologically inert” and can trigger common toxicity mechanisms such as oxidative stress, inflammation, and cellular dysfunction [8, 9]. These mechanisms are particularly important in terms of gut health, microbiota balance, and metabolic regulation in chronic and low-dose exposure scenarios through diet [6].

2.2. Toxicity Mechanisms

2.2.1. Reactive Oxygen Species (ROS) and Oxidative Stress

The most commonly identified mechanism in the toxicity of metal oxide nanoparticles is the increased production of intracellular and extracellular reactive oxygen species (ROS) [8].

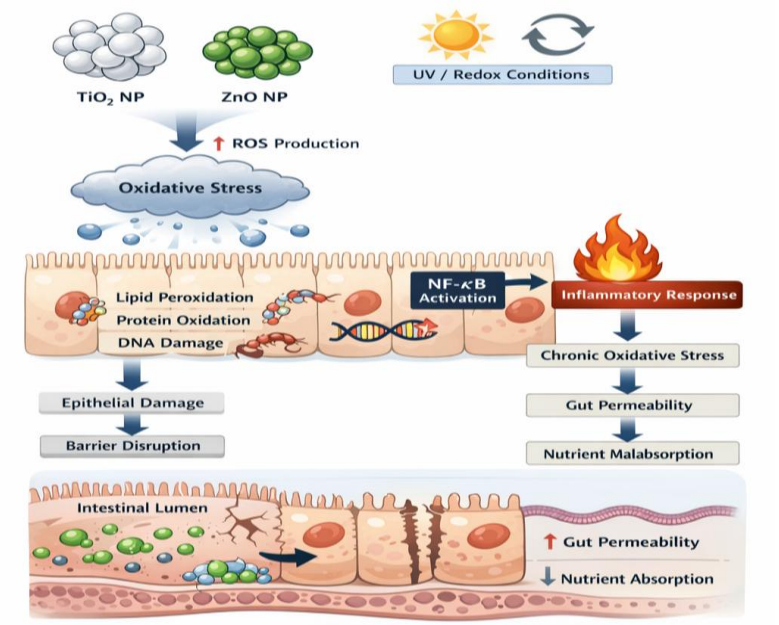

Figure 2 Toxic effects of metal oxide nanoparticles on the gut [7].

TiO_2 and ZnO nanoparticles can trigger cellular oxidative stress responses by increasing ROS production, especially under light or biological redox environments [11]. Increased ROS levels can initiate cellular damage processes such as lipid peroxidation, protein oxidation, and DNA damage [3]. This oxidative stress state, combined with the activation of inflammatory signaling pathways (e.g., NF-κB), leads to the deepening of tissue damage [8]. Continuous exposure of gastrointestinal system cells to nanoparticles can lead to chronic oxidative stress and weakening of intestinal epithelial integrity [6]. This process is considered a risk factor that may indirectly affect nutrient absorption and intestinal barrier function [7,12] (Figure 2).

2.2.2. Reactive oxygen species (ROS) and oxidative stress

The most commonly described mechanism for the toxicity of metal oxide nanoparticles is the increased production of intracellular and extracellular reactive oxygen species (ROS) [8]. TiO_2 and ZnO nanoparticles can trigger cellular oxidative stress responses by increasing ROS production, particularly under light or biological redox environments [11]. Increased ROS levels can initiate cellular damage processes such as lipid peroxidation, protein oxidation, and DNA damage [3]. This oxidative stress state, combined with the activation of inflammatory signaling pathways (e.g., NF-κB), leads to the deepening of tissue damage [8]. Continuous exposure of gastrointestinal system cells to nanoparticles can lead to chronic oxidative stress and weakening of intestinal epithelial integrity [6]. This process is considered a risk factor that may indirectly affect nutrient absorption and intestinal barrier function [7].

2.3. Cell membrane Integrity, cell-to-cell interaction and Ion Emission

Metal oxide nanoparticles can disrupt membrane integrity by directly contacting the cell membrane and can be taken up into the cell via endocytosis [11]. The entry of nanoparticles into the cell can lead to disruption of lysosomal membrane stability and increased cellular stress responses. Specifically for ZnO nanoparticles, ion release (Zn^{2+}) has been reported to play a significant role in the toxicity mechanism. This ion release is associated with mitochondrial dysfunction, impaired energy metabolism, and the triggering of apoptosis processes [8]. TiO_2 nanoparticles, on the other hand, cause cellular damage mainly through surface reactivity and physical interactions [3]. These differences indicate that the toxicity of metal oxide nanoparticles is not uniform and that each compound should be evaluated separately [4].

2.4. Toxic Effects In The System

While the primary target organ of metal oxide nanoparticles after oral exposure is the gastrointestinal system [6], some studies have reported low-level accumulation and functional changes in organs such as the liver, kidneys, and brain [4,8]. It is thought that metal oxide nanoparticles can cause not only local toxicity but also multiple system effects through food-microbiota-barrier interactions [9]. This can trigger systemic inflammation by creating a "leaky gut"-like condition [7]. It has been shown that TiO_2, ZnO, and SiO_2 nanoparticles can reduce the expression of tight junction proteins in intestinal epithelial cells and weaken barrier integrity [6,9]. These changes in intestinal barrier integrity are critical for nutrient absorption, immune tolerance, and microbiota-host interaction [6]. Nanoparticle-induced barrier disruption is considered a risk factor that may lead to long-term metabolic and immune consequences, especially during developmental periods [8].

2.5. Biodispersion and Tissue Distribution

Although the passage of metal oxide nanoparticles from the gastrointestinal system to the systemic circulation is generally low, studies have reported detectable accumulation in organs such as the liver, spleen, and kidneys [4]. This accumulation is reported to be related to the size, surface properties, and exposure time of the nanoparticles [3]. Ti element has been shown to be more prominently retained in intestinal and lymphoid tissues, and this has been associated with low-intensity inflammatory responses [4]. These findings suggest that metal oxide nanoparticles are not completely eliminated and may have the potential for cumulative effects with long-term dietary exposure [1].

3. Effects on Microbiota

Recent in vivo and in vitro studies have shown that metal oxide nanoparticles can lead to significant changes in the composition and metabolic activity of the gut microbiota [6,13]. These microbiota changes have been reported to result in a decrease in short-chain fatty acid (SCFA) production, which can have negative effects on gut barrier integrity and immune regulation [7] and are associated with inflammation [6]. This suggests that nanoparticles ingested with food can have effects not only on the gastrointestinal tract but also indirectly on the central nervous system [9]. Microbiota disruption and weakening of barrier integrity due to metal oxide nanoparticle exposure have been shown to lead to systemic and neurological effects via the microbiota–gut–brain axis, and are associated with behavioral changes and neuroinflammation [7]. The sensitivity of microbiota development and the gut-brain axis, particularly during childhood, highlights the need for more careful consideration of metal oxide nanoparticle exposure in this population [8].

3.1. Risks and Safety Concerns Regarding Child Nutrition

Children are considered a more sensitive population to environmental and food contaminants due to their ongoing physiological development, high metabolic rates, and higher food intake relative to their body weight [8]. This necessitates that children be considered a special risk group for the ingestion of metal oxide nanoparticles through food and food packaging [5].

3.2. High Exposure Relative to Body Weight

Since children have higher energy and food intake per kilogram compared to adults, higher nanoparticle exposure may occur as a result of consuming the same food product [8]. Frequent consumption of products containing TiO_2 and SiO_2, such as candies, chewing gum, coated baked goods, and packaged snacks, by children increases the risk of exposure [3]. The formation of dietary habits at an early age can lead to nanoparticle exposure becoming a long-term and repetitive characteristic [1]. This chronic low-dose exposure scenario carries more difficult-to-predict risks from a toxicological perspective compared to short-term high-dose exposures [4]. Childhood is a period when the intestinal barrier, immune system, and microbiota are not yet fully mature, which increases susceptibility to nanoparticles [6]. It has been reported that even small changes in intestinal epithelial integrity can have more significant effects on systemic inflammation and immune response in children [7].The ability of metal oxide nanoparticles to alter microbiota composition can negatively impact microbial colonization processes, which are critical during childhood [6].This is considered a risk factor that may lead to disruptions in physiological processes directly related to nutrition, such as energy metabolism, vitamin synthesis, and the development of immune tolerance [7].Furthermore, the high plasticity of the microbiota-gut-brain axis in early life makes nanoparticle exposure significant in terms of neurodevelopmental effects [9].

3.3. Exposure and Risk of Toxicity in Children

Packaged and ready-to-eat foods, frequently consumed by children, are a significant source of indirect exposure through the migration of metal oxide nanoparticles from packaging to food [10]. Long-term storage, high fat content, and heating processes can increase nanoparticle migration, raising the daily intake of children [2]. Since this exposure usually occurs at low doses, it can delay the onset of clinical symptoms and make it difficult to recognize the risk [1]. This raises concerns that nanoparticle exposure may have cumulative effects throughout life [4]. In assessments conducted by EFSA, it has been stated that TiO_2 cannot be considered safe as a food additive because its genotoxicity potential cannot be completely ruled out [5].This decision is considered a reflection of the precautionary approach principle, particularly in terms of protecting vulnerable groups such as children [7].However, the limited available data for silicon dioxide (E551) and other metal oxide nanoparticles indicate that significant uncertainties remain in safety assessments [3]. From the perspective of child nutrition, it is emphasized that current regulations do not adequately consider long-term, low-dose, and combined exposures to nanoparticles [8]. Therefore, it is stated that nanoparticle-based risk assessments for foods and packaging materials intended for children should be addressed separately and in a more protective manner [1].

4. Discussion

While the use of metal oxide nanoparticles in the food industry and food packaging provides significant technological advantages, the long-term effects of dietary exposure are not yet fully understood [1]. In particular, oxidative stress, disruption of barrier integrity, and changes in microbiota composition stand out as common toxicity mechanisms of metal oxide nanoparticles [3]. The fact that these mechanisms largely operate at a subclinical level makes it difficult to detect the effects of chronic dietary exposure in the short term [4]. Current safety assessments largely rely on adult populations and short-term toxicity data, increasing uncertainties for vulnerable groups such as children [8]. It is emphasized that future studies should focus on low-dose and long-term exposure models that reflect realistic dietary scenarios [1]. Furthermore, evaluating the combined exposure (combined effect) of different metal oxide nanoparticles and their interactions with the food matrix will improve the accuracy of risk analyses [2].

Metal oxide nanoparticles have become a significant component of the modern food system due to the functional advantages they provide in food production and packaging technologies [2]. However, the entry of these nanoparticles into the human diet through foods and packaging materials carries potential health risks, particularly through the gastrointestinal system and microbiota [3]. Current findings suggest that TiO_2, ZnO, and SiO_2 nanoparticles can exert biological effects through mechanisms such as oxidative stress, disruption of barrier integrity, and microbiota imbalance [6,8].These effects may become more pronounced during childhood, and the risk level can increase when combined with factors such as high exposure relative to body weight, developmental susceptibility, and long-term exposure [8]. EFSA's cautious approach to TiO_2 reveals that uncertainties remain significant in the safety assessments of nanoparticle-based additives [5]. In the field of nutrition and dietetics, these uncertainties are thought to necessitate the development of more protective approaches, particularly for foods intended for children [1].

5. Conclusion

The literature findings evaluated in this study reveal that despite the functional advantages provided by metal oxide nanoparticles (TiO_2, ZnO, and SiO_2) in food production and packaging technologies, they may have potential biological effects as a result of dietary exposure. In particular, the induction of oxidative stress, weakening of gastrointestinal barrier integrity, and changes in gut microbiota composition are identified as the prominent mechanisms of action of these nanoparticles. Current data indicate that these effects are mostly low-level and subclinical, making them difficult to detect in the short term, but they may become biologically significant with long-term and repeated exposure. In vulnerable groups such as children, the higher exposure level relative to body weight and their sensitivity due to developmental stages can make the potential risks more pronounced. Current safety assessments are mostly based on individual nanoparticles, short-term toxicity data, and predominantly animal experiments. This does not adequately reflect the actual exposure conditions encountered in daily diets. Therefore, more comprehensive risk assessments based on human-based, long-term studies are needed, taking into account the co-exposure of metal oxide nanoparticles and their interactions with the food matrix. In conclusion, the use of metal oxide nanoparticles in the food chain should be considered not only in terms of technological gains but also in terms of long-term dietary exposure, effects on the gastrointestinal system and microbiota, and potential risks to vulnerable populations. It is believed that the findings obtained in this regard will contribute to the development of food safety policies and the adoption of more cautious approaches, especially in products aimed at children.

References

[1] Domingo, J. L. (2025). Nanoparticles in food: formation during cooking, migration from packaging, and release of nanoplastics-food safety implications. Food additives & contaminants. Part a, Chemistry, analysis, control, exposure & risk assessment, 42(11), 1447-https://doi.org/10.1080/19440049.2025.2565014

[2] Muthu, A., Nguyen, D. H., Neji, C., Törős, G., Ferroudj, A., Atieh, R., ... & Béni, Á. (2025). Nanomaterials for smart and sustainable food packaging: Nano-Sensing mechanisms, and regulatory perspectives. Foods, 14(15), 2657.

[3] Akagi, Ji., Mizuta, Y., Kumada, H. et al. Titanium dioxide nanoparticles with a diameter of 6 nm; crystallite Oral toxicological study in rats. Part Fibre Toxicol 20, 23 (2023). https://doi.org/10.1186/s12989-023-00533-x

[4] Lin, H., Tan, J., Wang, J., Xie, C., Chen, B., Luo, M., Liu, Y., Liao, W., Huang, W., Wang, H., Jiang, Y., Wang, K., Lu, C., & Zhao, M. (2023). Subchronic oral toxicity Study of food-related Gut Microbiota in rats and Biodistribution involved in Ti Titanium dioxide Nanoparticles. Journal of agricultural and Food Chemistry, 71(3), 1713-https://doi.org/10.1021/acs.jafc.2c05341

[5] The European Food Safety Authority (EFSA). (2021). Guidance on risk assessment of nanomaterials applied to food and feed chain: human and animal health. EFSA Journal, 19(8), ehttps://doi.org/10.2903/j.efsa.2021.6768

[6] Chen, Z., Han, S., Zhou, D., Zhou, S. , & Jia, G., (2019). Effects of oral exposure to titanium dioxide nanoparticles pre-gut microbiota and gut-associated metabolism in vivo. Nanoscale, 11(46), 22398-https://doi.org/10.1039/c9nr07580a

[7] Zhang, S., Jiang, X., Cheng, S., Fan, J., Qin, X., Wang, T., Zhang, Y., Zhang, J., Qiu, Y., Qiu, J., Zou, Z., & Chen, C. (2020). Titanium dioxide nanoparticles via oral exposure and locomotor activity in adult mice leads to disturbance of the gut microecology adverse. Archives of toxicology, 94(4), 1173-https://doi.org/10.1007/s00204-020-02698-2

[8] Bautista-Perez, R., Cano-Martinez, A., Herrera-Rodriguez, M. A., Ramos-Godinez, M. d. P., Perez-Reyes, O. L., Chirino, A. I., Rodriguez Serrano, Z. J., & Lopez-Marure, R. (2024). Oral exposure to zinc oxide and E171 titanium dioxide Nanoparticles Induces Multi-organ damage in Rats: Role of Ceramide. International Journal of Molecular Sciences, 25(11), https://doi.org/10.3390/ijms25115881

[9] Du, L., Wang, B., Wang, X. et al. Gastrointestinal exposure to silica nanoparticles induced Alzheimer's disease-like neurotoxicity in mice, relying on pre-and gut microbiota modulation through TLR4/NF-kB and HDAC. J Nanobiotechnol 23, 406 (2025). https://doi.org/10.1186/s12951-025-03481-0

[10] The European Food Safety Authority (EFSA). (2025). Literature review of ten micro - and nanoplastic release from food contact materials during their use. EFSA Supporting Publications, 2025(EN-9733), 1-https://doi.org/10.2903/sp.efsa.2025.EN-9733

[11] Gupta, R. K., A, P., & Srivastav, P. P. (2024). Investigating the toxicological effects of nanomaterials in food packaging is associated with human health and the environment. Journal of hazardous materials letters, 5, https://doi.org/10.1016/j.hazl.2024.100125

[12] Rathore, C., Yadav, V. K., Gacem, A., AbdelRahim, S. K., Verma, R. K., Chundawat, R. S., ... & Patel, A. (2023). Microbial synthesis of titanium dioxide nanoparticles and their importance in wastewater treatment and antimicrobial activities: a review. Frontiers in microbiology, 14, 1270245.

[13] Yang, C., Tan, Y., Li, F., Wang, H., Lin, Y., Lu, F., & Zhao, H. (2022). Intestinal Microecology of Mice Exposed to TiO2 Nanoparticles Foods and bisphenol A., 11(12), https://doi.org/10.3390/foods11121696

Occupational Health and Safety Practices in the Solar Energy Sector

Hüseyin Güllüce[1,*], Selçuk Sincar[1,*]

[1] Department of Machine, Technical Sciences Vocational School, Ataturk University, Erzurum, Türkiye

* *Corresponding authors E-mail: hgulluce@atauni.edu.tr; sscincar@atauni.edu.tr*

Keywords

Renewable Energy

Solar Energy

Occupational Health and Safety Practices

Risk Assessment Hazard Mitigation

Abstract

This study evaluates the importance of occupational health and safety (OHS) practices in the rapidly growing solar energy sector and examines preventive strategies for sector-specific risks. Although renewable energy technologies have environmental and economic advantages, occupational risks faced by workers, especially during photovoltaic (PV) panel installation, maintenance processes, and electrical operations, are increasing. This study emphasizes the necessity of developing a safety culture and adopting systematic OHS management approaches in solar energy projects. The study first classifies the hazards commonly encountered in solar energy applications. These hazards include risks of working at height, electric shock, thermal burns, cuts and injuries due to panel breakage, musculoskeletal disorders due to heavy lifting, and long-term health problems related to UV radiation. The analysis shows that most of these risks can be eliminated or minimized with appropriate training, the use of protective equipment, and a systematic risk assessment approach. This study comparatively examines the policies and procedures that should be implemented in solar energy projects within the framework of the Occupational Health and Safety Law No. 6331, international OHS standards (ISO 45001), European Union directives, and relevant legislation in Turkey. The findings reveal that effective OHS management should not be limited to technical measures alone; a holistic approach, including employee participation, regular training programs, field inspections, and emergency planning, is essential. In conclusion, the study shows that ensuring safe working conditions in the solar energy sector is directly related to sustainable production goals. That well-planned OHS practices significantly reduce both work accidents and operational costs. Therefore, it is recommended that sector stakeholders give importance to safety culture as much as technological progress.

1. Introduction

The rapid increase in global energy demand and the adverse impacts of fossil fuels on environmental sustainability have made the transition toward renewable energy sources imperative. Within this transformation, solar energy—particularly photovoltaic (PV) power systems—has gained a strategic position in ensuring energy supply security due to its clean, renewable, and inexhaustible nature [1]. However, the rapid expansion of the solar energy sector has introduced distinct occupational health and safety (OHS) risks across all phases, including installation, operation, maintenance, and decommissioning [2]. Unlike conventional energy production facilities, the installation and operation of PV systems involve a complex structure in which electrical hazards, working at height, physical strain, and environmental conditions are intertwined [3].

One of the most distinctive safety characteristics of PV systems is their continuous electricity generation as long as they are exposed to sunlight, making it difficult to fully de-energize them. This creates ongoing risks of electric shock and arc formation for installation teams, maintenance personnel, and emergency responders such as firefighters [4]. Particularly on the direct current (DC) side, insulation faults, loose connections, and the use of incompatible connectors constitute the main factors increasing the likelihood of fire incidents [5]. Moreover, the frequent installation of panels on rooftops or in challenging terrain exposes workers to additional hazards such as falls, slips, musculoskeletal strain, and ergonomic risks [6, 7].

In Türkiye, Law No. 6331 on Occupational Health and Safety imposes proactive obligations on employers to ensure worker safety and mandates systematic risk management practices [8]. Nevertheless, a review of the literature shows that a comprehensive, sector-specific regulatory framework for solar energy has not yet been fully established. Risk

management practices are predominantly guided by general OHS legislation and international standards (IEC, EN, etc.) [2, 9]. In this context, the effective implementation of risk assessment methods such as the L-Type and Fine-Kinney approaches, the training of qualified personnel (e.g., MYK Level 5), and the use of process-based checklists are of vital importance for preventing occupational accidents [10].

This study aims to identify OHS risks encountered throughout the life cycle of solar power plants (SPPs), analyze existing risk assessment approaches, and propose technical and administrative measures to enhance worker safety.

2. Materials and Methods

Lorem This study examines the management of occupational health and safety (OHS) risks throughout the life cycle of Photovoltaic (PV) power systems, including the planning, installation, commissioning, operation/maintenance, and decommissioning stages. The methodology employed in the study integrates national regulations (e.g., Occupational Health and Safety Law No. 6331), international standards (IEC, EN), and sector-specific risk analysis matrices. Within this framework, systematic data collection and conducting risk assessments based on these data are crucial for ensuring an effective OHS management system.

2.1. Data Collection Tools and Technical Equipment

The materials used in field operations and risk analyses include electrical measurement devices, personal protective equipment (PPE), and various digital monitoring technologies.

2.1.1. Personal Protective Equipment (PPE) and Safety Devices

In the installation, operation, and maintenance phases of solar power plants, personal protective equipment serves as a fundamental safety barrier in situations where engineering controls cannot completely eliminate hazards. The PPE used in this study is selected in accordance with the definition established by the Vocational Qualifications Authority (MYK), which describes PPE as “tools that protect against risks arising from the work performed and affecting the health and safety of employees” [13]. The equipment and their relevant standards are categorized below.

2.1.1.1 Protective Equipment for Electrical Hazards

PV systems continuously generate electricity as long as they are exposed to sunlight, making full system de-energization difficult. This condition necessitates the implementation of live working procedures and increases the risks of electric shock and arc-flash. For this reason, equipment meeting specific electrical safety standards is utilized.

Electrician Gloves (Class 0): During PV installation and maintenance, particularly on the DC side where voltage levels may reach up to 1000 V, Class 0 insulated gloves (1000V AC / 1500V DC rated) are used. These gloves provide adequate high-voltage protection while allowing the dexterity required for tool handling [6].

Face Shields and Arc-Protective Clothing: To protect against the high heat and explosive effects of potential electrical arcs caused by short circuits or connection faults, flame-resistant face shields are used. Ensuring compliance with the protection classes defined in TS EN 61140 is intended to minimize thermal burn risks [4].

Antistatic and Insulated Shoes: To prevent electrical current from flowing through the body to the ground, insulated and antistatic footwear is employed. As noted by Keçeci [6], such shoes provide secondary protection particularly against “step voltage” hazards.

2.1.1.2 Fall Protection Equipment for Working at Height

Since rooftop PV system installations are typically performed at heights exceeding 2 meters, falls constitute one of the most critical physical hazards.

Full Body Harnesses and Lifelines: Full Body Harnesses, which distribute the shock load across the body in the event of a fall and reduce the risk of spinal injury, are used instead of simple waist belts. These systems are integrated with fall-arrest mechanisms such as anchor points and rope grabs in accordance with EN 361 standards [6, 7].

Mobile Lifelines and Anchors: On rooftops with slopes ranging from 20° to 45°, mobile lifelines and fixed anchor systems are installed to ensure worker safety without significantly restricting mobility [6].

2.1.1.3 Head and Physical Protection Equipment

Due to risks such as falling objects, impacts, and various environmental hazards, the use of standardized basic physical protection equipment is essential in field operations.

Reinforced Safety Helmets: During installation activities, reinforced helmets with enhanced shock-absorbing properties are used to protect against impacts from lifted panels or dropped tools. Beny [5] emphasizes that such helmets must also have insulating properties to protect against accidental electrical contact.

Workwear and High-Visibility Clothing: In open-field areas or work zones involving vehicular or crane movement, high-visibility vests and UV-protective long-sleeved workwear are used to improve worker visibility and protection [7, 5].

2.2. Measurement and Monitoring Technologies

Several technological tools are used to detect risks early and verify the safety of PV systems:

Thermal Imaging: Thermal cameras or unmanned aerial vehicles (UAVs) equipped with thermal sensors are employed to detect loose connections, cable defects, and the formation of hotspots on PV modules. This technique plays a significant role in predicting and preventing fire risks [11].

Electrical Test Devices: During system commissioning and periodic inspections, calibrated devices capable of performing insulation resistance tests, open-circuit voltage measurements, and grounding continuity tests in compliance with IEC 62446-1 are used [4].Vivamus a tellus. Pellentesque habitant morbi tristique senectus et netus et malesuada fames ac turpis egestas. Proin pharetra nonummy pede. Mauris et orci. Aenean nec lorem.

2.3. Risk Assessment Methodology

Risk management in solar power plants (SPPs) involves the systematic identification of hazards, analysis of the likelihood that these hazards may materialize, and evaluation of the potential consequences. In this study, quantitative risk assessment was conducted using the L-Type (5×5) Matrix and Fine-Kinney methods. Both methods were applied in accordance with the Occupational Health and Safety Law No. 6331 and the TS 18001 Occupational Health and Safety Management System standard to determine the “acceptable risk” threshold and to establish appropriate action plans [9].

2.3.1. L-Type (5×5) Matrix Method and Application Examples

The L-Type Matrix is a practical evaluation method that enables rapid risk classification based on expert knowledge and the ability to establish cause–effect relationships. The risk score (R) is calculated using the formula:

R=O×SR = O \times SR=O×S

where *O* represents Likelihood and *S* represents Severity, each scored between 1 and The resulting scores are categorized as follows (Aycan, 2018):

1–6: Insignificant

8–12: Tolerable

15–20: Significant

25: Intolerable

Table 1 L-Type Matrix Evaluation Scale

Value	Likelihood (O)	Severity (S)
5	Very High (Daily)	Very Severe (Fatality, Permanent Disability)
4	High (Weekly)	Severe (Long-term treatment, Occupational disease)
3	Medium (Monthly)	Moderate (Treatable injury)
2	Low (Every 3 months)	Minor (No lost workday, First aid)
1	Very Low (Yearly)	Very Minor (No time loss)

(Source: Aycan, 2018; Dündar & Ertem, 2016)

Application Example: Panel Dropping During Manual Handling

Hazard: Manual handling of PV panels

Risk: Dropping the panel and worker injury

Likelihood (O): 5

Severity (S): 3

Risk Score (R): 15 (Significant Risk)

Conclusion: Immediate corrective action or suspension of work is required. Mechanical lifting equipment or handling procedures in line with the Manual Handling Regulation should be implemented [9].

2.3.2. Fine-Kinney Method and Application Examples

The Fine-Kinney method provides a more detailed assessment by incorporating the frequency of exposure into the calculation. The Risk Value (RV) is determined using:

RV=P×F×SRV = P \times F \times SRV=P×F×S

where *P* (Probability), *F* (Frequency), and *S* (Severity) are multiplied. The frequency factor ranges from **0.5 (Very Rare)** to **10 (Continuous)**. Risk values are classified as follows [12]:

< 20: Acceptable

20–70: Notable

70–200: Significant

200–400: High

> 400: Very High Risk

Application Example: Working Near a High-Voltage Line

Probability (P): 3

Frequency (F): 6

Severity (S): 40 (Fatality)

Risk Value (RV): 720 (Very High Risk)

Conclusion: Work must be stopped immediately, the line de-energized, and the area isolated [12].

2.4. Safe Work Method Statement (SWMS)

The installation, maintenance, and testing activities carried out in solar power plants (SPPs) are classified as forms of "high-risk construction work" due to their operational characteristics [7]. To ensure that such high-risk tasks are conducted safely, a formal document that identifies the work steps, potential hazards, associated risks, and the control measures required to mitigate these risks is prepared. This document is known as the Safe Work Method Statement (SWMS).

Beyond being a regulatory requirement, the SWMS serves as a safety agreement between site personnel and management, defining mutual responsibilities for safe work practices. The primary purpose of the SWMS is to identify hazards prior to the commencement of high-risk activities and to implement the most effective control measures that are **"reasonably practicable"** to eliminate or reduce risks to an acceptable level [7].

Accordingly, an SWMS outlines the scope of work, responsibilities, equipment to be used, environmental considerations, emergency procedures, competency requirements, and the application of the hierarchy of risk controls, thereby contributing to the establishment of a robust safety culture in solar energy system operations.

2.5. Personnel Competence and Certification Standards

Solar power plants (SPPs) contain both Low Voltage (LV) and High Voltage (HV) components within the same facility, making them complex technical environments that require a high level of professional competence. Therefore, the qualifications of personnel involved in installation, operation, and maintenance activities constitute a fundamental component of the risk assessment methodology. The key competence and certification requirements expected from technical personnel are outlined below.

2.5.1. EKAT Certificate (Authorization for Working on High-Voltage Electrical Installations)

In Türkiye, technical personnel working on high-voltage installations exceeding 1 kV are legally required to hold an EKAT certificate, as mandated by Article 60 of the Regulation on Electrical Power Installations. This certification verifies that personnel are competent in applying safe working procedures in HV environments, executing isolation–grounding protocols, and performing fault interventions correctly. Within the scope of this study, it is assumed that personnel working in transformer substations and overhead power lines have completed the **120-hour theoretical and practical training** provided by TEİAŞ or other authorized institutions [13, 14].

2.5.2. MYK Vocational Qualification Certificates

For personnel involved in the installation, assembly, and commissioning of photovoltaic systems, the national qualification **15UY0208-5 Photovoltaic Power Systems Personnel (Level 5)** defined by the Vocational Qualifications Authority (MYK) has been taken as a reference. This qualification framework requires personnel to demonstrate competence in:

applying occupational health and safety (OHS) procedures,

interpreting risk assessment results,

executing emergency response protocols,

performing technical installation tasks in accordance with standards [10].

These certification standards enhance the technical reliability and safety of all activities conducted within SPP sites and contribute to maintaining a high and sustainable level of OHS performance.

2.6. Energy Isolation Procedure: Lockout/Tagout (LOTO)

During maintenance and repair activities in solar power plants (SPPs), the unintentional re-energization of equipment poses a critical hazard that may lead to severe injuries or significant equipment damage. Therefore, under the framework of "Control of Hazardous Energy," the internationally recognized **Lockout/Tagout (LOTO)** procedure is implemented. LOTO is not merely the placement of a warning tag; rather, it is a physical isolation method that relies on individual lock mechanisms to prevent accidental re-energization [15].

In this study, maintenance operations were carried out using the standardized **six-step LOTO procedure**:

2.6.1. Preparation

Before initiating isolation, the type and magnitude of all energy sources—such as PV arrays, DC cabling, inverters, AC grid connections, and battery storage systems—are identified. This step is essential for selecting the appropriate isolation point.

2.6.2. Shutdown

The system is shut down in a controlled manner following manufacturer guidelines. Inverters, AC circuit breakers, and intermediate switches are turned off systematically.

2.6.3. Isolation

All devices enabling energy transmission (DC disconnect switches, AC breakers, fuse blocks) are set to the open position, physically interrupting energy flow.

2.6.4. Lockout/Tagout Application

Each authorized employee attaches **their personal lock** and identification **tag** to the isolation point. This ensures complete prevention of unauthorized re-energization and establishes individual responsibility for safe isolation.

2.6.5. Dissipation of Stored Energy

Any residual or stored energy—such as inverter capacitor charge, battery module energy, or capacitive charge in cables—is safely discharged or otherwise controlled [16].

2.6.6. Verification (Zero-Energy Test)

Prior to commencing work, the absence of electrical energy is verified using appropriate test instruments. This step is one of the most critical phases of the LOTO process, as a significant proportion of accidents occur when verification is neglected [15].

This procedure highlights that the presence of multiple energy sources in PV systems (DC/AC hybrid operation, battery storage units) makes the LOTO protocol both indispensable and highly sensitive to proper implementation.

3. Results and Discussion

Lorem ipsum dolor sit amet, consectetuer adipiscing elit. Maecenas porttitor congue massa. Fusce posuere, magna sed pulvinar ultricies, purus lectus malesuada libero, sit amet commodo magna eros quis urna. Nunc viverra imperdiet enim. Fusce est. Vivamus a tellus. Pellentesque habitant morbi tristique senectus et netus et malesuada fames ac turpis egestas. Proin pharetra nonummy pede.

This study analyzed the occupational health and safety (OHS) risks encountered during the installation, operation, and maintenance stages of solar energy systems. The findings were categorized under four main themes: electrical hazards, physical risks, fire safety, and chemical exposure.

3.1. Assessment of Electrical Risks: DC Arc and Electric Shock Hazards

The results indicate that the most critical hazard in photovoltaic (PV) systems arises from their "always on" operational nature. Unlike conventional AC systems, PV modules continue generating DC voltage as long as they are exposed to sunlight, making a complete Zero Energy State nearly impossible during emergencies or maintenance activities [4, 5].

The analysis demonstrates that DC arc flash is significantly more dangerous than AC arcing. While AC current naturally extinguishes at its 100 zero crossings per second (50 Hz), DC current lacks such a point, allowing arc temperatures to exceed 3000°C [17, 18]. These findings confirm the necessity of higher class protective equipment—such as Class 0 gloves and arc rated clothing—for personnel working on the DC side [6].

Field observations further show that a substantial proportion of PV fires result from the use of incompatible (cross mated) connectors. Connecting male and female MC4 connectors from different manufacturers leads to microscopic mechanical mismatches, increased contact resistance, and eventual arcing [4, 18].

3.2. Physical Risks and Working-at-Height Safety

Risk assessments conducted on rooftop PV installations confirm that falls from height are the most frequent type of accident. Findings indicate that roof slope directly influences the required preventive measures. On roofs with slopes between 20° and 45°, personal protective equipment (e.g., full body harnesses) alone is insufficient; instead, fixed anchor points, lifelines, and guardrail systems (collective protection) are essential [6].

Additionally, manual handling of PV panels introduces ergonomic risks, while wind load creates a "sail effect," potentially destabilizing workers. This highlights the need for real time monitoring of meteorological conditions—particularly wind speed—during installation planning [3, 4].

3.3. Fire Safety and Firefighter Intervention Strategies

One of the most critical findings concerns firefighters' reluctance to intervene in PV fires due to persistent DC voltage generation during daylight. Research indicates that safe intervention can be performed using a straight water stream from **20 feet (6 m)** or a fog nozzle from **5 feet (1.5 m)** [5].

Although shutting down the inverter's AC side removes grid power, voltage remains in DC conductors, demonstrating the necessity of **Rapid Shutdown systems** and **rooftop DC isolation switches** (Salmanoğlu & Korkmaz, 2024). Additionally, toxic materials released during panel combustion—such as cadmium telluride (CdTe) and lead (Pb)—pose significant chemical exposure risks to firefighters and nearby populations [2, 19].

3.4. Operational and Maintenance Findings

Thermal drone inspections conducted during operation reveal that **hotspots** are among the earliest indicators of fire risk. These localized temperature increases, caused by cell cracks or shading, can ignite the module's backsheet [1].

Another critical finding concerns the risk of **thermal shock** during cleaning. Spraying cold water onto hot panels leads to micro-cracks, reduced efficiency, and moisture ingress—ultimately causing insulation failures. Therefore, cleaning operations must be performed during **early morning or late evening**, when module temperatures are low [20].

4. Conclusion

This study demonstrates that occupational health and safety (OHS) standards in the rapidly growing solar energy sector must evolve in line with technological advancements. The findings reveal that photovoltaic (PV) systems, due to their "always-energized" nature, pose continuous and dynamic risks throughout installation, operation, and decommissioning stages.

One of the most significant results is that electrical hazards in PV systems differ fundamentally from those in conventional AC systems. Since direct current (DC) lacks a zero-crossing point, DC arcs do not self-extinguish and can reach temperatures exceeding 3000°C. This makes compliance with specialized standards such as NFPA 70E and IEC 62446 essential when selecting protective devices (AFCI, DC disconnect switches) and personal protective equipment (PPE) [4, 17]. Additionally, the integration of Rapid Shutdown technologies is crucial for ensuring safe firefighting operations during PV-related fires [1, 5].

Regarding human factors, the study shows that certifications such as EKAT and the national vocational qualifications issued by MYK are not merely regulatory formalities but constitute the most effective administrative controls for reducing human-error-related incidents [13, 10]. Fall-from-height incidents—frequently observed during installation—can be significantly reduced through proactive risk assessment methods (L-Type Matrix, Fine-Kinney) and the implementation of appropriate anchorage and fall-protection systems [2, 3].

In the operation and maintenance (O&M) phase, the use of remote-assessment technologies such as thermal drones and robotic cleaning systems enhances safety by enabling hazard detection without requiring personnel to enter high-risk DC arc boundaries [11, 21].

In conclusion, achieving the "zero-accident" objective in solar power plants requires not only regulatory compliance but also the adoption of the Prevention through Design (PtD) philosophy across the entire sector. In future projections, it is essential to establish a dedicated OHS regulatory framework tailored specifically to PV systems and for industry stakeholders to consider safety not as a cost factor but as a cornerstone of sustainability.

References

[1] Salmanoğlu, F., & Korkmaz, S. (2024). Fire risk in photovoltaic power systems: Prevention strategies and emergency action plans. International Fire Symposium and Exhibition with Participation, 1–14. İzmir.
[2] Uncu, G. (2022). Effectiveness of occupational health and safety practices in the solar energy sector [Master's thesis, Pamukkale University]. Pamukkale University Institute of Science.
[3] Acar, B., & Sönmez, İ. (2020). Occupational health and safety measures to be taken during the installation phase of solar power plants. Journal of Eastern Science (Doğu Fen Bilimleri Dergisi), 3(2), 95–108.
[4] yprus Turkish Chamber of Electrical Engineers (KTEMO). (2021). Application guide for grid-connected photovoltaic solar systems (M. Görgü, Trans.).
[5] Beny (2024, February 1). Understanding solar panel safety: Risks and preventive measures. https://www.beny.com
[6] Keçeci, A. (n.d.). Occupational health and safety in PV systems [Presentation]. TMMOB Chamber of Electrical Engineers.
[7] T WorkSafe. (2020). Information bulletin: Work health and safety requirements for solar PV installers (Version 1.0). Northern Territory Government.
[8] Yöntem Akademi. (2025, November 7). Duties and responsibilities of an OHS specialist – What does an occupational safety specialist do? https://www.yontemakademi.com.tr
[9] Dündar, U. U., & Ertem, M. A. (2016). Risk assessment guide for the installation of solar power plants. TMMOB Chamber of Mechanical Engineers Symposium Paper, Çankaya University.
[10] MYK (Vocational Qualifications Authority) (2022). Photovoltaic power systems personnel level 5 national qualification (Rev. No: 01, Ref: 15UY0208-5). (Original work published 2014 under the title IET Code of Practice for Grid Connected Solar Photovoltaic Systems.)
[11] SolarPower Europe. (2021). Operation & maintenance: Best practice guidelines (Version 5.0).
[12] Aycan, H. (2018). Risk analysis and assessment in solar power plants [Master's thesis, Süleyman Demirel University]. Isparta.
[13] Vocational Qualifications Authority (MYK). (2022). National qualification for photovoltaic power systems personnel, Level 5 (Rev. No: 01, Ref: 15UY0208-5).
[14] TEDAŞ. (2025, February 7). Who should apply for the EKAT certificate? TEDAŞ Training Portal.
[15] Vector Solutions. (n.d.). LOTO safety procedures: 6 steps for effective lockout tagout. https://www.vectorsolutions.com
[16] ABB. (n.d.). Lockout-Tagout procedures in 8 steps. https://new.abb.com
[17] ELEHUB. (2025, April 28). Explanation of DC arc flash: Risks and mitigation strategies. https://elehub.com
[18] Allianz Sigorta. (n.d.). Fire risks in solar panel (PV) systems. https://www.allianz.com.tr
[19] Beny. (2022, June 13). Firefighting and solar panels: Everything you need to know. https://www.beny.com
[20] Daxler Energy. (2025, October 2). How to clean solar panels? https://daxlerenergy.com
[21] Cleanerji. (n.d.). The importance of occupational safety in solar panel cleaning. https://cleanerji.com

Advances in Albumin-Based Nanocarriers: Novel Engineering Strategies and Functional Enhancements

Ferdane Danışman Kalındemirtaş[1], Betül Çicek[1]

[1]Department of Physiology, Faculty of Medicine, Erzincan Binali Yildirim University, Erzincan, Türkiye

* *Corresponding author E-mail: betul.cicek@erzincan.edu.tr*

Keywords

Albumin-based nanocarrier

Nanoparticles

Functional enhancement

Abstract

Albumin-based nanocarrier systems are increasingly gaining attention in cancer treatment due to their biocompatibility, long circulation times, and tumor-specific targeting capabilities. Albumin nanocarriers can be naturally taken up into tumor tissue via gp60 and SPARC-mediated mechanisms. Three-dimensional tumor models and in vivo studies demonstrate that albumin nanocarriers distribute within tumor tissue like a natural biomaterial, and conjugation with RGD, folate, transferrin, and aptamers significantly enhances cellular uptake. Furthermore, albumin nanocarriers enable tumor-specific drug delivery and significantly reduce systemic toxicity by exploiting their sensitivity to the tumor microenvironment (pH, ROS, and enzyme-sensitive nanocarriers). These controlled release strategies also offer advantages in overcoming multidrug resistance (MDR). Furthermore, albumin is highly successful in drug delivery in 3D tumor models and, when combined with imaging agents, becomes a multi-purpose carrier. All these features make albumin-based nanocarriers a strong clinical candidate for targeted, controlled drug delivery with reduced side effects and safe drug delivery systems.

1. Introduction

Rapid advancements in nanotechnology make it feasible to create drug delivery systems for cancer treatment that are safer, more effective, and specific to cancer cells. Due to the short half-life, poor bioavailability, systemic toxicity, and off-target effects of traditional chemotherapeutic agents, there is a greater need for biocompatible and functional nanocarriers. Albumin is one of the nanocarriers closest to clinical success, despite the fact that many other nanocarriers, including polymers, lipid-based carriers, inorganic nanoparticles, and proteins, are presently under investigation [1,2].

Albumin is a versatile protein used as a drug carrier and is a non-toxic, non-immunogenic, biocompatible, and biodegradable protein. As a result, it is thought to be the best material for creating drug-carrying nanoparticles. Albumin nanoparticles have garnered significant attention due to their high binding capacity and favorable tolerance in biological environments without significant adverse effects [3].

The primary effect of albumin-based drug delivery systems is related to tumor targeting and the ability to increase nanoparticle accumulation within tumors. For instance, an increased tumor accumulation is the consequence of an increased uptake, which is passively mediated by enhanced permeability and retention effects [4,5].

The most prevalent and durable blood protein, albumin, has unique characteristics as a carrier that can significantly improve the pharmacological activity of therapeutic payloads. Albumin has been demonstrated to accumulate inside the tumor environment or inflammatory tissues by receptor-mediated active transport, in addition to passive trafficking through increased permeability and retention effect. This makes albumin a suitable scaffold for targeted drug administration. Recently, it was shown that albumin scavenges amyloid-β and may be used to treat neurodegenerative illnesses. Albumin's hydrophobic binding pockets, conjugatable thiol residue, and surface-exposed N- and C-termini are all naturally helpful locations for transporting a variety of peptidyl and non-peptidyl medications. Albumin has long been used as a half-life extender, but it is now being used as a flexible drug carrier to help several therapeutic medicines with poor pharmacokinetics, targetability, solubility, and instability in vivo [4].

Tumor cells overexpress surface markers that are not found on normal cells. This helps distinguish cancer cells from non-target cells for ligand-directed targeting. However, tumor heterogeneity prevents the establishment of a clear model for a specific target marker. As a result, a subset of cancer cells remains untargeted during treatment, which

subsequently increases drug resistance and cancer recurrence. Along with the problems that arise in targeting cancer cells in cancer treatment, the search for suitable markers for effective targeted therapy continues in order to create new targets. Furthermore, to track and facilitate the targeting of cancer cells with more effective ligands, it is important to develop the therapeutic and diagnostic potential of different approaches, their underlying mechanisms, and the methods established for different nanocarrier systems in particular [4,6].

In particular, protein-based nanocarriers possess many positive characteristics compared to other nanocarriers and can be safely used in biological environments, making them more preferred than other nanomaterials. Albumin can bind to specific receptors overexpressed in cancer cells and enhance the binding and internalization of nanoparticles. Various tumors overexpress the 60 kDa glycoprotein (gp60) receptor [7] and also secrete the protein acidic and cysteine-rich (SPARC) [8]. Albumin can specifically bind to gp60 and SPARC and thus actively enhance nanoparticle uptake. This specific uptake mechanism prevents albumin-based nanoparticles from being excreted from tumor cells [9]. Furthermore, albumin is known to be rich in carboxyl and amino groups, which may allow for surface functionalization for active targeting. Therefore, albumin-based nanocarriers increase uptake by suppressing drug efflux and enhancing drug uptake into the cell, thereby increasing drug accumulation in the tumor and potentially overcoming cancer drug resistance [2]. It has been shown that the binding of nab-paclitaxel to the endothelium is 9.9 times higher than that of Cremophor EL-paclitaxel, and paclitaxel is transported 4.2 times more efficiently [2,9].

2. Surface-Functionalized Albumin Nanoparticles for Targeted Delivery

Also, the rich functional group structure of albumin enables chemical modifications, ligand immobilization, and adaptable drug release mechanisms. Thus, albumin-based NPs can be transformed into complex systems that include not only chemotherapeutic carriers but also imaging agents, biosensor modules, and responsive nano-mechanisms.

In recent years, active targeting techniques have been developed by conjugating ligands to multiple reactive sites on albumin. It has been demonstrated that the uptake of NPs bound to albumin modified with arginine-glycine-aspartic acid (RGD), folate, transferrin, aptamers. When targeting ligands are conjugated to the surfaces of albumin NPs, these ligands bind to specific receptors on the target cell surface, facilitating the uptake of nanoparticles into the cell via receptor-mediated endocytosis, thereby enhancing the passive EPR effect. This increases selectivity at the cellular level and accumulation within the cell.

Arginine-glycine-aspartic acid (RGD) peptides, and monoclonal antibody fragments is significantly increased by tumor cells. In one study, RGD-modified albumin NPs were shown to be internalized in tumors overexpressing integrin αvβIn the context of pancreatic cancer research, the integrin αvβ3 receptor has been identified as a critical target molecule in tumor progression. This receptor, expressed in pancreatic cancer cells, has been found to play a pivotal role in the development and progression of these tumors. Concurrently, albumin nanoparticles that had been modified with the arginine-glycine-aspartic acid (RGD) peptide, which demonstrated a high affinity for αvβ3, were developed, and a significant increase in cellular uptake was observed [10].

Similarly, aptamer-conjugated albumin NPs are noteworthy for their target specificity and low immunogenicity. Furthermore, it has been demonstrated that folic acid enhances the functional intracellular uptake of albumin NPs and exhibits minimal binding to hemoglobin, collagen, and other serum proteins. Consequently, all these developments support the idea that ligand selection can enhance the efficacy and selectivity of albumin-based carriers.

Additionally, studies conducted in three-dimensional (3D) cell cultures, which better reflect physiological conditions, report a significant increase in the penetration of albumin nanoparticles into tumors. Considering tumor stroma and extracellular matrix (ECM), albumin's potential to disperse as a natural compound makes it more advantageous in 3D models.

Combining albumin with synthetic or natural materials to create innovative composites for cardiac, neural, hard, and soft tissue engineering is another possible use. The globular albumin protein can now be electrospun thanks to recent material advancements, creating new opportunities for albumin-based scaffolds in cell treatment. Using serum albumin's superior biological, regulatory, manufacturing, and clinical properties, a number of reported technologies have already advanced to the clinical stage [11].

3. Stimuli-Responsive Albumin Nanocarriers

Albumin nanoparticles can be engineered to respond to tumor microenvironment-specific biochemical stimuli or exogenous triggers. This enables the control of drug release, reduction of systemic toxicity, and enhancement of therapeutic efficacy. Smart nanocarrier technologies based on albumin can accomplish targeted and regulated release in a way that is consistent with the pH of the tumor microenvironment. The bonds in pH-sensitive albumin-based nanocarriers can hydrolyze in the acidic tumor microenvironment, allowing the medicine to be released effectively at low pH [12] . Reactive oxygen species (ROS) are more prevalent in cancer cells than in healthy ones. ROS may readily

break the unique bonds that bind the medication to albumin in ROS-responsive albumin systems. Only the cancer cell releases the medication when these connections are broken by the elevated ROS level in the tumor cell. As a result, the medicine is delivered into drug-resistant cells (MDR) more easily and with greater effectiveness [13–15]. However, in enzyme-responsive albumin systems, the drug and albumin have unique peptide bonds that can be broken by enzymes like MMP-2 and MMP-9, which are abundant in the tumor area. The bonds are only broken and the medication is only released in the tumor because these enzymes are only active in the tumor. This greatly lowers off-target toxicity while safeguarding healthy tissues [16,17].

4. Conclusion

Albumin-based nanocarriers have the potential to overcome the limitations of traditional chemotherapeutics due to their biocompatibility, high drug-binding capacity, long half-life, and tumor targeting mechanisms as a natural compound. Both passive targeting (EPR effect) and active transport mechanisms via gp60 and SPARC increase the selective accumulation of albumin nanoparticles in tumor tissue, reducing systemic toxicity and increasing therapeutic efficacy.

Especially in recent years, with the development of functionalization strategies in compounds such as albumin, albumin has emerged as an important carrier in targeted therapy. Moreover, albumin is not only a drug carrier; it has also become an important bioplatform for imaging agents, sensor modules, ligands, aptamers, and immunotherapeutic molecules. Conjugations with RGD, folate, transferrin, and aptamers significantly increase cellular uptake, and three-dimensional tumor models and in vivo studies show that albumin nanocarriers distribute in tumor tissue like a natural biomaterial.

Furthermore, albumin nanocarriers provide tumor-specific drug delivery by utilizing their sensitivity to the tumor microenvironment (pH-, ROS-, and enzyme-sensitive nanocarriers), significantly reducing systemic toxicity. These controlled release strategies also offer advantages in overcoming multidrug resistance (MDR).

References

[1] Spada A, Emami J, Tuszynski JA, Lavasanifar A. The Uniqueness of Albumin as a Carrier in Nanodrug Delivery. Mol Pharm 2021;18:1862–https://doi.org/10.1021/ACS.MOLPHARMACEUT.1C00046.

[2] Hassanin I, Elzoghby A. Albumin-based nanoparticles: a promising strategy to overcome cancer drug resistance. Cancer Drug Resistance 2020;3:930–https://doi.org/10.20517/CDR.2020.68.

[3] Elzoghby AO, Samy WM, Elgindy NA. Albumin-based nanoparticles as potential controlled release drug delivery systems. Journal of Controlled Release 2012;157:168–https://doi.org/10.1016/J.JCONREL.2011.07.031.

[4] Rahimizadeh P, Yang S, Lim SI. Albumin: An Emerging Opportunity in Drug Delivery. Biotechnology and Bioprocess Engineering 2020 25:6 2020;25:985–https://doi.org/10.1007/S12257-019-0512-9.

[5] Elzoghby AO, Samy WM, Elgindy NA. Albumin-based nanoparticles as potential controlled release drug delivery systems. Journal of Controlled Release 2012;157:168–https://doi.org/10.1016/J.JCONREL.2011.07.031.

[6] Seidi F, Jenjob R, Crespy D. Designing Smart Polymer Conjugates for Controlled Release of Payloads. Chem Rev 2018;118:3965–https://doi.org/10.1021/ACS.CHEMREV.8B00006.

[7] Lee ES, Youn YS. Albumin-based potential drugs: focus on half-life extension and nanoparticle preparation. Journal of Pharmaceutical Investigation 2016 46:4 2016;46:305–https://doi.org/10.1007/S40005-016-0250-3.

[8] Vaz J, Ansari D, Sasor A, Andersson R. SPARC: A Potential Prognostic and Therapeutic Target in Pancreatic Cancer. Pancreas 2015;44:https://doi.org/10.1097/MPA.0000000000000409.

[9] Kratz F. A clinical update of using albumin as a drug vehicle — A commentary. Journal of Controlled Release 2014;190:331–https://doi.org/10.1016/J.JCONREL.2014.03.013.

[10] Ji S, Xu J, Zhang B, Yao W, Xu W, Wu W, et al. RGD-conjugated albumin nanoparticles as a novel delivery vehicle in pancreatic cancer therapy. Cancer Biol Ther 2012;13:206–https://doi.org/10.4161/CBT.13.4.18692;WGROUP:STRING:PUBLICATION.

[11] Kuten Pella O, Hornyák I, Horváthy D, Fodor E, Nehrer S, Lacza Z. Albumin as a Biomaterial and Therapeutic Agent in Regenerative Medicine. International Journal of Molecular Sciences 2022, Vol 23, Page 10557 2022;23:https://doi.org/10.3390/IJMS231810557.

[12] Aziz A, Sefidbakht Y, Rezaei S, Kouchakzadeh H, Uskoković V. Doxorubicin-loaded, pH-sensitive Albumin Nanoparticles for Lung Cancer Cell Targeting. J Pharm Sci 2022;111:1187–https://doi.org/10.1016/J.XPHS.2021.12.006.

[13] Fu S, Zheng A, Wang L, Chen J, Zhao B, Zhang X, et al. Tuneable redox-responsive albumin-hitchhiking drug delivery to tumours for cancer treatment. J Mater Chem B 2024;12:6563–https://doi.org/10.1039/D4TB00751D.

[14] Bhushan B, Gopinath P. Antioxidant nanozyme: a facile synthesis and evaluation of the reactive oxygen species scavenging potential of nanoceria encapsulated albumin nanoparticles. J Mater Chem B 2015;3:4843–https://doi.org/10.1039/C5TB00572H.

[15] Danışman-Kalındemirtaş F, Sert E, Kariper İA, Korkut IN, Erdem-Kuruca S. UV-synthesized albumin-based doxorubicin nanoparticles induce apoptosis and modulate leukemia surface markers while overcoming drug resistance. Naunyn-Schmiedeberg's Archives of Pharmacology 2025 2025:1–https://doi.org/10.1007/S00210-025-04803-7.

[16] Zhou K, Zhu Y, Chen X, Li L, Xu W. Redox- and MMP-2-sensitive drug delivery nanoparticles based on gelatin and albumin for tumor targeted delivery of paclitaxel. Materials Science and Engineering C 2020;https://doi.org/10.1016/j.msec.2020.111006.

[17] Li M, Zhao G, Su WK, Shuai Q. Enzyme-Responsive Nanoparticles for Anti-tumor Drug Delivery. Front Chem 2020;8:https://doi.org/10.3389/FCHEM.2020.00647/BIBTEX.

A Two-Stage Evaluation Model Based on LBWA for Evaluating KOSGEB Entrepreneurship Support Projects

Halil Barış Gezmiş[1,*], Elif Kılıç Delice[1]

[1] Industrial Engineering Department, Faculty of Engineering, Atatürk University, Erzurum, Türkiye

* *Corresponding author E-mail: halilbarisgezmis@hotmail.com*

Keywords

Entrepreneurship

KOSGEB

Project Evaluation

LBWA

Abstract

The proper allocation of public resources to entrepreneurial projects is critical for their efficient use. Because the use of public resources in the right projects also impacts economic growth, project evaluation processes must be conducted meticulously. This study proposes a two-stage evaluation model using the Level-Based Weight Assessment (LBWA) method to eliminate the subjectivity of the KOSGEB Entrepreneur Support Program's current evaluation system and to evaluate projects more accurately and consistently. The first stage of the model, the board evaluation, involved evaluations conducted by KOSGEB experts and academics based on seven main criteria and 23 sub-criteria. The second stage, the jury evaluation, evaluated projects that passed the first stage based on five main criteria and nine sub-criteria by jury members. The weightings of the criteria were determined using the LBWA method. Additionally, the contributions of the evaluators to the evaluation process were weighted differently, taking into account their opinions, professional experiences, and project evaluation expertise. As a result of the study, it was found that there was a significant divergence in the focus of the evaluator groups. Experts viewed the main criterion of "Technical Infrastructure and Experience" as more important in project evaluations, while academics prioritized "Economic and Strategic Contribution." Furthermore, based on LBWA method calculations, the main criterion of "Economic and Strategic Contribution" was determined to be the most important criterion in board evaluations, while the main criterion of "Entrepreneur Competence" was found to be the most important in jury evaluations. The study demonstrates that a delicate balance must be struck between the technical feasibility of projects and their economic and strategic contributions for the success of project evaluation processes. This study fills a significant gap in the literature as one of the pioneering applications of the LBWA method adapted to public support mechanisms in Turkey.

1. Introduction

Entrepreneurship, acting as a primary driving force of the global economy, plays a critical role in augmenting both economic growth and innovation capacity. Consequently, various grant and incentive schemes are implemented at the national level to support entrepreneurial initiatives. Small and Medium-Sized Enterprises Development and Support Administration (KOSGEB), one of the principal bodies administering these programs, operates as a public institution dedicated to facilitating the development of Small and Medium-sized Enterprises (SMEs) in Turkey and enhancing the competitive capabilities of such ventures.

The efficacy of support mechanisms administered by organizations such as KOSGEB is contingent not merely on the magnitude of allocated funds, but fundamentally on the capacity to objectively appraise the scientific, technical, and economic potentials of proposed projects. Nevertheless, the evaluation process for entrepreneurial projects entails an inherently high degree of complexity. Such assessments necessitate the simultaneous consideration of numerous criteria, including entrepreneur competence, technical feasibility, financial sustainability, market potential, and economic contribution. While the current evaluation framework employed within the KOSGEB Entrepreneur Support Program is functional in project scoring, it presents limitations regarding the comprehensive reflection of this multidimensional structure.

Specifically, the ambiguity regarding the precise weights of evaluation criteria, scoring discrepancies observed among evaluators, and procedural variations encountered during the two-stage (board and jury) process can be identified as

critical points requiring improvement in terms of system objectivity and efficiency. Consequently, the identified structural deficiencies and the imperative to enhance procedural objectivity necessitate the use of Multi-Criteria Decision Making (MCDM) methods that can rationalize criterion weighting.

MCDM methods serve as widely utilized analytical tools in the resolution of complex decision problems characterized by numerous conflicting criteria. Fundamentally, these methods execute the functions of weighting criteria, selecting the optimal alternative, and ranking alternatives according to their performance during the evaluation process. The determination of criterion weights constitutes one of the most critical phases directly influencing the accuracy and reliability of the decision-making framework. Within the literature, weighting methodologies are classified into objective, subjective, and integrated approaches, contingent upon the source and structure of the data employed.

In particular, the Level Based Weight Assessment (LBWA) method has secured a distinguished position among next-generation weighting techniques, primarily due to its capacity to yield reliable and objective weight values while necessitating a minimal number of pairwise comparisons, and its ability to transmute the subjective intuitions of decision-makers into a systematic structure.

A review of the extant literature reveals the absence of a comprehensive analytical study addressing the evaluation systematics of the KOSGEB Entrepreneur Support Program, one of Turkey's preeminent entrepreneurship support mechanisms. Specifically, the lack of clarity regarding evaluation criterion weights, variations among evaluators, and inconsistencies stemming from the two-stage (board and jury) process emerge as distinct factors limiting the system's efficacy.

Consequently, this study was undertaken to address this identified gap in the literature. The research aims to develop an integrated evaluation model designed to radically improve the evaluation systematics of the KOSGEB Entrepreneur Support Program and enhance objectivity. By introducing a methodological novelty to KOSGEB evaluation processes, the study targets the rendering of decision-making mechanisms into a more transparent, measurable, and balanced state.

Within the scope of the relevant literature, the comprehensive applicability of the LBWA method and its hybrid extensions in solving complex multi-criteria decision-making problems in multidisciplinary fields has been examined. The literature review conducted revealed a significant concentration in the field of transportation and logistics optimization in the use of this method, while also demonstrating its effectiveness in strategic assessments related to smart cities, renewable energy, and healthcare service performance. The LBWA method has been used in many areas and on various topics, including financial performance comparison, sustainable supply chain management, the integration of risk-focused energy planning, public administration, and the defense industry [1-19].

2. Materials and Methods

The precise determination of criterion weights within MCDM problems constitutes a factor of critical importance regarding the reliability and validity of the decision-making framework. In this context, the LBWA method, developed by Žižović and Pamučar [20], has been introduced to the literature as a novel weighting technique grounded in a subjective approach. The fundamental objective of the method is to transmute the intuitions of decision-makers into a systematic structure, thereby establishing the importance relationships among criteria in a rational and consistent manner. In particular, its capacity to generate reliable results with a minimal number of pairwise comparisons, coupled with its high practical applicability, distinguishes LBWA among next-generation weighting techniques [21].

The application steps of the LBWA method are as follows [20]:
Step Determining the most important criterion

The decision maker determines the most important criterion from the set of criteria

$$S = \{c_1, c_2, \dots, c_n\} \quad (1)$$

Step Grouping criteria according to their level of importance

At this stage, level sets of criteria are created.

Step Assigning integer values to criteria

Each criterion is assigned an integer value based on its level of importance. The most important criterion is always assigned a value of ‘0’. Criteria of lower importance are assigned values such as 1, 2, 3 in ascending order.

The following equality is satisfied such that r is a maximum integer.

$$r = maks\ \{|s_1|, |s_2|, \dots\dots, |s_k|\} \quad (2)$$

Step Determining the flexibility coefficient

The flexibility coefficient r_0 is determined such that it is greater than r: r_0>r, $r_0 \in$

Step Calculation of impact functions

The impact value of each criterion is calculated using Equation (2):

$$f(c_{i_P}) = \frac{r_0}{i \cdot r_0 + I_{i_P}} \quad (3)$$

r_0: Flexibility coefficient

i: Level order

I_{i_P}: Represents the integer value assigned to the criterion.

Step Calculating the weights of the criteria

First, the weight of the most important criterion is calculated using Equation (3).

$$w_i = \frac{1}{1+f(c_2)+\cdots+f(c_n)} \quad (4)$$

Subsequently, the importance weights of the other criteria are calculated using Equality (5).

$$w_j = f(c_j).w_i \quad (5)$$

3. Results and Discussion

A suggested and implemented two-stage evaluation model based on LBWA was designed to enhance the current evaluation method of the KOSGEB Entrepreneurship Support Program. The model consists of a board evaluation and a jury evaluation stages. For the evaluators who took part in the board and jury evaluations, a weighting process was carried out according to certain standards. For the evaluation process, three different examinations were given to the jury, academics, and KOSGEB personnel. The evaluator's prior participation in entrepreneurship evaluations and professional experience form the basis of this weighting mechanism. Accordingly, the weight values obtained for Expert 1, Expert 2, Expert 3, Academician 1, and Academician 2 are 0.25, 0.49, 0.26, 0.31, and 0.69, respectively. The values for Jury 1, Jury 2, and Jury 3 are 0.44, 0.26, and 0.30, respectively.

3.1. Stage Board Evaluation Question Weighting Using the LBWA Method

The board evaluation phase utilized the inquiry set contained within the Board Evaluation form, which is accessible via the official KOSGEB Entrepreneur Support Program portal, to assess entrepreneurial projects. This phase encompasses twenty-three distinct questions dedicated to project content scrutiny. Additionally, two specific items are designated for the examination of the project in terms of form and documentation.

Table 1 Categorisation of board assessment questions

Main Category	Question Numbers	Category Description
c_{b1}- Entrepreneur and Business Profile	1,2	The project owner's and/or team's knowledge base and experience in the sector.
c_{b2}-Project Objectives and Strategies	3,4,5,6	The alignment and feasibility of the project's objectives, targets and activities with the business strategy.
c_{b3}-Technical Infrastructure and Competence	7,8,9,11,15	The level of technical infrastructure and personnel suitability required for the project.
c_{b4}-Financial Structure and Budget Management	10,12,19	The financial sustainability of the project and the efficient use of resources.
c_{b5}-Risk Management and Sustainability	13,14	Measures taken against project risks and long-term sustainability plans.
c_{b6}-Innovation and Added Value	16,17,18,20	The project's potential to bring innovation to the sector, generate solutions to problems and be applicable in different areas.
c_{b7}-Economic and Strategic Contribution	21,22,23	The project's potential contribution to the national economy and its potential to reduce external dependency.

The twenty-three questions addressing project content were subjected to a detailed analysis. From the perspective of evaluation systematics, the categorization of these inquiries was deemed appropriate to ensure a coherent assessment structure. For this purpose, seven distinct categories, the details of which are delineated in Table 1, were defined within the scope of the study.

The process of weighting the criteria was initiated after the project evaluation questions were categorized. While the categories presented in Table 1 were determined as the main criteria, the questions forming these main categories were determined as sub-criteria. After weighting the main criteria using the LBWA method, the sub-criteria were weighted and the resulting weights were used to determine the maximum points to be awarded to the criteria, i.e., the evaluation questions. As a result, a two-level weighting structure was obtained, encompassing both the main criterion level and the sub-criterion level. However, due to page limitations in this study, only calculations and results for the main criteria are presented.

The application steps of the LBWA method for Expert 1 are explained below. Similar steps were applied to other evaluators to determine the criteria weights.

Step Determining the most important criterion

Step 1 aims to determine the most important criterion. According to Expert 1's response, c_{b3} was found to be the most important criterion.

Step Grouping criteria according to their level of importance

In this step, Level 1 and Level 2 criterion groups were created. The level groups have been determined according to the level of importance determined by the evaluator.

$S_1 = \{c_{b3}, c_{b1}, c_{b4}, c_{b6}, c_{b7}\}$

$S_2 = \{c_{b2}, c_{b5}\}$

Step Assigning integer values to criteria

The value of 'r', which is the maximum number of elements in the level set, was found to be 5 using Equation (2). Furthermore, a comparison was made based on the importance levels of the criteria in Step As a result, whole numbers were assigned to the criteria. In the application of the method, the value ‘0’ was assigned as the whole number for the most important criterion specified.

Level 1 integer assignments;

$I_3 = 0$, $I_1 = 3$, $I_4 = 1$, $I_6 = 2$, $I_7 = 4$

Level 2 integer assignments;

$I_2 = 2$, $I_5 = 1$

Step Determining the flexibility coefficient

In this step, as r_0 >5, the value of r_0 has been set to 6.

Step Calculation of impact functions

The impact functions were calculated using Equation (3) as shown in Table 2.

Table 2 Effect function table

Level 1 - Effect Functions	f(c_{b3})	1.000
	f(c_{b1})	0.667
	f(c_{b4})	0.857
	f(c_{b6})	0.750
	f(c_{b7})	0.600
Level 2 - Effect Functions	f(c_{b2})	0.429
	f(c_{b5})	0.462

Step Calculating the weights of the criteria

First, the weight of the most important criterion was determined using Equation (4). Later, the weights of the other criteria were calculated using Equation (5). The calculated criterion weights are presented in Table 3.In the current

evaluation system, the questions in Table 1 are evaluated out of 100 points, while in this study, they are evaluated out of 80 points. An additional 20 points in the current and proposed model are allocated for the formal evaluation of the project. 80 points were distributed among the criteria, taking into account the criterion weights. Thus, the maximum points to be awarded for the questions represented by the criteria have been determined. Table 3 shows the scores for the criteria. Additionally, when determining the weighted score for expert 1, the weight value assigned to expert 1 (0.25) was multiplied by the criterion weights.

Table 3 Criteria weights and scores determined for expert 1

Criteria weights	w_{b1}	w_{b2}	w_{b3}	w_{b4}	w_{b5}	w_{b6}	w_{b7}
	0.140	0.090	0.210	0.180	0.097	0.157	0.126
Criteria scores	c_{b1}	c_{b2}	c_{b3}	c_{b4}	c_{b5}	c_{b6}	c_{b7}
	11.20	7.20	16.79	14.39	7.75	12.59	10.08
Expert weighted scores	c_{b1}	c_{b2}	c_{b3}	c_{b4}	c_{b5}	c_{b6}	c_{b7}
	2.8	1.80	4.20	3.60	1.94	3.15	2.52

In the computation of the final aggregate score, a weighting distribution of 60% for KOSGEB experts and 40% for the academic group was implemented. This special allocation was deemed appropriate based on the operational expertise of KOSGEB experts in the entire life cycle management of entrepreneurship projects, covering the stages of examination, evaluation, control, and monitoring. The results obtained are presented in Table 4.

Table 4 Final scores of criteria for board evaluation

Criteria	c_{b1}	c_{b2}	c_{b3}	c_{b4}	c_{b5}	c_{b6}	c_{b7}
Expert weighted score total	8.71	4.89	9.45	5.69	4.31	7.04	7.90
Academic weighted score total	3.04	2.53	2.91	3.33	4.67	7.46	8.06
Final scores	11.75	7.42	12.37	9.02	8.98	14.51	15.95
Modified scores	12	7	12	9	9	15	16

Table 4 shows that the c_{b1} criterion represented questions had scores ranging from 0 to 11.Experts or academics may find it challenging to assign a value within this range. As a result, the criterion scores obtained using the LBWA method were rounded to 80 points to obtain modified scores. In this instance, the two questions listed in Table 1 and contained in criterion c_{b1} should be assessed using maximum 12 points.

Stage Jury evaluation question weighting using the LBWA method

The questions in the Jury Evaluation form on KOSGEB's website were used to evaluate the entrepreneurial projects included in the jury evaluation stage. This stage comprises ten distinct questions dedicated to the review of project content, the evaluation of which is conducted on a 100-point scale. The ten items contained within the jury evaluation form were subjected to a comprehensive analysis. From the perspective of evaluation systematics, the categorization of these inquiries was deemed appropriate to facilitate a structured assessment. To this end, five distinct categories, the particulars of which are delineated in Table 5, were defined within the scope of the study.

Table 5 Categorisation of jury assessment questions

Category	**Question Number**	**Category Description**
c_{j1}-Entrepreneurial Competence	1,2	The entrepreneur's command of the project and presentation skills.
c_{j2}-Project Specifications	3,4,5	The originality of the project, its potential solutions for the sector, and its feasibility.
c_{j3}-Financial and Marketing Aspects	6,7,8	The financial sustainability of the project, its potential in local and foreign markets, and its contribution.
c_{j4}-Business and Growth Potential	9	The project's impact on the business's growth potential and development.
c_{j5}-Overall Assessment	10	General opinion and conclusion about the project.

Similar steps to those in the board evaluation procedure were applied at this stage as well, and the criteria scores obtained for jury evaluation were as shown in Table Additionally, the weight value assigned to each jury member was taken into account when determining the weights of the criteria.

In the current evaluation system and proposed model, the questions in Table 5 are evaluated out of 90 points. An additional 10 points in the current and this model are allocated for c_{j5}. 90 points were distributed among the criteria, taking into account the criterion weights. Thus, the maximum points to be awarded for the questions represented by the criteria have been determined.

Table 6 Final scores of criteria for jury evaluation

Main Criterion	c_{j1}	c_{j2}	c_{j3}	c_{j4}
Jury 1	30.92	24.73	20.61	13.74
Jury 1 weighted score	13.60	10.88	9.07	6.05
Jury 2	34.52	14.79	25.89	14.79
Jury 2 weighted score	8.98	3.85	6.73	3.85
Jury 3	13.14	23.65	29.56	23.65
Jury 3 weighted score	3.94	7.09	8.87	7.09
Weighted Total Scores	26.52	21.82	24.67	16.99
Modified Weighted Total Scores	26	22	25	17

As seen Table 6, the criterion scores obtained using the LBWA method were rounded to 90 points to obtain modified scores. In this instance, the two questions listed in Table 5 and contained in criterion c_{j1} should be assessed using maximum 26 points.

4. Conclusion

This study centered upon addressing the structural deficiencies inherent within the existing evaluation systematics of the KOSGEB Entrepreneur Support Program and proposed an innovative, integrated model utilizing the LBWA method to remedy these limitations. The issue of criterion weight ambiguity, arising from the absence of any explicit weighting explanation regarding score distribution in the current system, has been effectively resolved through the application of the LBWA method. By restructuring subjective evaluations into rational and transparent weight coefficients, this model has fortified the objectivity of the evaluation framework.

Upon examination of the empirical findings obtained regarding the board evaluation stage, it is evident that the evaluators (experts and academics) prioritized macro-objectives. As a result of the analysis, the "Economic and Strategic Contribution" criterion was determined to be the main criterion with the highest weight, followed by the "Innovation and Added Value" criterion. This circumstance reveals that in the board phase, the potential contribution of the project to the national economy and its effect on reducing import dependency are the determinant factors, rather than the technical details of the project.

When we look at the focus of the findings obtained from the jury evaluation stage, a clear criterion stands out. As a result of the evaluations by the jury members, the "Entrepreneurial Competence" criterion ranked first, surpassing all other criteria. The fact that the "Financial and Marketing Aspects" criterion took second place in the jury evaluation serves as proof that the sustainability of the project is viewed as more critical than its technical specifications.

These obtained results demonstrate that the proposed two-stage model establishes a balanced structure that complements one another. While the board stage audits the project's "strategic fit," the jury stage measures the entrepreneur's "implementation capacity." Contrary to the ambiguity in the current system, with this study, the mathematical weight of each criterion in the system has been clarified, and the impact of decision-makers (KOSGEB personnel and academics) on the process has been optimized according to their areas of expertise. Consequently, the developed two-stage evaluation model based on LBWA is presented to the literature and practice as a decision support mechanism that enhances transparency, accountability, and strategic focus in the process of allocating public resources to the most appropriate projects.

References

[1] Adalı, E. A., Öztaş, G. Z., Öztaş, T., & Tuş, A. (2022). Assessment of European cities from a smartness perspective: An integrated grey MCDM approach. Sustainable Cities and Society, 84, https://doi.org/10.1016/j.scs.2022.104021

[2] Ayough, A., Shargh, S. B., & Khorshidvand, B. (2023). Utility Additive Method and Base-Criterion Method: A new approach for assessing supplier selection criteria. Expert Systems With Applications, 221, https://doi.org/10.1016/j.eswa.2023.119740

[3] Biswas, S., Pamučar, D., Božanić, D., & Halder, B. (2022). A new spherical Bulanık LBWA-MULTIMOOSRAL framework: Application in evaluation of leanness of MSMEs in India. Mathematical Problems in Engineering, 2022, 1–https://doi.org/10.1155/2022/5480848

[4] Božanić, D., Pamučar, D., Badi, I., & Tešić, D. (2023). A decision support tool for oil spill response strategy selection: Application of LBWA and Z MABAC methods. Opsearch, 60(1), 24–https://doi.org/10.1007/s12597-022-00605-0

[5] Božanić, D., Ranđelović, A., Radovanović, M., & Tešić, D. (2020). A hybrid LBWA - IR-MAIRCA multi-criteria decision-making model for determination of constructive elements of weapons. Facta Universitatis, Series: Mechanical Engineering, 18(3), 399–https://doi.org/10.22190/FUME200528033B
[6] Demir, G. (2020). LBWA method. In H. Bircan (Ed.), Criteria weighting methods in multi-criteria decision-making problems (pp. 137–158). Nobel Academic Publishing.
[7] Deveci, M., Özcan, E., John, R., Covrig, C.-F., & Pamucar, D. (2020). A study on offshore wind farm siting criteria using a novel interval-valued Bulanık-rough based Delphi method. Journal of Environmental Management, 270, Article https://doi.org/10.1016/j.jenvman.2020.110916
[8] Dündar, S., & Karadağ, İ. (2024). Selection of a Facility Location for a Cosmetics Company by Integrated F-LBWA and I-RAWEC Methods. International Journal of Bulanık Systems. https://doi.org/10.1007/s40815-024-01960-4
[9] Ecer, F., Pamucar, D., Mardani, A., & Alrasheedi, M. (2021). Assessment of renewable energy resources using new interval rough number extension of the level based weight assessment and combinative distance-based assessment. Renewable Energy, 170, 1156–https://doi.org/10.1016/j.renene.2021.02.004
[10] Ersoy, N. (2022). Comparative analysis of MCDM methods for the assessment of ICT development in G7 countries. Kafkas University Journal of Economics and Administrative Sciences Faculty, 13(25), 55-73.
[11] Özekenci, E. K. (2023). Assessing the logistics market performance of developing countries by SWARA-CRITIC based CoCoSo method. Logforum, 19(3), https://doi.org/10.17270/J.LOG.2023.857
[12] Pamučar, D., Behzad, M., Božanić, D., & Behzad, M. (2021). Decision making to support sustainable energy policies corresponding to agriculture sector: Case study in Iran's Caspian Sea coastline. Journal of Cleaner Production, 292, 125302.
[13] Pamučar, D., Deveci, M., Canıtez, F., & Lukovac, V. (2020). Selecting an airport ground access mode using novel Bulanık LBWA-WASPAS-H decision making model. Engineering Applications of Artificial Intelligence, 93, Article https://doi.org/10.1016/j.engappai.2020.103703
[14] Pamučar, D., Gokasar, I., Torkayesh, A. E., Deveci, M., Martinez, L., & Wu, Q. (2023). Prioritization of unmanned aerial vehicles in transportation systems using the integrated stratified Bulanık rough decision-making approach with the hamacher operator. Information Sciences, 622, 374–https://doi.org/10.1016/j.ins.2022.11.143
[15] Pamučar, D., & Görçün, Ö. F. (2022). Evaluation of the European container ports using a new hybrid Bulanık LBWA-CoCoSo'B techniques. Expert Systems With Applications, 203, https://doi.org/10.1016/j.eswa.2022.117463
[16] Pawlewicz, K., & Cieślak, I. (2022). The Use of Level Based Weight Assessment (LBWA) for Evaluating Public Participation on the Example of Rural Municipalities in the Region of Warmia and Mazury. Sustainability, 14, https://doi.org/10.3390/su142013612
[17] Torkayesh, A. E., Pamucar, D., Ecer, F., & Chatterjee, P. (2021). An integrated BWM-LBWA-CoCoSo framework for evaluation of healthcare sectors in Eastern Europe. Socio-Economic Planning Sciences, 78, https://doi.org/10.1016/j.seps.2021.101052
[18] Yazdani, M., Pamucar, D., Chatterjee, P., & Torkayesh, A. E. (2022). A multi-tier sustainable food supplier selection model under uncertainty. Operations Management Research, 15, 116–145.
[19] Ye, Y., Lin, H., & Zhang, C. (2023). Research on effective asset risk assessment of power grid enterprises based on LBWA-Vague set. In Proceedings of 2023 IEEE/IAS Industrial and Commercial Power System Asia (I&CPS Asia), 50–54.
[20] Žižović, M., & Pamučar, D. (2019). New model for determining criteria weights: Level Based Weight Assessment (LBWA) model. Decision Making: Applications in Management and Engineering, 2(2), 126–https://doi.org/10.31181/dmame1902102z
[21] Yılmaz Özekenci, S. (2024). Financial performance measurement of companies in the BIST Sustainability 25 Index with LBWA and MEREC-based CRADIS Methods. Çağ University.

Data-Driven Quality Control in Iron and Steel Production: Evaluating the Impact of Carbon Content and Process Parameters Using Machine Learning

Hümeyra Ulaş[1], Tuba Irmak[2*]

[1] Department of Industrial Engineering, Faculty of Engineering, Atatürk University, Erzurum, Türkiye

* *Corresponding author E-mail: tuba.adar@atauni.edu.tr*

Keywords

Machine Learning

Steel Production

Quality Control

Process Parameters

Carbon Analysis

Abstract

High-quality steel production is influenced by numerous factors, including chemical composition (particularly carbon content), process parameters (heat-treatment durations, charge amounts, preheating values), scrap quality, and the control mechanisms utilized during the production cycle. The relationships among these variables and the impact of process parameters on steel quality can be identified using machine learning methods. This study presents a data-driven approach for determining steel quality classes by using three months of steel production data obtained from a manufacturing company in Türkiye. The operational dataset consists of 38 variables, including preheating values, scrap charge information, process durations, and chemical composition measurements. On the raw dataset, missing-value analysis, removal of inconsistent records, scaling of numerical variables, encoding of categorical variables, and splitting into training (80%) and test (20%) sets were performed. Ultimately, machine learning models—Support Vector Machine (SVM), Light Gradient Boosting Machine (LightGBM), Extreme Gradient Boosting (XGBoost) and Random Forest (RF)—were trained using 3,817 observations to predict steel quality classes (B420 – S220). The results indicated that the quality class was clearly separated by the carbon content in the chemical composition; when carbon analysis values were included in the models, RF, XGBoost, LightGBM, and SVM all achieved 100% accuracy and AUC = 1.This finding demonstrates that carbon content is the primary determinant of the quality decision. To further examine the effect of carbon, the carbon variable was removed from the dataset, and the models were retrained using 5-fold cross-validation. In this case, the accuracy of tree-based methods decreased to approximately 86%, while the SVM model achieved 65% accuracy. ROC analyses performed without cross-validation showed that AUC values ranged between 0.93 and 0.95 in the absence of the carbon variable. This indicates that process parameters contribute to quality classification to a certain extent.

1. Introduction

Global steel production began in the 1800s and has now exceeded 1 billion tons. A rapid increase in steel output was observed between 1950 and 1970; thereafter, up to the 2000s, production followed a more moderate growth trend accompanied by fluctuations [1]. Türkiye is the second-largest steel producer in Europe and the seventh-largest worldwide, and the iron and steel sector plays a strategic role in the national economy by supplying inputs to numerous industries, including automotive, construction, machinery, and durable consumer goods. Steel production is widely regarded as a cornerstone of industrialization processes and infrastructure investments.

Iron and steel production in Türkiye started in 1928 with the establishment of the Machinery and Chemical Industry Corporation (MKE) in Kırıkkale to support the defense industry. Following MKE's initial operations for military purposes, Karabük Iron and Steel Works (Kardemir) was founded in 1939 as Türkiye's first integrated iron and steel plant. While Kardemir focused on long product manufacturing, the increasing demand for flat steel led to the commissioning of Ereğli Iron and Steel Works (Erdemir) in 1965, initiating flat steel production. Another integrated facility, İskenderun Iron and Steel Works (İsdemir), was established in 1977 and later became part of the Erdemir Group in These plants represent integrated iron and steel production structures capable of processing primary raw materials, such as iron ore, into final products [2].

The quality of steel produced in these plants directly influences the performance, durability, and reliability of final products, thereby determining manufacturers' competitiveness and customer satisfaction. Producing high-quality steel is critical in terms of both cost-effectiveness and sustainability. In modern secondary steelmaking facilities operating through scrap procurement and control, electric arc furnace (EAF) melting, ladle metallurgy, and continuous casting processes, the production of high-quality steel billets is closely associated with the chemical and physical properties of steel [3].

Steel quality is influenced by a wide range of factors, including chemical composition (particularly the carbon content), process parameters (e.g., heat-treatment durations, charge amounts, and preheating conditions), scrap quality, and control mechanisms throughout the production process. Monitoring and optimizing these factors are essential for improving the effectiveness and efficiency of quality control procedures.

In this context, this study employs machine learning models to determine steel quality in an automated, data-driven manner. The main objective is to develop a data-driven quality prediction model for the production line by analyzing the chemical composition and process parameters that are influential in identifying the steel grade (B420–S220) within the iron–steel manufacturing process. To this end, three months of operational data collected from an iron and steel plant located in Hatay, Türkiye, were used to train Random Forest, XGBoost, LightGBM, and SVM models, and the resulting models were utilized to predict the quality grade of the produced steel. The research questions investigated in this study are as follows:

RQ1: To what extent can machine learning models predict steel quality classes with high accuracy?

RQ2: Which variables are the most influential in determining the quality grade in iron and steel production?

RQ3: How does classification performance change when carbon analysis is included in the model versus when it is excluded?

When studies employing machine learning methods in the iron and steel sector are reviewed, the literature is seen to focus on a range of problem domains. For instance, prior work has addressed forecasting future values of iron and steel imports [4], predicting employee turnover risk in the sector [5], and modeling the relationship between the iron and steel industry, economic growth, and air pollution [6]. With respect to steel quality, to the best of the authors' knowledge, there is no study aligned with our approach that aims to directly determine the "steel quality grade" from production process data. Nevertheless, there are studies that focus on mechanical behavior parameters that indirectly represent quality. Shahen et al. [7] developed an artificial neural network (ANN)-based model to predict the strength degradation of high-strength steels exposed to elevated-temperature conditions such as fire. Assuming that not only temperature but also the chemical composition of steel (e.g., C, Si, Mo, Ni) could be a key determinant of this degradation, they compiled a total of 366 data points from 19 studies reported in the literature. In their model, temperature and chemical composition values (and, where applicable, holding time) were used as input variables, while the output variables were reduction factors for mechanical properties such as ultimate tensile strength, yield strength, 0.2% proof strength, and elastic modulus. Although this study demonstrates the applicability of machine learning in the context of steel quality, it does not focus on directly classifying the quality grade of produced steel, as addressed in the present work.

In their study, Li et al. [8] proposed a quality prediction system driven by real-world plant data to overcome the time and cost disadvantages of laboratory-test-based quality control in steel production. The problem was formulated as a regression task, and a solution was developed using ensemble learning approaches that combine multiple algorithms on historical production data. In a related work, Wang et al. [9] argued that many existing approaches for product quality prediction in the iron and steel industry remain "manually designed" and often rely solely on macro-scale data (e.g., process parameters) while neglecting meso-scale information (e.g., grain structure) that may significantly affect quality, which can limit accuracy and generalizability in practice. To address this limitation, they proposed the MOCNNEL-MSDF method, which constructs a dataset enriched via multi-scale (macro/meso) data fusion, develops 1D-CNN-based models through multi-objective evolutionary search, and then derives the final predictor using a sparse ensemble. They reported competitive and improved accuracy and robustness on both benchmark datasets and practical continuous annealing processing line (CAPL) data, suggesting that the approach can be generalized to different iron and steel processes.

A key aspect that differentiates this study from similar quality classification works in the literature is that, beyond reporting high accuracy, it experimentally isolates which variable(s) predominantly "carry" the quality decision. In particular, after demonstrating that the carbon variable in the chemical composition can almost perfectly separate the quality classes on its own, the models were retrained with carbon removed from the dataset, allowing the contribution of process parameters to quality prediction to be quantitatively assessed under a separate scenario.

The remainder of this paper is organized as follows. Section 2 describes the dataset, data preparation steps, the machine learning models employed, and the evaluation strategy. Section 3 presents the experimental findings and compares

the performance obtained with and without the carbon analysis variable. Finally, Section 4 summarizes the study, highlights the main conclusions, and outlines directions for future work.

2. Materials and Methods

In this section, we present the scope and main characteristics of the dataset compiled from process data, chemical composition measurements, and analysis results obtained from the steel production line for model training. Next, the machine learning methods used to predict the steel quality grade—Support Vector Machine (SVM), Light Gradient Boosting Machine (LightGBM), Extreme Gradient Boosting (XGBoost), and Random Forest (RF)—are introduced, and the rationale for employing these models in the classification task is explained. Finally, the SHAP (SHapley Additive exPlanations) approach is summarized as an interpretability technique used to quantify the relative contributions of features to the quality classification decision; specifically, it is described how SHAP-based importance/weight values are utilized to assess the impact of factors affecting steel quality.

2.1. Dataset

The dataset used in this study was obtained from a steel manufacturing plant operating in Türkiye and includes three months of production records from an electric arc furnace (EAF) steelmaking process. It has an integrated operational structure consisting of process parameters monitored along the production line, product-level chemical analysis measurements, and production performance indicators related to the process. The dataset comprises a total of 3,817 observations, with the target variable (quality grade) defined as a binary category; 1,958 observations belong to the B420 quality grade. The independent variables used in the modeling stage consist of 38 features representing information from different stages of the production process. Detailed definitions and descriptions of these features are provided in Table 1.

Table 1 Summary of input features and target variable (operational, process, and chemical composition)

Features	**Description**	**Unit**	**Features**	**Description**	**Unit**
Ebat	Dimension profile of the produced steel product (e.g., 150×12, 130×12)	mm	D.Gaz (Nm3/t)	Other gas consumption (per ton)	Nm³/ton
On_Isıtma_Suresi	Preheating duration	minute	Sure (dk)	Total operation duration	minute
On_Isıtma_Giris_Sicaklik	Preheating inlet temperature	°C	PO_Enerji (kWh)	Ladle Furnace (LF) energy consumption	kWh
On_Isıtma_Cikis_Sicaklik	Preheating outlet temperature	°C	PO_Enerji (kWh/t)	LF energy consumption (per ton)	kWh/ton
Hurda_Sarj_Sayisi	Number of scrap charges	count	CCM_Sure (dk)	Continuous Casting Machine (CCM) duration	minute
Hurda_Tonaj	Scrap tonnage used	kg	FeSi (kg)	Ferrosilicon addition amount	kg
Hurda_Verim	Scrap yield / efficiency	%	SiMn (kg)	Silicomanganese addition amount	kg
Std_ad	Number of standard products	count	C (kg)	Carbon addition amount	kg
Std_kg	Standard product weight	kg	Kirec (kg)	Lime addition amount	kg
Kutuk_Std_Disi_mt	Off-standard billet length	meter	CaF2 (kg)	Calcium fluoride addition amount	kg
Kutuk_Std_Disi_kg	Off-standard billet weight	kg	Enjekte C (kg)	Injected carbon amount	kg
TTT (dk/dok)	Total turnaround/throughput time (per casting)	min/cast	Analiz_C	Carbon (C) percentage	%
P.ON (dk/dok)	Planned preheating time (per casting)	min/cast	Analiz_Si	Silicon (Si) percentage	%
Ariza (dk/dok)	Downtime due to failures (per casting)	min/cast	Analiz_Mn	Manganese (Mn) percentage	%
Proses (dk/dok)	Process time (per casting)	min/cast	Analiz_P	Phosphorus (P) percentage	%
EAO_Enerji_kWh	Electric Arc Furnace (EAF) energy consumption	kWh	Analiz_S	Sulfur (S) percentage	%
EAO_Enerji_kWh/t	EAF energy consumption (per ton)	kWh/ton	Analiz_Cu	Copper (Cu) percentage	%
Oksijen (Nm3/t)	Oxygen consumption (per ton)	Nm³/ton	Analiz_V	Vanadium (V) percentage	%
VLB (Nm3/t)	Vacuum/auxiliary gas consumption (per ton)	Nm³/ton	Celik_Sinif	Steel quality class of the produced product	-

Representative samples from the constructed dataset are presented in Table 2 by reporting the first five rows to illustrate the data structure and how the variables are represented.

Table 2 Sample rows from the constructed dataset

Ebat	On_Ist_S	On_Ist_Gr_Sic	On_Ist_Ck_Sic	Hurda_Sarj_S	Hurda_Tonaj	Hurda_Verim	…	Ana_C	Ana_Si	Cel_Sin
150x12	30	492	33	3	118650	85,18	…	0.19	0.17	B420
130x12	30	492	33	3	118650	85,18	…	0.19	0.17	B420
150x12	31	550	26	3	120800	81,90	…	0.18	0.18	B420
130x12	31	550	26	3	120800	81,90	…	0.18	0.18	B420
150x12	27	465	33	3	120250	82,73	…	0.23	0.20	S220

The distribution of the target variable—steel quality grade (B420 and S220)—in terms of the number of observations is presented in Figure As shown in the figure, the class counts are relatively similar, indicating that there is no pronounced class imbalance in the dataset.

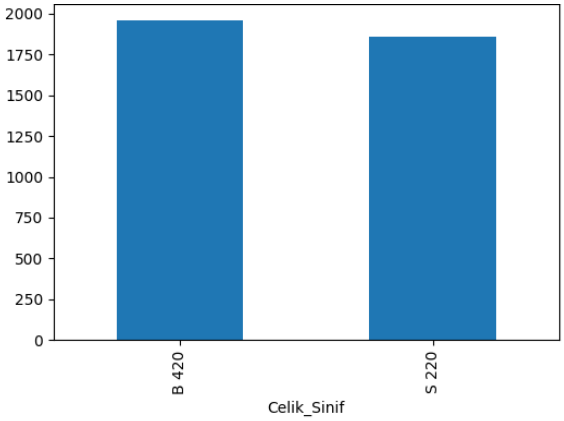

Figure 1 Distribution of steel quality classes (B420 and S220) in the dataset

As shown in Figure 1, the numbers of observations for the B420 and S220 classes are very similar, which reduces the risk of class-imbalance–driven bias during training and enables a more reliable evaluation of model performance.

In this study, four supervised machine learning models were employed to predict steel quality grades using features derived from process data and chemical composition measurements. These models were selected because they are widely used in industrial classification tasks, can capture nonlinear relationships, and typically achieve strong performance on tabular datasets. Brief descriptions of the employed models are provided below.

Support Vector Machine – SVM: Support Vector Machine (SVM) is a supervised learning model developed by Vladimir Vapnik in 1995 [10]. The main objective of SVM is to identify the decision boundary that best separates the data points. Specifically, SVM determines the hyperplane that maximizes the margin between two classes, where the support vectors are the critical samples that define this margin. For nonlinearly separable problems, SVM can construct complex decision boundaries through kernel functions and can be particularly effective for high-dimensional data structures [11].

Random Forest – RF: Random Forest is an ensemble-based approach in which multiple decision trees are trained on different bootstrap samples and their predictions are aggregated (majority voting) to obtain the final output. In this algorithm, random samples are drawn from the training data to generate t subsets, and each subset is used to train a decision tree model [12]. At each split node of a tree, a randomly selected subset of features is evaluated to determine the best split. After all trees are trained, their individual predictions are combined, and the class receiving the highest number of votes is selected as the final prediction [13]. Owing to its robustness to noise, its ability to capture interactions among variables, and its strong generalization performance, Random Forest is frequently preferred in industrial datasets.

Extreme Gradient Boosting – XGBoost: XGBoost builds decision trees sequentially based on the gradient boosting principle, where each new tree aims to reduce the errors of the previous trees. Owing to its regularization mechanisms and efficient optimization scheme, it can achieve strong performance on tabular data [14–15].

Light Gradient Boosting Machine – LightGBM: LightGBM (LGBM) is a gradient boosting framework based on tree-based learning algorithms, proposed by Microsoft in 2017 [16]. It was developed to achieve high speed and

scalability. Owing to its histogram-based splitting strategy and leaf-wise tree growth approach, LightGBM can reduce computational cost on large datasets while maintaining competitive predictive accuracy [17].

2.2. Model Interpretability Using SHAP (SHapley Additive exPlanations)

In this study, the SHAP method was employed to quantify the relative contribution of each feature to the steel quality classification decision and to make the models' decision mechanisms interpretable. Based on Shapley values from cooperative game theory, SHAP computes, on a per-instance basis, how much each variable contributes to the model output (i.e., the predicted class or probability) and reports these contributions quantitatively along with their positive or negative effects. This enables a transparent analysis of which chemical composition variables and process parameters drive the model decisions, and allows a comparative assessment of the decisive role of the carbon variable in classification performance versus the contributions of process variables other than carbon to the quality decision [18].

2.3. Performance Evaluation Metrics

The descriptions and formulas of the performance metrics used in this study are provided in Table These metrics are computed based on the confusion matrix shown in Figure The confusion matrix includes the following four fundamental terms [11]:

True Positives (TP): The number of instances that are actually positive and are correctly predicted as positive by the model.

False Positives (FP): The number of instances that are actually negative but are incorrectly predicted as positive by the model.

True Negatives (TN): The number of instances that are actually negative and are correctly predicted as negative by the model.

False Negatives (FN): The number of instances that are actually positive but are incorrectly predicted as negative by the model.

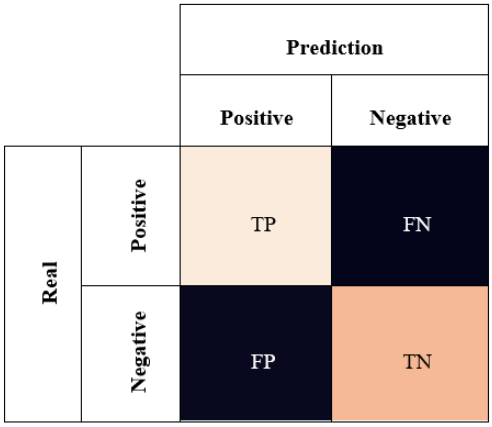

Figure 2 Confusion matrix

Table 3 Definitions and formulas of classification performance metrics [11]

Metric	Definition	Formulation
Accuracy	Accuracy is a metric that represents the proportion of correct predictions made by a classification model relative to the total number of observations.	$Accuracy = \frac{(TP+TN)}{(TP+TN+FP+FN)}$
Precision	Precision is a metric that measures the proportion of predicted positive instances that are actually positive.	$Precision = \frac{TP}{(TP+FP)}$
Recall	Recall is a metric that measures the proportion of actual positive instances that are correctly identified.	$Recall = \frac{TP}{(TP+FN)}$
F1 Score	The F1-score is the harmonic mean of precision and recall, and it is used as a performance metric that balances both measures.	$F_1\ Score = \frac{2 * Recall * Precision}{Precision + Recall}$

3. Experimental Setup and Results

In this section, we first describe the hardware/software infrastructure and the experimental environment used in the study, and then summarize the data preprocessing steps applied to make the raw data suitable for analysis. Finally, the performance of the employed models is reported using the specified evaluation metrics, and the findings are interpreted with the support of tables and figures.

3.1. Experimental Environment

All data processing steps, model training procedures, and analyses in this study were conducted in the Google Colab environment. Google Colab is a cloud-based Python runtime provided by Google, enabling users to perform machine learning, data analytics, and deep learning tasks without requiring local setup. Built on the Jupyter Notebook infrastructure, Colab offers free access to hardware accelerators such as GPUs (e.g., NVIDIA Tesla T4) and TPUs, making it possible to work efficiently with large datasets and computationally intensive models. Owing to its convenient file sharing, seamless integration with Google Drive, rapid library installation, and the ability to present code, outputs, and documentation within a single platform, it is widely used in both research and educational settings.

3.2. Data Preprocessing

The raw dataset used in this study was subjected to a comprehensive preprocessing pipeline to make it suitable for modeling. First, missing-value analysis was performed, and empty or physically inconsistent records were identified and removed from the dataset. Next, outliers in process and operational parameters were examined, and anomalies that could compromise data consistency were filtered out. All numerical variables were normalized using standard scaling to reduce model sensitivity to errors and eliminate differences in feature scales. Among the categorical variables, ebat and celik_sinifi were transformed into numerical representations via one-hot encoding. Finally, the dataset was split into 80% training and 20% testing sets using a stratified strategy to preserve the class distribution, thereby preparing the data for model training.

Following data preprocessing, model training was performed. To ensure a reliable performance evaluation, 5-fold cross-validation was employed. Accordingly, the dataset was partitioned into five folds; in each iteration, four folds were used for training and one-fold for validation, and the procedure was repeated five times. The reported performance values are presented as the average of the results obtained across all folds.

3.3. Model Training Results with Carbon Analysis Included

When the carbon analysis variable was included in the feature set, three of the machine learning models—RF, XGBoost, and LightGBM—achieved perfect classification performance, yielding 100% accuracy, precision, recall, and F1-score, with confusion matrices indicating that all samples in both steel quality classes were correctly predicted. This result clearly demonstrates that the carbon content is a dominant and highly discriminative feature in determining steel quality. The SVM model also exhibited very high performance, achieving 99.24% accuracy, 99.25% precision, 99.24% recall, and 99.24% F1-score. Its confusion matrix shows that only a small number of instances were misclassified. Overall, the models' near-perfect performance confirms that carbon analysis provides strong separability between the B420 and S220 classes, enabling highly accurate data-driven quality prediction in steel manufacturing. The confusion matrix for the SVM model is presented in Figure 3.

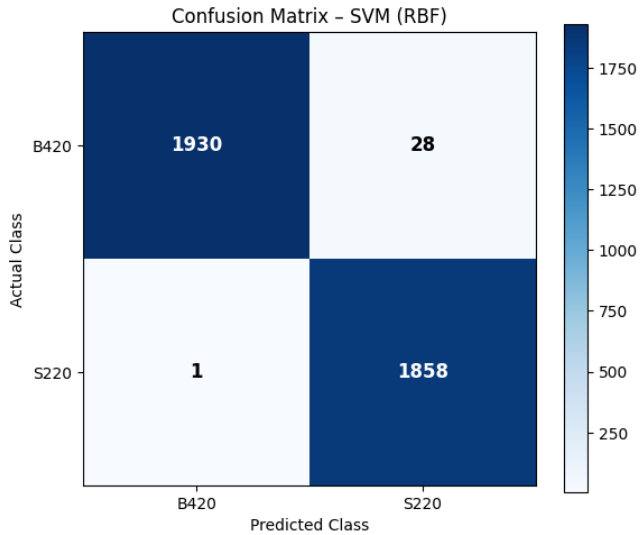

Figure 3 Confusion matrix for SVM classification results

The confusion matrix obtained for the SVM model indicates that the two steel classes are separated with high accuracy. Of the samples belonging to the B420 class, 1,930 were correctly classified as B420, while 28 were predicted as S220; conversely, 1,858 S220 samples were correctly classified, and only 1 sample was labeled as BThis distribution suggests that the model exhibits a very low overall error rate and identifies the S220 class almost perfectly. Most of the remaining errors appear to arise from B420 samples located near the class boundary being confused with S220.

In steel classification, a deterministic relationship was observed between the Analiz_C value and the steel grade. According to the company procedure and the TSE 708 standard, the classification rule is defined as follows: when Analiz_C > 0.22, the quality grade is assigned as "S220", whereas when Analiz_C ≤ 0.22, it is assigned as "B420." The threshold analysis conducted in Google Colab confirmed this pattern and yielded an optimal cutoff value of 0.These results indicate that the carbon content is a highly discriminative feature that can almost entirely distinguish the steel quality classes.

When the distribution of the carbon (Analiz_C) variable across steel classes is examined, a clear separation between the classes is observed (Figure 4).

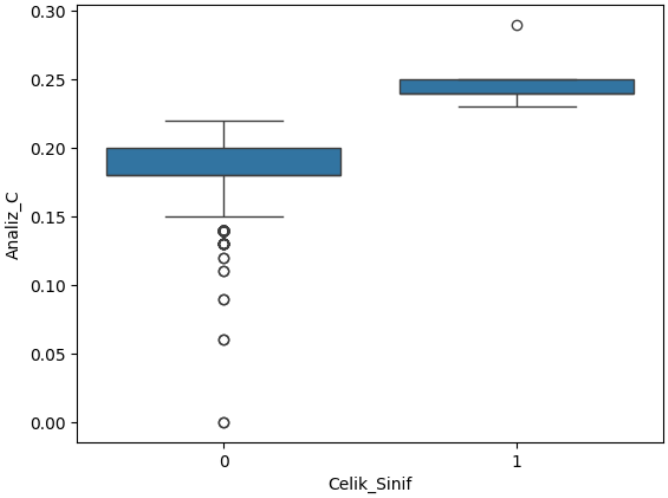

Figure 4 Distribution of carbon (C) content by steel class (box plot)

This box plot shows that the carbon (Analiz_C) values differ markedly across the steel classes. For class 1, carbon values are concentrated within a narrower range, with a median of approximately 0.24–0.25, suggesting a more homogeneous carbon content in this class. In contrast, class 0 exhibits a lower median (around 0.18–0.20) and a relatively wider distribution, along with numerous outliers at lower carbon levels. Overall, the observed separation between the classes indicates that carbon content is a strong and discriminative variable for distinguishing steel grades.

3.4. Model Training Results Without Carbon Analysis

In this section, the training performance of different machine learning models is comparatively reported when the carbon analysis variable (Analiz_C) is excluded from the dataset (Table 4).

Table 4 Performance comparison of ML models without carbon analysis (Analiz_C removed)

Model	**Accuracy**	**Precision**	**Recall**	**F1-Score**
RF	0.8745	0.8747	0.8745	0.8744
XGBoost	0.8682	0.8682	0.8682	0.8682
LightGBM	0.8677	0.8678	0.8677	0.8677
SVM	0.6581	0.6589	0.6581	0.6581

The results reported in Table 4 indicate that tree-based ensemble methods (RF, XGBoost, and LightGBM) achieved similarly strong performance on the classification task. The best performance was obtained with the Random Forest (RF) model (Accuracy = 0.8745; F1 = 0.8744), followed closely by XGBoost (Accuracy = 0.8682; F1 = 0.8682) and LightGBM (Accuracy = 0.8677; F1 = 0.8677). In contrast, the SVM model exhibited substantially lower performance than the other methods (Accuracy ≈ 0.6581; F1 ≈ 0.6581). Overall, the proximity of the metrics suggests that class imbalance is limited and that the models display similar error characteristics; these findings further indicate that tree-based ensembles provide a more suitable solution for this dataset.

After excluding the carbon (Analiz_C) variable from the dataset, the classification performance of the Random Forest model and the distribution of its errors were examined using the confusion matrix (Figure 5).

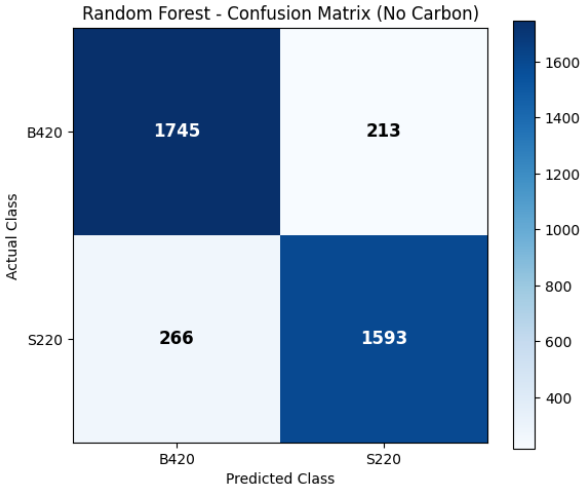

Figure 5 RF confusion matrix without carbon (Analiz_C)

The confusion matrix presented in Figure 5 shows that the RF model's ability to discriminate between classes decreases noticeably when the carbon feature is not used. Of the 1,958 samples in the B420 class, 1,745 were correctly classified, while 213 were predicted as S220; similarly, among the 1,859 S220 samples, 1,593 were correctly classified and 266 were labeled as BThe increase in errors in both classes—particularly the relatively high number of misclassifications from S220 to B420—suggests that carbon is an important feature that strengthens the separation between classes, and that removing it increases overlap near the class boundary.

3.5. SHAP-Based Feature Importance Results

In this section, feature importance was analyzed using SHAP to make the decision mechanisms of the developed models interpretable. The resulting feature attributions are presented in Figure 6.

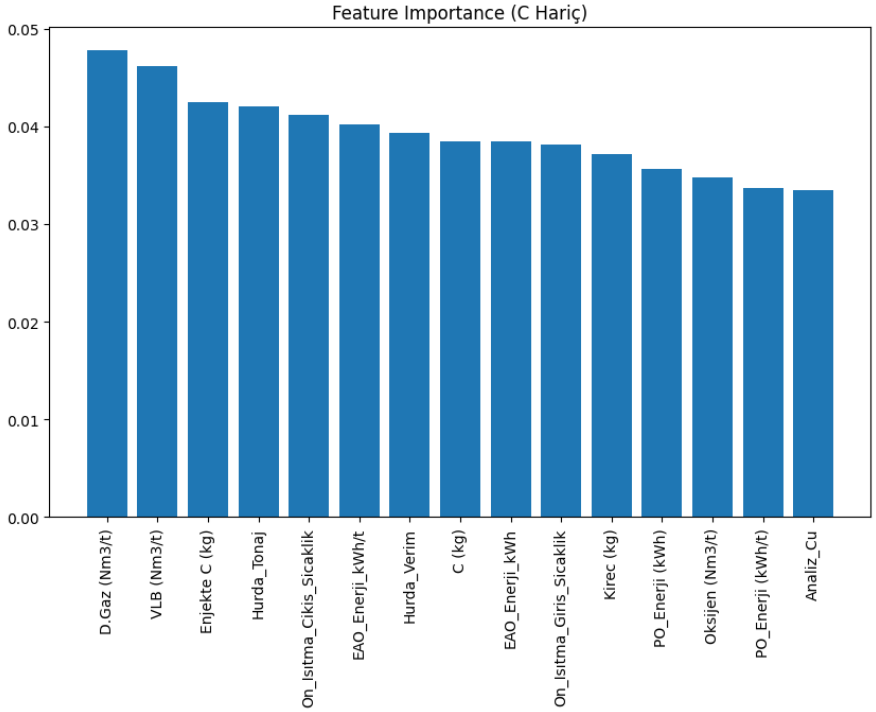

Figure 6 Feature importance distribution when carbon (Analiz_C) is excluded

Figure 6 illustrates the feature attributions that become prominent in the model's decision process after the carbon variable is removed. Accordingly, other gas consumption (D.Gaz) and the VLB variable exhibit the highest importance values and emerge as the primary determinants of the classification decision. These are followed by process-related parameters that are directly linked to production, such as injected carbon (Enjekte C), scrap tonnage, and preheating/outlet temperature. Although energy-related variables (e.g., EAF energy and PO energy) and oxygen

consumption also provide meaningful contributions, the relatively close importance values suggest that the decision is not driven by a single variable but rather by the combined effect of multiple process indicators. This finding indicates that, in the absence of carbon information, the model relies more heavily on indirect signals—particularly energy consumption, fuel usage, and process temperatures—to maintain class separability.

4. Conclusion

This study addressed the classification of steel quality grades using machine learning methods based on process and chemical analysis variables, with a particular focus on the impact of the carbon feature (Analiz_C) on model performance. The findings obtained via 5-fold cross-validation indicate that tree-based ensemble models generally deliver consistent and strong performance, whereas the SVM model achieves comparatively lower accuracy than the other approaches. When the carbon variable was excluded from the dataset, a noticeable decline was observed in the performance metrics, and the confusion matrix results further showed an increase in misclassifications. Feature-importance analyses and SHAP-based interpretations suggest that, in the absence of carbon, the model decisions are mainly shaped by energy consumption, fuel usage, and key process parameters (e.g., other gas, oxygen, temperature, and production inputs); however, these variables cannot fully substitute for the discriminative contribution of carbon.

Overall, the results confirm that carbon content is a critical determinant for steel grade separation and that data-driven quality monitoring can be made more reliable by jointly considering carbon analysis and operational process indicators.

Future work will focus on validation with larger datasets, the adoption of alternative modeling strategies (e.g., hyperparameter optimization and robustness analyses), and testing generalization under real production conditions.

References

[1] Öztürk, R., & Fındık, M. (2012). Türkiye'de Demir Çelik Sektörü'nün Yapisal Analizi. This preprint research paper has not been peer reviewed. Electronic copy available at: https://ssrn. com/abstract, 4505114.

[2] Çeştepe, H., & Tunçel, A. (2018). Türkiye Demir Çelik Sektörünün Uluslararasi Rekabet Gücü Analizi. Electronic Turkish Studies, 13(15).

[3] Özaksoy, M. G. (2004). Türkiye Demir Çelik Sektörünün Uluslararasi Rekabet Gücü Analizi. Electronic Turkish Studies, 13(15).

[4] Gür, Y. E., & Eşidir, K. A. (2024). Türkiye hurda demir çelik ithalatının gelecek değerlerinin derin öğrenme, makine öğrenmesi ve topluluk öğrenme yöntemleri ile öngörülmesi. Alanya Akademik Bakış, 8(3), 885-908.

[5] Süllü, N., & Kurt, A. (2025). İşten Ayrılma Durumunun Tahminlenmesinde Makine Öğrenmesi Algoritmaları Kullanımı–Demir Çelik Sektöründe Bir Uygulama. Osmaniye Korkut Ata Üniversitesi Fen Bilimleri Enstitüsü Dergisi, 8(4), 1525-1543.

[6] Mele, M., & Magazzino, C. (2020). A machine learning analysis of the relationship among iron and steel industries, air pollution, and economic growth in China. Journal of Cleaner Production, 277, 123293.

[7] Shaheen, M. A., Presswood, R., & Afshan, S. (2023, June). Application of machine learning to predict the mechanical properties of high strength steel at elevated temperatures based on the chemical composition. In Structures (Vol. 52, pp. 17-29). Elsevier.

[8] Li, F., Wu, J., Dong, F., Lin, J., Sun, G., Chen, H., & Shen, J. (2018, December). Ensemble machine learning systems for the estimation of steel quality control. In 2018 IEEE International Conference on Big Data (Big Data) (pp. 2245-2252). IEEE.

[9] Wang, X., Wang, Y., Tang, L., & Zhang, Q. (2023). Multiobjective ensemble learning with multiscale data for product quality prediction in iron and steel industry. IEEE Transactions on Evolutionary Computation, 28(4), 1099-1113.

[10] C. Cortes, V. Vapnik, "Support-vector networks," Machine learning, vol. 20, pp. 273-297, 1995.

[11] Irmak, T. (2023). Sağlık sektöründe yapay zekâ temelli bir klinik karar destek sisteminin geliştirilmesi. Doktora Tezi, Atatürk Üniversitesi Endüstri Mühendisliği Ana Bilim Dalı, Fen Bilimleri Enstitüsü.

[12] T.K. Ho, "Random decision forests," In Proceedings of 3rd international conference on document analysis and recognition, IEEE, vol. 1, pp. 278-282, 1995.

[13] L. Breiman, "Random forests," Machine learning, vol. 45, pp. 5-32, 2001.

[14] Chen, T., He, T., Benesty, M., Khotilovich, V., Tang, Y., Cho, H., ... & Zhou, T. (2015). Xgboost: extreme gradient boosting. R package version 0.4-2, 1(4), 1-4.

[15] Irmak, M. C., Aydın, T., & Yağanoğlu, M. (2025). A novel integration of multiple learning methods for detecting misleading information from different datasets during the pandemic. Engineering Applications of Artificial Intelligence, 142, 109944.

[16] Ke, G., Meng, Q., Finley, T., Wang, T., Chen, W., Ma, W., ... & Liu, T. Y. (2017). Lightgbm: A highly efficient gradient boosting decision tree. Advances in neural information processing systems, 30.

[17] Yıldız, D., Yıldız, G., & Demirci, S. Makine Öğrenmesi Tekniklerinin Sürüş Stili Sınıflandırmasında Kullanımı. Black Sea Journal of Engineering and Science, 7(4), 756-763.

[18] Irmak, T. (2025, June). Defect Detection in Manufacturing: A Comparative Study of Machine Learning and Fuzzy Rule-Based Systems. In 2025 9th International Symposium on Innovative Approaches in Smart Technologies (ISAS) (pp. 1-6). IEEE.

New Approaches to Microneedle Technology and Alzheimer's Vaccine Applications

Hayrunnisa Nadaroğlu [1,2]

1 Department of Food Technology, Vocational College of Technical Sciences, Ataturk University, 25240 Erzurum, Türkiye
2 Department of Nano-Science and Nano-Engineering, Institute of Science, Ataturk University, 25240 Erzurum, Türkiye

* *Corresponding author E-mail: hnisa25@atauni.edu.tr*

Keywords

Microneedle, Vaccine, Bioavailability, Alzheimer's disease (AD)

Abstract

The integration of microneedle technology into drug and vaccine delivery systems offers an innovative approach due to its advantages, such as applicability against a wide range of diseases, applicability in the field of immunology, minimally invasive structure, and high bioavailability. Microneedles, which are micron-sized needles designed to penetrate the outer layer of the skin and are widely used and currently in widespread use, offer a minimally invasive method for the administration of therapeutic agents, including vaccines. The microneedles proposed in our project will not only increase the bioavailability of drugs but also improve patient compliance due to their painless application and ease of use. The application of microneedle technology in vaccine development for Alzheimer's disease (AD) represents a promising frontier in immunization strategies. Micro-needles, which are small, minimally invasive devices, facilitate the direct delivery of vaccines into the skin, where they can effectively stimulate immune responses. This method has been shown to increase the immunogenicity of various vaccines, including those targeting neurodegenerative diseases such as Alzheimer's.

1. Introduction

Research suggests that microneedles can be used for transdermal delivery of therapeutic agents such as donepezil hydrochloride, a cholinesterase inhibitor used to treat Alzheimer's disease. This approach not only improves drug absorption but also minimizes the pain associated with traditional injection methods. Furthermore, microneedles have been successfully used to deliver amyloid β peptides, which are critical in the pathogenesis of Alzheimer's disease, and thus may serve as a potential vaccine against AD (Wu *et al.*, 2024).

The immunogenicity of vaccines delivered via microneedles is significantly enhanced due to the localized delivery of antigens to the skin, which is rich in immune cells such as Langerhans and dendritic cells (Mansoor *et al.*, 2022). This localized response can be further enhanced by the mechanical stress induced during microneedle insertion, which acts as a physical adjuvant and promotes a strong adaptive immune response.

Studies have shown that microneedle patches can induce higher antibody levels compared to traditional intramuscular injections, demonstrating their effectiveness in eliciting strong immune responses (Feng *et al.*, 2023). urthermore, the use of dissolvable microneedle arrays (MNAs) provides a painless vaccination experience while ensuring stability and ease of storage. They have been highlighted for their capabilities (Mistilis *et al.*, 2017; Rawson *et al.*, 2019). The dissolvable nature of these microneedles eliminates the need for cold chain logistics, making them particularly advantageous in resource-limited settings (Ray *et al.*, 2022). The potential for self-administration of microneedles also addresses barriers to vaccination, such as needle phobia and the need for skilled healthcare professionals for vaccine distribution (Prausnitz and Langer, 2008; Blicharz *et al.*, 2018). I n terms of economic viability, microneedles have been considered a “game changer” in global vaccination efforts, offering a cost-effective solution for mass immunization campaigns (Nguyen and Nguyen, 2023). Their ability to generate long-lasting immune responses further supports their application in vaccines targeting chronic conditions such as Alzheimer’s disease, where sustained immunity is vital (Netea *et al.*, 2020; Arunachalam, 2024).

All of these, for these reasons, polymeric microneedles, which will be synthesized, offer significant advantages for the development of vaccines against Alzheimer's disease. Microneedles, which will be obtained with enhanced efficacy using nanotechnological methods, will significantly impact the way vaccines are administered, particularly

for diseases that require long-term immune responses, by enhancing their immunogenicity, providing a painless application method, and facilitating self-administration.

2. The Basic Structure and Types of Microneedle Technology

Microneedles are microscale structures, generally 50–900 µm long, that can painlessly penetrate the stratum corneum of the skin and reach the dermal region. Microneedles designed for vaccine and drug applications are divided into five main classes based on their structure:

The materials used to make microneedles are selected based on their intended use, production method, and physical properties (Xu *et al.*, 2021). Produced microneedles are classified into five types:

These are:

➢ Solid Microneedles

➢ Coated Microneedles

➢ Dissolvable Microneedles

➢ Hollow Microneedles

➢ Hydrogel Microneedles

The appearance of the vaccine during skin application is shown in Figure 1.

This diversity allows for the design of suitable delivery systems for different formulations of Alzheimer's vaccines (peptide, DNA, nanoparticle, conjugated antigen, etc.).

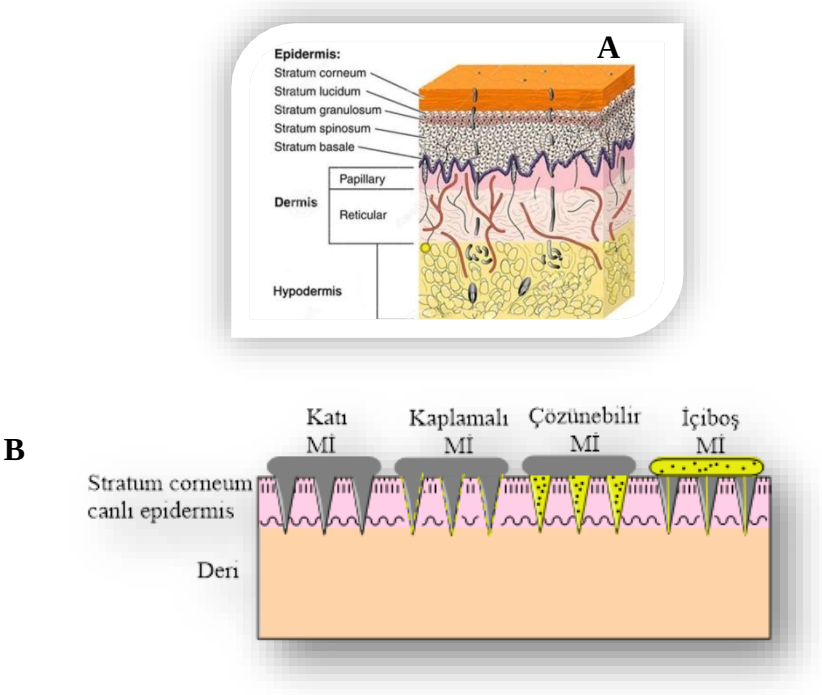

Figure 1 Illustration of skin layers (A) and microneedle types and drug delivery methods (B)

3. Advantages of Microneedles in Vaccine Applications

Microneedles are an innovative platform, particularly preferred for immunization. Their advantages can be summarized as follows:

Painless application: This is critical for long-term treatment compliance in Alzheimer's patients.

Direct access to dermal immune cells: This region, where Langerhans and dermal dendritic cells are densely located, generates a more potent and targeted immune response.

High efficacy with low dose: Reduced antigen loss reduces production costs.

Self-administration: Advantageous for elderly individuals receiving home care and in care centers.

Cold chain advantage: Antigen stability is increased, especially with dissolvable microneedle patches.

Does not generate sharps or medical waste.

These features significantly increase the applicability of Alzheimer's vaccines to the general population.

4. Alzheimer's Vaccines: Current Status and Approaches

Vaccine studies for Alzheimer's disease are based on two main goals:

4.1. Amyloid-β (Aβ)-targeted vaccines

Initial clinical trials targeted the Aβ42 peptide. However, the AN1792 vaccine, administered by conventional injection, was discontinued due to meningoencephalitis related to neuroinflammation. This experience highlighted the need for safer delivery systems. Microneedles offer the potential to reduce these side effects thanks to their low dose and local immunization(Smyth Templeton, 2015).

4.1.1. Tau-targeted vaccines

Therapeutic vaccines developed against tau protein aim to prevent the formation of neurofibrillary tangles. Dermal application of tau peptide vaccines has been reported to induce a more balanced immune response through controlled release (Tan *et al.*, 2024).

4.1.2. DNA and nanoparticle-based Alzheimer's vaccines

DNA/tRNA-based Alzheimer's vaccines combined with polymeric or lipid nanoparticles provide a platform compatible with microneedle delivery systems. Dissolvable microneedles increase delivery efficiency by preserving DNA stability (Vicidomini *et al.*, 2023).

5. Conclusion

Microneedle technology represents a transformative approach for the development and delivery of Alzheimer's disease vaccines and therapeutic agents. The ability to painlessly penetrate the skin, target immune-rich dermal layers, and provide controlled, effective antigen delivery makes microneedles a powerful alternative to traditional injection-based immunization methods. The enhanced immunogenicity achieved through localized antigen delivery, combined with the mechanical adjuvant effect of microneedle placement, supports the development of more effective and safer Alzheimer's disease vaccines. Dissolvable polymeric microneedles, in particular, offer additional advantages such as improved stability, elimination of cold chain requirements, and the ability to self-administer; these features are particularly valuable for elderly populations and long-term disease management.

Advances in nanotechnology-driven microneedle production are further enhancing the sensitivity, loading capacity, and biocompatibility of these systems, making them compatible with a variety of vaccine platforms, including peptide-based, DNA, mRNA, and nanoparticle-conjugated formulations. Given the limitations observed in previous Alzheimer's vaccine trials (particularly neuroinflammatory side effects), microneedles offer a safer, more targeted, and more dose-efficient vaccination route.

Acknowledgments

The study received funding from the Ataturk University, Scientific Research Projects Commission with grant number FBA-2025-The authors want to thank Ataturk University for its assistance, through the Scientific Research Projects initiative.

References

[1] Arunachalam, A.B. (2024) Vaccines Induce Homeostatic Immunity, Generating Several Secondary Benefits. *Vaccines* **12**: 396.

[2] Blicharz, T.M., Gong, P., Bunner, B.M., Chu, L.L., Leonard, K.M., Wakefield, J.A., et al. (2018) Microneedle-based device for the one-step painless collection of capillary blood samples. *Nature Biomedical Engineering* **2**: 151–157.

[3] Feng, Y.-X., Hu, H., Wong, Y.-Y., Yao, X., and He, M.-L. (2023) Microneedles: An Emerging Vaccine Delivery Tool and a Prospective Solution to the Challenges of SARS-CoV-2 Mass Vaccination. *Pharmaceutics* **15**: 1349.

[4] Mansoor, I., Eassa, Heba A., Mohammed, K.H.A., Abd El-Fattah, M.A., Abdo, M.H., Rashad, E., et al. (2022) Microneedle-Based Vaccine Delivery: Review of an Emerging Technology. *AAPS PharmSciTech* **23**: 103.

[5] Mistilis, M.J., Joyce, J.C., Esser, E.S., Skountzou, I., Compans, R.W., Bommarius, A.S., and Prausnitz, M.R. (2017) Long-term stability of influenza vaccine in a dissolving microneedle patch. *Drug Delivery and Translational Research* **7**: 195–205.

[6] Netea, M.G., Domínguez-Andrés, J., Barreiro, L.B., Chavakis, T., Divangahi, M., Fuchs, E., et al. (2020) Defining trained immunity and its role in health and disease. *Nature Reviews Immunology* **20**: 375–388.

[7] Nguyen, H.X. and Nguyen, C.N. (2023) Microneedle-Mediated Transdermal Delivery of Biopharmaceuticals. *Pharmaceutics* **15**: 277.

[8] Prausnitz, M.R. and Langer, R. (2008) Transdermal drug delivery. *Nature Biotechnology* **26**: 1261–1268.

[9] Rawson, T.M., Gowers, S.A.N., Freeman, D.M.E., Wilson, R.C., Sharma, S., Gilchrist, M., et al. (2019) Microneedle biosensors for real-time, minimally invasive drug monitoring of phenoxymethylpenicillin: a first-in-human evaluation in healthy volunteers. *The Lancet Digital Health* **1**: e335–e343.

[10] Ray, S., Wirth, D.M., Ortega-Rivera, O.A., Steinmetz, N.F., and Pokorski, J.K. (2022) Dissolving Microneedle Delivery of a Prophylactic HPV Vaccine. *Biomacromolecules* **23**: 903–912.

[11] Smyth Templeton, N. ed. (2015) Gene and Cell Therapy, CRC Press.

[12] Tan, W., Thiruppathi, J., Hong, S.H., Puth, S., Pheng, S., Mun, B.-R., et al. (2024) Development of an anti-tauopathy mucosal vaccine specifically targeting pathologic conformers. *npj Vaccines* **9**: 108.

[13] Vicidomini, C., Borbone, N., Roviello, V., Roviello, G.N., and Oliviero, G. (2023) Summary of the Current Status of DNA Vaccination for Alzheimer Disease. *Vaccines* **11**: 1706.

[14] Wu, C., Yu, Q., Huang, C., Li, F., Zhang, L., and Zhu, D. (2024) Microneedles as transdermal drug delivery system for enhancing skin disease treatment. *Acta Pharmaceutica Sinica B*.

[15] Xu, J., Xu, D., Xuan, X., and He, H. (2021) Advances of Microneedles in Biomedical Applications. *Molecules (Basel, Switzerland)* **26**:.

The Study and Methodological Support for the Development of Natural Science Competencies in 5th-Grade Students of Secondary School No. 117 Named After Ch. Aitmatov in Bishkek

Gulnara A. Sharshenalieva[1], Tursunbek kyzy Almagul [2], Nurjamal Omurzakova [2]

1 Department of General Biology and Technology of its Teaching, Institute of Natural Sciences, Kyrgyz State University named after I. Arabaev, Bishkek, Kyrgyzstan

2 Department of Biology, Faculty of Sciences, Kyrgyz-Turkish ManasUniversity, Bishkek, Kyrgyzstan

Corresponding author: sharshenalieva@mail.ru

Keywords

Natural Science Competencies,

Methodological Support,

Event-Participation Method,

5th Grade Education,

Inquiry Skills.

Abstract

This study addresses the urgent necessity of creating effective pedagogical and methodological tools to enhance students' thinking structures and natural science competencies (NSCs) within modern education. Highlighting contradictions between National Education Standards and students' low competency levels, the research aims to provide a theoretical justification and experimental verification of a new methodological support system for 5th-grade students. The research conducted diagnostic, formative, and control experiments involving 56 students (Control Group, n=28; Experimental Group, n=28) at Ch. Aitmatov Secondary School No. 117 in Bishkek. Initial diagnostics revealed that a majority of students across both groups possessed medium to low levels of cognitive activity and environmental culture. To address this, the study developed and implemented a new methodological framework centered around the "situational–event participation" method. This four-stage model focuses on integrating topics into real-life events, creating motivational engagement, promoting productive (interactive) activity, and concluding with analytical reflection. Post-experiment results demonstrated a significant positive dynamic in the Experimental Group compared to minimal changes in the Control Group. Specifically, the number of students in the Experimental Group demonstrating a high level of competence development increased dramatically (from 18% to 36%), while the number of students at the low level decreased by 41% (from 46% to 7%). The study successfully clarified the concept of NSCs for 5th graders and proved the high effectiveness of the event-participation method in enhancing student engagement, subject knowledge, and ecological awareness. The developed materials offer a practical resource for biology teachers and are adaptable for other middle and upper grades.

1. Relevance of the Study

The necessity to develop students' thinking structures and form their natural science competencies at the school age requires the creation of pedagogical and methodological tools that ensure this process. This is one of the most relevant issues in modern natural science education. The content of natural science education should foster a scientific understanding of the world and develop students' inquiry skills. Natural science competencies form the foundation of general education.

Modern researchers - E. Mambetakunov (2018), M.A. Nogaev (2023), M.J. Chorov (2020), R.R. Chynybaev (2023), I.Yu. Aleksashina (2017), V.I. Golubtsova (2000), V.A. Ignatova (2013), M.V. Klarin (2018), and V.A. Lvovsky (2018) - emphasize that the formation of natural science competencies is a key task of contemporary schooling.

Based on theoretical analysis, the following contradictions were identified:

Between the requirements of the National Education Standard and the low level of students' natural science competencies.

Between the increasing complexity of content and the lack of effective teaching methods.

Between the need for scientifically based methodological support and its shortage in schools.

1.1. Purpose of the Study

To provide theoretical justification and experimental verification of methodological support for the development of natural science competencies among 5th grade students.

1.2. Place of the Study

The research was conducted among 5th-grade students of Ch. Aitmatov Secondary School No. 117 (Bishkek).

2. Research Methods and Materials

To achieve the objectives, the following methods were used: theoretical: analysis of psychological, pedagogical, and methodological literature; study of internet sources; interpretation and generalization of pedagogical experience, empirical: interviews, observation, diagnostic, formative, and control experiments and analytical: quantitative and qualitative analysis of the data obtained.

3. Results and Discussion

The level of development of natural science competencies among 5th-grade students (formed in grades 1–4) was assessed. A total of 56 students participated: control group - Grade 5 “Zh” - 28 students. Experimental group - Grade 5 “Z” - 28 students

Diagnostic tools were based on questionnaires by B.K. Pashnev, N.O. Polyanicheva, and Yu.A. Poleshchuk, which assessed: Students’ cognitive and creative activity. The level of subject knowledge. Value-based attitudes toward living nature (Figure 1).

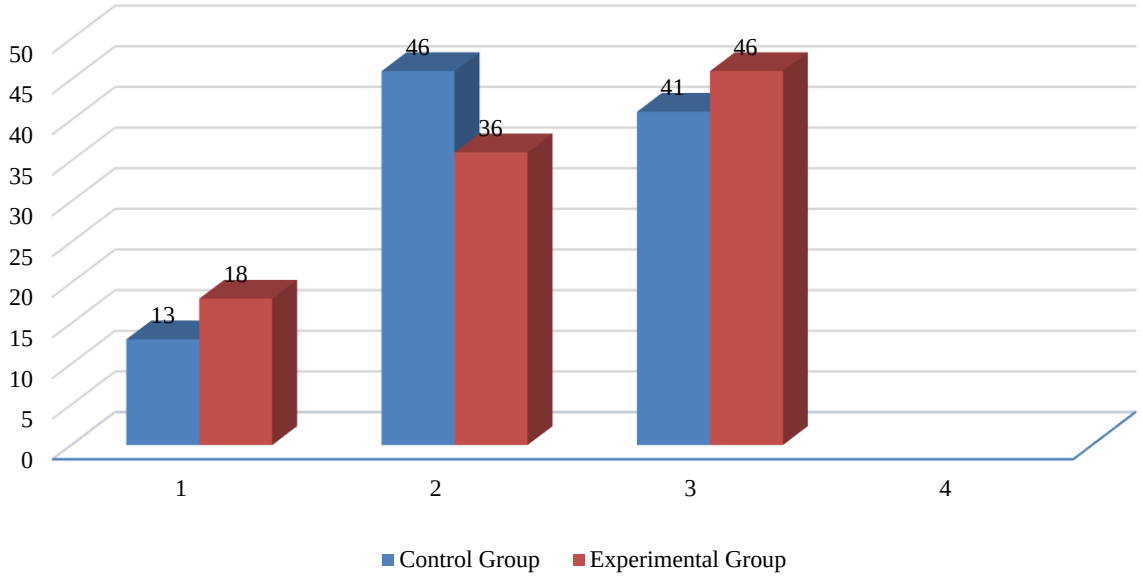

Figure 1 Level of Cognitive Activity (Before Experiment), %

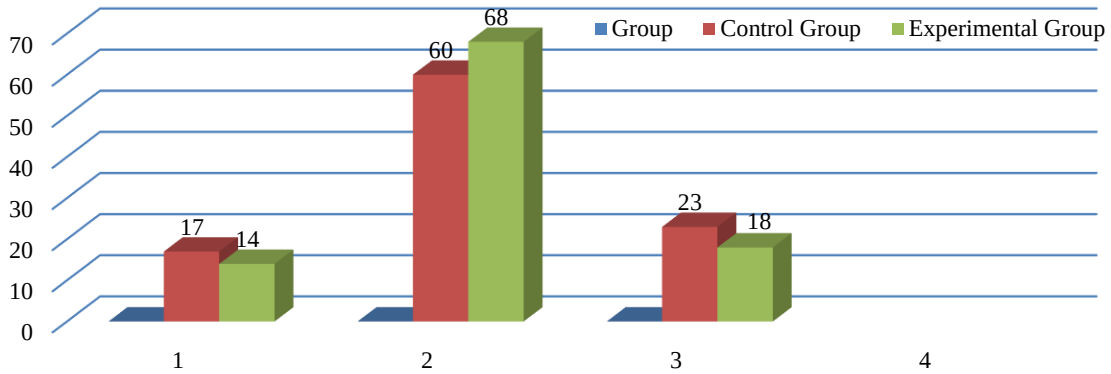

Figure 2 Level of Environmental Culture (Before Experiment), %

3.1. Methodology of the Pedagogical Experiment

To test the effectiveness of the methodological support, the situational–event participation method was applied, consisting of four stages: 1.Integrating the topic into a real-life event 2.Creating motivational engagement (introduction) 3.Productive activity (interactive lessons, experiments, role-based participation) Analytical conclusion (reflection, conceptualization, self-assessment).

Example Lesson (Biology, Grade 5):

Section: “Living Systems: Organisms, Environment, Ecosystems”. Topic:“Habitats of Living Organisms” , Practical Work: “What living organisms are made of and how they function.”

3.2. Results After the Experiment:

After implementing the methodological support, positive dynamics were recorded (Figure 3,4).

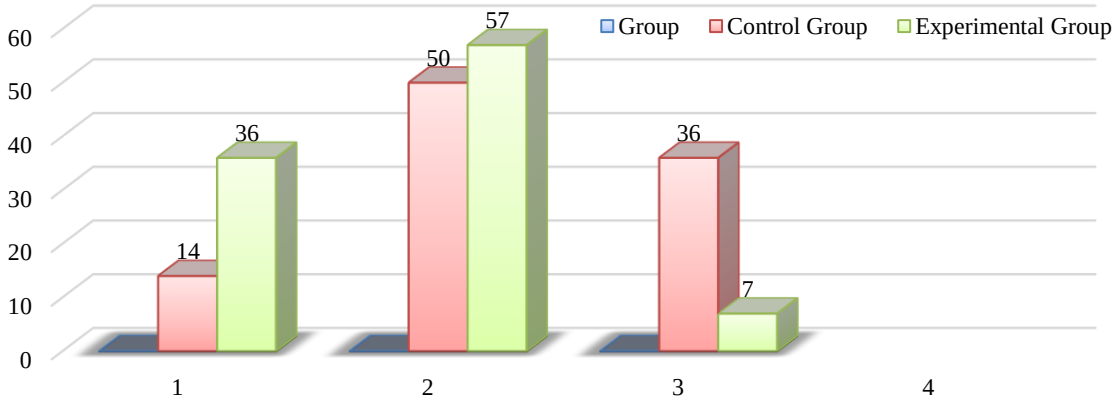

Figure 3 Changes in Cognitive Interest (After Experiment), %

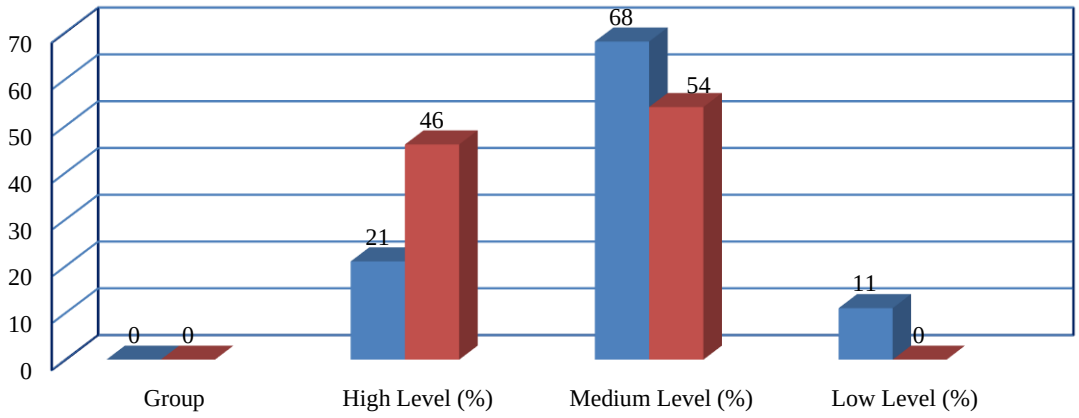

Figure 4 Formation of Environmental Culture (After Experiment), %

4. Conclusions

Components and indicators of methodological support were developed: subject knowledge, cognitive and creative activity, research and practical engagement, ecological awareness, generalization, and reflection skills. The event-participation method proved highly effective - every student became actively involved in the learning process. After the introduction of methodological support:

- The number of students with a low level decreased by **41%**.
- The number of students with a high level increased by **19%**.

References

[1] Mambetakunov E., Ryazantsev V.A. Natural Science. – Grade Textbook for general education schools. – Bishkek. – 2018.
[2] Stakhieva Elena Valerievna. Practically-Oriented Approach in the Professional Training of a Public Relations Specialist: Dissertation ... Candidate of Pedagogical Sciences: 13.00.08 / [Place of defense: Moscow State University of Culture and Arts]. Moscow, – 2020.
[3] Subject Standard for Natural Science for Grade 5 of General Education Organizations of the Kyrgyzstan // Developers: A.R. Nasyrova, R.R. Chynybaev, V.V. Savochkina, M.A. Nogaev, et al. – Bishkek. – 2022.
[4] Curriculum for Natural Science for General Education Organizations, Grade 5 // Developers: A.R. Nasyrova, R.R. Chynybaev, V.V. Savochkina, N.A. Znamenskaya, G.M. Zhamankulova, M.A. Nogaev. – Bishkek. – 2023.
[5] State Standard of Education in General Secondary Schools of the Kyrgyzstan, Resolution of the Cabinet of Ministers of the Kyrgyzstan No. 393, July 22, 2022.
[6] Program for the Development of Education in the Kyrgyzstan for 2021 – 2040 and Action Plans for its Implementation.
[7] On Measures to Ensure Environmental Safety and Climate Resilience of the Kyrgyzstan – Decree of the President of the Kyrgyzstan dated March 19, 2021, UP No. 77.
[8] State Educational Standard for School General Education of the Kyrgyzstan, approved on July 21, 2014, approved by Resolution of the Government of the Kyrgyzstan No. 403 dated July 21, Basic Curriculum for General Education Schools of the Kyrgyzstan.
[9] Questionnaire for Studying the Level of Cognitive Activity of Students (B.K. Pashneva) [Electronic resource] // Vash Psikholog. URL: http://www.vashpsixolog.ru/psychodiagnostic-school-psychologist/69-diagnosis-emotional-and-the-personal-sphere/2645-oprosnik-izucheniya-urovnya-poznavatelnoj-aktivnosti-uchashhixsya-bkpashneva
[10] Sharshenalieva G.A., Tashibekova Z.M., Kazakova N.O., Azhieva A.T. The Importance of Using Career Guidance in Teaching Biology in the Senior Grades of General Secondary School // Vestnik Kyrgyzstana No. 2 (1) – P. 334-355.

Synergistic Effects of *Thymus vulgaris* Essential Oil Combined with Antibiotics Against Methicillin-Resistant *Staphylococcus aureus*

Torkan Haghi [1], Murat Özdal [1]

[1] Department of Biology, Faculty of Science, Atatürk University, 25240, Erzurum, Türkiye

* *Corresponding author E-mail: torkan.haghi20@gmail.com*

Keywords

Thymus vulgaris

Essential oil

MRSA

Antibiotic synergy

Antimicrobial resistance

Abstract

The worldwide increase in antibiotic resistance has greatly diminished the efficacy of many traditional antimicrobial agents, and has made it imperative to develop complementary therapeutic strategies. Methicillin-resistant *Staphylococcus aureus* (MRSA) is one of the most challenging multidrug-resistant pathogens, that cause severe infections in hospitals and communities. Plant-based essential oils are becoming more and more popular as antimicrobial adjuvants owing to their various bioactive components and multiple mechanisms of action. The current study aimed to assess the possible synergistic effects of thyme (*Thymus vulgaris*) essential oil in combined with erythromycin (15 µg) and amoxicillin (10 µg) against MRSA (ATCC 67106). Antibacterial activity was tested by disk diffusion method through comparing inhibition zone diameters of antibiotics alone and in combination with 10 µL of thyme essential oil. MRSA showed resistance to both antibiotics when tested separately with no measurable inhibition zones. The combination of thyme essential oil with amoxicillin gave an inhibition zone about 13 mm, while its combination with erythromycin resulted in an inhibition zone of about 9 mm. These results prove that thyme essential oil is capable of significantly potentiating the antibacterial activity of antibiotics that are otherwise ineffective against MRSA. The results also support the use of essential oil–antibiotic combinations as a promising strategy for improving antimicrobial efficacy to meet the challenge posed by increasing antibiotic resistance.

1. Introduction

Antibiotic resistance has emerged as one of the greatest threats to public health worldwide, reversing decades of advancement in the management of infectious diseases [1, 2]. The global spread of multidrug-resistant bacteria has resulted in higher rates of death and disease; causing significant increases in health care costs. Of resistant pathogens, methicillin-resistant S. aureus (MRSA) stands out as being the most problematic with regard to its potential for causing chronic and invasive disease while also displaying resistance to multiple antibiotic classes [3].

The small number of newly developed antibiotics has heightened interest in alternative methods to increase the efficacy of current antimicrobial agents [4]. This can be achieved through the application of natural products as antibiotic adjuvants. Essential oils extracted from medicinal plants are complex mixtures containing volatile compounds, such as phenolics, terpenoids, and aldehydes, that show broad-spectrum antimicrobial activity by different mechanisms including membrane disruption, enzyme inhibition, and interference with cellular metabolism [5, 6].

Essential oil from thyme (Thymus vulgaris) is very well known for its strong antimicrobial activity due to its major constituents such as thymol and carvacrol [7, 8]. Some previous studies have shown that thyme essential oil has activity against a wide variety of Gram-positive and Gram-negative bacteria. Besides this, more recent evidence supports the idea that thyme essential oil could possibly work in synergy with some conventional antibiotics by restoring or enhancing their effect against resistant strains [9, 10].

This study was designed to explore the synergistic antibacterial effects of thyme essential oil in combination with erythromycin and amoxicillin against MRSA. Such understanding could lead toward developing new combination therapies that would enhance treatment outcomes while slowing down the process of antimicrobial resistance.

2. Materials and Methods

2.1.1. 2.Bacterial Strain

Methicillin-resistant *Staphylococcus aureus* (MRSA) ATCC 67106 was used in this study. This strain was kept on Mueller–Hinton agar (MHA) and subcultured before testing for viability and purity.

2.1.2. 2.Essential Oil and Antibiotics

The essential oil from Thyme (Thymus vulgaris) was acquired from a commercial vendor and stored at 4 °C in a dark container until required. Erythromycin (15 µg) and amoxicillin (10 µg) antibiotic disks were used as standard antimicrobial agents.

2.1.3. 2.Disk Diffusion Assay

Antibacterial activity was tested using the disk diffusion method, bacterial suspensions were prepared in sterile saline and adjusted to the turbidity of 0.5 McFarland standard. The suspensions were uniformly spread uniformly over MHA plates using sterile cotton swabs.

Antibiotic disks were placed on the agar surface either alone or supplemented with 10 µL of thyme essential oil. Plates were incubated at 37 °C for 18–24 h, after which, inhibition zone diameters were measured in millimeters. All experiments were done in triplicate, and mean values were recorded.

2.1.4. 2.Assessment of Synergistic Effects

To assess synergism between compounds, comparisons of inhibition zones diameters with antibiotics alone and those observed in combination with thyme essential oil were made; an increase in inhibition zone diameter would be interpreted as proof of synergism or additivity.

3. Results and Discussion

MRSA showed total resistance to erythromycin and amoxicillin when tested separately since no inhibition zones were seen around the antibiotic disks proving that thyme essential oil by itself has very limited antibacterial activity under these conditions

However, a combination of thyme essential oil with amoxicillin produced a clear inhibition zone of about 13 mm, while an equivalent combination with erythromycin gave an inhibition zone of about 9 mm; this substantial enhancement indicated synergy when antibiotics are used together with thyme essential oil.

Thyme essential oil has been shown in this study to significantly potentiate erythromycin and amoxicillin against MRSA, a pathogen characterized by multidrug resistance, indicating that the activity of the antibiotics has been restored. This is likely due to synergy between thyme essential oil and the respective antibiotics, as has been reported for other combinations of essential oils and antibiotics [9–11].

The synergistic effects may be mediated through the ability of thyme essential oil to disrupt cell membrane integrity and increase permeability, thereby enhancing penetration of antimicrobial agents into bacterial cells [5, 7]. Furthermore, bioactive components like thymol and carvacrol could potentially interfere with stress response pathways, efflux systems, and resistance mechanisms in MRSA [8, 12].

Synergism between plant-derived essential oils and antibiotics against Gram-positive pathogens including MRSA has previously been documented [9, 13], hence supporting the proposition that essential oils can serve as resistance-modifying agents to restore the efficacy of antibiotics that have decreased in effectiveness due to resistance mechanisms [10, 14].

While disk diffusion assays are valuable for preliminary screening since they are qualitative methods and do not reflect the actual events of antimicrobial interactions quantitatively; hence further studies involving quantitative methods such as MIC determination checkerboard assay, FICI analysis as well as time-kill studies should be carried out to confirm and determine mechanistically any synergy observed [15, 16].

4. Conclusion

This study confirms that thyme (Thymus vulgaris) essential oil possesses a profound synergistic effect with erythromycin and amoxicillin against MRSA. The revitalization or enhancement of antibiotic activity by thyme essential oil points towards its prospect as a natural antimicrobial adjuvant. Increasing literature supports the application of essential oils as complementary agents in antimicrobial therapy [9, 10, 14].

Given the global burden of antibiotic resistance and the limited pipeline of new antibiotics, essential oil–antibiotic combinations may represent a promising and sustainable strategy to improve treatment outcomes and mitigate the spread of multidrug-resistant pathogens [1, 4, 17].

References

[1] World Health Organization (WHO). *Global action plan on antimicrobial resistance*. Geneva: WHO Press; 2015.
[2] Ventola CL. The antibiotic resistance crisis: Causes and threats. *Pharmacy and Therapeutics.* 2015;40(4):277–283.
[3] Chambers HF, DeLeo FR. Waves of resistance: *Staphylococcus aureus* in the antibiotic era. *Nature Reviews Microbiology.* 2009;7(9):629–641. https://doi.org/10.1038/nrmicro2200
[4] Tacconelli E, Carrara E, Savoldi A, et al. Discovery, research, and development of new antibiotics: The WHO priority list of antibiotic-resistant bacteria. *The Lancet Infectious Diseases.* 2018;18(3):318–327. https://doi.org/10.1016/S1473-3099(17)30753-3
[5] Burt S. Essential oils: Their antibacterial properties and potential applications in foods—A review. *International Journal of Food Microbiology.* 2004;94(3):223–253. https://doi.org/10.1016/j.ijfoodmicro.2004.03.022
[6] Nazzaro F, Fratianni F, De Martino L, Coppola R, De Feo V. Effect of essential oils on pathogenic bacteria. *Molecules.* 2013;18(12):14511–14531. https://doi.org/10.3390/molecules181214511
[7] Marchese A, Orhan IE, Daglia M, et al. Antibacterial and antifungal activities of thymol: A brief review of the literature. *Food Chemistry.* 2016;210:402–414. https://doi.org/10.1016/j.foodchem.2016.04.111
[8] Ultee A, Bennik MHJ, Moezelaar R. The phenolic hydroxyl group of carvacrol is essential for action against food-borne pathogens. *Applied and Environmental Microbiology.* 2002;68(4):1561–1568. https://doi.org/10.1128/AEM.68.4.1561-1568.2002
[9] Langeveld WT, Veldhuizen EJA, Burt SA. Synergy between essential oils and antibiotics: A review. *Journal of Applied Microbiology.* 2014;117(4):1023–1041. https://doi.org/10.1111/jam.12600
[10] Hemaiswarya S, Kruthiventi AK, Doble M. Synergism between natural products and antibiotics against infectious diseases. *Phytomedicine.* 2008;15(8):639–652. https://doi.org/10.1016/j.phymed.2008.06.008
[11] Yap PSX, Lim SHE, Hu CP, Yiap BC. Combination of essential oils and antibiotics reduce antibiotic resistance in plasmid-conferred multidrug resistant bacteria. *Phytomedicine.* 2013;20,710-https://doi.org/10.1016/j.phymed.2013.02.013
[12] Di Pasqua R, Betts G, Hoskins N, Edwards M, Ercolini D, Mauriello G. Membrane toxicity of antimicrobial compounds from essential oils. *Journal of Agricultural and Food Chemistry.* 2007;55(12):4863–4870. https://doi.org/10.1021/jf0636465
[13] Nostro A, Blanco AR, Cannatelli MA, et al. Susceptibility of methicillin-resistant staphylococci to oregano essential oil, carvacrol and thymol. *FEMS Microbiology Letters.* 2004;230(2):191–195. https://doi.org/10.1016/S0378-1097(03)00890-5
[14] Yap PSX, Yiap BC, Ping HC, Lim SHE. Essential oils, a new horizon in combating bacterial antibiotic resistance. *The Open Microbiology Journal.* 2014; 8:6–14. https://doi.org/10.2174/1874285801408010006
[15] Balouiri M, Sadiki M, Ibnsouda SK. Methods for in vitro evaluating antimicrobial activity: A review. *Journal of Pharmaceutical Analysis.* 2016;6(2):71–79. https://doi.org/10.1016/j.jpha.2015.11.005
[16] Odds FC. Synergy, antagonism, and what the chequerboard puts between them. *Journal of Antimicrobial Chemotherapy.* 2003;52(1):1–4. https://doi.org/10.1093/jac/dkg301
[17] O'Neill J. *Tackling drug-resistant infections globally: Final report and recommendations.* London: Review on Antimicrobial Resistance; 2016.

Combining Black Seed Oil with Antibiotics: A Promising Strategy Against *Klebsiella pneumoniae* and *Acinetobacter baumannii*

Torkan Haghi [1,*], Murat Özdal [1]

[1] Department of Biology, Faculty of Science, Atatürk University, 25240, Erzurum, Türkiye

* *Corresponding author E-mail: torkan.haghi20@gmail.com*

Keywords

Nigella sativa

Essential oil

Antimicrobial synergy

Multidrug-resistant bacteria

Pathogens

Abstract

The rapid emergence of antibiotic-resistant bacteria coupled with the poor development of new antimicrobial agents has necessitated the search for alternative therapeutic strategies. An approach that holds promise in this aspect is the synergistic combinations of antibiotics and essential oils, which may enhance antibacterial efficacy through complementary mechanisms. Essential oils have broad-spectrum activity and have been gaining increasing attention as potential adjuvants to improve the performance of antibiotics and reduce the required dose of these drugs. This study assessed the synergistic effect on antibacterial activities between Black seed (Nigella sativa) essential oil with two antibiotics: Oxolinic acid (2 µg) and Netilmicin (30 µg), against Klebsiella pneumoniae ATCC 70063 and *Acinetobacter baumannii*. The disk diffusion assay was employed to measure inhibition zone diameters for antibiotics alone and in combinations with black seed essential oil. In *A. baumannii*, netilmicin gave an inhibition zone of 2.0 mm which increased to 2.3 mm in combination with essential oil; oxolinic acid had an inhibition zone of 1.0 mm rising to 1.1 mm upon addition of black seed oil. For *K. pneumoniae*, netilmicin increased from 2.4 mm to 2.7 mm in the presence of essential oil while oxolinic acid increased from 0.9 mm to 1.1 mm when combined with the oil as well so overall black seed essential oil exhibited limited yet significant synergistic potential with both antibiotics particularly against gram-negative bacteria thus such combinations might be a way to increase antimicrobial activity helping resistance development mitigation.

1. Introduction

The worldwide diffusion of bacteria that resist antibiotics has turned out to be one of the most important public health issues in this century [1,2]. Gram-negative pathogens, for example, *Klebsiella pneumoniae* and *Acinetobacter baumannii* are highly alarming due to their inherent resistance mechanisms and capability to quickly obtain additional resistance determinants [3]. These organisms are mostly connected with hospital-acquired infections like pneumonia, bloodstream infections, wound infections as well as urinary tract infections; they frequently demonstrate resistance against multiple classes of antibiotics [4].

The restricted pipeline of newly developed antibiotics has heightened the search for alternative or complementary antimicrobial strategies [5]. Among these, the use of natural products as antibiotic adjuvants has gained increasing attention. Essential oils derived from medicinal plants are complex mixtures of bioactive compounds; terpenes, phenolics, and alkaloids may exert antimicrobial effects through membrane disruption enzyme inhibition and interference with cellular metabolism [6,7].

Nigella sativa is referred to as black cumin or black seed. It has a place in medicine going back to ancient history. Its essential oil has a variety of activities, including, but not limited to, antimicrobial effects, antioxidant effects, immunomodulatory effects, and anti-inflation activities [8,9]. Several authors have reported that thymoquinone, the essential oil of black seed, increases the efficacy of many antibiotics in use, as it enhances the permeability of bacterial membranes and inhibits the expulsion of antibiotics from resistant bacteria and or enhances the susceptibility of bacteria to their antibiotics [10,11].

This study aimed to evaluate whether there are any synergistic antibacterial effects from the combination of *Nigella sativa* essential oil, oxolinic acid and netilmicin antibiotics towards *K. pneumoniae* ATCC 70063 and *A. baumannii* ATTC BAThese interactions could provide insight on the potential development of combination therapy to enhance treatment effectiveness while minimizing the risk of antimicrobial resistance.

2. Materials and Methods

2.1. Bacterial Strains

The strains of bacteria were Acinetobacter baumannii ATTC BA1609 and Klebsiella pneumoniae ATCC These isolates represented strains that were clinically significant and had established resistance patterns. In order to preserve viability, the cultures were subcultured prior to the experiments and kept on Mueller-Hinton agar (MHA).

2.2. Essential Oil and Antibiotics

The essential oil of black seed (Nigella sativa) was purchased from a commercial source and stored at 4 °C in a dark container until needed. the use of antibiotics.

2.3. Disk Diffusion Assay

Antibacterial activity was assessed by the disk diffusion method as per standard protocols. Briefly, bacterial suspensions in sterile saline were prepared and adjusted to a turbidity equivalent to the 0.5 McFarland standard. The suspensions were evenly spread on Mueller–Hinton agar plates using sterile swabs. Antibiotic disks were placed on the agar surface either alone or impregnated with a defined volume of black seed essential oil. Plates were incubated at 37 °C for 18–24 hours, and after incubation, inhibition zone diameters were measured in millimeters. All experiments were performed in triplicate, and mean values were calculated.

2.4. Evaluation of Synergistic Effects

Zones of inhibition for antibiotics alone were compared with those obtained from antibiotic–essential oil combinations to determine synergy. An increase in the zone of inhibition diameter in the presence of essential oil was taken as evidence of a synergistic or additive interaction.

3. Results and Discussion

The results of antibacterial activities of netilmicin and oxolinic acid, alone and in combination with black seed essential oil, are presented here. Netilmicin alone gave an inhibition zone of 2.0 mm which increased to 2.3 mm when combined with black seed essential oil, indicating approximately a 15% increase in the size of the zone. Oxolinic acid alone produced a 1.0 mm inhibition zone that increased to 1.1 mm in the presence of the essential oil, representing an approximate 10% increase. For *K. pneumoniae*, netilmicin produced an inhibition zone of 2.4 mm when used alone; this increased to 2.7 mm when it was combined with black seed essential oil (approximately 12.5% increase). The oxolinic acid increased from 0.9 mm to 1.1 mm upon combination with the essential oil which corresponds to an approximate increase by about 22.2%.

Black seed essential oil has shown a limited but consistent enhancement of antibiotic activity, particularly against Gram-negative pathogens. This study has proved that black seed essential oil can slightly improve the antibacterial activity of netilmicin and oxolinic acid against *K. pneumoniae* and *A. baumannii*. Though small increases in inhibition zone diameters were noted, these effects were reproducible and indicated a measurable synergistic or additive interaction consistent with previous reports on essential oil-antibiotic combinations [12,13].

The increased effect seen in the combinations might be due to the many ways that essential oils work. *N. sativa* essential oil has some parts, like thymoquinone and other active compounds, which are known to break bacterial cell membranes, block metabolic pathways, stop the making of toxins, and lessen biofilm creation. This kind of action might increase the permeability of bacterial membranes, hence making it easier for antibiotics to enter and work effectively. With the aminoglycoside antibiotic netilmicin, the trends were more pronounced. This implies that the essential oil's membrane-disruptive properties may especially improve antibiotics that need intracellular access to function at their best. It should be noted that disk diffusion assays are used for a preliminary evaluation of antimicrobial interactions. Because diffusion-based methods are not capable of capturing dynamic bactericidal effects accurately, the minor variations observed in this case may actually underestimate the real synergistic potential. Hence, further studies will be necessary to confirm and more precisely assess these interactions through checkerboard assays, fractional inhibitory concentration index analysis, minimum inhibitory concentration determination, and time kill kinetics.

4. Conclusion

In this study, it was shown that black seed (*Nigella sativa*) essential oil, when used with netilmicin and oxolinic acid, had low, but reliable synergistic effect against *K. pneumoniae* and *A. baumannii*. These results are in line with other studies to support essential oils use with antibiotics as adjuvants to enhance their antibacterial efficacy [12,13,20]. Higher therapeutic successes can arise from only slight increases in antibiotic activity; hence, the observed synergy is likely clinically relevant when it comes to infections with multidrug-resistant Gram-negative pathogens [2,5]. The

evidence has supported the use of essential oil and antibiotics in combination and is aimed to help resolve the growing problem of antimicrobial resistance. Future studies should aim to elucidate the molecular mechanisms as well as confirm this observation using rigorous quantitative *in vitro* and *in vivo* systems.

References

[1] World Health Organization (WHO). Global action plan on antimicrobial resistance. Geneva: WHO Press; 2015.

[2] Ventola CL. The antibiotic resistance crisis: Causes and threats. Pharmacy and Therapeutics. 2015;40(4):277–283.

[3] Rice LB. Federal funding for the study of antimicrobial resistance in nosocomial pathogens: No ESKAPE. Journal of Infectious Diseases. 2008;197(8):1079–https://doi.org/10.1086/533452

[4] Peleg AY, Hooper DC. Hospital-acquired infections due to Gram-negative bacteria. New England Journal of Medicine. 2010;362(19):1804–https://doi.org/10.1056/NEJMra0904124

[5] Tacconelli E, Carrara E, Savoldi A, et al. Discovery, research, and development of new antibiotics: The WHO priority list of antibiotic-resistant bacteria. The Lancet Infectious Diseases. 2018;18(3):318–https://doi.org/10.1016/S1473-3099(17)30753-3

[6] Burt S. Essential oils: Their antibacterial properties and potential applications in foods—A review. International Journal of Food Microbiology. 2004;94(3):223–https://doi.org/10.1016/j.ijfoodmicro.2004.03.022

[7] Nazzaro F, Fratianni F, De Martino L, Coppola R, De Feo V. Effect of essential oils on pathogenic bacteria. Pharmaceuticals. 2013;6 (12):14511–https://doi.org/10.3390/ph6121451

[8] Ali BH, Blunden G. Pharmacological and toxicological properties of Nigella sativa. Phytotherapy Research. 2003;17(4):299–https://doi.org/10.1002/ptr.1309

[9] Randhawa MA, Alghamdi MS. Anticancer activity of Nigella sativa (black seed): A review. American Journal of Chinese Medicine. 2011;39(6):1075–https://doi.org/10.1142/S0192415X1100941X

[10] Salman MT, Khan RA, Shukla I. Antimicrobial activity of thymoquinone against multidrug-resistant strains of Staphylococcus aureus. Fitoterapia. 2008;79(6):456–https://doi.org/10.1016/j.fitote.2008.04.005

[11] Bakathir HA, Abbas NA. Detection of the antibacterial effect of Nigella sativa ground seeds with water. African Journal of Traditional, Complementary and Alternative Medicines. 2011;10(3):377–https://doi.org/10.4314/ajtcam.v8i2.63203

[12] Hemaiswarya S, Kruthiventi AK, Doble M. Synergism between natural products and antibiotics against infectious diseases. Phytomedicine. 2008;15(8):639–https://doi.org/10.1016/j.phymed.2008.06.008

[13] Langeveld WT, Veldhuizen EJA, Burt SA. Synergy between essential oils and antibiotics: A review. Critical Reviews in Microbiology. 2014;40(1):76-https://doi.org/10.1111/jam.12600

[14] Forouzanfar F, Bazzaz BSF, Hosseinzadeh H. Black cumin (Nigella sativa) and its constituent thymoquinone: A review on antimicrobial effects. Iranian Journal of Basic Medical Sciences. 2014;17(12):929–938.

[15] Ultee A, Bennik MHJ, Moezelaar R. The phenolic hydroxyl group of carvacrol is essential for action against the food-borne pathogen Bacillus cereus. Applied and Environmental Microbiology. 2002;68(4):1561–https://doi.org/10.1128/AEM.68.4.1561-1568.2002

[16] Krause KM, Serio AW, Kane TR, Connolly LE. Aminoglycosides: An overview. Cold Spring Harbor Perspectives in Medicine. 2016;6(6):ahttps://doi.org/10.1101/cshperspect.a027029

[17] Yap PSX, Lim SHE, Hu CP, Yiap BC. Combination of essential oils and antibiotics in overcoming antibiotic resistance. Frontiers in Microbiology. 2014; 5:https://doi.org/10.3389/fmicb.2014.00672

[18] Balouiri M, Sadiki M, Ibnsouda SK. Methods for in vitro evaluating antimicrobial activity: A review. Journal of Pharmaceutical Analysis. 2016;6(2):71–https://doi.org/10.1016/j.jpha.2015.11.005

[19] Odds FC. Synergy, antagonism, and what the chequerboard puts between them. Journal of Antimicrobial Chemotherapy. 2003;52(1):1–https://doi.org/10.1093/jac/dkg301

[20] Yap PSX, Yiap BC, Ping HC, Lim SHE. Essential oils, a new horizon in combating bacterial antibiotic resistance. The Open Microbiology Journal. 2015; 8:6-https://doi.org/10.1016/j.tibtech.2015.07.003

Characterization of Annealed and Unannealed Iron-Doped Tungsten Oxide Thin Films Grown by Co-Sputtering

Hilal Kübra Sağlam[1,3*], Sevda Sarıtaş[2,3]

[1] Department of Electrical and Electronics Engineering, Faculty of Engineering, Atatürk University, Erzurum, Türkiye
[2] Department of Electrical and Energy, İspir Hamza Polat Vocational School, Atatürk University, Erzurum, Türkiye
[3] Department of Nano-Science and Nano-Engineering, Institute of Science and Technology, Ataturk University, Erzurum, Türkiye

* *Corresponding author E-mail: hilalk.saglam@atauni.edu.tr*

Keywords

Thin film
Optical analyses
Magnetron sputtering
Tungsten oxide
Nanomaterial

Abstract

Metal oxides, such as tungsten oxide, are frequently investigated in electronic technology due to their practical applications and low cost. The positive effects of iron doping are documented in the literature. The changes in characterizations caused by the annealing process applied to the films were examined. According to XRD graphs, the crystal structure is homogeneous in both films. When considering absorptions, film F2 has a more stable structure than film FThe bandgap decreased by approximately 0.15 eV after annealing. According to SEM images, polycrystalline nanostructures were obtained in both films.

1. Introduction

Nanostructured materials have become a subject of research for devices such as gas sensors, solar cells, and photocatalysts due to their unique properties compared to their counterparts. Nanostructured oxide semiconductors are attracting attention because of their potential applications. The performance of oxide semiconductors can be improved by doping with transition metals. Smooth structures consisting of ultra-fine nanowires can be obtained. For example, Co-doped tungsten oxide nanoblocks, lens-shaped bundled Zn-doped tungsten oxide nanorods, and plate-shaped or flower-like Fe-doped tungsten oxide particles. Studies involving transition metal-doped tungsten oxide nanostructures are particularly available in the literature. Fe-doped tungsten oxide flowers have formed due to the regular arrangement of single nanoplates [1,2].

Tungsten oxide among MOSs has high electrical conductivity, a stable structure, and is inexpensive. Therefore, it has been used in various fields such as sensors, optical modulation devices, and displays. In fact, since the thin film is the main component of the sensor, the structural, optical, and morphological characterization of the Fe-doped WO_3 film is being investigated. Characterization analysis is necessary because there are few studies on Fe-doped WO_3 used as the sensing layer [3].

The gas sensing properties of metal oxides, although dependent on characteristic properties, can be improved with some modifications. These modifications include: modifying the surface morphology of the films, reducing the particle size, and adding impurities. Because thin films are generally compact, the sensing layer is limited to the surface. However, thick films are generally porous and therefore can interact with all types of gases. If this porous structure can be controlled, the sensor performance of nanostructures can be improved. Furthermore, the sensitivity to specific gases increases when dopant metals are added to oxide thin films. An increase in response to specific gases has also been observed in iron oxide-doped tungsten oxide thin films [4].

Nanomaterials offer more advantages for surface-gas interaction due to their high surface-to-volume ratio and are open to new opportunities in sensing properties. In addition to these gains, thin-film nanostructured metal oxide sensors continuously monitor various gases without the need for additional infrastructure such as power supplies. When this enormous potential is explored, it is found that the sensing behavior of these sensors depends on the electrical resistance between the film surface and the target gases. In addition to the previously mentioned grain size, film thickness, and porous structure, crystallinity and film stoichiometry are also affected by charge transport mechanisms. As a result, a change in resistance occurs [5].

In addition to sensor research, transition metal oxide thin films are also quite useful in the design of many optical devices. WO_3 thin films, preferred for radiation measurement due to their structural sensitivity, are creating a new

platform in smart windows. These devices control incoming solar radiation and visible radiation, providing a comfortable environment. Furthermore, these films have the ability to optimize coloring efficiency, optical modulation, and switching time due to their electrochromic properties. Thus, they make efficient films possible for applications such as display devices and electrochemical mirrors [6].

In this study, films obtained using the co-sputter growth technique, which differs from other growth techniques in the literature, were investigated. The structural, optical, and morphological properties of iron-doped tungsten oxide films, both untreated and heat-treated after the growth process, were analyzed. The effects of heat treatment on characterization were investigated. Characterization analyses included XRD, absorbance, band gap, and SEM data.

2. Materials and Methods

The iron doped WO_3 structure was grown with the co-sputtering. The sputter technique is the growth of ions, atoms and molecules broken from the metal target on the heated substrate cleaned by chemical processes as a thin film with the help of inert gas. To break the material to be grown from the metal target, argon is turned into an inert gas carrier plasma with the help of an RF or DC power source and the plasma performs the detachment process by beating the surface of the target metal. The iron sputtering foil target has 2 inches (dia) x 0.005 inches (thickness) and the W sputtering metal target has 2 inches (dia) x 0.005 inches (thickness). An iron target was placed in the DC power gun and a W target was placed in the RF gun source. The sputter technique has been preferred because it is a reproducible, relatively low cost, and low surface roughness film growth technique that can more easily control the optical and structural properties of the grown film. In the sputter technique, due to the vacuum environment, the pollution rate is lower and higher quality binary and triple compounds are grown. In this experimental study, an iron thin foil was attached to the DC power supply and a W metal target was attached to the RF power supply part. While the DC power supply is 90 watts, the RF power supply is set to 50 watts. The glass substrates placed for the vacuum chamber up to $6*10^{-6}$ Torr pressure (base pressure) were heated up to 400 degrees. Then 100 sscm of inert argon gas was sent in and plasma was formed. Then, 45 sscm of argon and 5 sscm of oxygen gas were given to grown pressure of $8{,}2*10^{-3}$ Torr and growth was made for 38 minutes. In this study, the structural, optical properties of iron-doped WO_3 structures grown by RF-DC co-sputtering were investigated by scanning electron microscopy (SEM), X-ray diffraction (XRD), and UV-VIS spectroscopy.

To investigate the effect of annealing on characterization, some of the films grown using the co-sputter growth technique were subsequently subjected to heat treatment. Annealing was performed at 560°C. Thus, the structural, optical, and morphological properties of unannealed and annealed iron-doped tungsten oxide films were compared. Unannealed films are named as F1, while annealed films are named as F2.

3. Results and Discussion

3.1. Crystal structure

Examination of the XRD graphs revealed that the crystal structure was uniform in both constructs (Figure 1). Characteristic WO_3 peaks were observed. According to the graphs, the main peaks occurred at the same degree. However, it was observed that the quality of the crystal structure improved after annealing at 560°C.

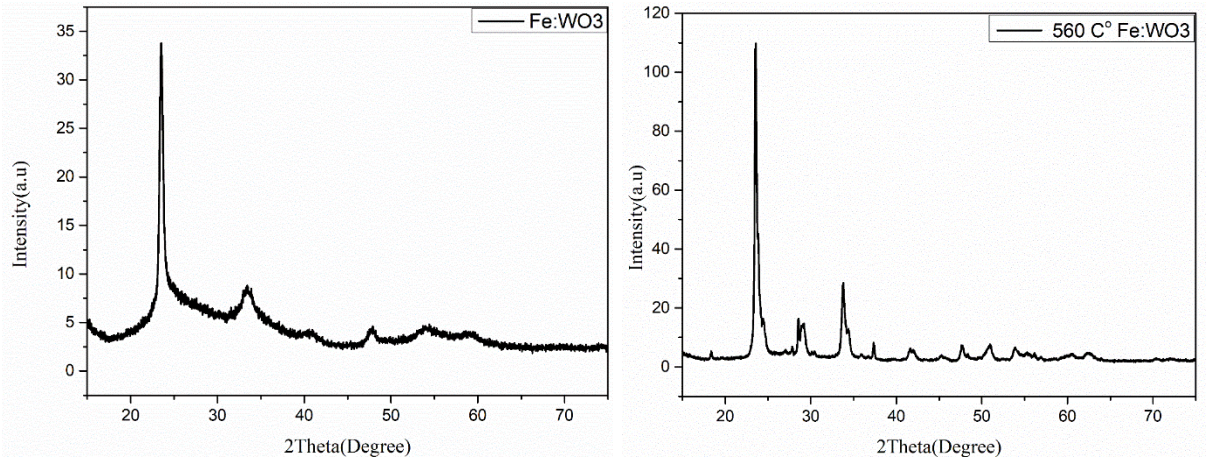

Figure 1 XRD graphs of films a) F1 and b) F2 [7]

3.2. Optical properties

Absorption graphs support the XRD analyses. The film structure annealed at 560°C is more stable (Fig. 2b). This is because absorption was measured in the Fe:WO_3 film, which was not subjected to annealing (Fig. 2a), even at low energies and high wavelengths.

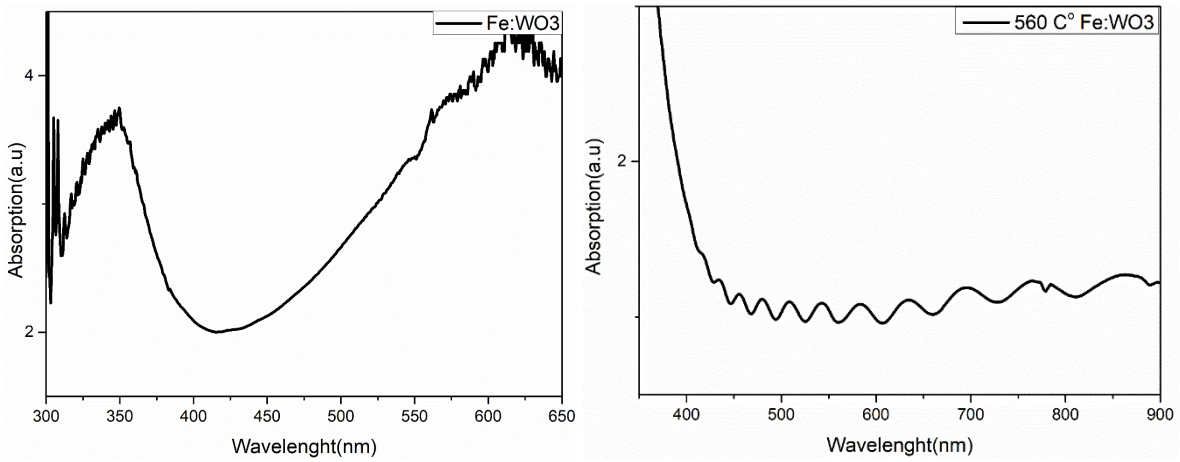

Figure 2 Absorbance graphs of films a) F1 and b) F2

Optical band gap (Eg) values were calculated from the well-known Tauc equation. The band gap of the unannealed thin film is 3,3 eV, while the band gap of the annealed film is approximately 3,15 eV (Fig. 3). A decrease of approximately 0,15 eV was measured after annealing.

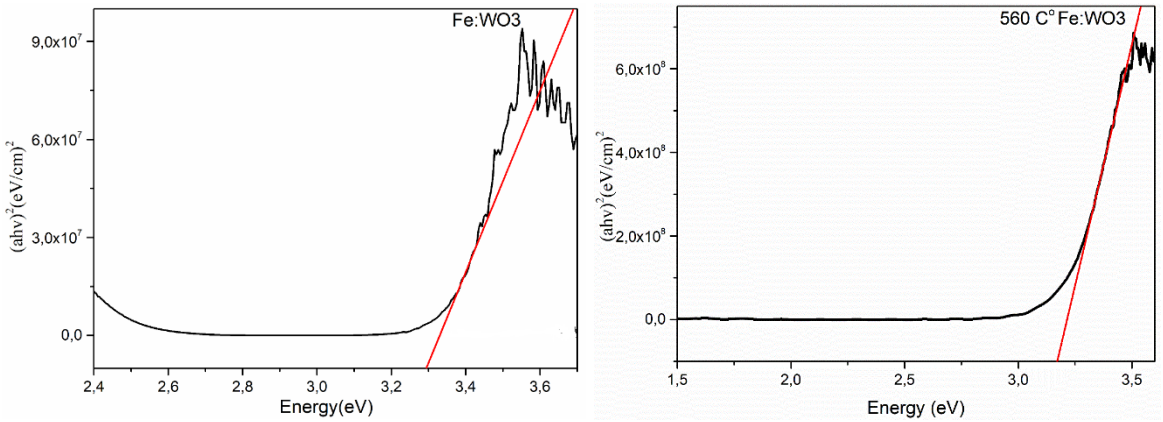

Figure 3 Bandgap graphs of films a) F1 and b) F2

3.3. Surface morphology

After annealing, polycrystalline structures and nanostructures on their surfaces were observed in the film. SEM images of the samples are shown at x40,000 and 20,000 magnification (Fig.4).

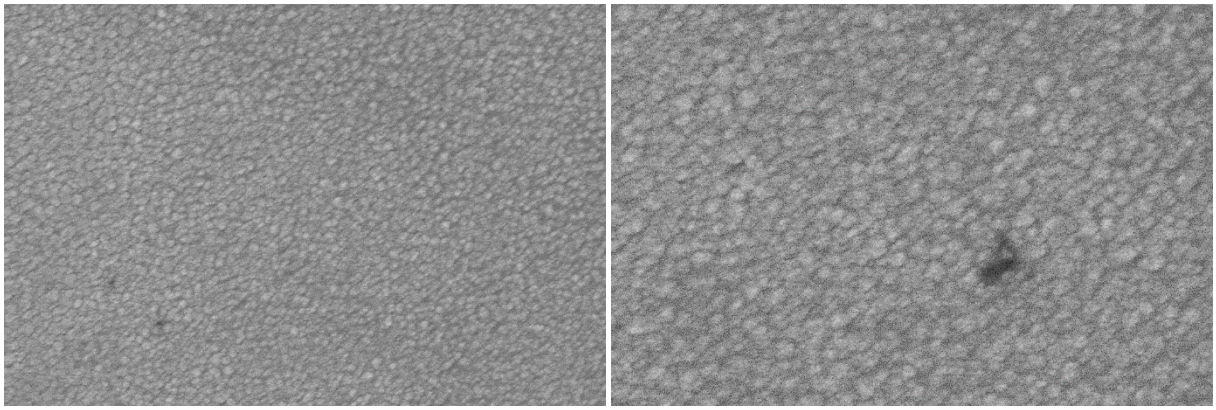

Figure 4 SEM graphs of F2 a) 20.000x and b) 40.000x

4. Conclusion

Metal oxide nanomaterials are a subject of research in electronic technology due to their unique properties. Tungsten oxide is preferred in thin film growth of electronic devices due to its low cost, high electrical conductivity, and stability. Performance improvement is observed when transition metals are selected as dopant materials.

This study includes the crystal structure, optical, electrical, and surface morphology properties of iron-doped tungsten oxide thin films. Properties before and after annealing were compared. The properties investigated are: crystal structure, optical-electrical properties, and surface morphology. Homogeneous polycrystalline structures were successfully formed in F1 and F2 films. F2 films obtained after annealing have a more stable structure. A decrease of 0.15 eV was measured when F1 films were subjected to annealing. Initially, this study, which includes characterization analyses, aims to test the sensor performance of iron-doped tungsten oxide thin films due to their efficient properties.

References

[1] Chang, X., Sun, S., Xu, X., & Li, Z. (2011). Synthesis of transition metal-doped tungsten oxide nanostructures and their optical properties. Materials Letters, 65(11), 1710-

[2] Si, P. Z., Choi, C. J., Brück, E., Klaasse, J. C. P., Geng, D. Y., & Zhang, Z. D. (2007). Synthesis, structure and magnetic properties of iron-doped tungsten oxide nanorods. Physica B: Condensed Matter, 392(1-2), 154-158.

[3] Osiac, M., Cioatera, N., & Jigau, M. (2020). Structural, morphological, and optical properties of iron doped WO3 Thin film prepared by pulsed laser deposition. Coatings, 10(4), 412.

[4] Tesfamichael, T., Arita, M., Bostrom, T., & Bell, J. (2010). Thin film deposition and characterization of pure and iron-doped electron-beam evaporated tungsten oxide for gas sensors. Thin Solid Films, 518(17), 4791-4797.

[5] Tesfamichael, T., Ponzoni, A., Ahsan, M., & Faglia, G. (2012). Gas sensing characteristics of Fe-doped tungsten oxide thin films. Sensors and Actuators B: Chemical, 168, 345-353.

[6] Pandurangarao, K., Purnachand, N., & Kumar, V. R. (2020). Studies on magnetron sputtered deposited nanocrystalline tungsten oxide films useful for electrochromic devices. Optical Materials, 101, 109791.

[7] Sarıştaş, S. Structural investigation of the effect of annealing temperature on the Fe:WO3 structure on a silicon substrate (In-Press). NanoEra

Microcontroller-Based Smart Monitoring Solutions for Critical Communication and Energy Infrastructures

Tuba Çakıcı Can [1,2,*]

[1] Department of Electrical and Automation, Technical Sciences Vocational School, Ataturk University, 25250 Erzurum, Türkiye
[2] Department of Nano-Science and Nano-Engineering, Institute of Science and Technology, Ataturk University, 25240 Erzurum, Türkiye

* *Corresponding author E-mail: tuba.cakici@atauni.edu.tr*

Keywords

Microcontroller-Based Systems
Smart Infrastructure
RF Monitoring
Embedded Systems
Fault Detection

Abstract

This study presents two complementary microcontroller-based smart monitoring platforms developed to enhance situational awareness, fault diagnosis, and operational reliability in critical communication and energy infrastructures. The first platform is an intelligent interruption detection unit capable of distinguishing between feed-side and subscriber-side faults in less than one second, significantly reducing diagnosis time and operational uncertainty. The second platform is a modular RF monitoring and active privacy simulation system designed for portable spectrum analysis, signal direction estimation, and experimental evaluation of hidden or deceptive communication modes. Both systems are implemented using cost-effective embedded control architectures based on Arduino Nano and ESP32 microcontrollers, enabling rapid development, flexible expansion, and seamless integration with sensors and communication interfaces. Experimental evaluations demonstrate that the proposed solutions provide practical, low-cost, and field-deployable alternatives to conventional centralized monitoring systems. In addition, the modular RF platform, developed within the scope of a TÜBİTAK 2209-A undergraduate research project, extends the system toward wireless security, interference analysis, and smart infrastructure protection..

1. Introduction

Communication and energy infrastructures play a critical role in sustaining modern life by enabling uninterrupted access to electricity, data transmission, and communication services. As these infrastructures expand and become more interconnected, operational reliability and rapid fault management have emerged as key challenges. Even short-term interruptions can lead to significant economic losses, service disruptions, and safety risks, particularly in systems that support industrial facilities, data centers, and communication networks [1,2].

In many real-world scenarios, when an interruption occurs, it is not immediately clear whether the fault originates from the energy provider or from the subscriber side. This uncertainty often results in parallel field interventions by multiple institutions, unnecessary deployment of technical teams, and prolonged resolution times. Traditional monitoring approaches generally rely on centralized measurement equipment or manual testing procedures, which are not always suitable for fast, on-site diagnosis and continuous monitoring [3].

Recent advances in embedded systems have enabled the development of compact, low-cost, and flexible monitoring solutions that can be deployed directly within operational environments. Microcontroller-based platforms such as Arduino and ESP32 offer practical advantages including low power consumption, modular design, and easy integration with sensors and communication interfaces. These features make embedded architectures particularly attractive for smart infrastructure applications where scalability, affordability, and real-time response are essential [4,5]. Alongside fault detection in energy and communication lines, the growing complexity of wireless environments has created an increasing need for portable RF monitoring solutions. Dense wireless deployments, shared frequency bands, and unauthorized or interfering transmissions can significantly affect system performance and security. Conventional RF analysis tools are often laboratory-based, expensive, and impractical for routine field use. As a result, there is a growing interest in lightweight, embedded RF monitoring systems capable of spectrum observation, signal characterization, and basic security-oriented analysis [7,8].

In this study, an integrated smart monitoring framework is proposed to address these challenges through two complementary platforms. The first platform is an intelligent interruption detection unit designed to rapidly distinguish between feed-side and subscriber-side faults in communication and energy infrastructures. The second platform is a modular RF monitoring and active privacy simulation system that extends the framework toward wireless environment analysis and security-related applications. This RF monitoring platform was developed within the scope of a TÜBİTAK 2209-A undergraduate research project and is designed as a scalable extension of the main monitoring architecture. By combining practical fault diagnosis with modular RF monitoring capabilities, the proposed framework bridges operational infrastructure needs with experimental and educational applications. The resulting system not only supports faster and more reliable fault management but also provides a flexible platform for research, training, and future developments in smart infrastructure monitoring.].

2. Materials and Methods

The proposed smart monitoring framework was developed with a modular and application-oriented design approach, aiming to provide practical solutions for fault diagnosis and wireless monitoring in communication and energy infrastructures. The system consists of two complementary hardware platforms: an intelligent interruption detection unit and a modular RF monitoring and active privacy simulation platform. While each platform can operate independently, they are designed to function cohesively within a unified monitoring architecture. The overall system structure and interconnections are illustrated in Figure 1.

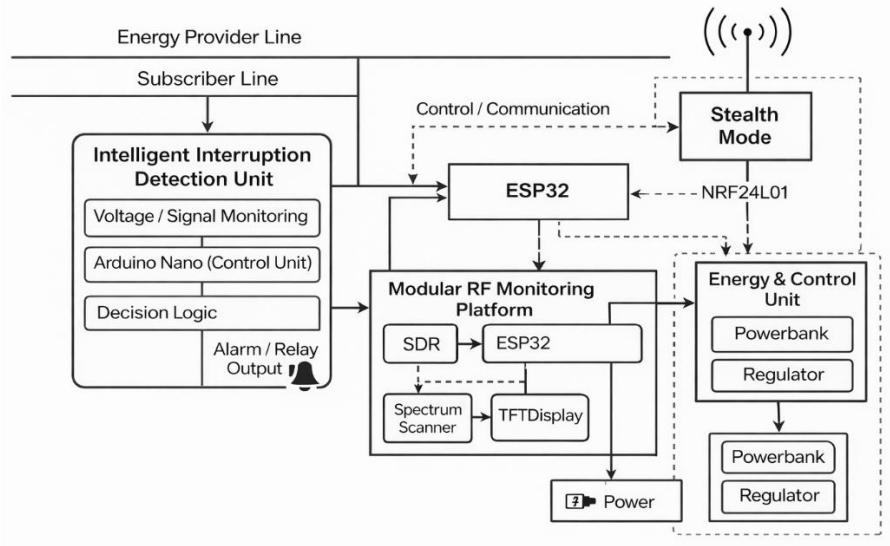

Figure 1 Block diagram of the microcontroller-based intelligent interruption detection and modular RF monitoring system.

2.1. Intelligent Interruption Detection Unit

The intelligent interruption detection unit was designed to identify the source of service interruptions by distinguishing between feed-side and subscriber-side faults in real time. The system is built around an Arduino Nano microcontroller, selected due to its compact size, low power consumption, and suitability for continuous monitoring applications. To enable fault localization, voltage and signal monitoring points were placed on both the input line (energy provider side) and the output line (subscriber side). During normal operation, the microcontroller continuously evaluates the presence and stability of signals at both monitoring points. When an interruption occurs, the system compares the signal states and applies a threshold-based decision logic combined with simple time-domain analysis. This approach allows the system to determine whether the interruption originates upstream or downstream of the monitoring unit. The decision process is completed within less than one second, enabling rapid response without the need for manual testing or external measurement equipment.

The system provides immediate feedback through visual indicators and audible alarms, allowing operators to quickly recognize the type and location of the fault. In addition, relay-based outputs were incorporated to support integration with external alarm, notification, or supervisory systems. The hardware layout was designed to be compact and robust, facilitating installation within existing infrastructure cabinets and field environments. A three-dimensional view of the printed circuit board, illustrating the placement of control, power regulation, and alarm components, is presented in Figure 2.

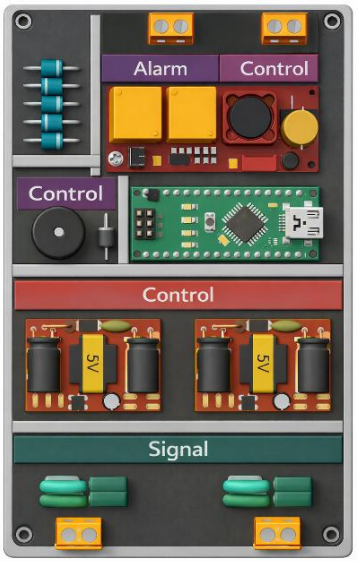

Figure 2 Three-dimensional PCB layout of the proposed smart monitoring unit, including control, power regulation, alarm, and signal interfaces.

2.Modular RF Monitoring and Active Privacy Simulation Platform

To complement the interruption detection functionality, a modular RF monitoring and active privacy simulation platform was developed as an extension of the overall system architecture. This platform was implemented within the scope of a TÜBİTAK 2209-A undergraduate research project and is primarily focused on the portable analysis of wireless environments. The system is based on an ESP32 microcontroller, selected for its higher processing capability, integrated wireless communication interfaces, and compatibility with external RF modules.



Figure 3 Two-dimensional labeled layout highlighting the control, signal, and alarm modules of the proposed system.

The RF monitoring platform enables real-time observation of wireless activity by scanning predefined frequency bands and evaluating signal presence and strength. External antennas and RF modules are employed to support directional analysis and to enhance sensitivity during portable operation. Owing to its modular design, the RF platform can operate independently or be directly integrated with the intelligent interruption detection unit, depending on the intended application scenario. Beyond passive monitoring, the platform also supports experimental active privacy simulation through the generation of controlled RF signals. This feature allows the investigation of interference scenarios and basic security-oriented experiments under controlled conditions. Such capabilities are particularly valuable for educational, training, and research applications where flexible, low-cost, and field-deployable RF experimentation tools are required. The functional organization of the modular RF monitoring and active privacy

simulation platform is illustrated in Figure 3, which presents a two-dimensional labeled layout highlighting the separation of the alarm, control, and signal modules. This intentional separation improves system clarity, scalability, and ease of modification. Within this structure, the control module coordinates data acquisition and processing tasks, while the signal module manages power and signal distribution. The alarm module operates independently to provide timely user notification when abnormal conditions are detected. The simplified two-dimensional representation enhances system readability and emphasizes the adaptable and scalable nature of the proposed platform without introducing unnecessary hardware-level complexity.

3. Results and Discussion

The performance of the proposed smart monitoring framework was evaluated under controlled test conditions designed to reflect common scenarios encountered in communication and energy infrastructures. The experimental implementation demonstrates that the integration of intelligent interruption detection with modular RF monitoring can be achieved using a compact and well-organized embedded architecture. The physical realization of the system, shown in Figure 2, confirms that all critical hardware components can be accommodated on a single PCB without compromising operational stability or modularity. For the intelligent interruption detection unit, multiple interruption scenarios were introduced by selectively disabling the input and output lines. In all test cases, the system successfully identified whether the interruption originated from the energy provider side or the subscriber side. The decision process was consistently completed within less than one second, representing a significant improvement compared to conventional manual testing procedures. This rapid response capability enables technical teams to quickly determine the responsible intervention point, thereby reducing unnecessary field operations and shortening service restoration times. Beyond response speed, system stability was carefully observed during repeated interruption cycles. The monitoring unit maintained consistent behavior without false triggering or misclassification, indicating that the applied threshold-based decision logic provides sufficient robustness for practical deployment. The hardware layout presented in Figure 2 reflects a deliberate placement strategy in which control, power regulation, and alarm-related components are arranged to minimize signal interference and ensure reliable operation under continuous monitoring conditions. From an operational perspective, the use of clear visual and audible indicators proved effective in conveying fault information without requiring specialized technical interpretation, which is particularly important in distributed infrastructure environments.

The modular RF monitoring platform demonstrated reliable performance in portable spectrum observation and wireless activity analysis. During testing, the system detected active signals within predefined frequency ranges and provided qualitative information regarding signal presence and relative strength. While the platform is not intended to replace laboratory-grade spectrum analyzers, the obtained results confirm that low-cost embedded hardware can deliver meaningful insight into wireless environments when portability and accessibility are prioritized. The functional organization of the system was further examined using the modular layout illustrated in Figure This two-dimensional representation clarifies the separation between alarm, control, and signal modules and offers insight into how system tasks are distributed across different functional layers. Such modular separation proved beneficial during testing, as it allowed individual subsystems to be analyzed, modified, or extended without affecting the overall architecture. Within this structure, the control module acted as the central coordination unit, managing data acquisition and decision-making processes, while the signal module ensured stable power and signal distribution to all subsystems. The alarm module operated independently, providing immediate user feedback when abnormal conditions were detected.

The integration of RF monitoring with the interruption detection unit significantly enhances overall situational awareness. While the interruption detection unit focuses on energy continuity and fault localization, the RF platform provides complementary information about the surrounding wireless environment. This combined perspective is particularly valuable in modern infrastructures where communication systems and energy networks are increasingly interconnected. Moreover, the capability to experimentally simulate controlled RF activity enables the evaluation of interference scenarios and basic security-related behaviors in a safe and flexible manner. From a broader viewpoint, the experimental results highlight the practical advantages of microcontroller-based system architectures for smart infrastructure monitoring. The consistency between the physical layout in Figure 2 and the functional abstraction in Figure 3 demonstrates a coherent design approach in which hardware implementation and system logic are closely aligned. The modular design strategy supports incremental system evolution and future extensions without requiring fundamental changes to the core hardware.

Overall, the results indicate that the proposed framework offers a balanced combination of speed, reliability, and practicality. By addressing both fault diagnosis and wireless environment monitoring within a unified architecture, the system provides a versatile solution that aligns well with the evolving needs of smart communication and energy infrastructures.

4. Conclusion

This study presented a practical and integrated smart monitoring framework designed to address common challenges in communication and energy infrastructures. By combining an intelligent interruption detection unit with a modular RF monitoring and active privacy simulation platform, the proposed system offers a unified approach to fault diagnosis and wireless environment awareness. The interruption detection unit demonstrated the ability to rapidly and reliably distinguish between feed-side and subscriber-side faults, enabling faster decision-making and more efficient use of technical resources. This capability directly contributes to reducing unnecessary field interventions and minimizing service downtime. The clear and intuitive feedback mechanisms further support ease of use in real-world deployment scenarios.

The modular RF monitoring platform extended the system beyond basic fault detection by providing portable insight into wireless activity and enabling experimental evaluation of RF-related scenarios. Its low-cost and flexible design makes it suitable not only for operational monitoring but also for educational and research-oriented applications. When used together, the two platforms enhance overall situational awareness by addressing both energy continuity and communication environment conditions within a single framework. Overall, the results indicate that microcontroller-based embedded architectures can provide effective, scalable, and accessible solutions for smart infrastructure monitoring. The modular nature of the proposed system allows future expansion without significant redesign, supporting evolving requirements in communication technologies and infrastructure management. Future work will focus on system-level integration, software-based intelligence enhancements, and broader field testing to further strengthen the applicability of the proposed framework in real operational environments.

References

[1] Gungor, V. C., Sahin, D., Kocak, T., Ergut, S., Buccella, C., Cecati, C., & Hancke, G. P. (2011). Smart grid technologies: Communication technologies and standards. IEEE Transactions on Industrial Informatics, 7(4), 529–539.

[2] Mahmood, A., Javaid, N., Razzaq, S., & Khan, Z. A. (2015). A review of wireless communications for smart grid. Renewable and Sustainable Energy Reviews, 41, 248–260.

[3] Ghayvat, H., Mukhopadhyay, S. C., Gui, X., & Suryadevara, N. K. (2015). Internet of Things for smart homes and buildings: Technologies, applications, and challenges. IEEE Sensors Journal, 15(12), 6074–6089.

[4] Al-Fuqaha, A., Guizani, M., Mohammadi, M., Aledhari, M., & Ayyash, M. (2015). Internet of Things: A survey on enabling technologies, protocols, and applications. IEEE Communications Surveys & Tutorials, 17(4), 2347–2376.

[5] Sousa, E. L. d., Marques, L. A. d. A., Lima, I. d. S. F. d., Neves, A. B. M., Cunha, E. N., Kreutz, M. E., & Neto, A. J. V. (2023). Development of a low-cost wireless smart meter with power quality measurement for smart grid applications. Sensors, 23(16), 7210.

[6] Lin, Y.-C., & Shih, Z.-S. (2018). Design and simulation of a radio spectrum monitoring system with a software-defined network. Computers & Electrical Engineering, 68, 271–285.

[7] Silva, B. N., Khan, M., & Han, K. (2018). Towards sustainable smart cities: A review of trends, architectures, components, and open challenges. Sustainable Cities and Society, 38, 697–713.

[8] Akyildiz, I. F., Lee, W. Y., & Chowdhury, K. R. (2009). CRAHNs: Cognitive radio ad hoc networks. Ad Hoc Networks, 7(5), 810–836.

[9] Mudaliar, M. D., & Sivakumar, N. (2020). IoT based real-time energy monitoring system using Raspberry Pi. Internet of Things, 12, 100292.

[10] Zanella, A., Bui, N., Castellani, A., Vangelista, L., & Zorzi, M. (2014). Internet of Things for smart cities. IEEE Internet of Things Journal, 1(1), 22–32.

[11] Raza, S., Wallgren, L., & Voigt, T. (2013). SVELTE: Real-time intrusion detection in the Internet of Things. Ad Hoc Networks, 11(8), 2661–2674.

[12] Palattella, M. R., Dohler, M., Grieco, L. A., Rizzo, G., Torsner, J., Engel, T., & Ladid, L. (2016). Internet of Things in the 5G era: Enablers, architecture, and business models. IEEE Journal on Selected Areas in Communications, 34(3), 510–527.

Effect of Concrete Strength Class, Maximum Aggregate Particle Size, and Curing Type on Ultrasonic Pulse Velocity

İbrahim İshaq M. Alkhattab[1,*], Remzi Şahin[1]

1 Atatürk University, Engineering. Faculty, Dept. of Civil Engineering, Erzurum, TR

*Corresponding author e-mail: ibm.19th@gmail.com

Keywords

Concrete Compressive Strength,

Ultrasonic Pulse Velocity,

Concrete Curing,

Maximum Aggregate Particle Size,

Fresh Concrete Tests

Abstract

The Ultrasonic Pulse Velocity (UPV) method, although being a non-destructive testing technique, has certain limitations and may yield different results due to factors related to the internal structure of concrete. In this study, strength measurements were carried out using the UPV method on concrete mixtures produced by considering several parameters that are frequently varied in practice. For this purpose, concretes of different strength classes were produced by varying the water/cement ratio (W/C) and cement content (C), and these concretes were cured under different curing conditions (water, air, and moisture). The maximum aggregate particle size (8 mm, 16 mm, and 22.4 mm) was also defined as a parameter in the study. Fresh concrete tests included air content, unit weight, and slump tests. Hardened concrete tests were conducted on a total of 54 cube specimens with dimensions of 15×15×15 cm³ at the age of 28 days. The results obtained from the experiments indicated that the behavior of fresh concrete varied depending on the concrete strength class achieved by changing the water/cement ratio and cement dosage, as well as on the maximum aggregate particle size. As the concrete strength class increased, UPV values also increased. Likewise, as the maximum aggregate particle size in the mixtures increased, UPV values were observed to increase depending on the concrete strength class. For all three concrete strength classes, the highest UPV values were obtained from specimens cured in water.

1. Introduction

The evaluation of the mechanical properties of concrete is of critical importance for quality assurance, assessment of structural integrity, and maintenance of existing structures. For this purpose, various non-destructive testing (NDT) and semi-destructive testing (SDT) methods have been developed. Table 1 provides an overview of the principal techniques used in this field [1,2].

Table 1 Selection of Concrete Evaluation Tests [3]

Name	Type	Principle	Advantages	Limitations
Schmidt Rebound Hammer	Non-Destructive	Measures surface hardness and correlates rebound values with compressive strength.	Simple, portable, and fast.	Sensitive to moisture, carbonation, and surface texture.
Ultrasonic Pulse Velocity	Non-Destructive	Measures the velocity of ultrasonic waves; detects cracks and voids and evaluates homogeneity.	Detects internal defects; non-invasive.	Interpretation can be complex; affected by moisture content.
Windsor Probe	Semi-Destructive	Estimates strength based on the penetration depth of a fired steel probe..	Provides direct in-situ assessment without coring..	Causes minor surface damage; calibration is required.
Resonance Frequency	Non-Destructive	Evaluates elastic properties and detects cracks by measuring the natural frequency.	Sensitive to small defects; does not cause surface damage..	Requires precise setup and interpretation.
Pin Penetration	Semi-Destructive	Estimates surface strength by measuring pin penetration depth..	Fast and economical for early-age concrete.	Not standardized; provides localized results.

Name	Type	Principle	Advantages	Limitations
Pull-Out	Semi-Destructive	Measures the force required to pull out an embedded anchor; correlated with compressive strength.	Reliable for in-situ strength estimation.	Surface damage; requires pre-installed anchors.
Break-Off	Semi-Destructive	Measures the force required to break off a portion of concrete..	Provides direct local strength assessment..	Requires specific preparation; causes visible damage.
Pull-Off	Semi-Destructive	Measures the tensile force required to pull a bonded disc from the surface.	Evaluates surface tensile strength and bond quality.	Surface damage; adhesion plays a critical role.
Combined Methods	Non-Destructive /Semi-Destructive	Verifies or improves measurements by combining multiple methods..	Increased reliability; broader evaluation..	Time-consuming; requires expertise.

In the UPV test, a longitudinal vibration pulse is generated by an electro-acoustic transducer in contact with the concrete surface. This pulse propagates through the concrete by reflecting from the boundaries of different material phases within the concrete, producing a complex stress wave system that includes both longitudinal and shear waves. The first waves to reach the receiving transducer are longitudinal waves, which are converted into an electrical signal by another transducer. Electronic timing circuits then measure the pulse transit time (t) [4].

UPV measurements performed on reinforced concrete structures can be used for quality control purposes. Pulse velocity measurements are more directly related to the concrete within the structure compared to mechanical tests carried out on control specimens such as cubes or cylinders. Control specimens, however, may not always represent the actual concrete in the structure. Nevertheless, for pulse velocity test results to be compatible with the results obtained from structural elements, it is more appropriate to establish a correlation between strength or other significant properties. Such correlations can be readily developed for prefabricated components and field applications. Empirical correlations can also be established between the dynamic and static elastic moduli and the strength of concrete. However, UPV results should be evaluated with greater caution, especially when dealing with concrete strengths exceeding 60 MPa [5].

The purpose of the study is to reveal the effect of concrete class, maximum aggregate particle size, and curing environment—parameters that are frequently changed in practice—on UPV readings. The present paper includes the results of fresh concrete tests and UPV measurements obtained from a comprehensive thesis study.

2. Material and Method

2.1. Material

In the experiments, CEM I 42.5 R type cement produced in accordance with TS EN 197-1 by the Erzurum Cement Plant of Aşkale Çimento San.&Tic. A.Ş. was used. The chemical and physical properties of the cement obtained from the manufacturer were presented in Table 2.

Table 2 Chemical and Physical Properties of the Cement

Chemical Analyses	Standards	Results (%)
SiO2	-	18,12
Insoluble Residue	Max. 5,0	0,81
Al2O3	-	4,90
Fe2O3	-	3,18
CaO	-	62,50
MgO	-	2,91
SO3	Max. 4,0	2,99
Na2O	-	0,24
K2O	-	0,76
CI-	Max. 0,1	0,0079
Free CaO	-	1,68
Heating Loss	Max. 5,0	3,90
Physical Analyses	Standards	Results (%)
Residue on 32 µm sieve (%)	-	11,2
Residue on 90 µm sieve (%)	-	-

Specific surface area (cm2/g)		-	3740
Specific gravity (g/cm3)		-	3,11
Setting time (minutes)	initial	Min. 60	155
	final	-	210
Water demand (%)		-	29
Volume expansion (mm)		Max. 10	0

In the experiments, two classes of fine aggregates (0–2 mm and 2–4 mm) and three classes of coarse aggregates (4–8 mm, 8–16 mm, and 16–22.4 mm) were used. The fine aggregates were river sand, while the coarse aggregates were of limestone origin. The filler added to the specimens was also obtained from limestone. The specific gravity values and water absorption ratios of the aggregates used in the experiments, determined in accordance with TS EN 1097-6, were given in Table 3.

Table 3 Specific Gravity and Water Absorption Properties of Aggregates

Particle Size Class	**Water Absorption (%)**	**Specific Gravity**
Filler		2,60
0/2	6,8	2,60
2/4	7,4	2,66
4/8	1,2	2,58
8/16	1,88	2,61
16/22.4	2,05	2,62

In the study, a chemical admixture produced by Sika and marketed under the trade name ViscoCrete SKY 608 was used as a superplasticizer. The properties of this admixture as declared by the manufacturer were given in Table 4.

Table 4 Product Information of the Superplasticizer Admixture

Chemical Structure	Aqueous solution of modified polycarboxylates
Packaging	Bulk and IBC (container) packaging Refer to the current price list valid for the available packaging types.
Shelf Life	12 months from the date of production
Appearance / Color	Greenish, liquid
Density	1,06 - 1,10 g/cm³ (ISO 758)
pH-Value	4,00 - 8,00
Total Chloride Ion Content	≤No.1 of mass

In the experiments, Atatürk University tap water was used as the mixing water for concrete. Integrated steel plants produce Ground Granulated Blast Furnace Slag (GGBFS) as a by-product of pig iron production. The properties of the GGBFS used in this study were given in Table 5.

Table 5 Chemical Properties of GGBFS

No.	**Component**	**Weight (%)**	**No.**	**Component**	**Weight (%)**
1	SiO2	38,6	6	Fe2O3	0,28
2	Al2O3	7,16	7	TiO2	0,22
3	CaO	46,04	8	K2O	0,51
4	MgO	4,91	9	Na2O	0,32
5	SO3	1,61	10	FeO	0,49

2.2. Method

2.2.1. Determination of Aggregate Gradations Based on Maximum Particle Size

Sieve analyses of the aggregates obtained for the mixtures were carried out in accordance with TS EN 933-After the sieve analysis tests, the aggregates were separated into particle size classes. Since the maximum aggregate size was also defined as a parameter in the study, optimum gradation curves (see Fig. 1) were established for each maximum particle size based on the cohesion of the mixtures produced in the preliminary tests.

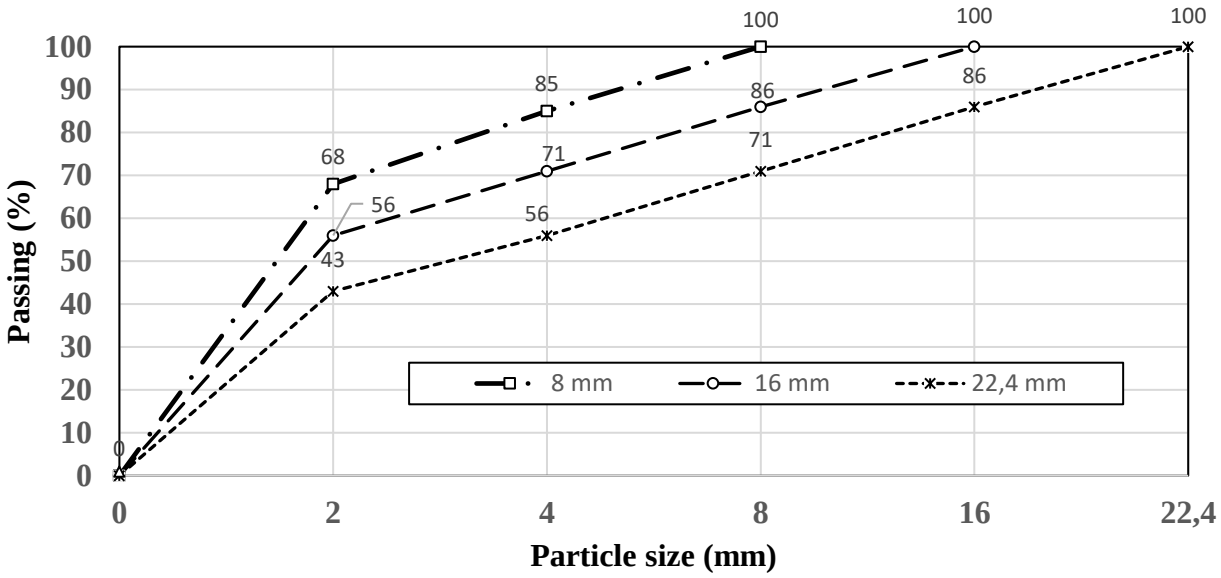

Figure 1 Gradation curves varying according to maximum aggregate particle size

2.2.2. Parameters and Levels

Within the scope of the study, concrete strength class, maximum aggregate particle size, and curing condition were selected as parameters.

Concrete mixtures were produced in three different strength classes: C35, C40, and CThe concrete strength classes were differentiated by varying the water/cement (W/C) ratio and cement content (C) of the mixtures. Accordingly, the concrete classes were produced by selecting W/C=0.55 and C=300 for C35; W/C=0.50 and C=330 for C40; and W/C=0.45 and C=360 for CThe levels of the maximum aggregate particle size parameter were defined as 8 mm, 16 mm, and 22.4 mm. The levels of the curing condition were selected as water curing (W), air curing (laboratory environment, D), and moisture curing (M).

2.2.3. Coding

The coding system was divided into three main components. The first indicates the concrete strength class, the second represents the curing method, and the third denotes the maximum aggregate particle size. When coding the concrete classes, the designations CI for C35, CII for C40, and CIII for C45 were adopted. For instance, the code “CIW8” represents a mixture with a compressive strength of 35 MPa, cured in water, and having a maximum aggregate particle size of 8 mm. Based on this information, Table 6 presents the parameters, levels, and codes corresponding to each mixture.

2.2.4. Number of Specimens

A total of 18 specimens were produced by preparing 9 different mixtures for each strength class and 2 specimens of 15×15×15 cm^3dimensions for each mixture. Considering that three different strength classes (CI, CII, and CIII) were selected, the total number of specimens was

Table 6 Parameters, Levels, and Codes of the Mixtures

	Concrete class	CI = C35 (W/C=0,55; C=300)								
	Dmax (mm)	8			16			22,4		
Parameter	Curing condition	W	D	M	W	D	M	W	D	M
Code		CIW8	CID8	CIM8	CIW16	CID16	CIM16	CIW22,4	CID22,4	CIM22,4
	Concrete class	CII = C40 (W/C=0,50; C=330)								
	Dmax (mm)	8			16			22,4		
Parameter	Curing condition	W	D	M	W	D	M	W	D	M
Code		CIIW8	CIID8	CIIM8	CIIW16	CIID16	CIIM16	CIIW22,4	CIID22,4	CIIM22,4
	Concrete class	CIII = C45 (W/C=0,45; C=360)								
	Dmax (mm)	8			16			22,4		
Parameter	Curing condition	W	D	M	W	D	M	W	D	M
Code		CIIIW8	CIIID8	CIIIM8	CIIIW16	CIIID16	CIIIM16	CIIIW22,4	CIIID22,4	CIIIM22,4

2.2.5. Concrete Mix Design and Specimen Production

The concrete mix design was calculated based on the TS 802 standard. The ground granulated blast furnace slag (GGBFS) used in the mixtures was substituted for cement. Based on the theoretically obtained values, eight preliminary tests were conducted, and the final mix proportions were determined by checking the workability and cohesion of the concrete. After the preliminary tests, the finalized mix design calculations were presented in Table 7.

Table 7 Mix Proportions (kg/m³)

No	Code*	Cem.	Water	GGBFS	SA	Filler	0/2	2/4	4/8	8/16	16/22,4
1	CI(W/D/M)8	270	165	30	3	94,25	1217,69	311,45	266,54	-	-
2	CI(W/D/M)16	270	165	30	3	94,25	1002,8	274,81	266,54	251,67	-
3	CI(W/D/M)22,4	270	165	30	3	94,25	770,01	238,17	266,54	269,64	252,63
4	CII(W/D/M)8	297	165	33	3,3	92,95	1200,89	307,15	262,87	-	-
5	CII(W/D/M)16	297	165	33	3,3	92,95	988,97	271,02	262,87	248,19	
6	CII(W/D/M)22,4	297	165	33	3,3	92,95	759,39	234,88	262,87	265,92	249,14
7	CIII(W/D/M)8	324	162	36	3,6	92,04	1189,13	304,14	260,29	-	-
8	CIII(W/D/M)16	324	162	36	3,6	92,04	979,29	268,36	260,29	245,76	-
9	CIII(W/D/M)22,4	324	162	36	3,6	92,04	751,95	232,58	260,29	263,32	246,71
* Since separate specimen production was not required, different curing conditions (W, D, and M) were shown in the same row.											

2.2.6. Fresh Concrete Tests

Within the scope of the study, fresh concrete tests were carried out as follows: unit weight determination in accordance with TS EN 12350-6, slump test in accordance with TS EN 12350-2, and determination of air content in concrete in accordance with TS EN 12350-

2.2.7. Curing of Specimens

As stated above, the curing condition was also defined as a parameter in the study. After production, the specimens were exposed to three different curing conditions by being stored in water (W), dry (D), and moist (M) environments. The water curing condition was selected to represent ideal curing conditions, while the laboratory environment was chosen to represent a curing method frequently used in practice. The moist environment was included in the study in order to determine the performance of reinforced concrete elements that cannot be subjected to long-term water curing and are instead wrapped with wet burlap. Accordingly, the curing regime defined for the study was given in Table 8.

Table 8 Storage Periods of Hardened Concrete Specimens According to Curing Conditions

W:	3 Days water curing	+ 18 Days water curing	+ 7 days air curing
D:	3 Days water curing	+ 25 days dry curing	
M:	3 Days water curing	+ 18 days moist curing	+ 7 days air curing

2.2.8. Ultrasonic Pulse Velocity Test

The Ultrasonic Pulse Velocity (UPV) test was conducted in accordance with TS EN 12504-4 using a Proceq device obtained from the market. An image of the device was shown in Figure The device transmits high-frequency ultrasonic waves through the specimen, which are received by a sensing probe at the opposite end. By recording the transit time of the ultrasonic waves passing through the specimen, the pulse velocity is calculated, providing information on the internal structure and homogeneity of the material.



Figure 2 Experimental setup image of the UPV device

For accurate and reliable measurements, the dimensions of each specimen were carefully determined prior to testing. Measurements were taken at three different points along the length of each specimen, and average values were used in the calculations in order to minimize potential dimensional variations. In addition, a small amount of grease oil was applied to the probe surfaces to minimize signal loss and optimize wave transmission. The probes were centrally placed on opposite faces of the specimen to ensure optimal propagation of the ultrasonic waves. In the experiments, the ultrasonic wave transit time recorded in microseconds (μs) was divided by the specimen length to calculate the wave velocity (V).

3. Research Findings and Discussion

In the study, unit weight, slump, and air content tests were conducted as fresh concrete properties. The results obtained from the experiments were collectively presented in Table 9.

Table 9 Results of Fresh Concrete Tests

Code	Unit Weight(g/cm³) (g\cm3)	Slump (cm)	Air Content (%)
CI(W\D\M)8	2217	2	4,20
CI(W\D\M)16	2239	5,5	3,50
CI(W\D\M)22.4	2283	13,5	2,00
CII(W\D\M)8	2201	2	4,50
C1I(W\D\M)16	2247	5	2,80
CII(W\D\M)22.4	2297	12,5	1,20
CIII(W\D\M)8	2236	1,5	3,20
CIII(W\D\M)16	2267	5,5	3,00
CIII(W\D\M)22.4	2315	7,5	2,00

3.1. Evaluation of Unit Weight Test Results

As seen in Table 9, the unit weights of the concrete mixtures ranged between 2201 kg/m³ and 2315 kg/m³. According to TS EN 206+A2, concretes with unit weight values between 2000 kg/m³ and 2600 kg/m³ are defined as normal-weight concrete. Therefore, it can be stated that the study was conducted on normal concretes, which are the most commonly used in practice.

In the study, concretes in three different strength classes were produced by varying the water/cement (W/C) ratios and cement contents (C) of the mixtures. For this purpose, the selected values were W/C = 0.55 and C = 300 for C35; W/C = 0.50 and C = 330 for C40; and W/C = 0.45 and C = 360 for CFrom the values given in Table 9, the average unit weight values were calculated as 2246 kg/m³ for CI, 2248 kg/m³ for CII, and 2273 kg/m³ for CIII class concretes. As expected, although the W/C ratio decreased, increases in the unit weight of concretes occurred due to the increase in cement content in the mixtures. The increase rates were approximately 0.1% for CII concretes and 1.2% for CIII concretes relative to the unit weight of CI concretes.

The unit weight values given in Table 9 were graphically illustrated in Figure 3.

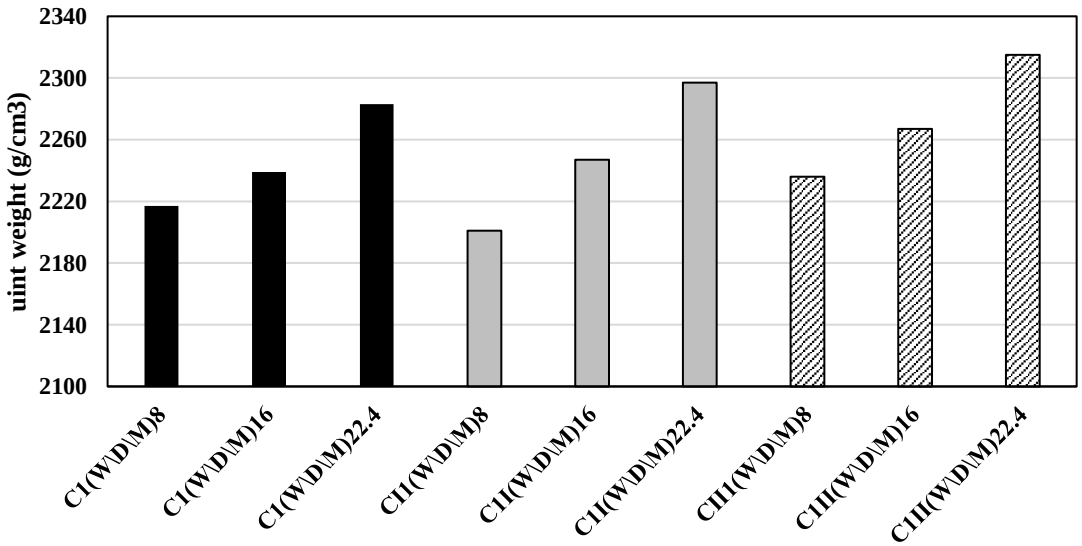

Figure 3 Variation of unit weight with maximum aggregate particle size and con. strength

As can be seen from Figure 3, for all three concrete strength classes, unit weight values increased as the maximum aggregate particle size increased. Compared to concretes with a maximum aggregate particle size of 8 mm, the increases observed in concretes with aggregate sizes of 16 mm and 22.4 mm were determined as 1% and 3% for CI class concretes, 2.1% and 4.4% for CII class concretes, and 1.4% and 3.5% for CIII class concretes. These results indicate that increasing the maximum aggregate particle size in the mixture leads to higher unit weight values of concrete, regardless of the W/C ratio and cement content (C). However, the rate of increase is influenced by the W/C ratio and cement dosage (C). It was also considered that the density differences among aggregate classes may have contributed to this outcome. Indeed, as seen from Table 3, the specific gravity values are 2.68 g/cm³ for the 4/8 aggregate size class, 2.61 g/cm³ for the 8/16 size class, and 2.62 g/cm³ for the 16/22.4 size class.

From the data obtained in the study, it was clearly determined that the unit weight increased with increasing maximum aggregate particle size. Accordingly, mixtures with a maximum aggregate particle size of 8 mm had an average unit weight of 2218 kg/m³, those with a maximum aggregate particle size of 16 mm had 2251 kg/m³, and those with a maximum aggregate particle size of 22.4 mm had 2298 kg/m³.

3.2. Evaluation of Slump Test Results

The slump test is the most commonly used test to determine the consistency of fresh concrete, which is an indicator of its workability. As can be seen from Table 9, the slump values of the concretes produced within the scope of the study ranged between 1.5 cm and 13.5 cm. According to TS EN 206+A2, slump classes are defined as S1 (1–4 cm), S2 (5–9 cm), S3 (10–15 cm), S4 (16–21 cm), and S5 (≥22 cm). Based on these classifications, three of the tested concrete specimens fall into the S1 class, four into the S2 class, and two into the S3 class. All mixtures classified in the S1 group were concretes with a maximum aggregate particle size of 8 mm. In contrast, the two mixtures classified in the S3 group used aggregates with a maximum particle size of 22.4 mm. The lowest slump value, 1.5 cm, was observed in the mixtures coded CIII (W/D/M)8, while the highest slump value, 13.5 cm, was observed in the mixtures coded CI (W/D/M)22.4.

The slump values given in Table 9 were graphically presented in Figure 4.

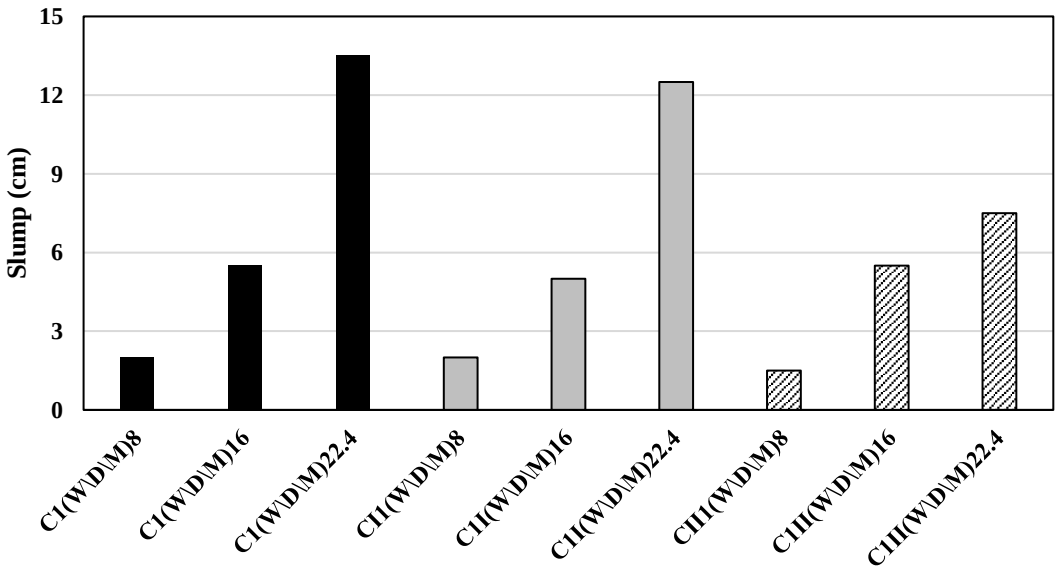

Figure 4 Variation of slump values with maximum aggregate particle size and con. strength

As can be seen from Figure 4, for all three concrete strength classes, the slump values increased as the maximum aggregate particle size increased. Compared to concretes with a maximum aggregate particle size of 8 mm, the increases observed in concretes with aggregate sizes of 16 mm and 22.4 mm were determined as 175% and 575% for CI class concretes, 150% and 525% for CII class concretes, and 267% and 400% for CIII class concretes. These results indicate that increasing the maximum aggregate particle size in the mixture leads to a significant increase in slump values, regardless of the W/C ratio and cement content (C). However, the rate of increase is influenced by the W/C ratio and cement dosage (C).

On the other hand, the average slump values within each concrete class were found to be 7 cm for CI, 6.5 cm for CII, and 4.8 cm for CIII. As observed, as the W/C ratio decreases and cement content increases, a reduction in workability occurs. Based on the slump values of CI class concretes, the reduction rates were 7% for CII class and 31% for CIII class concretes.

This experimental study clearly demonstrated that increasing the maximum aggregate particle size also increases slump values. Accordingly, mixtures with a maximum aggregate particle size of 8 mm had an average slump of 1.8 cm, those with 16 mm had 5.3 cm, and those with 22.4 mm had 11.2 cm.

3.3. Evaluation of Air Content Test Results

The air content of fresh concrete is an important factor for both strength and durability. Examination of the values given in Table 9 shows that the air content of the tested specimens ranged between 1.2% and 4.5%. The lowest air content, 1.2%, was observed in the mixture coded CII (W/D/M)22.4, while the highest air content, 4.5%, was observed in the mixture coded CII (W/D/M)A graphical representation of the air content values given in Table 9 is presented in Figure 5.

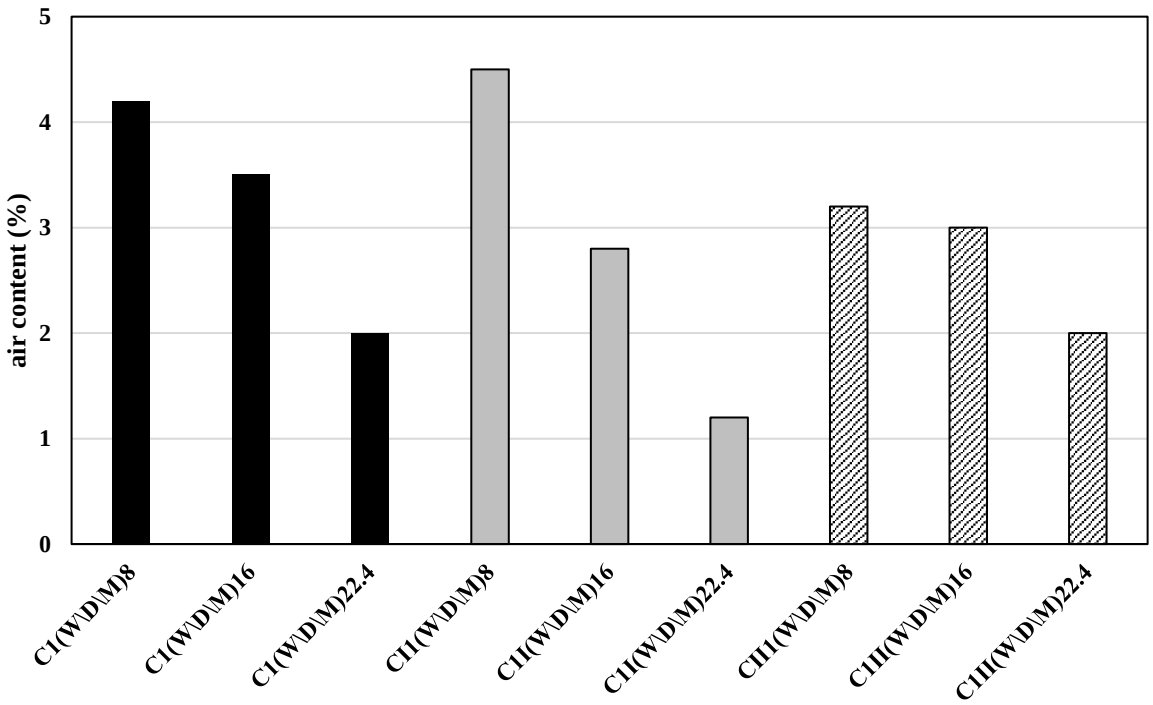

Figure 5 Variation of air content with maximum aggregate particle size and con. strength

Analysis of the graph in Figure 5 shows that, within the same concrete class, increasing the maximum aggregate particle size leads to a decrease in the air content of the mixtures. Compared to concretes with an 8 mm maximum aggregate particle size, the decreases observed in concretes with 16 mm and 22.4 mm aggregates were determined as 17% and 52% for CI class concretes, 38% and 73% for CII class concretes, and 6% and 38% for CIII class concretes. These results indicate that increasing the maximum aggregate particle size in the mixture reduces the air content of the concrete, regardless of the W/C ratio and cement content (C).

The combined analysis of Table 9 and Figure 5 also shows that the average air contents differ among concrete classes. The average air contents were found to be 3.2% for CI, 2.8% for CII, and 2.7% for CIII. As observed, as the W/C ratio decreases and the cement content increases, the air content of the concrete decreases. Based on the CI class concrete air contents, reductions of 12% and 15% were observed in CII and CIII class concretes, respectively.

Except when air-entraining admixtures are added to improve freeze-thaw resistance, it is generally desirable to keep the air content in concrete as low as possible. Accordingly, the mix design in this study assumed an air content of 1% as a general target. The experimental results showed that the lowest air content approached this target, with 1.2% in the CII (W/D/M)22.4 sample. Furthermore, the mixtures with a maximum aggregate particle size of 22.4 mm had an average air content of 1.7%, those with 16 mm had 3.1%, and those with 8 mm had 4.0%. These results clearly indicate that as the aggregate size decreases, the air content in fresh concrete increases.

3.4. Ultrasonic Pulse Velocity (UPV) Test Results and Evaluation

The results of the UPV measurements performed on the specimens in the study were presented in Table The values in the table represent the averages of two specimens.

Table 10 28-Day UPV Readings Conducted on Concretes

Num.	Code	UPV (m/s)	Num.	Code	UPV (m/s)
1	CIW8	4057	15	CIID22.4	3995
2	CIW16	4169	16	CIIM8	4054
3	CIW22.4	4286	17	CIIM16	4168
4	CID8	3844	18	CIIM22.4	4221
5	CID16	3895	19	CIIIW8	4165
6	CID22.4	4000	20	CIIIW16	4344
7	CIM8	3947	21	CIIIW22.4	4349
8	CIM16	4003	22	CIIID8	4061
9	CIM22.4	4162	23	CIIID16	4001
10	CIIW8	4109	24	CIIID22.4	4166
11	CIIW16	4225	25	CIIIM8	4049
12	CIIW22.4	4224	26	CIIIM16	4222
13	CIID8	3942	27	CIIIM22.4	4344
14	CIID16	3943			

Ultrasonic pulse velocity (UPV) values provide valuable information about the quality and strength development of concrete. The values proposed by Malhotra (1976) [6] for the relationship between ultrasonic transit velocity and concrete quality were presented in Table 11.

Table 11 Evaluation of Concrete Quality Based on UPV [6]

Ultrasonic pulse velocity (V, m/s)	Classification
V > 4575	Excellent
4575 > V > 3660	Good
3660 > V > 3050	Questionable
3050 > V > 2135	Weak
V < 2135	Vary weak

As seen in Table 10, by the 28th day, the lowest UPV value among the concretes produced in the study was 3844 m/s for the CID8 specimen, while the highest UPV value was 4349 m/s for the CIIIW22.4 specimens. When these values are compared with the ranges provided in Table 11, it can be concluded that all the concretes produced in the study are of "good" quality.

The variation of the 28-day UPV values with respect to D_{max}, as given in Table 10, was illustrated in Figure 6.

As shown in Figure 6, the 28-day UPV values of the mixtures varied depending on the experimental parameters. The variation rates were discussed below according to the parameter.

For mixtures with D_{max} = 8 mm, the average UPV values obtained from CI, CII, and CIII concretes were 3949 m/s, 4035 m/s, and 4091 m/s, respectively. According to these data, compared to CI concrete, the UPV increased by 2.5% for CII concrete and 3.6% for CIII concrete.

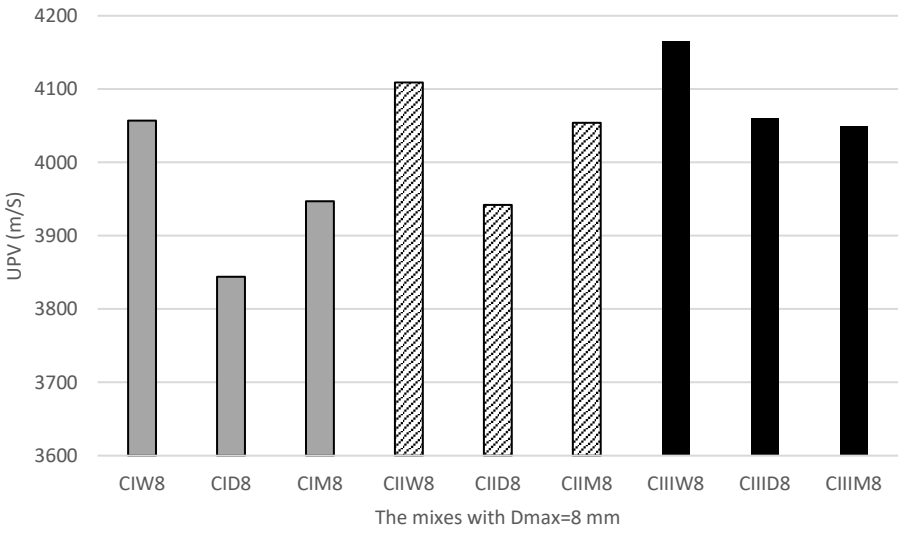

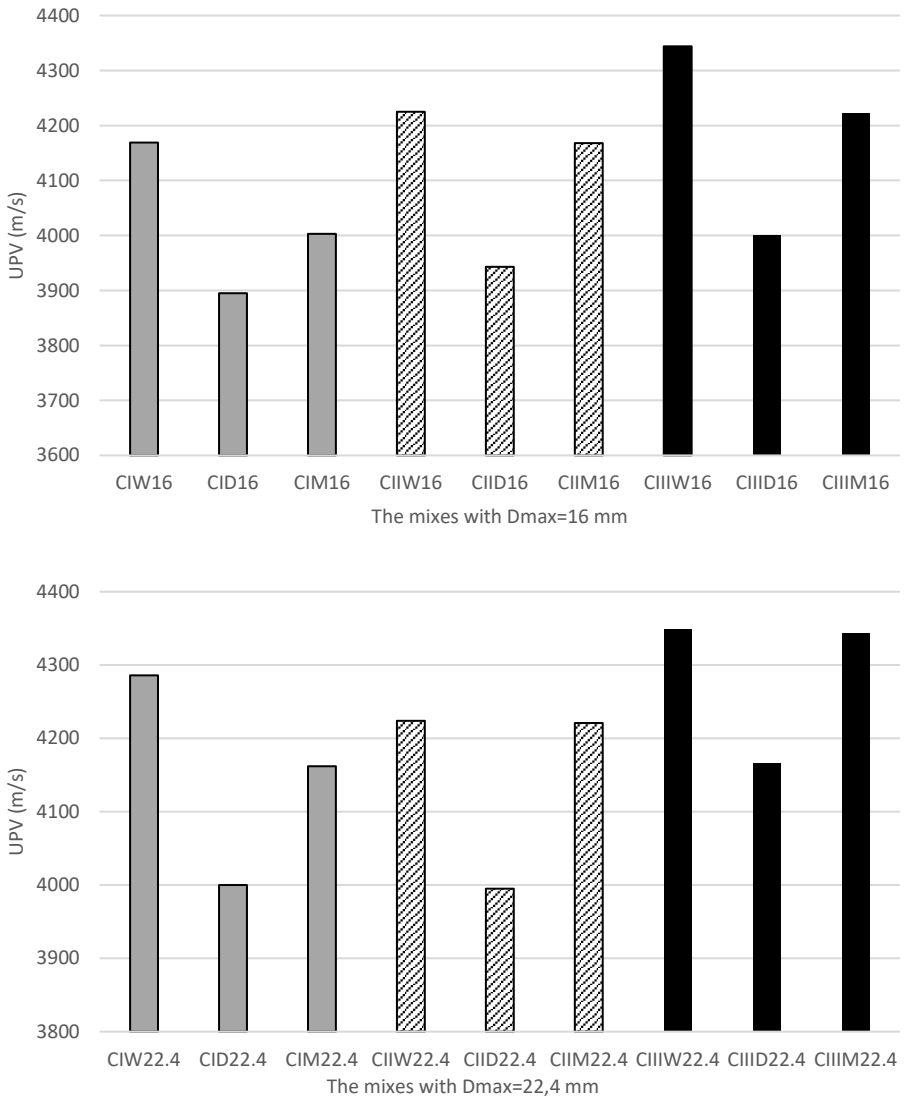

Figure 6 Variation of 28-day UPV values with maximum aggregate particle size

For specimens with D_{max} = 16 mm, the average UPV values for CI, CII, and CIII concretes were 4022 m/s, 4112 m/s, and 4189 m/s, respectively. Based on these data, compared to CI concrete, the UPV increased by 2.2% for CII and 4.1% for CIII concretes.

For specimens with D_{max} = 22.4 mm, the average UPV measurements for CI, CII, and CIII concretes were 4149 m/s, 4148 m/s, and 4286 m/s, respectively. These results indicate that CI and CII concretes in this group had nearly the same UPV averages, while CIII concrete had an average 3.3% higher than the other two.

Furthermore, it was observed that increasing the maximum aggregate particle size also led to higher UPV values, depending on the concrete class. Compared to mixtures with D_{max} = 8 mm, concretes produced with 16 mm aggregates showed increases of 1.8%, 1.9%, and 2.4% for CI, CII, and CIII classes, respectively. Similarly, concretes produced with 22.4 mm aggregates showed increases of 5.1%, 2.8%, and 4.8% for CI, CII, and CIII classes, respectively.

The average UPV values presented in the above four paragraphs represent the mean of specimens stored in water (W), air (D), and moist (M) curing conditions for each concrete class. Evaluations based on UPV values calculated separately for each curing condition are provided below.

As also seen in Figure 6, for all three concrete classes, the highest UPV values were obtained from specimens cured in water. For D_{max} = 8 mm mixtures, compared to water curing, CI class concretes cured in air and moist conditions showed UPV reductions of 5.3% and 2.7%, respectively; CII class showed reductions of 4.1% and 1.3%; and CIII class showed reductions of 2.5% and 2.8%.

For D_{max} = 16 mm specimens, compared to water curing, CI class concretes cured in air and moist conditions exhibited UPV reductions of 6.6% and 4.0%, respectively; CII class showed reductions of 6.7% and 1.3%; and CIII class showed reductions of 7.9% and 2.8%.

Concretes with D_{max} = 22.4 mm, compared to water curing, UPV reductions were calculated for CI class concretes cured in air and moist conditions as 6.7% and 2.9%, respectively; for CII class concretes, 5.4% and 0.1%; and for CIII class concretes, 4.2% and 0.1%.

The study also examined how UPV values change with concrete class when specimens are stored under the same curing condition. The results are summarized below.

For D_{max} = 8 mm concretes stored in water, CII and CIII concretes had UPV values 1.3% and 2.7% higher than CI concretes, respectively, while CIII concretes were 1.4% higher than CII concretes. In air-cured specimens, CII and CIII concretes had UPV values 2.5% and 5.6% higher than CI concretes, and CIII concretes were 3.0% higher than CII concretes. In moist curing, CII and CIII concretes showed UPV values 2.7% and 2.6% higher than CI concretes, while CIII concretes were 0.1% higher than CII concretes.

For D_{max} = 16 mm concretes stored in water, CII and CIII concretes had UPV values 1.3% and 4.2% higher than CI concretes, and CIII concretes were 2.8% higher than CII concretes. In air curing, CII and CIII concretes were 1.2% and 2.7% higher than CI concretes, and CIII concretes were 1.5% higher than CII concretes. In moist curing, CII and CIII concretes showed UPV increases of 4.1% and 5.5% compared to CI concretes, while CIII concretes were 1.3% higher than CII concretes. For D_{max} = 22.4 mm concretes stored in water, CII and CIII concretes had UPV values −1.4% and 1.5% relative to CI concretes, and CIII concretes were 3.0% higher than CII concretes. In air curing, CII and CIII concretes had UPV values −0.1% and 4.2% compared to CI concretes, and CIII concretes were 4.3% higher than CII concretes. In moist curing, CII and CIII concretes showed UPV increases of 1.4% and 4.4% relative to CI concretes, while CIII concretes were 2.9% higher than CII concretes.

4. Conclusions

With the increase in cement dosage in the mixes, the unit weights of the concretes also increased. For all three concrete classes, it was observed that as the maximum aggregate particle size increased, the unit weight values increased as well. The data obtained from the study clearly indicate that larger maximum aggregate particle sizes lead to higher unit weights.

Similarly, the slump values of the mixes increased with the increase in maximum aggregate particle size for all three concrete classes. As the water/cement (W/C) ratio decreased and the cement dosage increased, a reduction in workability was observed. Compared to the CI class concretes, the slump loss was 7% for CII concretes and 31% for CIII concretes. It was clearl`y determined that increasing the maximum aggregate particle size also increases slump values.

Independent of the W/C ratio and cement dosage (C), increasing the maximum aggregate particle size in the mix was found to reduce the air content percentages in the concrete. For all three concrete classes, slump values increased with larger maximum aggregate particle sizes. As the W/C ratio decreased and cement dosage increased, reductions in air content were observed. Compared to CI class concretes, air content decreased by 12% in CII concretes and 15% in CIII concretes.

As the concrete class increased, UPV values also increased. It was determined that increasing the maximum aggregate particle size also led to higher UPV values, depending on the concrete class. For all three concrete classes, the highest UPV values were obtained from specimens cured in water.

References

[1] Malhotra, V. M., and Carino, N. J. (2004). Handbook on Nondestructive Testing of Concrete (2nd ed.). CRC Press.

[2] American Concrete Institute (ACI). (2013). ACI 228.2R-13: Report on Nondestructive Test Methods for Evaluation of Concrete in Structures. American Concrete Institute.

[3] Polat, R., Gencer, Y. G., and Yüzer, N. (2020). Evaluation of mechanical properties of existing concrete structures with NDT methods. Engineering Sciences, 15(2), 81–

[4] Komlos, K., Popovics, S., Nürnbergerová, T., Babal, B., and Popovics, J. S. (1996). Ultrasonic pulse velocity test of concrete properties as specified in various standards. Cement and Concrete Composites, 18(5), 357-

[5] Crawford, G. I. (1997).Guide to nondestructive testing of concrete (No. FHWA-SA-97-105). United States. Federal Highway Administration.

[6] Malhotra, V. M., Testing Hardened Concrete: Nondestructive Methods. ACI Monograph No. 9, ACI. Iowa Sate University Press. Ames. Iowa.

Remediation of Heavy Metal and Dye Pollution in Kyrgyzstan Using Nanotechnological and Biological Methods

Fatma Melike Yeşilyurt [1,*]

[1] Kyrgyz-Turkish Manas University, Faculty of Science, Department of Biology, 720038 Bishkek, Kyrgyzstan

*Corresponding author e-mail: 2552D1201002@manas.edu.kg

Keywords

Heavy metals,
Dye removal,
Biotechnology,
Nanotechnology,
Kyrgyzstan

Abstract

Industrial and mining industries cause heavy metal and chemical pollution in many regions around the world. Synthetic dyes are an example of chemical pollutants and pose a threat to the environment due to the aromatic rings, azo bonds or metal complexes they contain. Kyrgyzstan is a country in Central Asia consisting largely of mountainous areas. Since the Soviet era, it has become a significant center for minerals such as gold, uranium and mercury. The chemical processing agents used in these mines contain synthetic reagents, metal complex dyes and heavy metals. The country's economy currently relies heavily on mining. Inadequate treatment means that the textile and leather industries can release azo and reactive dyes directly into the environment. Regional water systems, which are mountainous and composed of closed basins, cannot sufficiently dilute these pollutants, thereby increasing the environmental risk. These pollutants degrade very slowly in the natural environment, forming toxic by-products. New, sustainable, environmentally friendly biological and nanotechnological methods can eliminate these pollutants that accumulate in nature. Biological methods such as biosorption, bioaccumulation, microbial reduction and bioremediation can eliminate accumulated chemical pollution via environmentally friendly processes. These methods work by actively absorbing pollutants into cells, converting toxic substances into harmless ones or accumulating them within organisms. Additionally, nanomaterials can bind metal ions due to their large surface area, reduce heavy metals using light energy, or convert them into less toxic forms. Nanotechnological methods, such as nanoadsorbents, nanocomposite filters, nanophotonics and photocatalytic applications, can clean aqueous environments. Biological and nanotechnological applications are expected to contribute to environmental sustainability.

1. Introduction

Global industrialization and technological advances around the world have serious impacts on the environment. The waste generated as a result of these developments causes heavy metal and chemical dyes accumulation in the environment [1]. Heavy metals are toxic substances for the environment due to their high density and atomic weight. They are also persistent in the environment because they are not biodegradable. The accumulation of these toxic substances in the environment inevitably causes harm to humans and ecosystems [2]. Although industry is often cited as the source of heavy metals, large amounts of fertilizers and pesticides applied to agricultural fields to increase yields are also among the main causes of soil pollution. Heavy metals commonly found in soil and having toxic effects include cadmium (Cd), copper (Cu), lead (Pb), cobalt (Co), arsenic (As), mercury (Hg), and zinc (Zn). The estimated persistence times of some of these metals range from 70–510 years for Zn to 740–5900 years for Pb [1]. As soil and water are an important part of life, the toxic substances they contain pose a threat to the entire ecosystem. Heavy metals in soil threaten human health by being transported through plants. Ninety percent of human exposure to heavy metals comes from fruits and vegetables, while the remaining 10% comes from dermal contact and inhalation of contaminated dust. Through biological accumulation, heavy metals can be transferred through all links of the food chain. Another major problem with heavy metals today is that they are powerful carcinogens and mutagens [2].

Chemical dyes, like heavy metals, are hazardous and toxic substances present in ecosystems as a result of industrial and agricultural activities. The developing dye industry and textile waste, in particular, form the basis for the formation of these toxic substances [3]. Dyes may contain azo bonds, aromatic rings, functional groups, metal complexes, and

reactive groups in their structures. Dyes containing azo bonds are called azo dyes. The nitrogen-containing structure forming this bond gives the dye its color. A dye may contain one or more aromatic rings; these impart color and chemical stability to the dyes [4], [5]. Functional groups determine the dye's solubility, binding, and environmental behavior. Some dyes, including those containing complexes, form complexes with metals such as chromium and copper, while reactive groups are used for the covalent bonding of the dye to the textile. This chemical structure of dyes makes degradation in nature even more difficult [6].

A study conducted in the textile industry area of Kolkata (India) has revealed that heavy metals (Pb, Cd, and Zn) in the waste from small-scale textile bleaching and dyeing (BD) units may cause gastrointestinal disorders (GI), ulcers, and cancer risk in the local population. In people consuming daily agricultural products and using surface water in this region, the identified toxic metals (Pb, Cd, Ni) were found to be 2 to 40 times above WHO/FAO limits [7]. These toxic substances, which are naturally resistant to degradation in the environment, accumulate in water and soil, posing serious threats to the environment and human health.

Kyrgyzstan is a country located in the center of Central Asia, with a large part of its territory consisting of mountainous terrain and generally high altitude. Kyrgyzstan has more than 2,000 lakes, most of which are small and high-altitude. The country has abundant rivers and lakes. The country's economy is based on agriculture and mining. Historically, mining was traditional and small-scale before the Soviet era, while the Soviet period included large state-supported mining exploration projects. During this period, large reserves of various minerals, such as uranium and mercury, were discovered and mined. The chemical processing used for mining also took place during this period. The mining sector, which began in the 1970s, is developing rapidly. Gold is one of Kyrgyzstan's most valuable natural resources. Like the country's other mineral resources, such as oil, natural gas, coal, lead, zinc, copper, iron ore, nepheline, mercury, and bismuth, gold has not yet been fully exploited. During the Soviet era, Kyrgyzstan was a major supplier of uranium, but uranium is no longer mined. These mining activities, carried out with little regard for the environment, have caused significant pollution in the region [8]

Kyrgyzstan's environmental problems are not as bad as those of other former Soviet republics, but the lack of funds allocated for cleaning up environmental pollutants means that heavy metal contamination from the past and ongoing industrial development pose serious problems for the region. Poor agricultural practices lead to increased soil salinity and erosion, inefficient water use, and overgrazing of livestock. Furthermore, fertilizers and pesticides used in agriculture cause soil and water pollution due to the harmful substances they contain. In Kyrgyzstan, especially in densely populated areas, inadequate infrastructure and sewage treatment cause waterborne diseases. The uranium mining town of Mailuu-Suu in southern Kyrgyzstan was once the center of the Soviet nuclear program. The mine produced more than 10,000 tons of uranium since 1945 and ceased operations in 1968. During the mine's operation in 1958, the collapse of a dam holding mining waste caused up to 600,000 tons of hazardous radioactive material to mix into the Mailuu-Suu River. The soil and water near the mine and metallurgical facilities have been contaminated due to these radioactive materials being toxic waste [9, 10]

The toxic legacy of uranium mining continues in Kyrgyzstan today, with many local residents still having no water source other than the poisoned river. This situation has led to birth abnormalities in the region. The anomaly rate remains at 2.77%, and cancer rates in the region are the highest in the country.

In addition to heavy metal concentrations originating from mines, chemical dyes used in the country's leather processing and textile industries today also pose a serious threat to the environment. Lead-containing toxic paints found in the region are still available for sale in Kyrgyzstan, or paints sold in the past may still be in use. This situation poses a risk of lead exposure, particularly in older homes, as paint deteriorates over time, cracks, and turns to dust, which can be inhaled or ingested. Lead poisoning has been a serious health problem for centuries, and the World Health Organization (WHO) has identified lead as one of the 10 most important chemicals for public health, emphasizing that there is no safe level of lead exposure in the region. Lead is also found in products such as paint, ceramics, toys, and cosmetics, and can contaminate drinking water through old plumbing systems. A comprehensive study was conducted in the country on blood lead levels in preschool children, and the results of the study found that one in five children (21%) in Kyrgyzstan had blood lead levels above the values recommended by the WHO [11].

In many parts of the world, including Kyrgyzstan, it is crucial to remove toxic substances that pollute the soil and water and pose a threat to the ecosystem in an environmentally friendly and sustainable manner. Therefore, environmentally friendly methods for removing heavy metals and chemical toxins must be promoted and encouraged [10]

This study aims to comprehensively reveal the sources and effects of these pollutants in the environment and, in particular, the potential of nanotechnological and biological treatment methods in reducing this pollution. In this regard, the study aims to compile the existing literature, introduce innovative treatment techniques, and propose solutions suitable for Kyrgyzstan's unique geographical and industrial conditions. Thus, the study aims to provide a scientific basis for contributing to regional environmental management approaches and promoting the use of sustainable treatment technologies.

2. Biological Treatment Methods

2.1. Bioremediation

Bioremediation provides an environmentally friendly, low-cost, and sustainable remediation that aims to remove, recover, or completely eliminate harmful pollutants in the environment using cells or their components. It can be used to remove or eliminate toxic pollutants such as heavy metals and synthetic dyes from their environment. Compared to traditional physical and chemical treatment methods, which are costly, energy-intensive, and produce toxic sludge, bioremediation offers a powerful alternative to these problems.

2.2. Biosorption

Biosorption facilitates the removal of heavy metal ions and toxic pollutants such as synthetic dyes from aqueous solutions using cells or their components (biomass). This process is a rapid and reversible physicochemical adsorption event that does not require metabolic energy. The mechanism of action varies depending on the chemical structure and surface properties of the biomass. The mechanism involves ion exchange, physical adsorption, complexation, chelation, and combinations thereof. Ion exchange is one of the fundamental components of biosorption and occurs through the replacement of metal ions on the biomass with other ionized ions. Physical adsorption is based on the principle of metal ions adhering to the biosorbent surface through weak physical forces. The complexation and chelation mechanism involves metal ions forming complexes on the biosorbent surface with active groups such as carboxyl, hydroxyl, amine, phosphate, sulfate, and sulfhydryl. [12, 13].

2.3. Bioaccumulation

Bioaccumulation is the process by which living organisms such as bacteria, algae, plants, fungi, and yeasts accumulate pollutants from the environment within their cells using active metabolic processes. Unlike biosorption, bioaccumulation involves an active metabolic process that requires an energy source and therefore only occurs with living biomass. This process consists of two stages. The first stage involves the rapid adsorption of metal ions onto functional groups on the cell surface, independent of metabolism [14]. The second stage is metabolism-dependent and involves the transport of metal species across the cell membrane into the cell (cytoplasm) [15].

2.4. Microbial reduction

Microbial reduction is one of the bioremediation methods used to remove pollutants that cannot be broken down in nature or take a long time to break down, such as heavy metals or dyes. It typically involves converting toxic pollutants into less harmful, more stable, or inert forms through redox reactions. This process can be carried out through metabolic pathways or via enzymes [14]. Since enzymes are specific working protein structures, they provide detoxification by enzymatically converting specific toxic metals or toxic chemicals in this process.

3. Nanotechnological Purification Methods

3.1. Nanoadsorbents

Nanoadsorbents are materials with different sizes smaller than 100 nanometers (nm). They are used especially in water treatment processes to clean contaminants in the environment. The process occurs through the adsorption principle of pollutants onto the surfaces of these nano-sized materials [16]. These nano-sized structures are known for their unique physical and chemical properties, such as large surface area, reactivity, selectivity, reusability, and magnetic properties, due to their size. These properties provide advantages such as high efficiency, ease of application, cost, and reusability potential. Additionally, compared to traditional chemical or physical purification methods, they are considered an effective, low-cost, and environmentally friendly alternative [17].

3.2. Nanocomposite filters

Nanocomposites are hybrid materials, typically designed with dimensions smaller than 100 nm, used to remove contaminants from aqueous environments. Nanocomposite filters are created by combining two or more materials and exhibit high functionality and performance [16]. These materials represent a powerful alternative to traditional purification methods in combating environmental pollution due to their physical and chemical structures at the nanoscale. These filters remove pollutants through physicochemical adsorption or photocatalytic degradation processes [18].

3.3. Nanophotonic photocatalytic techniques

Nanophotonic photocatalytic techniques are among the advanced oxidation processes used in the treatment of environmental pollutants. They eliminate toxicity by using light energy to break down organic pollutants with metal oxides or semiconductor nanoparticles, and are a sustainable method. This method offers advantages over traditional treatment methods due to its high efficiency, low cost, and lack of toxic byproducts. Semiconductor metal oxide

nanoparticles such as Titanium Dioxide (TiO2), Zinc Oxide (ZnO), Cerium Oxide (CeO2), and Tin Oxide (SnO2) are commonly used.

4. Conclusion and Recommendation

In Kyrgyzstan, toxic substances accumulate in the environment, particularly due to mining activities left over from the Soviet era, improperly stored waste, and, today, increasing industrial discharges. These pollutants pose persistent risks to the ecosystem and threaten ecological balance. The literature shows that hybrid treatment systems combining multi-stage, biological, physicochemical, and nanotechnological components provide the highest efficiency compared to using a single method for such difficult pollutants. Furthermore, Kyrgyzstan is a region with high levels of pollution from mining and textiles, and its climate conditions, high altitude, and mountainous terrain create extreme conditions. Therefore, the use of local biosorbents, the selection of cold-adaptive microorganisms, and the use of solar-assisted photocatalysis options provide suitable environmental conditions.

Biotechnological (bioremediation, biosorption, bioaccumulation, and microbial reduction) and nanotechnological (nanoadsorbents, nanocomposite filters, nanophotonics, and photocatalytic techniques) methods offer solutions suitable for Kyrgyzstan's geological and socioeconomic conditions. Biosorption and microbial degradation are considered to be a sustainable option in rural areas due to their low costs and use of local biomass and microorganisms. Nanoadsorbents and photocatalytic advanced oxidation systems, on the other hand, can offer advantages in urban or semi-industrial areas due to their efficiency, fast kinetics, and low volume of waste. It is anticipated that a hybrid system combining these two approaches will effectively remove high concentrations of metal loads and complex aromatic dye compounds. However, when assessing the applicability of these treatment methods in the country, it is evident that while there is potential to implement these technologies, there are significant infrastructure deficiencies. Although the legal framework and institutional structure required for environmental improvement exist in the country, technical guidelines and control mechanisms for advanced treatment technologies are limited. Universities have sufficient equipment infrastructure for heavy metal analysis, microbiology, and biotechnology studies, but there are deficiencies in the amount of chemical substances. For nanotechnological production, technical capacity is insufficient for advanced applications such as photocatalytic reactors and nanocomposite filter development. Currently, there are academic institutions equipped to carry out pilot-scale biological treatment projects. However, international funding support for equipment investments and the development of university-industry collaboration are required for the field application of nanotechnology-based systems. Financially, the national budget is insufficient for environmental investments. Therefore, international grants and joint projects are largely needed for the implementation of advanced treatment technologies. Considering the current conditions, it is understood that biotechnological methods can be applied in Kyrgyzstan, but nanotechnological treatment techniques can be developed.

If the current situation is improved or joint projects are undertaken, it is believed that Kyrgyzstan's environmental problems will be best addressed by the proposed hybrid system. In this process, it is recommended that pollutant sources first be analyzed and controlled, followed by the development of a treatment system.

For treatment, pollutants can first be removed using pretreatment processes such as sedimentation and coagulation. In the second stage, high removal rates of heavy metals and dye concentrations can be achieved using biosorption and nanoadsorption filters; in the third stage, the degradation of dissolved organic dyes should be supported using TiO2 or ZnO-based photocatalytic systems. This ensures that water is returned to the natural cycle and the soil is improved in the long term. The literature shows that Kyrgyzstan's environmental pollution problem can be solved with high technical efficiency and reduced operating costs by hybrid treatment models that combine the biological, environmentally friendly, and low-cost advantages of nanotechnology with its high efficiency. This solution, once developed, will improve soil and water quality while also benefiting important areas such as human health and increased agricultural productivity.

References

[1] Sönmez, O., & Kılıç, FN (2021). Heavy Metal Pollution in Soil and Removal Methods. Turkish Journal of Agricultural Engineering Research, 2(2), 493-507.

[2] K. K. Sodhi, L. C. Mishra, C. K. Singh, and M. Kumar, "Perspective on the heavy metal pollution and recent remediation strategies," Curr. Res. Microb. Sci., vol. 3, no. September, p. 100166, 2022, doi: 10.1016/j.crmicr.2022.100166.

[3] M. Tripathi et al., "Microbial biosorbent for remediation of dyes and heavy metals pollution: A green strategy for sustainable environment," Front. Microbiol., vol. 14, no. April, pp. 1–9, 2023, doi: 10.3389/fmicb.2023.1168954.

[4] Y. Liu, C. Li, J. Bao, X. Wang, W. Yu, and L. Shao, "Degradation of Azo Dyes with Different Functional Groups in Simulated Wastewater by Electrocoagulation," Water (Switzerland), vol. 14, no. 1, 2022, doi: 10.3390/w14010123.

[5] Kusumlata, B. Ambade, A. Kumar, and S. Gautam, "Sustainable Solutions: Reviewing the Future of Textile Dye Contaminant Removal with Emerging Biological Treatments," Limnol. Rev., vol. 24, no. 2, pp. 126–149, 2024, doi: 10.3390/limnolrev24020007.

[6] F. Eltaboni et al., "Issue 4 of Azo Dyes: A Comprehensive Review," J. Chem. Rev, vol. 4, no. 4, pp. 313–330, 2022, [Online]. Available: https://doi.org/10.22034/JCR.2022.349827.1177

[7] B. G. Gupta and R. Mukhopadhyay, "Heavy metal contamination from textile wastewater and its health impacts: a case study from

West Bengal with sustainable remediation approaches," Sci. Rep., vol. 15, no. 1, pp. 1–16, 2025, doi: 10.1038/s41598-025-13357-w.

[8] Aliprandini, M. (2025). Kyrgyzstan. EBSCO Research Starters. Retrieved December 10, 2025, from https://www.ebsco.com/research-starters/geography-and-cartography/kyrgyzstan?utm_source=chatgpt.com EBSCO

[9] Kähler, K. N. (2025). Pesticides and pest control. EBSCO Research Starters. Retrieved December 10, 2025, from https://www.ebsco.com/research-starters/agriculture-and-agribusiness/pesticides-and-pest-control

[10] Satke, R. (2025, July 12). Uranium mine in Kyrgyzstan spreads pollution for 53 years. Dialogue Earth. Retrieved December 10, 2025, from https://dialogue.earth/en/energy/uranium-mine-radioactive-waste-kyrgyzstan/

[11] United Nations in Kyrgyzstan. (2024, November 11). Protecting children and families in Kyrgyzstan from lead exposure. Retrieved December 10, 2025, from https://kyrgyzstan.un.org/en/283244-protecting-children-and-families-kyrgyzstan-lead-exposure

[12] Baran, M. F. (2017). Removal of some toxic metals from water using biosorption method (Doctoral dissertation). Dicle University, Diyarbakır, Turkey.

[13] A. K. Priya, L. Gnanasekaran, K. Dutta, S. Rajendran, D. Balakrishnan, and M. Soto-Moscoso, "Biosorption of heavy metals by microorganisms: Evaluation of different underlying mechanisms," Chemosphere, vol. 307, no. P4, p. 135957, 2022, doi: 10.1016/j.chemosphere.2022.135957.

[14] V. H. T. Pham, J. Kim, S. Chang, and W. Chung, "Bacterial Biosorbents, an Efficient Heavy Metals Green Clean-Up Strategy: Prospects, Challenges, and Opportunities," Microorganisms, vol. 10, no. 3, pp. 1–16, 2022, doi: 10.3390/microorganisms10030610.

[15] A. Hansda, V. Kumar, and Anshumali, "A comparative review towards potential of microbial cells for heavy metal removal with emphasis on biosorption and bioaccumulation," World J. Microbiol. Biotechnol., vol. 32, no. 10, pp. 1–14, 2016, doi: 10.1007/s11274-016-2117-1.

[16] K. Piaskowski and R. Swiderska-d, "Carbon-Based Nanomaterials in Water and Wastewater Treatment Processes," pp. 1–34, 2025.

[17] F. Farahmandzadeh, E. Molahosseini, K. Kermanshahian, and M. Molaei, "Diamond & Related Materials Fe 3 O 4 / activated carbon / EDTA magnetic nanocomposite : A high-performance and cost-efficient nano adsorbent for treatment of water from heavy metal ions and organic dyes," Diam. Relat. Mater., vol. 159, no. PA, p. 112751, 2025, doi: 10.1016/j.diamond.2025.112751.

[18] S. Dutta, B. Gupta, S. K. Srivastava, and A. K. Gupta, "Materials Advances Recent advances on the removal of dyes from wastewater using various adsorbents : a critical," pp. 4497–4531, 2021, doi: 10.1039/d1ma00354b.

A Comparative Study of Optimization-Based Control Strategies for a Two-Tank Liquid Level System

Kaan Can[1,*]

[1] Department of Electrical & Electronics Engineering, Faculty of Engineering, Atatürk University, Erzurum, Türkiye

* *Corresponding author E-mail: kaan.can@atauni.edu.tr*

Keywords

Linear control,

Optimization-based control,

Metaheuristic algorithms,

Liquid level control,

Coupled tank system

Abstract

In this paper, the parameters of the PI-type linear controller designed to regulate the liquid level in a coupled-tank system were optimized using three nature-inspired algorithms such as Fata Morgana (FATA), Fox Optimization (FOX), and Moss Growth (MOSS). First, a nonlinear mathematical model of the coupled-tank system was derived to accurately represent the system dynamics. Subsequently, the transfer function corresponding to the required control configuration was obtained, and the PI controller gains, *Kp* and *Ki*, were optimized by using the FATA, FOX, and MOSS algorithms. For comparative assessment, the PI controller parameters were also tuned using the classical Ziegler–Nichols (Z–N) method, and all controllers were evaluated under two different step + time varying reference signal. The simulation results demonstrated that the controller parameters optimized by the FOX algorithm, have achieved superior reference tracking performance compared to those obtained using the FATA and MOSS techniques. Furthermore, the FOX-based controller has provided approximately 52% better reference tracking performance compared with the controller tuned using the Z–N method.

1. Introduction

Liquid level control of tank systems is a fundamental problem in process control engineering due to its inherent nonlinear dynamics, parameter uncertainties, and strong coupling effects [1-4]. Such systems are widely encountered in chemical processes, water treatment plants, and industrial fluid transport applications, where accurate and robust level regulation is critical for safe and efficient operation. Classical control strategies, particularly proportional–integral (PI) controllers tuned using heuristic rules such as the Z–N method, have been extensively employed owing to their simplicity and ease of implementation. However, the Z–N tuning approach often leads to large overshoot, long settling time, and poor tracking performance, especially under time-varying reference signals and nonlinear operating conditions. On the other hand, in literature, there are some metahuiristic optimization methods are available.

For instance, the FOX optimizaiton methods has been used and applied different systems to tune their control parameter soas to enhance system performance [5-7]. As an example, Mohammed and Rashis, have proposed a study that introduces a novel metaheuristic algorithm, referred to as FOX, inspired by the hunting behavior of foxes in nature [8]. The algorithm employs a best-position-based random walk during the exploration phase, while a distance measurement mechanism is used to estimate the distance between the fox and its prey. Furthermore, a jumping action is incorporated in the exploitation phase to capture the prey. Another nature-inspired approach, known as FATA, is a method developed by heuristically modeling hallucination-like phenomena observed in nature [9, 10]. Wei et al. proposed an improved version of the algorithm, referred to as IMFATA, which incorporates a circular chaotic map and an adaptive t-distribution–based perturbation mutation strategy to overcome the premature convergence and local optimum stagnation issues of FATA [10]. The effectiveness of IMFATA was validated against the original FATA using 23 benchmark functions and the CEC2021 test suite, and its performance was further compared with several well-known metaheuristic algorithms, including the Goose Algorithm (GOOSE), Beluga Whale Optimization (BWO), Honey Badger Algorithm (HBA), Whale Optimization Algorithm (WOA), Dung Beetle Optimization (DBO), and Eagle Optimization Algorithm (AO). The experimental results demonstrate that IMFATA significantly enhances computational accuracy and convergence speed, while exhibiting superior global optimization capability compared to the competing methods. As an another method, MOSS growth optimization inspire the moss ecosystem [11, 12]. For instance, Steen et al. integrated the MGO algorithm with a graph-based approach using MAKLINK Graph Theory to enable efficient map representation and path planning [13]. While an initial path is rapidly generated through the

graph-based framework, MGO enhances global exploration and refines the solution via local optimization. The incorporation of a Line-of-Sight Reduction technique further improves the search efficiency. Simulation results and comparative analyses confirm that, particularly in complex environments, the proposed approach achieves faster convergence and shorter path lengths compared to existing methods.

In this paper, the tuning of a linear PI controller for liquid level control of a two-tank system is carried out using the FOX, FATA, and MOSS optimization methods to evaluate their comparative performance. The resulting controller parameters were evaluated under two different step + time-varying reference signals. Moreover, to assess the effectiveness of the proposed optimization approaches and to provide a benchmark for comparison, the controller parameters obtained using the classical Z–N method were also applied under the same reference conditions. Along with the graphical results obtained from the simulation studies, the performance of each method was quantitatively evaluated using the mean absolute error (MAE) criterion, and the results were presented in tabular form. The findings clearly demonstrate that metaheuristic optimization methods achieve better reference tracking performance compared to the conventional Z–N tuning method.

2. Materials and Methods

2.1. The Mathematical Model of Tank System

The two-tank system is a challenging control problem due to its nonlinear dynamics, single-input structure, and two different operating configurations [14]. The upper tank (Tank 1) is directly supplied by the pump, whereas the lower tank (Tank 2) is fed only through the outflow from the upper tank. As a result of this configuration, the dynamics of Tank 2 are more complex than those of Tank 1, making its level control significantly more difficult. For this reason, in this paper, the liquid level control of Tank 2 was selected in order to evaluate the effectiveness of the optimized controller parameters under a more realistic and demanding control scenario. Moreover, in Fig. 1, the system figure is depicted [14].

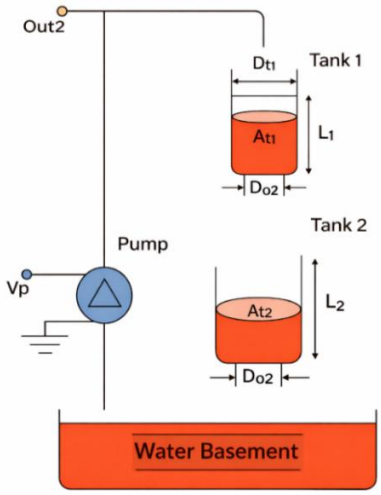

Figure 1 The two tank system [14].

In addition, the mathemaitcal model of the tank 2 to be controlled, can be expressed as given below [14].

$$\frac{dL_2}{dt} = \frac{A_{01}\sqrt{2}\sqrt{gL_1} - A_{02}\sqrt{2}\sqrt{gL_2}}{A_{t2}} \tag{1}$$

where g is the gravitational acceleration, A_{t2} is the area of tank 2, A_{02} and A_{01} the cross-sectional area of the outlet of the tank 1 and tank 2, respectively.

2.2. The Optimization Methods

In this paper, the optimization methods employed for liquid level control of the two-tank system, are choosen as FOX, FATA, and MOSS, respectively. Using these methods, the controller parameters of Tank 2, namely Kp_2 and Ki_2 obtained.

2.2.1. The FOX Optimization Method

The FOX method, is a population-based metaheuristic method inspired by the hunting behavior of foxes. The algorithm alternates between global exploration and local exploitation by adaptively adjusting the step size of each agent (fox) [5-8]. Candidate solutions are guided toward the best solution found so far, while random perturbations are introduced to avoid premature convergence to local minima [5-8].

In FOX method, each fox represents a candidate solution in the search space and can be defined as [5-8],

$$x_i = [x_{i1}, x_{i2}, \dots, x_{id}] \tag{2}$$

where *d* denotes the dimensionality of the optimization problem. For PI controller tuning, the decision vector can be expressed as [5-8],

$$x_i = [K_p, K_i] \tag{3}$$

where *Kp* and *Ki* are the proportional and integral gains, respectively. An initial population of ***N*** foxes is randomly generated within the search bounds as given below [5-8].

$$x_{ij}^{(0)} = l_j + (u_j - l_j) rand(0,1) \tag{4}$$

This ensures a wide coverage of the search space at the beginning. Each fox is evaluated using an objective (fitness) function such as,

$$f(x_i) = MAE, ITAE, IAE, ISE, etc. \tag{5}$$

The best solution in the population is identified as [5-8];

$$x_{best} = \arg\min_{x_i} f(x_i) \tag{6}$$

This best solution is considered the **prey location.** Each fox moves toward the best solution found so far [5-8];

$$x_i^{(t+1)} = x_i^{(t)} + a_t r_t \left(x_{best}^{(t)} - x_i^{(t)}\right) \tag{7}$$

where $r_t \in (0,1)$ is a random number and a_t is an adaptive step-size parameter, respectively. This step models the fox approaching the prey. The adaptive transition from global to local search, the step size decreases over iterations according to [5-8, 15];

$$a_t = a_0 \left(1 - \frac{t}{T_{max}}\right) \tag{8}$$

where a_0 is the initial step size and T_{max} is the maximum number of iterations. This adaptive mechanism is key to fast and stable convergence. Based on a predefined probability, the fox initiates a random movement in the search space [5-8];

$$x_i^{(t+1)} = x_i^{(t)} + \beta N(0,1) \tag{9}$$

where β is a scaling factor and $N(0,1)$ denotes a standard Gaussian random variable [15]. For boundary control; each decision variable is constrained within its limits as given below [5-8, 15].

$$x_{ij}^{(t+1)} \in [l_j, u_j] \tag{10}$$

Values outside the allowable range are constrained to the nearest boundary. For the selection process, if the updated position produces a better fitness [5-8],

$$[\![f(x)]\!]_i^{(t+1)}) < [\![f(x)]\!]_i^{(t)}) \tag{11}$$

then, the update is accepted; otherwise, the previous position is retained.

The algorithm is halted upon reaching the maximum iteration limit or when successive improvements become negligible. Besides, the algorithm express the following properties;

- ✓ Exploration (global search of the solution space),
- ✓ Exploitation (local refinement around promising solutions),
- ✓ Random perturbation (escaping local optima).

2.2.2. The FATA Optimization Method

The FATA method is a population-based metaheuristic method inspired by the optical mirage phenomenon [9, 10]. The algorithm introduces adaptive distortion operators to generate new candidate solutions, enabling effective global exploration while gradually shifting toward local exploitation [9, 10]. By combining mirage-based perturbations with guided attraction toward the best solution, the FATA demonstrates strong performance in complex optimization problems such as controller parameter tuning. The key advantages of FATA depends on [9, 10];

- ❖ Strong global exploration via mirage distortion,
- ❖ Adaptive transition to local exploitation,
- ❖ Simple structure with few control parameters,
- ❖ Effective for nonlinear and multimodal problems, as well.

In order to obtain the mathematical expression of the FATA method, one can consider the following continuous optimization problem [9, 10, 16];

$$\min_{x \in w} f(x), \quad w = \{x \in \mathbb{R}^d \mid l \leq x \leq u\} \tag{12}$$

where $f(x)$ is the objective (fitness) function, l and u are the lower and upper bounds and d is the dimenson of the decision vector, respectively [9, 10, 16, 17]. Moreover, an initial population of N candidate solutions is randomly initialized as given below [17].

$$x_i^{(0)} = l + (u - l) \odot rand_i, \qquad i = 1, 2, \ldots, N \tag{13}$$

Here, $\odot$ denotes element-wise multiplication as well as $rand_i \sim U(0,1)^d$. In the mirage-based perceptual attraction mechanism, $x_{best}^{(t)}$ represents the best solution identified at iteration *t.* Each agent experiences an attraction toward this perceived optimal point [9,10,16],

$$A_i^{(t)} = x_{best}^{(t)} - x_i^{(t)} \tag{14}$$

in which this term represents the perceived proximity of the global optimum, analogous to the illusionary nature of a mirage. Due to environmental and perceptual distortions, the attraction is perturbed by a stochastic mirage term [9,10];

$$M_i^{(t)} = \gamma_t \xi_i^{(t)}, \ \xi_i^{(t)} \sim N(0, I) \tag{15}$$

where γ_t is the mirage distortion coefficient and $\xi_i^{(t)}$ models uncertainty and environmental fluctuation, as well. Furthermore, the candidate solutions are updated as in (16) [9,10,16].

$$x_i^{(t+1)} = x_i^{(t)} + \alpha_t A_i^{(t)} + M_i^{(t)} \tag{16}$$

where α_t is the perceptual attraction coefficient. This equation balances exploitation (first term) and exploration (stochastic term). To enhance convergence, the coefficients are updated adaptively, one can write the following expressions [9,10,16].

$$\alpha_t = \alpha_{max} - \frac{t}{T_{max}}(\alpha_{max} - \alpha_{min}); \qquad \gamma_t = \gamma_{max} exp\left(\beta \frac{t}{T_{max}}\right) \tag{17}$$

Here, T_{max} represents the maximum number of iterations and $\beta > 0$ is the decay constant of the expression, as well. On the other hand, each updated solution is projected back into the feasible domain [9,10,16],

$$x_{i,j}^{(t+1)} = \min\left(\max\left(x_{i,j}^{(t+1)}, l_j\right), u_j\right). \tag{18}$$

A greedy selection mechanism is applied as in (19) [9, 10, 16, 17].

$$x_{i,j}^{(t+1)} = \begin{cases} x_i^{(t+1)}, & if\ f\left(x_i^{(t+1)}\right) < f(x_i^{(t)}) \\ x_i^{(t)}, & otherwise \end{cases} \tag{19}$$

For the termination criterion, the algorithm terminates when the following expression satisfied.

$$t \geq T_{max} \quad or \quad \left|f_{best}^{(t)} - f_{best}^{(t-1)}\right| < \varepsilon \tag{20}$$

2.2.3. The MOSS Optimization Method

The MOSS algorithm is a nature-inspired metaheuristic algorithm that models the adaptive growth behavior of moss colonies [11-13]. By combining gradual local expansion with attraction toward favorable environments, the algorithm achieves a balanced trade-off between exploration and exploitation, making it well suited for controller parameter optimization problems. The advantages of MOSS methods can be given as below [11-13].

- ❖ Strong local exploitation capability,
- ❖ Smooth convergence behavior,
- ❖ Few control parameters,
- ❖ Effective for nonlinear control systems.

In order to define a problem, one can taking into account the expresion as given in (12). Afterthat, an initial set of *N* moss agents is generated as [11-13];

$$x_i^{(0)} = l + (u - l) \odot rand_i, \qquad i = 1, 2, \ldots, N \tag{21}$$

where $rand_i \sim U(0,1)^d$. During the local exploitation phase, moss grows toward favourable conditions, represented by the current best solution [11-13].

$$x_i^{(t+1)} = x_i^{(t)} + \alpha_t(x_{best}^{(t)} - x_i^{(t)}) \tag{22}$$

Here, α_t is a growth rate. To colonize new areas, moss spreads randomly as given below [11-13].

$$x_i^{(t+1)} = x_i^{(t+1)} + \delta_t \xi_i^{(t)},\ \xi_i^{(t)} \sim N(0, I) \tag{23}$$

where δ_t controls exploration and typically decays over time [11-13]. Besides, the healthier colonies dominate [17, 18],

$$x_i^{(t+1)} = \begin{cases} x_i^{(t+1)}, & f\left(x_i^{(t+1)}\right) < f(x_i^{(t)}) \\ x_i^{(t)}, & otherwise. \end{cases} \tag{24}$$

For the adaptive parameter α_t, a common schule can be expressed as in (17) with boundary handling given in (18). For the stop criteria can be taking in to account when $t \geq T_{max}$ or $improvement < \varepsilon$ as given in (20). In addition, Table 1 provides the controller parameter values derived from all optimization methods.

Table 1 The optimized controller parameter values for all optimization methods

Methods	K_p	K_i
Z-N	5.0939	1.7438
FATA	7.7301	4.8113
FOX	8.037	4.5317
MOSS	7.7921	4.4109

3. Results and Discussion

In this section, the simulation results obtained using the proposed optimization methods are presented. In Fig. 2, the results obtained under a step + sinusoidal reference signal are presented. For the step section, it is seen that the FOX method has reached the reference signal earlier than the other methods, and settled faster while exhibiting an overshoot of nearly the same magnitude as the FATA and MOSS methods. On the other hand, although the Z–N method has reached the reference signal in approximately the same time as the MOSS and FATA methods, it is observed to has had the longest settling time. For the sinusoidal part, it is observed that the Z–N method exhibited a steady-state error while tracking the reference signal and has had difficulty in accurately following the reference trajectory. Conversely, the remaining optimization-based control approaches have provided enhanced reference tracking performance compared with the Z–N method, accompanied by reduced steady-state errors.

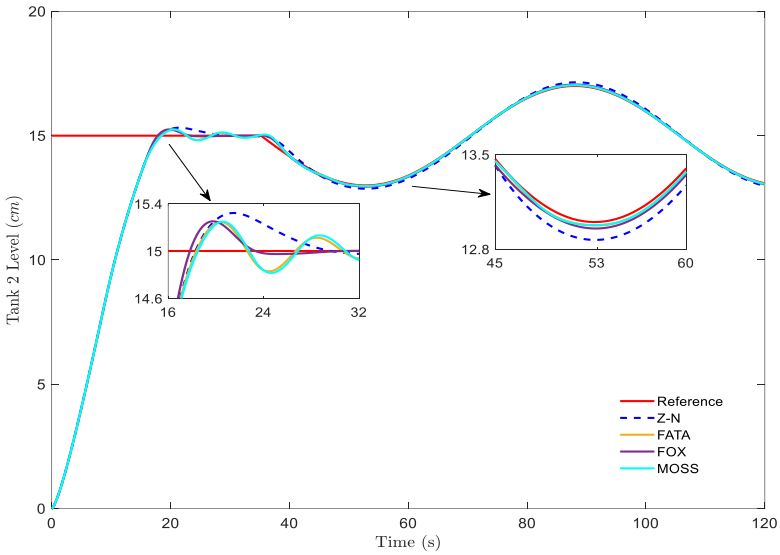

Figure 2 Comparative simulation results of all optimization-based control approaches under step and sinusoidal reference signals

In Fig. 3, the error signals of all optimization methods have been depicted. For the step part, it is observed that all methods initially exhibited an error value of 15 cm, and as the liquid level increased, the error values gradually approached to zero. Subsequently, due to the FOX method settled to the reference signal in a shorter time, its error was reduced to zero earlier than the others and was maintained around zero with slight oscillations. Moreover, it is observed that the error variations of the MOSS and FATA methods were similar and fluctuated within the range of approximately −0.3 to 0.3 cm. On the other hand, the Z–N method has showed the largest reference tracking error over the full duration of the reference signal.

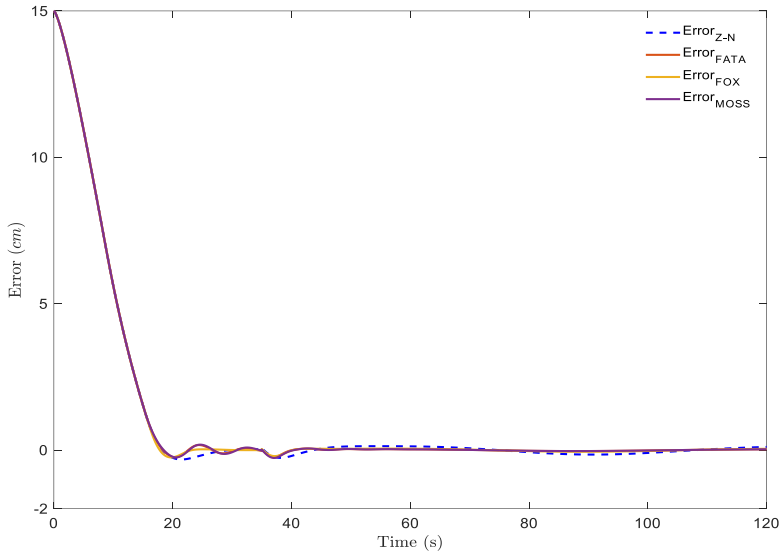

Figure 3 Tracking error signals of all optimization-based control approaches under a combined step and sinusoidal reference signal

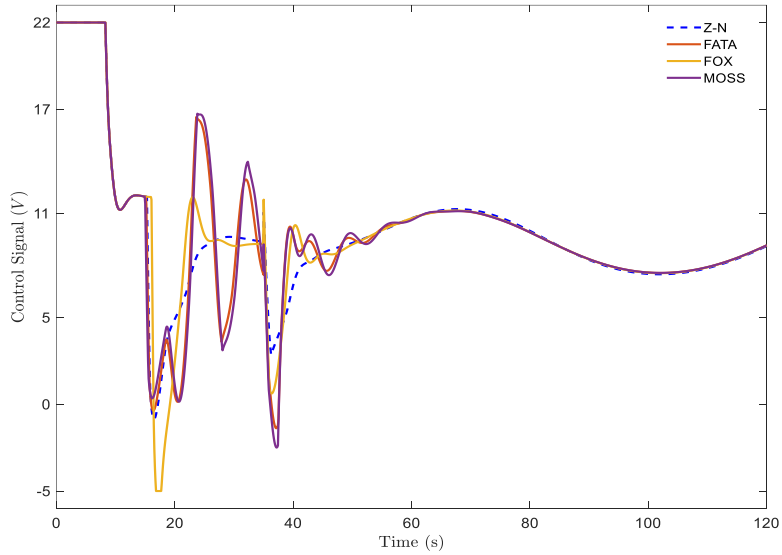

Figure 4 Comparative control signals of all optimization-based control approaches for step and sinusoidal reference signals

In Fig. 4, the control signals of all optimization methods have been given under step + sinusoidal reference signal. As seen in the figure, sudden changes and oscillations occurred in the control signal during the step + sinusoidal reference transition in all methods. Differences between methods are particularly noticeable during the initial transition (approximately 15–40 seconds). The FOX method initially exhibited a more aggressive control behaviour, creating a deeper but shorter-lived drop in the control signal to guide the system to the reference more quickly. This contributed to a shorter settling time, consistent with previous error analyses. The FATA and MOSS methods exhibited similar control profiles; although more pronounced oscillations occurred in the control signal, these oscillations remained within a limited band. The control signals of these methods were slightly smoother compared to FOX but more effective than Z-N. By contrast, the Z–N tuning approach exhibited a slower and less responsive behaviour during the transient phase. Its control input magnitude was relatively constrained compared to the optimization-based methods, which resulted in delayed reference convergence and increased tracking errors. Following the transition to the sinusoidal reference segment (approximately after 50 s), the control inputs generated by all controllers converged to comparable shapes and amplitudes, indicating that the system had reached steady-state operation. Nevertheless, even under these conditions, the Z–N method continued to apply a less efficient control action, leading to inferior reference-following performance.

Furthermore, Table 2 presents the MAE values obtained by all optimization methods under a step + sinusoidal reference signal. For the step part of the reference signal, the FOX, FATA, and MOSS methods have very similar MAE values, all of which are significantly lower than that of the Z–N method. In the sinusoidal reference, the FOX method obtained the lowest MAE value, demonstrating superior tracking performance for time-varying references.

On the other hand, the Z–N method has the highest MAE value approximately with 2.4906. Considering the entire reference signal, the FOX method obtained a minimum MAE value of 1.0901, which corresponds to a performance improvement of 56.23% compared to the Z–N method. The FATA and MOSS methods also showed significant improvements of 42.82% and 42.76%, respectively. These results clearly demonstrate that the proposed optimization-based methods perform significantly better than the traditional Z–N tuning approach, and that the FOX method provides the best overall tracking accuracy.

Table 2 The calculated MAE values obtained for all optimization methods subjected to a combined step and sinusoidal reference signal

Algorithms	Step	Sinusoidal	Step + Sinusoidal	Total Improvement % (Wrt. Z-N)
FOX	4.5745	0.0296	1.0901	%56.2314
FATA	4.5564	0.0374	1.4242	%42.8169
MOSS	4.5784	0.0320	1.4255	%42.7647
Z-N	5.5994	0.0907	2.4906	--------

Figure 5 shows the simulation results obtained using all optimization methods under step and sinusoidal reference signals. As seen in the figure, all methods successfully guided the liquid level to the target value after applying the step reference. However, performance differences between the methods become particularly noticeable in the transition regime and at the peaks of the sinusoidal reference. The FOX method reached the reference level faster in the step transition and exhibited a shorter settling time with limited overshoot. As can be seen from the zoomed-in graphs, the FOX method quickly dampens oscillations, keeping the liquid level stable around the reference. The FATA and MOSS methods showed similar dynamic behavior. Although these methods exhibited a marginally higher overshoot than the FOX approach, the resulting oscillatory behavior remained well within acceptable bounds. In contrast, the Z–N tuning method resulted in a noticeably larger overshoot and significantly prolonged settling times, both during step changes and at the transition points of the sinusoidal reference. It is evident that the Z–N method had difficulty maintaining accurate reference tracking, leading to more severe oscillations, particularly in the zoomed-in sections. During the sinusoidal tracking phase, the optimization-based techniques (FOX, FATA, and MOSS) demonstrated reduced amplitude deviations and improved phase alignment with the reference signal, whereas the Z–N method suffered from comparatively larger tracking errors. Overall, these findings confirm that metaheuristic-based controller tuning strategies achieve substantially improved control performance for the two-tank liquid level system when compared with the conventional Z–N approach.

Figure 6 illustrates the tracking error responses of all optimization methods under the step + sinusoidal reference signal. For the step part of the reference signal, all methods started with an initial error of approximately 15 cm, which rapidly decreased as the liquid level approached the reference value. During this phase, the FOX method reduced the error to zero earlier than the other methods and maintained it around zero with minimal oscillations. After the second step change in the reference signal, a sudden increase in the tracking error was observed for all methods. Nevertheless, the FOX method exhibited faster error convergence and smaller oscillations compared to the FATA and MOSS methods. In contrast, the Z–N method showed relatively larger error fluctuations and slower convergence throughout the entire response.

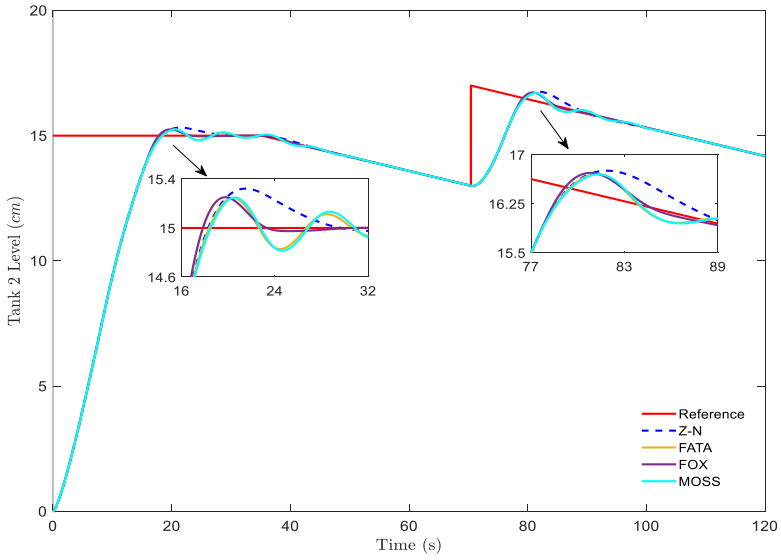

Figure 5 Comparative simulation results of all optimization-based control approaches under step and sawtooth reference signals

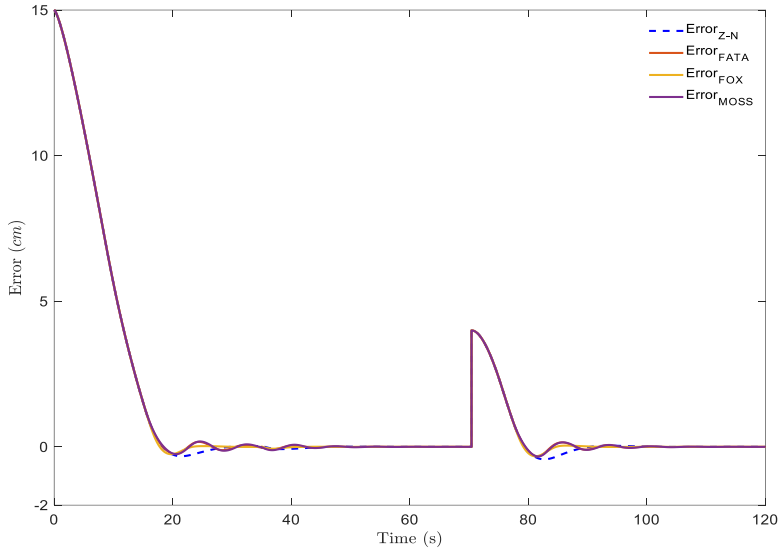

Figure 6 Tracking error signals of all optimization-based control approaches under a combined step and sawtooth reference signal

In Fig. 7, the control signal responses generated by all optimization methods under the step + sinusoidal reference signal are presented. For the step part of the reference signal, all methods exhibited aggressive control actions to rapidly settle to the liquid level towards the reference value, displaying sharp variations in the control signal. During this transient phase, the FOX method produced a relatively strong but short-lived control effort, resulting in faster convergence to the reference with a shorter settling time. Although the FATA and MOSS methods had a similar control signal form characterized by larger oscillations during the transient response, these oscillations remained within acceptable limits. In contrast, as previously observed, the Z-N method exhibited a relatively smoother but slower control action, resulting in delays in reference tracking and larger tracking errors. For the time-varying part of the reference signal, similar control behaviors were observed for all methods. However, the FOX method again provided faster stabilization of the control signal with smaller oscillations, while the Z-N method required a longer settling time.

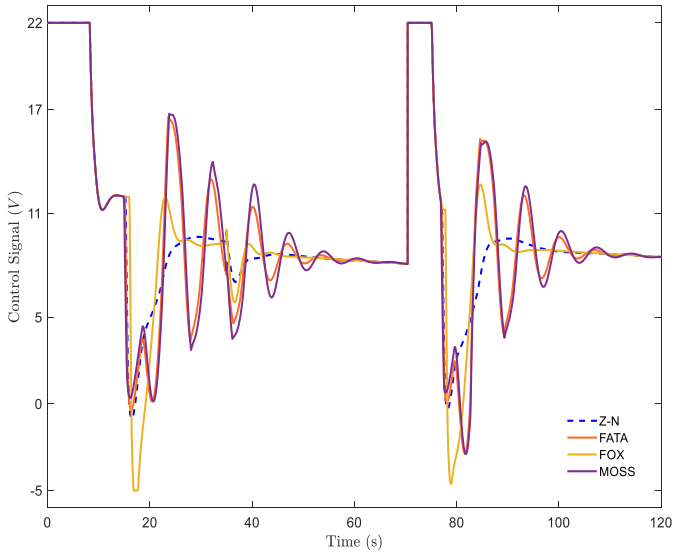

Figure 7 Comparative control signals of all optimization-based control approaches for step and sawtooth reference signals

Table 3 presents the calculated MAE values obtained under the combined step and sawtooth reference signal. For the step segment, the FOX, FATA, and MOSS methods exhibit very similar MAE values, all of which are significantly lower than that obtained using the conventional Z–N tuning method. Under the sawtooth reference signal, the FOX method achieves the lowest MAE, indicating superior tracking performance for rapidly varying reference inputs, whereas the Z–N method yields the highest error. Considering the entire reference signal, the FOX method attains the minimum MAE value of approximately 1.2583, corresponding to an overall improvement of 52.68% compared to the Z–N method. This performance is followed by the FATA and MOSS methods, which provide substantial improvements of approximately 38.95% and 38.03%, respectively.

Table 3 The calculated MAE values obtained for all optimization methods subjected to a combined step and sawtooth reference signal

Algorithms	Step	Sawtooth	Step + Sawtooth	Total Improvement % (Wrt. Z-N)
FOX	4.5745	0.2189	1.2583	%52.6830
FATA	4.5564	0.2368	1.6236	%38.9463
MOSS	4.5784	0.2545	1.6480	%38.0288
Z-N	5.5994	0.2594	2.6593	--------

4. Conclusion

This paper investigates the performance of three meta-heuristic optimization algorithms (FOX, FATA, and MOSS) for tuning the PI controller's parameter so as to control of a two-tank liquid level system. The proposed optimization-based controllers were systematically evaluated and compared with the classical Z-N tuning method under step + sinusoidal and sawtooth reference signals to assess their liquid level tracking performance. Simulation results revealed that all optimization-based methods significantly outperformed the traditional Z-N method in terms of reference tracking accuracy. Specifically, the FOX method consistently exhibited faster rise and settling times for both reference signals, resulting in less steady-state and lower reference tracking error levels. Furthermore, as seen in the calculated MAE results, the FOX method had the lowest error values and the highest overall improvement rates compared to the Z-N method under both step + sinusoidal and step + sawtooth reference signals. The FATA and MOSS methods also showed significant improvements compared to the Z-N method, exhibiting comparable and stable reference tracking performance with acceptable oscillation levels. Overall, the results confirmed that metaheuristic optimization-based tuning approaches offer a more robust and efficient alternative to classical tuning rules for nonlinear liquid level control problems.

Future studies will focus on experimental verification, robustness analysis under disturbances and parameter uncertainties, and real-time implementation of the proposed optimization-based controllers.

References

[1] Sekban, H.T., Can, K., & Başçi, A. (2020). Model-based Dynamic Fractional-order Sliding Mode Controller Design for Performance Analysis and Control of a Coupled Tank Liquid-level System. Advances in Electrical and Computer Engineering, 20(3), 93-100.

[2] Sekban, H.T., Can, K., & Başçi, A. (2016). Real-Time Application of Sliding Mode Controller for Coupled Tank Liquid Level System. International Journal of Applied Mathematics, Electronics and Computers, 2016(4), 301-307.

[3] Yılmaz, M., Can, K., & Başçi, A. (2021). PI + Feed Forward Controller Tuning Based on Genetic Algorithm for Liquid Level Control of Coupled-Tank System. Journal of the Institute of Science and Technology, 11(2), 1014-1026.

[4] Can, K. (2025). İkili Tank Sisteminin Sıvı Seviye Kontrolü için Farklı Optimizasyon Yöntemlerinin Kıyaslanması ve Performans Analizi. In Proc. 26th National Conf. on Automatic Control, Samsun, Türkiye, Sept. 18–21, 735–741.

[5] Hamed, A., Torky, M., AlJanah, S., et al. (2025). A Blockchain-Based Fox Optimization Algorithm for Optimizing and Securing Electrical Vehicles Charging. IEEE Tran. on Intelligent Vehicles, 10(9), 4479-4498.

[6] Manivannan, R., Senthilkumar, S. (2025). Intrusion Detection System for Network Security Using Novel Adaptive Recurrent Neural Network-Based Fox Optimizer Concept. Int J Comput Intell Syst, 18(37), 24 pages.

[7] Majhi, B., Prastavana A. (2024). feature selection model using binary FOX optimization and v-shaped transfer function for network IDS. Peer-to-Peer Netw. Appl., 17, 3556–3570.

[8] Mohammed, H. & Rashid, T. (2023). FOX: a FOX-inspired optimization algorithm. Applied Intelligence, 53(2023), 1030-1050.

[9] Aljaidi, M., Jangir, P., Agrawal, S.P. et al. (2025). Optimizing FACTS Device Placement Using the Fata Morgana Algorithm: A Cost and Power Loss Minimization Approach in Uncertain Load Scenario-Based Systems. J. Appl. Prob., 56, 830–857.

[10] Wei, P., Jia, C., Shi, Z. et al. (2025). An Improved Fata Morgana Algorithm for Global Optimization. Arab J Sci Eng., 50, 19993–20013

[11] Hou, L., Wang, Y., Lin, X. et al. (2025). An enhanced alpha evolution moss growth optimizer for prognostic prediction in spontaneous intracerebral hemorrhage. J Big Data 12(122), 31 pages.

[12] Li, P., Wang, H., Wang, Z., Wang, K. & Wang, C. (2024). Swin Routiformer: Moss Classification Algorithm Based on Swin Transformer with Bi-Level Routing Attention. IEEE Access, 12, 53396-53407.

[13] Steen, S., Lei, T., Luo, C. et al. (2025). A Moss Growth Optimization Apprach to Robot Path Planning, In Proc. 2025 IEEE Congress on Evolutionary Computation (CEC), Hangzhou, China, June 08-12, 4 pages.

[14] Quanser Two Tank manuel. https://www.quanser.com/products/coupled-tanks/#panel1v

[15] Blanchet, J., Kang, Y. & Murthy, K. (2019) Robust Wasserstein Profile Inference and Applications To Machine Learning. Int J Comput Intell Syst., 18, 12, 38 pages.

[16] Lucidi, S., Piccialli, V., Sciandrone, M. (2005) An Algorithm for Mixed Variable Programming. SIAM Journal on Optimization, 15(4), 1057-1084.

[17] Karadabağ, F. & Can, K. (2026). Performance Comparison of Different Optimization Techniques for Temperature Control of A Heat-Flow System. Applied Science, 16(1), 363, 24 pages. https://doi.org/10.3390/app16010363

[18] Moreno-Diaz, R., Pichler, F., Quesada-Arencibia, A. (2009). Computer Aided Systems Theory - EUROCAST 2009. In Proc. 12th International Conference, Las Palmas de Gran Canaria, Spain, February 15-20. https://doi.org/10.1007/978-3-642-04772-5

Pharmacological Properties of Curcumin-Encapsulated Nanoclays

Shahriyar Karimdoust[1*], Ekrem Kalkan[2,3], Yalçın Kemal Bayhan[4], Hayrunnisa Nadaroğlu[5], Yousef Vasigh[6]

[1] Department of Geology, Faculty of Science, Payame Noor University, Ardabil, Iran
[2] Department of Civil Engineering, Faculty of Engineering, Ataturk University, Erzurum, Türkiye
[3] Earth Sciences Application and Research Center (YEBIM), Ankara University, Ankara, Türkiye
[4] Department of Environmental Engineering, Engineering Faculty, Ataturk University, Erzurum, Türkiye
[5] Department of Food Technology, Vocational School of Technical Sciences, Ataturk University, Erzurum, Türkiye
[6] Department of Geography, Islamic Azad University, Ardabil Branch, Ardabil, Iran

* *Corresponding author E-mail: karimdoust_sh@yahoo.com*

Keywords

Curcumin,
Nanoclay,
Pathogens,
Bioavailability

Abstract

In recent years, the use of naturally derived bioactive compounds as adjunct therapeutic agents for the treatment of various diseases has received increasing attention in the medical and pharmaceutical sciences. Curcumin, as demonstrated in numerous studies, exhibits potent anti-inflammatory, antimicrobial, antiviral, and antiphrastic activities, and has proven beneficial in the management of several chronic disorders. Moreover, curcumin possesses notable anticancer properties. Curcumin (Diferuloyl Methane) is the principal active constituent of turmeric and a powerful antioxidant with significant therapeutic potential, particularly in enhancing the immune system and counteracting inflammatory and infectious pathogenic factors. Despite its broad pharmacological benefits, curcumin suffers from extremely low aqueous solubility and poor bioavailability, which substantially restrict its clinical applicability. Nanoclays hydrated silicate minerals with a layered architecture and at least one dimension in the nanoscale range have emerged as promising materials in modern industrial applications, especially in the fields of healthcare and therapeutics, due to their unique structural and physicochemical characteristics. The utilization of advanced nanotechnology and clay-based nanoparticles to improve drug delivery performance and overcome clinical limitations has become a major contemporary research focus. Reducing curcumin to the nanoscale significantly increases its solubility and enhances its therapeutic efficacy. The incorporation of plant-derived compounds into nanoclay matrices has enabled the development of a new generation of eco-friendly, biocompatible, non-chemical therapeutic agents. Modern biomedical formulations produced through micro and nanostructural engineering, combined with enhanced cell mediated therapeutic performance, represent a remarkable advancement an impressive convergence of traditional medicine with state of the art therapeutic technologies.

1. Introduction

Recent research in the pharmaceutical and healthcare sectors has increasingly focused on the development of non-toxic, organic, and environmentally friendly nanomaterials, as well as biosynthesized nanotherapeutics. Among green synthesis approaches, plant-mediated nanoparticle synthesis (phytosynthesis) has emerged as a sustainable alternative to conventional physical and chemical methods. Plants are particularly suitable for biological nanoparticle production due to their abundance, ease of cultivation, and ability to produce nanoparticles with high purity, controlled size distribution, and good stability. Advances in green nanotechnology and studies on clay minerals, especially montmorillonite, have facilitated the development of plant-based nanoclay composites with promising pharmaceutical properties. A safe and chemical-free strategy involves the modification and encapsulation of optimized nanoclay with curcumin molecules to produce herbal drug delivery systems. This novel approach enhances the bioavailability of herbal compounds by overcoming limitations such as poor solubility and rapid metabolism, while enabling effective transport and controlled release of active ingredients. These biocompatible and eco-friendly mineral–plant nanocomposites represent a promising platform for antibacterial and therapeutic applications.

2. Materials and Methods

Modified and optimized layered clay minerals with at least one nanoscale dimension have attracted significant attention in the pharmaceutical industry due to their structural versatility, low toxicity, lack of side effects, and high biocompatibility with various organs. In this study, the primary objective was the green synthesis of montmorillonite nanoclay modified with curcumin or turmeric plant extract (Figure 1) as a chemical-free nano-mineral drug [1,2].



Figure 1 Extended chemical structure of curcumin.

Raw bentonite samples (Figure 2) were collected from northeastern bentonite deposits, mechanically crushed, and pulverized to particle sizes below 1 cm using a jaw crusher and a laboratory disc mill. Particle size distribution was analyzed using laser particle size analysis [3,4].

The morphology and encapsulation efficiency of the synthesized nanomaterials were examined using electron microscopy techniques, including TEM and SEM. Elemental composition and spatial distribution were further characterized by EDX/EDAX analysis coupled with SEM [5].



Figure 2 Crushed raw bentonite sample

3. Results and Discussion

Because the purification and extraction of montmorillonite nanoclay from raw bentonite were based on mechanical separation and particle size classification, particle size analysis (PSA) played a critical role in evaluating the efficiency of the purification and dispersion process. Comparison of PSA results for the raw sample and the size-purified sample showed a homogeneous (Figure 3) and narrow particle size distribution after purification, confirming the successful separation of montmorillonite nanoparticles from the heterogeneous bentonite matrix [5].

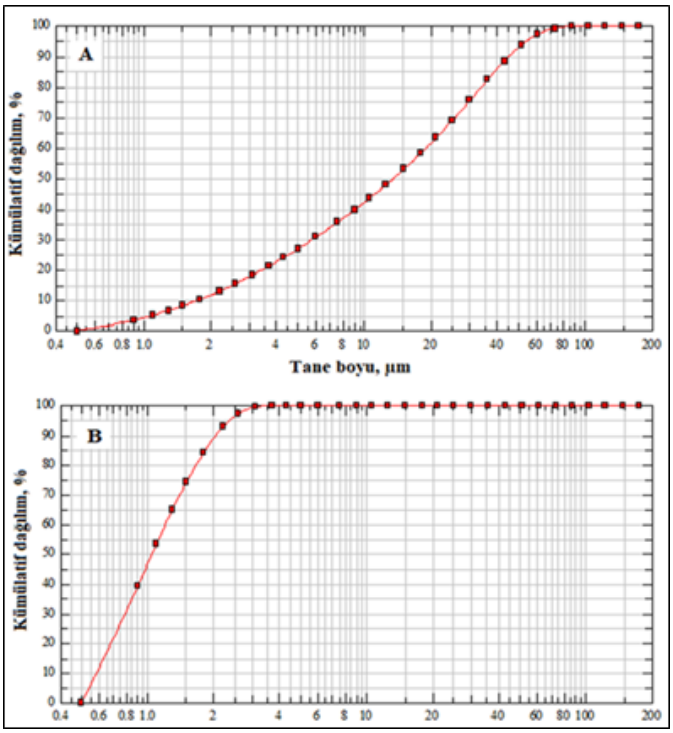

Figure 3 Particle size distribution curves of raw bentonite (A) and purified bentonite (B) samples.

The effectiveness of the green synthesis and modification process was further evaluated using SEM/EDX and microstructural analyses. While SEM images alone cannot confirm chemical composition, comparison between raw and curcumin-modified montmorillonite revealed a noticeably smoother and more uniform surface after modification.

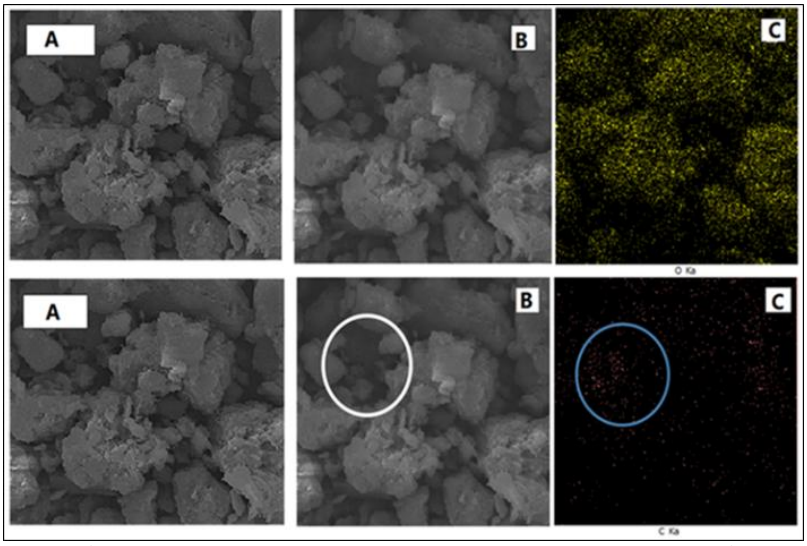

Figure 4 SEM/EDX analysis results of nano-clay samples not treated with curcumin (A) and the accumulation of curcumin particles in high-energy regions (B) and the elemental point distribution of elements on nano-clay (C)

Electron microscopy results indicated that curcumin preferentially adsorbs onto high-energy regions of the montmorillonite surface, such as peaks and valleys, leading to surface smoothing of the modified nano/microspheres. This interaction was further supported by SEM–EDS analysis, which confirmed the presence and distribution of curcumin on the montmorillonite surface (Figure 4).

Comparative examination of TEM images obtained from microscopic analysis of the studied samples shows that curcumin molecules are visible and dispersed in the form of amorphous and non-crystalline aggregates around the nano-montmorillonite crystals. When organic materials such as curcumin are adsorbed on the surfaces, the crystallization becomes almost invisible. It is shown that the process is positive because the montmorillonite crystal grains are covered with curcumin (Figure 5).

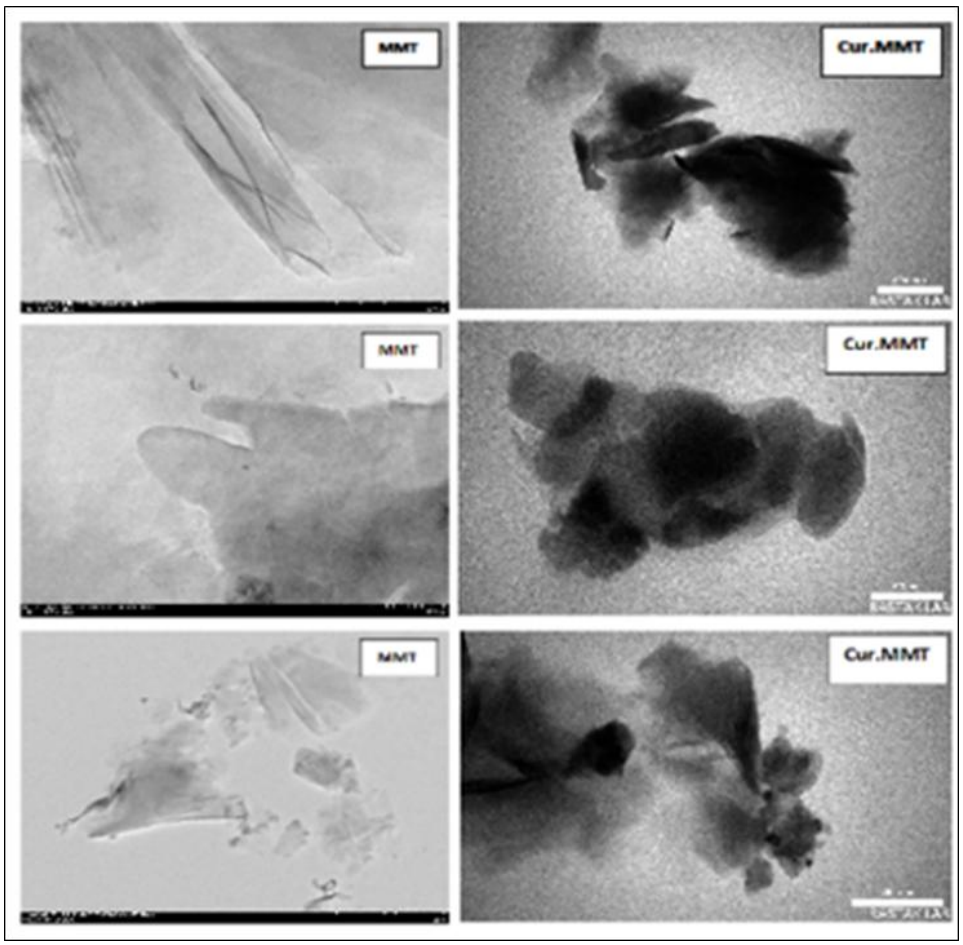

Figure 5 TEM images showing amorphous aggregates of curcumin on montmorillonite and modified montmorillonite.

Overall, these results demonstrate that the applied purification and green modification methods were effective in producing homogeneous, curcumin-loaded montmorillonite nanocomposites with improved surface characteristics, supporting their potential application in pharmaceutical and drug delivery systems.

4. Conclusions

The results of this study demonstrate that the use of physical, non-chemical methods to produce montmorillonite-rich materials with particle sizes below 2 μm is an effective and suitable approach, particularly for pharmaceutical and human health applications. Laser-based particle size analysis (PSA) proved to be a reliable and practical technique for evaluating the mechanical purification of montmorillonite from bentonite by monitoring particle dispersion and size distribution. Particle separation based on average diameter represents a simple, cost-effective, and efficient differential purification method for the successful extraction of montmorillonite nanoclay.

Electron microscopy combined with elemental mapping provided an effective and straightforward tool for assessing surface microstructure, elemental distribution, optimization efficiency, and the presence of impurities in the synthesized samples. Overall, the integrated analyses indicate that physically purified nanoclays enable more effective curcumin loading and modification. Given that impurities significantly reduce the pharmacological performance of nanomaterials, the proposed purification and modification strategy offers a promising route for producing high-purity nanoclays with enhanced medicinal and pharmaceutical properties.

References

[1] Hughes, G.A., 2005. Nanostructure-mediated drug delivery. Nanomedicine 1, 22-30.
[2] Gomes, C.S.F., Silva, J.B.P., 2007. Minerals and clay minerals in medical geology. Applied Clay Science 36, 4-21.
[3] D.Mubarak-Ali, N., Thajuddin, K., Jeganathan, M., 2011. Gunasekaran, Colloids and Surfaces B: Biointerfaces, 85: 360.
[4] Sangeetha, G., Rajeshwari, S., R. Venckatesh, R., 2011. Mater Res Bull, 46, 2560.
[5] Veiskarami, M., Sarvi, M.N., Mokhtari, A.R., 2016. Influence of the purity of montmorillonite on its surface modification with an alkyl-ammonium salt. Applied Clay Science, 120: 111-120.

Evaluation of Liquefaction Potential in Erzurum Aziziye District

Onur Temiz [1*], Hamit Çakıcı [2]

[1] Department of Architecture and Urban Planning, Pasinler Vocational School, Ataturk University, Erzurum, Türkiye
[2] Graduate Student, Department of Geological Engineering, Institute of Science, Atatürk University, Erzurum, Türkiye

* *Corresponding author E-mail: onurtemiz5355@gmail.com*

Keywords

Liquefaction,
Erzurum,
Aziziye,
SPT,
Sieve Analysis

Abstract

The aim of this study is to evaluate the liquefaction potential of Aziziye District in Erzurum Province and to determine the seismic safety of the region in terms of soil properties. In this context, the liquefaction potential of the study area was calculated using the methods proposed by Iwasaki et al. (1982) and Sönmez and Gökçeoğlu (2005). As part of the field studies, boreholes were drilled at designated points and Standard Penetration Test (SPT) was applied. In addition, disturbed and undisturbed soil samples taken from the research pits were subjected to consistency limits, natural and saturated unit weight, sieve analysis, and hydrometer tests in the laboratory. Using all the data obtained from the field and laboratory tests, liquefaction potential analyses were performed according to the criteria of Iwasaki et al. (1982) and Sönmez and Gökçeoğlu (2005). The liquefaction potential for Erzurum province was evaluated using the Liquefaction Potential Index (LPI) and Liquefaction Severity Index (LSI) methods, and a liquefaction potential map was prepared in a GIS environment according to different earthquake scenarios. As a result of the evaluation of the data obtained within the scope of the study; it was determined that the average SPT-N value was 25.36, the natural unit weight was 16.20 kN/m³, and the saturated unit weight was 17.45 kN/m³. Furthermore, the plasticity index was determined to be 13.8%, the clay content 11.12%, and the fine grain ratio 32.34%. In the liquefaction analyses performed using these soil properties, the liquefaction potential at different points of the study area was calculated according to the methods of Iwasaki et al. (1982) and Sönmez and Gökçeoğlu (2005). The liquefaction potential for Erzurum province was evaluated, and maps were prepared according to different earthquake scenarios. According to the results obtained from field and laboratory studies, it has been determined that the probability of liquefaction occurring is high at the SK-1, SK-4 and SK-7 borehole locations in the study area, while the liquefaction potential is at a very low level at the SK-2, SK-3, SK-5 and SK-6 locations.

1. Introduction

Accurate determination of the local soil properties on which structures are built is crucial in understanding and mitigating the damage caused by earthquakes. How seismic waves behave in the soil is directly related to the engineering properties of the soil conditions. Therefore, to minimize the potential effects of earthquakes in a region, it is necessary to accurately define the physical, mechanical, and dynamic properties of the soil [1].

In Turkey, engineering measures to be taken against earthquake hazards have been updated through earthquake regulations issued over the years. Earthquake regulations in our country have been revised nine times since 1940 [2]. With the latest Turkish Building Earthquake Regulation [3], which came into force in 2018, the provisions regarding the determination of soil class, the determination of groundwater level, and the evaluation of possible soil liquefaction have been revised according to modern scientific methods, and a standard building design framework has been established.

Liquefaction is a critical phenomenon that causes a significant reduction in soil bearing capacity and rigidity during earthquakes. More frequently observed in saturated, loose, and sandy soils, this condition results in the soil behaving like a liquid, leading to settlement, toppling, or severe damage to the load-bearing systems of structures. Past earthquakes clearly demonstrate that liquefaction has caused large-scale destruction worldwide [4].

Various methods are used to accurately assess liquefaction potential. In recent years, evaluating data obtained from Standard Penetration Testing (SPT) together with the physical properties of the soil (liquid limit, plastic limit, natural unit weight, etc.) has become an important approach that increases the reliability of liquefaction analyses. Therefore, comprehensive investigation of soils through both laboratory and field tests is an indispensable engineering method in reducing earthquake damage.

2. Introduction to the Field of Study and Examination of the Methods of Study

2.1. Area of Study

Erzurum province, due to its higher altitudes compared to the interior and western regions of Turkey, constitutes one of the country's important elevation zones. The deep valleys formed by the Çoruh River and its tributaries, and the plains connected to these valleys, create the province's natural transportation corridors with the Eastern Black Sea Region. In the west, access is provided from the Tercan Mountains to the Keşiş Mountains, and from there, via Kop Mountain and Kop Pass, to the Kelkit Valley. In the southwest, the Sansa Gorge opens to the Erzincan Plain; the southern part of this area continues with the Munzur Mountains range via the Mercan Mountains. The Palandöken Mountains, extending in the south, enable access to the Şakşak and Bingöl Mountains and the Murat Basin [5].

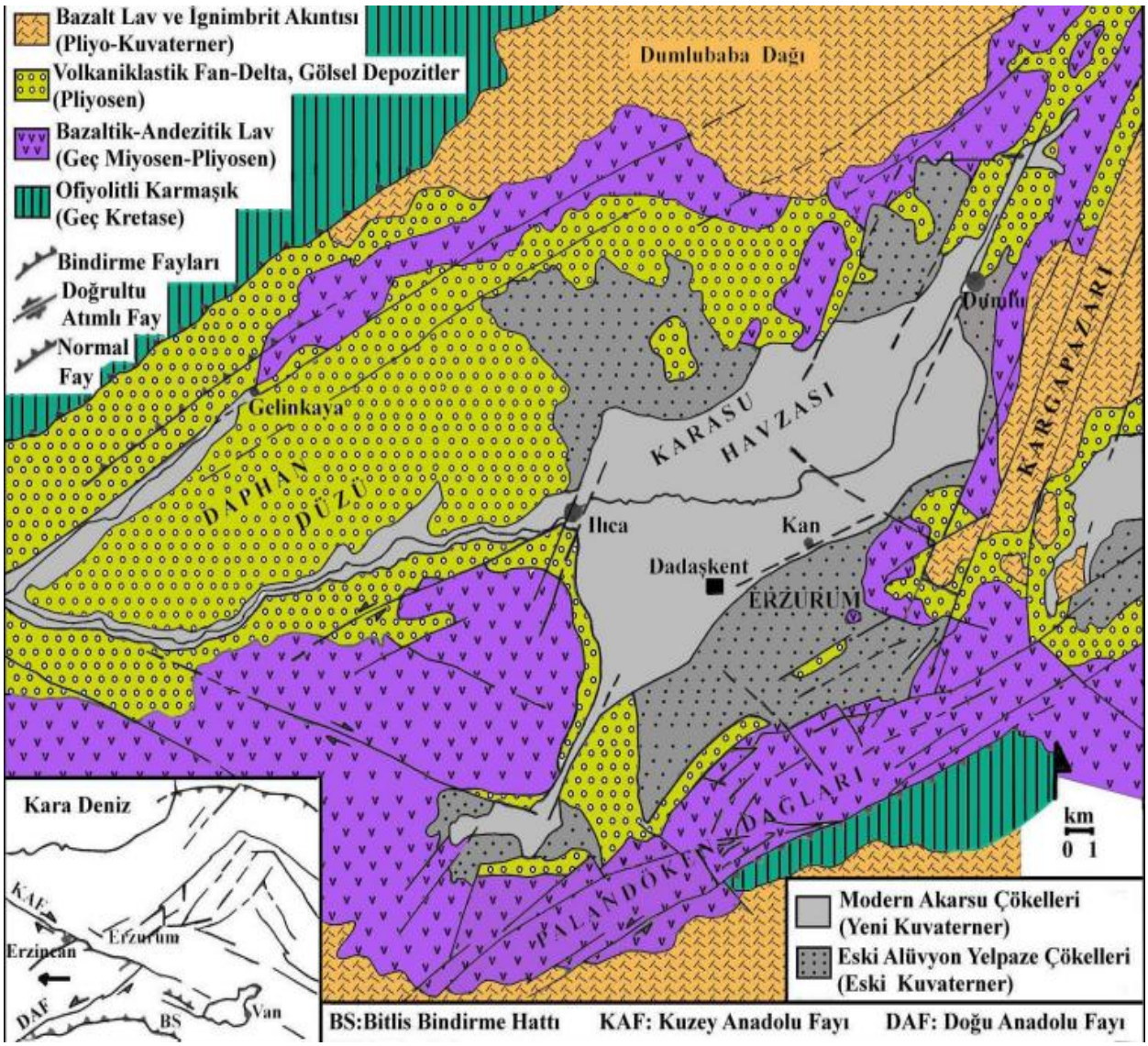

Figure 1 Geological map of Erzurum and its surroundings, covering the study area. (Scale: 1/100.000 MTA-2003)

Although the districts of İspir, Narman, Oltu, Olur, Pazaryolu, Tortum, and Uzundere, located north of Erzurum, are geographically within the borders of the Eastern Black Sea Region, these areas constitute approximately 30% of the total area of the province. The remaining 70% is located within the Eastern Anatolia Region. The average elevation of the province is 1,859 meters [6].

Located in the northeast of the Eastern Anatolia Region, Erzurum is the largest city in the region and the fourth largest in Turkey, with an area of 25,066 km². Accounting for approximately 3.2% of the country's total area, Erzurum is situated between 40°15'–42°35' east longitudes and 39°10'–40°57' north latitudes [5].

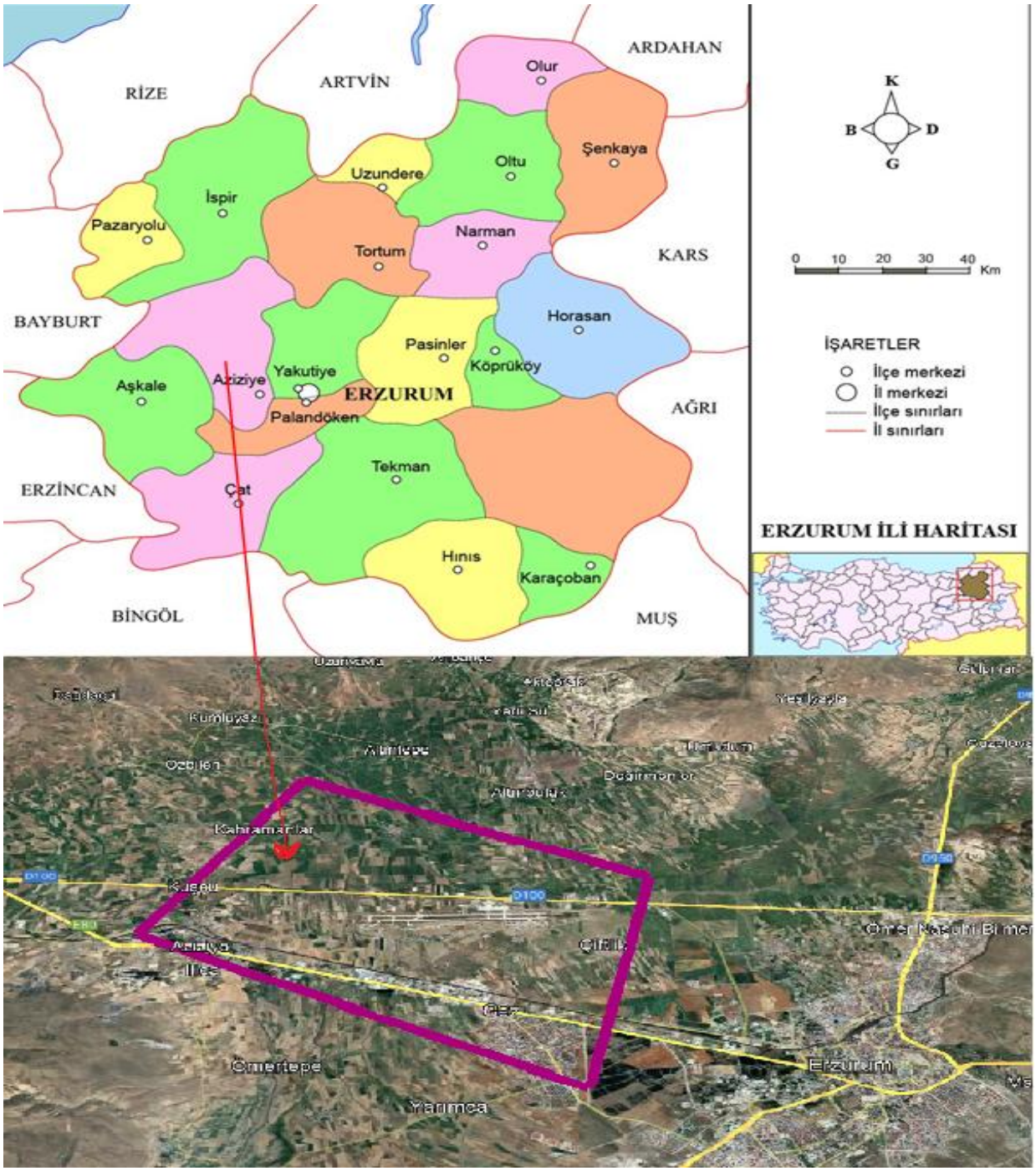

Figure 2 Location map of the study area

2.2. Geology of the Study Area and Its Immediate Surroundings

The city center of Erzurum is largely situated on alluvial soils. Alluvial structures, due to their weak engineering properties, tend to transmit earthquake vibrations more effectively and amplify the effects of shaking. Therefore, structures may experience a higher level of damage compared to soils that better dampen seismic waves. Furthermore, such soils can be susceptible to various geotechnical problems during an earthquake, including liquefaction, settlement, lateral spreading, and landslides [6].

In the immediate vicinity of the study area, units consisting of alternating gneiss, amphibolite, schist, and marble are observed. These rocks surface as a tectonic window beneath complex assemblages containing ophiolites. The

ophiolitic complex structure consists of diabase, gabbro, serpentinite, and peridotite rocks. Lithological units dating between the Maastrichtian and Pliocene exhibit transgressive-regressive sequences and unconformably overlie older masses. The study area shows Middle-Upper Miocene characteristics. While thin andesitic-basaltic interbeds are found within the Oligocene sedimentary sequence, volcanic products of dacite-andesite composition developed first, followed by andesitic basalt, basaltic pyroclastics, and lava flows during the Miocene-Pliocene time interval [6].

The research area contains fractured and fissured siltstone units, mostly light gray in color, with occasional greenish clayey silt, at depths of 7.50–19.50 m. Between 3.00–7.50 m, clayey silt is observed in shades ranging from light brown to cream, with some sections showing dark brown. Weathered siltstone is also present at these levels. In the upper section, between 0.50–3.00 m, there are poorly sorted gray gravel-sand mixtures mixed with clayey silt units.

2.3. Seismicity of the Study Area and Its Immediate Surroundings

According to the Turkish Earthquake Hazard Map, the study area is located in a second-degree earthquake zone (Figure 3), and there are active fault lines in the region and its immediate surroundings [7]. These faults are the Palandöken, Aşkale, and Kandilli fault zones. The Palandöken Fault Zone, located in the south of the study area, extends along Palandöken Mountain and exhibits left-lateral strike-slip characteristics. This zone, consisting of numerous parallel faults, passes through the Börekli and Tuzcu neighborhoods and progresses towards the city center, then continues in a northeasterly direction [7].

The Kandilli Fault is a multi-segmented right-lateral strike-slip fault approximately 27 km long. It starts around Küçükgeçit neighborhood in Aşkale district and ends west of Özbek neighborhood. [6].

Two earthquakes, with instrumental magnitudes of 5.1 and 5.3 respectively, occurred on this fault on March 25 and 28, 2004 [8]. These earthquakes resulted in 10 deaths and 56 injuries.

The Aşkale Fault exhibits a left-lateral strike-slip structure and is a fault zone approximately 6 km wide and 140 km long. This fault extends from the southwest of Tortum to the Aşkale district [9].

Table 1 Major Earthquakes in Erzurum (http://www.koeri.boun.edu.tr/) [10]

History	Local Time	Place	Violence	Mag (Ms)	Loss Of Life	Damaged Building
13.9.1924	16:34	Horasan (Erzurum)	Ix	6.8	60	380
3.1.1952	08:03	Hasankale (Erzurum)	Viii	5.8	41	701
30.10.1983	07:12	Erzurum – Kars	Viii	6.8	1155	3241
18.9.1984	15:26	Balkaya (Erzurum)	Viii	6.4	3	570
25.3.2004	21:30	Kandilli- Aşkale(Erzurum)	Vii	5.6	9	1280

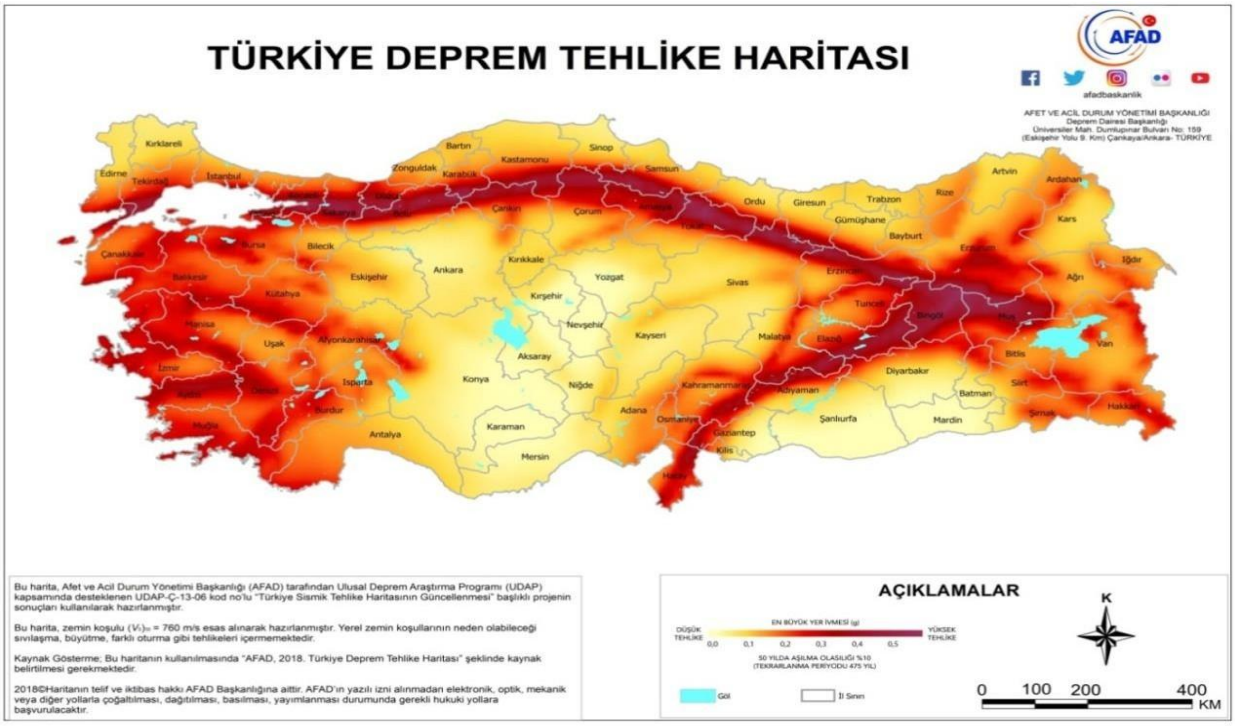

Figure 3 Earthquake Hazard Map of Türkiye. https://www.afad.gov.tr/turkiye- deprem-tehlike-haritasi [11]

3. Field and Laboratory Studies

The drilling operations conducted in the field were carried out by Eras Engineering under the supervision of a Geological Engineer, using a drilling machine with a TSM-750 model rotary drilling system mounted on a truck and a team of two people [5]. A total of 7 boreholes and 7 exploration pits were drilled in the area. The exploration pits, drilled vertically near the surface, are constructed to observe the soil without disturbing its natural structure, to collect samples, to conduct in-situ tests, and to determine general soil properties. A total of 7 exploration pits, each reaching a depth of approximately 4 meters, were drilled in the study area.

In liquefaction analyses, it is generally accepted that the effective depth should be examined up to at least 20 m. However, the fact that the geotechnical boreholes used in this study reached a maximum depth of 15 m and the exploration pits reached a depth of 4 m constitutes a limitation. Nevertheless, considering that the effects of liquefaction on the surface decrease as the depth increases, all evaluations were carried out based on the geotechnical data obtained within the scope of the available borehole depths and exploration pits.

In this study, Standard Penetration Test (SPT) was applied to the boreholes drilled in the field. In addition, consistency limits, natural and saturated unit weight, sieve analysis, and hydrometer tests were carried out on samples taken from the research pits in the laboratory. Using the data obtained from field and laboratory tests, the liquefaction potential of the soils was evaluated in accordance with the methods of Iwasaki et al. [12] and Sönmez and Gökçeoğlu [2].

As a result of the evaluation of the data obtained within the scope of the study; it was determined that the average SPT-N value was 25.36, the natural unit weight was 16.20 kN/m³, and the saturated unit weight was 17.45 kN/m³. In addition, it was determined that the plasticity index was 13.8%, the clay content was 11.12%, and the fine grain ratio was 32.34%. In the liquefaction analyses performed using these soil properties, the liquefaction potential at different points of the study area was calculated according to the methods of Iwasaki et al. [12] and Sönmez and Gökçeoğlu [2].

According to the results obtained from field and laboratory studies, it was determined that the probability of liquefaction occurring is high at borehole locations SK-1, SK-4, and SK-7 in the study area, while the liquefaction potential is very low at points SK-2, SK-3, SK-5, and SK-6.

4. Assessment of Liquefaction Potential According to Different Earthquake Scenarios

In assessing soil liquefaction, not only is the safety factor calculated for a specific depth level, but also holistic approaches that consider the entire soil profile from the surface are used. In this context, the Liquefaction Potential Index (LPI) concept, which is based on the soil layer from the surface to a depth of 20 m, was first developed by Iwasaki et al. [12]. Sönmez et al. [2] made a classification of liquefaction potential while preserving the basic principle of LPI.

Sönmez and Gökçeoğlu [2] in their probability approach based on the safety factor value against liquefaction, considered the relationship presented by Juang et al. (2005) and the liquefaction probability classification proposed by Chen & Juang (2000), and developed the Liquefaction Severity Index (LSI) formula and its related classification, based on the general approach of Iwasaki et al. [12].

In this study, using the existing data in the study area, the classifications related to the LPI method proposed by Iwasaki et al. [10] and the LSI method developed by Sönmez & Gökçeoğlu [11] were taken into consideration, and liquefaction maps revealing the liquefaction potential of the region for different earthquake scenarios were produced.

The parameters for the different earthquake scenarios evaluated for the study area are presented collectively in Table 1.

Table 2 Major Earthquakes in Erzurum (http://www.koeri.boun.edu.tr/)

Scenarios	Earthquake magnitude	Maximum acceleration value, PGA (g)	Explanation
1	7,8	0.8	The 1939 Erzincan earthquake was recorded by taking into account the records of Erzurum Station.
2	6,8	0.5	1983 Earthquake Scenario for the Horasan-Narman Region Based on the New Earthquake Regulations
3	6,4	0.4	The 2003 Bingöl earthquake was recorded by taking into account the Erzurum Station records.

In the study reported by Iwasaki (1982), calculations were made using the following equations, taking into account the thickness of liquefiable layers and safety factors.

$$LPI = \int_0^{20} F(z) * W(z) * dz \tag{1}$$

$$\begin{aligned} F(z) &= 1 - FS\ (for\ FS < 1.0) \\ F(z) &= 0\ (for\ FS \geq 1.0) \\ W(z) &= 10 - 0{,}5z\ (for\ z \leq 20\ m) \\ W(z) &= 0\ (for\ z > 20\ m) \end{aligned} \tag{2}$$

The liquefaction potential index, expressed as LPI, is calculated using Equation (1) based on values varying with depth up to 20 m from the ground surface, taking into account changes in the safety factor (F) and weighting function (W). According to LSI, the total liquefaction potential of liquefiable layers up to 20 m is determined by depth depending on the liquefaction probability ratio (PL) [13].

Detailed field and laboratory data were used for the liquefaction analysis of the settlement area. During the analyses, various earthquake scenarios determined based on the current Turkish Earthquake Regulations [3], which came into force in 2019, were taken into consideration. Within the scope of these scenarios, both the Liquefaction Potential Index (LPI) and the Liquefaction Severity Index (LSI) values were calculated for all geotechnical borehole points.

$$L_s = \int_0^{20} P_l(z) * W(z) * dz \tag{3}$$

$$P_L(z) = \frac{1}{1 + \left(\frac{F_L}{0{,}96}\right)^{4{,}5}}\ (for\ F_L \leq 1{,}411) \tag{4}$$

$$P_L(z) = 0\ (for\ F_L > 1{,}411) \tag{5}$$

In the earthquake scenario decision-making phase, the maximum horizontal ground acceleration (PGA) values were first examined for a 50% probability of an earthquake, corresponding to the probability of an earthquake occurring, using the online application of the new regulation. This evaluation was carried out using horizontal acceleration distribution maps for values of 475, 72, and 43 gal in the region covering Erzurum and its surroundings (Figure 4). The analyses reveal that the PGA value in the study area and its immediate vicinity can reach levels of 0.5 g according to the current regulation. However, in Considering the magnitudes of 7.8 and 6.8 measured in the Erzincan and Horasan-Narman earthquakes, and the maximum horizontal ground acceleration of 0.8 g recorded, a total of three different earthquake scenarios were determined (Table 1).

For each of the three selected earthquake scenarios, LPI and LSI values were calculated based on geotechnical drilling data. Subsequently, liquefaction maps were generated in a Geographic Information Systems (GIS) environment using the Inverse Distance Weighting (IDW) interpolation method. In preparing these maps, the class boundary values proposed by Iwasaki [12] for LPI and by Sönmez and Gökçeoğlu [2] for LSI were used as references (Figure 5).

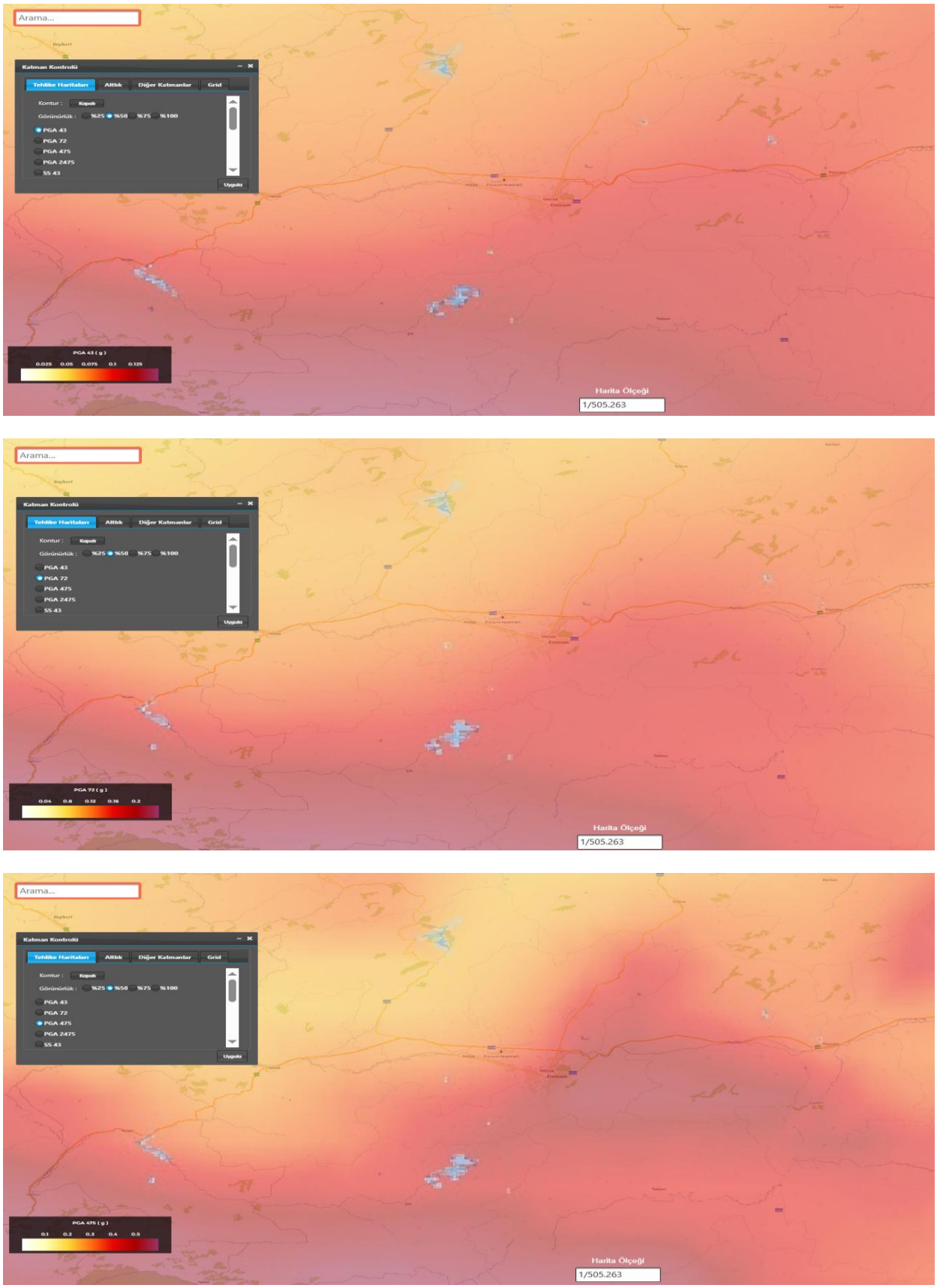

Figure 4 Distribution of maximum ground acceleration values for different exceedance probability in interactive web application (https://tdth.afad.gov.tr/) [14]

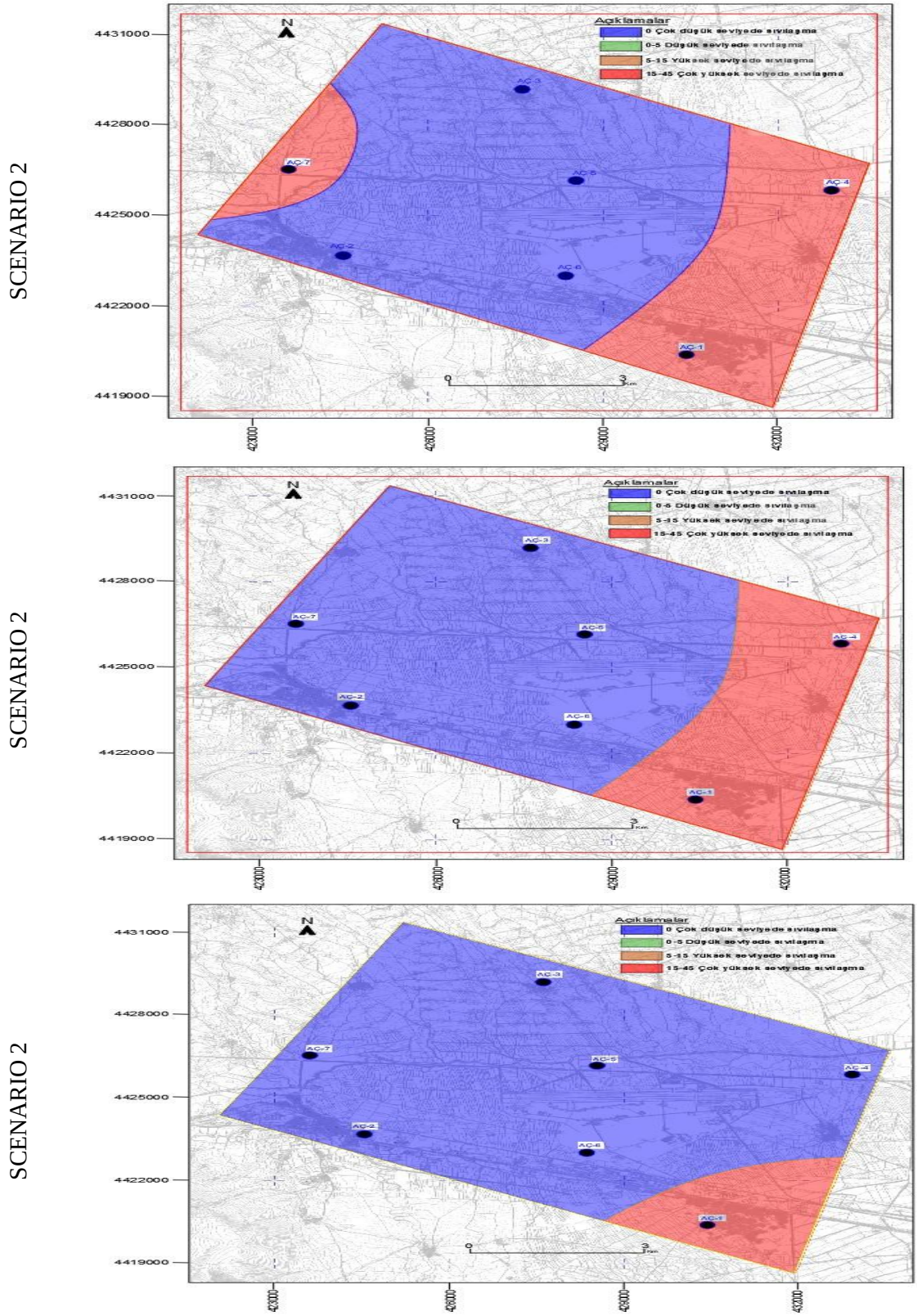

Figure 5 Common liquefaction map produced using LPI (Iwasaki et al., 1982) and LSI (Sonmez and Gokceoglu, 2005) methods for different earthquake scenarios

In conclusion, it can be said that in the event of possible earthquake scenarios in the eastern and western parts of the area where liquefaction mapping was conducted, the surface effects of liquefaction events may be observed more intensely. As presented in previous sections, the geotechnical borehole depths in the field generally reach a maximum of 15 m. However, LPI and LSI calculations require the evaluation of the profile extending up to a depth of 20 m. Therefore, when evaluations are made up to a depth of 20 m, it is possible to obtain relatively higher LPI and LSI

values depending on the soil properties at greater depths, when compared with the liquefaction maps prepared in this study for preliminary evaluation purposes.

5. Results

The findings of this study indicate that areas with concentrated new construction in Erzurum province, particularly in the Aziziye district, have a high liquefaction potential. The Aziziye district is located on the Erzurum Plateau, which consists of loose alluvial soils. The concentration of damage in certain areas during past earthquakes strengthens the possibility that these zones formed in places with high groundwater levels. Therefore, local soil conditions played a decisive role in the distribution of damage in Erzurum.

The study identified a very high liquefaction potential, particularly in the eastern and western parts of the study area. While the potential decreases in the north and south, the LPI (Liquefaction Potential Index) and LSI (Liquefaction Severity Index) methods still indicate a low-to-moderate risk in some parts of these regions. The study identified a very high liquefaction potential, particularly in the eastern and western parts of the study area. While the potential decreases in the north and south, the LPI (Liquefaction Potential Index) and LSI (Liquefaction Severity Index) methods still indicate a low-to-moderate risk in some parts of these regions.

For Erzurum province, which harbors significant seismic resources such as the North Anatolian Fault Zone, different earthquake scenarios must be considered both at the parcel level and during the planning phase. For structures to be built in areas with a high risk of liquefaction, geotechnical parameters must be determined in detail, and liquefaction analyses must be carried out realistically and thoroughly. As a result of these analyses, the application of appropriate soil improvement methods in high-potential areas is mandatory. In other words, when examining soil-structure interaction, liquefaction and related surface deformations (settlement, lateral spreading) should not be ignored.

One finding of the study is that the maps produced according to the LSI method show very little difference despite the moment magnitude and acceleration values in different earthquake scenarios. In this context, the results obtained from different methods evaluating liquefaction potential should be examined with detailed analyses in terms of the magnitude of surface deformations (settlement, lateral spreading) that may occur. To be on the safe side and to consider the possibility of ground amplification, local-scale liquefaction analyses and models should be performed based on horizontal ground acceleration values.

References

[1] Babadan, K. (2023). Investigation of the liquefaction potential of Erzurum Ilıca neighborhood using different methods (Publication No. 847718) [Master's thesis, Atatürk University]. National Thesis Center of Türkiye (YÖK).

[2] Sonmez, H., Gokceoglu, C., 2005. A liquefaction severity index suggested for engineering practice. Environmental Geology, Volume 48, Issue 1, pp 81–91.

[3] Republic of Türkiye, Disaster and Emergency Management Authority (AFAD). (2018). Turkish Building Earthquake Code. Official Gazette No. 30364 (Repeated), March 18, 2018. https://www.resmigazete.gov.tr/eskiler/2018/03/20180318M1-2.htm

[4] Alpaslan, N. (2013). Soil liquefaction and its mechanisms. Batman University Journal of Life Sciences, 3(2).

[5] Erzurum Metropolitan Municipality. (2011). Geological–geotechnical survey report prepared as a basis for the 1/5000-scale master zoning plan. Prepared by: Anakent Planlama Ltd. Şti., Erzurum.

[6] General Directorate of Mineral Research and Exploration (MTA). (1988). 1:100,000 scale geological maps of Turkey series: Erzurum F32 sheet. MTA.

[7] Şaroğlu, F., Emre, Ö., & Kuşçu, İ. (1992). Active fault map of Turkey. General Directorate of Mineral Research and Exploration (MTA).

[8] Tarhan, N., (2004). Aşkale (Erzurum) Depremi Üzerine , Jeoloji Mühendisleri Odası, 67-70

[9] Özer, C. (2018). Investigation of local site effects in Erzurum and its surroundings using SSR and HVSR methods.

[10] Major Earthquakes That Occurred in Erzurum http://www.koeri.boun.edu.tr/

[11] Turkish Building Earthquake Regulations, 2018.

[12] Iwasaki, T., Arakawa, T., Tokida, K., 1982. Simplified procedures for assessing soil liquefaction during earthquakes. Proceedings of the Conference on Soil Dynamics and Earthquake Engineering, Southampton, UK, pp. 925-939

[13] Akın, M. (2019). Evaluation of liquefaction potential of soils in Düzce city center. Journal of Geological Engineering, 43(1), 39–56.

[14] Disaster and Emergency Management Authority (AFAD). (2018). Turkey earthquake hazard map. https://www.afad.gov.tr/turkiye-deprem-tehlike-haritasi

Chair's Closing Speech

My dear professors, colleagues and dear students,

We have successfully completed the 2025 event of the International Congress on Trends and Advances in Global Research and Applications (TAGRA). It was a great honor and pleasure for me to be here with you and to be a part of this inspiring scientific journey.

Within the framework of the theme of our congress, "Discover the New Faces of Science", we discussed the latest developments in various fields of science and engineering for the last three days, exchanged ideas and prepared the ground for very valuable collaborations.

During the congress, while we followed the visionary presentations, we understood once again how important interdisciplinary collaboration is. These face-to-face and online presentations once again revealed that scientists work with a passion that knows no bounds and are open to innovations.

From energy systems to materials science, from artificial intelligence to environmental science, the topics covered not only meet today's needs but also offer a glimmer of hope for the future. In particular, I believe that the discussions held throughout our congress provided new perspectives and enabled concrete steps to be taken towards interdisciplinary collaboration.

I would like to thank our valuable speakers for their presentations and sharings that provided us with new perspectives. And of course, I would like to express my gratitude to you, the participants, who made this congress meaningful. Every presentation you made here, every discussion you contributed to, and every idea you put forward was an important step towards the advancement of science.

The environment we created together has proven once again that science knows no boundaries and that interdisciplinary collaboration is powerful. I hope TAGRA 2025 brings new connections, collaborations, and inspiring ideas for you.

As I conclude my closing speech, I hope to meet again at the TAGRA Congress next year. I wish you all a healthy, happy, and productive year. Thank you.

Author Index

A
Abayomi O Adelaja 113
Abbas Jahanbani 148
Abbas Razmi 101, 126
Abdollah Esmaeili 114
Abolfazl Taghavi 189
Adam Zafry 86
Afiq Irham 85
Afonso Cesar Rodrigues Nogueira 114
Afranur Timur 130
Ahmad Ali 71
Ahmed N Nusari 206
Ahmet Hacımüftüoğlu 116
Aichurok Mazhitova 110
Akylai Chynalieva 110
Aleyna Karaosman 134
Ali Khodayari 78, 80
Ali Sharifi 88
Ali Taghizadehghalehjoughi 245, 250
Annissa Delfira 119
Artka Zildzia Riawan 119
Arzu Kavaz Yüksel 164
Asan Omuraliev 72
Aslı Yılmaz 120, 121
Aslıhan Esringü 297, 301
Asylbek Kulmyrzaev 90
Aydan Akkök 124
Aynur Babagil 306
Aysan Mansournia 97
Ayşe Cebeci 108
Ayşenur Şuvak 167
Aysu Kirali 306
Azizeh Shadidizaji 116
B
Babasola Aiyeku 113
Bahman Rahmatinejad 174, 182, 189
Bahram FathiAchachlouei 74, 95
Behina Asadoghli 310
Behnaz Ashtari 104, 105, 132
Bermet Kydyralieva 83
Bermet Sultanova 110
Betül Çicek 323
Beytullah İsmet Toprak 209
Bilal Usanmaz 274
Binita Mandal 71
Bishnu Pada Bose 111
Bülent Çetin 306
Büşra Aydın 235
C
Cem Yamalı 239
Charles Olubunmi Ogunkoa 118
D
Dalmo S Amorim Jr 137
Damilola Omoboyowa 113
E
Ebru Bozkurt 239
Ebru Kılıç 129
Edmilson S Moutinho 137
Efe Çetin Yılmaz 152, 156, 160
Ekrem Kalkan 391
Elif Kılıç Delice 326
Eliyana Ruslan 84
Ella Abylaeva 72
Emin Argun Oral 206
Emine Çoruh 131
Emrah Turan 279
Emre Koşar 102
Ercan Doğan 209
Esen Taşğın 306, 310
Eslam Pourbasheer 75
Esra Çelik 256
Ezo Palavan 121
F
Fadime Şimşek 202
Faiz Arith 70, 98, 117, 122, 133
Falek Bamme 71
Farideh Ghalamfarsa 116
Farshad Lotfollahzadeh 96
FarzinAzimpour Shishevan 174
Fatemeh Barati 104, 105, 132
Fatemeh Ghanbary 92
Fatemeh Ghannadiasl 74
Fatma Bayrakçeken 167
Fatma Betül Özgeriş 129
Fatma Melike Yeşilyurt 376
Fatma Yavuz Takım 124
Fauziyah Salehuddin 70, 98, 133
Ferdane Danışman Kalındemirtaş 323
Fevzi Erdoğan 81, 82
Feyza Gündoğdu 297
G
Gulnara A Sharshenalieva 346
H
Habibollah Eskandari 78, 80

Hadi Ghasemi Zavaragh 174, 182, 189
Haidar Abd Ali Abdulsada 78
Hairat Banaru 228
Halil Barış Gezmiş 326
Halise İnci Gül 239
Hamed Niroumand 65
Hamit Akbulut 128
Hamit Çakıcı 220, 395
Hatice Yüncü 293
Hayrunnisa Nadaroğlu 293, 306, 342, 391
Hilal Kübra Sağlam 356
Hirdan K M Costa 137
Hülya Öztürk Doğan 164
Hümeyra Ulaş 333
Hüseyin Güllüce 284, 316
Hüseyin Gündüz 128
I
I Made Dwi Mertha Adnyana 119
İbrahim Elebeyd 152
İbrahim İshaq M Alkhattab 365
İbrahim Yücel Özbek 206
Iduseri O Murphy 99, 100
İlhan Volkan Öner 88
İsmail Solmaz 209
Ismayadi Ismail 66, 123
J
Jalal Pourahmad 92
Jamila Smanalieva 107
Jatau BS 228
Juraina Md Yusof 91, 123
K
Kaan Can 381
Kadir Bilen 88
Kagan Tolga Cinisli 116
Koray Babadan 220
M
Magdi E A Zaki 113
Mahmut Sinan Taşpınar 116
Mahmut Yeşilyurt 112
Mansur Mustafaoglu 88, 89
Maruf A Bello 99, 100
Maryam Fathinejad 170
Maryam Khosravi 104, 105, 132
Maryam Nouri Majd 75
Md Habibur Rahman 67
Mehdi Jafarian 101
Mehmet Yılmaz 120, 121
Mehrdad Lakestani 81
Melda Şişecioğlu 130
Melike Alemdağ 108
Meral Oltulu 279
MirJalal Hosseini 92
Mohamad Javad Hadi 104, 105
Mohammad Reza Zamanloo 79
Mohd Ali Mat Nong 91, 123
Mohd Asyadi Azam 117
Mohd Zobir Hussein 125
Mohit Agrawal 113
Mucize Beldek Tomuk 127
Muhammed Taha Topcu 88
Muhammet Harun Osta 216
Muhammet Kaan Yeşilyurt 160
Muhammet Kaan Yeşilyurt 88, 102
Murat Özdal 350, 353
N
Nabilah Ahmad Jalaluddin 133
Nabilah Ahmad Jaluluddin 70
Nazgul Imanberdieva 87
Nazreen Waeleh 93
Neslihan Çelebi 164
Ni Luh Gede Sudaryati 119
Niken Irfa Nastiti 119
Nikhat Shaikh 71
Nurbek Aldayarov 83, 87, 94
Nurgul Ermekova 94
Nurjamal Omurzakova 346
Nursu Koyunoğullarından 131
Nurul Farina Mohd Nazli 115
O
Ohwoharhohwo Etaoghene 100
Ömer Çoban 93
Omid Khanmohammadi 189
Omsri Vinasha Aliyaselvam 117
Onifade Yemi Sikiru 99
Onur Temiz 395
Özlem Ütme 245
P
Parisa Nami 101
Parvaneh Naserzadeh 92, 103, 132
Pawan Sharma 71
Peruzet Aydın 274
Peyil Esengul Kyzy 72
Pınar Anlar Daldal 164
Prathap Singh S 69
R
Rabah Sabah Khamees 80
Rabiye Kılıç 206
Rafet Çağrı Öztürk 108, 109
Raja Ahmad Arifikri Raja Ismail 93
Ramin Jannesar 116
Remzi Şahin 365
Rezvan Shaddel 95
Rosnah Nawang 125
S
Sadiq Abdulmaliqq 228
Saleh Alhaji Saleh 99, 100
Saliha Erentürk 235
Sana Ghaffarzadeh 92
Sedaghat Shahmorad 82
Selçuk Sincar 316

Senanur Seher Ağbaba 301
Şerafettin Alpay..... 127
Sevda Sarıtaş 356
Shahdad Mousavi 101
Shahriyar Karimdoust..... 101, 391
Shayesteh Hassanloo 74
Sıdıka Genç 245, 250
Simin Tolouei 95
Şirin Firidin 108
Siti Amaniah Mohd Chachuli .. 77, 84, 85, 86, 93
Siti Asma Che Aziz 84, 85, 86
Siti Halma Johari 84, 85, 86
Somayeh Fekri..... 148, 170
Suhaidi Shafie 123
Suzila Sabil..... 91
T
Tabassum Khan 71
Taha Yasin Bayram 120
Taiwo Kamorudeen Alasi..... 118
Tanko IY 228
Temitope C Aribigbola..... 113
Thanies Murugan..... 122
Torkan Haghi..... 350, 353
Tuba Çakıcı Can..... 360
Tuba Irmak.....333
Turgut Seçkin Gül.....239
Tursunbek kyzy Almagul.....346
W
Wasiu Osisanya.....99, 100
Y
Yagoub Mansoori.....148, 170
Yahya Terzi.....108, 109
Yalçın Kemal Bayhan 391
Yasemin Gültepe.....134
Yaser Shokri.....189
Yavar Nour Mohammadi Ziba 101
Yousef Fazli 116
Yousef Vasigh.....391
Yudesh Kumar Kumara Raja 77
Yunus Emre Aydın.....250
Yusnita Yusuf 123
Z
Zahra Frizki Asty 119
Zainab Yunusa 68
Zekeriya Kutlu 209
Zhazgul Kelgenbaeva.....106
Zhyldyzai Ozbekova 90
Zulfanizam Abdul Wahab 98



Publishing